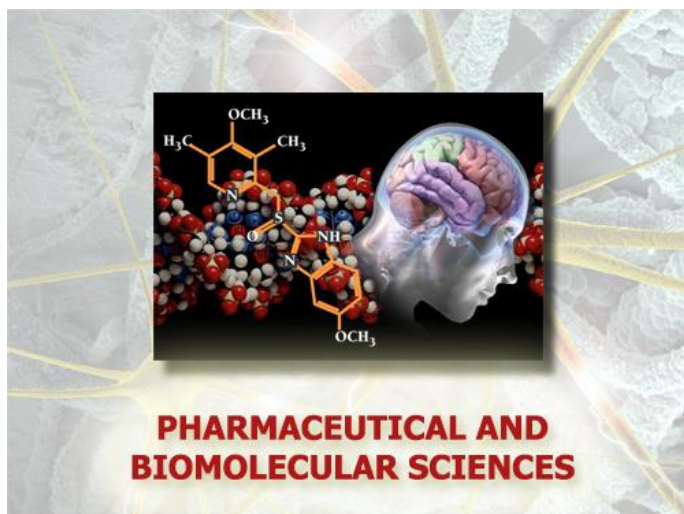**Università degli Studi di Torino**

Scuola di Dottorato in

Scienze della Natura e Tecnologie Innovative

Dottorato in Scienze Farmaceutiche e Biomolecolari

CICLO: XXXIV

NEW TECHNOLOGIES FOR THE PREPARATION AND APPLICATION OF NANOCATALYSTS FOR SUSTAINABLE SYNTHETIC PROCESSES

Candidato: Federica Calsolaro   **Supervisor: Prof.ssa Katia Martina**

Università degli Studi di Torino

Dottorato in

Scienze Farmaceutiche e Biomolecolari

Tesi svolta presso il Dipartimento di Scienza e Tecnologia del Farmaco

CICLO: XXXIV

TITOLO DELLA TESI:

NEW TECHNOLOGIES FOR THE PREPARATION AND APPLICATION OF NANOCATALYSTS FOR SUSTAINABLE SYNTHETIC PROCESSES

TESI PRESENTATA DA: Federica CALSOLARO

SUPERVISOR: Prof.ssa. Katia MARTINA

COORDINATORE DEL DOTTORATO: Prof. Roberta CAVALLI

ANNO ACCADEMICO: 2018-2021

SETTORE SCIENTIFICO-DISCIPLINARE DI AFFERENZA: Chimica Organica (06/C1)

Alla spensieratezza, alla libertà

Abstract

This PhD project aimed at developing new heterogeneous systems, investigating unconventional technologies, such as ultrasound (US) and microwave (MW) irradiation for materials preparation and application. Different supporting materials were chosen to prepare a series of heterogeneous systems, that were investigated for their potential as well-defined supports, catalysts or nanoparticles. The importance of the structure design was investigated with a view to gaining insight into their structure-property relationships. Also flow chemistry, as non-classical synthetic method, was exploited to study its efficacy towards sustainable synthetic processes.

Organic-inorganic hybrid catalysts, composed of silica-cyclodextrin-Cu(II) derivatives, were synthesized to study the influence of flexible amino spacers, interposed between the ligands and the inorganic surface, on the catalytic activity and efficiency. In order to obtain a highly reproducible and efficient synthetic protocol, a deep investigation into the influence of US and MW irradiation on the reaction rate of silica derivatisation, to obtain cyclodextrin-grafted silica, was performed. Their catalytic activity was tested on click azido-alkyne cycloadditions and detailed information on the surface functionalization, as well as on the oxidation state, local coordination environment and aggregation of the encapsulated/anchored Cu(II) species was obtained by complementary characterization techniques.

A deep investigation into carbon-based materials preparation and derivatization was carried out. Graphene and nanodiamonds were finely and covalently functionalized by 1,3-dipolar cycloadditions. To extend the scope of this type of functionalization, a comparative study of azomethine ylides, nitrile oxides and nitrones cycloaddition was performed. The influence of dipolarophile alkyl or aryl substituents on carbon-material derivatization was investigated. The introduction of various substituents gave us the possibility to study their influence on derivatization degree and on material structural modification. The beneficial effect of MW irradiation on reaction rate and derivatization degree was demonstrated. Aware of these results, carboxylate-functionalized graphene composites were developed as Ru(II) supporting systems.

A further study on carbon-based materials focused on the development of cobalt supported on activated carbon derived from pinecones. Variation of the preparation technique (conventional, US, MW and combined MU-US irradiation), introduction of *N*-doping and polyphenol as stabilizers and ligands of cobalt, provided the achievement of differently active electrocatalytic systems for the oxygen evolution reaction. The influence of the synthetic procedure demonstrated that both MW and US techniques provided a greater number of active sites than conventional heating procedures, with US being the most effective one; the importance of doping with nitrogen, as well as the good cobalt stabilization through polyphenol coating were proven by the electrocatalytic tests and confirmed by a deep structural characterization.

The sonochemical technique was also exploited as innovative method in offering a better control of particle size distribution, morphology and structure of nanoparticles. Thus, multifunctional amino-citrate-cyclodextrin coated iron oxide magnetic nanoparticles were prepared as promising nanosystems for magnetic resonance imaging. Careful studies in synthesizing coated nanoparticles were conducted and a fine choice of coating agents was evaluated to enhance stability, hydrophilicity and biocompatibility.

The last study focused on the use of flow reactors to study their efficacy on continuous synthetic processes. The research began from the optimization of two liquid-phase multicomponent reactions, for the synthesis of Praziquantel and Camptothecin analogues. Reduced reaction time, enhanced chemical selectivity and improved yields were observed due to the efficient mixing and the accurate control of the reaction parameters. Then, the successful reduction reaction of an aromatic nitro compound, as Itraconazole intermediate, was studied using continuous flow solid supported catalysis. Celite-supported copper nanoparticles were prepared and used for the controlled and selective transfer hydrogenation of the nitro derivative, using glycerol as hydrogen source. The results were compared to continuous flow reduction on packed activated-carbon-supported palladium.

Overall, this study provided insight into the preparation and application of heterogeneous systems. The use of non-conventional technologies for aiming at sustainable synthetic processes shows excellent promises, and it remains open for exploration.

Publications and conferences

Publications:

Martina, K.; Calsolaro, F.; Zuliani, A.; Berlier, G.; Chávez-Rivas, F.; Moran, M. J.; Luque, R.; Cravotto, G., Sonochemically-promoted preparation of silica-anchored cyclodextrin derivatives for efficient copper catalysis. *Molecules* **2019**, *24* (13).

Calsolaro, F.; Martina, K.; Borfecchia, E.; Chávez-Rivas, F.; Cravotto, G.; Berlier, G., β-Cyclodextrin-silica hybrid: a spatially controllable anchoring strategy for Cu(II)/Cu(I) complex immobilization. *Catalysts* **2020,** *10* (10).

Zuliani, A.; Cano, M.; Calsolaro, F.; Puente Santiago, A. R.; Giner-Casares, J. J.; Rodríguez-Castellón, E.; Berlier, G.; Cravotto, G.; Martina, K.; Luque, R., Improving the electrocatalytic performance of sustainable Co/carbon materials for the oxygen evolution reaction by ultrasound and microwave assisted synthesis. *Sustainable Energy & Fuels* **2021,** *5* (3), 720-731.

Martina, K.; Caporaso, M.; Calsolaro, F.; Sacco, M.; Orio, L.; Barge, A.; Tagliapietra, S.; Cravotto, G.; Picollo, F.; Mino, L.; Turci F., Azomethine ylide, nitrile oxide and nitrone cycloaddition on surface modification of carbon-based nanomaterial: a study to obtain high degree of functionalization with different dipols – *manuscript in preparation.*

Calsolaro, F.; Garello, F.; Cavallari, E.; Valsania, M. C.; Magnacca, G.; Cravotto, G.; Terreno, E.; Martina, K., Multifunctional amino-citrate-β-cyclodextrin coated iron oxide nanoparticles: an efficient nanosystem for magnetic resonance imaging – *manuscript in preparation.*

Calsolaro, F; Magnano, A.; Lemcoff, G.; Baldino, S.; Cravotto, G.; Martina, K., Advances in heterogeneous catalyst design and applications for metathesis reactions – *manuscript in preparation.*

Conference and workshop participation:

- VIII National Workshop, Green Chemistry, 29th September **2020**.

Poster presentation: Role of non-innocent ligands in β-cyclodextrin-silica hybrid systems.

- Catalysis Talks, Euchems, 22nd July **2020**.

Oral presentation: Efficient study of amino bearing spacers in β-cyclodextrin-silica systems for Cu(II)/Cu(I) stabilization.

- New Trends in Organic Synthesis 2019, XXXIV Ed., Milano, 25th November **2019**.

- VII National Workshop, Green Chemistry, Padova, 5th July **2019**.

Poster presentation: Combined microwave and ultrasound irradiation for efficient production and grafting of nanomaterials (best poster award).

Abbreviations

1,3-DCA	1,3-Dipolar Cycloadditions
AC	Activated Carbon
AEM	Adsorbate Evolution Mechanism
AEPS	3-(2-aminoethylamino)propyltrimethoxysilane
β-CD	Beta-cyclodextrin
CA	Citric acid
CFD	Chemical Functionalization Degree
CMDx	Carboxymethyl dextran
CNT	Carbon Nano Tube
CuAAC	Copper Azide Alkyne Cycloaddition
DCM	Dichloromethane
DETA	Diethylenetriamine
DLS	Dynamic Light Scattering
DMF	Dimethylformamide
DR UV-Vis	Diffuse Reflectance UV-Vis spectroscopy
DRIFT	Diffuse Reflectance Infrared Fourier Transform
EXAFS	Extended X-ray Absorption Fine Structure
FRET	Fluorescence Resonance Energy Transfer
FT-IR	Fourier Transform Infrared Spectroscopy
GEDT	Global Electron Density Transfer
GO	Graphene Oxide
GQD	Graphene Quantum Dots
ICP	Inductively Coupled Plasma
ICP-MS	Inductively Coupled Plasma Mass Spectrometry
IONPs	Iron Oxide Magnetic Nanoparticles
MOF	Metal Organic Framework
MNPs	Magnetic Nanoparticles

MRI	Magnetic Resonance Imaging
MW	Microwave
NDs	Nanodiamonds
NMR	Nuclear Magnetic Resonance
OER	Oxygen Evolution Reaction
Php	Phenolphthalein
RL	Reflection Loss
rGO	Reduced Graphene Oxide
SAED	Selected Area Electron Diffraction
SEM	Scanning Electron Microscopy
SEM-EDX	Energy-Dispersive X-ray Spectroscopy
SOMC	Surface Organometallic Chemistry
SSA	Specific Surface Area
SWCNT	Single Wallet Carbon Nanotube
TEM	Transmissions Electron Microscopy
TGA	Thermogravimetric Analysis
XAS	X-ray Absorption Spectroscopy
XANES	X-ray Absorption Near-Edge Spectroscopy
XPS	X-ray Photoelectron Spectroscopy
XRD	X-ray Diffraction
US	Ultrasound
UV-Vis	Ultra-Violet and Visible

Table of contents

Chapter 1

Catalysis and sustainable approaches

1.1. **Green chemistry**

The concept of green chemistry was first formulated at the beginning of the 1990s and it is aiming to address chemical industries towards eco-sustainable processes. Chemistry, in fact, is the field of science more involved in environmental problems. The transformation of conventional technologies in new clean processes, the design of new products and synthetic pathways, as well as the reduction of consumption of non-renewable resources, represent a big challenge towards the sustainability. Green chemistry is defined as the "design of chemical products and processes to reduce or eliminate the use and generation of hazardous substances".[1] In 1998, Paul Anastas and John Warner published a set of principles to guide the practice of green chemistry. The twelve principles, listed in Table 1, suggest different ways to reduce the environmental and health impacts of chemical production and indicate research priorities for the development of green chemistry technologies.

Table 1. Green Chemistry's principles (early 1990s by Anastas and colleagues).

Prevention	It is better to prevent waste, than to treat it or clean up after it is formed
Atom Economy	Synthetic methods should be designed to maximize the incorporation of all materials into the final product
Less Hazardous Chemical Syntheses	Synthetic methods should be designed to use and generate substances that possess little or no toxicity to human health and the environment
Designing Safer Chemicals	Chemical products should be designed to preserve efficacy of the function while reducing toxicity
Safer Solvents and Auxiliaries	The use of auxiliary substances should be made unnecessary wherever possible and, when used, innocuous
Design for Energy Efficiency	Energy requirements of chemical processes should be recognized for their environmental and economic impacts and should be minimized.
Use of Renewable Feedstocks	Raw material or feedstock should be renewable rather than depleting whenever technically and economically practicable
Reduce Derivatives	Unnecessary derivatization should be minimized or avoided if possible, because such steps require additional reagents and can generate waste
Catalysis	Catalytic reagents (as selective as possible) are superior to stoichiometric reagents
Design for Degradation	Chemical products should be designed so that at the end of their function they break down into innocuous degradation products and do not persist in the environment
Real-time analysis for Pollution Prevention	Analytical methodologies need to be further developed to allow for real-time, in-process monitoring and control prior to the formation of hazardous substances
Inherently Safer Chemistry for Accident Prevention	Substances used in a chemical process should be chosen to minimize the potential for chemical accidents, including releases, explosions, and fires

Later, in 2003, Anastas and Zimmerman proposed a set of twelve principles of green engineering.[2] This was since the twelve principles of green chemistry do not include several important concepts, highly relevant to environmental impact. Green engineering focuses on how to achieve sustainability through science and technology, considering environmental, economic, and social factors.

Recently, these principles have been summarized in the acronyms *PRODUCTIVELY*[3] and *IMPROVEMENTS*,[4] for green chemistry and green engineering, respectively (Table 2).

Table 2. The condensed twelve Principles of Green Chemistry (left) and twelve Principles of Green Engineering (right).

P	Prevent waste	*I*	Inherently non-hazardous and safe
R	Renewable materials	*M*	Minimize material diversity
O	Omit derivatization steps	*P*	Prevention instead of treatment
D	Degradable chemical products	*R*	Renewable material and energy inputs
U	Use safe synthetic methods	*O*	Output-led design
C	Catalytic reagents	*V*	Very simple
T	Temperature, pressure ambient	*E*	Efficient use of mass, energy, space and time
I	In-process monitoring	*M*	Meet the need
V	Very few auxiliary substances	*E*	Easy to separate by design
E	E-factor, maximize feed in product	*N*	Networks for exchange of local mass and energy
L	Low toxicity of chemical products	*T*	Test the life cycle of the design
Y	Yes, it is safe	*S*	Sustainability throughout product life cycle

Two parameters, E-factor (environmental impact factor) and atom economy, were introduced since the early 1990s to focus the attention of the chemical industry world-wide on the problem of waste generation in chemicals manufacture. E-factor is defined as the mass ratio of waste to desired product. The atom efficiency or atom economy is measured as the ratio of the molecular weight of the desired product over the molecular weights of all reactants used in the reaction. They represent valid tools to quantify the amount of waste generated by alternative processes per kilogram of product, assessing the "environmental acceptability" of a manufacturing process. They provide the impetus for developing cleaner and more sustainable processes.[5]

1.2. Catalysis

The role of catalysis as a primary tool in the design, development and implementation of green chemistry has been extensively demonstrated, since it is recognized as accomplishing a wide range of green chemistry goals and it is a system able to increase reaction efficiency, yield, and selectivity.[6] The catalysis involves the acceleration of chemical reactions, that occurs by substances not consumed in the reactions themselves, known as catalysts. The catalysts act providing a different reaction mechanism, with lower activation energy, thanks to a specific interaction between the catalyst and the reaction components, allowing the system to reach the equilibrium more quickly, without influencing the equilibrium constant. They accelerate both the forward and the reverse reactions rate and are regenerated in the process. The catalytic activity is expressed as turnover number (TON), that is a measure of the catalyst stability, and it is calculated as the average number of catalytic cycles a site can undergo until it deactivates; or calculating the number of molecules converted per active site per unit time (turnover frequency, TOF).

The catalyst development began during the end of the nineteenth century, when the growth of academic knowledge was translated into industrial applications. Firstly, the demand for bulk chemicals and minimization of by-products was aimed on explosives based upon nitric acid; successively, the industrial production shifted towards the manufacturing of synthetic fuels and new innovative processes such as Fisher-Tropsch, petrochemical industry and various catalytic processes for the manufacturing of synthetic polymers.

At the early 70s the catalysis was subjected to a new trend of applications, and it was applied to almost every process, including the production of fine chemicals for pharmaceutical applications, the production of bulk chemicals and exhaust gas catalyst systems, to the use of enzymatic bio-catalysis.

The search for optimization and good quality products forced the chemical companies and the academia to improve catalyst chemo- and enanctioselectivity, productivity, activity and sensitivity. The separation of the catalyst from the final product, represents one of the most important step to remove trace metal contamination, in particular from pharmaceutical compounds, especially when developing homogeneous catalytic processes.[7] Distillation, product crystallization and extraction were the separation procedures most frequently applied; however, metal scavengers and heterogeneous systems are more accurate technique to remove residual metals.

Heterogeneous catalysts are in a different phase than the reactants, are generally solids and, for this reason, can be easily removed by filtration.[8, 9] Heterogeneous catalysts are most commonly made of metals and/or metal oxides, adsorbed on solid surfaces, and for this reason called supported catalysts. They are composed of a inert support upon which an active phase is finely distributed. The exposed active surface is fundamental to establish interactions

between the solid catalyst with the reactant molecules. The interaction can occur by chemisorption or physisorption, depending on the created bonds: chemical bonds for the former, and weak van der Waals interactions for the latter. The interactions of the reactant molecules with the surface of the catalyst influence the catalytic efficiency, because the transformation of the reactants to products occurs through processes of diffusion toward and adsorption on the surface-active sites, activation, modification and desorption, leaving the active centers available for new incoming reactants. Thus, the adsorption and the subsequent conversion reactions critically depend on the properties of the catalysts, where the performance of catalytic active sites depends on both structural and electronic effects.[10]

Significant industrial processes that involve the use of heterogeneous catalysts include the preparation of sulfuric acid, the preparation of ammonia, the oxidation of ammonia to nitric acid, the synthesis of methanol and the hydrogenation of polyunsaturated to saturated fats and oils using nickel as catalyst. Heterogeneous catalysts are widely employed in many aspects of national economy, including petroleum refining, synthesis of fertilizers and other chemicals, and pollution control. Indeed, heterogeneous catalysts also find application in environmental catalysis, as innovative technologies for reducing emissions of environmentally unacceptable compounds. An example is the development of preheated catalytic converters to reduce the amount of toxic emissions produced by burning gasoline in internal combustion engines. Selected catalytically active metals, generally platinum-rhodium catalyst, are used to affect the combustion of all carbon-containing compounds to carbon dioxide while also reducing the output of nitrogen oxides. They catalyze the conversion of nitric oxide into dinitrogen and oxygen as well as the conversion of carbon monoxide and hydrocarbons such as octane into carbon dioxide and water vapor, as follows:

$$2NO_2(g) \rightarrow N_2(g) + 2O_2(g)$$

$$2CO(g) + O_2(g) \rightarrow 2CO_2(g)$$

$$2C_8H_{18}(g) + 25O_2(g) \rightarrow 16CO_2(g) + 18H_2O(g)$$
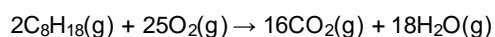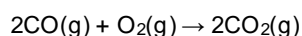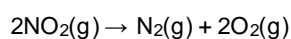
1.2.1. Organic-inorganic hybrid catalytic systems

The concept of heterogeneous catalysts was born to satisfy the request of higher stability and robustness provided by inorganic materials. The creation of inorganic or hybrid organic-inorganic catalytic systems that maintain high activity and selectivity, with enhanced stability under temperature, pressure, and solvents, represent a big challenge. The key feature of this type of system is that its characteristics arise not only from the individual contributions of the phases, but also from the properties of the inner interface, which can also be predominant. The unique active behavior of these hybrid systems is therefore not observed when the single

components are used alone.[11] Organic-inorganic hybrid systems have emerged as winning combinations in the general field of catalysis due to their enhanced heterogeneous properties. In fact, the immobilization and stabilization of organic active sites over inorganic solids has strongly improved recovery and recyclability characteristics.[12, 13] Moreover, the interposition of an organic flexible spacer between the ligand and the inorganic support allows to increase the accessibility and the stability of metallic sites.[14] Multidentate *N*-donor ligands have been largely employed in the preparation of organic–inorganic hybrid catalysts due to their versatile coordination modes.[15, 16]

In order to prepare organic–inorganic hybrid systems, an efficient surface modification of the inorganic part is required[17] and different synthetic strategies can be followed. According to the nature of the organic-inorganic interface this type of material can be divided into two classes.[18] Class I materials possess organic and inorganic components bonded together *via* weak interactions, such as van der Waals forces, electrostatic and hydrogen bond interactions. However, several problems, such as inhomogeneous dispersions of the organic layer, can be observed when weak physical interactions are present between the organic and the inorganic portions.[19] Class II compounds are made up of stronger covalent or ion-covalent interactions.[20] This latter class has attracted much more interest from the field of catalysis due to the higher stability of its hybrid systems, where the structure, the morphology and the porosity of the supporting material are preserved.[21] Covalent bonds generate atomic scale connections with a good control of functional groups density on the material surface.[22] Indeed, class II materials can be used under harsher reaction conditions, whereas class I systems are more sensitive and may be irreversibly damaged. For example, mesoporous silica, such as SBA-15 and MCM-41, has been functionalized with numerous organic ligands for several catalytic applications.[23-26] The evolution of Class II hybrid components has led to the growth of materials in which catalytically active coordination-metal complexes are covalently anchored to inorganic substrates.[27-31]

Among organic-inorganic hybrid systems a wide range of hybrid networks were designed by following different chemical pathways. Sol-gel chemistry, hydrolysis of organically modified metal alkoxides, formation of bridged precursors (such as silsesquioxanes) and hydrothermal synthesis for the synthesis of Metal Organic Frameworks represent simple, low-cost ad effective strategies to obtain amorphous nanocomposite hybrid materials.[32] On the other hand, assembly procedures were proven to be a suitable method to reach a better definition of the inorganic component, where the hybrid interfaces can be tuned and controlled. Recent strategies consist of the use of organic surfactants, specific bridged and polyfunctional precursors, where the organic spacers have been improved by using two terminal functional groups.[33] Ordered dispersions of organic-inorganic matrices, mesoporous hybrid systems with organic functionality within the walls, as well as highly-ordered nanoporous materials available for further organic functionalisation through surface grafting reactions have been obtained.[34]

Especially for heterogeneous catalysis, the nature of the material surface plays a key role in determining the chemical and physical properties of the system. Talking about supported metallic catalysts, the surface properties of the support influence the catalytic behavior by affecting the formation of metal nanoparticles, interacting with reactants and active metallic species by stabilizing the metal particles, changing the chemical oxidation state of the active sites or affording the formation of unique active species. This is particularly evident when the inorganic surface is modified with active moieties, obtained by inorganic surface chemical modification. The grafting of the surface with specific ligands can tune the catalytic activity of supported metal sites, acting on leaching and catalytic efficiency. This is due to the fact that the metal complex structure is strictly correlated to the catalytic activity, the choice of the metal and its coordination sphere. Consequently, the choice of ancillary ligands and inorganic surface structure represent fundamental factors that must be considered in order to generate well-defined systems, that can directly enter into the catalytic cycle or as immediate precursor. [35, 36] The key role of the ligand is well recognized since it can impose stereo electronic effects, modify the electronic structure of metal, and interfere with the metal/solvent boundaries. [37] The vast majority of these approaches relied on the use of innocent ligands, not responsible of any redox-activity, but they can impart improvements to the desired catalytic transformation. For instance, *n*-alkanethiol coated Pd catalysts greatly improved selectivity thanks to the metal-sulphur interactions,[38] hexadecyl(2-hydroxyethyl)dimethylammonium dihydrogen phosphate was used as suitable ligand for the synthesis of ruthenium nanoparticles, in order to act as a pH buffer, controlling the local acidity and the interactions between the ligand and the metal were deeply demonstrated.[39] Pd/polyaniline/Pd sandwich-structured nanotube arrays were designed as electrocatalysts for ethanol electrooxidation for direct alcohol fuel cells. They showed high electrocatalytic activity and long-term durability thanks to the strong synergistic coupling between the inorganic Pd and the organic polyaniline support, with high electron delocalization between Pd d orbitals and polyaniline π-conjugated ligands and electron transfer from Pd to polyaniline.[40] However, while the use of innocent ligands is extensively reported, literature research in organic–inorganic hybrid systems revealed that, only recently, non-innocent ligands are achieving growing importance, especially in catalytic applications.[41] Non-innocent ligands are able to import novel reactivity to the adjacent metal complexes, and multifunctional redox-active ligands have been demonstrated to act on proton or electron transfer and are directly involved in the catalytic cycle.[42, 43] However, the active interaction between the ligand framework and metal complexes is not well documented, especially in heterogeneous catalysis, where a discussion of the possible ligand-metal participation is in general not reported. Moreover, most studies have focused on the interaction between redox-active ligands and precious metals. Thus, a major effort in the investigation of ligand-metal coordination chemistry and heterogeneous catalysis is indispensable.

1.2.2. Importance of catalyst structure design

In the case of supported metal catalysts, several approaches have been developed for the immobilization of the metal on suitable supports, achieved through covalent or non-covalent interactions,[44, 45] including impregnation, ion exchange, and precipitation techniques. Ionic and hydrogen interactions, physisorption, entrapment in porous supports, immobilization *via* π–π interactions and charge-transfer complex interactions are the most used strategies to obtain non-covalent immobilized catalysts.[46] The properties of heterogeneous catalysts supported *via* non-covalent immobilization are dependent on reaction conditions, such as temperature, substrates, support, solvents, as well as leaching and reuse.[47] Furthermore, as-prepared supported-metal systems result in a mixture of undetermined and numerous active species, characterized by particle size and composition inhomogeneity.[48] The non-uniformity of sites negatively affect the balance between activity, selectivity, and stability. This limit can be overcome designing well-prepared systems, through an excellent control of the preparation procedures or a deep knowledge of the structure of the metal active sites at the molecular level,[44] where the interaction between the molecular complex and the surface is carefully evaluated and uniform "single-site" heterogeneous catalysts can be generated.[49] The selection of specific preparation procedures allows to obtain high reactive heterogeneous supported systems by the modulation of the catalyst structure (i.e. defects, electronic and geometric states) and the subsequent modification of the surface properties (i.e. size, morphology, specific surface area, composition and electron transfer), exploiting the material design and the structure-property correlation.[50] The metal electronic and structural properties can be tuned and optimized designing the catalyst structure, by complexing the metal with specific ligands.[51] In fact, the reactivity of the metal center can be influenced by the ligands characteristic properties originating, for example, from their Lewis acidity or basicity, aromatic chelating structure and redox activity.[52, 53] The cooperativity between the metal and the ligands, as well as the capability of the ligands to stabilize metal oxidation states and coordination geometries can improve the activity and selectivity of the system.[36] This is evident illustrating the properties of *cis*- and *trans*-dichlororuthenium benzylidenes complexes (Figure 1). *Cis*-ruthenium-based systems are latent metathesis catalysts, which means that remain inactive until they undergo a specific external stimulus, responsible of the ligand dissociation, necessary for the catalyst activation. The latency can be modulated by exchanging the ligand shell around the metal center, acting on the strength of the ligand-metal bond to lower the initiation rate, generally reached by forming a bidentate chelate, which hinders dissociation. *Cis*-isomers are more stable than the *trans*-counterpart, so their latency is improved.[54] The chelation given by tethered, carbene, alkylidene and anionic ligands decelerates both initiation and propagation. The steric effects on the benzylidene or on the *N*-heterocyclic carbene (NHC) positions tune the latency in ruthenium precatalysts.[55] Interestingly, the simple substitution of an oxygen atom with a sulfur atom represents an efficient strategy to impose higher latency in ruthenium-based catalysts. Sulfur-

based ruthenium complexes have been isolated in a *cis*-dichloro geometry, this is due to the sulfur atom inability to coordinate to the strongly σ-electron-donating NHC ligand, which would give *trans*-isomers. Therefore, the *trans* influence is reduced, and the complex remains inactive at ambient temperatures. The sulfur−ruthenium bond could be dissociated by applying UV irradiation or when exposed to thermo treatments.[56-59]
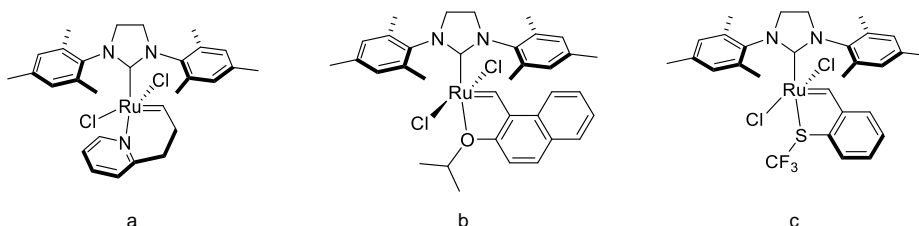
Figure 1. Ru(II) complexes: (a), (c) *cis*-isomers; (b) *trans* isomer.

A common way to efficiently control heterogeneous supported metal chemical composition and atomic coordination and obtain well-defined systems is *via* the surface organometallic chemistry (SOMC).[60, 61] SOMC is a methodology through which organometallic complexes can be directly attached to inorganic carriers: organometallic fragments (i.e. alkyl, alkoxide, or halogen groups) interact with reactive functionalities of the inorganic support, whose surface plays a crucial role as support and ligand, and it is directly involved in the coordination sphere of the metal, establishing covalent or ionic bonds or acid-base Lewis interactions.[62] Otherwise, well-defined active sites (i.e. Lewis acids, redox sites) can be introduced in the framework of zeo-types and mesoporous materials, generating pore-selective functionalities toward different potential transition states and metal ions or clusters.[63] Another way to control the synthesis of catalytic materials on the atomic scale, is, for instance, the atomic layer deposition. It allows to control metal and metal oxides sites, as well as the size, shape, morphology, facets and composition of dispersed nanoparticles, and an enhancement of the catalytic activity, selectivity and durability is explained by the atomic precise growth effect.[64] Moreover, a good control of the chemical composition, the atomic coordination and the surface layers structure of nanocatalysts determines their performance in catalysis and it can be achieved by monitoring the nucleation and growth rates, by modulating the synthesis parameters, like temperature, precursors, pH, concentration and protective agents. A number of synthetic procedures including wet chemical synthesis, solid-state and physical chemical reaction can be employed to synthesize well-defined nanostructures, with a high selective display of catalytic facets, composition tuning surface engineering *via* heteroatom doping, and dimension/structure engineering and interface engineering with selected supporting material.[65] The most applied techniques for the controlled synthesis, result in the use of non-conventional technologies, such as microwave and ultrasound irradiation, that will be discussed later.

1.2.3. Nanomaterials and nanocatalysts

Nanomaterials have gained importance in technological developments due to their tunable physical, chemical and biological properties with enhanced performance over their bulk counterparts. They can be classified depending on the size, shape, and origin, but the main categorization divides the nanomaterials basing on their composition:

- carbon-based nanomaterials, such as fullerenes, carbon nanotubes, graphene, black carbon, etc.,

- inorganic-base nanomaterials, such as metal and metal oxide nanoparticles,

- organic-based nanomaterials, made of organic matter and transformed into dendrimers, micelles, liposomes and polymers,

- composite-based nanomaterials, such as hybrid organic-inorganic nanoparticles, or combined nanoparticles and bulk-materials or more complicated structures, such as metal organic framework.[66]

The chemistry of nanomaterials mainly depends on the synthesis of nanoparticles, controlling size, shape and morphology, and on the molecular approach to find out ever more selective applications. During the years, well-controlled synthesis of nanomaterials has been achieved by using stabilizing or capping agents, surfactants, polymers, etc. It has been demonstrated that the appropriate choice of the stabilizing agents is fundamental to control the surface properties of the nanomaterials, since they can modify the active sites, the chemical environment, as well as the selectivity and reactivity, due to steric and electronic effects.[67, 68] Moreover, an accurate control of the reaction parameters for the nanoparticle formation is essential to obtain highly organized nanosystems. Some long-established approaches may successfully produce pure, well-defined nanoparticles, but the relative high cost of production and the elevated environmental impact are asking for more cost-effective and environmentally benign alternatives.[69] This can be achieved by the use of innovative preparation methodologies, such as the application of ultrasound or microwave irradiation (Figure 2), or by the choice of renewable resources as capping agents, such as plant extracts (like polyphenol anti-oxidants from tea and coffee), biodegradable polymers, reducing sugars (such as vitamins) and agricultural residual waste. Moreover, recently, with the aim at pursuing eco-friendly alternatives, the attention on magnetic nanoparticles is rapidly growing. Magnetic nanosystems have been recognized as promising materials in different field of application, from the catalysis, electrochemistry, biomedicine, to the pollutant removal, toxicity mitigation or water treatments,[70] thanks to their ease surface chemical modification, coating and recoverability.[71]
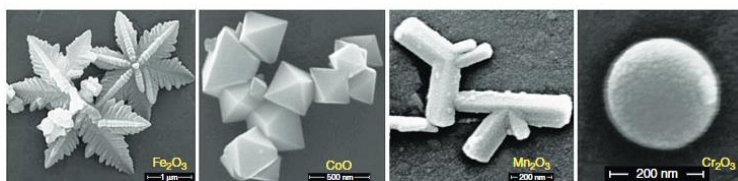
Figure 2. Metal oxides with well-defined morphologies, obtained by microwave-controlled nanoparticle preparation. Figure obtained from the paper of Varma.[72]

Nanomaterials have gained importance in catalysis due to their excellent physicochemical properties. They combine the rapid and selective chemical transformations with excellent product yield and ease of separation and recovery. Nanocatalysts have been studied during the years to improve the performance of supported metal catalysts by downsizing the metal particles and combine advantages of both the homogeneous and heterogeneous catalytic systems.[73] Nanocatalysts are composed of metal components finely dispersed on a high-surface-area support. The size of metal particles becomes one of the most critical factors determining the reactivity and specificity of supported metal catalysts. Nano dimensions and high exposed surface areas are responsible of enhanced coordination environment of metal centers, improved metal-support interactions and charge transfer, as well as quantum size effects, where confinement of electrons leads to a discrete energy level distribution. Thus, the amount of active surface species and the electron transfer between the catalyst surface and the reactive species increase dramatically, while the insolubility into the reaction mixture makes the recoverability easy.[74] The heterogeneity of nanosystems can be achieved by the fixation of single atoms, metal cluster or metal nanoparticles onto suitable supports (such as silica, alumina, other oxides or carbon nanomaterials).[75] More recent approaches consists of the use of magnetic supports, such as iron oxide magnetic nanoparticles, to immobilize the metal center, that could be easily recovered from the catalytic media by simply applying a magnet.[76]

1.2.3.1. Single atoms, nanoclusters or nanoparticles?

The interaction between single atoms, nanoclusters or nanoparticles and the supports and the reactants has been extensively investigated.

The electronic structure of mononuclear metal complexes is strongly related to the coordination environment, including ligands and solvent. They are stabilized by the cooperation between the metal and the support, that occurs through chemical bonding, *via* direct interaction or through functional groups. In the first case their geometric structures are partially restricted by the support, while, when single atoms are supported with functional groups, they may adapt their coordination environment. Moreover, a strong metal-support interaction is important to prevent aggregation of single atoms on the surface. Thus, the choice of the surface anchoring sites, has an essential role in stabilizing single-atom metal species.[77] The utilization of supported

single-atom catalysts in heterogeneous catalysis provides wide applications, but their limit rely on the request of multi-metal active sites.

Metal clusters and nanoparticles show the orbital overlapping between metal atoms. Metal clusters are composed of less than 20 atoms and the geometric structures of such nanoparticles are quite flexible and can be strongly affected by the environment. When supported on solid supports, different geometric configurations can be observed even in the same local environment, making the catalytic efficiency more variable and difficult. The study of the influence of geometric structure on the catalytic properties of metal clusters is rarely reported and the controlled preparation of metal clusters is still a challenge. Indeed, a lot of factors influence the preparation of supported metal cluster with well-defined structures, where size, shape and the electronic properties are strictly under control, such as the nature of the support, metal−support interaction, the presence of other metals and impurities. However, it has been demonstrated that the introduction of organic ligands allows to obtain well-defined metal clusters. Moreover, the development of more robust synthetic methodologies is necessary to understand and improve the catalysis based on supported metal clusters.[78]

Metal nanoparticles are usually composed of more than 40 atoms and show a diameter size more than 1 nm. Their geometric structures are stable and less sensitive. Since the electronic properties depend on the particle size, the electron transfer between the support and the metal species, that affect the catalytic properties, is also strongly dependent on it. The electron transfer is also influenced by the geometric location of the metal species on the support, where metal nanoparticles can be located at crystal edges, corners, and facets during different catalytic reactions. When catalytic nanoparticles are located into a specific environment, the local space applies a physical restriction on them and provides a unique electronic microenvironment that modulates electron transfer processes. For these reasons, the choice of the correct solid support is fundamental to design highly active nanocatalytic systems. In addition, the nanoparticles selectivity can also be modulated by controlling its intrinsic composition. For instance, bimetallic nanocatalysts are emerging as new field of nanocatalysis, because they do not only combine single properties, but they show new properties and abilities due to a synergistic effect between the metals.[79]

Figure 3 shows a schematic representation of the surface free energy and the specific activity per metal atom with metal particle size and the support effects on stabilizing single atoms. The bulk material can be turned into nanoparticles, subnanoclusters, and single metal atoms. An increase of unsaturated coordination environment of the metal species is proportional to the size. Accordingly, the surface free energy of the metal components increases, and the metal sites become more and more active for chemical interactions with the support and adsorbates.
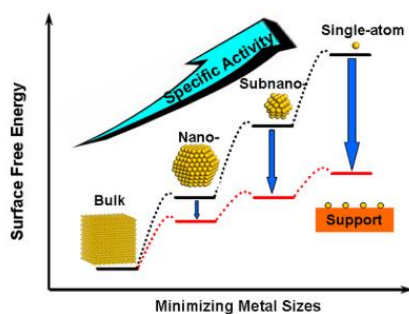
Figure 3. Surface free energy and specific activity per metal atom related to metal particle size. Figure obtained from the paper of Singh.[77]

1.3. Non-conventional technologies

1.3.1. Microwave

The concept of green chemistry is aiming to address chemical industries towards eco-sustainable processes. The development of innovative energy-saving, economically viable and environmentally safe technologies is gaining great attention. In the last two decades, the use of microwave (MW) irradiation in organic synthesis attracted increasingly interest, as indicated by the number of publications in this field that is increasing from year to year, starting from the 1986, when the first studies on MW activation in organic chemistry have been published by Gedye and co-workers.[80] It is surprising that even now, when MW irradiation is a well-established methodology, the number of publications is still increasing, indicating the high interest of academia and chemical industries in its application and development (Graph 1).
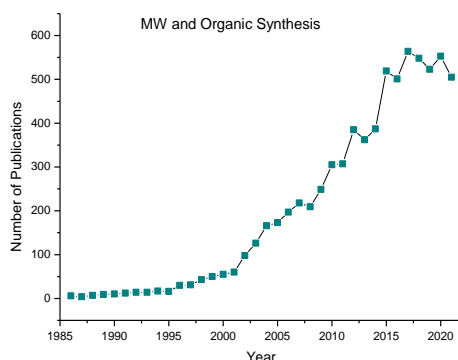
Graph 1. Number of publications in Microwave-Assisted Organic Synthesis (MAOS). Number of references resulted from a SciFinder research.

In the electromagnetic spectrum (Figure 4), the MW radiation region is located between infrared radiation and radio waves (wavelengths of 1 mm-1 m and frequencies between 0.3 and 300

GHz), but industrial and domestic MW apparatus operates at a frequency of 2.450 GHz. Within this region of electromagnetic energy, only molecular rotations are affected. MW photons energy (0.037 kcal/mole) is not enough to affect the structure of organic molecules: the effect of MW adsorption is purely kinetic. Electromagnetic radiation combines both electric and magnetic field, propagating through the space and carrying out the energy. Material heating occurs through molecular interaction with the MW electric field, through two different mechanisms: dipolar polarization and ionic conduction. Dipolar polarization refers to the effect of the alternated electromagnetic field on polar molecules, causing the antiparallel orientation of the molecule dipole moments to the force field lines, rotation and conversion of MW energy into kinetic energy. The second method of energy transfer is the ionic conduction, that originates from the presence of ionic species or free ions in the material. Vibrational motion of ions and resistance of the medium to ion flux are generated under the alternated electric field and the electromagnetic energy is converted into thermal energy. Indeed, as seen, MW heating involves a process of energy conversion instead of heat transfer as in conventional heating.[81] It results in instantaneous localized superheated centers, high temperature homogeneity and the possibility to heat selectively within a composite material.[82, 83]
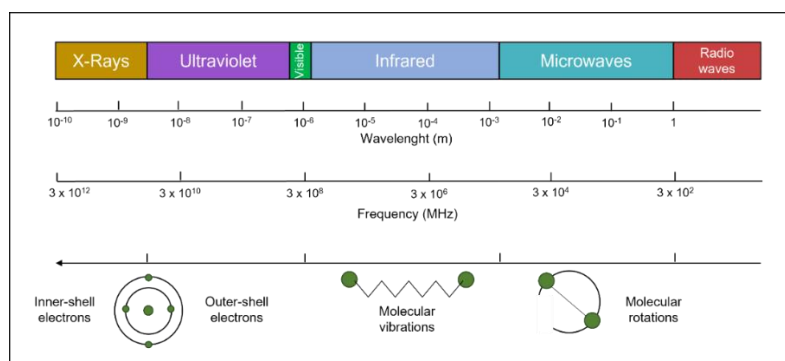
Figure 4. The electromagnetic spectrum.

MW-assisted chemical reactions strongly depend on the ability of the reaction mixture to efficiently absorb MW energy, that often depends on the choice of the solvent. The ability of a specific material or solvent to absorb and convert MW energy into heat, at a given frequency and temperature, is determined by the three main dielectric parameters: tangent delta, dielectric constant, and dielectric loss. These parameters are correlated in the equation:

$$\delta = \frac{\varepsilon''}{\varepsilon'}$$

where δ is the so-called loss tangent, ε'' is the dielectric loss (that represents the conversion efficiency of the electromagnetic radiation into heat), and ε' is the dielectric constant (that describes the polarizability of molecules in the electric field). The dielectric parameters strongly affect the MW penetration depth, which is the point where 37% of the initially irradiated MW power is still present. The MW penetration depth is inversely proportional to the loss tangent.

13

Some of the penetration depths of the microwaves in common solvents at room temperature are listed in Graph 2. Particularly significant is that the penetration depth of the 2.45 GHz microwaves into almost all non-polar solvents tends to be rather extensive compared to the one in polar solvents.[84] Generally, the loss tangent and consequently the absorption of MW irradiation decreases with temperature and is proportional to the wavelength of applied MW. It means that MW absorption may become somewhat difficult at high temperatures and a solvent can be penetrated at different depths by varying frequencies. The higher the δ value, the better the solvent is for MW absorption and the more efficient the solvent converts MW energy into thermal energy. The solvents employed for MW-assisted chemistry are classified as high (tan δ > 0.5), medium (0.1 < tan δ < 0.5), and low MW absorbing (tan δ < 0.1), as gathered in the Table 1.[85] The use of a very low absorbing solvent (i.e. hexane, benzene, toluene) can help to selectively heat the other absorbing molecules in the media, allowing a selective and efficient heating process.
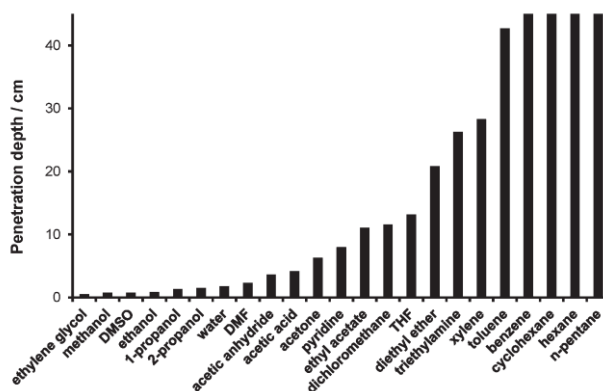
Graph 2. Penetration depths of the 2.45 GHz microwaves for some common solvents. Figure obtained from the paper of Serpone *et al.*[84]

Table 1. Dielectric constant (ε), tan δ, and dielectric loss (ε") for some common solvents (measured at room temperature and 2450 MHz). Table obtained from the website https://cem.com/it/microwave-chemistry/solvent-choice.[86]

Solvent (bp °C)	Dielectric Constant (ε')	Solvent	Tan δ	Solvent	Dielectric Loss (ε")
Water (100)	80.4	Ethylene Glycol	1.350	Ethylene Glycol	49.950
Formic Acid (100)	58.5	Ethanol	.941	Formic Acid	42.237
DMSO (189)	45.0	DMSO	.825	DMSO	37.125
DMF (153)	37.7	2-Propanol	.799	Ethanol	22.866
Acetonitrile (82)	37.5	1-Propanol	.757	Methanol	21.483
Ethylene Glycol (197)	37.0	Formic Acid	.722	Nitrobenzene	20.497
Nitromethane (101)	36.0	Methanol	.659	1-Propanol	15.216
Nitrobenzene (202)	34.8	Nitrobenzene	.589	2-Propanol	14.622
Methanol (65)	32.6	1-Butanol	.571	Water	9.889
NMP (215)	32.2	Isobutanol	.522	1-Butanol	9.764
Ethanol (78)	24.3	2-Butanol	.447	NMP	8.855
Acetone (56)	20.7	2-Methoxyethanol	.410	Isobutanol	8.248
1-Propanol (97)	20.1	o-Dichlorobenzene	.280	2-Butanol	7.063
MEK (80)	18.5	NMP	.275	2-Methoxyethanol	6.929
2-Propanol (82)	18.3	Acetic Acid	.174	DMF	6.070
1-Butanol (118)	17.1	DMF	.161	o-Dichlorobenzene	2.772
2-Methoxyethanol (124)	16.9	1,2-Dichloroethane	.127	Acetonitrile	2.325
2-Butanol (100)	15.8	Water	.123	Nitromethane	2.304
Isobutanol (108)	15.8	Chlorobenzene	.101	MEK	1.462
1,2-Dichloroethane (83)	10.4	Chloroform	.091	1,2-Dichloroethane	1.321
o-Dichlorobenzene (180)	9.9	MEK	.079	Acetone	1.118
Dichloromethane (40)	9.1	Nitromethane	.064	Acetic Acid	1.079
THF (66)	7.4	Acetonitrile	.062	Chloroform	0.437
Acetic Acid (113)	6.2	Ethyl Acetate	.059	Dichloromethane	0.382
Ethyl Acetate (77)	6.0	Acetone	.054	Ethyl Acetate	0.354
Chloroform (61)	4.8	THF	.047	THF	0.348
Chlorobenzene (132)	2.6	Dichloromethane	.042	Chlorobenzene	0.263
o-Xylene (144)	2.6	Toluene	.040	Toluene	0.096
Toluene (111)	2.4	Hexane	.020	o-Xylene	0.047
Hexane (69)	1.9	o-Xylene	.018	Hexane	0.038

It has been demonstrated that under MW irradiation, faster and more selective organic reactions can be obtained, by choosing appropriate MW parameters.[87] Based on Arrhenius reaction rate equation ($k = Ae^{\frac{-Ea}{RT}}$), the reaction rate constant (k) increases proportionally with the increase of the absolute temperature (T) and the frequency factor (A) and decreases proportionally with the increase of transition state energy (energy activation, E_a). Thus, the increase in the pre-exponential factor A, which is representative of the probability of molecular impacts, could enhance reaction rates. This collision efficiency can be effectively influenced by mutual orientation of polar molecules involved in the reaction. However, it should be underlined that MWs do not influence orientation molecule collisions or the reaction activation energy but act on temperature control. Increasing the temperature, the molecules movement becomes more rapid, and a greater number of more energetic collisions is generated. The temperature increase happens much faster under MW irradiation than under conventional heating, due to the high immediate heating of the reaction mixture above the normal bulk temperature. Furthermore, the MW energy affects the level of instantaneous heating: the higher the MW

energy, the higher is the reached temperature. Thus, a simultaneous cooling during the MW irradiation is a powerful method to remove latent heat and provide a higher level of MW power. Thanks to the elevated molecular energy generated by the transfer of MW energy, reaction times shorten from several h or even days to a few min.[88]

In recent years, the attention is also moving to the use of MW on the synthesis of heterogeneous systems and nanostructured materials, as a potential alternate heating for material processing, as well as on their application. It is well-known that the growth of nanomaterials, metal nanoparticles and nanostructures is highly dependent on the reaction conditions and a controlled and efficient synthesis can be achieved by MW irradiation, whose rapid temperature profile is unique.[89] Indeed, it has been demonstrated that the dispersity, the morphology and the size of nanosystems are dependent on heating method, uniformity and rapidity of the heat.[90] Moreover, given the usually excellent MW absorption capability of most solid catalysts, it is beyond doubt that the combination of MW activation with heterogeneous catalysis carries almost unlimited opportunities in synthesis design for environmentally benign processes.

1.3.2. Ultrasound

Ultrasound (US) covers the frequency range between 20 KHz and 5 MHz (Figure 5), that is the sound beyond which the human ear can respond. It does not affect chemical species at molecular level, being the molecular dimension too small compared to the acoustic wavelength. It consists of alternate compression and decompression cycles and sound waves propagate longitudinally into liquid media. Under the effect of sonic waves, the generation of micro bubbles or cavities into the liquid is observed, with subsequent growth to a maximum size and a final violent implosion, that leads to a local strong energy dissipation, with the creation of local hot spots, characterized by rather extreme temperatures and pressures of around 5000 K and 1000 atm. Furthermore, in addition to the chemical cavitation effects, also physical effects are observed as the generation of high liquid movement, responsible of elevate mass transfer rates. Thus, homogeneous reactions take advantage of the local hot spots generation, radical mechanisms can be accelerated because the better ability of radical species formation under ultrasonic waves, while heterogeneous reactions benefit from the intense liquid agitation and the implosion of cavities in the proximity of a solid surface that produces micro-jets of liquid that act on the outer solid layers, renewing the exposed area and prolonging the solid activity (i.e. in heterogeneous catalysis).
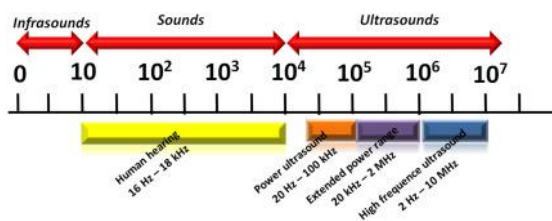
Figure 5. The frequency range of the sound. Figure obtained from the chapter 10 of the book of Konieczka *et al.*[91]

The choice of the solvent is fundamental in sonochemistry because when it is combined to US irradiation can dramatically affect reactivity and product yield. Each solvent can dissipate ultrasonic power (U_p) differently and the higher is U_p, the higher is the cavitation effect. Viscous solvents show elevates cohesive forces that oppose to the negative pressure required for the cavitation; however, if the onset of cavitation is longer, the dissipated power is higher. Then, high solvent surface tension is correlated to high dissipation power, while volatility and dissipated power are inversely correlated.[92]

Solvent	Vapour pressure (kPa)	Viscosity (mPa.s)[a]	Surface tension (Dyn/cm)[b]	U_p (W)[c]
Acetone	24.53	0.33	23.3	1.98
Chloroform	26.66	0.57	27.1	1.93
Methanol	12.8	0.6	22.6	2.93
Hexane	16	0.31	18.4	2.46
Ethanol	5.9	1.08	22.3	3.47
Benzene	42.66	0.65	28.9	2.91
CH_3CN	9.7	0.38	29.1	3.40
1-Propanol	2.77	1.72	23.7	4.00
Water	2.4	0.89	72.75	6.35
Toluene	2.90	0.59	28.5	2.87
1-Butanol	16.66	3.0	24.6	4.61
Acetic Acid	1.5	1.13	27.4	4.72
DMSO	0.06	2	43.7	5.5
[BMIM][BF_4]	0	219	46.6	7.02

[a] Determined at 25 °C.
[b] Determined at 20 °C.
[c] Average ultrasonic dissipated pressure (U_p) at 20, 25 and 30% amplitude (A) determined by calorimetric method.

Table 2. Average ultrasonic dissipated pressure (Up) and physical properties of several solvents. Figure obtained from the paper of Colacino *et al.*[92]

Many factors influence the effect of sonochemistry efficacy. It is reported that, generally, an increase in the ultrasonic power results in greater generation of cavitation bubbles, that is higher cavitational intensity, leading to faster reaction rates. However, this effect must be evaluated on a case-by-case basis. Indeed, it has been demonstrated that the conversion of organic and enzymatic reactions can increase until an optimum value increasing the US power, beyond which uninteresting or even worst results can be obtained. This is for example the case of the Knoevenagel condensation between benzaldehyde and ethyl cyanoacetate, where a decrease of the conversion is registered when using more than 30% of power intensity.[93] The size of the cavities, the implosion time and the physical or chemical effects ratio are correlated to the ultrasonic frequency. Higher frequencies generate smaller bubbles, reduce the time required for collapsing and increase the number of free radicals that move from the cavitation site to the bulk mixture, reducing the degree of the physical effects in favour of the chemical effects.

17

Moreover, US efficacy is negatively affected by the temperature: the formation of vapour cavities resulting from higher temperatures would alleviate the bubble collapse due to the cushioning effect. However, a good relationship between the ultrasonic and the kinetic effect, given by the temperature increase, was demonstrated to be helpful for reactions outcome.[94][95]

Two different methods for the introduction of US into a system can be principally describe, the ultrasonic cleaning bath and the ultrasonic prob. Both systems rely upon the piezoelectric transducer as an US source. One of the main disadvantages is the fact of having an optimum performance when a fixed frequency (that depends on the transducer) is applied. In most cases, the optimum frequency for commercial baths is around 40 kHz and for commercial probes is around 20 kHz. Although the ultrasonic bath is the cheapest and widely used source of ultrasounds, some disadvantages can be named if comparing with the probes. Like any other sound wave, US is propagated *via* a series of compression and rarefaction waves induced in the molecules of the medium through which it passes. This fact supposes that the amount of energy that reaches the reaction while working with the sonic-bath is very low (normally between 1 and 5 W cm^{-2}).

The nature of sonochemical reactions has been widely studied and a set of empirical rules has been established in order to provide some clues and better understand the effects of this irradiation:

- in homogeneous reaction, the chemical effects can be explained by assuming that sequential electron transfers are favored by ultrasonic irradiation,

- in heterogeneous liquid-liquid or solid-liquid reactions, bubbles cavitation near the interface will cause disruption and mixing, resulting in the formation of fine emulsions, and therefore being particularly beneficial in the enhancement of phase-transfer catalysis,

- in heterogeneous reactions, the biphasic system will also be subjected to the mechanical component of shock waves, in addition to the chemical activation.

US has seen widespread use in the promotion of organic and polymeric synthesis,[96, 97] heterogeneous phase reactions,[98, 99] and in the preparation of inorganic nanostructures and catalysts.[100-102] Moreover, significant effort has been devoted to organic synthesis with supported catalysts and reagents on the surfaces of cheap and recyclable mineral supports, such as clay, silica, alumina.[103] However, if sonochemistry has become one of the most powerful heating and stirring methods for laboratory scale operations, as demonstrated by the rapid increase of the number of scientific publications during the last decades (Graph 3), the replace of conventional methodologies in commercial scale processing is slowly happening.
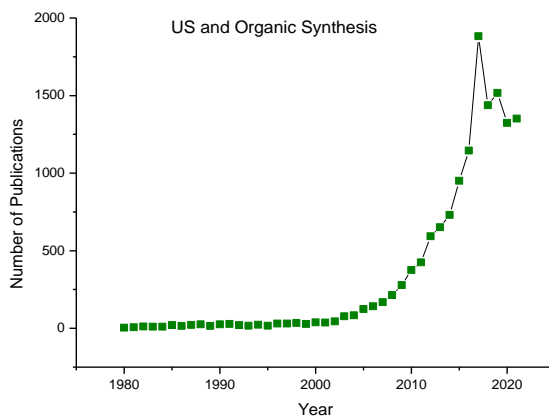
Graph 3. Number of publications in Ultrasound-Assisted Organic Synthesis. Number of references resulted from a SciFinder research.

1.3.3. Flow chemistry

Continuous flow processes are defined as a type of chemistry performed in continuous flowing streams, where the reactions take place in narrow channels with inner diameters ranging from several μm to mm. The tremendous advantages it presents are attributed to the small channel dimensions, to the ease with which hazardous reagents can be handle. In addition, the continuous flow properties eliminate the need of isolation of intermediates, sometimes toxic and hazardous. The large surface area to volume ratio of flow reactors, as a result of the small dimensions, provides efficient mass and heat transfer rates. The rapid heat transfer is easily achieved in microstructured flow devices, where energy exchange can be controlled in a very different way in flow devices compared to classical batch reactors. Moreover, several external energy input can be applied, combining the continuous flow synthetic methodologies to other enabling technologies leading to an improved efficiency. Typical combinations with flow chemistry are MW irradiation, photochemistry, supported reagents or catalysts, inductive heating, electrochemistry. [104, 105] Continuous flow processes show also many other advantages, including precise controlling of reaction parameters, reaction time and temperature, thanks to the ease and safe pressurization of the system, efficient mixing and automation and efficient set-up of multistep reactions, where reagents can be introduced into the stream of reactants anywhere in the flow system. [106-108] Compared to the batch alternative, continuous flow processing specifically address the scale-up needs and exhibit several benefits that make it particularly attractive for the industrial synthesis, in terms of efficacy, cost, equipment size, energy consumption, safety and waste generation, among other things. Three different approaches can be exploited to produce large amount of compounds *via* continuous flow systems: running the process longer, performing the reaction in multi-reactors in parallel, or using larger continuous reactors. Moreover, it has been demonstrated that the reaction scale-

up in continuous flow reactors is easier than in batch, because the possible inefficient mixing or by-product formation are easily avoided.[109, 110]

The continuous flow systems can be designed into three types, as schematically shown in Figure 6:

- the reagents are dissolved into suitable solvents, poured into syringes and flowed through the reactor. At the end, the product is collected. Homogeneous catalysts are allowed,

- one of the reagents is supported onto a solid and confined into the reactor; the substrate is passed through. The collected solution contains the product,

- the heterogeneous catalyst is confined into the reactor, the reagents are passed through. In principle, no separation of the product from the catalyst is needed; and the catalyst could be easily recycled.[111]
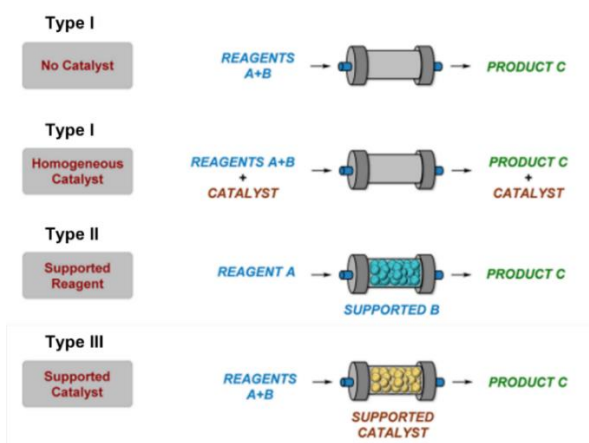
Figure 6. Types of continuous flow systems. Figure obtained from the paper of Kobayashi *et al.*[111]

Since catalytic methodologies are nowadays essential for the development of sustainable and efficient processes, continuous flow systems involving the use of a heterogeneous catalysts are grown rapidly.[112] Moreover, they are acquiring increasing importance for the preparation of Active Pharmaceutical Ingredients (APIs). For instance, the synthesis of Aliskiren hemifumarate in continuous flow systems was reported by Novartis-MIT Center.[113] It involves continuous flow reactions and additional operations (quench, work up, isolation, and purification), where all the steps are integrated in a fully automated continuous process. In this way, 100 g / hour of Aliskiren can be produced. Moreover, while the batch reactions need refluxing conditions for 48 h, the continuous process is done in 1 h, and it operates in solvent free conditions. Many other examples of API production, such as the synthesis of Olanzapine (Figure 7), Amytriptyline, Tamoxifen, Rufinamide, etc are reported in literature.[114] However, pharmaceutical industries

still rely on batch reactors, but the growing interest toward continuous flow manufacturing of APIs is evident.
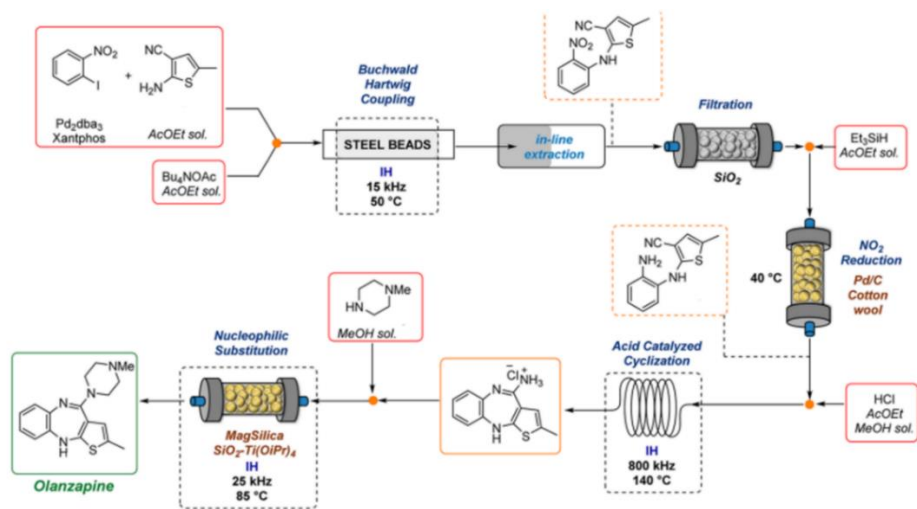
Figure 7. Continuous flow synthesis of Olanzapine. Figure obtained from the paper of Puglisi *et al.*[113]

Chapter 2

Sonochemically-promoted preparation of β-cyclodextrin-silica hybrid systems for efficient copper catalysis

2.1.   Introduction

As explained in Chapter 1.2.1, organic-inorganic hybrid materials have achieved great attention in recent years and numerous innovative studies have enriched the literature on these types of compounds.[115-118] The design of novel organic-inorganic hybrid systems provided considerable success in several fields, including catalysis, photochemistry, biochemistry and optoelectronics.[12] Hybrid nanostructures for catalytic applications have been studied and synthesized since the 1990s and still represent a big challenge for the scientific community, merging the heterogeneous and homogeneous worlds.[119] The modification of the composition on the molecular scale of hybrid catalysts makes them suitable for the design of smart and efficient systems,[120, 121] where the inorganic surface modification *via* the ligand grafting can enhance and tune the catalytic activity of supported metal sites.[122] Good control of the organic functional groups on the inorganic surface and well-defined supporting materials are obtained by the selective covalent grafting between the organic and the inorganic portions,[47] where atomic scale connections are generated and a good control of functional groups density on the material surface is obtained.

Most explored inorganic supports are mesoporous materials,[123-126] polymers,[127, 128] nanostructured supports,[129, 130] metal organic frameworks (MOF).[131, 132] Surface exposed nucleophilic or electrophilic functions, vacant coordination sites and unsaturated functional groups can be used as active sites for specific derivatizations.[21, 133] Among the inorganic materials, porous silicas particles achieved great attention as strong support matrix, useful in several technological applications. The outstanding chemical and physical properties, as well as the ease of functionalization of both internal and external surfaces of the pores with various organic functional groups, made silica an excellent catalyst support material.[134] The surface properties of silica depend on the concentration and the distribution of different types of OH groups (single, geminal or vicinal silanols, Figure 8), on the presence of siloxane bridges and on the porous structure of the silica. The silanols are considered strong adsorption sites, can interact with H-bond interactions, and are responsible of the silica hydrophilic properties. The distribution and the density of the surface hydroxyls, that is dependent on the type of silica material (crystalline or amorphous), determine the number of H-bonds and their contacts. On the other hand, siloxane sites are usually considered hydrophobic and can interact with other molecules by means of dispersion forces. Their concentration at the surface is increased by

heating the silica material at high temperature, and by the condensation of two H-bonded Si-OH groups with the loss of a H_2O molecule.[135] The chemical modification of the silica surface allows to modify and modulate adsorption properties and technological features of composite materials.[136] Moreover, the modification of the functional groups, by the addition of ligands and spacers on the silica surface represents a possibility to control the morphology and the local coordination environment at the catalytic sites to generate selectivity and to change hydrophilic/hydrophobic properties. Thus, the possibility to manage the silica surface modification and to exploit the adsorption properties, as well as the excellent chemical and thermal stability, the uniform pore size and distribution, high surface area, that affect the possibility to incorporate various nanomaterials (such as catalysts), made porous silica materials great potentials as strong support matrix in catalytic applications.[137]

| Geminal | Vicinal | Isolated | Interacting |
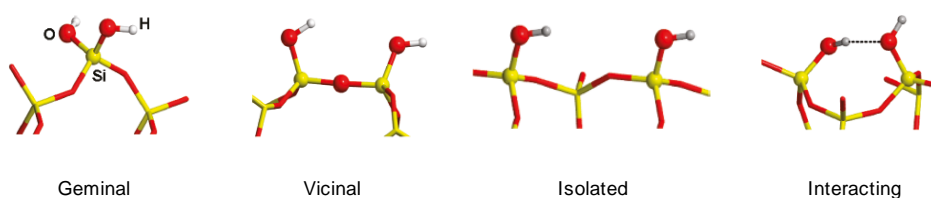
Figure 8. Different types of surface silanols commonly found at the silica surfaces. Figure obtained from the paper of Sodupe *et al.*[135]

The nature and the properties of a material surface, understood in its organic-inorganic entirety, play a key role in determining the physical and chemical properties of the materials, especially talking about heterogeneous catalysts.[138] The surface properties of a support can influence the metallic catalytic behavior by interacting with active metal sites, changing the chemical oxidation state, or affecting the formation of metal nanoparticles. This is particularly evident looking at metal ligands interactions, since they can impose stereo electronic effects, modify the electronic structure of the metal, and interfere with the metal/solvent boundaries.[37] On the other hand, the interposition of an organic flexible spacer between the ligand and the inorganic support represents an important strategy to increase the accessibility and the stability of metallic sites.[14]

Due to the impractical nature of infinitely recycling the metals, research is being directed to the utilization of more abundant and inexpensive metals, such as iron, cobalt, copper and nickel, in the place of precious metals.[139-144] Specifically, copper catalysis has received a great deal of attention in recent years.[145-149] In fact, copper has undergone thorough investigations in its role as a homogeneous catalyst and remarkable results have been achieved in many reactions, including oxidations, additions, C-C bond cleavage and Michael addition reactions.[150-154] Therefore, the development of stable Cu catalysts that can be used in heterogeneous conditions has recently attracted considerable interest. For example, copper nanoparticles that are supported over silica have been studied as efficient catalysts for the hydrogenation of

alkynes.[155] Furthermore, Cu that is supported over manganese oxide octahedral molecular sieves has been demonstrated to be an efficient catalyst for the synthesis of imidazoles.[156]

The purpose of Cu organic-inorganic hybrid systems resides in the possibility of synthesizing heterogeneous catalysts with the lowest possible metal dimensions in order to increase active surface area. The ambitious major objective in this field is therefore that of producing atomic-scale particles. This can be achieved *via* the selection of stable ligands for Cu that can be strongly anchored over the various solid supports. β-cyclodextrin (β-CD) has been demonstrated to be an attractive macromolecule for this purpose. β-CD is a cyclic oligosaccharide composed of seven linked D-glucopyranose units and that can be represented as a toroid structure with narrow and wide openings corresponding to the primary and secondary hydroxyl groups, respectively (Figure 9).[157] This peculiar structure means that β-CD can easily encapsulate copper and numerous other compounds.[158-160] They can be used as carriers and stabilizers and, when grafted on the external surface of inorganic supports,[161] can be exploited for the preparation of heterogeneous catalysts.[129, 162-165] They can be employed for the spatial control of the catalyst as a result of a chemical confinement of the metallorganic species.[166] β-CDs can be directly bound on the external surface of the inorganic support,[167] or they can be bound to the inorganic surface with the interposition of organic spacers.[14, 168, 169] Interestingly, β-CDs have been efficiently employed for coordinating Cu(II) in a sandwich-type coordinative inclusion complex[170] and the Cu(II)-CD complex has been already employed to perform click azide-alkyne cycloadditions,[171] C-C coupling of aryl boronic acids[172] and synthesis of oxazolidinones.[173] Interestingly, the click azide-alkyne cycloaddition is known to be catalyzed by Cu(I), which should be produced *in situ* from the CD-Cu(II) complexes.[174, 175] Moreover, several studies have proposed ingenious strategies for supporting Cu/β-CD complexes. For example, Moradi *et al.*, have recently stabilized Cu(II)/β-CD complexes over fibrous nanosilica and have successfully employed the material as a catalyst in the synthesis of oxazolidinones.[176] Xia and co-workers have prepared a magnetically recoverable catalyst made of Cu(II)/β-CD complexes anchored over ferric oxide and covered by silica.[177] Shafiee and co-workers, have reported the preparation of functionalized PEGylated mesoporous silica nanoparticle-graphene oxide as a catalyst for the synthesis of imidazoles.[163]
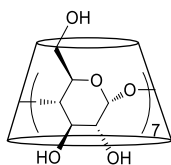
Figure 9. General structure of β-CD.

Herein, a detailed investigation into the influence of US irradiation on the reaction rate of silica derivatization to obtain β-CD-grafted silica is described. A number of routes were explored and compared with the aim of obtaining this class of peculiar organic-inorganic hybrid material using a highly reproducible, efficient synthetic protocol. Commonly employed silica-grafting

procedures entail long reaction times at high temperatures and the capability of US to shorten reaction times and operate at lower temperatures was demonstrated. Different covalently grafted silica-β-CD hybrid catalysts were prepared to study the influence of different flexible amino-bearing spacers on the catalytic activity and efficiency in catalytic applications. By supporting Cu(II) on the CD grafted silica, green and sustainable single-atom catalysts for click azido-alkyne cycloadditions were synthesized. The click 1,3-dipolar cycloaddition was optimized without the addition of a reducing agent because of the presence of CD. Complementary characterization techniques (infrared, X-ray absorption spectroscopy, TEM, UV-Vis in diffuse reflectance) were used to obtain detailed information on the surface functionalization of the silica support, on the oxidation state, local environment, and aggregation of the encapsulated/anchored Cu species, focusing on the stability and recyclability of the prepared materials.

2.2.   Results and discussion

2.2.1   Preparation of silica-β-CD derivatives

The silica surface modification was studied to investigate the importance of obtaining organic-inorganic hybrid systems *via* the grafting of silica material with organic compounds, that can lead to improve catalytic activity and may increase sorption capacity. The strategy focused on the use of β-CDs as stable ligands for Cu species, strongly anchored to the porous silica surface *via* flexible amino spacers to prepare silica-β-CD-Cu(II) derivatives, where the organic linker can contribute to Cu binding strength, influencing the catalytic activity and efficiency of organic-inorganic silica-based Cu(II) catalysts. Furthermore, the influence of US irradiation on the reaction rate of silica derivatization was investigated. Indeed, commonly employed silica-grafting procedures entail long reaction times at high temperatures and the capability of US to shorten reaction times and operate at lower temperatures was demonstrated. US irradiation is a non-conventional means to achieve efficient heating, dispersion, deagglomeration of solids and improvements in mass transfer. It offers a facile, versatile synthetic tool for the preparation of nano/microstructured materials that are often unavailable *via* conventional methods.

With the aim of offering highly reproducible and efficient synthetic protocol and in order to study the effect of amino-bearing spacers on metal stabilization, different hybrid systems were prepared by comparing three alternative synthetic routes:

(I) amino-β-CD was directly bound to the silica surface (procedure **a**, **d**, Scheme 1),

(II) β-CD was anchored to silica *via* a diethylentriamino spacer (procedure **a**, **b**, **c**, Scheme 1),

(III) or the silica was grafted with monoalkyl-trialkoxysilane derivatives by a condensation reaction (procedures **e, f** or **e**, **g**, Scheme 1).

25

In detail, procedure **a** follows the preliminary conversion of the silanol groups on the silica surface to silica chloride (Si-Cl) in the presence of thionyl chloride, as described in literature,[178, 179] and the resulting chloride ions were titrated with a silver nitrate solution in the presence of a potassium chromate solution, used as an indicator. 6^I-Amino-6^I-deoxy-β-CD was then reacted to obtain the Si-NH-CD derivative (procedure **d**). In the second route (procedure **b**), chlorinate silica was reacted with diethylenetriamine (DETA) and a nucleophilic substitution with 6^I-tosyl-β-CD was performed to obtain the Si-DETA-CD (procedure **c**). Alternatively, the preparation of Si-MonoAm-CD, Si-DiAm-CD and Si-TriAm-CD derivatives proceeds through the condensation reaction between the surface silanol groups and the monoamino, diamino and triamino alkoxysilanes (procedure **e**), followed by nucleophilic substitution with 6^I-tosyl-β-CD, respectively (procedure **f**). In a similar way Si-Gly was obtained reacting silica with an epoxy alkoxysilanes (procedure **e**), followed by the addition of 6^I amino-6^I-deoxy-β-CD (procedure **g**) to obtain Si-Gly-CD derivative. The structure of the above-mentioned and obtained organic-inorganic hybrid systems are clearly reported in Figure 10.
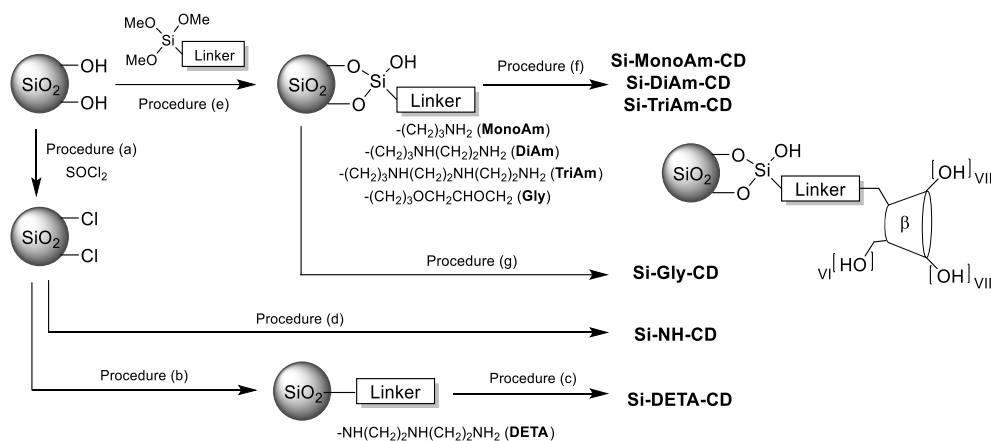
Scheme 1. Synthetic scheme for the preparation of silica-β-CD derivatives. Reaction conditions of procedure (a): silica was functionalized with SOCl₂; (**b**) Si-Cl was grafted with diethylenetriamine; (**c**) Si-DETA was reacted with 6^I-tosyl β-CD; (**d**) Si-CL was reacted with 6^I amino-6^I-deoxy-β-CD; (**e**) silica was grafted with alkyl alkoxysilanes; (**f**) Si-MonoAm, Si-DiAm, Si-TriAm were reacted with 6^I-tosyl β-CD; (**g**) Si-Gly was reacted with 6^I amino-6^I-deoxy-β-CD.
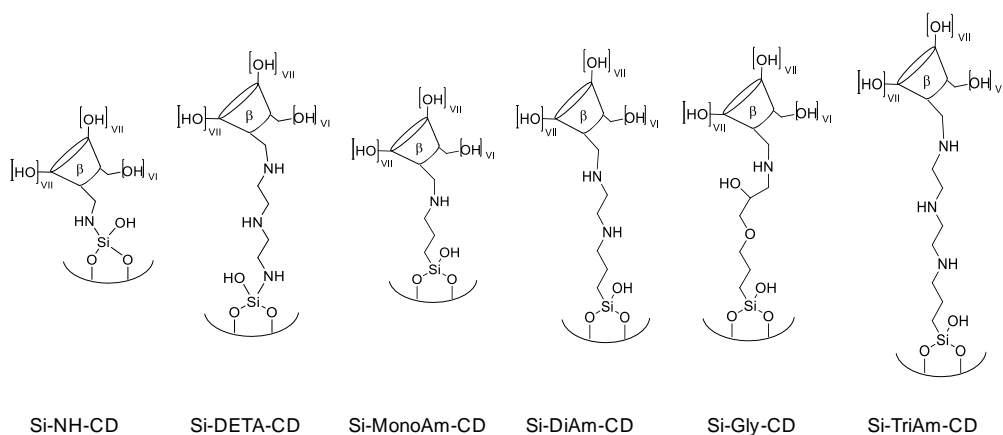
Figure 10. Structures of prepared silica-β-CD derivatives.

The loading and the identity of the synthesized silica derivatives were confirmed by thermogravimetric analysis (TGA) and UV-Vis spectroscopy. Complementary characterization techniques (infrared (FT-IR), X-ray absorption spectroscopy (XAS), TEM, UV-Vis in diffuse reflectance) were used to obtain detailed information about the surface functionalization of the silica support, the oxidation state, the local coordination environment and the aggregation of the encapsulated/anchored Cu species, focusing on the stability and recyclability of the prepared materials. TGA allows the grafting efficacy to be quantified by calculating the percentage weight loss in the TGA curve, assuming that water is the only compound removed from the starting silica by surface dehydroxylation. To circumvent any possible solvent influence on yield calculations, the curves are all normalized to 150 °C. In combination with TGA, the amount of β-CD was measured *via* titration with phenolphthalein (Php) in the buffer solution (pH = 10.5) at 0.008 mM.[180] The amount of grafted β-CD was measured on the basis of the loss of UV absorbance of Php when included in the β-CD cavity, *via* interpolation from the standard curve (Scheme 2). The change in Php absorbance was recorded on a UV spectrophotometer at 553 nm. The interaction between β-CD and Php was used to achieve the dual aims of measuring the amount of β-CD that maintains its inclusive properties when grafted onto the silica, and of investigating the inclusion capacity of the grafted β-CD.
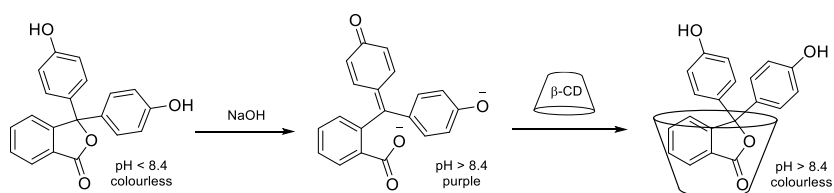
Scheme 2. Php and cyclodextrin inclusion complex.

More in detail, SIPERNAT 320 was used as amorphous silica, with a medium particle size and moderate absorption capacity. In order to optimize the reaction parameters for the silica derivatization, the preparation of Si-DETA-CD and Si-NHCD was first performed under different reaction conditions, as depicted in Table 4. When DETA was reacted with silica chloride, a number of solvents were compared under conventional conditions and a suspension of Si-Cl in toluene (entry 3, Table 4), chloroform (entry entry 1, Table 4) and DMF (entry 2, Table 4) was treated with the triamine derivative at 60 °C for 12 h. As represented in Figure 11, the TGA analyses of Si-DETA showed a higher degree of derivatization when toluene was used as the solvent. The first derivative peak temperature (315 °C) indicates the point of greatest rate of change on the weight loss curve, and the profile was consistent in all three samples. The synthetic process was also performed under US irradiation in order to reduce the reaction time and improve functionalization. Several different US irradiation frequencies (40 – 80 – 120 kHz) were used and compared. The reaction was irradiated for 2 (entries 4-6, Table 4) and 4 h (entries 10-12, Table 4), using toluene as solvent. For the sake of comparison, the results obtained in toluene, were compared to neat reactions (entries 7-9, 13-15, Table 4), where diethylenetriamine was used as solvent and reagent as well. As depicted in Table 4, the same degree of substitution, that was measured by TGA after 2 h of US irradiation (entry 5, Table 4), was achieved after 12 h at 60 °C (entry 2, Table 4), while after 4 h of US irradiation (entry 11, Table 4) the degree of substitution was maintained without improvement. Figure 12 shows the TGA profiles of Si-DETA batches obtained at different US frequencies, both in toluene and neat in 2 h. An increase in weight loss was observed when the reactions were subjected to 80 kHz irradiation. 40 kHz and 120 kHz fail to give the maximum degree of substitution under both sets of reaction conditions.

Entry	Product	Reaction condition	Time	Loading (w/w %)	Loading (µmol/g)
1	Si-DETA	Si-Cl, DETA, CHCl₃, reflux	12 h	14.1[a]	$1.37 \cdot 10^3$ [b]
2	Si-DETA	Si-Cl, DETA, DMF, 60 °C	12 h	10.0[a]	$0.96 \cdot 10^3$ [b]
3	Si-DETA	Si-Cl, DETA, toluene, 60 °C	12 h	15.7[a]	$1.49 \cdot 10^3$ [b]
4	Si-DETA	Si-Cl, DETA, toluene, US, 40 kHz	2 h	9.5[a]	$0.87 \cdot 10^3$ [b]
5	Si-DETA	Si-Cl, DETA, toluene, US, 80 kHz	2 h	14.8[a]	$1.35 \cdot 10^3$ [b]
6	Si-DETA	Si-Cl, DETA, toluene, US, 120 kHz	2 h	11.5[a]	$1.12 \cdot 10^3$ [b]
7	Si-DETA	Si-Cl, DETA, neat, US, 40 kHz	2 h	7.1[a]	$0.69 \cdot 10^3$ [b]
8	Si-DETA	Si-Cl, DETA, neat, US, 80 kHz	2 h	13.9[a]	$1.26 \cdot 10^3$ [b]
9	Si-DETA	Si-Cl, DETA, neat, US, 120 kHz	2 h	8.2[a]	$0.79 \cdot 10^3$ [b]
10	Si-DETA	Si-Cl, DETA, toluene, US, 40 kHz	4 h	10.3[a]	$0.97 \cdot 10^3$ [b]
11	Si-DETA	Si-Cl, DETA, toluene, US, 80 kHz	4 h	14.3[a]	$1.12 \cdot 10^3$ [b]
12	Si-DETA	Si-Cl, DETA, toluene, US, 120 kHz	4 h	10.9[a]	$0.97 \cdot 10^3$ [b]
13	Si-DETA	Si-Cl, DETA, neat, US, 40 kHz	4 h	8.2[a]	$0.77 \cdot 10^3$ [b]
14	Si-DETA	Si-Cl, DETA, neat, US, 80 kHz	4 h	13.5[a]	$1.26 \cdot 10^3$ [b]
15	Si-DETA	Si-Cl, DETA, neat, US, 120 kHz	4 h	9.1[a]	$0.88 \cdot 10^3$ [b]

Preparation of Si-DETA: Si-Cl (0.100 g), solvent (0.500 mL) and diethylenetriamine (0.500 mL). a) the w/w % grafting was measured on the basis of TGA; b) mmol/g values were measured on the basis of TGA considering the organic moiety anchored to the silica surface.
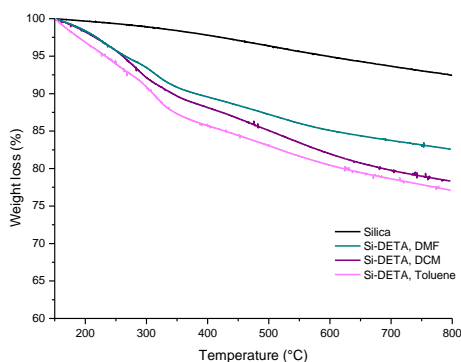
Figure 11. TGA profiles of starting silica and Si-DETA prepared using three different solvents.
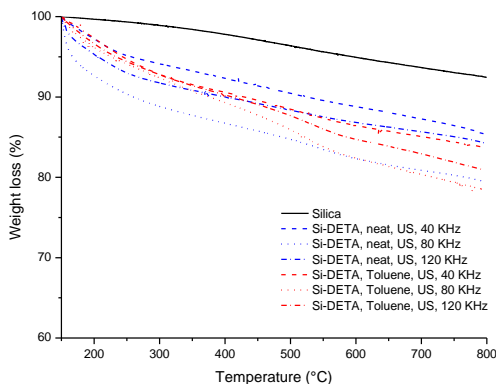
Figure 12. TGA profiles of silica and Si-DETA obtained using US irradiation at different frequencies (40 – 80 – 120 kHz), in neat conditions and in toluene.

When β-CD was grafted onto Si-DETA *via* the nucleophilic replacement of 6^I-tosyl β-CD, the reaction was performed conventionally in DMF at 70 °C for 24 h. Looking at TGA (Figure 13), an instability of the system was observed, due to the detachment of DETA from the silica surface, as the organic moiety was reduced in weight after the reaction, when compared to the starting material. When the grafting of β-CD was performed under conventional heating, by UV absorbance of the Php solution the presence of solid supported β-CD was detected and measured a w/w % of grafting of 1.3 mg/100 mg (entry 1, Table 4). The same sample analyzed by TGA showed a decrease in total weight loss in the range 150 °C - 800 °C when compared to the starting Si-DETA derivative. Based on this fact, the instability of the precursor under the reaction conditions was assumed, as furthermore confirmed by infrared analysis described below. Under US irradiation at 80 kHz, the grafting percentage increased to 3.3% w/w, and PhP titration confirmed the derivatization data (entry 2, Table 4). Unfortunately, it was observed that the preparation of Si-DETA-CD was not reproducible, and so a direct grafting of 6^I amino β-CD to Si-Cl was performed (procedure **d**, Scheme 1).

As described in Table 4, when 6^I-amino-6^I-deoxy-β-CD was reacted with Si-Cl for 12 h at 60 °C in DMF, a w/w % degree of derivatization of 4% was detected by TGA (entry 3, Table 4), while PhP titration detected only 1.0% of β-CD, providing an inconclusive answer to the preservations of its inclusive properties. When the reaction was tested under US irradiation at 80 kHz, comparing DMF and H_2O as solvents, a higher percent of grafting was observed when water was used (entries 6, 8, Table 4). When the reaction was repeated to compare longer reaction times, the reaction reached the same degree of derivatization in 2 h (entries 5-6, Table 4). After 4 h no improvement was observed (entries 7-8).

Table 4. Synthesis of β-CD grafted silica

Entry	Product	Reaction condition	Time	Loading (w/w %)	Loading (µmol/g)
1	Si-DETA-CD	Si-DETA, 6-tosyl β-CD, DMF, 70 °C	24 h	1.3[b]	11[d]
2	Si-DETA-CD	Si-DETA, 6-tosyl β-CD, DMF, US, 80 kHz	4 h	3.3[a]-3.4[b]	30[c]
3	Si-NHCD	Si-Cl, 6-amino β-CD, DMF, 60 °C	12 h	4.0[a]-1.0[b]	35[c]
4	Si-NHCD	Si-Cl, 6-amino β-CD, H$_2$O, 60 °C	12 h	2.6[a]-0.8[b]	20[c]
5	Si-NHCD	Si-Cl, 6-amino β-CD, DMF, US, 80 kHz,	2 h	3.8[a]-0.7[b]	30[c]
6	Si-NHCD	Si-Cl, 6-amino β-CD, H$_2$O, US, 80 kHz,	2 h	7.1[a]-0.6[b]	60[c]
7	Si-NHCD	Si-Cl, 6-amino β-CD, DMF, US, 80 kHz,	4 h	3.5[a]-0.7[b]	30[c]
8	Si-NHCD	Si-Cl, 6-amino β-CD, H$_2$O, US, 80 kHz,	4 h	6.8[a]-0.7[b]	60[c]

Preparation of Si-DETA-CD: Si-DETA (0.100 g), DMF (1.7 mL), 6^I-tosyl-β-CD (0.100 g). Preparation of Si-NHCD: Si-Cl (0.100 g), solvent (2 mL), 6-amino β-CD (0.163 g). a) the w/w % grafting was measured on the basis of TGA; b) the w/w % grafting was based on PhP titration; c) mmol/g values were measured on the basis of TGA considering the organic moiety anchored to the silica surface; d) mmol/g of β-CD based on PhP titration.
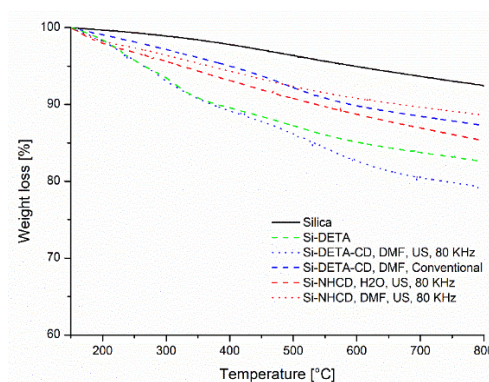
Figure 13. TGA profile of starting silica, Si-DETA, Si-NHCD and Si-DETA-CD prepared conventionally or under US irradiation.

2.2.2. *Preparation of copper supported on Si-NH-CD and Si-DETA-CD*

Based on the fact that copper(II) forms a complex with CD in alkaline solution, Si-DETA-CD and Si-NH-CD were loaded with Cu(II). CuSO$_4$ was chosen as Cu(II) ion source. The complexation reaction was performed reacting CuSO$_4$ with silica-CD derivatives in a NaOH water solution and a blue colored catalyst was obtained (Figure 14). The CD-Cu(II) complexes with α- and β-CDs have already been isolated and characterised.[181, 182] The efficacy of β-CD to direct and bind Cu when CD is bonded to silica has been already studied and its catalytic activity as a Lewis acid has been demonstrated.[173] As the literature has focused mainly on the non-

covalent bonding of β-CD onto the silica surface,[164, 165, 183] the efficacy of covalently grafted β-CD onto silica was explored and its ability to chelate Cu(II) was investigated. These systems were exploited as catalyst for alkyne-azide cycloaddition (CuAAC).

Figure 14. Illustration of Si-DETA-CD and Si-DETA-CD-Cu(II).

2.2.3. *Characterization of Si-NH-CD, Si-DETA-CD and related copper-supported derivatives*

Si-DETA, Si-DETA-CD and Si-NHCD were characterized by IR to prove the identity of the grafted silica. The same was done for Si-DETA-CD-Cu and Si-NHCD-Cu. As shown in Figure 15, the presence of the diethylentriamino spacer on Si-DETA can be observed in spectrum a. This is characterized by a broad absorption band centred around 3000 cm^{-1}, which can be ascribed to hydrogen-bonded Si-OH and N-H groups.[184] The expected νNH bands can be only seen as a modulation of the intense absorption, between 3400 and 3200 cm^{-1}. The corresponding weak δNH$_2$ mode is vibrating at similar frequency as physisorbed water (around 1600 cm^{-1}), while the band at 1510 cm^{-1} can be ascribed to the δNH vibrations of the secondary amines. Important changes can be observed in the spectrum (curve b) after the reaction with 6^{I}-tosyl-β-CD (and subsequent Cu inclusion). Namely, the high frequency region is dominated by an intense band centred at 3360 cm^{-1} (νOH), with clear νCH/νCH$_2$ bands at 2930 cm^{-1} (shoulder at 2860 cm^{-1}). The low frequency region shows the typical bending mode of physisorbed water δH$_2$O centred at 1603 cm^{-1} (shoulder at 1662 cm^{-1}), and a complex group of bands with between 1500 and 1250 cm^{-1} (δCH and δOH). These features can be safely ascribed to the presence of β-CD, even if the assignment of the shoulder at 1662 cm^{-1} to physisorbed water alone is not straightforward. Similar results were obtained with the sample prepared with direct Si-NH-CD (curve e). The main difference is in the relative intensity of the bands assigned to δH$_2$O modes. A comparison of the spectra of β-CD and Cu-CD has led us to propose that this vibrational mode is sensitive to the presence of the Cu(II) ions included in the cavity and at the rim of the CD cavity. These results thus confirm the presence of β-CD on the silica in the various preparations. However, the changes in the high frequency region passing from Si-DETA to Si-DETA-CD (curves a and b), suggest a decrease in the amount of the diethylentriamino spacer, confirming the instability of Si-DETA when submitted to reaction with 6^{I}-tosyl-β-CD. Hydroxyl group of CD may act as nucleophile, as well as DETA cannot be efficiently and

reproducibly washed from the silica surface because of strong interactions with surface silanol/ silanolate groups.[185]
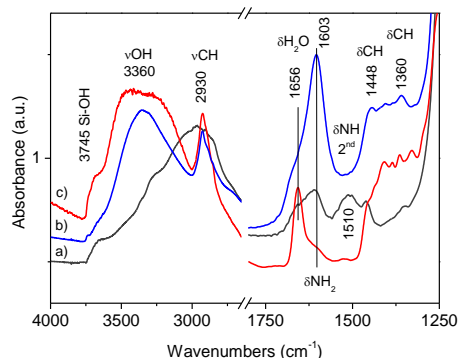
Figure 15. Infrared spectra of a) Si-DETA; b) Si-DETA-CD-Cu, c) Si-NHCD. All samples were degassed at 80 °C before measurements.

The presence of Cu on the catalysts was monitored by Diffuse Reflectance UV-Vis-NIR spectroscopy (Figure 16). For example, the spectrum of Si-NHCD-Cu (blue curve) is compared to the spectra of the reference materials (β-CD, SiO_2 and Si-NHCD). The spectra can be divided into three regions: i) UV (200-400 nm), corresponding to $O^{2-} \rightarrow$ Cu(II) Charge Transfer (CT) transitions; ii) Visible (400-800 nm), corresponding to the ligand-field d-d transitions of Cu(II) ions; and iii) NIR (800-2500 nm), where the overtone and combination modes of infrared modes can be observed. The NIR region analysis allows us to further confirm the presence of the CDs that are linked to the silica support, and to confirm the involvement of OH groups in the coordination of the Cu ions. Indeed, all the hybrid-material spectra show signals, in this region, that are a mixture of the vibrational modes of SiO_2 (Si-OH overtone $\nu_{0-2\ OH}$, $\nu+\delta_{H2O}/\nu+\delta_{OH}$ combination modes of physisorbed water and of Si-OH groups) and those of CD ($\nu_{0-2\ OH}$, $\nu+\delta_{H2O}$, $\nu_{0-2\ CH}$, $\nu_{OH}+\nu_{CO}$). On the other hand, the UV-Vis region of Si-NHCD-Cu clearly shows the typical fingerprint of hexacoordinated Cu(II) ions, with a CT component at 260 nm and an intense and broad d-d band at 700 nm.[186] These results are in agreement with the structures proposed in Ref [187], which involve hexacoordinated Cu(II) ions in the cavity and at the rim of the CD cavity, coordinated by H_2O molecules, OH/O^- CD groups and/or extra ligands.

ICP analyses of Si-NHCD-Cu and Si-DETA-CD-Cu quantified the Cu content on the Silica: at 10.1 mg/g and 7.2 mg/g of Cu, respectively.
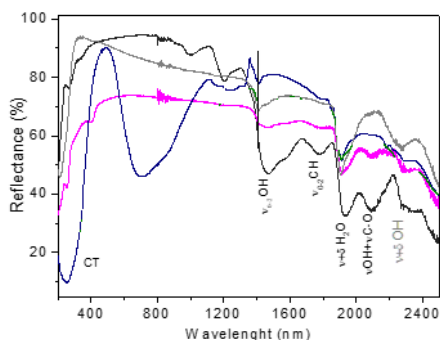
Figure 16. DR UV-Vis-NIR spectra of: SiO$_2$ (grey); β-CD (black); Si-NHCD (pink) and Si-NHCD-Cu (blue).

2.2.4. *Preparation of silica-polyamino-β-CD derivatives*

In order to obtain a stable silica-supported β-CD derivative with a polyamino spacer, the synthetic approach was changed, moving from the direct functionalization of silica surface with amino function, to the condensation reaction between the silanol group of the silica surface and alkoxysilane derivatives, to interpose an alkylic portion between silica atoms and the amino functionalities. The external surface of the inorganic material was grafted with a thin organic layer thanks to the beneficial effects of US irradiation that maximize the grafting loading. Preliminary, Si-diAm-CD was synthesized: silica was derivatized with 3-(2-aminoethylamino)propyltrimethoxysilane (AEPS) to obtain Si-diAm. As described in Table 5, US irradiation reduced the reaction time to 2 h (entries 3-5, Table 5), whereas the same degree of substitution was achieved after 36 h at 80 °C under conventional heating and magnetic stirring entry 2, Table 5). No differences in activation were observed comparing the use of 40 and 80 kHz and both were very efficient (entries 3-4, Table 5). In order to obtain the efficient grafting of β-CD, 6-O-tosyl β-CD was reacted at 60 °C for 60 h and 4.7% w/w derivatization was observed by TGA, while 2.15% was measured by Php titration (entry 6, Table 5). US irradiation at 80 kHz in a US bath was insufficient to obtain a satisfactory grafting percent, because of the low reaction temperature (45 - 50 °C) (entry 8, Table 5). An increase in grafting percentage was observed when the reaction was prolonged to 6 days (entry 7, Table 5). The synergic effect of combined MW and US irradiation was also exploited. Enhancing the silica dispersion, increasing the active surface and allowing a selective MW irradiation, the combined system permit to obtain high efficacy of grafting in short time, 4 h, and 6.1% w/w derivatization was afforded (entry 9, Table 5). As depicted in Figure 17, the first derivative TGA profile of Si-diAm indicated that the degradation peak was approximately at 314 °C, when CD was grafted two degradation steps were visible, the peaks were at 298 °C and at 413 °C.

Table 5. Synthesis of Si-diAm-CD

Entry	Product	Reaction conditions	Time	Loading (w/w%)	Loading (µmol/g)
1	Si-diAm	Silica, AEPS, toluene, 80 °C	6 h	6.5[a]	290[c]
2	Si-diAm	Silica, AEPS, toluene, 80 °C	36 h	13.6[a]	610[c]
3	Si-diAm	Silica, AEPS, toluene, US, 40 kHz	2 h	14.0[a]	640[c]
4	Si-diAm	Silica, AEPS, toluene, US, 80 kHz	2 h	12.1[a]	540[c]
5	Si-diAm	Silica, AEPS, toluene, US, 80 kHz	4 h	13.3[a]	600[c]
6	Si-diAm-CD	Si-diAm, 6^I-tosyl-β-CD, DMF, 60 °C	60 h	4.7[a]-2.15[b]	42[c]
7	Si-diAm-CD	Si-diAm, 6^I-tosyl-β-CD, DMF, 60 °C	6 days	6.1[a]-2.8[b]	54[c]
8	Si-diAm-CD	Si-diAm, 6^I-tosyl-β-CD, DMF, US, 80 kHz	4 h	1.7[a]-1.18[b]	15[c]
9	Si-diAm-CD	Si-diAm, 6^I-tosyl-β-CD, DMF, MW/US, 100 °C	4 h	6.1[a]-2.09[b]	54[c]

Preparation of Si-diAm: silica powder (0.100 g), toluene (1 mL), AEPS (0.040 mL). Preparation of Si-diAm-CD: Si-diAm (0.100 g), DMF (1.5 mL), 6^I-tosyl-β-CD (0.100 g). a) measured by TGA, the weight loss was calculated on the basis of the starting material; b) the w/w % grafting was based on PhP titration; c) mmol/g of organic moiety grafted on silica surface.
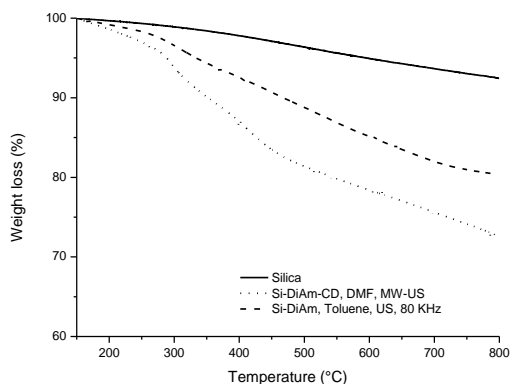
Figure 17. TGA profile of Si-DiAm obtained in US at 80 kHz, 2 h, toluene and Si-DiAm-CD obtained in MW-US combined irradiation at 100 °C, 4 h, DMF.

The same preparation procedure was followed to prepare Si-monoAm-CD and Si-TriAm-CD. Efficient grafting of β-CD was achieved in 4 h at 100 °C in a combined MW–US reactor (procedure **f**, Scheme 1). In the same way, 6^I amino-6^I-deoxy-β-CD was reacted with Si-Gly to obtain Si-Gly-CD (procedure **g**, Scheme 1).

The loading and the identity of the synthesized silica derivatives were confirmed by TGA and infrared spectroscopy. As shown in Figure 18, TGA analyses of Si-Gly, Si-MonoAm, Si-DiAm and Si-TriAm showed a high degree of derivatization, from 6 to 12 w/w %, as reported in Table 6. The first derivative peak temperature was detected at 406 °C in Si-TriAm, 486 °C in Si-Gly, 495 °C in Si-MonoAm and 314 °C in Si-DiAm, and profiles were consistent in all samples. When

Si-MonoAm-CD, Si-DiAm-CD and Si-TriAm-CD were analyzed, 3.8% w/w, 7.6% w/w and 7.7% w/w of β-CD derivatization were observed by TGA (34; 67, 68 µmol/g, respectively). The Php titration showed that from 1.3% to 3.6% w/w of CD was available for making inclusion complexes (11 to 32 µmol/g). In Si-Gly-CD, 6.1% w/w (54 µmol/g) of derivatization was afforded by TGA and 1.0% w/w (9 µmol/g) was registered by Php titration. As shown in Figure 18, the TGA profile of Si-MonoAm-CD indicated that two degradation peaks, approximately at 360 °C and 519 °C, were visible, as well as in Si-Gly-CD (347 °C and 572 °C). When CD was grafted to Si-DiAm, two degradation steps were visible and were at 298 °C and 413 °C, as well as in Si-TriAm (339 °C and 584 °C). Moreover, from TGA it was confirmed that the use of condensation reaction between silanol groups of the silica surface and alkoxy silane generated more stable amine-bearing silica materials then the Si-DETA derivative, which showed a lower thermal stability. Finally, Si-Gly-CD, Si-MonoAm-CD, Si-DiAm-CD and Si-TriAm-CD were loaded with Cu(II) in basic conditions, as previously described for Si-NHCD and Si-DETA-CD, and characterized by IR and DR UV-Vis-NIR.

Table 6. Synthesis of grafted silica.

Entry	Product	Linker	Loading (w/w%)	Loading (µmol/g)
1	Si-MonoAm	$-(CH_2)_3NH_2$	$9.2^{(a)}$	$513^{(a)}$
2	Si-TriAm	$-(CH_2)_3NH(CH_2)_2NH(CH_2)_2NH_2$	$10.4^{(a)}$	$390^{(a)}$
3	Si-Gly	$-(CH_2)_3OCH_2CHOCH_2$	$6.1^{(a)}$	$259^{(a)}$
4	Si-MonoAm-CD	$-(CH_2)_3NH-β-CD$	$3.8^{(b)}–1.3^{(c)}$	$34^{(b)}–11^{(c)}$
5	Si-TriAm-CD	$-(CH_2)_3NH(CH_2)_2NH(CH_2)_2NH-β-CD$	$7.7^{(b)}–3.6^{(c)}$	$68^{(b)}–32^{(c)}$
6	Si-Gly-CD	$-(CH_2)_3OCH_2CHOHCH_2-β-CD$	$6.1^{(b)}–1.0^{(c)}$	$54^{(b)}–9.2^{(c)}$

Preparation of Si-Gly, Si-MonoAm, Si-DiAm, Si-TriAm: silica powder (0.100 g), toluene (1 mL), epoxy, mono or poly amino alkoxy silane derivatives (0.040 mL), US (80 kHz, 2 h). Preparation of Si-MonoAm-CD, Si-DiAm-CD, Si-TriAm-CD: Si-MonoAm, Si-DiAm or Si-TriAm (1 g), DMF (15 mL), 6^I-tosyl-β-CD (1 g), MW/US (100 °C, 4 h). Preparation of Si-Gly-CD: Si-Gly (1 g), DMF (15 mL), 6^I amino-6^I-deoxy-β-CD (1 g), MW/US (100 °C, 4 h) (a) measured by TGA; (b) β-CD grafting measured by TGA; (c) β-CD grafting measured by PhP titration.
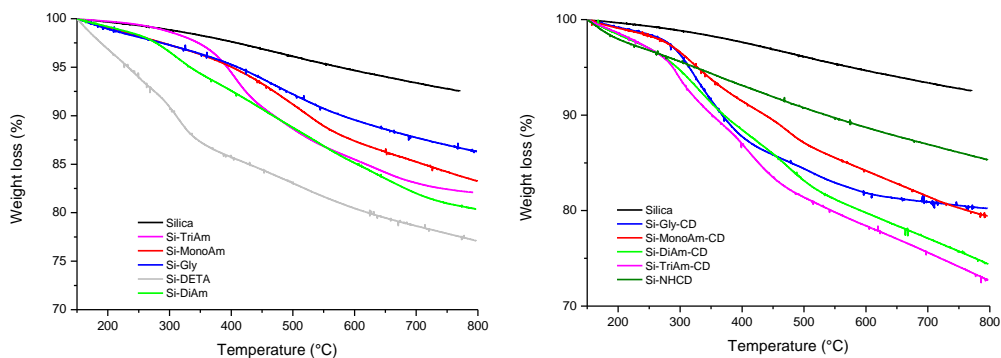
Figure 18. TGA profiles of organic inorganic silica derivatives.

2.2.5. *Characterization of silica-polyamino-β-CD derivatives*

The prepared materials were characterized by infrared and diffuse reflectance (DR) UV-Vis spectroscopies, to assess the molecular structure of the final products. The infrared spectra of the four samples (Figure 19a) showed the fingerprint modes of CD between 1500 and 1250 cm^{-1} (δCH and δOH bending modes) with variable intensity and shape. The intense peak at 1664 cm^{-1}, labeled with a star, can be ascribed to the presence of residual DMF solvent. The effective bonding of the functional groups was furthermore proven by the intense CH/CH$_2$ stretching modes (νCH/CH$_2$) at 2928 and 2856 cm^{-1}. These are superimposed to the broad absorption related to hydrogen bonded -OH and -NH groups, including OH groups from the CD rings and Si-OH groups from the silica surface.[175, 184] Both Si-DiAm-CD-Cu and Si-TriAm-CD showed a component around 1596 cm^{-1}, typical of the bending mode of primary amines (δNH$_2$), which would indicate an incomplete reaction of the amino groups with CDs.

Weak overtone modes of the νCH and νNH vibrations (ν_{0-2}) can be also appreciated in the low energy region of the corresponding DR UV-Vis spectra (Figure 19b), which are reported in reflectance mode (negative peaks), to avoid artefacts related to the Kubelka–Munk conversion. Apart from sample Si-Gly-CD-Cu, which showed relatively weak peaks in the whole spectral range, the three samples functionalized with amino groups very clearly showed the typical d-d transition of Cu(II) ions around 700 nm, though with some difference in the band width and position. In agreement with previous reports, this can be used as a fingerprint of Cu(II) ions stabilized in the cavity. These could be hexacoordinated, as a result of coordination by H$_2$O, OH/O$^-$ CD groups or extra-ligands,[188] or have lower coordination, in square planar geometry.[189]

ICP analysis of Si-DiAm-CD-Cu(II) and Si-TriAm-CD-Cu(II) showed a loading of 15.5 and 14.9 mg/g of copper, respectively.

37
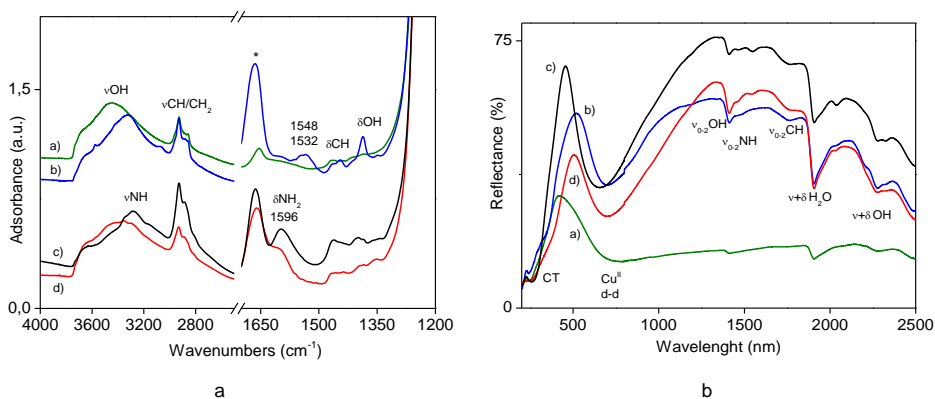
Figure 19. (a) Infrared and (b) diffuse reflectance UV-Vis spectra of (spectrum a) Si-Gly-CD-Cu; (spectrum b) Si-MonoAm-CD-Cu; (spectrum c) Si-DiAm-CD-Cu; (spectrum d) Si-TriAm-CD-Cu. Before infrared measurements samples were outgassed at 80 °C to remove adsorbed water and impurities. The peak labeled with * can be related to DMF residual solvent.

2.2.6. *Catalytic activity of organic-inorganic silica-supported β-CD-Cu(II)*

The catalysts were tested in CuAAC reaction without the addition of a reducing agent, because of the presence of β-CD.[190] The cyclisation of benzyl azide and phenylacetylene was chosen as model reaction (Scheme 3). It was repeated under a number of reaction conditions and different copper sources were compared. The reaction was performed under conventional heating or MW irradiation, and similar results were obtained reducing the reaction time from 1 h in batch to 20 min in the MW reactor. $Cu(OAc)_2$ and $CuSO_4$ were tested as Cu(II) salts, and the reaction was compared to a click reaction that was catalyzed by a previously prepared Cu(II)-β-CD complex, and a reaction using a physical mixture of $CuSO_4$ and β-CD. Only the Cu(II)-β-CD complex gave satisfactory results and a 55% yield was obtained, confirming the importance of the Cu(II)-β-CD complex to exploit the reductive ability of the β-CD. Si-NHCD-Cu and Si-DETA-CD-Cu showed different catalytic activities. In fact, only the second acted as an efficient catalyst for CuAAC (Table 7). As already observed in the Php titrations, it shows a higher inclusion capability when CD is bound to the silica with a spacer, furthermore, the triamino spacer can stabilize Cu(II) species. Si-DETA-CD-Cu shows high efficiency even when used in very small amounts. However, a reduction of activity was observed when the catalyst amount was decreased to 0.5 mol%. In order to understand the influence of silica and the amino spacer on the reaction outcome, Si-Cu and Si-DETA-Cu were tested to further confirm that the complex between the copper ions and β-CD plays a key role in the performance of the reaction, in which β-CD acts as ligand for copper and reducing agent. The interaction between β-CD and Cu ions could implicate the reduction of Cu(II) to Cu(I), as proven afterwards by XAS.

38
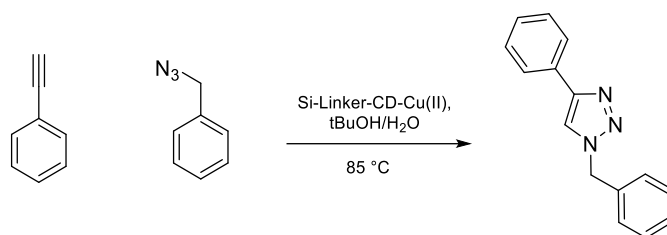
Scheme 3. Model reaction for CuAAC test of Si-Linker-CD-Cu.

Table 7. Panel test of CuAAC reaction.

Entry	Catalyst, Cu mol%	Cu mol%	Yield (%)[a]
1	Cu(OAc)$_2$	5	14
2	CuSO$_4$	5	0
3	β-CD-CuSO$_4$ (physical mixture)	5	0
4	β-CD-Cu (complex)	5	55
5	Si-NHCD-Cu	4	5
6	Si-DETA-CD-Cu	4	>99
7	Si-DETA-CD-Cu	2	>99
8	Si-DETA-CD-Cu	1	>99
9	Si-DETA-CD-Cu	0.5	80
12	Silica-Cu	5	4
13	Si-DETA-Cu	5	0

Reaction conditions: benzyl azide (0,0676 mmol, 1 eq), phenylacetylene (1 eq), H$_2$O:tBuOH (1:1; 500 μL), 85 °C, 1 h or 85 °C, 20 min. (a) Determined by GC-MS.

Based on the catalytic activity of silica-supported β-CD-Cu(II) previously reported, the silica-polyamino-CD-Cu(II) derivatives, obtained *via* the condensation reaction, were tested in alkyne-azide cycloaddition, as well. CuAAC were conducted in the absence of reducing agents because of the interaction between β-CD and Cu ions, that could implicate the reduction of Cu(II) to Cu(I), as already mentioned and proven afterwards by XAS. Again, the model reaction between benzyl azide and phenylacetylene was chosen to compare the catalytic activity of the silica-polyamino-CD-Cu(II) derivatives. Among them, the most active silica catalysts towards the CuAAC model reaction in absence of reducing agents, were proven to be Si-DiAm-CD-CU and Si-TriAm-CD-Cu, assuming that the amino-bearing spacer can stabilize Cu(II) species and it allows Cu ions to be more accessible (Table 8). When the catalytic activity was tested using a different combination of alkylic and arylic azido and alkynes derivatives, a slightly higher amount of catalyst was employed in order to obtain full conversion, as well as when more demanding synthesis of dimers, in the presence of diazide or dialkynyl derivatives, were tested.
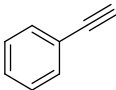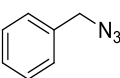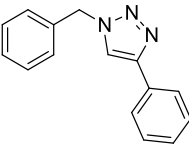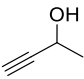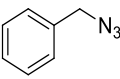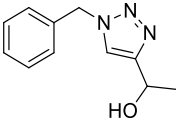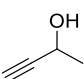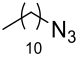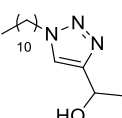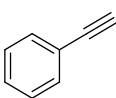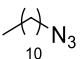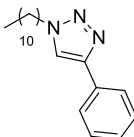
These reactions were fully converted in the presence of 4 or 8.7 mol% of catalyst, and the products were isolated without further purification. Thus, the reaction applicability on different types of reagents, the efficacy and the versatility of the systems were proven.

Table 8. Panel test of CuAAC reaction.

Entry	Catalyst	Cu mol%	Yield (%)[a]
1	Si-DiAm-CD-Cu	4	>99
2	Si-DiAm-CD-Cu	2	65
3	Si-Gly-CD-Cu	4	45
4	Si-MonoAm-CD-Cu	4	4
5	Si-TriAm-CD-Cu	4	>99
6	Si-TriAm-CD-Cu	2	>99
7	Si-TriAm-CD-Cu	1	85

Reaction conditions: benzyl azide (0.0676 mmol, 1 eq), phenylacetylene (1 eq), H_2O:tBuOH (1:1; 500 µL), 85 °C, 1 h. (a) Yields determined by GC-MS.
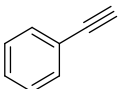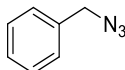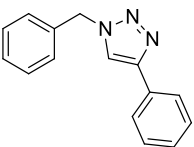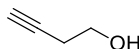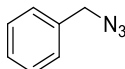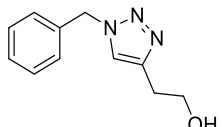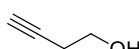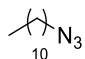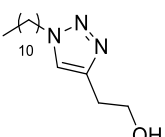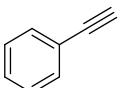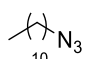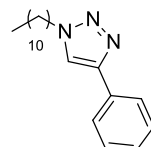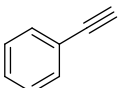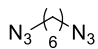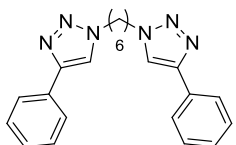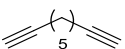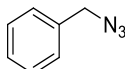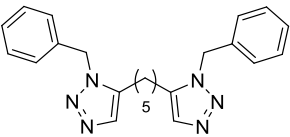
Table 9. Synthetic results of CuAAC, using Si-DiAm-CD-Cu.

Entry	Alkyne	Azide	Product	Yield (%)[a]
1				99
2				95
3				92
4				89

Reaction conditions: azide (0,0676 mmol, 1 eq), terminal alkyne (1 eq), H_2O (250 µL), tBuOH (250 µL), 11 mg of catalyst (4 mol %), 85 °C, 1 h or MW, 85 °C, 20 min. a) Yields determined by GC-MS.

Table 10. Synthetic results of CuAAC, using Si-TriAm-CD-Cu.

Entry	Alkyne	Azide	Product	Yield (%)[a]
1				99
2				99[b]
3				99[b]
4				99[b]
5				99[c]
6				99[d]

(a) Yields determined by GC-MS. Reaction conditions: azide (0.0676 mmol, 1 eq), terminal alkyne (1 eq), H_2O (250 µL), tBuOH (250 µL), catalyst (4 mol%), 85 °C, 1 h; (b) catalyst (8.7 mol%), reaction time 5 h; (c) terminal alkyne (2 eq), catalyst (8.7 mol%), reaction time 5 h; (d) azide (2 eq), catalyst (8.7 mol%), reaction time 5 h.

A study on the recoverability and recyclability of Si-DiAm-CD-Cu and Si-TriAm-CD-Cu catalysts was performed on a CuAAC model reaction. The following reaction conditions were used: reaction temperature of 85 °C; H_2O/tBuOH ratio of 1:1; reaction time of 1 h; amount of catalyst 4 mol%. The catalysts were recovered by filtering the reaction mixture and washing with water, methanol and chloroform. After drying, they were reused in the reaction. Graph 4 displays the performance of the reused catalysts. After four cycles, the reaction yield using Si-TriAm-CD-Cu was 44%. The recovery of the catalyst indicates its good structural stability and high reactive activity. If compared to Si-DiAm-CD-Cu catalyst, it shows higher stability. The reaction yield of Si-DiAm-CD-Cu was 78% in the second reuse, and 30% in the third cycle.
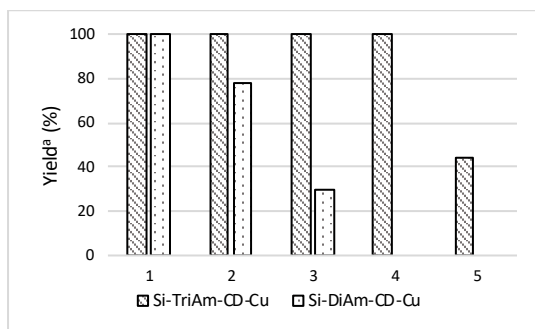
Graph 4. Recyclability of Si-TriAm-CD-Cu, compared to Si-DiAm-CD-Cu, in the CuAAC model reaction.

2.2.7. *Characterization of aged Si-TriAm-CD-Cu catalyst*

Sample Si-TriAm-CD-Cu was further characterized after the catalytic tests by infrared, DR UV-Vis and X-ray absorption (XAS) spectroscopies. The infrared spectrum measured on the sample recovered after catalytic tests was indistinguishable from that of the as-prepared material, indicating the stability of the grafted groups (Figure 20a). Some differences instead were observed in the DR UV-Vis spectra (Figure 20b), particularly in the intensity of the Cu(II) band. The comparison is not quantitative, since the exhaust sample (five-time reused catalyst) was measured after dilution in Teflon, due to the small amount recovered from the catalytic tests. The reported spectrum was indeed roughly normalized with respect to the overtone/combination modes in the NIR region ($v + \delta$ of H_2O and OH). Notwithstanding these limitations, the results were in agreement with a decrease in the amount of Cu(II) in the catalyst, which can be tentatively related to a partial reduction to Cu(I), which was silent in the UV-Vis d-d region being a closed shell d^{10} ion. This hypothesis was further investigated by XAS (see below).

a

b
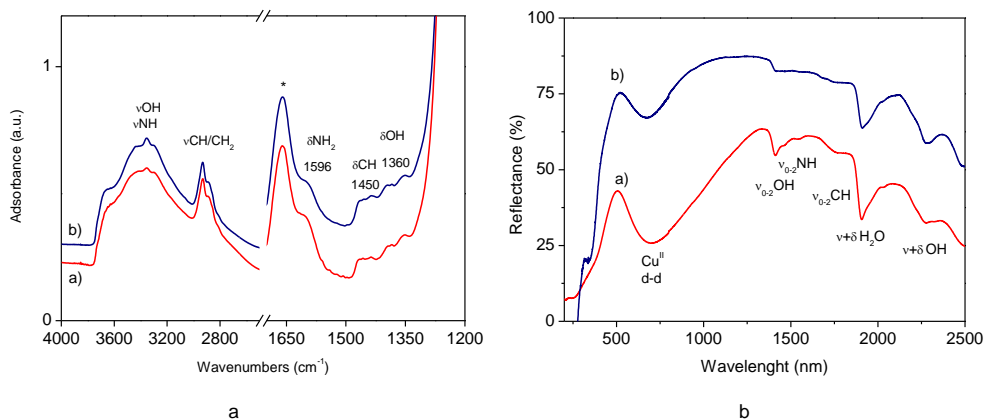
Figure 20. (a) Infrared and (b) diffuse reflectance UV-Vis spectra of (spectrum a) Si-TriAm-CD-Cu; (spectrum b) Si-TriAm-CD-Cu-exhausted. Before infrared measurements samples were degassed at 80 °C to remove adsorbed water and impurities. Sample Si-TriAm-CD-Cu-exhausted was diluted in Teflon for Diffuse-Reflectance (DR) UV-Vis

measurement. The corresponding curve was arbitrarily normalized to the intensity of the overtone/combination modes of the support (X 2.5).

To obtain more insight on the oxidation state and local coordination environment of the Cu centers in Si-TriAm-CD-Cu, the as-prepared vs. exhaust catalyst by Cu K-edge XAS were characterized. The technique, combining element-selective response with simultaneous sensitivity to local electronic and structural properties of Cu-species,[191, 192] is complementary to the IR and UV-Vis results discussed before.

Figure 21 reports the obtained results for Si-TriAm-CD-Cu, in both the X-ray absorption near edge structure (XANES) and the extended X-ray absorption fine structure (EXAFS) regions (Figure 21-a,b, respectively). The XAS spectra of the as-prepared and exhaust catalyst were compared to the ones obtained for selected model compounds, including Cu(II) and Cu(I) oxides. A Cu(II) complex with mixed N/O ligation was also considered, characterized as $[Cu^{II}(NH_3)_3(NO_3)]^+$ in a previous study,[193] where Cu(II) was coordinated in a pseudo-square planar fashion to three $N(NH_3)$ and to one $O(NO_3)$ atom.
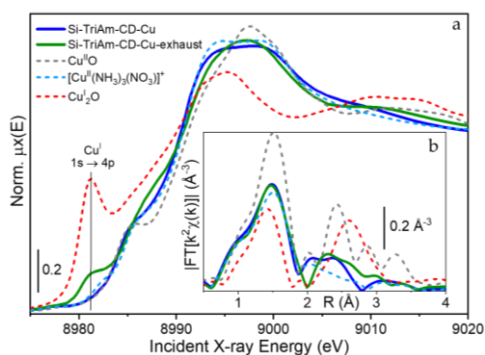
Figure 21. Cu K-edge (a) X-ray absorption near edge structure (XANES) and (b) extended X-ray absorption fine structure (EXAFS) spectra of Si-TriAm-CD-Cu and Si-TriAm-CD-Cu five times reused reported as thick solid lines. The spectra of the sample are compared to the ones of selected model compounds, namely $Cu^{II}O$, Cu^{I}_2O, and $[Cu^{II}(NH_3)_3(NO_3)]^+$, reported as thin dashed lines.

XAS revealed that as-prepared Si-TriAm-CD-Cu exclusively contains Cu(II) species, based on the absorption edge position, as well as on the presence of a characteristic rising-edge peak at ca. 8986 eV. Indeed, this XANES feature, observed for both $Cu^{II}O$ and $[Cu^{II}(NH_3)_3(NO_3)]^+$ model compounds was assigned to three/four-fold coordinated Cu^{II} metal centers.[192] The XANES line shape observed for Si-TriAm-CD-Cu in correspondence of the intense resonance at ca. 8995 eV ("white-line" peak region) resembled the one observed in the $[Cu^{II}(NH_3)_3(NO_3)]^+$, pointing to a possible mixed ligation to both O (e.g., from OH groups), and N atoms (most likely from the N^1-(3-trimethoxysilylpropyl) diethylenetriamine spacer) of Cu-species in the as-prepared catalyst. EXAFS spectra also indicated for Si-TriAm-CD-Cu a ligand environment similar to the one in $Cu^{II}(NH_3)_3(NO_3)]^+$, resulting in almost overlapped first-shell peaks. Notably, the first-shell intensity was, in these cases, intermediate between the one detected for Cu^{I}_2O (two O neighbors) and $Cu^{II}O$ (four O neighbors in ideal square planar coordination). This observation was consistent with the presence in Si-TriAm-CD-Cu of four-fold-coordinated Cu(II) sites with

43

both N- and O-containing ligands. Comparing the EXAFS of Si-TriAm-CD-Cu with the ones of bulk Cu-oxides at higher R-values, it clearly emerged that no trace of high-intensity Cu-Cu scattering contributions compatible with large oxidic or metallic aggregates was detected, while a well-defined second-shell peak was observed. This was consistent with the presence of highly dispersed Cu-species, in the form of monomers or very small clusters.

In line with the UV-Vis results, XAS analysis of exhausted Si-TriAm-CD-Cu unambiguously indicated the formation of a small fraction of Cu(I). Indeed, the appearance of an additional rising-edge peak at ca. 8982 eV was observed, occurring at the same energy position as seen in Cu^I_2O and representing a fingerprint of Cu(I) species.[192, 194] On the other hand, the EXAFS signals of the two samples were very similar, apart from small differences in correspondence of the second shell peak around 2.5 Å, which were not compatible with the formation of large metal or oxidic aggregates (compare with grey and red dashed lines in Figure 21b). This indicated that, besides the change in the oxidation state of a fraction of the copper, the average local environment and agglomeration of the metal centers was not sensibly affected by catalysis. This was an important observation, confirming on one hand the stabilizing effect of the amino spacer and CD on the copper catalytic centers, and on the other hand the formation of catalytically active Cu(I) ions during the reaction.

The high dispersion of Cu on the silica functionalized material was further confirmed by Transmission Electron Microscopy (TEM). The sample was characterized by aggregates of silica nanoparticles with sizes of around 10–15 nm, which were not affected in size, morphology, and aggregation by the catalytic tests (Figure 22a, referring to the two times reused catalyst). Higher magnification images of Si-TriAm-CD-Cu (as prepared and two times reused catalyst, Figure 22-c,b, respectively) suggested the presence of very small (a few nanometers) Cu nanoparticles, which could be seen as dark spots in both materials. The particle size was too small to give electron diffraction, which would give more detailed information on their structure. No diffraction spots could be observed by selected area electron diffraction (SAED) on different portions of the samples. Putting together this piece of information with EXAFS data, which exclude the presence of a significant fraction (≥10%) of large aggregates, a high dispersion of the Cu species was established. Obviously, this was only a qualitative observation, and more specific measurement (such as N_2O chemisorption) would be necessary for a quantitative analysis of copper dispersion, which was outside the scope of this work.

ICP analysis was performed on the freshly prepared and exhaust catalyst. The data demonstrated a copper quantity of 14.9 mg/g and 14.1 mg/g, respectively, showing 5% leaching. What was relevant, was that copper species (β-CD-Cu and Cu NPs) were highly dispersed on the support and hardly affected by the catalytic tests, confirming the stabilizing effect of β-CD, and likely of the N^1-(3-trimethoxysilylpropyl) diethylenetriamine spacer, as suggested by XAS data.

44
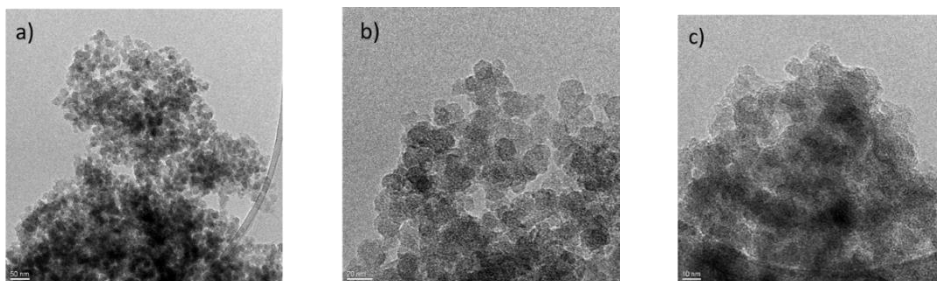
Figure 22. TEM images of Si-TriAm-CD-Cu-two times reused (**a,b**) Si-TriAm-CD-Cu (**c**).

2.3.   Conclusions

In conclusion, the ability of sonication to speed up the synthetic procedures for silica grafting was demonstrated. New β-CD grafted silicas were synthesized and fully characterized. The influence of US at different frequencies (40–80 and 120 KHz) was studied and compared to conventional conditions. MW combined with US was also employed in grafting β-CD to functionalized silica. β-CDs supported on silica were used as non-innocent ligands for copper species, resulting in the production of atomic-scale catalysts. The influence that β-CD had on directing and activating Cu(II) on the silica surface for CuAAC reactions, in absence of a reducing agent, was studied and confirmed. The study provided evidence for the synergistic activity of silica, β-CD and of a polyamino spacer in obtaining spatially isolated and well-characterized active catalytic sites. The Cu(II)/β-CD complex was proven to act as an efficient source of Cu(I) species and multidentate N-donor ligands were able to activate and stabilize the catalytic species. A deep level of understanding was achieved by the combination of IR, DR UV-Vis, XAS and TEM analysis on the fresh and the post-reaction catalyst. The applied characterization methods consistently demonstrated: (i) the successful incorporation and stability of the grafted functionalities; (ii) the exclusive presence of Cu(II) in the fresh catalysts, most likely occurring in a O/N mixed-ligand environment; (iii) the formation of few Cu(I) species in the catalyst after usage without substantial perturbations in the Cu local coordination environment and aggregation state. Complementary insights by TEM, in agreement with EXAFS results, confirmed that Cu remains highly dispersed on the support after the catalytic tests. The novel Cu-supported hybrid heterogeneous catalysts showed excellent performances in click reactions for the synthesis of small molecules and dimers, without the addition of a reducing agent.

Chapter 3

Surface modification of carbon-based nanomaterials: the efficacy and versatility of dipolar cycloaddition in the derivatization of rGO and nanodiamonds

3.1.   Introduction

Carbon based nanomaterials have been intensively investigated in the past two decades and nowadays their production is highly dedicated to technological applications.[195] Drug delivery, hydrogen storage, fuel and solar cells, batteries, electromagnetic shields, conductive paints and reinforcement for polymer are part of the wide range of studied applications.[196, 197] The general classification scheme for carbon nanomaterials comes from their allotropic structure or their valence orbital hybridization.[198] Distinct archetypical allotropic forms are determined by their specific valence orbital hybridization state and are characterized by their own polymeric connectivity. sp^3-, sp^2-, sp-type of hybridization corresponds to a spatial (3D-), planar (2D-), linear (1D-) polymer of carbon, such as diamond, graphite, carbyne, respectively.[199] They are characterized by a fully conjugated structure with unusual molecular symmetries, with good mechanical strength, high electrical conductivity and ion diffusivity.[200] Electronic, mechanical, thermal and optical properties of the different allotrope forms are correlated to the hybridization state of carbon and to their structure, therefore a wide range of applications can be foreseen.[201]

Graphene is the elusive two-dimensional form of carbon. It is the planar, hexagonal arrangement of carbon atoms in a 2D crystal with mono-atomic layer, where carbon atoms have a trigonal planar structure with sp^2 hybridization. It can be wrapped up into 0D fullerenes, rolled into 1D nanotubes or stacked into 3D graphite[202] (Figure 23).
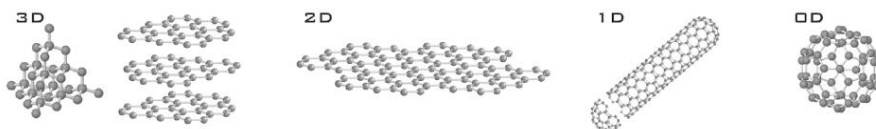
Figure 23. Crystal structure of the different allotropes of carbon. (Left to right) Three-dimensional diamond and graphite (3D); two-dimensional graphene (2D); one-dimensional nanotubes (1D); and zero-dimensional buckyballs (0D). Figure obtained from the paper of Katsnelson.[203]

The length of the σ bond between carbon atoms is 1.42 Å. The σ band is responsible for the robustness of the lattice structure in all allotropes. According to the Pauli principle, these bands have a filled shell and, hence, form a deep valence band. The unaffected p orbital, which is perpendicular to the planar structure, can bind covalently with neighboring carbon atoms, leading to the formation of a π band. Since each p orbital has one extra electron, the π band is

half filled.[200,] Graphene has a unique 2D crystal structure, where its charge carriers behave as massless relativistic particles or Dirac fermions, and under ambient conditions they can move with little scattering. This specific behavior offers many excellent properties in graphene. First, graphene is a zero-bandgap 2D semiconductor with a tiny overlap between valence and conduction bands. Second, it exhibits a strong ambipolar electric field effect along with ballistic conduction of charge carriers. Third, a quantum Hall effect (QHE) at room temperature has been observed. In addition, graphene shows great specific surface area (2630 m^2 g^{-1}),[204] high electron mobility (200 000 cm^2 $(V\ s)^{-1}$), high thermal conductivity (5000 W $(m\ K)^{-1}$),[205] high optical transmittance (97.7%)[206] and capability to carry high current densities.[207] Furthermore, it is highly transparent, with an absorption of ~ 2.3% towards visible light, it possesses excellent mechanical strength and high elasticity.[206]

The crystal structure of graphene can contain a certain number of defects and disorders, that can affect the mechanical properties as well as the thermal and electrical conductivities of graphene and graphene-based nanocomposites.[208] The topology, the curvature and the structure of graphene can be changed depending on the types of defects. Defects can be produced during the preparation process. Therefore, a good understanding of defects and impurities is useful for the improvement of graphene-based nano-engineering.[209] In general, defects in graphene can be categorized into two different groups: *intrinsic defects*, which are composed of non-sp^2 orbital hybrid carbon atoms in graphene. These defects are usually caused by the existence of non-hexagonal rings surrounded by hexagonal rings, and *extrinsic defects*, where the crystalline order is perturbed with non-carbon atoms in graphene.[210] Moreover, a structural and/or chemical modification of the graphene structure can be achieved through deposition of molecules on top or through intercalation, using different substrates that modify the final electronic structure. The modification of the electronic structure and the electrical conductivity of graphene is correlated to the electronic properties of the added molecules: electron-donor molecules decrease the conductivity of graphene while electron-acceptor molecules increase it.[211]

The existence of defects, on one side, destroys the symmetry and integrity of graphene crystals and influence the electronic transmission, on the other, it opens the possibility of ion transport path and enhances interaction between atoms and graphene. Furthermore, the bond length of the interatomic valence bond and the type of the hybrid trajectories of the partial carbon atoms change when defects are present. Generally, a decrease of conductivity is registered when intrinsic defects are present, because they form an electron scattering centre on the surface of graphene, that affects electron transfer. Compared with intrinsic defects, the effect of the foreign atom defects on the electrical properties of graphene is more complicated and interesting. In literature some speculative studies report a decrease of conductivity when oxygen atoms and oxygen containing functional groups are present. However, theoretical studies suggest that conductivity is maintained if the position of oxygen atoms is reasonable. Instead, a large number of studies have pointed out that in-plane foreign atom defects formed by nitrogen and boron

atoms can improve the conductivity of graphene. Heteroatoms cause resonance scattering on graphene, which affects the electrical properties of graphene. Furthermore, the adsorption of molecules influence the electronic properties of graphene.[209, 210]

In order to obtain large amounts of graphene and to control its particle size, several methods have been developed by using graphite as starting material. Indeed, graphene is composed of isolated sheets of graphite and it is produced by graphite exfoliation. The exfoliation can be achieved through *mechanical* or *thermal processes*, generally supported by sonication. However, these methods are expensive and juts few amounts of graphene are obtained and particle size is not under control. Therefore, derivatives of graphene are used to replace pure graphene. The most commonly used are graphene oxide, in their oxidized and reduced form, synthesized by *chemical exfoliation*. The chemical exfoliation of graphite gives rise to graphene oxide (GO) by inserting functional groups between its layers,[212] improving also the processability of graphene-based materials, by overcoming the problems of low solubility, poor reactivity and the limited accessibility.[213] In fact, GO consists of graphene-like sheets, chemically functionalized with oxygen functionalities, such as hydroxyl, carbonyl, epoxy and carboxyl functional groups, which stabilize the sheets in water and provides a remarkable GO hydrophilic character.[214] This functionalization results in randomly distributed aromatic regions (sp^2 carbon atoms) and oxygenated aliphatic regions (sp^3 carbon atoms), which causes the disruption of the electronic structure of graphene.[215] In fact GO becomes an insulator rather than a semi-metal as graphene. While the functionalities can be removed by reduction, large defect populations, which continue to disrupt the electronic properties, remain. The epoxy and hydroxyl groups are the major components and are located above and below each graphene layer; carbonyl and carboxyl groups are minor and are usually distributed at the edges of the layers.[216] Structure and properties of GO depend on the synthesis method and degree of oxidation, while rapid heating of GO results in expansion and delamination, due to evaporation of the intercalated water and evolution of gases from pyrolysis of the oxygen containing functional groups.[215] Today, the Hummers method is the most commonly used. However, despite the presence of oxygen functionalities, GO forms unstable dispersions in water and polar organic solvents, since the exfoliated GO sheets tend to aggregate through π-π interactions and form large particles of graphite oxide. The addition of protective agents, such as octadecylamine, 1-octyl-3-methyl-imidazolium, large aromatic molecules, didodecyldimethyl-ammonium bromide, polystyrene, and poly(sodium 4-styrenesulfonate) and also elastomeric silicon foams and DNA, can be added to stabilize GO nanoplatelets in solution. Thanks to the rich chemistry of hydroxyl, carboxyl, and epoxy groups, GO has been selected very often as the starting material for the formation of graphene derivatives through the covalent attachment of organic groups on its surface, where the added groups are linked through the oxygen atoms of GO.[217]

The reduction of graphene oxide removes the oxygen groups and rehybridizes the effected sp^3 carbon atoms to sp^2, to give reduced graphene oxide (rGO). rGO resembles graphene

structurally and can partially restore the conductive features of pristine graphene. However, it has been demonstrated experimentally, that after reductive treatment of GO a critical number of oxygen groups and defects remain. These defects affect the properties of rGO, mainly it exhibits lower electron mobility than graphene.[218] The reduction of GO can be performed under various conditions and, among them, chemical reduction and thermal annealing routes have been widely explored. The chemical reduction is performed at low temperature by using a wide range of reducing agents. Among them, hydrazine is extensively used for its high reduction efficiency. However, it presents some disadvantages such as its chemical toxicity and the introduction of nitrogen impurities, likely in the form of hydrazone, aziridine, or amine, covalently bonded to the reduced GO surface. Different mechanisms (Figure 25, route 1 to 3) were identified for reducing epoxy groups of GO using hydrazine treatment. Route 1 is the exclusive mechanism for epoxides protruding from GO; routes 2, 2' and 3 are dominant for epoxides attached to the aromatic domain of GO. In these mechanisms, epoxy rings are opened by hydrazine to form hydrazino alcohols, which react further via the formation of an aminoaziridine moiety with the loss of an H_2O molecule, and finally undergo thermal elimination of diimide to form a double bond. No reaction path has been determined for the reduction of hydroxyl, carbonyl, or carboxyl groups with hydrazine as a reducing agent, and they must be eliminated through thermal treatment. The hydroxyl, carbonyl and carboxyl thermal reduction mechanisms are represented in routes 4-5, 6 and 7, Figure 25, respectively. The hydrazine de-epoxidation and thermal dehydroxylation of GO have opposite dependencies on the reaction temperature. For this reason, it is possible to improve the reduction efficiency through a combined route with low temperature hydrazine reduction and high-temperature thermal reduction.[219]

49
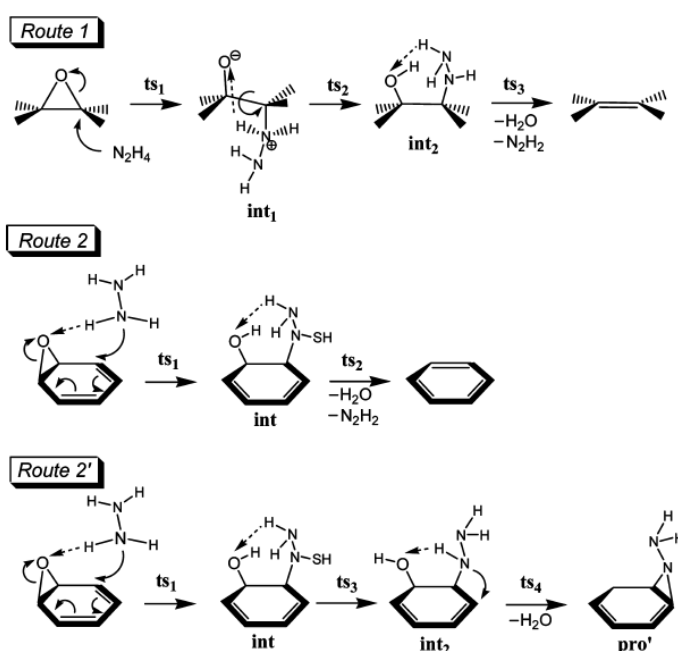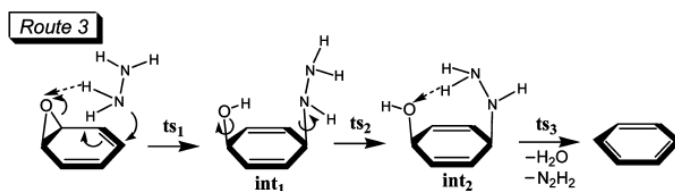
Figure 24. GO reduction mechanisms. Routes 1 to 3 represent the mechanisms for the hydrazine de-epoxidation of GO. Figure obtained from the paper of Chen *et al.*[219]
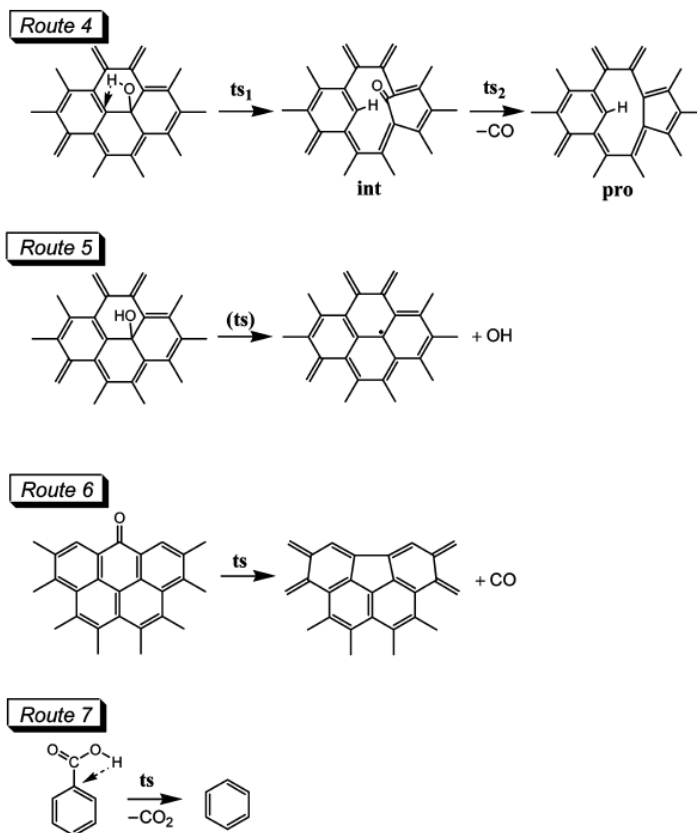
Figure 25. GO reduction mechanisms. Routes 4 and 5 refer to the mechanism for the thermal de-hydroxylation of GO. Routes 6 and 7 respectively show the mechanisms for thermal de-carbonylation and thermal de-carboxylation of GO. Figure obtained from the paper of Chen *et al.*[219]

The thermal treatment is typically achieved under a rapid heating of GO in inert or reducing environments (up to 1050 °C in an oven under argon gas or up to 800 °C under hydrogen gas) or under mild conditions by using MW techniques. These conditions cause the decomposition of oxygen-containing groups in GO, and the instability of carbon monoxide (CO), carbon dioxide (CO_2) and water cause the deoxygenation of the material (Figure 25, route 4 to 7).[212, 216]

In order to improve the processability of graphene-based materials, their chemical derivatization has been extensively studied. The functionalization with organic functional groups can be achieved through covalent functionalization and non-covalent functionalization and interactions. Covalent functionalization is based on the binding of organic functionalities, like free radicals and dienophiles, to C=C bonds on graphene surface. It causes the disruption of the extended π-conjugation on the graphene surface and aromatic character perturbation, unlike non-covalent functionalization. Moreover, the organic covalent functionalization can be achieved through the formation of covalent bonds between organic functional groups and the oxygen groups of graphene derivatives. Furthermore, the *covalent attachment of hydrogen and halogens* allows to obtain graphane and fluorographene. Finally, the *deposition of nanostructures* on graphene surface, such as nanoparticles like noble metals, metal oxides, quantum dots, polymers, has been extensively studied.[217, 220-222] Thanks to the functionalization, the dispersibility of graphene in organic solvents is increased, and organic functional groups offer new properties that could be combined with the properties of graphene. During the covalent functionalization, sp^2 carbon atoms are rehybridized into sp^3 configuration accompanied by simultaneous loss of electronic conjugation. The degree of oxidation or a covalent functionalization reaction can be measured by the ratio between carbon atoms with sp^2 and sp^3 hybridization in the graphitic lattice, using Raman spectroscopy. I_D/I_G ratio is measured, where I_D and I_G are the intensities of the peaks at 1350 and 1580 cm^{-1}, which correspond to the number of sp^3 and sp^2 C atoms, respectively.[219, 223] On the other hand, non-covalent functionalization offers the possibility of attaching functional groups to graphene without disturbing the electronic network.[224, 225] Graphene has a large binding affinity for aromatic compounds, because non-covalent functionalization generally involves π−π interactions, that are important driving forces for supramolecular self-assembly.

Graphene powder, thanks to its large surface-to-volume ratio, high conductivity, and unusual electronic properties is a promising candidate for electronic applications. Graphene shows possible uses in touch screens, capacitors, spintronic devices, fuel cells, batteries, sensors, transparent conductive films, high-frequency circuits, toxic material removal, and flexible electronics.[226] Otherwise, graphene powder can be used as field emitters and solid-state gas sensor.[227] The electronic properties of graphene are strongly affected by the adsorption of molecules, which makes this material very attractive for gas sensing applications. In this case, graphene is widely used in gas sensors for detecting gas concentration, by monitoring changes in resistivity.[228] It can be used as hydrogen storage[211] and, if biofunctionalized with biomolecules (proteins, peptides, etc.), graphene-based nanostructures may open a gateway to new fields in biotechnology. Graphene itself possesses zero band gap as well as inertness to reaction, which weakens the competitive strength of graphene in the field of semiconductors and sensors, moving the researchers to investigate the graphene functionalization with organic and inorganic molecules. Band gap opening of graphene by doping, intercalation, and striping would be useful for functional nano electronic devices.[217] Recently, thanks to the excellent

electrical and mechanical properties of graphene, as well as the large active surface area per mass unit, the immobilization of metallic and other nanoparticles on graphene sheets has been extensively studied. In addition, it is characterized by high conductivity and mechanical strength, and it is free of metallic or carbon impurities since the preparative methods are not catalytic. The composite materials, obtained from the dispersion of metallic nanoparticles or oxides on graphene surface, are applied in catalytic or optoelectronic applications, supercapacitors, fuel cells, batteries.[217] Furthermore, thanks to its electronic properties, it acts as electron acceptor and transporter, and it is able to enhance photoinduced charge transfer for improving catalytic activity.[229] The properties of graphene (and hence the pool of applications where it can be used) depend very much on the quality of the material, type of defects, substrate, which are strongly affected by the production method.[230]

Nanodiamonds (NDs) are composed of a sp^3 carbon core surrounded by a middle sp^{2+x} core and a graphitized sp^2 outer layer, that often shows partial oxidation. They are characterized by a variety of sizes, shapes and surface chemistry, that can be modulated by varying the synthetic approach.[231] NDs surface functional groups determine the chemical state of the carbon material and their modification, resulting in the tune of both macroscopic and microscopic properties, makes the well-prepared NDs suitable for the desired application.[232] NDs are resistant to chemical attack and their functionalization is necessary for their processing. Functionalization can be achieved by exploiting the physical properties of the diamond core or, more commonly, the chemical properties of the graphitic surface or of the surface functional groups.[233] Due to the high surface-to-volume ratio, the surface properties of NDs play an important role and different strategies were pursued to obtain homogeneous and reactive surface species distribution. Well-defined and well-distributed functional groups on NDs surface have been commonly obtained by convenient methodologies, such as hydrogenation or oxidation of raw NDs, annealing under reducing atmosphere, under oxygen or in air,[234] and further chemical functionalization by mechanical bundle disruption, non-covalent or covalent techniques.[235] The graphitic sp^2 surface provides NDs with the most important properties of graphene.

Thanks to the sp^2 graphitic structure of rGO and NDs surface, NDs and rGO are considered as carbon-based MW absorbing materials. The absorbing properties depend on the dielectric losses, that come from conductivity loss and polarization loss (ionic, electronic, dipole orientation and interfacial polarization) arising from defects and functional groups, and conductive dissipation, that involve the motion of conductive electrons, as well as on the high specific surface area, low density, low thickness, wide bandwidth, high conductivity, and unique geometry structure. They can absorb and dissipate incident electromagnetic waves and transform their energy into thermal energy.[236, 237] Their ability in absorbing MW electromagnetic waves depends on the relative complex permittivity and the relative complex permeability, that are expressed in the reflection loss (RL) parameter, that represents the electromagnetic absorption ability. An efficient synergism between the relative permittivity and permeability determines excellent MW absorption properties. In graphene materials, the permeability is very

low due to the weak magnetic characteristic in the MW band, the permittivity must be low for good impedance matching, so abundant defects and functional groups, such as hydroxyl, epoxy, and carboxyl groups of rGO result in low permittivity, which is beneficial for the MW absorption, introducing defects polarization relaxation and groups' electronic dipole relaxation.[238] Moreover, the RL parameter is also dependent on the absorber thickness. Figure 26 shows the calculated theoretical RL curves for a composite with 1 wt% of rGO at different thicknesses in the frequency range of 3-18 GHz. The thickness of the absorber influences the MW absorbing property, that is also dependent on the electromagnetic wave frequency. Usually, the RL is improved shifting the resonance to a higher-loss frequency.[239]
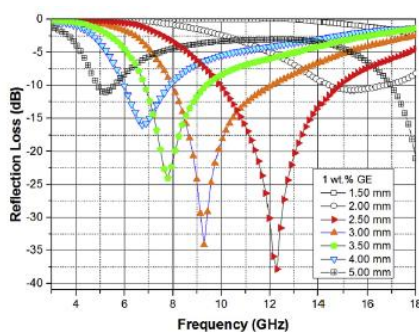
Figure 26. Calculated RL vs. frequency for the composite with 1 wt% of rGO (GE) at different thicknesses. Figure obtained from the paper of Zhou *et al.*[239]

Chemistry can play an important role in the development of new carbon-based nanomaterials, not only in promoting new technological ways for large-scale production, but also acting on structure control, improving their dispersibility in water, aimed at increased concentration and stability, and synthesizing new stable carbon systems by functionalization. Chemical treatments can dramatically alter carbon-based nanomaterial properties, by adding defects and impurities, changing the structure and the topology, affecting the mechanical properties and the thermal and the electrical conductivities.[240] However, some imperfections may increase the local reactivity and be exploited for some applications, to create defined properties and to achieve new functionalities.[210] As a result, new studies have been dedicated to functionalize the carbonaceous network with the aim to modulate properties, improve limits or to approach new applications. Despite the high chemical inertness of the carbon-based nanomaterial, some relevant examples of organic functionalization have been successfully addressed.[241] Direct covalent modification of graphitic surface, without oxidation or any other pre-treatment, has attracted large interest and 1,3-dipolar cycloadditions (1,3-DCA) represent a special class of organic reactions whose applicability is reported in experimental reports[242-245] and several theoretical studies.[246-248] The cycloaddition of azomethine ylides onto single-walled (SW) carbon nanotubes (CNTs), graphene and NDs represents a powerful tool for producing derivatized and highly dispersed systems,[249-251] also applied to carbon encapsulated nanoparticles.[252] Nevertheless other dipoles have emerged with the aim to integrate new

53

functions on the carbonaceous network. Several attempts to fullerene, SWCNT and multi-walled CNT derivatization with nitrile oxide, nitrile imine, nitrile ylide, pyrazolium ylides have been proposed,[253-256] while just few publications refer to the use of nitrone for SWCNT[257] and graphene quantum dots (GQDs),[258] as well as carbonyl ylides functionalization.[259] Recently also a mechanochemical activation was exploited to make oxazol-5-(4H)-one reactive as dipoles to limit its reactivity respect to Diels Alder cycloaddition.[244]

Based on our knowledge, 1,3-dipolar cycloaddition (1,3-DCA) represents a versatile and efficient methodology for carbon-based nanomaterial stable functionalization nevertheless synthetic protocol are often limited because of the harsh reaction conditions, high temperature for long time. The aim of this study is to optimize mild and efficient synthetic protocols based on 1,3-DCA, starting from the well-known azomethine ylide derivatization, moving to the use of nitrile oxide and giving origin to nitrone derivatives for stable covalent functionalization of carbon-based materials. Initially the covalent derivatizations were investigated on rGO surface, in order to validate the different derivatization strategies, to be extended to the use of variable dipoles; to fine-tune an accurate and non-destructive quantification method, and, as final goal, to translate their use to hard-to-change, promising and highly interesting NDs. The beneficial effect of MW irradiation on this type of functionalization was investigated and a comparative study of cycloaddition reactions using classical heating and MW activation is presented with the aim to reduce reaction time and improve efficacy. In order to carefully measure the degree of functionalization, the reaction products were characterized by several spectroscopic and analytical techniques and an indirect evaluation of the reaction outcome by Fmoc deprotection and quantification has been performed. The structural, chemical and physical properties of the functionalized systems were investigated through TGA, FT-IR/DRIFT and Raman spectroscopy.

3.2.   Results and discussion

3.2.1.   Study of a new derivatization degree quantification method: 1,3-DCAs of azomethine ylides

In order to study an environmentally friendly derivatization of graphene-based materials, three different approaches based on 1,3-DCAs of azomethine ylides, nitrile oxide, and nitrones were compared. The first step was based on the preparation of rGO. Naturally abundant graphite underwent to a chemical oxidation method, following the commonly used modified Hummers method.[260] The graphite was oxidized to GO by treatment with $KMnO_4$ and $NaNO_3$ in concentrated H_2SO_4, followed by suspension in water and hydrogen peroxide (H_2O_2). The chemical exfoliation of graphite gives rise to GO by inserting functional groups (such as hydroxyl, carbonyl, epoxy and carboxyl) between its layers and a highly oxidized GO was obtained, as shown by TGA. The major weight loss was registered at 200 °C, which

corresponds to CO, CO_2, and steam release from the most labile functional groups such as hydroxyl, epoxy, and carbonyl groups. Between 400 and 800 °C, a slower mass loss was observed and was attributed to the removal of more stable oxygen functionalities.[261] Successively, GO underwent to hydrazine reduction, to partially remove the oxygen groups and rehybridize the effected sp^3 carbon atoms to sp^2, to give rGO (the final graphitic structure is shown in Figure 27). As demonstrated by TGA, rGO exhibited higher thermal stability than GO, indicating the removal of labile oxygen functional groups during the hydrazine reduction step (Figure 28). The reductive step was carried out using both conventional and MW heating, resulting, in the last case, in shorter reaction times (2 h versus 10 min). The graphitic structure was restored and the thermal stability was confirmed by TGA, comparing the thermal trend with the one of the commercial rGO and conventionally-prepared rGO. The use of MW to accelerate carbon-based material preparation and derivatization was driven by the intense MW-material interactions. MW heating occurs *via* conduction mechanism, superheated centers are generated, and the reactivity is promoted.
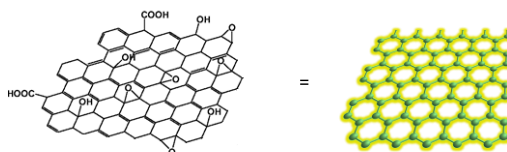
Figure 27. Representation of rGO structure and stylised model used to represent graphitic layer in the present work.
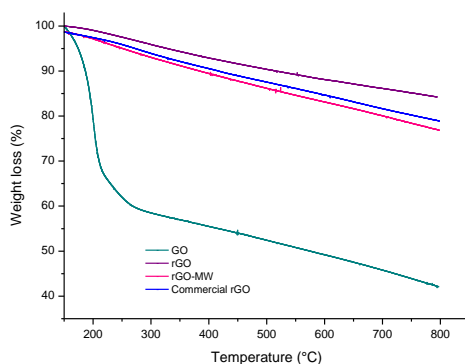
Figure 28. TGA spectra of commercial rGO, conventionally-prepared rGO, MW-prepared rGO and GO.

The first derivatization strategy was based on the 1,3-DCAs of *in situ* generated azomethine ylides which include both an amino acid and an aldehyde moiety. The influence of MW irradiation on rGO derivatization was also studied. Preliminarily, a model reaction was chosen and alanine and hexanal were reacted with rGO under conventional heating or MW irradiation (Scheme 4). On the basis of our research group's experience on SWCNT,[262] the optimized reaction conditions were 130°C for 2 h under MW irradiation and the same procedure was repeated under conventional heating. The reaction was performed in a constant temperature

55

mode. The power was automatically adjusted to reach the set temperature as quickly as possible and then to maintain it using a dynamic feedback power loop. The temperature and power profile in the MW instrument was registered and is reported in Graph 5. TGA analysis was performed on functionalized rGO, and a higher degree of substitution was observed when MW irradiation was employed (Figure 29). For sake of comparison, a blank experiment was performed by heating rGO in MW at 130°C for 2 h and a recorded TGA profile confirmed its thermal stability.
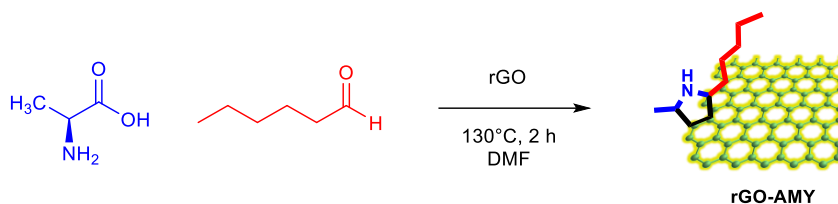
Scheme 4. rGO functionalization by azomethine ylide cycloaddition under conventional heating and MW irradiation
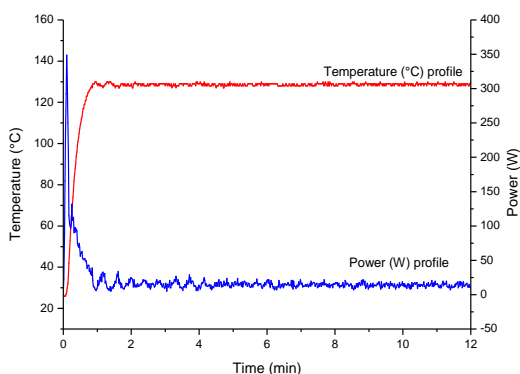
Graph 5. Temperature and power profile curves registered by MW instrument Anton Paar Monowave 300, Program: $P_{max} = 100\%$ heated as quickly as possible to reach 130 ℃, then T = 130 °C.
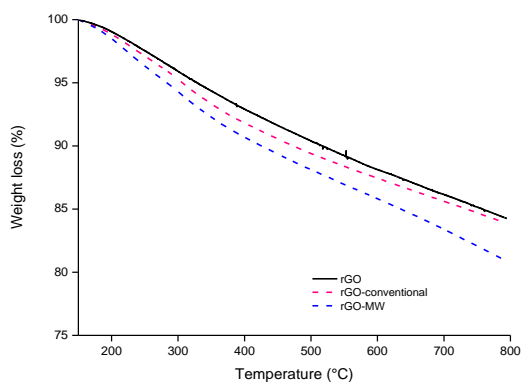
Figure 29. TGA spectra of pristine rGO, conventional grafted rGO, MW grafted rGO.

Table 11. Degree of substitution of rGO functionalization by azomethine ylide cycloaddition under conventional heating and MW irradiation.

56

Sample	Reaction condition	% w/w	μmol/g	Derivatisation/ C atoms
rGO-AMY-conventional	Alanine, hexanal, 130 °C, 2h	1.0	80	1033
rGO-AMY-MW	Alanine, hexanal, MW, 130 °C, 2h	3.3	260	312

In view of the low reactivity of rGO, the measure of derivatization degree still represents a big challenge. TGA is commonly used for measuring the degree of substitution, but its low selectivity prompted chemists to perform different analyses such as TGA, IR, TGA/MS, SEM, TEM, etc., to prove the identity and efficacy of the grafting reaction and to measure the degree of functionalization.[263, 264] With the aim to selectively quantify the grafted derivatives, a new methodology for the quantification of the derivatization degree was studied. It was decided to apply the Fmoc derivatization methodology as successfully demonstrated in peptide solid phase synthesis and to compare it to TGA analysis.[265] As reported, the substitution determination can be performed indirectly by deprotecting a small amount of Fmoc-protected rGO derivative (3-5 mg) in a solution of piperidine (20% v/v in DMF) : MeOH (1:1) to generate the dibenzofulvene–piperidine adduct that was quantified by UV-Vis spectroscopy at 301 nm (ε = 7800), the maximum absorption wavelength of the dibenzofulvene–piperidine adduct (Scheme 7).[266]

To prove the concept and to confirm the efficacy of MW-promoted 1,3-DCA with *in situ* generated azomethine ylides three Fmoc-protected alkylic aldehydes were synthesized from their amino alcohol precursor (Scheme 5). 3-Amino propanol, 5-amino pentanol and 6-amino hexanol were protected with Fmoc and the alcoholic moiety oxidized to its corresponding aldehyde. Unfortunately, the aldehyde obtained from 5-Fmoc-amino pentanol (1b) proceed with a cyclization of the aldehyde to the protected amino group, forming the cyclic enecarbamates (2c).[267]
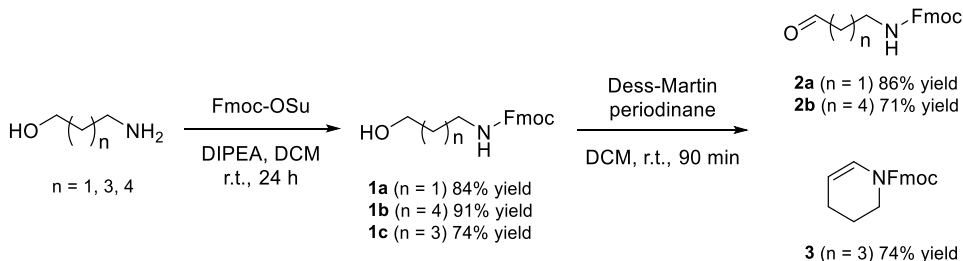
Scheme 5. Synthesis of Fmoc-aldehydes.
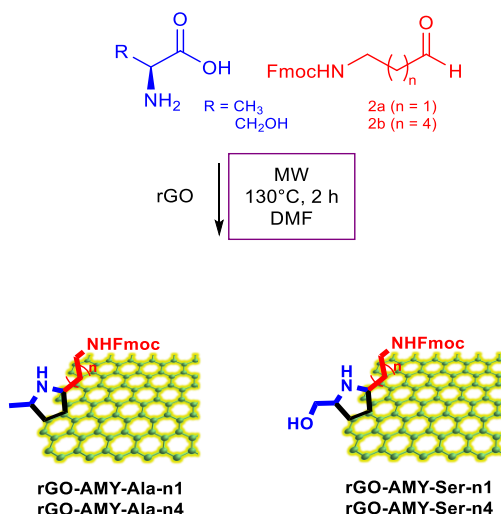
Scheme 6. Derivatization of rGO with azomethine ylides generated *in situ* from Fmoc-6-aminohexanal and alanine or serine.
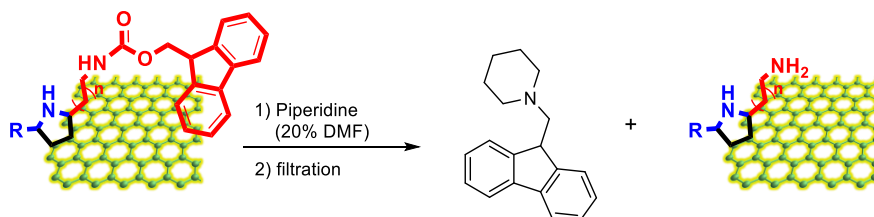
Scheme 7. Schematic representation of Fmoc deprotection to obtain the fulvene – piperidine adduct in solution.

The derivatization of rGO was performed by reacting the carbon-based material with the obtained aldehydes in presence of alanine (Ala) or serine (Ser), resulting in the corresponding azomethine ylide derivatized systems, named rGO-AMY-Ala-n1, rGO-AMY-Ala-n4, rGO-AMY-Ser-n1, rGO-AMY-Ser-n4. (Scheme 6). Dimethylformamide (DMF) was selected as solvent of choice to minimize the interfacial tension between solvent and graphene; initial sonication was used to promote exfoliation of the bulk material through acoustic cavitation; the reaction was carried out at 130°C for 2 h. The same procedure was repeated under conventional heating and MW irradiation. Following the latter synthetic conditions, higher derivatization degree was obtained, as confirmed by comparing the results with literature studies. In order to deny the possible π-π interactions between the Fmoc portion and the rGO electronic cloud and to confirm the covalent functionalization with azomethine ylide, the same reaction was performed by using hexanal, a Fmoc-lacking aldehyde, and alanine as azomethine ylide precursors. Thus, the effective covalent derivatization was demonstrated. The efficiency of rGO functionalization was

measured by TGA and compared with UV-Vis measurements (Table 12). The TGA curves were performed under inert atmosphere and were all normalized at 150 °C to circumvent any possible solvent influence on yield calculations. As described in Table 12, TGA and UV-Vis data were in accordance and a range of 10-15 % (w/w) of functionalization was measured. Because of the higher selectivity a slightly lower percentage of grafting was measured by UV-Vis indirect analysis. When the reactivities of 3-Fmoc amino propanal and of 6-Fmoc amino hexanal were compared, the latter resulted in higher functionalization degree. This is explained by the importance of the Fmoc level of freedom on the derivatization efficiency, that is influenced by the alkyl chain length through which the Fmoc portion is grafted on the sp^2 surface, demonstrating that the higher the distance between the Fmoc and the material surface, the higher is the grafting degree. The TGA curves showed that rGO under inert atmosphere shows a constant loss of weight, when grafted three degradation steps were observed at 241 °C, 325 °C and 408 °C, ascribed to azomethine ylides degradation. Here, a representative comparison of TGA curves of rGO-AMY-Ala-n1 and rGO-AMY-Ala-n4 is shown (Figure 30).
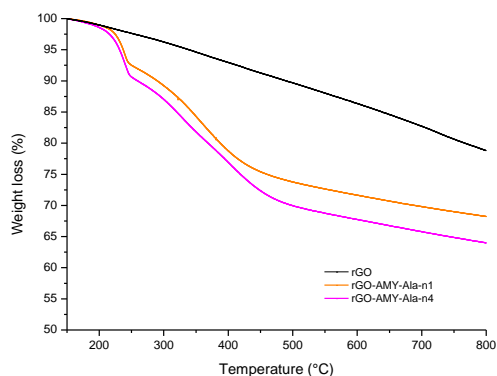
Figure 30. TGA spectra of pristine rGO, rGO-AMY-Ala-n1, rGO-AMY-Ala-n4.

Table 12. Functionalization degree of rGO and NDs by 1,3-DCA with azomethine ylides.

Sample	Aldehyde	aa	% UV		% TGA		Derivatisation/
			% w/w	µmol/g	% w/w	µmol/g	C atoms
rGO-AMY-Ala-n1	Fmoc-3-aminopropanal	Ala	10.3	320	12.1	375	196
rGO-AMY-Ala-n4	Fmoc-6-aminohexanal	Ala	12.4	340	14.5	398	187
rGO-AMY-Ser-n1	Fmoc-3-aminopropanal	Ser	6.9	204	8.5	251	305
rGO-AMY-Ser-n4	Fmoc-6-aminohexanal	Ser	10.1	265	11.8	310	247

Reaction conditions: 1.6 mmol aldehyde, 1.9 mmol amino acid, 50 mg rGO, DMF (13.3 mL), 2 h, 130 °C, MW.

The effectiveness of the derivatization reaction was also investigated by FT-IR (Fourier Transform Infrared Spectroscopy), while Raman spectroscopy was used to evaluate the chemical and physical properties of the synthesized nanomaterials. First of all, FT-IR profile of rGO was recorded at different concentration of rGO in KBr. Increasing the rGO/KBr ratio, an enhancement of peak intensity is achieved. The broad bands at 3433 and 3235 cm^{-1} correspond to the alcoholic and carboxylic acid O-H stretching, the peaks at 1648, 1557, 1317 and 1120 cm^{-1} correspond to the carbonyl and carboxyl C=O stretching, to the aromatic C=C stretching, to the phenolic and alkoxylic C-O, respectively, demonstrating the aromatic structure of the rGO layer and the partial presence of hydroxylic functions, that were not totally removed from the GO by the reductive step (Figure 31a). From Raman spectroscopy the sp^3-sp^2 content was evaluated. The pristine rGO sample shows the D-band (ca. 1350 cm^{-1}), also known as disorder band, is associated with the defects or vacancies present in the carbon structure and with the presence of sp^3 carbons, and the G-band (ca. 1580 cm^{-1}), related to the in-phase vibration of the graphite lattice, of sp^2-bonded carbon atoms. There are also three minor bands due to the Raman-active defects from the ideal structure of graphite: the 2D, (D + G) and 2D' band. The 2D peak, overtone of D peak, is attributed to double resonance transitions resulting in production of two phonons with opposite momentum, that confirms the low number of layers. Furthermore, unlike the D peak, which is only Raman active in the presence of defects, the 2D peak is active even in the absence of any defects. Its shift and shape have been correlated with the number of graphene layers. The 2D and 2D' overtones and the D + G combination modes produce a large, convoluted band at higher frequencies in the 2500-3500 cm^{-1} region. An increase in the relative Raman intensity of the D and D' bands, as compared to the G band, is generally observed when the disorder of graphite layers increases. The significantly high defect content, which is indicated by the high relative intensity of the D band with respect to the G band, is consistent with a high number of sp^3 carbon atoms introduced during the oxidative preparation of the material and only partially reconverted to sp^2 during the reduction step (Figure 31b).
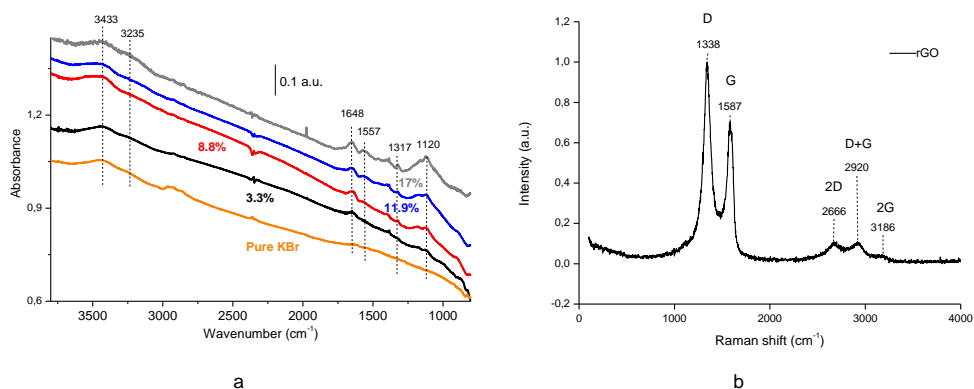
Figure 31. (a) FT-IR spectra, acquired in transmission mode, of rGO at different concentrations in KBr. The peak intensity increases by increasing the rGO concentration. (b) Raman spectrum of pristine rGO.

The first evidence of the successful covalent functionalization of rGO was obtained by FT-IR, by comparing the spectra of the functionalized materials with that of the starting rGO. A representative FT-IR spectrum of azomethine ylides derivatized rGO, rGO-AMY-Ala-n4, is shown (Figure 32). C-H, stretching and bending modes of aromatic system are observed (at 3090 cm^{-1} and 950-850 cm^{-1} respectively), the absorption bands around 2930 and 1350 cm^{-1} show the existence of a stretching vibration of C−H of the alkyl portion. The peaks centered at 1298, 1350, 1015 and 1125 cm^{-1} are attributed to the stretching vibrations of C-N, indicating the existence of the pyrrolidine ring. The absorptions of 1630−1580 cm^{-1} can be appointed to the stretching vibration of the amide group, indicating that azomethine ylide moiety had been successfully grafted on the surface of rGO.
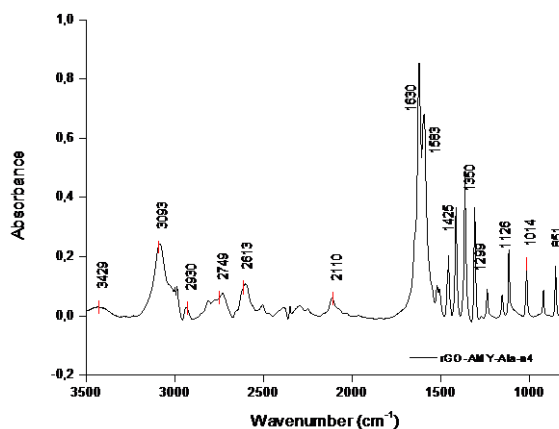
Figure 32. FT-IR spectrum of rGO-AMY-Ala-n4, acquired in transmission mode.

The formation of the pyrrolidine ring onto the rGO surface was also verified by Raman spectroscopy. The Raman spectra recorded for products rGO-AMY-Ala-n1 and rGO-AMY-Ala-n4 are similar to that of pristine rGO, but some differences elucidate the successful covalent functionalization by 1,3-DCA of azomethine ylides (Figure 35a). The average I_D/I_G ratio, a convenient parameter to estimate the overall defectiveness of graphitic materials, was 1.19 ± 0.04 and 1.20 ± 0.04 and 1.42 ± 0.06 for pristine rGO and product rGO-AMY-Ala-n1 and rGO-AMY-Ala-n4, respectively. This indicates that the functionalization by 1,3-DCA of azomethine ylides slightly altered the rGO defect content. The high I_D/I_G ratio (>1) measured for pristine rGO may be explained by a large number of polyaromatic domains with smaller overall size and the occurrence of patches with a highly defective carbon lattice that were induced by the oxidative processing of graphene. The increase in I_D/I_G ratio observed for the functionalized sample clearly indicates that the adopted synthetic approach followed during the synthesis slightly modify the hybridization of carbon, confirming the functionalization.

In order to finally prove the success of the cycloaddition reaction, attempts were made to deconvolute the Raman spectra into their possible constituent peaks, by following an established procedure, where an appropriate deconvolution model was developed to quantify

the observed spectral broadening and find relations with the chemical functionalization degree.[268, 269] Indeed, Raman spectroscopy is a useful technique for the characterization of carbon materials, not only for the crystal structure, but also for observing structural changes occurring at the molecular level. It is complementary to electron microscopy and X-ray diffraction to better understand morphological modifications at the long-range order. An accurate measurement of the chemical functionalization degree (CFD) could be obtained by the analysis of the deconvoluted Raman bands, by the ratio of bands assigned to sp^2 domains (which are the satellite bands S, S_r, D_l, D_r, G_l, G_r), and of the graphitic-type domains (the D and G bands) (Figure 33), which are associated with the initial graphitic-type structure of the carbon nanostructure.

$$CFD = \frac{S + S_r + D_l + D_r + G_v + G_l + G_r}{D + G}$$
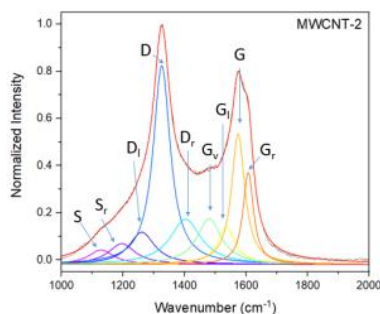
Figure 34-a,b shows a representative deconvoluted spectrum (rGO-AMY-Ala-n4), where multiple Lorentzians peak fit for the D and G bands. A total of four peaks could be fit as shown. The peaks centered at 1345 and 1587 cm^{-1} correspond to the conventional D and G bands. The broadening in the G band at the higher wavenumber side is due to the presence of the G_r band at 1620 cm^{-1}, this is due to the highly defective structure. In addition, one more peak could be fit at 1530 cm^{-1}, it is named G_v and is generally attributed to sp^3 rich phase of disordered carbons. Differently, the deconvoluted peak position of the 2D region corresponds to 2680, 2930, 3185 cm^{-1}. Based on the literature, the first signal can be assigned to the G* Raman modes. The band at 2930 cm^{-1} has been assigned to the $D+G_r$ or the D+G mode. Similarly, the peak at 3185 cm^{-1} has been identified with the 2D' and $G+G_r$ modes. Finally, the success of the cycloaddition reaction was further supported by the shift of the Raman G-band observed after the functionalization process (Figure 35). The G band was shifted to higher frequencies, confirming the doping of graphene.
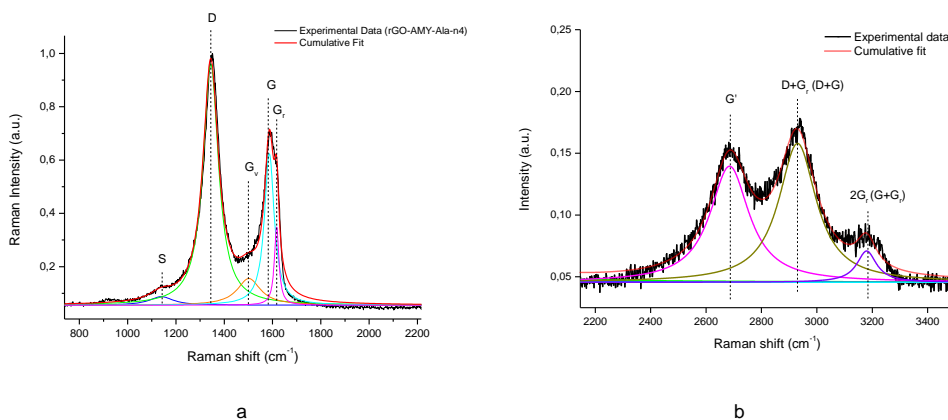
Figure 34. (a) Deconvolution of the observed D and G bands into D, G_v, G, and G_r bands of rGO-AMY-Ala-n4; (b) multiple peak-fit for 2D region of rGO-AMY-Ala-n4.
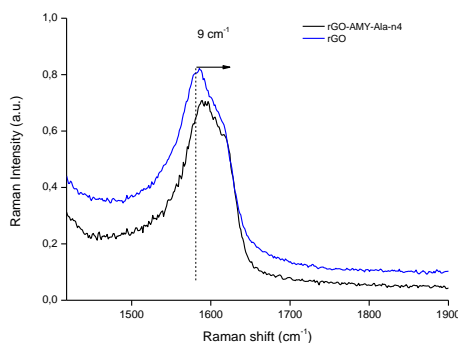
Figure 35. G band region of rGO-AMY-Ala-n4 in comparison with rGO.

Based on the excellent quantification strategy and derivatization efficiency, the same methodology was used to study the feasibility of NDs surface functionalization through 1,3-DCAs. The NDs used for this study were acquired by Adamas Nanotechnologies and were synthesized by exploiting high pressure and temperature reached during the detonation of explosive carbon-based compounds, TNT and RDX, (obtaining pristine NDs), followed by a thermal treatment at 800°C under vacuum pressure (10^{-1}-10^{-2} Pa) for 6 h to graphitize the amorphous carbon phases, while preserving the diamond core (annealed NDs).[270-272] This reductive step allows to increase the sp^2 phases, essential for the functionalization. On the other hand, it offers a better purification on the nanocrystal surface when the NDs are subjected to a further etching process, at 475 °C in O_2 atmosphere for 12 h, resulting in etched NDs. These oxidative conditions are responsible of the partial remotion of the surface graphitic layers. Qualitatively, annealed NDs present a darker color than the pristine ones, while the etching process give them a whitish aspect, probably due to the oxygenated surface, as showed in Figure 36.
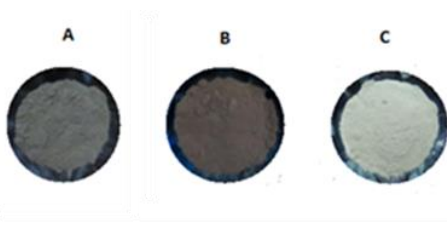
Figure 36. Qualitatively aspect of (A) Commercial pristine NDs, (B) annealed NDs and (C) etched NDs,

To evaluate the effect of the described processing steps on the sp^3/sp^2 content and on the surface chemistry, both Raman spectroscopy and DRIFT (Diffuse Reflectance Infrared Fourier Transform) spectroscopy were performed, respectively. However, from the analysis of Raman measurements, conducted on the different samples and assessed with a conventional micro-spectrometer (Horiba Jobin Yvon HR800), with optical excitation given by a continuous 532 nm laser focused with a 100× air objective, no significant differences were appreciable. No diamond peak at 1332 cm^{-1} was observed, while the main features at 1350 cm^{-1} and 1580 cm^{-1}, associated to the D and G, respectively, which are commonly attributed to amorphous sp^2 carbon-based system and to the stretching of the C-C bonds of graphitic carbon respectively, were not appreciably visible. Thus, Raman analysis was not exploited as characterization technique for functionalized NDs.

To explore the surface chemical terminations of these three samples of NDs, DRIFT analysis was carried out. As visible in Figure 37, all NDs show a broad and intense band in the 3750-2800 cm^{-1} spectral region associated to the v(OH) stretching vibration of hydrogen bonded water molecules. The adsorbed H_2O molecules give rise also to the bending vibration around 1630 cm^{-1}. In the NDs thermally treated, new signals could appear between 3000 and 2850 cm^{-1}, ascribed to v(CH) stretching modes, typical of aromatic portions, but they result overlapped to the v(OH) stretching vibration of adsorbed H_2O molecules. Moreover, during the annealing process, the reductive atmosphere induces a decrease of the oxygenated surface groups and the rehybridization of sp^3 carbon atom to sp^2. Conversely, a more intense band of the v(C=O) stretching (1790-1750 cm^{-1}) is present in the etched NDs: the etching process, in fact, introduces carbonyl groups on the surface.

NDs were also analyzed by TGA. Annealed NDs revealed a more constant and reduced loss compared to the commercial-pristine and etched ones. This is due to the annealing phenomena occurred in the NDs thermally treated that makes this material more stable and less subject of losing surface portions. The oxidative cleaning treatment, not only remove the graphitic amorphous component, but also make the NDs' surface more thermally unstable.
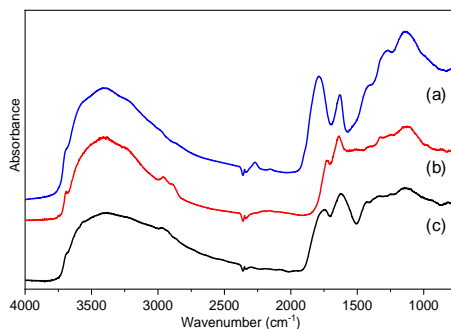
Figure 37. DRIFT spectra of pristine (spectrum c), annealed (spectrum b) and etched (spectrum a) NDs.

Based on our previous functionalization of rGO, the surface of NDs was decorated performing the azomethine ylides 1,3-DCA. The model reaction between hexanal and α-alanine was first studied with the different kinds of available NDs (pristine, annealed and etched NDs). The best functionalization degree was obtained with the thermally treated NDs (annealed NDs), this can be ascribed to the higher content of sp^2 surface of this sample that make it more reactive to the dipole. The etching process makes NDs more instable and less reactive to the azomethine ylide derivatization, due to the higher amount of impurities and sp^3 C atoms. Based on these reasons, the 1,3-DCA study proceed with the functionalization of the annealed NDs. Moreover, accurate and standard synthetic procedure for NDs preparation revealed to be fundamental to obtain reproducible and high-quality carbon-based product.
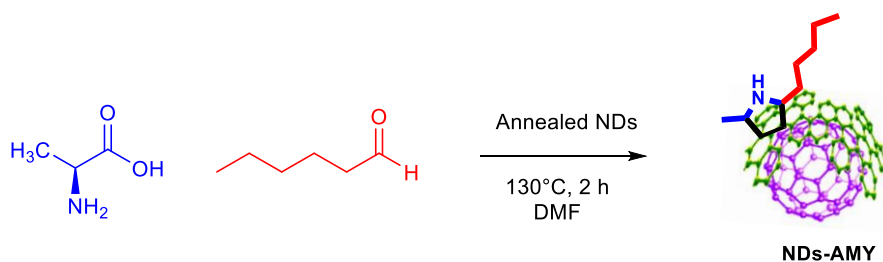
Figure 38. Model reaction of NDs through the 1,3-DCA reaction of azomethine ylides.

The reaction between the Fmoc protected hexanal and alanine or serine was carried out under MW irradiation at 130 °C for 2 h, obtaining a 3.3% and 4.7% (w/w) of derivatization degree of derivatized NDs, respectively, confirmed by UV-Vis Fmoc determination. A representative TGA curve is reported in Figure 39, showing a regular thermic degradation, with a slightly higher weight loss at 325 °C, typical of azomethine ylide portion. The successful derivatization of azomethine ylides onto NDs surface was also confirmed by infrared spectroscopy. A representative DRIFT spectrum corresponding to NDs-AMY-Ala-n4 is shown in Figure 40. The band at 3290 cm^{-1} is ascribed to the v(OH) stretching vibration of adsorbed H$_2$O molecules, where also the sp^2 C-H stretching could be present. The signals at 1080-735 cm^{-1} could be

65

attributed to the sp^2 C-H stretching and the aromatic sp^2 C-H bending. The aromatic portion is also visible by the peak centered at 1597 (C=C aromatic stretching), where also the N-H bending, associated to the pyrrolidine ring formation, is present. The peaks centered at 1444 and 2935-2871 cm^{-1} are attributed to the sp^3 C-H stretching and bending, respectively, while the peak at 1655 cm^{-1} is ascribed to the amide peak.
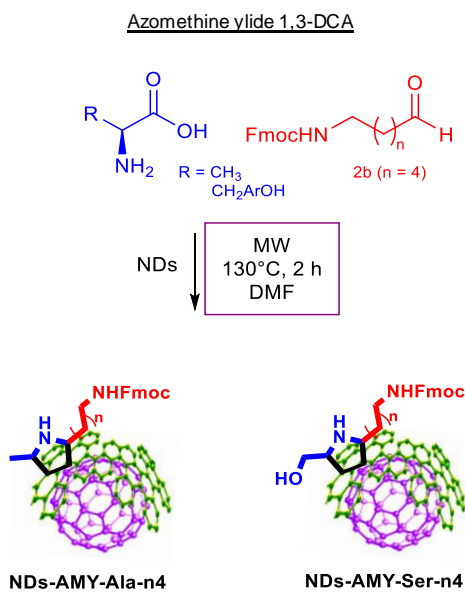
Scheme 8. Derivatization of NDs with azomethine ylides generated *in situ* from Fmoc-6-aminohexanal and alanine or serine.

Table 13. Functionalization degree of rGO and NDs by 1,3-DCA with azomethine ylides.

Sample	Aldehyde	aa	% UV		% TGA		Derivatisation/ C atoms
			% w/w	µmol/g	% w/w	µmol/g	
NDs-AMY-Ala-n4	Fmoc-6-aminohexanal	Ala	2.7	74	3.3	179	923
NDs-AMY-Ser-n4	Fmoc-6-aminohexanal	Ser	4.2	124	4.7	255	669

Reaction conditions: 1.6 mmol aldehyde, 1.9 mmol amino acid, 50 mg NDs, DMF (13.3 mL), 2 h, 130 °C, MW.
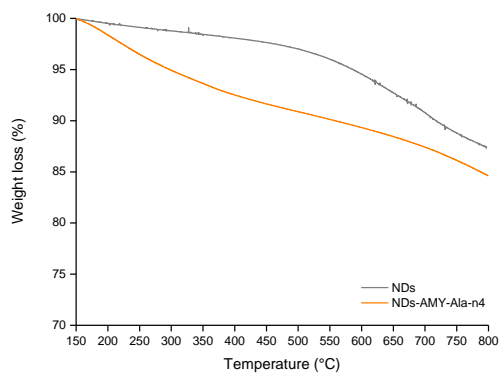
Figure 39. TGA of NDs-AMY-Ala-n4.
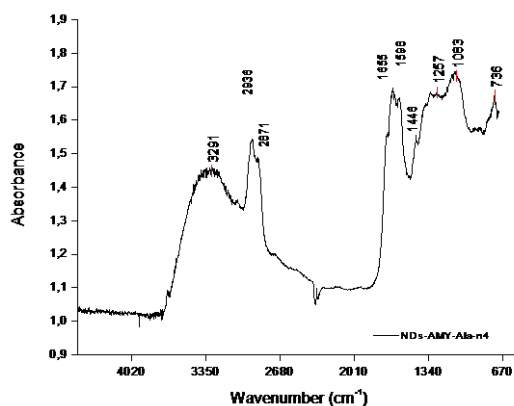
Figure 40. FT-IR spectrum of NDs-AMY-Ala-n4, acquired in transmission mode.

3.2.2. rGO and NDs functionalization by 1,3-DCA of nitrile oxides

In order to suggest a new and broader derivatization strategy of carbon materials, to optimize a synthetic protocol at lower temperature and to reduce the excess of reagent utilized, nitrile oxides were tested as different dipoles. They have been already employed for the derivatization of fullerene and good results were obtained under US irradiation or by mechanochemical activation starting from the oxime in presence of (diacetoxyiodo)benzene.[273] Here, the synthesis of aromatic and aliphatic chloroxime (Scheme 9 and Scheme 10) was attempted, followed by the 1,3-DCA on the sp^2 graphitic surface of rGO and NDs, through the nitrile oxide *in situ* generation (Scheme 11). Aliphatic and aromatic derivatives were synthesized starting from Fmoc-amino protected aldehydes, followed by the formation of the corresponding hydroxylamines and finally treated with *N*-chlorosuccinimmide for 3 h at room temperature in DMF, to obtain the final chloroxime derivatives (**5**) and (**11**).
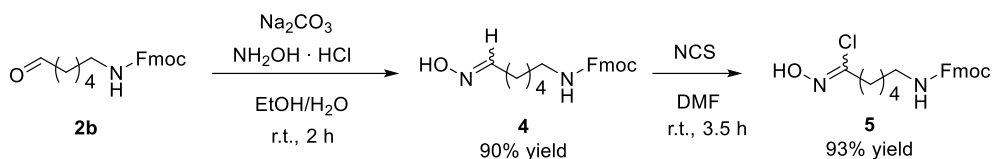
Scheme 9. Synthesis of aliphatic Fmoc-chloroxime.

2b → Na$_2$CO$_3$, NH$_2$OH · HCl, EtOH/H$_2$O, r.t., 2 h → **4** 90% yield → NCS, DMF, r.t., 3.5 h → **5** 93% yield
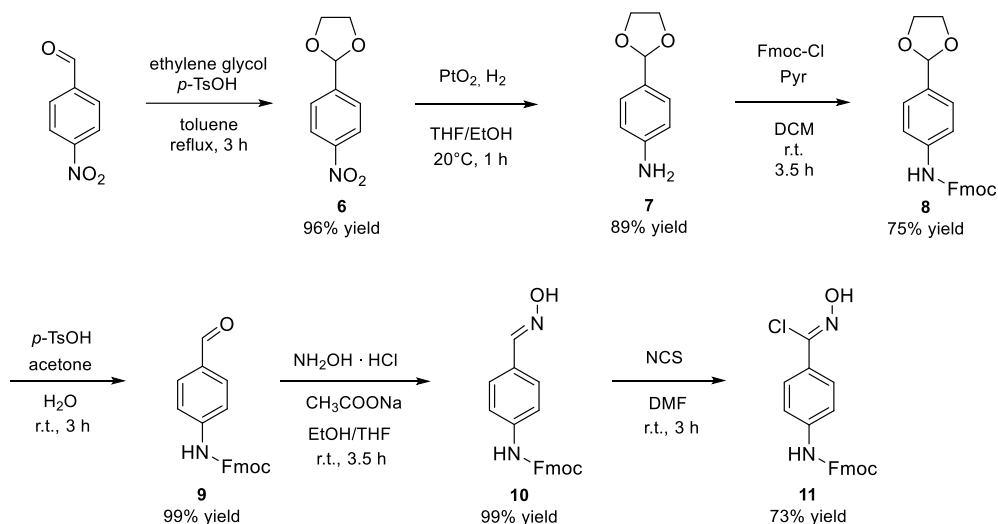
Scheme 10. Synthesis of aromatic Fmoc-chloroxime.

ethylene glycol, p-TsOH, toluene reflux, 3 h → **6** 96% yield → PtO$_2$, H$_2$, THF/EtOH, 20°C, 1 h → **7** 89% yield → Fmoc-Cl, Pyr, DCM, r.t., 3.5 h → **8** 75% yield

p-TsOH, acetone, H$_2$O, r.t., 3 h → **9** 99% yield → NH$_2$OH · HCl, CH$_3$COONa, EtOH/THF, r.t., 3.5 h → **10** 99% yield → NCS, DMF, r.t., 3 h → **11** 73% yield

As described in Table 14, the reaction optimization was obtained by performing the 1,3-DCA under different reaction conditions. A good derivatization degree was observed for both rGO (15.4% and 16% w/w by TGA, considering aromatic (rGO-NO-2) and aliphatic substrates (rGO-NO-1), respectively) and NDs (10.6% for NDs-NO-2 and 13.2% w/w for NDs-NO-1), even by reducing the amount of chloroxime to ¼. It was observed that the best functionalization degree was obtained performing the reaction under mild conditions, oil bath at 30 °C for 2 h, where the use of MW irradiation was not necessary, due to the low reaction temperature. When chloroximes were used as dipoles, the deep chemical modification on the sp^2 graphitic surface, fact that occurred after the chemical functionalization, has been clearly confirmed by the great difference in the profiles of TGA curves of the rGO cycloadducts from pristine rGO, where the first order derivative accurately defines the degradation temperature of the aromatic and aliphatic substituted 4,5-dihydroisoxazoles, at 190°C and 220°C, respectively, confirming the correct covalent functionalization and the influence of the Fmoc degree of freedom on derivatization degree (Figure 41a). The same was observed when NDs were grafted with aliphatic and aromatic chloroximes. From TGA two degradation steps were observed, due to the degradation of the isoxazole structure and its aliphatic or aromatic substituents (Figure 41b). Moreover, the same degradation trend between rGO-NO-1 and NDs-NO-1, as well as rGO-NO-

2 and NDs-NO-2, was visible looking at the highest point of degradation. Aliphatic nitrile oxides derivatized systems showed a slightly higher degradation temperature (ca 220 °C) than the aromatic ones, where the most evident degradation occured before 200 °C.

Nitrile oxides 1,3-DCA
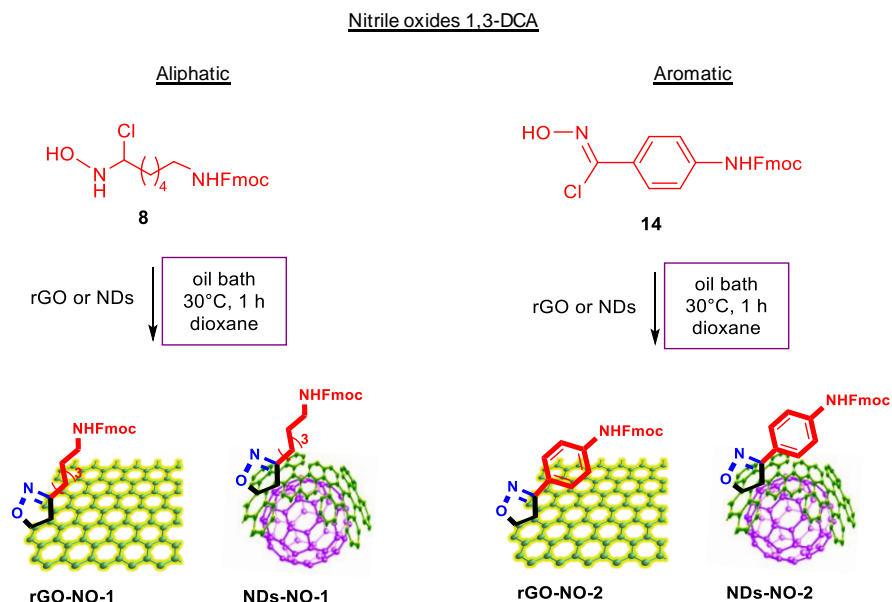
Scheme 11. Derivatization of rGO and NDs with nitrile oxides generated *in situ* from Fmoc-chloroxime derivatives.

Table 14. Functionalization degree and reaction conditions for 1,3-DCA of nitrile oxides onto rGO and NDs surface.

Sample	Chloroxime	Reaction conditions	% UV		% TGA		Derivatis/ C atoms
			% w/w	µmol/g	% w/w	µmol/g	
rGO-NO-1	Aliphatic[a]	MW, 60 °C, 1 h	10.2	285	15.3	453	169
rGO-NO-1	Aliphatic[b]	MW, 60 °C, 1 h	11.6	330	16.3	464	157
rGO-NO-1	Aliphatic[b]	MW, 45 °C, 1 h	12.0	342	15.8	450	163
rGO-NO-1	Aliphatic[c]	conventional, 30 °C, 2 h	17.0	484	22.8	649	103
rGO-NO-2	Aromatic[c]	conventional, 30 °C, 2 h	15.4	429	19.6	546	122
NDs-NO-1	Aliphatic[c]	conventional, 30 °C, 2 h	7.3	204	9.8	376	281
NDs-NO-2	Aromatic[c]	conventional, 30 °C, 2 h	8.9	247	10.6	294	253

Reaction conditions: rGO or NDs (50 mg), chloroxime (a) 1.6 mmol, (b) 0.8 mmol, (c) 0.42 mmol, KHCO$_3$ (0.417 mmol), dioxane (6.67 mL).

The successful covalent modification on rGO and NDs surface was also revealed by FT-IR and DRIFT spectroscopy. The broad band between 3100 and 3450 cm^{-1} is due to the presence of H_2O molecules adsorbed on carbon-based surface (O-H stretching), that can cover up the signal of the secondary amide and the sp^2 C-H stretching. The bands between 2600 and 2950 cm^{-1} are ascribed to the presence of alkyl portion, corresponding to the C-H stretching vibrations, that also generates the signal at around 1400 cm^{-1}, due to the sp^3 C-H bending. The split peak at around 1600 cm^{-1} can be ascribed to the presence of C=O and the C=N stretching. The sp^2 acyl C-O stretching is visible at 1370 and 1000-1100 cm^{-1}, indicating the existence of the 4,5-dihydroisoxazole ring, while the peak at 850 cm^{-1} could be ascribed to the sp^2 C-H bending for aromatic groups or the N-O stretching in the five-terms ring. (Figure 41-c,d. See Figure 77 and Figure 79, Appendix for rGO-NO-1 and NDs-NO-1 spectra).
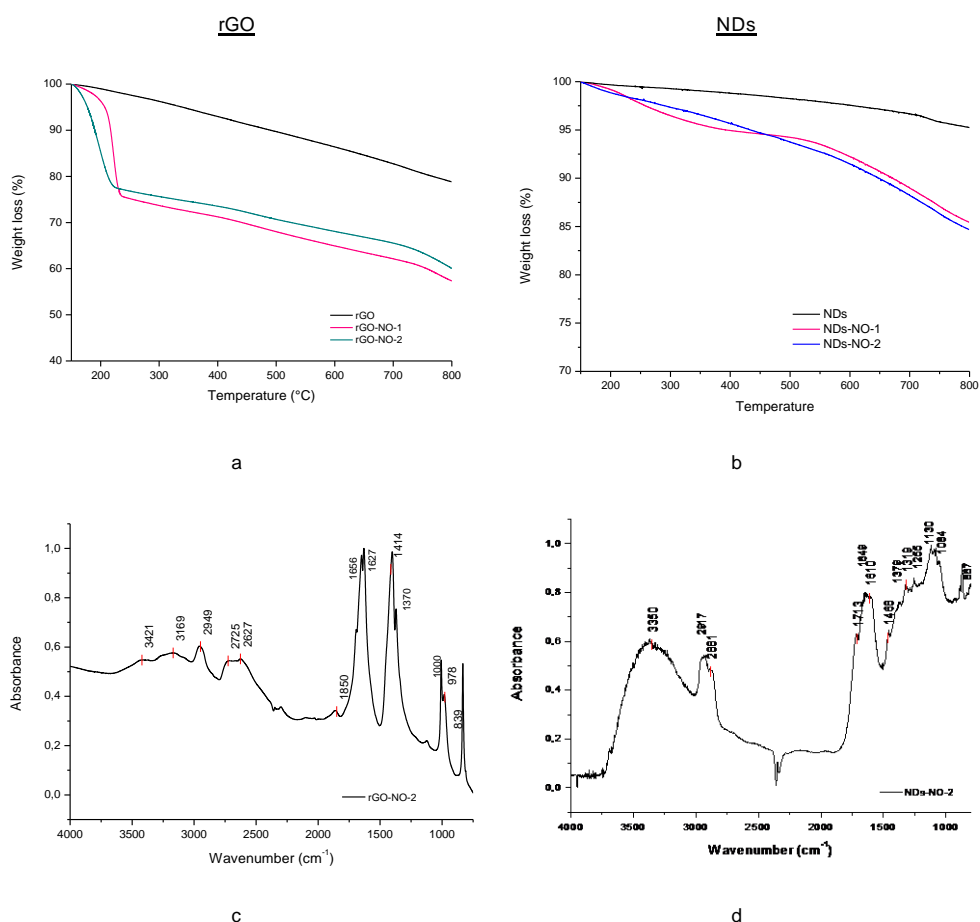
Figure 41. (a) TGA profiles of rGO and nitrile oxides derivatized rGO; (b) TGA profiles of NDs and nitrile oxides derivatized NDs; (c) FT-IR spectrum of rGO-NO-2; (d) FT-IR spectrum of NDs-NO-2.

Looking at Raman spectroscopy, apart from the prominent G band (~1600 cm^{-1}) and D band (~1350 cm^{-1}), significant band broadening and higher spectral intensity in the valley between the G and D bands are observed. The latter is in part the result of the increase in satellite bands

attributed to limit-sized sp^2 domains resulting from the covalent functionalization. The detailed Raman peak deconvolution was performed. The G_r, S and G_v bands are a demonstration of the high defective structure, and sp^3 content increment, caused by the surface functionalization. The G_v shoulder (1510 cm^{-1}) is related to amorphous phases, because it has been demonstrated, by previously studies, that its intensity decreases when the crystallinity increases. The S band (1125 cm^{-1}) is related to the disordered graphitic lattices provided by sp^2-sp^3 bonds. In addition, the G_r and D+G_r bands are related to defect features.[274] An illustrative example is provided in Figure 42 and corresponds to rGO-NO-2, but a similar spectrum was recorder for the aliphatic derivatized rGO (rGO-NO-1) (see Figure 78, Appendix).

a   b
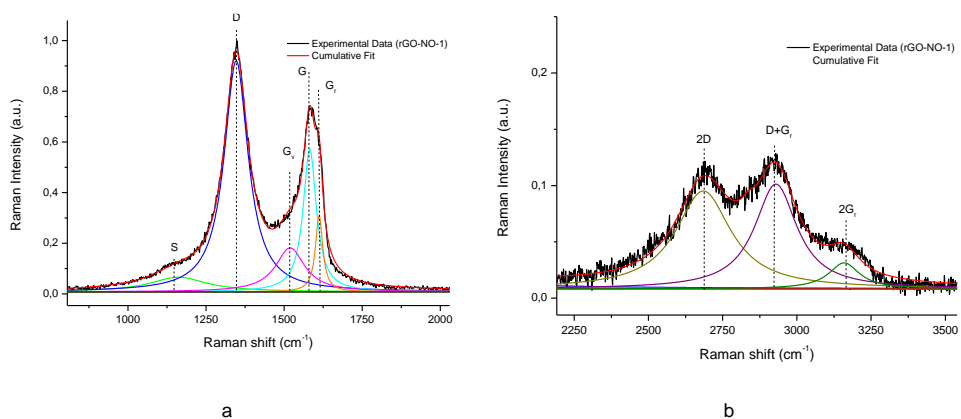
Figure 42. Deconvoluted Raman spectrum of rGO-NO-1.

3.2.3. Investigation of different nitrone's 1,3-DCAs for rGO and NDs functionalization

The acquired experience on the sp^2 graphitic surface functionalization through 1,3-DCA and the proven quantification method, through Fmoc-amino protected derivative as derivatizing agents, were exploited to directly functionalize rGO and NDs using a new and versatile cycloaddition reaction, pursuing eco-friendly and mild parameter conditions: the use of nitrones. Nitrones were chosen for their high known reactivity towards dipolarophiles and to allow for the introduction of new sites for further functionalization processes, thanks to their versatile structure. Nitrones are defined as allyl anions and enolates and their reactivity depends on their electronic structure, their high nucleophilicity and low electrophilicity. According to computation models, nitrones can be considered as strong/moderate nucleophiles with a uniform charge distribution along the conjugated C-N-O system, with a delocalized system of 4 e$^-$ on three atoms (Figure 43).

71
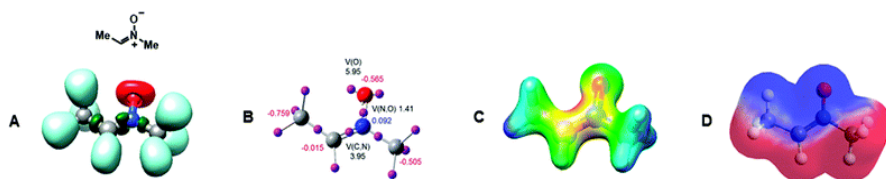
Figure 43. Electronic representations for a typical nitrone. (A) and (B) electron localization function, (C) total charge density, (D) electrostatic potential. Figure obtained from the paper of Matute *et al.*[275]

The reactivity of nitrones as dipoles in 1,3-DCA makes them important systems to obtain isoxazolidines, which are important structures for the synthesis of a large number of biologically active molecules. Several studies have been focused on the nitrone [3+2] cycloaddition mechanism. It has been demonstrated that the reactivity is controlled by the energy to distort the 1,3-dipole to the correct geometry for the interaction with the dipolarophile, instead of molecular orbital interactions or reaction thermodynamics. Moreover, a one-step mechanism where two new single bonds, C-O and C-C are formed, has been demonstrated. From the investigation of the reaction mechanism of the cycloaddition of C-phenyl-N-methyl nitrone with acrolein it has been shown that two regioisomeric channels are possible. When the reaction follows the meta channel, the C-C bond is formed after the C-O one, where the C-O bond formation begins at 1.58 Å, whereas the formation of the C-C bond begins at 2.02 Å. In the ortho channel the formation is opposite, where C-C and C-O bond formations occur at 2.02 and 1.63 Å, respectively and the C-C formation happens before the C-O one. However, in both cases the formation of the bonds occurs after the transition structure formation. Thus, this reaction was defined as one-step two-stages and asynchronous, where the processes take place in two different time even though they occur in one kinetic step and reactants are directly transformed into products, without being transformed into any intermediates. However, it has been demonstrated that, sometimes, a stepwise mechanism is possible and is predominant in polar solvents, while apolar ones encourage the concerted reaction pathway. Moreover, the reaction between nitrones and dipolarophiles also depends on the possible interactions between the reactants, where additional stabilization comes from π-π-interactions, H-bond formation, attractive electrostatic interactions and favored orbital overlapping.[275-277] Adequate substitution are important to perform the reaction under mild conditions, conjugated unsaturated systems react considerably faster than unconjugated alkenes and intramolecular addition of the *in-situ* generated nitrone group is often reported.[278]

Moreover, basing on the quantum chemical topology of electron density, formulated by Domingo in 2014, the global flux of electron density from the nucleophile to the electrophile at the transition state, is essential to determine the polarity of the reaction, as well as the activation energy. A strong correlation between the polar character of the reactions, measured by the global electron density transfer (GEDT) at the transition states and their feasibility was determined. Higher nucleophilic and electrophilic characters are correlated to higher GEDT and lower activation energy, where the GEDT at the transition states is computed and obtained from

the atomic charges, and the electron density transfer that takes place between the nucleophile and the electrophile is not a local process, but a concerted one. Non-polar processes require high activation energises, but adequate substitution can increase the nucleophilicity and electrophilicity of the reagents, favouring the reactions through polar processes.[279-282] Thus, the modulation and distribution of the electron density is crucial for the reactivity of nitrones.

The preparation of nitrones can be carried out by following different synthetic procedures, from oxidation of *N,N*-disubstituted hydroxylamines, oximes, oxaziranes, aromatic nitroso compounds etc.[283] Here, the synthetic procedure for the synthesis of nitrones followed the reaction between hydroxylamines and aldehydes compounds. Hydroxylamines were prepared starting from their aldehyde precursor, followed by the reaction with NH_2OH to obtain the corresponding oxime, reduced to the hydrogenated compound with $NaBH_3CN$. Fmoc protected aldehydes were used, to exploit the Fmoc deprotection procedure to quantify the grafting degree and were synthesized starting from their amino alcohol precursor (see Appendix for the detailed description of nitrones syntheses). In order to study the influence of alkyl or aryl substituents on nitrone derivatization, differently substituted hydroxylamines and Fmoc-amino protected carbonyl compounds were used. Corresponding nitrones utilized in this study are shown in Scheme 14.
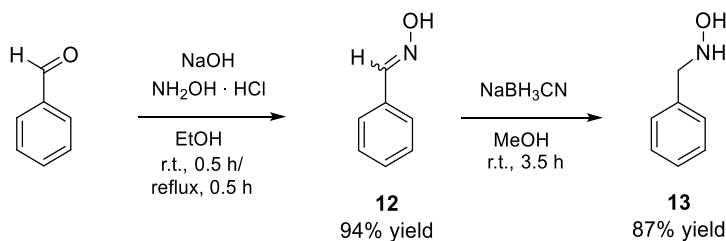
Scheme 12. Synthesis of *N*-benzylhydroxylamine.
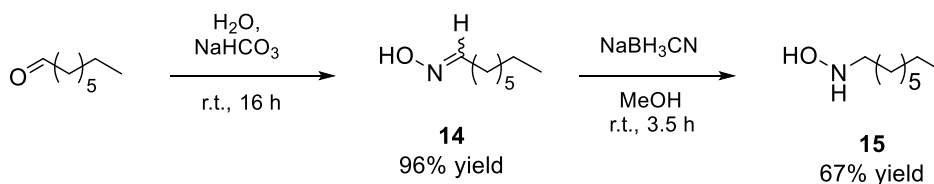
Scheme 13. Synthesis of *N*-octylhydroxylamine
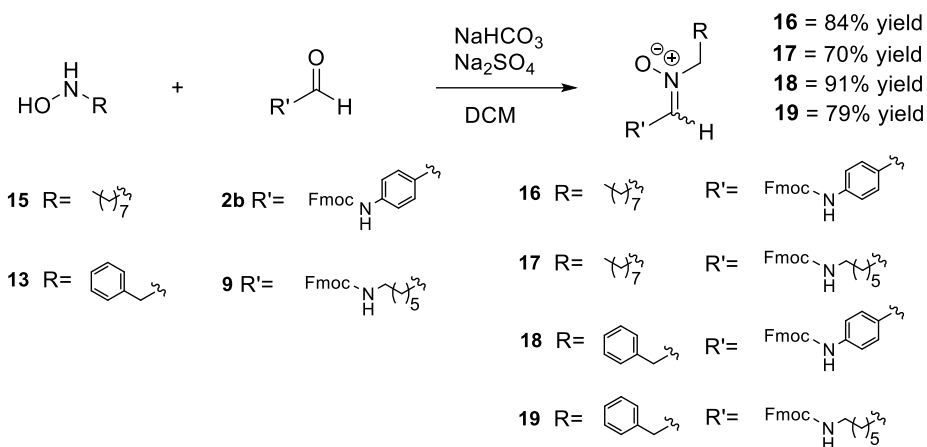
Scheme 14. General synthesis of nitrones used in this study.

The 1,3-DCA on the rGO surface was tested at 60 °C, for 12 h, using an excess of hydroxylamines and aldehydes (*ca.* 3 times more (w/w) than the carbon-based material). 1,4-dioxane, THF and toluene were tested as solvents (Scheme 15). It has been demonstrated that rGO is not stable when THF is used, while toluene revealed to be the optimal solvent of choice. Due to the low MW adsorption capacity of toluene, the 1,3-DCA of nitrones was carried out under conventional heating instead of MW irradiation and an optimization of the temperature conditions revealed that the best derivatization degree could be obtained at 100 °C in 12 h. The idea of introducing various substituents at the 4 and 5 positions of the dihydroisoxazole was done to study their influence on derivatization degree and on material structural modification.
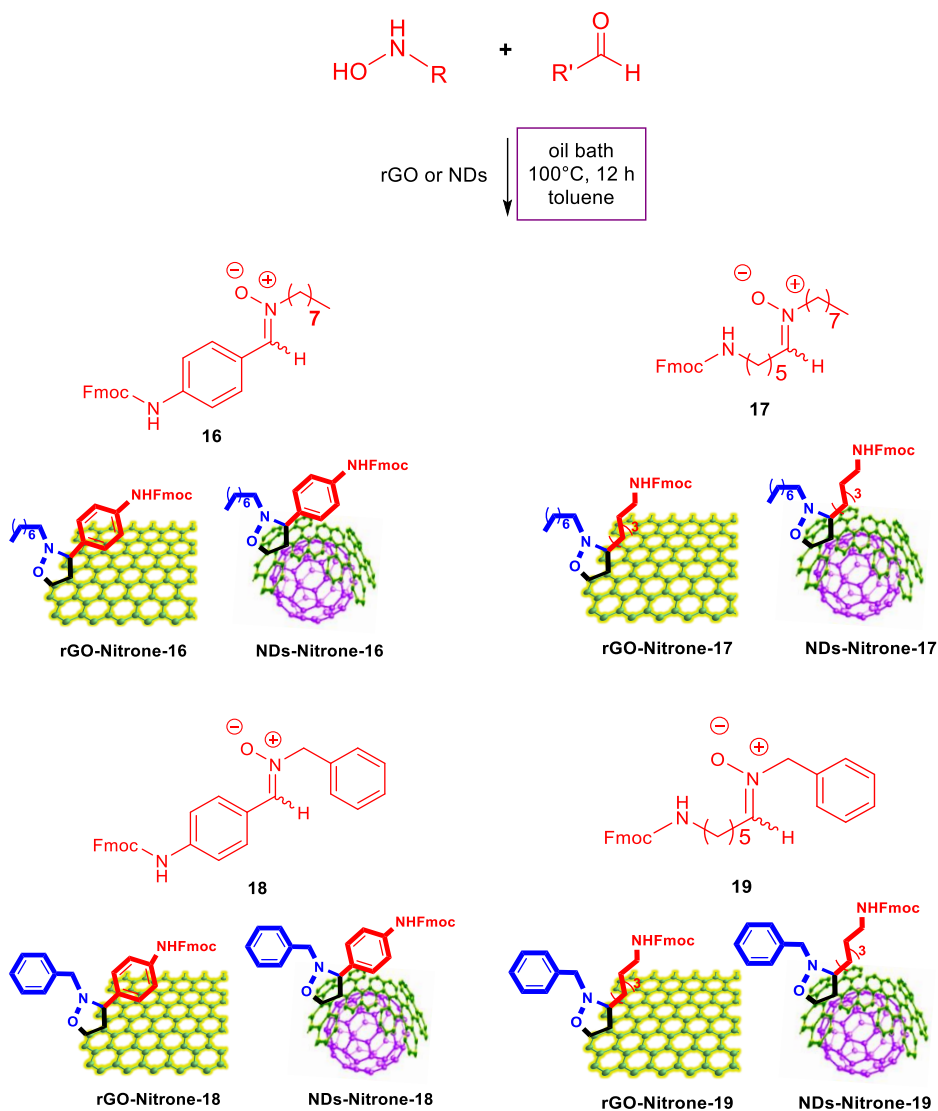
Scheme 15. Derivatization of rGO and NDs with nitrones.

From TGA curves and confirmed by UV-Vis measurements (Figure 44), it is possible to notice how rGO-Nitrone-16 and rGO-Nitrone-18, as well as NDs-Nitrone-16 and NDs-Nitrone-18, showed lower derivatization degrees. This can be ascribed to the position of the Fmoc portion, that, when it is directly bound to a benzene ring, does not allow a correct orientation of the dipole towards the graphitic surface. On the other hand, when the Fmoc portion is connected to the aliphatic portion (rGO-Nitrone-17, rGO-Nitrone-19, NDs-Nitrone-17, NDs-Nitrone-19), higher levels of derivatization were achieved. This is probably due to the possible more favored interaction between the Fmoc orbitals and the conjugated π-graphitic surface, where preferential stabilization comes from π-π-interactions and favored orbital overlapping.

However, the best functionalization occurred when two aliphatic substituents at the nitrone structure were present (rGO-Nitrone-17, NDs-Nitrone-17) (Table 15). This can be ascribed to the higher polar character of the systems, that influences the global electron density transfer (GEDT), the nucleophilicity of the reagents and the activation energy.

In general, excellent derivatization degrees were obtained and no deep modification of the graphite structure was observed, confirming a good structural conservation, as also confirmed by Raman spectroscopy, as reported below. All TGA curves showed a linear thermic decomposition, with a maximum weight loss between 300 and 400 °C, as observed for azomethine ylide and nitrile oxide derivatized rGO and NDs, confirming that the functionalization took place (Figure 44-a,b).

Table 15. Functionalization degree for 1,3-DCA of nitrone onto rGO and NDs surface.

Sample	Nitrone	% UV		% TGA		Derivatization/ C atoms
		% w/w	μmol/g	% w/w	μmol/g	
rGO-Nitrone-16	16	5.8	113	6.3	135	580
rGO-Nitrone-17	17	14.5	309	24.0	535	130
rGO-Nitrone-18	18	3.7	79	5.3	114	669
rGO-Nitrone-19	19	9.6	213	12.5	283	266
NDs-Nitrone-16	16	17.9	400	3.9	82	977
NDs-Nitrone-17	17	8.3	177	2.9	65	1360
NDs-Nitrone-18	18	2.8	38	3.4	390	1078
NDs-Nitrone-19	19	2.6	57	4.6	99	785

DRIFT analysis of nitrone-derivatized NDs reflected the extent of the covalent functionalization. Figure 44c compares the obtained spectra of the different functionalized NDs. All of them show the typical band at around 1650 cm^{-1} ascribed to the sp^2 C=O and the broad band at 3200-3500 cm^{-1} related to the O-H stretching due to the physisorbed water and to the secondary amide. The alkanes sp^3 C-H stretching at 2875-2944 cm^{-1} is also always present, as well as the sp^3 C-H bending at 1460 cm^{-1}. The C=C stretching of the aromatic bond is visible at 1593 cm^{-1}, and its intensity increases from NDs-Nitrone17, NDs-Nitrone-19, NDs-Nitrone16 to NDs-Nitrone18, because of the increasing number of aromatic portions in the structure. The sp^2 acyl C-O stretching at 1100-1350 cm^{-1} is overlapped to the sp^2 C-N stretching at 1235 cm^{-1}, as well as to the stretching of alkoxy C-O, generally at 1050-1150 cm^{-1}. These bands are not clearly visible in the sample NDs-Nitrone17, composed of two alkylic portions, where the broad band between 1100 and 1400 cm^{-1}, can covered up the most typical other signals. Finally, the sp^2 C-H bending

for aromatics is present at 757 cm^{-1} and the peak at 850 cm^{-1} can be ascribed to the N-O stretching.

a

b

c
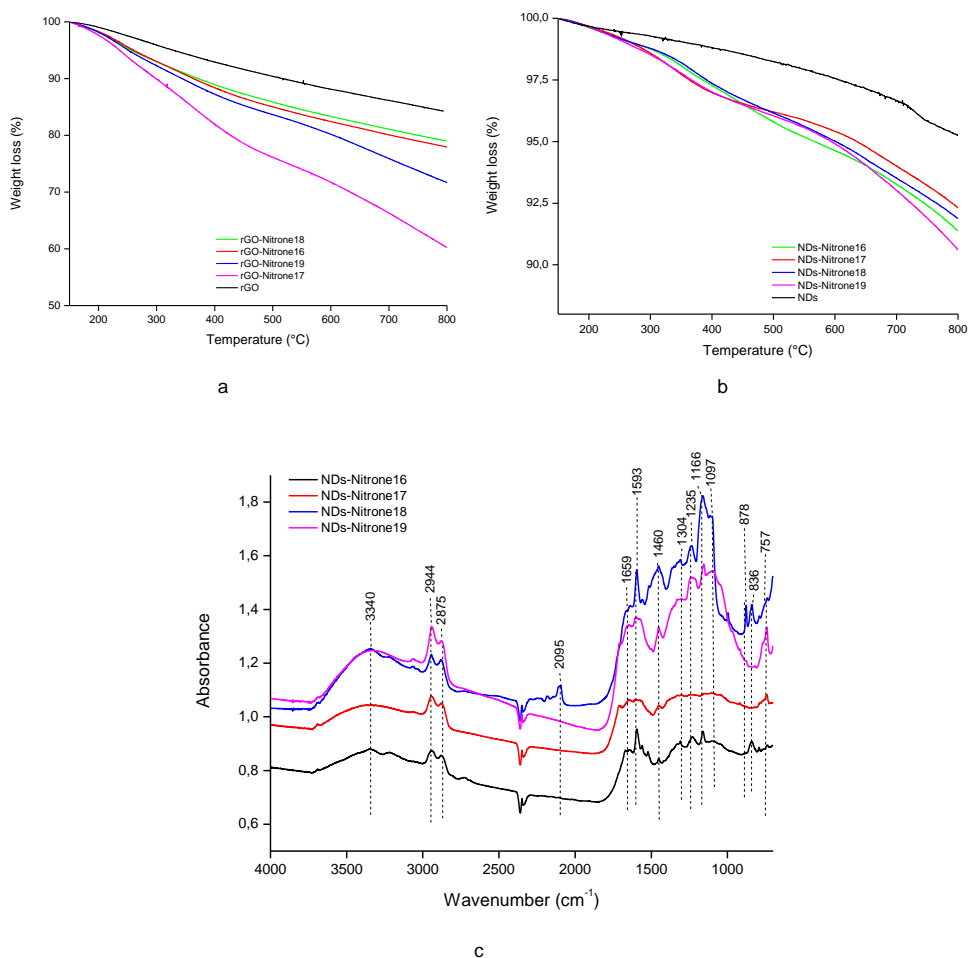
Figure 44. (a) TGA curves of rGO and nitrone divatized rGO; (b) TGA curves of NDs and nitrone derivatized NDs; (c) DRIFT spectra of nitrone derivatized NDs.

Raman spectroscopy was used to evaluate the chemical and physical properties of the synthesized nanomaterials. The average I_D/I_G ratio was measured to estimate the overall defectiveness of graphitic materials. It was 1.19 ± 0.04 for pristine rGO, 1.19 ± 0.02, 1.25 ± 0.03, 1.21 ± 0.05 and 1.52 ± 0.06 for product rGO-Nitrone16, rGO-Nitrone17, rGO-Nitrone18 and rGO-Nitrone19, respectively, as shown in Fgure 45, confirming an increment of the defect content, due to the derivatization and conversion of sp^2 to sp^3 C atoms. Moreover, a more similar I_D/I_G ratio of rGO-Nitrone16 and rGO-Nitrone18 to the one of pristine rGO reflects the lower derivatization degree of these systems, confirmed by TGA and UV-Vis analysis. This is due to a conservation of the graphitic surface and a small increase of the disorders. In Figure 45-a,b a representative Raman spectrum of nitrone derivatized rGO is shown (see Figure 80, Figure 81, Figure 82, Appendix for rGO-Nitrone16-17-19, respectively). The explanation of the

deconvoluted peaks follows the same of rGO-AMY and rGO-NO, where S and G_v are ascribed to the defect content and sp^3 carbon atom presence, also G_r and $D+G_r$ bands are related to defect features. Moreover, a higher spectral intensity in the valley between the G and D bands is observed, due to the increase of satellite bands attributed to limit-sized sp^2 domains resulting from the covalent functionalization. Moreover, from a deep evaluation of the Raman G-band it is possible to observe how the electronic and steric effects applied on the nitrogen function of the isoxazolidine ring determine a change of the G-band position. A shift to higher frequencies (+11 and +13 cm^{-1}) of the Raman G-band is registered in rGO-Nitrone-18 and rGO-Nitrone-19 spectra, respectively, while no appreciable shift is visible for rGO-Nitrone-16 and rGO-Nitrone-17, showing how the presence of the benzyl function, instead of the aliphatic one, on the nitrogen function of the isoxazolidine ring could be responsible of the registered shifts.

a

B

c
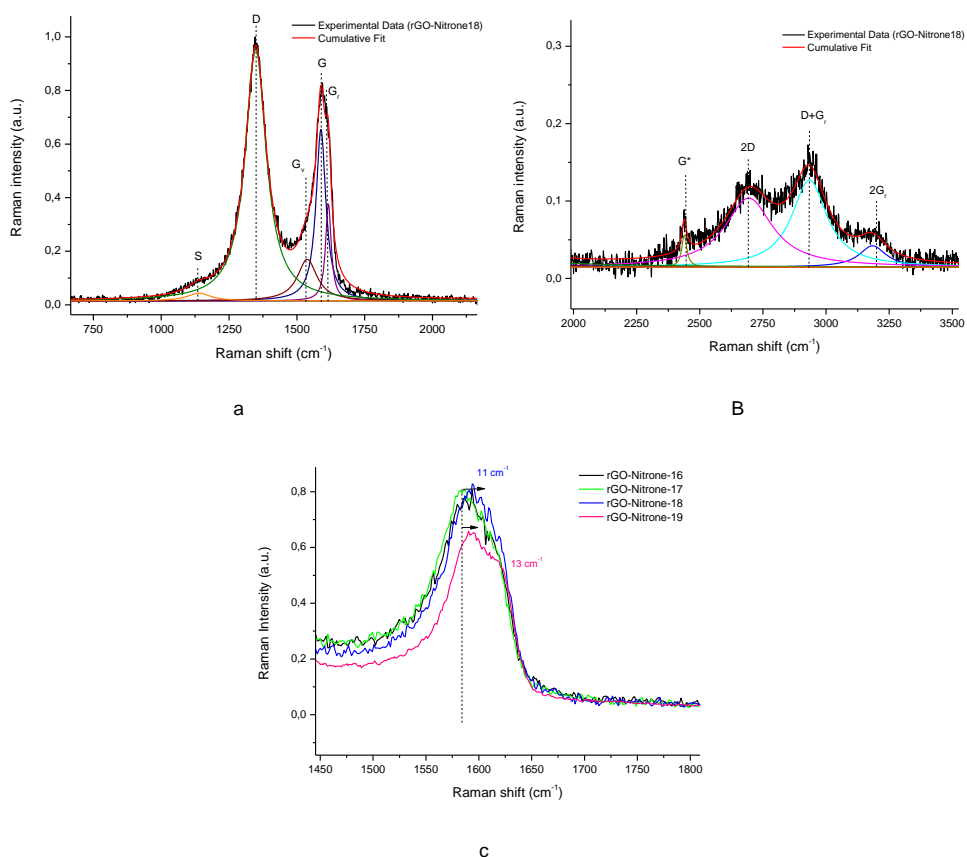
Figure 45. (d) and (e) deconvoluted Raman spectrum of rGO-nitrone18; (f) comparison of the G-band region of rGO-Nitrone-16-19.

As explained above, a possible measurement of the CFD could be obtained by the analysis of the deconvoluted Raman bands, by calculating the ratio of bands assigned to sp^2 domains and of the graphitic-type domains (the D and G bands). The CFD measurements for all the derivatized samples were object of a preliminary study; however, additional investigation on the Raman spectroscopy as quantification technique for graphene and related materials revealed

that such evaluation could be wrong because of the presence of overlapping effects. Indeed, the disorder-related D band, that document the covalent attack on the graphene surface, appears in the spectra, but additional peaks could be masked at exactly the same positions as the graphene bands. Moreover, looking at rGO Raman spectrum it is possible to notice how the disorder-related D band is also present, due to the partial derivatization with hydroxyl, carbonyl, carboxylic and epoxy groups. For these reasons, it was not possible to obtain reasonable results calculating the CFD through this technique.

3.3. Conclusions

In conclusion, three different dipolar cycloaddition reactions were successfully studied to demonstrate the versatility and the efficiency of this approach to derivatize carbon-based nanomaterials, such as rGO and NDs. To carefully prove the derivatization efficiency, different approaches were compared: the TGA analysis, Raman Deconvolution and indirect Fmoc deprotection. FT-IR and DRIFT demonstrated the identity of the grafted derivatives. MW irradiation was successfully exploited for the preparation of pristine rGO and derivatized rGO and NDs with azomethine ylides while nitrile oxide cycloaddition was efficiently performed at room temperature. A detailed evaluation of the influence of dipole substructure was performed and interestingly, the derivatization degree of nitrones varied in dependence of the aryl/alkyl balance in the dipole structure. High degrees of derivatization were always obtained under the optimized conditions.

Chapter 4

Study of heterogeneous catalyst design and applications for metathesis reactions

4.1.   Introduction

Thanks to a collaboration with Professor Gabriel Lemcoff, working at Ben-Gurion University of the Negev (Israel), specialist in ruthenium catalysts for olefin metathesis, an investigation on innovative heterogeneous supporting system for Ru(II) species, active in olefin metathesis, was performed. With this aim, an in-depth study of the design, the immobilization, and the applications of heterogeneous metathesis catalysts, by focusing on metal complexes, supporting material and metathesis type reactions, was carried out and gave rise to the composition of a broad review, that is still under final revision. Here, a short explanation of the main heterogeneous catalysts used in olefin, alkane and alkyne metathesis, whose activity and stereoselectivity is strongly dependent on the ligand structure, as described in Chapter 1.2.2., is reported.

During recent decades, metathesis-like reactions have gained considerable importance in the transformation of a wide range of compounds.[284-286] Olefin metathesis is the most extensively studied, but the related metathesis of alkynes and alkanes have been recently more investigated. Olefin and alkyne metathesis are organic reactions involving the transmutation of carbon carbon bonds, where the redistribution of substituents between the substrates takes place.[287] In the alkane metathesis, the saturated substrate is rearranged to give its lower and higher homologue.[288] Several strategies have been studied for the immobilization of metal complexes on suitable supports, such as supported homogeneous catalysis, supported metal oxides and surface organometallic chemistry (SOMC). In supported homogeneous catalysts a linker is used as intermediate spacer between the metal centre and the support,[44] while SOMC is a methodology through which organometallic complexes can be directly attached to inorganic carriers and the inorganic surface plays a crucial role as support and ligand, and it is directly involved in the coordination sphere of the metal. Following the latter immobilization procedure, uniform "single-site", well-defined heterogeneous catalysts can be generated through an excellent knowledge of the structure of the metal active sites at the molecular level.[44]

4.1.1. Olefin metathesis

The main metals used for the olefin metathesis appear in groups 6 and 7 of the periodic table, especially molybdenum, tungsten and rhenium in their higher oxidation state, whose complexes are generally known as Schrock-type catalysts.[289] Ruthenium complexes, also called Grubbs or Hoveyda-Grubbs complexes, also provide important systems for promoting alkene metathesis-like reactions.[290] A classification based on the immobilization strategy (supported metal oxides and SOMC) is here reported.

4.1.1.1. Supported metal oxides

Supported metal oxide catalysts consist of an active metal oxide species, rhenium, tungsten and molybdenum, immobilized on an inactive oxide support. They are characterized by lower activity than well-defined active sites catalysts. This is due to the incomplete knowledge of the active site structures and the presence of a mixture of surface species, among which only a very small fraction is active. The metal oxide, in fact, can be present as isolated mono-oxo and di-oxo or oligomeric surface species, essential for providing high metathesis activities, and inactive clusters or crystalline nanoparticles (Scheme 16). To avoid crystalline nanoparticles phase formation and to increase the dispersion and accessibility of the active species attention has to be paid on the choice of the metal oxide precursor, as well as its loading amount, pre-activation, synthetic methods and the support material.[291] The formation of inactive crystalline nanoparticles is promoted by conventional impregnation method and new synthetic procedures, such as one-step precipitation method,[292] ion exchange procedures,[293] framework trapping,[294] and thermolysis treatments,[295] have been studied to increase the number of the active sites. Pre-activation also influences catalyst activity and it is generally obtained by high temperature, inert gas purging and reduction treatments.[296, 297] Novel pre-treatment methods afford to prepare good quality catalysts using olefin-containing atmosphere and regeneration by inert gas purging at elevated temperatures.[45, 298] The choice of the solid supporting material can determine metathesis activity and lately, mesoporous supports exhibited higher catalytic activity due to their uniform and large pore volume, and higher BET surface area. The acidity of the support (silica or alumina-silica) was found to be beneficial for the olefin metathesis,[299, 300] as well as the addition of a binder agent, such as magnesium and/or zinc oxide.[301] Al_2O_3, SiO_2–Al_2O_3 and aluminium nitrate are commonly used as supports for rhenium oxides catalysts, while silica-based materials represent the first choice for tungsten and molybdenum oxide catalysts.
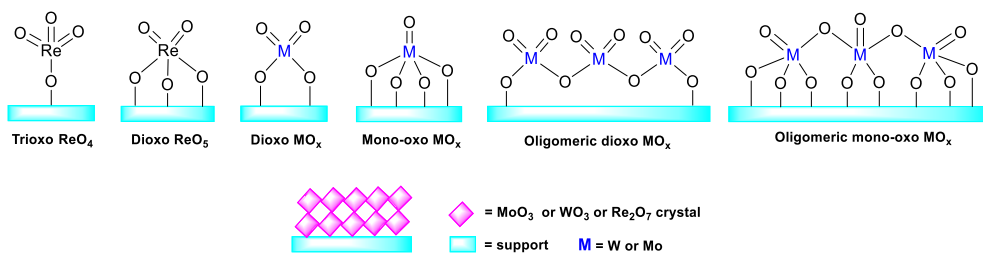
Scheme 16. Schematic representation of Re, W and Mo oxide catalysts, when supported on a solid material.

4.1.1.2.SOMC

Schrock-type catalysts

In the last decades, SOMC has been developed as efficient strategy to overcome heterogeneity of group VI metal oxides supported on inorganic materials. Supported metal oxo alkyl complexes, supported oxo-or imido-alkylidene metal complexes and homoleptic systems have gained considerable attention due to their high catalytic efficiency and resilience to the deactivation. Their general structure is represented in Figure 46.

When anchored on inorganic supports, the influence of supported metal oxo alkyl complexes podality was studied. Monopodal and bipodal metal oxo catalysts show different catalytic performance, and several studies, carried out since 2016, suggested the impact of the podality on the electrophilicity and flexibility around the metal center, and consequently, on the catalytic activity.[302] Monopodal species are demonstrated to be less active than the correspondent bipodal species, whose activation is faster. The lesser is the steric hindrance due to the ligands, the higher is the olefin coordination to the metal center. The podality is dependent on the silanol concentration and can be controlled by the temperature. Generally, monopodal species can be obtained at room temperature, however, heat treatment is necessary to initiate the formation of bipodal species. Furthermore, symmetric bipodal precatalysts are demonstrated to be more active and stable than unsymmetrical metal complexes.[303] Simultaneously, investigation of the structure-reactivity relationship in oxo-alkyl metal complexes have been carried out comparing different spectator ligands in propene metathesis.[304] The presence of bulky and coordinating ligands allows to isolate more stable oxo-alkyl metal complexes and it has been demonstrated that electron withdrawing groups increase the electrophilicity of the metal center and thereby the catalytic activity.[305]

The same was demonstrated when oxo-alkylidene metal complexes were grafted upon silica. They showed high activity and stability thanks to the imido ligands that act as stabilizing agents, preventing bimolecular decomposition. Moreover, the electron withdrawing property of ancillary ligands (X) positively affects the catalytic performance. Interestingly, in the case of imido-

82

alkylidene W complexes, the presence of electron donating groups, such as 2,5-dimethylpyrrole, N-heterocyclic carbenes,[306] imidazolin-2-iminato ligand[62] has a positive effect on the catalytic performance, due to a partial destabilization of the intermediates. Since electron donating ligands can prevent alkylidene protonation by the surface silanol groups, their presence can be crucial for the preparation of highly active catalysts.
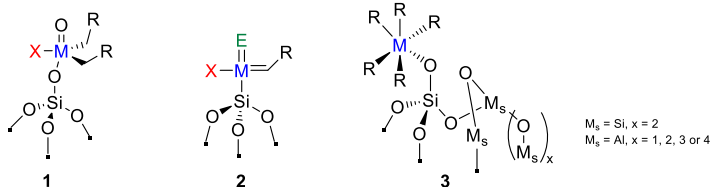
Figure 46. General structural motif of (1) supported metal oxo alkyl complexes, (2) supported oxo- or imido-alkylidene metal complexes and (3) homoleptic systems. M indicates W, Mo, Re; X the neutral or anionic ligand; E oxo or imido ligand.

Ruthenium-based catalysts

Grubbs and Hoveyda-Grubbs catalysts are stable ruthenium alkylidene complexes. They represent important systems for metathesis catalysis; however, the modification of the metal coordination sphere provided different designed Ru catalysts, characterized by high Z-selectivity. In heterogeneous metathesis, the selectivity of the catalyst can be achieved through the modification of the ligand environment of the metal centre, the alteration of the solid support properties, as well as the interactions between the complex and the support. However, not spectacular results were frequently obtained and a big effort is aimed for the preparation of selective Ru-supported catalysts for olefin metathesis. Covalent immobilization takes into account different parts of the catalyst: alkylidene ligand, neutral ligand and the halogen ligand and can be achieved through the replacement of one of them.

Alkylidene ligands can be successfully replaced exploiting alkylidene exchange reactions and, when the alkylidene portion is supported on solid materials, supported-ruthenium complexes can be obtained.[307] However, when modified alkylidene ligands are used as anchoring groups, the metathesis reaction is catalysed homogeneously. In fact, it is well demonstrated that the first step involved in the olefin metathesis reaction is the dissociation of the alkylidene ligand and the release of the 14e⁻ active species into the reaction mixture. After the metathesis reaction, the (pre)catalyst regenerates by the uptake of the active catalyst forms (the unstable 14 e⁻ ruthenium species) by the supported alkylidene ligand (boomerang reaction mechanism, Scheme 17). The heterogeneous boomerang effect was recently probed by supporting bis(quaternary ammonium)-tagged ruthenium complexes on solid supports (Figure 47a). In these cases, the supporting materials were doped with ammonium-tagged alkylidene

derivatives, as precursor of the benzylidene ligand to enhance the (pre)catalyst regeneration *via* the boomerang mechanism.[308, 309]
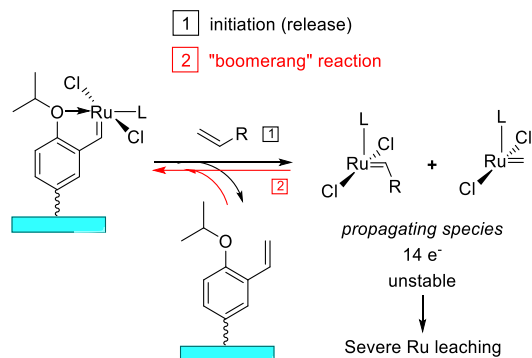
Scheme 17. Schematic representation of boomerang reaction mechanism.

When a neutral ligand is used as linker connection with the solid support, the boomerang effect is avoided. Recyclable single-site well-defined catalysts were obtained exploiting specific functional groups, such as phenolic hydroxyl or mercapto, as immobilization sites on suitable supports. It was demonstrated that the immobilization site influences the catalytic activity, due to the freedom of the catalytic center (Figure 47b).[310]

The replacement of chloride happens *via* anionic exchange. It generally involves the employment of carboxylate anions, however, lately, several homogeneous Ru-olefin metathesis catalysts containing thiolate ligands have been used for anchoring on suitable supports. The investigation of the difference between flexible mercaptopropyl linker and a more rigid and bulkier mercaptophenyl group revealed that the flexibility of the organic tether influences the catalytic properties of the resulting supported complex. The modification of the anionic ligands can result in different reactivity and selectivity of the catalysts (Figure 47c).[311]
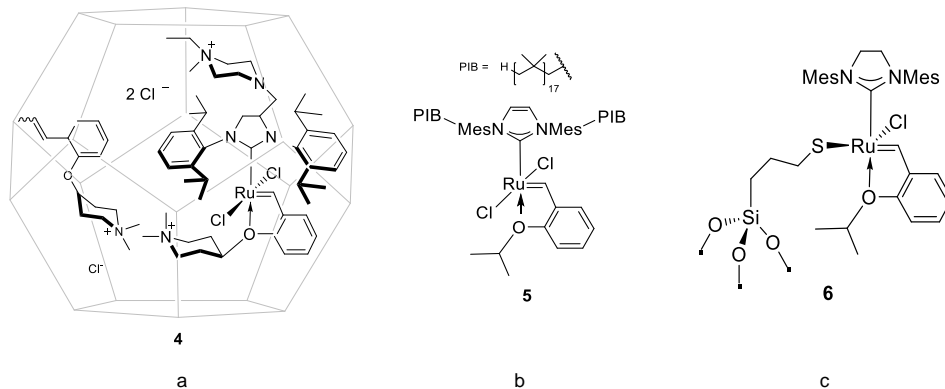
Figure 47. Examples of supported Ru(II) complexes, immobilized on suitable support exploiting (a) the alkylidene ligand (the support could be SiO_2, SBA-15, graphene-carboxylate), (b) the neutral ligand, (c) the anionic ligand.

4.1.2. Alkyne metathesis

The most commonly used catalysts in alkyne metathesis-like reactions are well-defined Schrock-type alkylidyne complexes,[312] where, differently from olefin metathesis catalysts, bis-alkoxide alkylidyne species are present, highlighting the importance of the metal coordination sphere.[313] The preparation of selective and robust alkyne metathesis catalysts, that do not undergo deactivation and do not promote undesired side reaction, such as alkyne polymerization, is a big challenge, especially for the metathesis of terminal and aryl alkynes. One strategy to increase the selectivity of molecular catalysts and to avoid deactivation mechanisms, is the grafting of metal complexes on isolated surface species, as well as the study of ancillary ligands. Recently, the catalyst investigation and the variations of the structure and the metal coordination environment led to the preparation of solid supported complexes differently stable and active, where the modification of the metal coordination sphere can modify the catalytic activity of the system through the modulation of the steric and electronic parameters.[314] Tuning the electronic properties of alkoxide ligands by introducing electron withdrawing atoms, the catalytic activity is dramatically influenced and higher efficiency is observed, due to the increased electrophilicity of the metal sites.[315] The steric and electronic properties of these types of catalysts can also be changed to avoid the deactivation, that occurs through bimolecular dimerization pathway[316, 317] or *via* α-hydrogen elimination.[314] The importance of the coordination sphere on the catalytic activity and selectivity of metal supported complexes was further proven by different research groups, confirming that the alkyne metathesis is favored when bulky alkoxide groups are present in the coordination sphere of the supported metal.[318, 319]
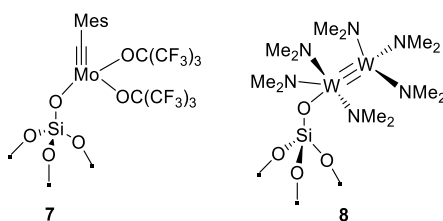
Figure 48. Examples of Schrock-type alkylidyne complexes.

4.1.3. Alkane metathesis

The activation of alkanes represents a challenge in chemistry due to the inertness of C-H and C-C bonds and alkane metathesis is a promising strategy for their transformation. It was for the first time discovered in 1997 by Basset and co-workers and involves the transformation of alkanes into their lower and higher homologues at moderate temperatures.[320] The catalyst investigation started with a single site Ta hydride catalyst supported on silica [(≡SiO)$_2$TaH] up

to well-defined supported metal alkyl catalysts (d^0 alkyl alkylidene complexes of Ta, Mo, Re, W, polyalkyl complexes of Ta, W carbynes and Ir pincer complexes).[288] The reactivity of metal hydrides and metal alkyl complexes has been recently described, and it was established that single site metal hydride carbenes (M-H(=CHR)) or metal alkyl carbenes (M-R(=CHR) represent the active intermediate species, respectively. The activation procedures consist of thermolysis for the formation of active metal alkyl carbene species, and hydrogenolysis for supported metal hydride, starting from supported metal alkyl complexes. The activation can be controlled varying the temperature, leading to different surface complexes, in term of structure and reactivity.[321] The variation of the activation reaction conditions, in fact, allows to obtain different single site alkylidyne, carbene or hydride species, that are actively involved in the reaction mechanism. Figure 49 describes the different alkylidyne, carbene or hydride species that can be formed upon hydrogenolysis and thermal activation. However, it is important to underline that, among them, mixtures of active species are formed and only the 50% of the active sites participates to the catalytic mechanism and undergo deactivation during the alkane metathesis reaction Moreover, to the best of our knowledge, no fine correlation between reaction activation conditions and catalyst structure modification is visible, when comparing same reaction conditions. Furthermore, the investigation of the catalytic role of the support as well as the nuclearity and coordination of the metal with the support is still object of study.[322] Despite the unknown influence of the catalyst structure and preparation, it has been demonstrated that metal hydride catalysts are more active than supported metal alkyl catalysts, due to their stronger ability to react with C-H bond of alkane by σ-bond metathesis or oxidative addition, followed by hydrogen and metal alkyl production.
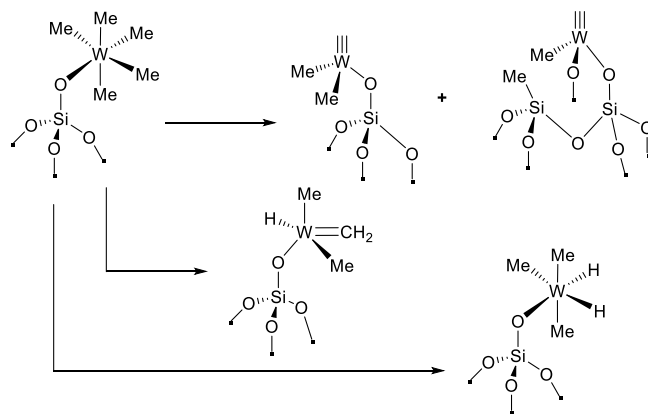
Figure 49. Activation of silica-supported tungsten pentamethyl complexes to different single site alkylidyne, carbene or hydride species achieved through hydrogenolysis and thermal treatments.

4.2. Design of a heterogeneous catalyst based on Ru(II) immobilized on carboxylate functionalized graphene for metathesis reactions

As reported above, heterogeneous Ru(II) systems can be covalently anchored on suitable supports *via* neutral, the anionic or the alkylidene ligand. Mesoporous materials, silica, aluminum silicate, resins and polymers are the most used supporting systems. Only a small portion of studies exploit the immobilization of ruthenium on graphene structures, by complexing it with covalently or non-covalently bonded ligands onto the graphene surface. Looking at graphene structure, as described in Chapter 3.1., the most used procedures for the preparation of nanohybrid ruthenium complex composites exploit the covalent functionalization of carboxylic functions by their activation and modification to amidinic portions,[323-325] or non-covalent functionalization through π-π interactions, thanks to the graphitic delocalized π-electronic system that allows immobilization of polyaromatic rings by π-stacking interactions, followed by ruthenium anchorage.[326] However, only a few number of these studies deeply consider the influence of the ligand on the catalytic efficiency. Especially talking about ruthenium catalysis, it is important to evaluate the impact of the ligands on the metal activity. Ligands confer high activity, selectivity, and stability to the catalyst by modifying the electronic and steric properties of the metal centre and a good cooperativity between the metal and the ligands, as well as the capability of the ligands to stabilize metal oxidation states and coordination geometries can improve the catalytic efficacy of the system. One of the platforms for the modification of catalyst properties are anionic ligands. If generally the anionic positions in ruthenium complexes are occupied by chloride ligands, the introduction of different halides, carboxylic, sulfonic and phosphonic groups have been extensively investigated. Some of these modifications can be used to immobilize catalysts, but the fine-tuning of the anionic ligands can result in different reactivity and selectivity of the catalysts.[56, 327, 328]

Here, a preliminary investigation of new carboxylate-functionalized rGO, designed as heterogeneous catalytic systems for the coordination and stabilization of Ru(II) species, was begun. As explained in Chapter 3.1., the GO surface is characterized by the presence of hydroxyl, epoxy and carboxylic acids groups. These reactive functional groups can efficiently bind metal ions or can be easily used as platforms for further covalent functionalization, as demonstrated by a conspicuous number of publications that declare the use of GO as support for catalytic systems.[264, 329, 330] However, GO nanosheets show some disadvantages, such as low dispersion stability and high defects content.[260, 331] Thus, in order to restore the honeycomb two-dimensional lattice structure and consequently the unique physicochemical properties of graphitic materials, including excellent conductivity, high surface area, high mechanical strength and ease of functionalization, rGO was used as starting material. Due to its superior properties it represents a promising candidate in the field of nanotechnology as suitable support for photocatalytic applications, thanks to its ability to improve charge transfer and separation.[332,

[333] For this reason it has been selected to be tested as potential support for Ru(II) species, suitable for metathesis reactions, induced by photocatalysis. In order to compare the complexing effect of anionic ligands, monocarboxylate or dicarboxylate derivatives were designed. The derivatization of rGO was performed by following the well-studied azomethine ylide (AMY) 1,3-DCA. Two different synthetic strategies were followed and the obtained derivatized systems were preliminary characterized by TGA. The first approach involved the reaction between rGO and formaldehyde in the presence of glutamic or aspartic acid, following by the optimized reaction parameters of the AMY 1,3-DCA (MW, 130°C, 2 h) and rGO-Glutamic and rGO-Aspartic were obtained, respectively (Scheme 18). The samples were analyzed by TGA and, as shown in Figure 50, the reaction occurring between rGO, formaldehyde and glutamic acid proceeded with a 6% (w/w) of derivatization degree, very differently from the 31% (w/w) obtained using aspartic acid. This can be explained by the possible ring closure reaction of glutamic acid to the corresponding amide, that does not happen using aspartic acid due to the higher tension forces and instability of the smaller cycle.

However, in order to satisfy the request for more flexible spacers, that could enhance the catalytic properties of the resulting supported complexes,[334] a second approach was studied: rGO was firstly reacted with formaldehyde in presence of lysine (rGO-Lys) and the final amine group was successively used as suitable reactive portion for acyl nucleophilic substitution of different anhydrides: succinic anhydride, citric acid anhydride and phthalic anhydride, obtaining rGO-Succinic, rGO-Citric and rGO-Phthalic, respectively. Thus, three different flexible portions were covalently anchored on rGO surface, and their structure allowed the comparison of the influence of aliphatic or aromatic spacers and the dicarboxylate chelating effect on metal species coordination, immobilization, and stabilization. The first reaction step was carried out in a MW reactor at 130 °C for 2 h, the second one involves the stirring of the reagents in dry DMF and pyridine at 40 °C for 24 h. Due to the low reaction temperature the reaction mixture was not irradiated under electromagnetic waves, but conventional heating was performed. Due to the low derivatization degree (in a range between 3-5%), observed through TGA, the samples were subjected to a second derivatization reaction. The same reaction conditions were followed, and a bit higher functionalization was obtained (up to 8%).

<u>First approach</u>
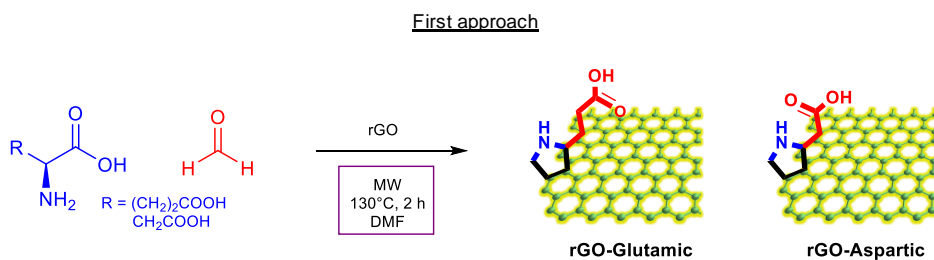
Scheme 18. rGO derivatization *via* AMY 1,3-DCA, to obtain monocarboxylate functionalized derivatives.
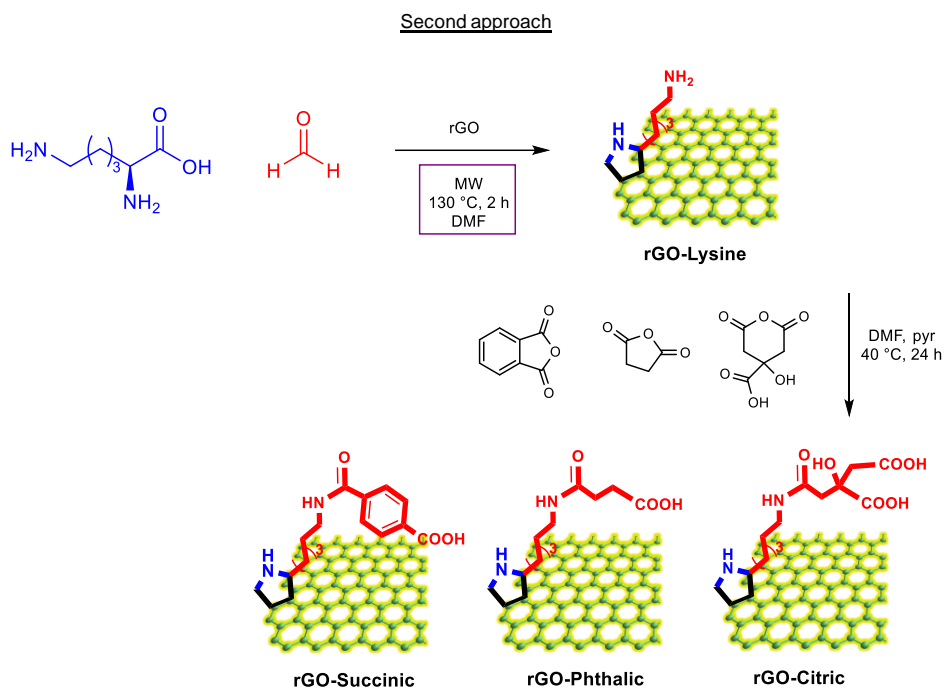
Scheme 19. rGO derivatization *via* AMY 1,3-DCA, to obtain more flexible mono- or bi-carboxylate functionalized derivatives.
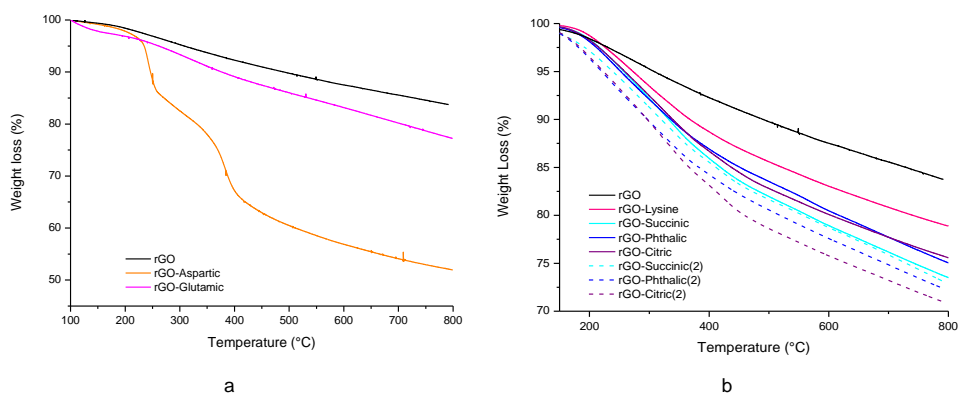
Figure 50. (a) TGA curves of rGO derivatized following the first approach; (b) TGA curves of rGO derivatized following the second approach. Dashed lines represent rGO reacted two times.

As previously mentioned, these supports were designed as innovative systems for heterogeneous catalysis. More precisely, the idea came from the investigation of the Prof. Lemcoff's research group on S-chelated ruthenium pre-catalysts for olefin metathesis, that need activation to the active form by means of either heat or UV irradiation. The latency property gives the opportunity to guide selectively catalytic sequences by UV light in chromatic-orthogonal processes and stereolithographic 3D printing,[57] and higher precision and ease of handling are some advantages.[335] The design of highly active metal supported heterogenous

systems represents a big challenge to evolve the framework of ruthenium-based complexes and to exploit all the benefits coming from the heterogeneous catalysis. The versatility of the ruthenium framework is easily suited to modification strategies. However, both neutral and anionic ligands have a significant impact on the stability and reactivity of such type of catalysts. Thus, the anionic exchange between the designed carboxylate-functionalized rGO and Hoveyda−Grubbs analogues, should be carefully investigated to afford highly stable and active complexes, where the combination between the excellent properties of graphitic structures and Ru(II) catalytic activity, could give an highly active, recyclable, innovative and versatile catalytic system. Figure 51 shows an hypothetical complexation and immobilization structure of Ru(II) supported on prepared rGO. This study still remains under investigation.
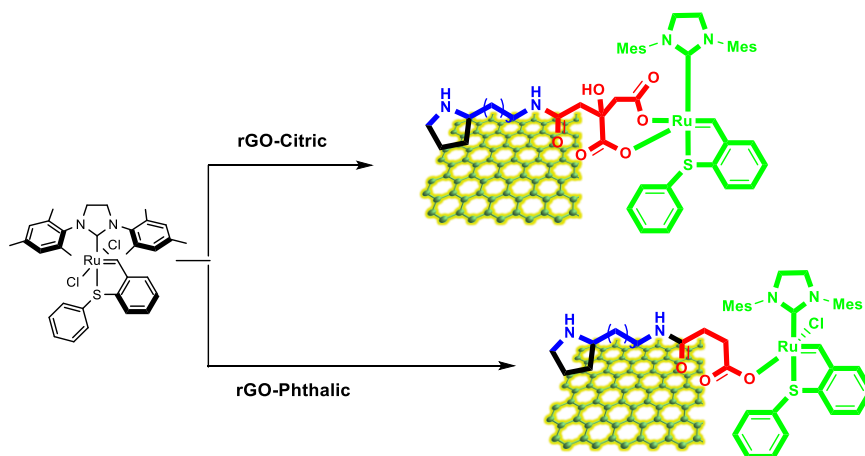
Figure 51. Hypothetical complexation and immobilization of a Hoveyda−Grubbs analogue onto carboxylate derivatized rGO.

4.3. Conclusions

Olefin metathesis is one of the new fundamental novel organic reactions discovered and improved in the last 60 years. It opened up new industrial routes to important petrochemicals, polymers, oleochemicals and chemicals.[336] In the academic field, many successful results were achieved through olefin metathesis, especially in polymer chemistry,[285, 337, 338] peptides and peptidomimetics synthesis,[339] protein modifications,[340] six-membered O-heterocycles synthesis,[341] steroid synthesis,[342] synthesis of biologically important alkaloids and other secondary metabolites,[343, 344] synthesis of bioactive agents,[345, 346] drug synthesis[347, 348] and natural products synthesis.[284] Relevant applications with alkyne and alkane metathesis are less present in literature, but the entire field is still in development, and progress are being made, such as synthesis of natural products *via* enyne metathesis.[349] However, most industrial processes and literature are focusing on homogeneous metathesis reactions with non-supported catalysts, while heterogenous metathesis reactions with supported catalysts are only

considered at the academic level. A well-defined, efficient, relatively inexpensive process which uses a supported metathesis catalyst might achieve the already mentioned applications, while retaining the typical advantages of the heterogenous reactions, such as easy catalyst separation and simple recycling. On the other hand, heterogenous systems could present critical issues, such as low selectivity and poorly-defined active sites. Thus, here a deep study on the main heterogeneous catalysts used in olefin, alkane and alkyne metathesis was performed. The focus of this investigation was to define the structure and the influence of the ligands on the catalytic activity and stereoselectivity, taking into account the metal coordination sphere, the type of immobilization, the type of catalyst and the support strategy. The final goal was to design a well-defined and efficient supported metathesis catalyst and a new carboxylate-functionalized rGO suitable for the coordination and stabilization of Ru(II) species through the anionic ligand was prepared. Two different derivatization approach were studied exploiting the azomethine ylide 1,3-DCA and the interposition of a flexible spacer between the rGO surface and the carboxylate functional groups was essential to prepare bi-carboxylate functionalized derivatives, that can be used as chelating ligands. Additional studies are needed in order to select the type of catalyst, according to the metal coordination sphere and the type of support, to study the immobilization degree and the catalytic activity.

Chapter 5

Improving the electrocatalytic performance of sustainable Co/carbon materials for the oxygen evolution reaction by ultrasound- and microwave-assisted synthesis

5.1.   Introduction

The ambitious challenge of developing cheap and efficient fuel cells, and metal–air batteries as well as systems for energy conversion or storage necessarily passes through the design of low-cost and highly active electrocatalyst materials.[350-355] For example, considering the case of water-splitting, i.e. "the electrolysis of water to hydrogen and oxygen",[356] the H_2 evolution reaction (HER) occurs at the cathode, while the oxygen evolution reaction (OER) takes place at the anode.[357] The design of cheap and stable active electrocatalyst materials for the OER is particularly attractive due to the elevated overpotential needed for the oxidation of water.[358] In fact, while the HER is a two-electron transfer reaction, the OER is a four-electron oxidation, having a higher kinetic barrier.[359]

Some precious metals, such as Pt, Ir and Ru, and their oxides, have been reported to develop the most active electrocatalysts for the OER.[360] However, high costs and, in some cases, low stability, make their commercial application impractical.[361]

The substitution of noble metals has focused on relatively inexpensive and Earth's crust abundant metals such as Mn, Fe, Cu, Ni and Co. Cobalt, whose market dramatically slumped in 2019 making the metal much more affordable, has been studied as an efficient OER catalyst since 1980s. Within that time, the literature has reported numerous successful novel Co-based OER catalysts, which can be divided into five different categories: nitrogen-doped (*N*-doped) carbon composites, oxides/hydroxides, chalcogenides, phosphides, and phosphates.[362] Based on the principles of green chemistry, cobalt-N-doped carbon composites have particularly emerged since they can be produced from biowaste-derived carbon, resulting in materials having a sensibly low carbon footprint.[363] For example, some commonly employed carbon bio-sources include inexpensive and abundant algae, chitin or eggshells.[364, 365] In addition, the porous nature of some of these biowaste can enhance the electrocatalytic properties of the final electrocatalysts.[366] It must also be highlighted that in cobalt-*N*-doped carbon composites, a synergism effect could be observed as apart from metal active sites the carbon itself can slightly catalyse the OER.

However, despite the ideal aim of creating sustainable catalysts, the preparation of *N*-doped carbon composites normally entails some environmental and ethical drawbacks. These

important limits are attributable to the massive use of cobalt or to the low efficiency of the synthetic methodologies. In fact, conventional technologies (i.e. conventional heating) are still the major techniques used for the preparation of electrocatalysts with remarkable energy-consumption disadvantages. In addition, and more importantly, a high content of cobalt is normally employed, ideally forcing the already intense and alarming mining of Co. Indeed, two-thirds of Co mines are present in the Democratic Republic of the Congo (DRC), where the population is suffering from toxic pollution (due to artisanal mining) and child exploitation.[367] As a result, if on one side Co remains economically convenient and catalytically efficient, its utilization should be diminished as much as possible.

The purpose of this work, that was carried out in collaboration with the PhD student Alessio Zuliani, working at Cordoba University under the supervision of Professor Rafael Luque, was to demonstrate the possibility of preparing active Co-based materials for the OER, having a low metal content, and employing low toxicity and biomass-derived reagents through environmentally friendly and energetically efficient synthetic techniques, such as MW-, US-assisted or both in combination (MW/US).[368, 369] Remarkably, US- and MW-assisted techniques are increasingly widely used in synthesis and catalysis.[370] Some of the most important advantages of the latter heating approaches are: (i) direct transfer of energy to the reactants instead of transferring heat, (ii) independence of heat convection, (iii) rapid heating rates, and (iv) the possibility of obtaining volumetric, local and material-selective heating, as explained in Chapter 1.3.[371-373] Carbon-based materials are, in general, very good MW and US absorbers. According to the literature, a synthetic strategy that takes into consideration all these aspects simultaneously has not been reported yet.

A sequence of electrocatalysts based on Co has been prepared using carbon derived from pinecones and employing US, MW and combined MW/US techniques. A low metal loading of ~4% (wt) was selected, alternatively to the 25–50%wt metal loading normally reported in the literature for this type of material.[374, 375] Carbon derived from pinecones has been selected due to large availability, the interesting composition in terms of cellulose and lignin contents, and the low cost.[376] In addition, it has been demonstrated that activated carbon from pinecones exhibits enhanced properties for the adsorption of metals at basic pH values.[377, 378] The *N*-doping of carbon have been performed using a low-toxicity nitrogen source, i.e. urea. Polyphenols extracted from green tea has also been used as stabilizers and ligands of cobalt, having similar phenolic functional groups of Co-ligands reported in the literature.[379, 380] With all of these considerations, a sequence of seven different samples was prepared and exhaustively characterized by powder X-ray diffraction (XRD), N_2 physisorption (Langmuir model), scanning electron microscopy (SEM) plus energy-dispersive X-ray spectroscopy (SEM-EDX), transmission electron microscopy (TEM), inductively coupled plasma mass spectrometry (ICP-MS) and X-ray photoelectronic spectroscopy (XPS). All the materials were tested as electrocatalysts for the OER, studying the influence of the use of carbon derived from pinecones (using commercially available activated carbon as the counterpart), doping with nitrogen,

stabilization with polyphenols and the influence of the different synthetic procedures (i.e. conventional heating vs. MW and US procedures) on the final electrocatalytic activities. The most active materials were also tested operating at 60 and 80 °C. According to the literature, the best sample was found to be classifiable as an "excellent" electrocatalyst for the OER.[381]

5.2. Results and discussion

5.2.1. Synthesis of Co-polyphenols supported on activated carbon

A series of electrocatalysts based on ~4% (wt) cobalt supported over activated carbon (AC) was developed using AC derived from pinecones, polyphenols and employing different synthetic techniques (US, MW and combined MW-US irradiation). The study aimed at investigating the difference between commercially available carbon and carbon derived from pinecones, the effect of doping with nitrogen, the influence of the synthetic procedure for the adsorption of the metal (conventional vs. MW vs. US vs. combined MW-US heating) and the impact of the utilization of polyphenols extracted from green tea as metal stabilizers. The synthetic procedure for the preparation of the samples involved a sequence of steps aimed to maximize the electrocatalytic activity of the materials for the OER, as summarized in Figure 52. First of all, the washed pinecones were carbonized exploiting their peculiar porous structure in order to enhance the metal adsorption properties.[382] As illustrated in TGA curve reported in Figure 53, around 70% of the total weight was lost during this procedure. Just like most of the thermal degradation of wood materials, the thermal degradation of pinecone biomass also occurred in three phases: (i) moisture evaporation at 30–150 °C, (ii) hemicellulose and cellulose decomposition at 200–350 °C, and (iii) lignin decomposition at 160–700 °C. Remarkably, the larger loss of weight was observed in the temperature range of 200–375 °C, corresponding to hemicellulose and cellulose decomposition. Before the second step, the carbonization step, the carbon was doped with nitrogen. The doping with nitrogen was performed using low-toxic and cheap urea.[383] Indeed, it can be also derived from waste, making it a promising *N*-source in the circular economy, in good accordance with the scope of the work to make environmentally friendly electrocatalysts.[384] Pinecones were ground together with urea using a blender (in order to obtain 10% (wt) of nitrogen in the final product). According to the literature, this procedure enhances the electrocatalytic-activity of the carbon by transforming the charge density and spin density of the carbon atoms.[385, 386] In addition, transition metals such as Co, Ni and Cu, showed a synergistic effect with the *N*-doped carbon for both the ORR and OER.[387] Sequentially, according to Chatha and co-workers,[388] the so-produced carbon was activated through a mild KOH washing (KOH : carbon = 2 : 1) in an US bath, in order to further increase its metal adsorption properties.[389] The milder KOH activation procedure allowed complete cleaning of the surface from remaining impurities without totally destroying the peculiar structure of the pinecone-based material. Finally, the carbon was filtered and again carbonized at 900 °C in an

Ethos MW, followed by the adsorption of the metals in an ethanol solution, for 24 h, at room temperature. Co(OAc)$_2$ was used as Cobalt ions source. Parallelly, a solution of polyphenols was prepared by extracting them from green Malaysian tea in ethanol through combined MW-US irradiation at 50 °C. Finally, the polyphenol solution was added to the mixture of metal/carbon aiming at chelating and stabilizing the cobalt ions over the carbon structure.[390] As reported in Table 16, the samples were denoted using the following abbreviations: "CC" stands for commercial charcoal, "PC" for pinecone charcoal, "pp" for polyphenols and "C", "M", "U" and "MU" respectively stand for "conventional-heating", "microwave-assisted", "ultrasound-assisted" and "combined microwave-ultrasound assisted" addition of polyphenols.

Table 16. List and description of the different prepared electrocatalysts.

Sample	Type of carbon	N-doping	Polyphenols
Co/CC	Commercial charcoal	No	No
Co/PC	Pinecone charcoal	No	No
Co/N-PC	Pinecone charcoal	Yes	No
Co/N-PC-pp-C	Pinecone charcoal	Yes	Yes
Co/N-PC-pp-M	Pinecone charcoal	Yes	Yes
Co/N-PC-pp-U	Pinecone charcoal	Yes	Yes
Co/N-PC-pp-MU	Pinecone charcoal	Yes	Yes
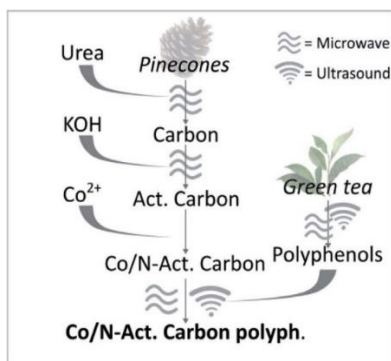
Figure 52. Schematic diagram for the preparation of the cobalt *N*-doped carbon materials.
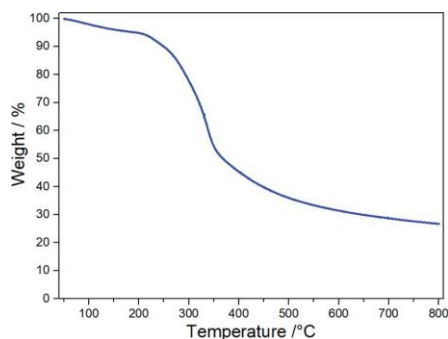
Figure 53. Thermogravimetric analysis (TGA) of washed pinecones.

5.2.2. *Co-polyphenol material characterization*

In order to evaluate the influence of the studied parameters (preparation technique, N-doping and polyphenol presence), the structural and physical properties of the prepared samples were analyzed. As shown in SEM images (Figure 54a), prior to the activation and to the adsorption of the metals and polyphenols, the carbonized pinecones exhibited pores in the micrometer range (i.e. around 20 mm in diameter). However, during the sequential steps of chemical activation, adsorption of metals and stabilization with polyphenols, the structure partially collapsed, as illustrated in the SEM images of the final samples, in Figure 54b. EDX-mapping micrographs allowed the examination of the surface distribution of Co, C, O and N. Remarkably, all the samples showed a homogeneous distribution of cobalt. Figure 54c presents the C, Co, N and O EDX-mapping of Co/N-PC-pp-U, the most active sample in the tests for the OER, as later described. In order to further analyze the state of the cobalt loading, TEM images have been obtained from Co/CC, N-PC, Co/N-PC-pp-M, Co/N-PC-pp-U and Co/N-PC-pp-MU samples (Figure 151, Appendix). As can be observed the size of the resulting cobalt-based particles drastically changed depending on the approach employed to synthesize the cobalt/carbon materials. More in detail, the Co/CC sample showed a larger particle size (diameters around 50 nm with a spherical and rod-like shape) than the cobalt *N*-doped carbon materials obtained by ultrasound (U), microwave (M) and MU assisted-methods, which showed smaller cobalt particle size in the nanocluster dimension. In addition, the material resulting from the ultrasound-assisted synthetic method (Co/N-PC-pp-U) showed a more homogeneous distribution and a monodispersed cobalt nanocluster loading, something that could also provide a better electrocatalytic performance for the OER.[391] XRD analysis was performed to investigate the phase purity and crystallinity of the synthesized samples. All the samples generally showed the amorphous carbon structure, as indicated by the wide peak ranging from a 2θ of around 10° to 30° in their XRD diffraction pattern; however, due to the low crystallinity of Co and the low content of the metal, no relevant peaks could be observed.[392] In order to determine the specific surface areas and the pore volumes (micro and meso) of the composite

materials, nitrogen physisorption was carried out (Table 17), (Figure 152, Appendix for the isotherms). Nevertheless, no significant correlations between surface areas and catalytic activities were observed. The metal loading of the samples was investigated through ICP-MS analysis. According to the results reported in Table 18 the average cobalt loading was found to be around 3.4%, with a standard deviation of 0.4. Remarkably, as explained in the electrocatalytic tests, a (slightly) higher metal loading did not directly imply a higher activity.

a   b   c
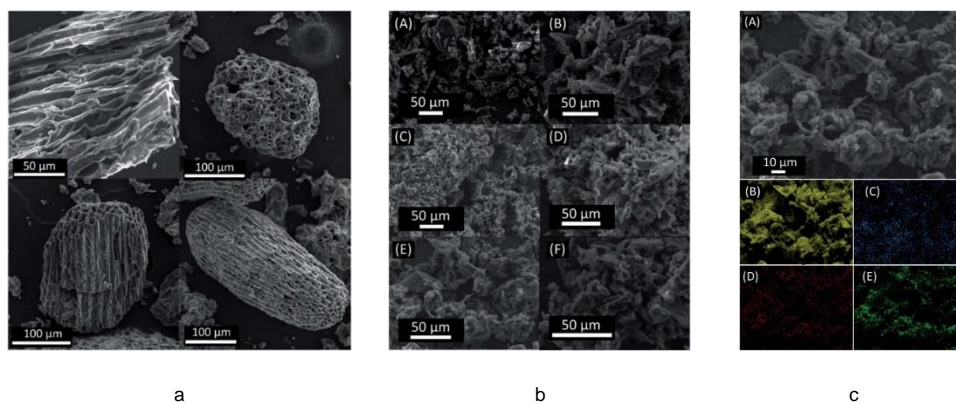
Figure 54. (a) SEM images of carbonized pinecones; (b) SEM images of finally prepared samples made from pinecone carbon. (A) Co/ PC; (B) Co/N-PC; (C) Co/N-PC-pp-C; (D) Co/N-PC-pp-M; (E) Co/N-PC-pp-U and (F) Co/N-PC-pp-MU; (c) SEM-EDX images with mapping analysis of the (A) Co/N-PC- pp-U carbon hybrid structure: (B) carbon; (C) cobalt; (D) nitrogen and (E) oxygen.

Table 17. Surface areas and pores volumes of the samples

Sample	SSA ($m^2 g^{-1}$)	Pores ($cm^3 g^{-1}$) (micro; meso)
Co/CC	1493	0.20; 0.54
Co/PC	456	0.12; 0.04
Co/N-PC	272	0.03; 0.09
Co/N-PC-pp-C	298	0.08; 0.03
Co/N-PC-pp-M	<60	Not detectable
Co/N-PC-pp-U	147	0.01; 0.08
Co/N-PC-pp-MU	147	0.02; 0.07

XPS measurements were performed in order to examine and study the chemical composition of the external surface of the solids as well as the chemical state of their different elements. More in detail, XPS analysis allowed the evaluation of the surface chemical composition (atomic concentration %) of C, O, N, K and Co. As reported in Table 18, K was not found in sample Co/CC, whereas P (3.26%) was observed in the form of phosphate (P 2p at 134.1 eV). In contrast, K derived from the addition of KOH was found in all the other samples, despite the intense sequential washing procedure, with Co/N-PC-pp-U and Co/NPC-pp-MU being the

samples with the lowest and highest K content at the surface, respectively. The surface-N content of the samples prepared by conventional-heating was lower than those using "unconventional-heating" (i.e. M, U and MU). Furthermore, it is remarkable that the Co content at the surface was found to be much higher than in the bulk (i.e. measured through ICP-MS) in all samples, being very wide for Co/PC and Co/N-PC samples but very close for Co/N-PC-pp-M and Co/N-PCpp-U. This fact was attributed to a more homogeneous distribution of cobalt in the latter case. Also, a higher content of O was observed in the case of Co/PC and Co/N-PC, as well as a lower C content. These variations of composition were attributed to the addition plus the subsequent treatment of polyphenols, which provokes a rearrangement of the Co distribution on the whole sample. Concerning the chemical state of the different constituent elements, Table 19 shows the binding energy in eV. In all cases, the C 1s signal can be decomposed into four contributions with different percentages at 284.8 eV assigned to adventitious carbon and –C–C– and –C=C– bonds, 286.0–286.4 eV to C–OH or C–O–C and C–N bonds, at about 288.0–288.5 eV assigned to urea and carboxylic or carboxylate groups, and finally at >289 eV due to carbonate. The percentage of the contribution assigned to C–OH or C–O–C and C–N bonds increased upon the addition of urea. All samples contained N, but N from urea was firstly detected in the case of sample Co/N-PC with a N 1s maximum at 395.8 eV.[89] In the case of the samples obtained by treating with MW or US, the N 1s signal can be decomposed into two contributions at 398.2 and 400.4 eV, which are attributed to pyridinic-N and pyrrolic-N, respectively. The latter results not only confirm the successful formation of *N*-doped active carbon species but also that the pyrrolic-N peak is higher than the pyridinic-N one, demonstrating that the electron pair on the pyrrolic nitrogen is involved in aromatic stabilization of cobalt ions (for the complete C 1s and N 1s spectra please see Figure 153 and Figure 154, Appendix).[393] Potassium, with a K $2p_{3/2}$ binding energy value of about 293.4 eV was, as expected, always as K^+. As illustrated in Figure 55, Co 2p core level spectra showed a maximum at high binding energy values (781.4–781.8 eV). According to the literature, these values correspond to Co(II) species having strong interactions with oxygen. Co $2p_{3/2}$ signals can be fitted into four contributions as observed in Figure 155 and Table 28 in the Appendix. The values of the maxima of these four contributions and the shape of the spectra are similar to Co(II) species such as $Co(OH)_2$ and CoO. The values of the observed doublet Co $2p_{1/2}$–Co $2p_{3/2}$ energy separation were in a range of 15.8–16.2 eV, values observed for $CoAl_2O_3$, and $Co(OH)_2$. However, the presence of Co(III) species cannot be ruled out. The satellites of the Co $2p_{3/2}$ signals for samples Co/PC, Co/N-PC and Co/N-PC-pp-C appeared in a range of 784.4–790.0 eV (peaks 2, 3 and 4 of Table 28, Appendix), more frequent for Co(II) species. These satellites were broader for samples Co/N-PC-pp-U, Co/N-PC-pp-M and Co/N-PC-pp-MU, probably due to the enhanced coordination of Co with polyphenols.

Table 18. Cobalt content % (wt), determined by ICP-MS (1st column) and XPS (2nd–6th columns) analysis (atomic concentration %) of the metal loading on the samples

Sample	Co % (wt)	C	O	N	K	Co
Co/CC	3.72	65.85	23.93	0.55	a	6.41
Co/PC	3.92	45.22	40.29	0.37	1.22	12.90
Co/N-PC	2.93	43.62	40.82	0.98	1.26	13.32
Co/N-PC-pp-C	2.94	59.01	32.96	0.68	1.47	5.88
Co/N-PC-pp-M	3.54	63.46	29.21	1.23	0.69	5.41
Co/N-PC-pp-U	3.51	62.68	30.37	1.19	0.26	5.50
Co/N-PC-pp-MU	3.58	56.64	32.19	1.04	2.84	7.29

a) K was not observed, but 3.26% of P.
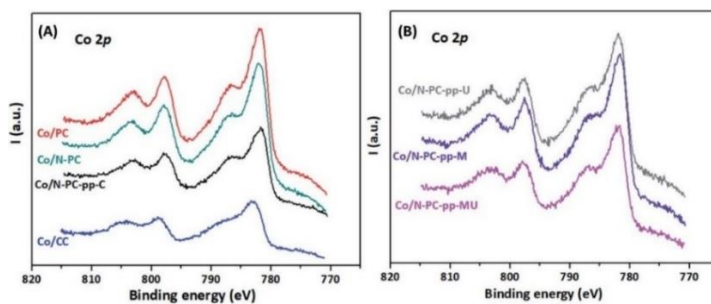
Figure 55. (A) Co 2p core level spectra for samples Co/CC, Co/PC, Co/N-PC and Co/N-PC-pp-C; (B) Co 2p core level spectra for samples Co/N-PC-pp-U, Co/N-PC-pp-M and Co/N-PC-pp-MU.

Table 19. Binding energy values, in eV, of the different constituent elements and percentages of each deconvoluted contribution, in brackets, of the studied samples

Sample	C 1s	O 1s	N 1s	Co 2p$_{3/2}$	K 2p$_{3/2}$
Co/CC	284.8 (76)	532.7	400.0	781.8	
	286.4 (16)				
	287.7 (5)				
	289.2 (3)				
Co/PC	284.8 (64)	532.1 (92)	400.2	781.7	293.4
	286.0 (18)	533.6 (8)			
	288.6 (4)				
	289.9 (14)				
Co/N-PC	284.8 (57)	532.1 (89)	399.5	781.9	293.6
	286.0 (26)	533.6 (11)			
	288.5 (3)				
	290.0 (14)				
Co/N-PC-pp-C	284.8 (56)	531.9 (68)	400.0	781.7	293.5
	286.4 (29)	533.3 (32)			
	288.1 (9)				
	289.5 (6)				
Co/N-PC-pp-M	288.4 (59)	531.9	398.2 (37)	781.6	293.0
	286.4 (25)		400.3 (62)		
	288.2 (9)				
	289.5 (7)				
Co/N-PC-pp-U	284.8 (53)	532.1 (63)	398.2 (38)	781.9	293.5
	286.4 (30)	533.5 (37)	400.4 (62)		
	288.0 (10)				
	289.5 (7)				
Co/N-PC-pp-MU	284.8 (53)	532.3	398.4 (42)	781.7	293.3
	286.4 (28)		400.7 (58)		
	287.7 (119)				
	289.4 (8)				

5.2.3. Electrochemical oxygen evolution

Electrochemical oxygen evolution (OER) electrocatalytic activities of the different Co–carbon samples were initially measured at room temperature. Figure 56 displays the resulting OER polarization curves of the Co functionalized carbonaceous materials obtained in 0.5 M KOH electrolyte at 2 mV s^{-1}. Remarkably, the electrocatalytic performance of the samples containing pinecone-derived carbon outperformed the electrocatalytic performances of commercially available carbons (Co/CC). As shown in Figure 56a and Table 20 the onset potentials values at j_{geo} = 10 mA cm^{-2} were significantly lower for the catalysts composed of pinecone derived carbon materials. These results most likely derived from the chemical activation of biomass waste with KOH, favoring the formation of a greater number of active sites that leads to considerable improvement in electrocatalytic performance. Interestingly, a remarkable enhancement of the electrocatalytic response was observed after the addition of polyphenols to the nitrogen-doped carbon materials. This behavior could be attributed to the lower difference of the Co content between the bulk (ICP) and surface composition (XPS) of these samples, indicating a better distribution of cobalt ions in these Co/carbon composites, which facilitates both accessibility to OH molecules and electronic connectivity within the whole system, shortening the ion-diffusion pathways. More in detail, the onset potential values at j_{geo} = 10 mA cm^{-2} decreased from 620 mV to 530 mV. In this sense, the polyphenolic networks (i.e. all samples named "Co/N-PC-pp-") had a dual function in the hybrid inorganic-organic architectures: (i) the stabilization of the Co^{2+} cations through highly stable metal-phenol complexes and (ii) the increasing of the surface density of the catalytically active sites providing enrichment in Co–OH (metal oxides) and Co–O–Co functional groups as evidenced by XPS, which notably boosts the catalytic activity by favoring the adsorption of OER intermediate species. Additionally, the hybrid organic-inorganic Co-based heterostructures were synthesized following different procedures for the adsorption of the metal (i.e. different heating methods): conventional heating, microwave-assisted heating, ultrasound heating and combined US-MW heating.
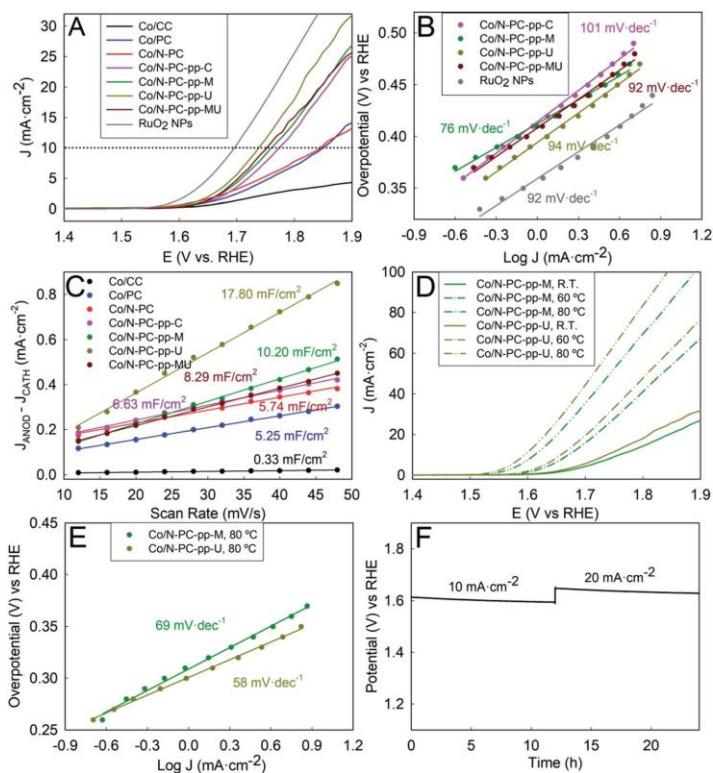
Figure 56. (A) LSV curves of GC modified with the different Co–carbon hybrid structures, and RuO_2 NPs as a reference material; (B) Tafel polarization plot obtained from (A); (C) plots of the difference of anodic and cathodic current densities against the scan rate for all samples; (D) effect of the temperature increase on the LSV curves of Co/N-PC-pp-M and Co/N-PC-pp-U samples, respectively; (E) Tafel polarization plot obtained from the latter samples at 80 °C; (F) chronopotentiometric curve obtained at current densities of 10 and 20 mA cm^{-2} for Co/N-PC-pp-U.

The OER measurements demonstrated that the synthetic route displayed an important influence on the surface chemical composition and, therefore, on the resulting electrocatalytic properties of the samples. In fact, according to the OER curves, all the catalysts prepared through ultrasound, microwave and US-MW-assisted heating procedures (Co/N-PC-pp-U, Co/N-PC-pp-MW, and Co/N-PC-pp-MU) showed better electrocatalytic performances than the catalyst prepared by the conventional heating procedure (Co/N-PC-pp-C). Indeed, US assisted techniques can lead to a uniform and homogeneous distribution of the treated compounds (i.e. the polyphenols), sensibly enhancing the electrocatalytic activity. On the other hand, also MW assisted techniques have been reported as efficient methods to boost the electrocatalytic activity of catalysts, due to rapid and uniform heating, which avoids the formation of thermal gradients (and consequent inhomogeneous particle distribution). This thesis was enforced by the strong interaction Co-polyphenols observed in XPS measurements. The comparison of the activity between these "unconventionally" (MW, US and MW-US) synthesized catalysts demonstrated that sample Co/N-PC-pp-U was the most active one. In order to investigate this behavior, the differences of anodic and cathodic current densities were plotted against the scan rates, obtaining slopes (areal capacitances) proportional to the number of active sites as well as to the electrochemical surface area of each sample (Figure 56c). The findings demonstrated

that Co/N-PC-pp-U provided the highest areal capacitance of 17.80 mF cm^{-2}, which was significantly higher than those of the other samples. As a result, the compositional and structural features of the Co/N-PC-pp-U sample provided the highest number of active sites with the most favorable material for charge transfer reactions and electronic connectivity within the whole system. Co/N-PC-pp-U provides the better electrocatalytic performance for the OER. According to the literature, the conventional electrochemical mechanism for OER processes in an alkaline medium is called the Adsorbate Evolution Mechanism (AEM) [394] which consists of 5 steps with multiple adsorbed intermediates:

(1) $M + OH^- \leftrightarrow M–OH^* + e^-$

(2) $M–OH^* + OH^- \leftrightarrow M–O^* + H_2O + e^-$

(3) $M–O^* + OH^- \leftrightarrow M–OOH^* + e^-$

(4) $M–OOH^* + OH^- \leftrightarrow M–OO^* + H_2O + e^-$

(5) $M–OO^* \leftrightarrow M + O_2$
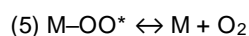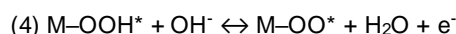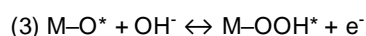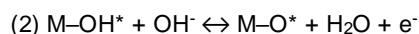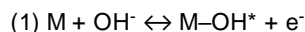
Based on the study reported by Nurlaela et al.,[395] the OER electrocatalytic performance of the two bests samples (i.e. Co/NPC-pp-U and Co/N-PC-pp-M), was sequentially evaluated at higher temperatures (Figure 56d). As reported in the Tafel polarization plots in Figure 56e, a higher temperature significantly improved the OER electrocatalytic response of both samples, providing a cathodic shift of the onset potential and increasing the maximum current density (Table 30 and Table 31 in the Appendix for the complete list of the obtained electrocatalytic parameters). More in detail, Figure 57a and Figure 57c display the Tafel plot trends of the OER curves obtained for the Co/N-PC-pp-M and Co/N-PC-pp-U samples at room temperature, 60 °C and 80 °C in 0.5 M KOH. Notably, the slopes of both materials slightly decrease at higher temperatures, which are related to the improvement of the OER efficiency of the samples from room temperature to 80 °C. According to the best results, the Co/N-PC-pp-U sample can be considered as an "excellent" OER catalyst in comparison with the literature, [381] requiring an overpotential of 365 mV to deliver a current density of 10 mA cm^{-2}, with a Tafel slope of 58 mV dec^{-1}. This performance was validated through durability tests performed by chronopotentiometry at current densities of 10 and 20 mA cm^{-2} (Figure 56f). As the potentials remained almost constant for 24 h at each current density, sample Co/N-PC-pp-U was demonstrated to have a good electrochemical stability and the best performance was confirmed. Finally, using the experimental Tafel curves, the values of currents at zero-overpotentials i_0 ($E = 1.23$ V vs. RHE) were obtained. The i_0 values were plotted versus the temperature following an Arrhenius representation (eqn (i), Figure 56b and Figure 56d), allowing the calculations of the activation energies.

$$(d\ln(i_0))/(d(T^{-1})) = -E_a/R \qquad\qquad (i)$$

where E_a, R and T are the apparent activation energy, the typical gas constant and the temperature.

The values obtained for Co/N-PC-pp-M and Co/N-PC-pp-U were 9.70 ± 0.06 kJ mol^{-1} and 9.97 ± 0.04 kJ mol^{-1}, respectively, which are smaller than the activation energies of almost all the metal transition-based OER electrocatalysts reported up to now in the literature.[396] These results strongly support the significant enhancement observed in the OER electrocatalytic behavior at higher temperatures for the Co-synthesized electrocatalysts, which may be linked with the increasing number of OER actives sites driven by some temperature-dependent structural changes at the polyphenolic networks. In order to verify the robustness of the best sample, a durability test was performed on the Co/N-PC-pp-U sample by performing 10 000 cyclic voltammetry cycles (CV). Figure 156 shows the polarization curves recorded before and after performing the cycles. As can be observed, the electrocatalytic performance for the OER remained almost identical after the CV cycling test, demonstrating its excellent long-term stability. Also, post characterization through SEM images and EDX analysis sample Co/N-PC-pp-U showed no relevant changes in the morphological structure.

Table 20. OER electrocatalytic parameters obtained from Figure 53A and B at room temperature

	Onset potential (V)	Overpotential (mV) at 10 mA·cm^{-2}	Maximum current density (mA·cm^{-2})	Tafel slope (mV·dec^{-1})
Bare GC	1.70	-	1.0	-
RuO$_2$ NPs	1.54	460	25.5	92
Co/CC	1.60	-	1.9	-
Co/PC	1.59	610	14.1	-
Co/N-PC	1.58	605	13.2	-
Co/N-PC-pp-C	1.57	540	25.2	101
Co/N-PC-pp-M	1.57	526	27.1	78
Co/N-PC-pp-U	1.56	497	32.0	94
Co/N-PC-pp-MU	1.57	520	26.3	92
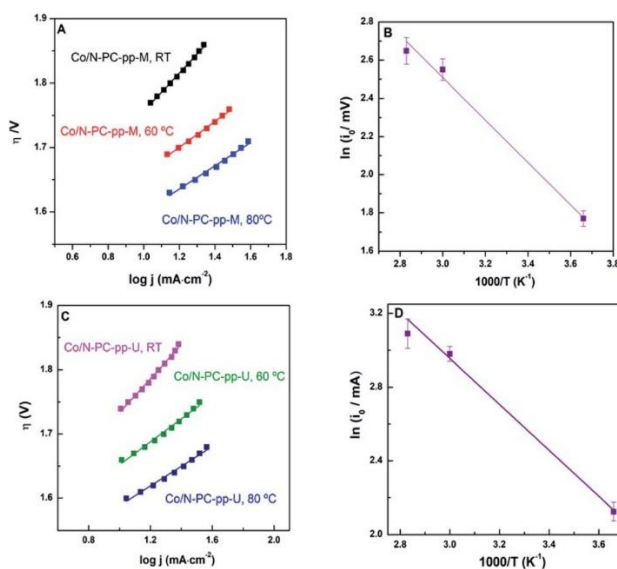
Figure 57. Tafel plots for OER polarization curves at RT, 60 °C and 80 °C of (A) Co/N-PC-pp-M and (B) Co/N-PC-pp-U, respectively. Arrhenius plots of (C) Co/N-PC-pp-M and (D) Co/N-PC-pp-U, respectively.

5.3.   Conclusions

A novel approach for the preparation of active and stable low metal content cobalt-based carbonaceous electrocatalysts for the OER was demonstrated. Materials were prepared exploiting the metal adsorbing properties of carbon derived from pinecones, and nitrogen doping with eco-friendly urea, as well as the metal chelating and stabilization characteristics of polyphenols extracted from green tea. Moreover, the approach allowed the investigation of different unconventional heating methodologies, including US, MW and combined US-MW techniques. The electrocatalytic tests demonstrated the co-activity and synergism of the carbon derived from pinecones, and the importance of doping with nitrogen, as well as the good stabilization and enhancement of the activity of cobalt thanks to the presence of polyphenols. Importantly, the influence of the synthetic procedure also demonstrated that both MW and US techniques provided a greater number of active sites than conventional heating procedures, with US being the most effective one.

Chapter 6

Multifunctional amino-citrate-β-CD coated iron oxide nanoparticles: an efficient nanosystem for Magnetic Resonance Imaging (MRI)

6.1.   Introduction

As explained in Chapter 1.2.3., the use of magnetic nanosystem is recently growing due to their promising activity in different field of application. In particular, over the last few years, iron oxide magnetic nanoparticles (IONPs) are undergoing intensive studies for biomedical purposes.[397] This is due to their versatility in drug targeting,[398] gene delivery,[399] and in several technological applications, such as magnetic resonance imaging (MRI),[400] magnetic hyperthermia,[401] tissue engineering, cell tracking and bioseparation.[402] In order to be used in biomedical applications, IONPs need to be water compatible.[403, 404] Hydrophilicity can be induced by adding coating agents, with hydrophilic portion, capable to bind the particle surface and to make hydrophilic particles.[405] Moreover, size, size distribution, shape, crystallinity, surface area and magnetic characteristics influence biological performances, and the search for innovative preparation methodologies is essential to provide pure and well-defined nanoparticles.[406, 407]

Among IONPs, magnetite (Fe_3O_4) is achieving great interest, thanks to its superior magnetic properties and higher biocompatibility. It shows a cubic inverse spinel structure with a ferrimagnetic behavior. Its structure is composed of oxygen atoms situated to form a face centered cubic configuration where Fe^{3+} ions occupy tetrahedral and octahedral sites, while all the Fe^{2+} ions occupy half of the octahedral sites. A ferromagnetic spin coupling between Fe^{3+} and Fe^{2+} ions takes place in the octahedral sites, but an antiparallel spin coupling occurs between moments in octahedral and tetrahedral sites and it is responsible of the ferrimagnetic behavior. The response to an external magnetic field determines different orientation of the magnetic moments in a particle, depending on the domain structure and on the dependence of the magnetic induction (M) on the magnetic field (H).[403] When a ferrimagnet is undergone to an external magnetic field the domains align themselves with it and the substance becomes magnetized. It can be driven to saturation by applying increasing magnetic field intensity. Once the material has been driven to saturation, the external magnetic field can be dropped to zero. However, even when the field is removed, part of the alignment is retained and the amount of magnetization it retains at zero driving filed is called remanence. The magnetizing field must be driven back to zero by a field in the opposite direction and the amount of reverse driving field is called coercivity. If an alternating magnetic field is applied to the material, its magnetization will trace out a loop called hysteresis loop. From the hysteresis loop a number of magnetic

properties of IONPs, such as the saturation magnetization, the remanence magnetization and coercivity, can be obtained.[408] When IONPs are superparamagnetic, no residual magnetic forces exist between the particles after the removal of the external magnetic field. This is due to their small dimension (below 15 nm) and the presence of only one domain, where the cooperative phenomenon of ferrimagnetism is no longer observed and no permanent magnetization remains after the removal of the external magnetic field. Thus, the M-H curve does not show hysteresis (Figure 58b).[409] Such superparamagnetic iron oxide nanoparticles were also approved by the US Food and Drug Administration (FDA) for in-vivo applications.
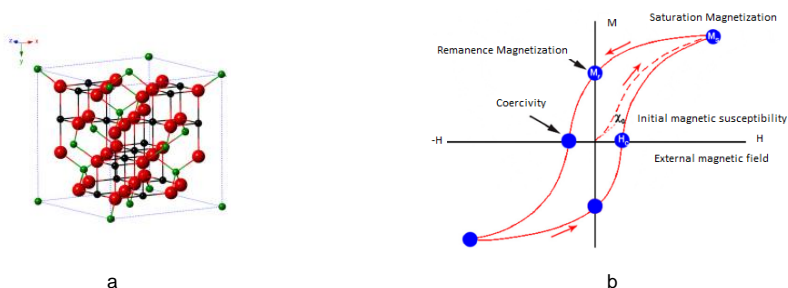
Figure 58. (a) Crystal structure and crystallographic data of magnetite (the black ball is Fe^{2+}, the green ball is Fe^{3+} and the red ball is O^{2-}); (b) representation of the hysteresis loop. Figure obtained from the paper of Kim *et al.*[408]

The request of new synthetic procedures that provide control over size, morphology, and nano/microstructure of particles represents a big challenge in magnetic NPs (MNPs) preparation.[410, 411] Lately, the sonochemical technique is representing a promising and innovative method in offering better control of particle size distribution, that is often unavailable by conventional approaches.[411-415]

Due to the high adsorption capacity of MNPs, careful studies in synthesizing IONPs as adsorbent materials have been recently conducted.[416, 417] Bare or functionalized Fe_3O_4 MNPs were used to adsorb metal ions, such as Ni(II), Cu(II), Cd(II) and Cr(VI), for wastewater treating.[418] Adsorbent performances, combined to magnetic separation technique make IONPs efficient, cost-effective, simple to use and environmental friendly compared to other adsorbents.[419] For these reasons, several examples of functionalized MNPs as nano-carriers are reported.[420, 421] The importance of coating agents in enhancing the loading and controlling the release of organic molecules has been demonstrated. For example, polymer-coated Fe_3O_4 NPs showed effective adsorption and desorption capacity for Enalapril loading and release.[422] Besides, the addition of cyclodextrins (CDs) as capping agents increases the active sites on MNPs surface for entrapping organic molecules by forming host-guest inclusion complexes.[423] Organic linkers can be used to indirectly coat the surfaces of IONPs with CDs.[424] Generally, silanes are used as organic linkers: they are chemically stable and versatile.[425-427] However, an accurate control of the layer quality, in term of monolayer or multilayer formation, is a difficult task.[428] Furthermore, this synthetic process requires several procedural steps.[429] Carboxylate anchoring groups have been proven to work well for ligand exchange processes and are

available for chemical functionalization.[430] Dextran-coated IONPs are the most widely used systems for medical purposes[431] and the transformation of dextran to carboxy-dextran was proven to enhance NPs physico-chemical properties.[432-436]

In addition, an important factor that must be considered in IONPs formulation is the surface charge. It is essential to prevent NPs aggregation through electrostatic repulsion and it influences the interaction of nanomaterials with cells and tissues. In general, cationic NPs enter cells with higher efficacy, due to the interaction with negative membrane cells. However, they tend to form large aggregates in the presence of plasma and have faster blood clearance than neutral particles. Negatively charged NPs are also massively incorporated by cells, show higher stability in plasma and consequently, their biocompatibility is improved and clearance is prevented.[437, 438]

Therefore, the combination of hydrophilic and negatively charged organic molecules and CDs, as adsorbent systems, on NPs surface becomes an important tool for obtaining biotechnological nanosystems. Just few examples, reported in literature, show the preparation and the application of similar systems. Jayaprabha and Joy reported the preparation of citrate modified β-CD functionalized magnetite NPs for targeting and delivery of curcumin to specific site through an external magnetic field.[169] Monteiro et al., demonstrated the importance of combining sodium citrate with CDs to obtain coated MNPs with high Irinotecan loading.[439]

Among the various applications, IONPs assume an important role as contrast enhancers in magnetic resonance imaging (MRI). Colloidal suspensions of IONPs are capable of providing both T_1- and T_2-weighted images,[440] and represent the most important class of T_2 contrast agents. Several studies show that NPs size influences MR relaxivity, as well as pharmacological features.[441, 442] For this reason, size-controlled synthesis of uniform NPs dispersions is essential for the fine control of MR relaxivity.[443] Furthermore, coating nature and thickness have important effects on R_1 and R_2 relaxivities. Coating materials influence the diffusion of protons and the chemical exchange processes. As coating thickness and hydrophobicity increase, R_2 and R_1 dramatically decrease.[444]

To develop versatile adsorbent nanomaterials for biomedical use in MRI, herein, negatively charged hydrophilic β-CDs grafted IONPs are prepared and characterized. Amino citrate modified β-CDs were chosen as coating agent to mimic and replace the widely used carboxy-dextran and to improve adsorbent performances. The combination of citric acid and amino citrate modified β-CDs, used as more flexible adsorbing device, is studied for the first time and an US-assisted IONPs preparation method is reported. Adsorption capacity, stability, cytotoxicity and relaxometric properties have been investigated in detail, in view of their potential.

6.2. Results and discussion

6.2.1. Preparation of carboxymethyl dextran and citric acid coated MNPs

With the aim of obtaining a novel, innovative and readily synthesized hydrophilic and biocompatible material, Fe_3O_4 MNPs were prepared as a core-shell nanostructured system. In order to circumvent common difficulties in controlling size, morphology and structure of NPs, MW and US irradiation, as alternative heating forces, were used as a non-conventional strategy to achieve efficient heating, dispersion and deagglomeration of solids, as well as mass transfer.

Following well-known procedures,[47,48] Fe_3O_4 MNPs were synthesized by a co-precipitation technique and nanoparticles growth was facilitated by the addition of ammonium hydroxide in an iron salts solution (Scheme 20). The solution was heated up at 80 °C comparing conventional heating and MW-US irradiation. When MW-US irradiation was employed, typical problems of homogeneity and reproducibility were avoided and the reaction time was reduced from 90 to 45 min.

$$Fe^{2+} + 2Fe^{3+} + 8OH^- \rightarrow Fe(OH)_2 + 2Fe(OH)_3 \rightarrow Fe_3O_4\downarrow + 4H_2O$$
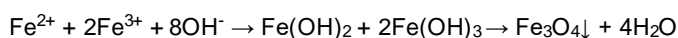
Scheme 20. Reaction scheme for the preparation of Fe3O4 nanoparticles by co-precipitation method.

To address water instability, oxidation and nanoparticle aggregation, iron oxide core was coated with hydrophilic organic ligands. As first attempt, in order to study the preparation technique and to validate non-conventional procedures, citric acid (CA) and carboxymethyl dextran (CMDx) were used to coat and stabilize the MNPs in solution, enhancing electrostatic stability and particles disaggregation. As described in literature,[445-447] the MNPs stabilization *via* these coating agents occurs by the coordination *via* the carboxylate functionalities. The free and exposed carboxyl groups can be used for other purposes, as anchoring functions for covalent bonding of additional molecules. CMDx is the most widely used coating agent: it offers biocompatibility, biodegradability and stability, to the extent that some CMDx coated NPs have been approved for human usage.[448] However, despite the preparation of coated IONPs has been known for a long time, the control of their properties still remains a challenge.

Here, core-shell nanostructured systems were prepared either *via* ligand exchange approach or *via* physical assembly, by means of conventional and non-conventional techniques. The choice of comparing different synthetic strategies wanted to investigate their impact on morphology, stability, dispersibility and degree of functionalization. The impact of the preparation technique on MNPs features was investigated by monitoring the hydrodynamic diameters and the dispersibility, through the Dynamic Light Scattering technique (DLS), that allows to determine the size distribution profile of MNPs and their stability in water suspension; the morphology through Trasmission Electon Microscopy (TEM), that revealed nanoparticle shape, core size and coating thickness; the degree of functionalization, through thermogravimetric analysis (TGA) and the field-dependent magnetization. Fourier Transform

Infrared (FT-IR) spectroscopy was used to prove the formation of coated MNPs and the measure of the Zeta potential allowed to investigate the surface charge.

Physical assembly was performed as first derivatization strategy (Scheme 21, approach A). Bare MNPs, obtained by MW-US-assisted co-precipitation technique, as previously described, were grafted with CA or CMDx, comparing conventional procedures or US irradiation, obtaining MNPs@CA and MNPs@CMDx, respectively. The reaction was performed in water and the reaction mixture was heated up at 80 °C, when conventional heating was used, or at 65 °C under US irradiation. It was operated at lower temperature when US irradiation was performed because, as reported in Chapter 1.3., the US efficacy is lower at higher temperature, where the formation of vapor cavities, resulting from higher temperatures, would alleviate the bubble collapse due to the cushioning effect. The reaction mixtures were stirred at the mentioned temperature for 1 h, as generally reported in literature. Comparable functionalization degrees (coating w/w %) were obtained comparing conventional heating and sonochemistry. However, more stable suspensions were obtained when US irradiation was employed, as visible comparing the polydispersion indexes (PDI) of the differently prepared nanosystems. This can be due to the formation of smaller MNPs, confirmed by the hydrodynamic diameter size, resulting in the absence of aggregated MNPs and dishomogeneous samples (

Table **21**).

Later, ligand exchange approach was chosen as comparative grafting procedure (Scheme 21, approach B). MNPs were synthesized and simultaneously coated with stearic acid (MNPs@StA) using a conventional or an US-promoted synthetic protocol. Following a known synthetic procedure, to a solution of $FeCl_3$, $FeCl_2$ and stearic acid in water, ammonium hydroxide was added dropwise, allowing the nanoparticles formation. A period of 24 h under conventional stirring was necessary to obtain the same degree of derivatization that was obtained after 30 min of sonication at 65 °C. Moreover, better suspensions of MNPs@StA in organic solvents (PDI 0.147 vs 0.240) and smaller nanoparticles (hydrodynamic diameter 23 nm vs 114 nm) were obtained when US irradiation was employed. For these reasons, US irradiation was decided as procedure of choice for MNPs@StA preparation. Subsequently, stearic acid was replaced with CA or CMDx and hydrophilic MNPs@CA and MNPs@CMDx were obtained. The ligand exchange occurred in a biphasic solution, where MNPs@StA were dissolved in toluene and were kept in touch with a water solution where the hydrophilic coating agents were previously dissolved. The combined solutions were refluxed for 24 h. Due to the high temperature requested, the solvent and the long reaction time, this synthetic step was carried out only under batch conditions. The happening of the ligand exchange was clearly visible by the movement of the MNPs from the organic to the water phase, indicated by the brown colored solutions. The as-synthetized MNPs@CA and MNPs@CMDx are water-dispersible and stable nanoparticle suspensions were obtained.

When the MNPs obtained by the two different synthetic strategies (physical assembly and ligand exchange) were compared, it was noticed that ligand exchange approach enhances the homogeneity of the suspensions, despite the slightly higher hydrodynamic diameter size, that can also be ascribed of a better coordination with the water molecules in the solution. Also the relaxometric properties (reported below) are enhanced, thanks to the higher stability of the suspensions. Thus, ligand exchange was chosen as preferential hydrophilic MNPs preparation method and as-prepared coated MNPs were further characterized.
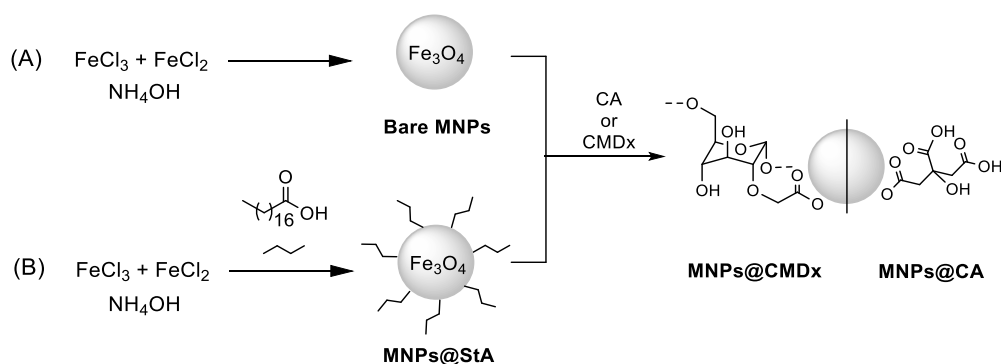
Scheme 21. Reaction scheme for MNPs@CMDx and MNPs@CA preparation using (A) physical assembly, (B) ligand exchange approach.

Table 21. Dispersibility, size and degree of functionalization.

Sample	Synthetic approach	Reaction conditions	PDI	Size (nm)	Coating (w/w%)
Bare MNPs	Co-precipitation	Conventional (80 °C), 1.5 h	-	6-17[a]	-
		MW-US (80 °C), 45 min	-	7-18[a]	-
MNPs@StA.5	Co-precipitation	Conventional (r.t.), 24 h	0.240[c]	114[d]	28.0
		US (65 °C), 30 min	0.147[c]	23[d]	29.2
MNPs@CMDx	Physical assembly	Conventional (80 °C), 1 h	0.200[b]	115[d]	23.2
		US (65 °C), 1 h	0.108[b]	69[d]	17.9
	Ligand exchange	Conventional (90 °C), 24 h	0.284[b]	73[d]	6.5
MNPs@CA	Physical assembly	Conventional (80 °C), 1 h	0.368[b]	40[d]	8.7
		US (65 °C), 1 h	0.340[b]	33[d]	10.5
	Ligand exchange	Conventional (90 °C), 24 h	0.187[b]	75[d]	14.6

[a] Diameter size acquired by TEM analysis. [b] Polydispersion index of water suspension of coated MNPs acquired by DLS analysis. [c] Polydispersion index of hexane suspension of coated MNPs acquired by DLS analysis. [d] hydrodynamic diameter size acquired by DLS analysis.

111

The effectiveness of the derivatization reaction was investigated by FT-IR (Fourier Transform Infrared Spectroscopy) and thermogravimetric analysis (TGA). The FT-IR bands characteristic of the iron oxide magnetic core are found at 620 cm^{-1} (ascribed to the torsional and stretching vibration of the Fe-O bond) and 3320-3240 cm^{-1} (assigned to O–H stretching vibration of hydroxyl group exposed on MNPs surface or to water residual).[449] In the spectrum of MNPs@StA the surfactant characteristic peaks are clearly visible. Peaks at 2920 and 2850 cm^{-1} are ascribed to CH$_2$ symmetric and asymmetric stretching. Typical peaks attributed to C-O symmetric and asymmetric vibrational modes are visible at 1555 and 1390 cm^{-1}. After exchange with CMDx and CA new absorbent peaks appear at 1140, 1010 cm^{-1} (due to the α-glucopyranose ring deformation modes)[448, 450, 451] and at 1080 cm^{-1} (assigned to C-H vibration), respectively. The peaks at 1590 and 1390 cm^{-1} are ascribed to the –COO– symmetric and antisymmetric stretching (Figure 59a).[452]

TGA allowed to measure the grafting and to confirm the identity of the synthesized MNPs systems. TGA curves are normalized to 100 °C to prevent any possible solvent influence on yield calculations and the small weight loss between 100 and 150 °C can be ascribed to the evaporation of adsorbed water molecules. TGA curves of bare and coated MNPs in the temperature range of 100 - 800 °C under nitrogen atmosphere are shown in Figure 59b (TGA curves of bare and coated MNPs obtained by physical assembly are reported in Figure 157, Appendix). TGA curve of MNPs@CMDx shows a degradation phase at 290 °C. This is lower than the temperature value registered in pure CMDx degradation profile (300 °C), due to the iron catalytic effect, as reported in literature.[409] TGA curves of MNPs@CA displays two degradation steps: at 270 °C and 610 °C. They are ascribed to the decomposition of citrate groups, chemically bounded to magnetite surface. The percentage of coating molecules attached to the surface of MNPs can be easily calculated *via* measuring the difference in residual weight between bare and coated MNPs and it is reported in

Table **21**.

a   b
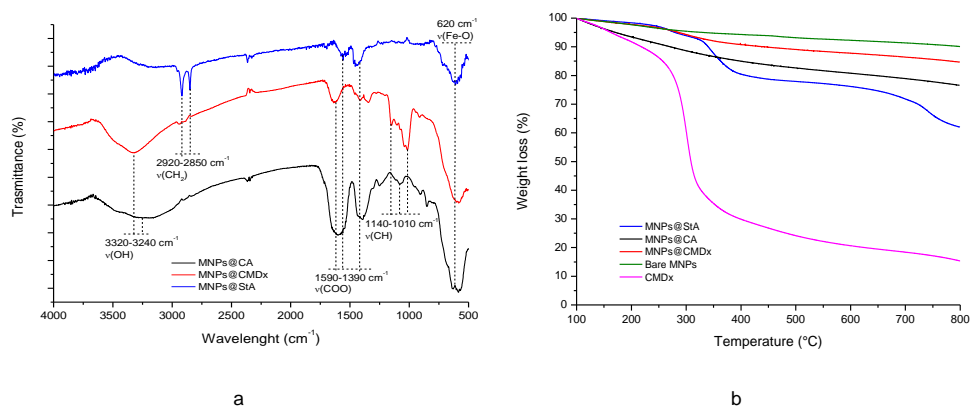
Figure 59. (a) FT-IR spectra and (b) TGA profiles of bare and coated MNPs, prepared by the ligand exchange approach.

6.2.2. Preparation of β-CD-coated MNPs

In order to meet the demand for biocompatible adsorbent nanomaterials, multifunctional nanocomposite IONPs, β-cyclodextrin (β-CD) and citric acid systems were prepared. β-CD is a cyclic oligosaccharide composed of seven linked D-glucopyranose units and that can be represented as a toroid structure with narrow and wide openings corresponding to the primary and secondary hydroxyl groups, respectively (Scheme 22). This peculiar structure means that β-CD can be exploited as adsorbing agents. β-CDs were chosen to replace the generally used dextran and their addition was fundamental to increase adsorption properties, thanks to their ability to act as vectors, by forming host-guest inclusion complexes. The addition of citric acid was essential to prevent NPs aggregation through electrostatic repulsion and its carboxylate functions can improve the ligand exchange process, as already demonstrated. Thus, the combination of MNPs, β-CD and citric acid represented an important tool for obtaining promising biotechnological nanosystems.
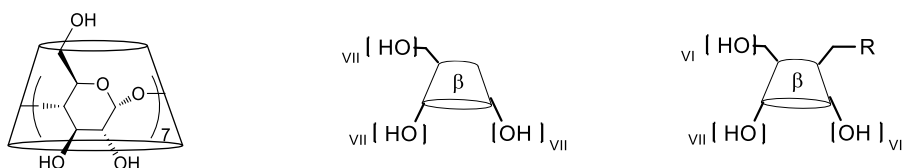
Scheme 22. Three representations of the general structure of β-CD. The numbers show the composition of the β-CD, made of seven linked D-glucopyranose units. When a hydroxyl function is replaced by a new functional group (R) the structure is represented as the figure on the right, where the new functionality is shown and just more six (VI) hydroxyl function on that position are present.

Here, two different multifunctional nanocomposite systems were prepared exploiting the acquired knowledge on MNPs covering through ligand exchange strategy, starting from MNPs@StA. A combination of citric acid and β-CD or citric acid and amino citrate β-CD (Citramide) were used to prepare versatile hydrophilic MNPs (MNPs@CA-β-CD and MNPs@CA-Citramide, respectively) (Scheme 24). Citramide was used to study the influence of an amino citrate spacer, between IONPs core and β-CD, with the aim to enhance the ability of inclusion complex formation, improve the cell incorporation and the biocompatibility. In fact, Citramide is able to chemisorb to the IONPs by forming a carboxylate function with Fe-OH groups present on NPs surface, exposing β-CD cavity, that can be used for inclusion complex formation and as adsorbent material. Moreover, the presence of aminic functions could promote the cell permeability. The preparation of Citramide was carried out starting from the reaction between 6^I-O-p-Toluenesulfonyl-β-CD and diethylentriamine, followed by the reaction of 6^I-diethylentriamine-6^I-monodeoxy-βCD with citric acid anhydride, *via* the formation of a stable amide bond (Scheme 23).
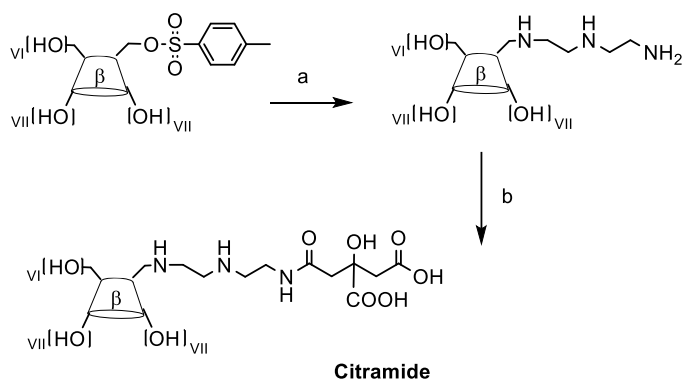
Scheme 23. Reaction scheme for the synthesis of Citramide. (a) diethylentriamine, 100 °C, 7 h; (b) citric acid anhydride, DMF, pyridine, 40 °C, 24 h.
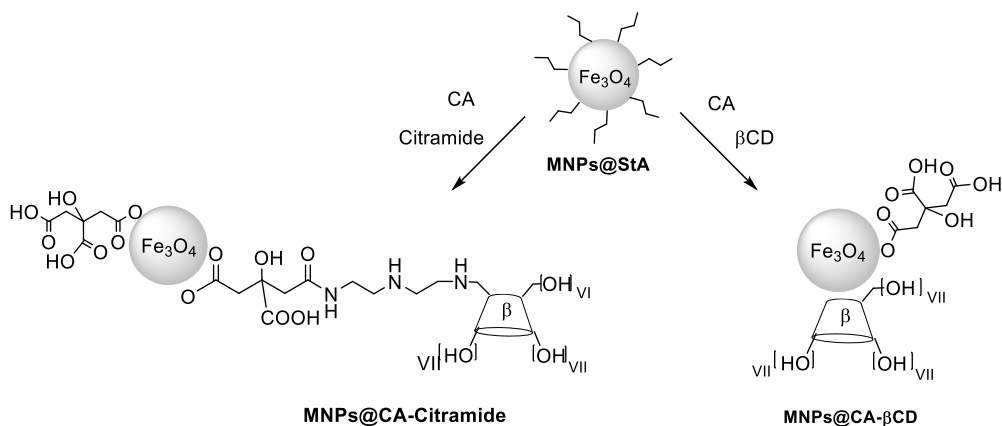
Scheme 24. Reaction scheme for MNPs@CA-β-CD, MNPs@CA-Citramide. Ligand exchange approach was used.

As visible from TGA profiles (Figure 60), highly coated systems were obtained. A w/w % grafting of MNPs@CA-β-CD and MNPs@CA-Citramide was calculated to be 66.4 and 27.2%, respectively. The hydrophilic coatings were important to produce water dispersible systems, that showed very high stability in aqueous solvents, as demonstrated by the measure of the PDI and stability assays, as reported below. In order to better understand the physical stability of these nanosuspensions, the surface charge was estimated by zeta potential measurement. The significance of zeta potential is that its value can be related to the short- and long-term stability of suspensions. Suspensions with high zeta potential (negative or positive, other than -30 mV to +30 mV) are electrically stabilized, while suspensions with low zeta potentials tend to aggregate or flocculate, due to the van der Waals attractive forces that act upon them, leading to poor physical stability. In general, when the zeta potential of an emulsion is high, the repulsive forces exceed the attractive forces, resulting in a relatively stable system. MNPs@CA-Citramide exhibited similar zeta potential to MNPs@CMDx. They resulted more positive than MNPs@CA-β-CD and MNPs@CA zeta potentials. This is due to absence of citrate functional

groups in the case of MNPs@CMDx and the presence of amino functional groups in MNPs@CA-Citramide, deriving from the amino citrate derivatized β-CD. Zeta potential values are reflected in the hydrodynamic size: as the negative zeta potential increases, MNPs aggregation decreases, improving the repulsion among them, as observed for MNPs@CA-β-CD, that exhibited smaller hydrodynamic diameter (47 nm) (Table 22).

Table 22. Dispersibility, size, degree of functionalization and zeta potential of coated MNPs.

Sample	PDI	Size (nm)[c]	Coating % (ww)[d]	Zeta potential (mV)
MNPs@StA	0.147[a]	23 ± 0.71	29.2	-
MNPs@CMDx	0.284[b]	73 ± 1.34	6.5	-30.3 ± 1.41
MNPs@CA	0.187[b]	75 ± 1.78	14.6	-35.7 ± 0.93
MNPs@CA-β-CD	0.446[b]	47 ± 1.98	66.4 - 10.17[e]	-33.4 ± 2.14
MNPs@CA-Citramide	0.335[b]	149 ± 2.05	27.2 - 9.89[e]	-30.6 ± 1.75

[a] Polydispersion index of hexane suspension of coated MNPs acquired by DLS analysis. [b] Polydispersion index of water suspension of coated MNPs acquired by DLS analysis. [c] hydrodynamic diameter size acquired by DLS analysis. [d] Coating w/w % measured by TGA. [e] β-CD w/w % grafting measured by php titration.

The evidence for the formation of MNPs coating was confirmed by FT-IR studies. The FT-IR spectra of MNPs@CA-β-CD and MNPs@CA-Citramide resemble the spectrum of CDs. The major bands at 3310, 2920, 1150, 1030 cm^{-1} correspond to the β-CD stretching vibrations of –OH, –CH$_2$, –C–C and β-CD bending vibration of –OH groups, respectively. The band at 1700 cm^{-1} is due to the vibration of the C=O group of the carboxylic acid. The band at 1630 cm^{-1} corresponds to the H–O–H deformation band of water present in the cavity of β-CD. It indicates that β-CD cavity is not occupied and it is available for host-guest inclusion complex formation. The stretching C-N (not very useful) and N-H, ascribable to the amino citrate portion, at 1000-1350 and 3100-3500 cm^{-1} are covered up by other signals. A typical FT-IR spectrum is reported in Figure 60.

a   b
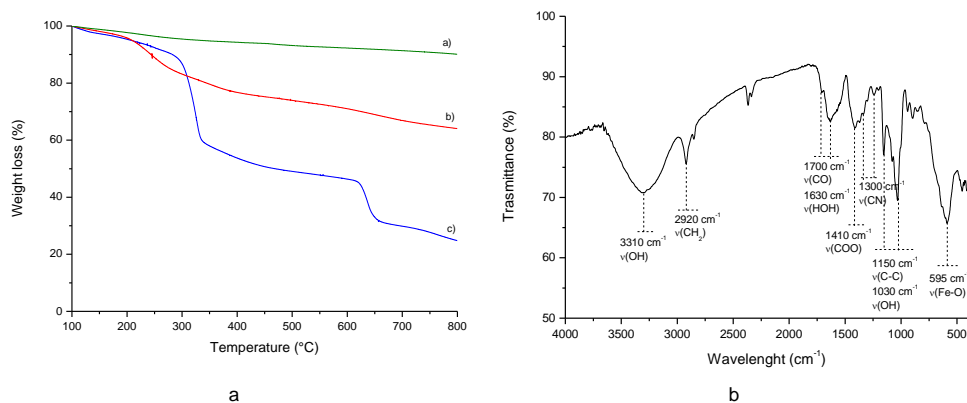
Figure 60. (a) TGA profiles and (b) FT-IR spectrum of multifunctional nanocomposite IONPs, β-CD and citric acid systems.

Adsorption performances were studied using phenolphthalein and adamantane amine. The interaction between β-CD and phenolphthalein (Php) is selective and allows to measure the amount of β-CD that maintains inclusive properties when grafted onto MNPs surface. The amount of β-CD was measured *via* titration with Php in the buffer solution (pH = 10.5) 0.008 mM and was measured on the basis of UV absorbance, *via* interpolation from the standard curve.[453] The change in Php absorbance was recorded on a UV spectrophotometer at 553 nm. By UV absorbance of the Php solution it was possible to detect the presence of solid supported β-CDs and measure a w/w % of grafting (ca 10 mg/100 mg, reported in Table 22). Despite the higher derivatization degree registered by TGA for the sample MNPs@CA-β-CD (66.7%), a lower w/w % grafting (10.17%) was recorded by UV analysis. This could be ascribed to the inability of all the β-CDs to act as inclusion vectors, due to the possible inappropriate conformation when used as coating of MNPs. When the amino spacer is interposed between the β-CD and the MNPs surface similar inclusion ability is obtained (9.89%), despite the 22% w/w registered by TGA. This means that, proportionally, more β-CDs maintain inclusion complex capability, probably due to the better exposure of the β-CD cavity.

On the other hand, the adsorption of adamantane amine was used to know the MNPs sorption capacity and to give addition information about the surface properties of the material. MNPs@CA-β-CD (2 mg) were added in 1 mL of adsorbate solutions of increasing concentrations and stirred in an US bath for 1 h. After the elimination of the NPs *via* magnetic recovery, the concentration of the solutions was analyzed using GC-FID and determined using a calibration curve. It has been observed that the adsorbed amount increased increasing the concentration of the adsorbate, till reaching a value of 2,50 mmol/g, confirming the interactions of adamantane amine with the surface MNPs functional groups and β-CDs.
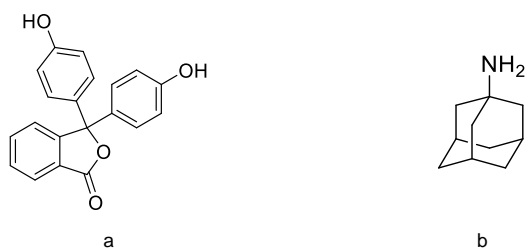
Figure 61. Adsorbed molecules (a) phenolphthalein, (b) adamantane amine, used for the study of MNPs@CA-β-CD sorption capacity.

6.2.3. Stability assays

For application of MNPs as delivery vectors for drug targeting and similar biomedical applications important features must be considered. Size, charge, surface chemistry and functionalization of the particles are particularly important since they strongly affect blood

circulation time, aggregation, mobility and bioavailability of the particles within the body. The study of stability and level of MNPs aggregation in physiological conditions is also very important in view of biomedical applications. Thus, the stability of MNPs@CA, MNPs@CMDx, MNPs@CA-CD and MNPs@CA-Citramide in three different media (bidistilled water, human serum and HEPES buffer added with 1.2 mM albumin) was investigated. The stability of these systems was evaluated by tracking the relaxivity for seven days. All the preparations displayed good stability in the tested media, thus laying the basis for potential future *in vivo* applications. Results for MNPs@CMDx, MNPs@CA, MNPs@CA-β-CD and MNPs@CA-Citramide are presented in the Appendix, Figure 160.

6.2.4. Structural characterization

The size and morphology of bare and coated MNPs were studied by HR-TEM analysis. The aggregation state and the size of the resulting iron oxide nanoparticles changed depending on the approach employed to synthesize the nanosystems. More in detail, when bare MNPs were prepared following the co-precipitation method under conventional heating, larger particle size (diameter around 14 nm) and more aggregated species than the bare MNPs obtained by combined MW and US irradiation were obtained. In addition, the resulting material obtained by the MW and US-assisted synthesis method showed a more homogeneous distribution and uniformity of size and morphology, with predominance of sphere-like shape particles in the nano dimension. The same can be observed analyzing the size and the shape of MNPs@CA, MNPs@CMDx, MNPs@β-CD-CA. Diameters around 6-14 nm are observed, as well as sphere-like morphology nanoparticles. In addition, the well-defined lattice fringes of crystallographic planes of iron oxide species are visible in all the samples, helping the nanoparticle identification and suggesting the sample crystalline structure typology. The small average size of the synthesized MNPs suggested the superparamagnetic behaviour of obtained nanoparticles. According to the literature, below some critical size, the number of magnetic domains decreases until one, characterized by a group of spins all pointing in the same direction and acting cooperatively.[454] Here, a representative image of MNPs coated with β-CD and citric acid is shown. The HR-TEM images of all of the samples can be found in the Appendix, Figure 164. Sphere-like morphology nanoparticles are visible, as well as the well-defined lattice fringes. The interplanar distances were calculated and the obtained values correspond to interplanar distances of (227) planes. These crystallographic planes are of Fe_3O_4 crystalline structure.

a

b
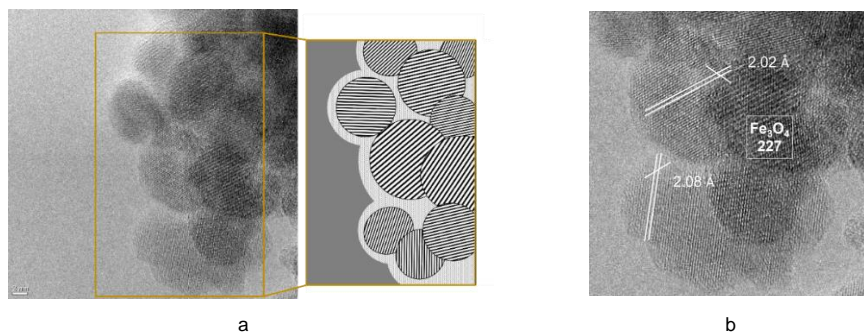
Figure 62. (a) representative HR-TEM image of MNPs@β-CD-CA, with schematic representation of nanoparticle morphology and alignment of the spacings between the observed diffraction fringes, directly visible in HR-TEM image (b); (c) particle size distributions.

The magnetic behaviour of MNPs@StA, MNPs@β-CD-CA and MNPs@Citramide-CA was studied by magnetization measurements. Measured magnetization, M, in an applied field, H, is a cumulative response of a large number of particles. The measured M(H) curve is therefore a statistical sum of the magnetization response of individual IONPs with different domains and different phases composition, depending also by density, size and dipolar interactions.[455] Figure 63 shows the magnetization curves at room temperature. Generally, the saturation magnetization increases with increasing MNPs size, due to a decrease of the cohesive energy, but it is also dependent on the different chemical composition of the surface and the surface effects on the magnetic field. The saturation magnetization values corroborate the superparamagnetic behavior of these systems, because of the absence of the hysteresis loop. The M_S values are consistent with generally reported M_S measurements for similar MNPs, normally between 60 and 30 emu/g.
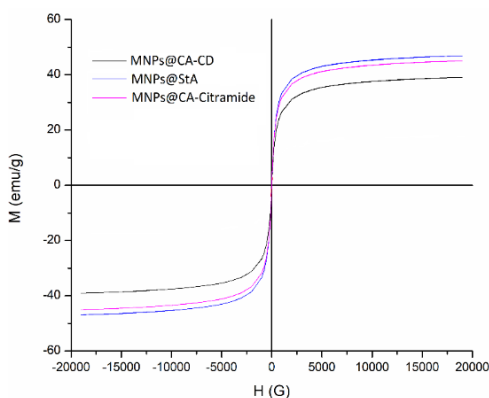
Figure 63. Magnetization measurement analysis of MNPs@CA-β-CD and MNPs@CA-Citramide.

6.2.5. Relaxometric properties

In view of potential applications of these MNPs for MRI purposes, the relaxometric properties of MNPs@CA, MNPs@CMDx, MNPs@CA-β-CD and MNPs@CA-Citramide were investigated. More in details, transverse and longitudinal relaxivities were measured and nuclear magnetic relaxation dispersion (NMRD) profiles were acquired. NMRD profiles, that report the dependence of the proton longitudinal relaxation rate (R_1) on the external magnetic field (B_0), are considered essential tools to estimate the efficiency and study magnetic properties of MNPs used as contrast agents for MRI. The experimental NMRD profiles of acquired MNPs suspensions have been fitted using the Roch's theory.[456] The fitting allows the determination of several MNPs physical parameters, such as size (A), Néel relaxation time (τ_N) and P/Q. This model can be applied to small nanosystems (metallic core less than 20 nm), supposing that the metallic core acts as a single magnetic domain. It considers that the relaxation is subject to two contributions: first, diffusion of solvent protons into the inhomogeneous nonfluctuating magnetic field created by the large magnetic moments of the superparamagnetic nanoparticles, aligned onto B_0 (Curie relaxation, predominant in the high field part of the NMRD profiles), and second, the fluctuations of the electronic magnetic moment or the Néel relaxation, dominating at low frequencies. The fluctuation of the nanoparticle magnetic moment is characterized by a relaxation time, τ_N, that is the inverse function of the magnetization flip rate from one direction along the axis to the opposite one. At low frequencies the magnetic moment of the particles is locked onto the anisotropy axis, due to the high crystal anisotropy, and the relaxation occurs both *via* Néel relaxation and water diffusion. At high frequencies, the magnetic moment is locked onto the magnetic field direction, thus, Néel relaxation does not happen, and the relaxation occurs only *via* water diffusion.

Figure 64 displays the R_1 magnetic field dependence (NMRD) of MNPs@CA, MNPs@CMDx, MNPs@CA-β-CD and MNPs@CA-Citramide. The shape of the curves is typical of the relaxation induced by superparamagnetic particles and some differences in shapes of NMRD profiles, especially at low magnetic fields, depend on particle properties, such as size, clustering, Néel relaxation time and saturation magnetization. The different profile of MNPs@CA-β-CD can be explained by the presence of more instable suspensions (as visible from PDI measurement: 0.446) characterized by higher aggregation. Table 23 reports the parameters obtained by the fitting of NMRD profiles for the different coated MNPs. The calculated diameter size (A) is similar to that registered by TEM, while P and Q factors are related to the magnetic anisotropy energy (E_A). P should decrease with increasing energy barrier, while Q should increase. τ_N is also reported.[406, 457]
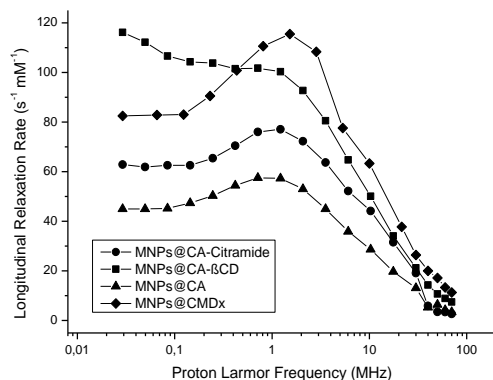
Figure 64. NMRD profiles of MNPs@CMDx, MNPs@CA, MNPs@CA-β-CD, MNPs@CA-Citramide.

Table 23. Interpolated parameters from NMRD profiles by the Roch's model fitting.

Sample	rDLS (nm)	rTEM (nm)	Ms (emu/g)	A (nm)	τN (ns)	P	Q	P/Q
MNPs@CA	37.5	8.9	30-60[a]	9.5	1.25E-07	0.01	0.64	0.016
MNPs@CMDx	36.5	10.7	30-60[a]	10.7	1.00E-06	0.07	0.37	0.190
MNPs@CA-β-CD	23.5	6.5	37	11	4.0E-07	0.61	0.39	1.572
MNPs@CA-Citramide	74.5	9.0	43	9.0	2.6E-07	0.02	0.59	0.037

(a) The Ms value of MNPs@CA and MNPs@CMDx has not been measured. For this reason, a variable Ms parameter was set during the fitting procedure.

From the calculation of the ratio between transverse relaxivity (r_2) and longitudinal relaxivity (r_1) it was possible to evaluate the efficiency of coated MNPs as T_2 contrast agents for MRI applications. The higher is the r_2/r_1 ratio, the higher is the predicted T_2 effect. The MR relaxivities of coated MNPs were measured, noticing an increase on their spin-spin (r_2) to spin-lattice (r_1) relaxation ratio (r_2/r_1) from 10 to 100, originating, therefore, a better negative contrast. While the calculated r_2/r_1 ratio at 20 MHz is comparable for all the preparations, increasing the magnetic fields the r_2/r_1 ratios change. MNPs@CA, MNPs@CA-β-CD and MNPs@CMDx show comparable r_2/r_1 ratios among them and with those reported in literature. MNPs@CA-Citramide shows higher r_2/r_1 ratio. Looking at the hydrodynamic diameter size of such system (149 nm), the higher r_2/r_1 values could conflict with the theory, that affirms that increasing the coating thickness the r_2/r_1 ratio should decrease.[458] However, it should be underlined that the effect of the coating size on r_2 and r_1 relaxivities is determined by two competing factors: the physical exclusion of protons from the magnetic field and the residence time for protons within the coating zone. So, probably, the higher hydrodynamic diameter size is only a reflection of a

better coordination between the coating and the water molecules, as confirmed by TEM images, where a small dimension of iron oxide core, as well as coating thickness is observed. Additionally, MRI tests have demonstrated an effective contrast, providing clear images, as shown in Figure 162.

6.2.6. *Cytotoxicity*

To study the biocompatibility of MNPs@CA-β-CD and MNPs@CA-Citramide, the MTT assay was performed following incubation of J774A.1 cells with different concentrations of MNPs for different time points (4 and 24 h) (Graph 6). Obtained results showed that cell metabolism was affected in a concentration-dependent manner. MNPs cytotoxicity increased with increasing iron concentration for both the preparations. Moreover, the cell viability slightly varied with the MNPs coating, demonstrating higher cytocompatibility when the cells are incubated with MNPs@CA-Citramide. A good cytocompatibility of the samples even at 10 µg/mL was demonstrated after 4 h of incubation and cell viability following 24 h of incubation was more than 70% at iron concentrations of 0.05 mM for both MNPs@CA-β-CD and MNPs@CA-Citramide, taking into account that 0.05 mM of iron nanoparticle concentration is considered to be far higher than the normal use and as far as the viability is higher than 70%, the carriers can be considered non-cytotoxic in accordance with ISO 10993-5:2009.[459]

a   b
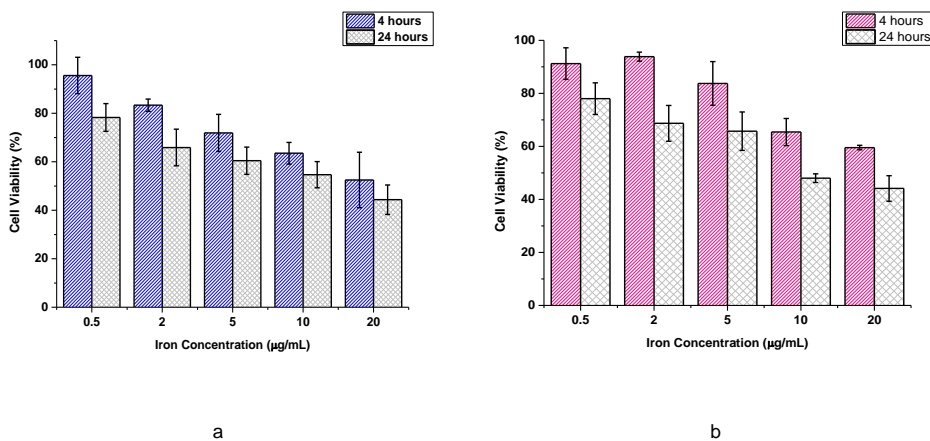
Graph 6. MTT assay results for concentration of 0.5, 2, 5, 10, 20 mg/mL of MNPs differently coated: [a] MNPs@CA-β-CD, [b] MNPs@CA-Citramide.

121

6.3.   Conclusions

A simple, effective, efficient and highly reproducible US-assisted IONPs preparation method is reported to obtain negatively charged β-CD-grafted IONPs. US technology provided control over size, morphology and nanostructure of particles. A ligand exchange approach was proven to be the most convenient synthetic procedure. High-quality coated MNPs were synthesized and versatile β-CDs coated MNPs combined with citric acid were successfully prepared and characterized. The introduction of an amino citrate spacer between the IONPs cores and the β-CDs was studied and it was demonstrated that a better inclusion complex capability, as well as higher biocompatibility was obtained. The addition of β-CDs as capping agents is fundamental for obtaining hydrophilic MNPs and stable water suspensions with good relaxometric properties, stability, cytocompatibility and adsorption capacity.

Chapter 7

Flow chemistry for the synthesis of drugs

7.1.   Introduction

A six-month period, spent in South Africa thanks to an Erasmus+ project and the collaboration with Professor Willem van Otterlo (Stellenbosch University, Stellenbosch) and Professor Paul Watts (Nelson Mandela University, Gqeberha), gave me the possibility to investigate the flow chemistry as innovative technology for the synthesis of drugs. Flow chemistry was chosen because of its well-known ability to overcome some of the challenges intrinsic of batch reaction conditions, and it represents a typical enabling technology aimed at the realization of green production processes of pharmaceuticals. Flow chemistry technology is an innovative methodology where reactions are carried out in continuous flowing streams. The application of this technology in the academia and in the industrial production of complex compounds has rapidly increased over the last few years, due to its several well documented advantages over the conventional batch processes, such us efficiency, reduced reaction time, enhanced chemical selectivity and improved yields, accurate control of the reaction parameters, efficient mixing, scale-up, enhanced safety and reproducibility.[108] A way to exploit the advantages of continuous flow reactors is the combination of sequential chemical reactions within one process. A multistep synthetic sequence in the flow mode imposes the transfer of the reaction mixture into several reactors in line with the benefit that the intermediates are not isolated but are directly transferred into the next flow reactor. However, the decomposition of the multistep flow synthesis could be required to the simple switch of solvents. Moreover, if the temperature, the homogeneity, the concentrations, and the choice of reagents are parameters that can be optimized for every single step, the back pressures, the solvents, the flow rates and the residence times are influenced by the first reactor conditions. Thus, every additional reaction step leads to an even more complex system.[460] Moreover, solid phase substances, such as heterogeneous reagents or catalysts, represent a problem, due to the blockage of the flowing system. However, packed-bed materials have been designed. They are composed of a chamber that contains catalyst particles, solid reagents, or they can be used for purification by the means of solid-phase scavengers or chromatographic separation.[461]

Multicomponent reactions (MCRs) provide a powerful tool for drug discovery and development. Combined with the power of flow chemistry they provide efficient tools for the modern medicinal chemistry. MCRs are defined as one-pot processes that combine three or more starting materials to selectively give a single product that contains all of the atoms of the reactants, thus satisfying the second principle of green chemistry, namely atom economy. MCRs offer the

ability to rapidly create molecular diversity and complexity, becoming essential in medicinal chemistry for the sustainable production of pharmaceuticals.[462] Some notable applications of MCRs in pharmaceutical industry for the synthesis of commercial drugs rely on the synthesis of lidocaine, that is produced by a three-component version of the Ugi reaction, as well as the antiplatelet agent clopidogrel.[463] The calcium channel blocker Nifedipine can be synthesized by the Hantzsch MCR,[464] the piperazine moiety of the HIV drug Indinavir by the Ugi 4CR,[465] the antiandrogen Bicalutamide using a Passerini-type reaction[466] and a two multi-step MCR for the synthesis of the anti-schistosomiasis Praziquantel follows the Ugi/Pictet-Spengler mechanisms.[467] However, despite this large number of examples the application of flow chemistry in manufacturing active pharmaceutical ingredients (API) is still not confirmed.

Thus, it was envisaged that an anticancer camptothecin analogue and the anti-schistosomiasis Praziquantel could be efficiently and cost-effectively synthesized in a continuous flow system to demonstrate the feasibility of MCRs in the production of drugs by the means of flow chemistry. Moreover, the multistep continuous flow synthesis of the Itraconazole substructure was supposed starting from the 4-[4-(4-methoxyphenyl)piperazin-1-yl]-aniline whose reduction from the 1-(4-methoxyphenyl)-4-(4-nitrophenyl)piperazine was studied in flow chemistry by using a packed-bed reactor.

7.2.   Results and discussion

This project began by preparing the starting materials for the MCRs and the synthesis of the 1-(4-methoxyphenyl)-4-(4-nitrophenyl)piperazine in batch conditions, following well-known procedures. Later, the MCRs for the synthesis of a Camptothecin analogue and Praziquantel, as well as the investigation of the reduction of the 1-(4-methoxyphenyl)-4-(4-nitrophenyl)piperazine to its corresponding aniline were firstly investigated following conventional approaches and successively studied in flow reactors.

7.2.1.   Continuous flow synthesis investigation of 6-aminouracil Camptothecin analogue

The 3-MCR for the synthesis of camptothecin analogues proceeds *via* the formation of a Knoevenagel adduct between benzaldehyde (**2**) and the activated 1,3-indanedione (**1a**) to afford intermediate (**4e**), that interacts with 6-aminouracil (**3**) and afford intermediate (**5**) *via* Michael addition. The intermediate (**5**) undergoes intramolecular cyclization with participation of the amino function and one of the 1,3-indandione carbonyl groups to form (**6**), that is finally oxidized to give the product (**7**) (Scheme 25).[468]
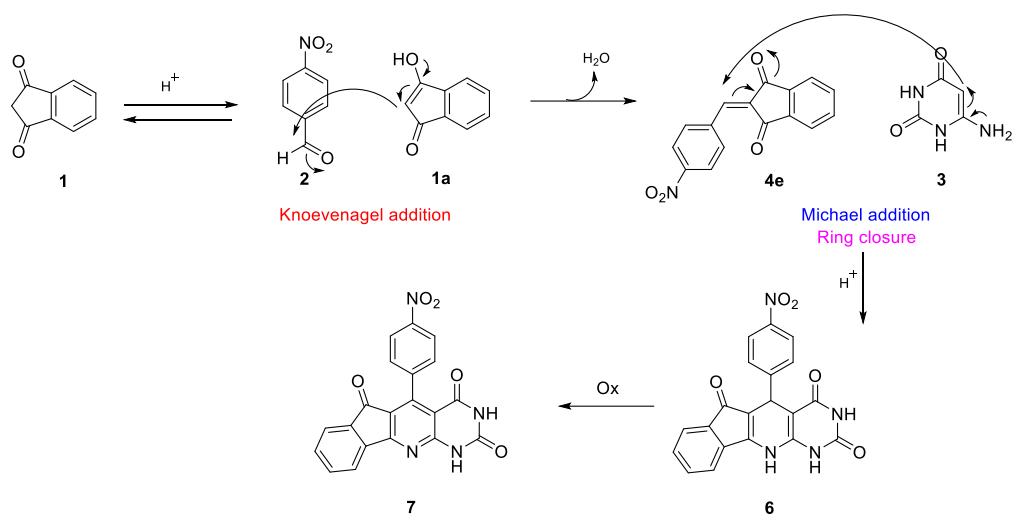
Scheme 25. Reaction mechanism of the MCR for the synthesis of a camptothecin analogue.

MCRs of camptothecin analogues have already been reported in literature. Deep eutectic solvents were used to develop a eco-friendly procedure[468] and libraries of differently substituted heterocycles were proposed by optimizing the reaction conditions, comparing solvents and additives.[469] The optimization of the reaction conditions suggested the use of DMF or a mixture of AcOH and glycol (2:1) at 120 °C as better solvent and temperature conditions, while the discovery of the beneficial effect of oxygenation of the reaction mixtures has led to an efficient multicomponent process to prepare various oxidized substrates, avoiding the final oxidative step, generally carried out using chloranil. Finally, it is reported that the isolation of the product was simply carried out by filtering the formed precipitate.[470]

However, the biggest challenge correlated to the use of continuous flow processing in chemical synthesis is the formation of and use of solids. The channel diameters of continuous flow reactors range from micrometers to millimetres and can hardly tolerate the presence of solids. Channel blockage is a common phenomenon and a serious drawback that must be alleviated. To circumvent this problem, the use of very dilute reactant solutions was employed.

As a starting point of this investigation, the batch synthesis of a 6-aminouracil Camptothecin analogue with a series of solvents at different concentrations was explored. From the comparison of DMF, glycol and THF, it was observed that the use of ethylene glycol or THF require very diluted solutions, not feasible for industrial production, due to the high wastefulness. For this reason, DMF was selected as solvent of choice and the maximum acceptable concentration was proven to be 0.5 M. Looking at the Knoevenagel mechanism, the first synthetic step is concluded by a dehydration reaction, resulting in the unsaturated intermediate (**4e**). The dehydration step can occur spontaneously or by the means of dehydrating agents. Molecular sieves or dry MgSO$_4$ are generally used as dehydrating additives; they were thus tested, and good yields were obtained. However, in order to get rid of the presence of solid reactants into the reaction mixture, not tolerable in continuous flow

reactors, the use of acetic anhydride was investigated as complementary dehydrating element. As reported in literature,[471] it was used in combination with acetic acid, also necessary as catalyst for the Knoevenagel product formation.[472] The proposed mechanism for the dehydration reaction, supported by acetic acid and acetic anhydride is outlined in Scheme 26. Following Path A, the reaction starts with the activation of the acetic anhydride by the acetic acid. The obtained complex delivers an acyl group to the hydroxyl group of the intermediate (**4a**), deriving from the Knoevenagel reaction between benzaldehyde and 1,3-indanedione, to yield the intermediate (**4d**) along with equimolar amounts of acetic acid and acetate. Abstraction of the proton in the intermediate (**4d**) by the acetate promotes deacetylation with the subsequent formation of the unsaturated function in the final intermediate (**4e**). Alternatively, following Path B, the hydroxy group might attack the carbonyl group of the acetic anhydride without the involvement of the acetic acid to provide the intermediate (**4f**), which, upon abstraction of the proton, leads to the formation of the desired intermediate (**4e**).
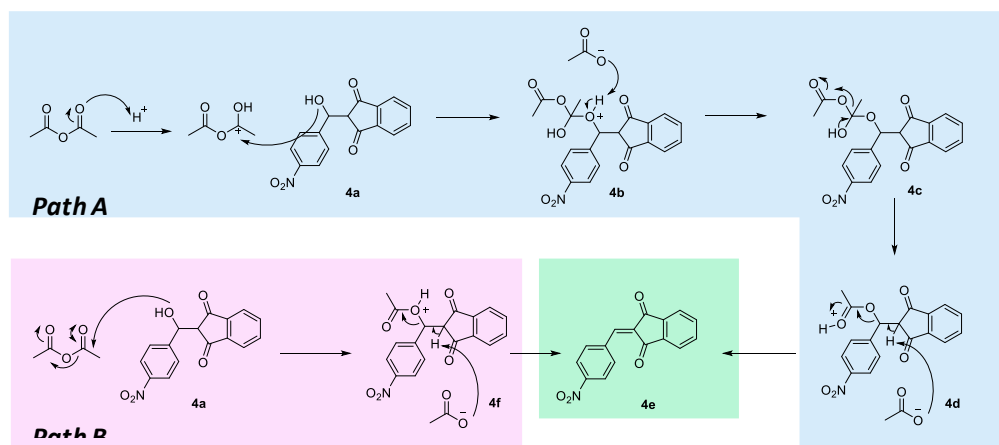
Scheme 26. Proposed mechanism of the dehydration reaction.

Subsequently, a Michael-type addition/cyclization process takes place (Scheme 27). First, a Friedel-Crafts alkylation between intermediate (**4e**) and 6-aminouracil (**3**) occurs to deliver the imine intermediate (**4g**). Next, an isomerization takes place with the formation of enamine intermediate (**5**). This intermediate undergoes intramolecular cyclization to give intermediate (**5a**), followed by dehydration and rearrangement to the product (**6**).[473-475] Product (**6**) is finally oxidized to give the final product (**7**).
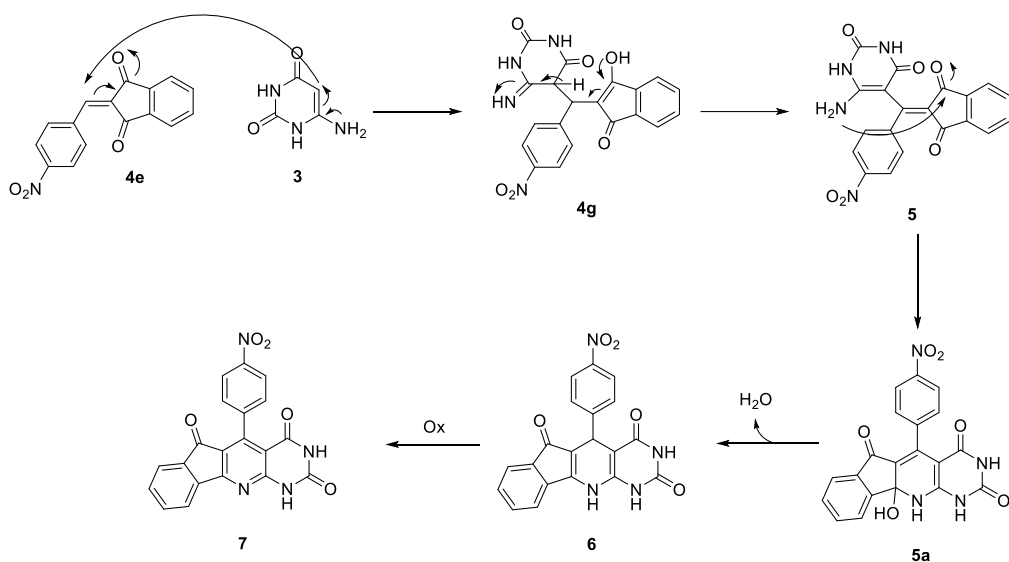
Scheme 27. Sequential steps for the synthesis of product (**7**) starting from intermediate (**4e**) and 6aminouracil (**3**).

Thus, the combination of DMF, acetic acid, acetic anhydride, at reflux conditions, was proven to be the best reaction set-up to carry out the reaction in batch reactors. However, a mixture of the final tetracyclic system (**7**) and the dihydropyridine intermediate (**6**) was always obtained. It was observed that when the reaction flask was opened to the atmosphere, only the tetracycle product was obtained after 16 h. As already demonstrated in other studies, the atmospheric oxygen might have a role in this improvement and the conduction of the reaction with saturated oxygen atmosphere resulted in the achievement of uniform formation of the product (**7**) after 4 h (99% yield). Another way that was explored to obtain the desired product (**7**) was based on the addition of CuCl$_2$ into the reaction mixture. The oxidative abilities of CuCl$_2$ have been already demonstrated,[476] and its influence on dihydropyridine intermediate (**6**) oxidation was here observed. It was fully converted into final product (**7**) after 4 h (94% yield). Moreover, the oxidative step was also conducted in the presence of a strong oxidizing agent, chloranil. While the yields remained the same (>99%), as well as the product isolation, through its precipitation by the addition of water, the supplementary step of chloranil oxidation was added. The final oxidative step was carried out after 5 h, at reflux conditions and it was 4 min long. Finally, the same MCR was studied under MW irradiation. MW conditions were set as follows: DMF, acetic acid, acetic anhydride, CuCl$_2$ at 160 °C. Fully conversion to the tetracycle product (**7**) was obtained in 1 hour (93% yield). In Table 24 all the tested reaction conditions are reported.

Table 24. Study of reaction parameters for the synthesis of product (**7**) in batch and MW conditions.

Entry	Reaction conditions	Concentration (M)	(6) : (7) ratio[a]
1	DMF, AcOH, Ac$_2$O, Reflux, 16 h	0.5 M	0 : 100
2	DMF, AcOH, Ac$_2$O, Reflux, 5 h	0.5 M	40 : 60
3	DMF, AcOH, Ac$_2$O, Reflux, O$_2$, 4 h	0.5 M	0 : 100
4	DMF, AcOH, Ac$_2$O, Reflux, CuCl$_2$ (0,10 eq), 4 h	0.5 M	0 : 100
5	DMF, AcOH, Ac$_2$O, MW, 160°C, CuCl$_2$ (0,10 eq), 1 h	0.5 M	0 : 100

Reaction conditions: 1,3-indanedione (0.4 mmol), 4-nitrobenzaldehyde (0.4 mmol), 6-aminouracil (0.4 mmol), DMF (0.8 mL), acetic acid (0.8 mmol), acetic anhydride (0.8 mmol). (a) Measured by NMR analysis.

In our preliminary studies on continuous flow synthesis, the division of the reagents into two pumped syringes forced us to change the solvent, from DMF to DMSO, due to the insolubility of the 6-aminouracil into DMF. Consequently, the utilization of CuCl$_2$, as promising oxidative agent, had to be discarded, due to the ability of DMSO to reduce Cu(II) species to Cu(0) nanoparticles, that, generated during the continuous flow process could led to pressure buildup, equipment failure and disruption of the flow process. Moreover, the combination of DMSO and acetic anhydride with the presence of a β-diketone, may give a number of by-products.[477] Thus, also the use of acetic anhydride was discarded.

The reaction was carried out in continuous flow reactor, using a mixture of DMSO and acetic acid as solvent. Syringe pumps were used to deliver reagents, which were added in stochiometric amount and were premixed in DMSO and acetic acid, as shown in Scheme 28. The 1.7 mL glass reactor was kept in an oil bath at 160 °C and the internal pressure was regulated by a back pressure regulator. Despite the possibility to use higher temperature conditions, thanks to the ease and safely pressurized system, temperatures higher than 160 °C were not used because of the possible dangerous degradation of DMSO, especially in the presence of acidic substances.[478] A conversion of the reagents into a mixture of the dihydropyridine intermediate (**6**) and the final product (**7**) was determined by following the product peaks on HPLC at 254 nm. The conversion to the tetracycle final product (**7**) increased by increasing the residence time, reaching 38% after 1 hour (Table 25 and Graph 7). However, due to the impossibility to pump molecular oxygen into the continuous flow reactor, and to avoid longer reaction times, the achievement of the fully conversion to the final product (**7**) was obtained *via* a multistep continuous flow reaction, by co-pumping chloranil dissolved in DMSO.

The first synthetic step for the synthesis of the intermediate (**6**) was optimized comparing different concentrations and reaction rates (Table 25). The faster conversion was achieved

using 0.5 M reagent solutions at 45 min residence time. After determining the optimum conditions for the synthesis of intermediate (**6**), the study was extended to the combined oxidative step (step 2, for the synthesis of product (**7**)). Flow unit 2 involved the oxidation of (**6**) with the presence of chloranil in DMSO at 160 °C for 5 seconds residence time (Table 26). Addition of water to the collected reaction mixture caused the precipitation of the final product (**7**), that was filtered and characterized without further purification. Our procedure demonstrated time economy in the total synthesis of 6-aminouracil camptothecin analogue.
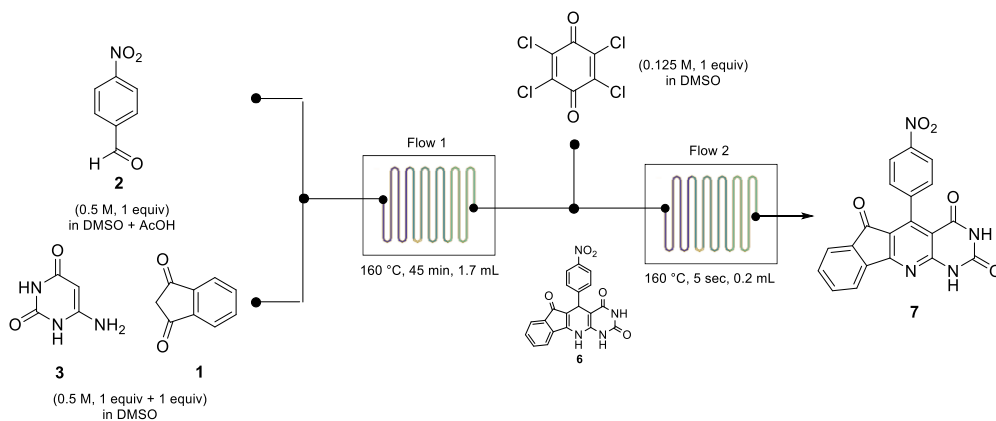
Scheme 28. Continuous flow synthesis of 6-aminouracil camptothecin analogue.
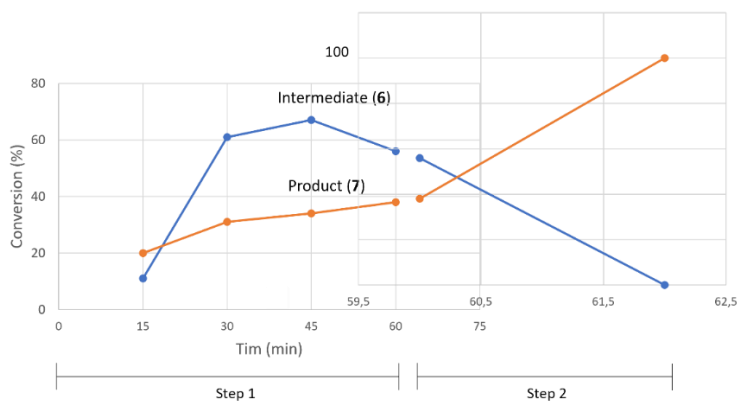
Graph 7. Graphical representation of selectivity to intermediate (**6**) or product (**7**), in continuous flow synthesis.

Table 25. Study of reaction parameters for the flow unit 1.

Entry	Reaction conditions	Molarity[a]	Time (min)	Conversion % to (6)[b]	Conversion % to (7)[b]
1			15	11	20
2	DMSO, AcOH, 160℃	0,5 M	30	61	31
3			45	67	34
4			60	56	38
5			15	36	3
6	DMSO, AcOH, 160℃	0,2 M	30	42	17
7			45	67	23
8			60	45	38
9			15	27	1
10	DMSO, AcOH, 160℃	0,1 M	30	24	1
11			45	21	1
12			60	37	11

(a) Molarity of the starting solutions; (b) measured by HPLC (H_2O : CH_3CN, 30 : 70, isocratic, 8 min) at 254 nm.

Table 26. Reaction parameters for the flow unit 2.

Entry	Reaction conditions	Molarity[a]	Molarity[b]	Time (sec)	Conversion % to (6)[c]
1	DMSO, 160°C	0,25 M	0,125	5	100

(a) molarity of (**6**) in DMSO at the end of flow step 1; (b) molarity of chloranil solution in DMSO; (c) measured by HPLC (H_2O : CH_3CN, 30 : 70, isocratic, 8 min) at 254 nm.

7.2.2. *Continuous flow synthesis investigation of Praziquantel*

The synthesis of Praziquantel, an anti-schistosomiasis drug, was prepared following a short MCR strategy, employing an Ugi reaction followed by Pictet–Spengler cyclization. The Ugi reaction is more efficient than the industrially employed 5-step synthesis. Praziquantel is administered as a racemate so stereoselectivity issues with the Ugi reaction (i.e., lack of a catalytic asymmetric version) do not represent a problem.[479] The reagents for the Ugi reaction are cheap, excluding phenethyl isocyanide, which can be synthesized from phenylethylamine. Here, a two-step procedure was followed for the synthesis of phenethyl isocyanide:

phenylethylamine was firstly reacted with formamide, to give the formylated product,[480] which was successively dehydrated by the use of $POCl_3$ in CH_2Cl_2 and Et_3N as base. It has been demonstrated that the latter step must be carried out under basic conditions, to avoid reduced yields of the product.[481] The work-up involved the direct purification of the product through chromatographic column and phenethyl isocyanide was obtained in high yield (83%) and purity.

The synthesis of Praziquantel was firstly studied under batch conditions, following well-known procedures.[482] The first step, the Ugi-four-component reaction, occurs between formaldehyde (**8**), amino acetaldehyde dimethyl acetal (**9**), cyclohexane carboxylic acid (**10**) and phenethyl isocyanide (**11**), to give the intermediate (**12**) (Scheme 29). It is interesting to notice how cyclohexane carboxylic acid acts both as acid and reagent. An equimolar ratio of reagents was dissolved into a mixture of MeOH and CH_3CN and was heated up at 80 °C for 1 hour, obtaining full conversion of the reagents to the intermediate (**12**), which was collected after liquid/liquid extraction and successively underwent to the Pictet–Spengler cyclization, *via* acetal deprotection by the use of methansulfonic acid (MsOH) and final intramolecular cyclization (6 h, 70 °C). The same synthetic steps were investigated under MW and continuous flow processes.

MW irradiation allowed a decrease in the reaction rates from 1 hour to 15 min, talking about the Ugi 4-MCR, and from 6 h to 30 min, when the second step was studied. MW-heating contributes to the efficacy of the Ugi reaction because of the high polarity of the intermediates.
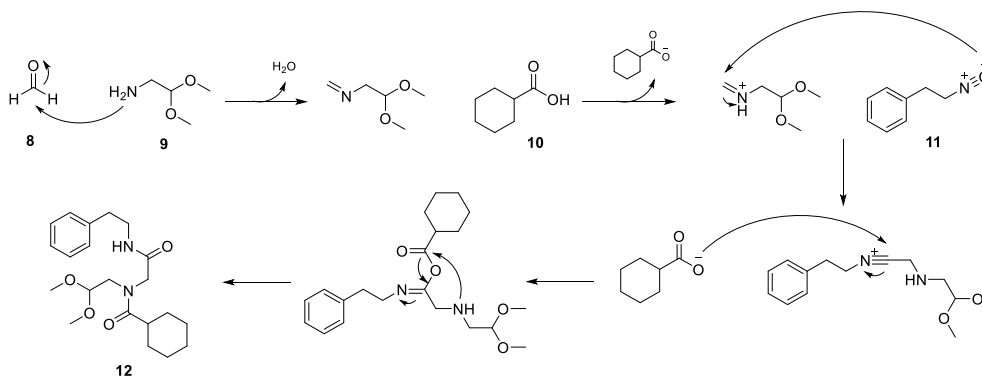
Scheme 29. Reaction mechanism for the Ugi four-component reaction.

The flow process for the synthesis of Praziquantel is shown in Scheme 30. The formation of intermediate (**12**) in continuous flow system was accomplished by the heating at 100 °C in a 1.7 mL mixing reactor for the reagents, that were pumped into the system by the means of two separate full glass syringes. Full conversion of the reagents to intermediate (**12**) was achieved after 15 min residence time. The intermediate (**12**) was subsequently treated with MsOH at 100 °C for 30 min residence time in the second reactor with full conversion to product (**13**), demonstrating the feasibility of the multistep synthesis of Praziquantel. Overall, this short two-step process affords Praziquantel from inexpensive and available starting materials in ~70%

yield. The importance to suggest an efficient, cost-effective, and alternative synthetic procedure for the preparation of Praziquantel is correlated to the annual mortality rate due to schistosomiasis (more than 280.000 people, only in the sub-Saharan Africa), also correlated to an increased susceptibility to HIV/Aids.
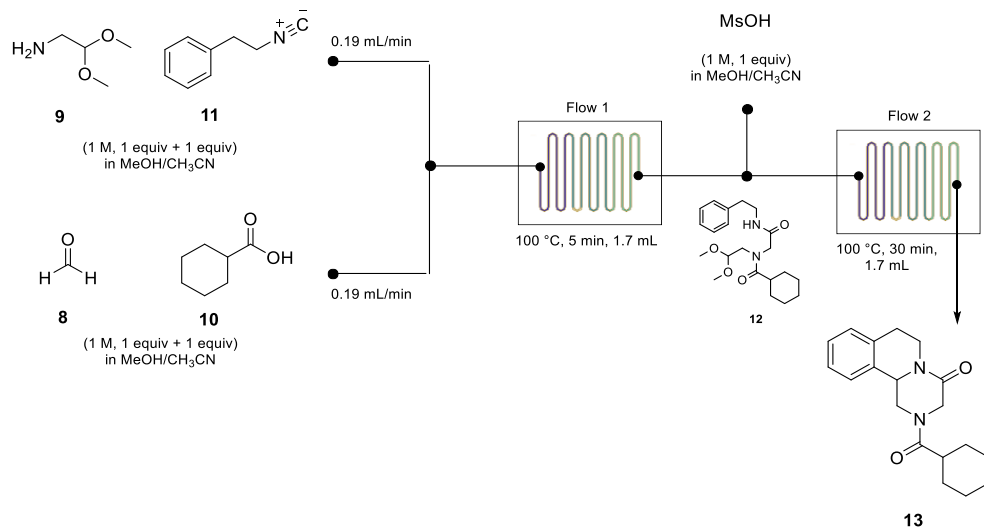
Scheme 30. Continuous flow synthesis of Praziquantel.

7.2.3. *Continuous flow synthesis investigation of 4-[4-(4-Methoxyphenyl)piperazin-1-yl]-aniline*

An investigation of the nitro reduction of 1-(4-methoxyphenyl)-4-(4-nitrophenyl)piperazine to 4-[4-(4-methoxyphenyl)piperazin-1-yl]-aniline was prepared adopting the strategies described in Scheme 31. An efficient procedure to prepare the *N*-aryl piperazine (**16**) was adopted reacting 4-methoxyaniline with bis(2-chloroethyl)amine hydrochloride (**15**), previously prepared from diethanolamine (**14**) and SOCl$_2$ in CHCl$_3$,[483] in the presence of nBuOH as described in the literature,[484] followed by the reaction with 1-chloro-4-nitrobenzene, to obtain the desired product (**17**).[485]
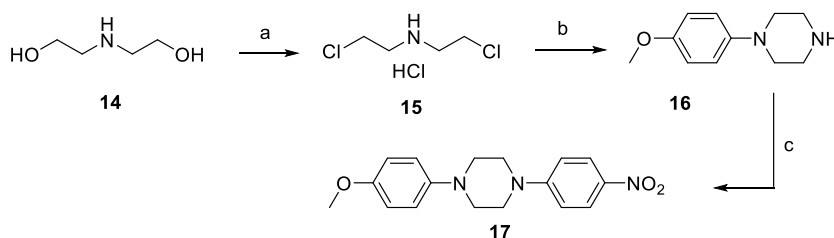
Scheme 31. Synthetic scheme for the synthesis of 1-(4-methoxyphenyl)-4-(4-nitrophenyl)piperazine. Reagents and conditions: (a) SOCl$_2$, CHCl$_3$, 5 h, 50 °C; (b) 4-methoxyaniline, nBuOH, reflux, 24 h; (c) DMSO, K$_2$CO$_3$, 1-chloro-4-nitrobenzene, 160 °C, 15 h.

As reported in literature, the hydrogenation reaction that reduces nitro to amino groups, is generally carried out in batch reactors, operated by Pd/C and ammonium formate in methanol, at reflux conditions for 3 h. Here, the nitro reduction was investigated to study the use of continuous flow system and to suggest an innovative and green reducing procedure, that involves the use of more environmentally friendly methodologies. This idea came from intensive studies, carried out in the laboratory of Professor Katia Martina, about the selective and exhaustive reductions of nitrobenzenes in the presence of glycerol, used as a sacrificial hydrogen source.[486, 487] Indeed, despite its main disadvantage, i.e. its high viscosity at room temperature, glycerol is an optimal solvent for catalysis purposes because of its high polarity and capacity to remain in the liquid phase over a large temperature range (from 17.8 to 290 °C). Moreover, it has low vapor pressure, a long relaxation time and high acoustic impedance, meaning that it can be used under MW and US irradiation conditions. Similarly to other polyols (e.g., ethylene glycol and polyethylene glycol), glycerol can act as both a solvent and reducing agent of metal precursors, and several applications have been developed in the field of metal-nanoparticle synthesis. Furthermore, glycerol can act as a stabilizer of nanometric species, leading to the straightforward recycling of the catalytic phase.[332]

Here, Cu(0)NPs were used as efficient catalytic system and a polyol (glycerol or ethylene glycol) as hydrogen source. Cu(0)NPs were thus efficiently prepared according to the "bottom-up" approach, using glycerol as protecting agent, stabilizer and solvent and supported Cu(0)NPs were prepared using celite as inert matrix.

The catalytic activity of Cu(0)NPs was investigated for the nitro reduction of 1-(4-methoxyphenyl)-4-(4-nitrophenyl)piperazine (**17**) to 4-[4-(4-methoxyphenyl)piperazin-1-yl]-aniline (**18**). Firstly, it was investigated under batch conditions, followed by its examination under continuous-flow process in a packed-bed reactor, thereby allowing the reaction mixture to pass through the catalyst without the need of subsequent removal by filtration (Scheme 32). An advantage to the application of the packed bed reactor approach is the presence of superstoichiometric amounts of catalyst, resulting in a significant reduction in the required residence time. Despite this superstoichiometric amount of Cu experienced by the limiting substrate, at any given time, in the reactor the overall flow system will become catalytic upon prolonged operation.
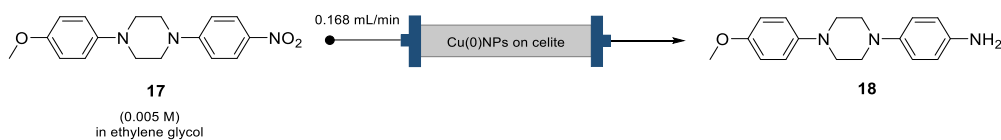
Scheme 32. Nitro reduction reaction under continuous flow process, using Cu(0)NPs/celite and ethylene glycol.

When batch reactors where used, the quantity of catalyst was set as 10 mol %. Freshly prepared Cu(0)NPs were sonicated for 10 min in an US bath until a perfectly dispersed black solution was obtained. Then, reagent (**17**), previously dispersed in a basic (KOH) solution of glycerol at the concentration of 0.08 M, was added and the reaction mixture was heated up at 130 °C and stirred for 5 h, to reach fully conversion of the reagent. The same result could be obtained after 8 h when supported Cu(0)NPs were tested.

Later, the 1-(4-methoxyphenyl)-4-(4-nitrophenyl)piperazine reduction was performed in a heated Cu(0)NPs/Celite packed column reactor (Omnifit EZ column 6.6 mm/100 mm, 0.1 g Cu(0)NPs/Celite mixture = 0.575 mL bed volume). As all reactants were mixed prior to entering the packed bed reactor, a one-pump set-up could be designed and the reaction mixture was loaded by a glass syringe pumped in the packed bed reactor. An oil bath was employed as the heating source and the packed bed reactor was immersed, allowing the system to reach the desired reaction temperature (130 °C). Finally, the outcome of the reactor was collected into a flask and a small amount of the reaction mixture was analyzed by HPLC to determine the conversion. The void volume of the packed bed reactor was determined by the weight difference of the dry and ethanol-loaded column at room temperature correlated to the density of the liquid (bed reactor). A freshly packed column was used for each experiment. The reductive step of compound (**17**) to product (**18**) was performed using ethylene glycol and KOH in continuous flow. In this case, ethylene glycol replaced the glycerol as solvent and hydrogen source in order to better allow the flow through the tubes and small bed packed reactor. Due to the poor solubility of (**17**) in ethylene glycol, a very diluted concentration was used (0.01 M). Pumping compound (**17**) through the packed column reactor held at 130 °C for 3.42 min residence time 87% of conversion to product (**18**) was afforded.

After the successful synthesis of compound (**17**) and its subsequent conversion to (**18**) using Cu(0)NPs and ethylene glycol as hydrogen source, the (**18**) synthesis from compound (**17**) was attempted *via* classical Pd/C reduction. Since a rapid reduction of compound (**17**) (5 h) with hydrazine was observed in batch reactors, it was found reasonable to use a Pd/C packed column reactor held at 100 °C for this study (Omnifit EZ column 6.6 mm/100 mm, 0.114 g Pd/C = 0.669 mL bed volume) (Scheme 33). Different flow rates were investigated (Graph 9). Each experiment was performed with a fresh catalyst cartridge. Operating the system at a flow rate of 0.620 mL/min, corresponding to a residence time of 1.08 min, resulted in full conversion to aniline with 90% of yield. When variations in the flow rate were applied, 0.465 and 0.387 mL/min, an increase in compound (**17**) reduction was observed, till to reach a 100% of conversion when a 0.310 mL/min, corresponding to 2.16 min residence time, was applied.
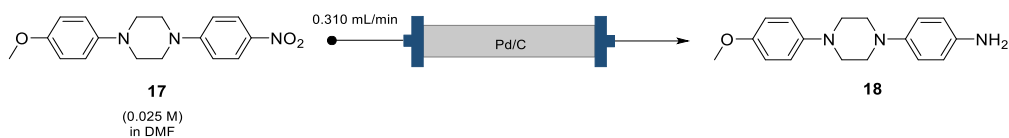
Scheme 33. Nitro reduction reaction under continuous flow process, using Pd/C and hydrazine.

Thus, increasing the residence time improved the conversion. The influence of the temperature on nitro reduction was also studied. An increase in temperature (from 80 °C to 100 °C) afforded better conversion to (**18**) (Graph 8 and Graph 9); when 120 °C is the set temperature a slightly lower conversion was obtained (Graph 10). Optimum conditions were found to be 100 °C and 2.16 min residence time to afford (**18**) in 100% conversion and 79% isolated yield.
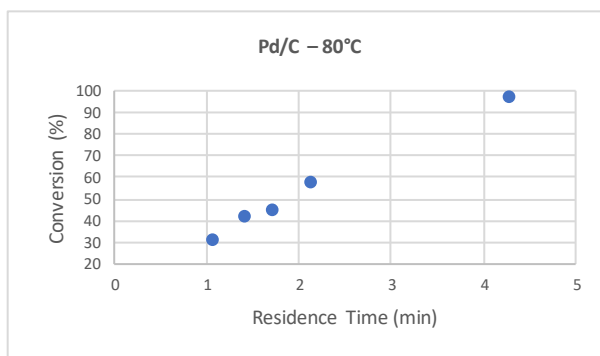
Graph 8. Conversion studies for the continuous reduction of (**17**) to (**18**), increasing the residence time, using Pd/C and hydrazine at 80 °C.
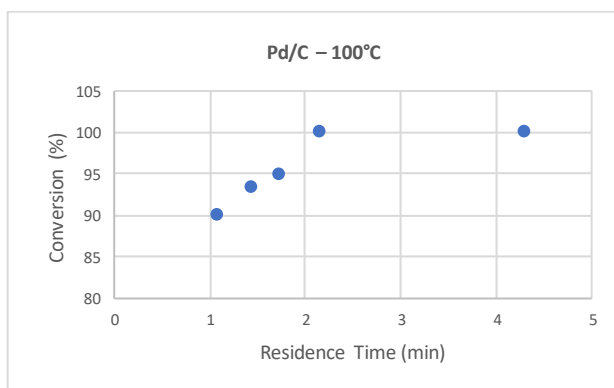
Graph 9. Conversion studies for the continuous reduction of (**17**) to (**18**), increasing the residence time, using Pd/C and hydrazine at 100 °C.

135
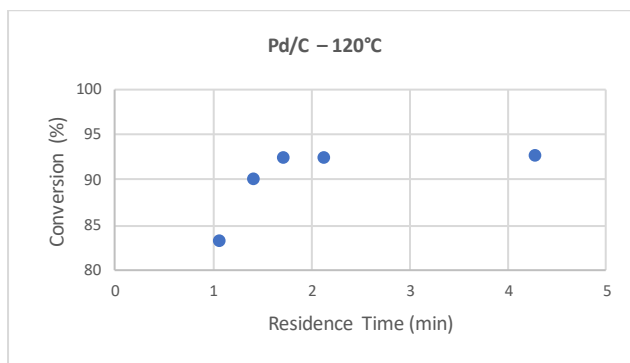
Graph 10. Conversion studies for the continuous reduction of (**17**) to (**18**), increasing the residence time, using Pd/C and hydrazine at 120 °C.

Guided by the above studies, it was decided to place special emphasis on monitoring the Pd/C-catalyzed reduction of 1-(4-methoxyphenyl)-4-(4-nitrophenyl)piperazine over a prolonged time period. Indeed, one of the most important features of immobilized catalysts in continuous applications derives, apart from the activity of the catalyst, from the ability to be used over several h. From the data seen in Graph 11, full conversion was retained for the first 2 h of operation. The batch begins to show traces of unconverted starting material after 130 min, and at 150 min the conversion dropped to 68%. Oversaturation of the catalytically active species or a deactivating mechanism could be a possible explanation for the observed decrease in conversion. In order to obtain again the fully reduction, catalyst reactivation was performed *via* fresh solvent flowing through the bed packed reactor. In this way, a new batch of reagent (**17**) and base was flowed through and full conversion to aniline was once again achieved for 20 min, after which the conversion dropped to 74%. The reactivation of the catalyst can occur through the cleaning of the catalyst surface from some reaction reagents or products that could act on the proper catalyst activity.
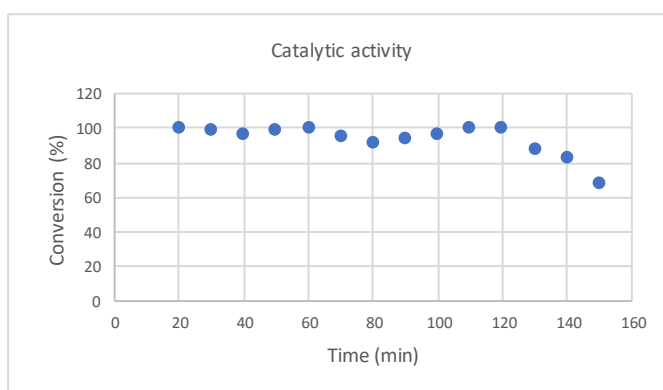
Graph 11. Prolonged studies of conversion for the continuous reduction of (**17**) to (**18**), using Pd/C and hydrazine at 100 °C.

Comparing the as-prepared catalytic systems and mentioned reaction conditions with commonly used procedures, similar yields were obtained (Table 27). A special mention goes to flow systems, where high conversion and yields were registered, while preserving green chemistry goals by the use of Cu(0) supported NPs and long recyclable Pd/C systems.

Table 27. Reaction conditions and yields for the synthesis of 4-[4-(4-Methoxyphenyl)piperazin-1-yl]-aniline. Comparison between published procedures and present investigation conditions under conventional ways and flow reactors.

Entry	Reaction conditions	Isolated yield	Ref
1	Pd/C 10%, MeOH, HCOONH$_4$, 3 h, reflux	60%	[485]
2	Pd/C 10%, NH$_2$NH$_2$·H$_2$O, 3.5 h, reflux	71%	[488]
4	Sn/HCl, CHCl$_3$, 3.5 h, reflux	68%	[489]
5	Pd/C 10%, DMF, NH$_2$NH$_2$·H$_2$O, 15 h, reflux	89%	This work
6	Cu(0) NPs, glycerol, 5 h, 130 °C	53%	This work
7	Cu(0) supported NPs 10%, glycerol, 8 h, 130 °C	62%	This work
8	Supported Cu(0) NPs, ethylene glycol, flow reactor, res. time 3.42 min, 130 °C	87%[(a)]	This work
9	Pd/C, DMF, NH$_2$NH$_2$·H$_2$O, flow reactor, res. time 2.16 min, 100 °C	79%	This work

(a) Conversion, measured by HPLC.

As shown in Scheme 34, the 4-[4-(4-methoxyphenyl)piperazin-1-yl]-aniline scaffold could be used as starting point for the multistep continuous flow synthesis of the Itraconazole substructure, where the steps must be optimized, in terms of the choice of solvents, concentrations, time and reagents. Indeed, the preparation of the triazolone derivative (**23**) requires several steps. Starting from the 4-[4-(4-methoxyphenyl)piperazin-1-yl]-aniline (**18**), the phenylcarbamate (**20**) could be obtained by the reaction with phenyl chloroformate (**19**) at 5 °C, followed by the treatment with hydrazine hydrate to give semicarbazide (**21**). The semicarbazide could be reacted with formamidine acetate at 130 °C to give the triazolone derivative (**23**). If the preparation of the intermediate (**20**) is generally performed in dichlorometane, while the second step requires 1,4-dioxane and the third one DMF; a unique solvent of choice has to be selected for a continuous flow system. Here, it has been hypothesized the use of DMF as solvent, demonstrated to be good in the reduction of the nitro compound to 4-[4-(4-methoxyphenyl)piperazin-1-yl]-aniline. Sequential additions of starting materials have been designed and the possibility to move the flow systems could give the opportunity to control the temperature of the reactors. The isolation of the intermediates would

be not required because they would be directly transferred into the next flow reactors; however, the flow rates and the residence times would be influenced by the first reactor conditions.
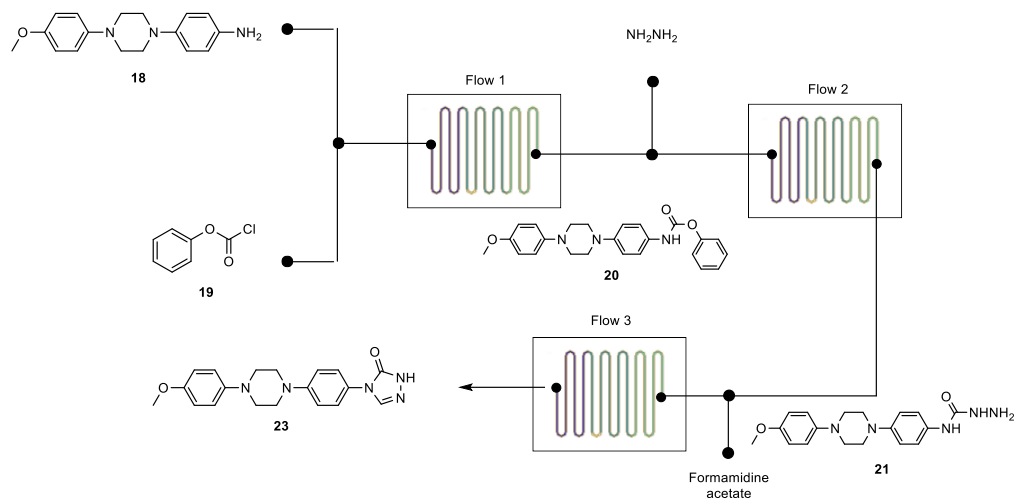
Scheme 34. Hypothetical representation of multistep continuous flow synthesis of compound (**23**), substructure of Itraconazole.

7.3. Conclusions

The MCRs for the synthesis of 6-aminouracil camptothecin analogue and Praziquantel were studied and optimized under batch, MW and continuous flow process conditions. Their preparation was proven to be more efficient, safer and faster when continuous flow chemistry was employed. Good conversion and isolated yields of the products were obtained, suggesting an innovative, green and cost-effective methodology for the application of MCRs for the synthesis of drugs. Two efficient methodologies for the reduction of 1-(4-methoxyphenyl)-4-(4-nitrophenyl)piperazine to 4-[4-(4-methoxyphenyl)piperazin-1-yl]-aniline were studied. The efficiency of ethylene glycol as hydrogen source and Cu(0)NPs/Celite, as non-noble metal catalyst, were proven in batch and continuous flow process. The same was done exploiting Pd/C and hydrazine, where deeper studies on temperature, efficiency and reusability confirmed their good activity at 100 °C, with short residence time and long activity and recyclability. The investigation of the multistep continuous flow synthesis of the Itraconazole substructure still remains open.

Chapter 8

Experimental details

The PhD Thesis herein described has been elaborated personally, but some external professional figures have been essential to carry on specific experimental procedures.

The characterization of β-cyclodextrin-silica hybrid systems, in terms of infrared spectroscopy, UV-Vis-NIR spectroscopy, XAS, XANES and EXAFS was performed by Prof. Gloria Berlier, Dr. Elisa Borfecchia and Dr. Fernando Chávez-Rivas (Department of Chemistry, Torino).

The preparation of NDs through Adamas technology as well as the UV-Vis, the infrared and the Raman measurements of derivatized-rGO and NDs were performed by Dr. Federico Picollo (Department of Physics, Torino), Dr. Lorenzo Mino and Dr. Francesco Turci (Department of Chemistry, Torino).

The XRD, ICP-MS, SEM, TEM, XPS and SSA characterization of Co/carbon materials were performed by Prof. Gloria Berlier (Department of Chemistry, Torino), Dr. Alessio Zuliani, Dr. Alain Rafael Puente Santiago, Dr. Juan J. Giner-Casares and Dr. Enrique Rodríguez-Castellón (Department of Organic Chemistry, Cordoba).

The characterization of amino-citrate-β-CD coated MNPs, in terms of TEM measurements was performed by Dr. Maria Carmen Valsania and Prof. Giuliana Magnacca (Department of Chemistry, Torino). The characterization through DLS, NMRD profiles, cytotoxicity and stability was done in collaboration with Prof. Enzo Terreno, Dr. Francesca Garello and Dr. Eleonora Cavallari (Department of Molecular Biotechnology and Health Sciences, Torino).

The continuous flow synthesis of APIs was feasible thanks to a collaboration project with Prof. Willem van Otterlo (Department of Chemistry and Polymer Science, Stellenbosch) and Prof. Paul Watts (Department of InnoVenton and The Downstream Chemicals Technology Station, Port Elizabeth).

8.1. Sonochemically-promoted preparation of β-cyclodextrin-silica hybrid systems for efficient copper catalysis

8.1.1. General working conditions

All commercially available reagents and solvents were purchased from Sigma-Aldrich (Milan, Italy) and used without further purification. SIPERNAT 320 amorphous silica was supplied by Evonik Degussa. β-CD was provided by Wacker Chemie (München, Germany). The synthesis

of 6^I-amino-6^I-deoxy-β-CD and 6^I-O-*p*-Toluenesulfonyl-β-CD was performed following published synthetic procedure.[490] US irradiation at 40-80-120 kHz was performed in a ultrasound bath supplied by Weber ULTRASONICS GMBH. When reactions were carried out in a combined system MW/US the device has been designed in our laboratory by inserting a sonic horn made of pirex inside a RotoShynth (Milestone) microwave chamber (Figure 65).

Thermogravimetric analyses were performed using a thermogravimetric analyzer TGA 4000 (PerkinElmer) at 10 °C min^{-1} operating with alumina crucibles that contained 10−20 mg of sample. The analyses were performed under an argon atmosphere at a starting temperature of 50 °C and an end temperature of 800 °C. Total mass loss was attributed to the functional groups that were covalently attached to the sidewalls. UV−vis absorption spectra were measured on a dual-beam spectrophotometer (Agilent Technologies Cary 60, G6860AA) equipped with a 1 cm path length quartz cuvette. Elemental analyses were performed on an EA 1108 (Fison Instruments). Reactions were carried out in professional MW reactor (Monowave 400/200, Anton Paar GmbH) using reaction vial G10. Reactions were monitored by TLC on Merck 60 F254 (0.25 mm) plates (Milan, Italy), which were visualized by UV inspection. TLC Merck 60 F254 (0.25 mm) plates (Milan, Italy) were used to monitor CuAAC reactions. For GC-MS analyses a 30 m capillary column, i.d. of 0.25 mm and film thickness 0.25 μm was used. GC-MS analyses were performed in a GC Agilent 6890 (Agilent Technologies, Santa Clara, CA, USA) that was fitted with a mass detector Agilent Network 5973, using a 30 m capillary column, i.d. of 0.25 mm and film thickness 0.25 μm. GC conditions were: injection split 1:10, injector temperature 250 °C, detector temperature 280 °C. Gas carrier: helium (1.2 mL/min), temperature program: from 50 °C (5 min) to 100 °C (1 min) at 10 °C/min, to 230 °C (1 min) at 20 °C/min, to 300 °C (5 min) at 20 °C/min. HRMS was determined using a MALDI-TOF mass spectra (Bruker Ultraflex TOF mass spectrometer, Milan, Italy). The cations were determined with a Perkin Elmer Optima 7000 (Perkin Elmer, Norwalk, Connecticut, USA) inductively coupled plasma-optical emission spectrometer (ICP-OES). Jeol ECZ-R at 25 °C, 600 MHz and 75 MHz for 1H and 13C, respectively, was used to record NMR spectra. Chemical shifts of NMR spectra were calibrated to the residual proton and carbon resonances of the solvent; CDCl$_3$ (δH = 7.26, δC = 77.16). Chemical shifts (δ) are given in ppm and coupling constants (J) in Hz.

Figure 65. Combined MW/US device.

Infrared spectra were recorded on a BRUKER FTIR-66 spectrophotometer with a resolution of 2 cm^{-1}, using a DTGS detector. Measurements were carried out using a home-made cell allowing *in situ* thermal treatment and room temperature measurement. Thin self-supporting pellets for transmission measurements (around 10 mg/cm^2) were prepared with a hydraulic press. Before the measurements the samples were outgassed at 80 °C for 2 h in the same cell used for the measurements. β-CD and Cu-CD were measured after dilution in KBr, without thermal treatment (spectra not reported).

UV-Vis-NIR spectra were recorded in the 2500-200 nm range at 1 nm resolution on Cary 5000 UV-Vis-NIR spectrophotometer (Agilent) equipped with a Diffuse Reflectance attachment with integrating sphere coated by BaSO$_4$. Prior to each measurement, a baseline spectrum was collected by using Teflon as a reference. Spectra are reported as relative reflectance (R%), defined as:

$$R_\% = R_{sample} / R_{reference} \cdot 100$$

Cu K-edge XAS data were collected at the B18 beamline[491] of the Diamond Light Source (UK). XAS spectra were acquired in transmission mode, using a fixed-exit double crystal water-cooled Si(111) monochromator and Pt-coated mirrors. Ionization chambers filled with different mixtures of He and Ar were employed to collect the incident (I_0) and transmitted ($I_{1,2}$) X-ray intensities. The third ionization chamber (I_2) was used for the simultaneous collection of the XANES spectrum of a Cu metal foil, for energy calibration purposes.[191] Si-TriAm-CD-Cu, in its as-prepared and exhausted state was measured at RT in air, in the form of self-supporting pellet, with optimized weight for transmission-mode XAS. The Cu^{II}O and Cu$^{I}_2$O model compounds were also measured in the form of self-supporting pellets, with optimized weights. Reported XAS spectra for $[Cu^{II}(NH_3)_3(NO_3)]^+$ are instead reproduced from ref.,[193] to which the reader is referred for additional details on data acquisition and interpretation. On B18, XAS spectra were acquired in Quick-EXAFS mode in the 8800 – 9783 eV range, with a constant energy step of 0.3 eV in the whole energy range. Each scan required 3 min. To characterize each pelletized

141

sample, five consecutive scans were collected, and averaged the corresponding μx(E) curves after checking for signal reproducibility. All the XAS spectra were normalized to unity edge jump and aligned in energy using the Athena software from the Demeter package.[492] The χ(k) EXAFS functions were also extracted by using the Athena program. Fourier-transform (FT) EXAFS spectra were obtained by transforming the $k^2\chi$(k) functions in the (2.4 – 12.0) Å^{-1} range.

8.1.2. Experimental procedures

Preparation of chlorinate silica (Si-Cl)

10.5 mL of $SOCl_2$ were added dropwise to 1 g of silica SIPERNAT 320. The mixture was left stirring under reflux, o.n. The suspension was filtered and the powder was washed with chloroform and dried under vacuum.[493]

Si-Cl titration.

The amount of chloride present in the sample was determined *via* argentometric titration. The Mohr method was followed. The sample solution was titrated against a solution of silver nitrate of known concentration. Chloride ions react with silver(I) ions to give insoluble silver chloride (1):

$$Ag^+ (aq) + Cl^- \rightarrow AgCl (s) \tag{1}$$

1 g of Si-Cl was dispersed in 100 mL of a $NaHCO_3$ solution (0.005 M). The solution was stirred for 1 h at room temperature. Potassium chromate was used as an indicator, giving red silver chromate after all the chloride ions have reacted:

$$2 Ag^+ (aq) + CrO_4^{2-} (aq) \rightarrow Ag_2CrO_4 (s) \tag{2}$$

398 μL of K_2CrO_4 0.25 M were added and the solution was titrated with $AgNO_3$ 0.1 M (2) to obtain the amount of chlorosilyl groups on silica surface (~0.9 mmol g^{-1}).

Preparation of Si-DETA

Diethylenetriamine (0.500 mL) was dissolved in 0.500 mL of solvent and Si-Cl was added (0.100 g). The suspension was heated under stirring in an oil bath (60 °C for 12 h). When the reaction was performed in a US bath (40, 80 or 120 kHz, power 200 W), the suspension was irradiated for 2-4 h in toluene or in diethylenetriamine. The modified silica was then filtered, washed with water, methanol and chloroform and dried under vacuum at room temperature for 12 h.

Preparation of Si-DETA-CD

6^{I}-tosyl-β-CD (0.100 g, 0.077 mmol) was dissolved in DMF (1.7 mL) and Si-DETA (0.100 g) was added. The suspension was heated to 70 °C under magnetic stirring for 24 h. When the reaction was performed under US irradiation, the suspension reacted 4 h (power 200 W, frequency 80 kHz). Silica was filtered, washed with water, methanol and chloroform, and dried under vacuum at room temperature for 12 h.

Preparation of Si-NHCD

6^{I}-amino-6^{I}-deoxy-β-CD (0.163 g, 0.14 mmol) was dissolved in DMF (2 mL) or water and then chlorinate silica (0.100 g) and pyridine (0.332 mL) were added. The suspension was either conventionally stirred at 60 °C for 12 h or was irradiated in an US bath at 80 kHz for 2-4 h. Modified silica was filtered, washed with water, methanol and chloroform, and dried under vacuum at room temperature for 12 h.

Preparation of Si-Gly

(3-Glycidyloxypropyl)trimethoxysilane (0.040 mL) was dissolved in toluene (1 mL) and silica (0.100 g) was added. The mixture was sonicated 2 h in US bath (Power 200 W, Frequency 80 kHz). The product was filtered and washed with toluene and chloroform. Finally, it was dried under vacuum at room temperature for 12 h.

Preparation of Si-MonoAm

3-(Trimethoxysilyl)-propylamine (0.040 mL) was dissolved in toluene (1 mL) and silica (0.100 g) was added. The mixture was sonicated 2 h in US bath (Power 200 W, Frequency 80 kHz). The product was filtered and washed with toluene and chloroform. Finally, it was dried under vacuum at room temperature for 12 h.

Preparation of Si-DiAm

3-(2-Aminoethylamino)propyltrimethoxysilane (0.040 mL) was dissolved in toluene (1 mL) and silica SIPERNAT 320 (0.100 g) was added. The suspension was either heated under stirring in an oil bath (80 °C for 36 h) or the reaction was performed in a US bath (power 200 W, comparing 40 and 80 kHz as frequencies). Silica was filtered, washed with toluene and chloroform, and dried under vacuum at room temperature for 12 h.

143

Preparation of Si-TriAm

N^1-(3-Trimethoxysilylpropyl)diethylenetriamine (0.040 mL) was dissolved in toluene (1 mL) and silica (0.100 g) was added. The mixture was sonicated 2 h in US bath (Power 200 W, Frequency 80 kHz). The product was filtered and washed with toluene and chloroform. Finally, it was dried under vacuum at room temperature for 12 h.

Preparation of Si-Gly-CD

6^I amino-6^I-deoxy-β-CD (1 g, 0.88 mmol) was dissolved in DMF (15 mL). Si-Gly (1 g) was added. The suspension was irradiated under MW and US combined irradiation at 100 °C for 4 h (MW power 20 W, US power 35 W). The product was filtered and washed with water, methanol and chloroform. Finally, it was dried under vacuum at room temperature for 12 h.

Preparation of Si-MonoAm-CD

6^I-O-*p*-Toluenesulfonyl-β-CD (1 g, 0.77 mmol) was dissolved in DMF (15 mL). Si-MonoAm (1 g) was added. The suspension was irradiated under MW and US combined irradiation at 100 °C for 4 h (MW power 20 W, US power 35 W). The product was filtered and washed with water, methanol and chloroform. Finally, it was dried under vacuum at room temperature for 12 h.

Preparation of Si-DiAm-CD

6^I-O-*p*-Toluenesulfonyl-β-CD (0.100 g, 0.077 mmol) was dissolved in DMF (1.5 mL) and Si-DiAm (0.100 g) was added. The suspension was either heated to 60 °C and stirred for 60 h, or was irradiated by US (4 h, power 200 W, frequency 80 kHz). The same procedure was repeated under MW and US combined irradiation: 1 g of Ts-CD was dissolved in 15 mL of DMF and 1 g of Si-DiAm was added. The suspension was heated at 100 °C for 4 h (average MW power 20 W, average US power 35 W). After cooling to room temperature, the modified silica was filtered, washed with water, methanol and chloroform, and dried under vacuum at room temperature for 12 h.

Preparation of Si-TriAm-CD

6^I-O-*p*-Toluenesulfonyl-β-CD (1 g, 0.77 mmol) was dissolved in DMF (15 mL). Si-TriAm (1 g) was added. The suspension was irradiated under MW and US combined irradiation at 100 °C for 4 h (MW power 20 W, US power 35 W). The product was filtered and washed with water, methanol and chloroform. Finally, it was dried under vacuum at room temperature for 12 h.

Synthesis of 6^I-O-p-Toluenesulfonyl-β-CD

The synthesis of 6^I-O-*p*-Toluenesulfonyl-β-CD was performed following published synthetic procedure.[494] Briefly, β-CD (1.30 g, 1.14 mmol) was dissolved in water (30 mL) and the solution was transferred to the cavitating-tube reactor. 1-(p-toluenesulfonyl)imidazole (1.01 g, 4.58 mmol) was added and the mixture was sonicated for 10 min (19.2 kHz, 20W). 2 mL of aqueous NaOH (0.560 g, 14 mmol) were added dropwise and after 30 min the suspension was transferred to a flask and NH_4Cl (1.67 g, 31.5 mmol) was added. After one night the mixture was filtered and washed with ice-cold water (5 mL) and acetone (5 mL). Finally, the solid was dried under vacuum.

^{1}H NMR (600 MHz, DMSO-d$_6$): δ 7.71 (d, *J* = 8.3 Hz, 2H), 7.39 (d, *J* = 8.2 Hz, 2H), 5.72 (dt, *J* = 24.0 Hz, 14H), 4.79 (d, *J* = 7.5 Hz, 5H), 4.73 (d, *J* = 3.2 Hz, 2H), 4.51 – 4.39 (m, 5H), 4.37 – 4.25 (m, 1H), 3.69 – 3.38 (m, 28H), 2.39 (s, 3H).

β-CD-Cu(II) Complexation

The silica-β-CD hybrid system (0.100 g) was dispersed in NaOH 0.5 M (0.675 mL). $CuSO_4$ 0.08 M (0.719 mL) was added dropwise, during US sonication. The suspension was immediately filtered and washed with water and methanol. Finally, the solid was dried under vacuum for 12 h.

Click chemistry reaction

Azide (0.0676 mmol, 1 eq) and terminal alkyne (1 eq) were dissolved in 0.500 µL of H_2O : tBuOH (1:1). Solid supported catalyst was added. The reaction was heated up at 85 °C, for 1 h or 5 h or under MW irradiation (85 °C) for 20 min. The resulting mixture was filtered, washed with methanol and chloroform. The solvent was removed under vacuum to afford the triazole. All products were confirmed by ^{1}H NMR and GC-MS.

1,5-bis(1-benzyl-1H-1,2,3-triazol-4-yl)pentane (white powder). ^{1}H NMR (600 MHz, CDCl$_3$): δ 7.39 – 7.31 (m, 6H), 7.24 (d, *J* = 6.4 Hz, 4H), 7.19 (s, 2H), 5.47 (s, 4H), 2.66 (s, 4H), 1.66 (s, 4H), 1.38 (s, 2H).

^{13}C NMR (151 MHz, CDCl$_3$): δ 135.26, 129.38, 128.95, 128.31, 54.40, 29.29, 28.96, 25.85.

1,6-bis(5-phenyl-1H-1,2,3-triazol-1-yl)hexane (white powder). ^{1}H NMR (600 MHz, CDCl$_3$): δ 7.84 (d, *J* = 7.1 Hz, 2H), 7.76 (s, 1H), 7.42 (t, *J* = 7.6 Hz, 2H), 7.34 (t, *J* = 8.0 Hz, 1H), 4.40 (t, *J* = 7.0 Hz, 2H), 2.02 – 1.93 (m, 2H), 1.45 – 1.35 (m, 2H).

^{13}C NMR (151 MHz, CDCl$_3$): δ 130.51, 128.95, 128.27, 125.74, 120.23, 49.82, 29.84, 26.09.

2-(1-benzyl-1H-1,2,3-triazol-4-yl)ethan-1-ol (white powder). ^{1}H NMR (600 MHz, CDCl$_3$): δ 7.39 – 7.32 (m, 4H), 7.26 (d, *J* = 1.6 Hz, 1H), 7.24 (d, *J* = 1.0 Hz, 1H), 5.48 (s, 2H), 4.10 (brs, 1H), 2.85 (s, 2H), 2.19 (s, 2H).

^{13}C NMR (151 MHz, CDCl$_3$): δ 145.73, 134.91, 129.45, 129.13, 128.47, 121.48, 61.72, 54.07, 29.62.

2-(1-undecyl-1H-1,2,3-triazol-4-yl)ethan-1-ol (white powder). ^{1}H NMR (600 MHz, CDCl$_3$): δ 4.32 (t, *J* = 6.8 Hz, 1H), 4.11 (q, *J* = 7.1 Hz, 2H), 2.95 – 2.79 (m, 2H), 1.91 – 1.85 (m, 2H), 1.29 (d, *J* = 11.7 Hz, 4H), 1.27 – 1.26 (m, 2H), 1.25 – 1.23 (m, 10H), 0.87 (t, *J* = 7.1 Hz, 3H).

^{13}C NMR (151 MHz, CDCl$_3$): δ 142.20, 132.09, 60.73, 32.20, 30.55, 29.85, 29.65, 29.32, 26.88, 22.99, 21.37, 14.47.

4-phenyl-1-undecyl-1H-1,2,3-triazole (white powder). ^{1}H NMR (600 MHz, CDCl$_3$): δ 7.82 (dd, *J* = 8.3, 2H), 7.73 (s, 1H), 7.42 (t, *J* = 7.7 Hz, 2H), 7.33 (dt, *J* = 9.1, 1H), 4.38 (t, *J* = 7.3 Hz, 2H), 1.96 – 1.90 (m, 2H), 1.38 – 1.30 (m, 4H), 1.29 – 1.15 (m, 12H), 0.86 (t, *J* = 7.1 Hz, 3H).

^{13}C NMR (151 MHz, CDCl$_3$): δ 130.92, 129.19, 128.51, 126.08, 119.79, 50.87, 32.22, 30.68, 29.77, 29.35, 26.84, 23.01, 14.44.

8.2. Surface modification of carbon-based nanomaterials: the efficacy and versatility of dipolar cycloaddition in the derivatization of rGO and nanodiamonds

8.2.1. General working conditions

All the reagents were purchased by Sigma Aldrich and used without further purification. TLC were carried out on Merck® Kieselgel 60 F254 precoated plates (0.25 mm) and visualized by UV inspection. HPLC-MS studies were carried out on a Waters Fraction Link autopurification system (flow rate of 1 mL/min) equipped with pump 525EF, PDA 2996 and MS (ESCI-ZQ) detectors and/or HPLC Waters Flexinject, pump 1525, PDA 2998, ELSD 2424 (Empower Pro software). Low-resolution mass spectra were recorded on a Finnigan-MT TSQ70 in electron impact (EI) or chemical ionization (CI) mode, using isobutane as reactant gas. NMR spectra were performed on Bruker 300 or 600 and 75 or 125 MHz Advance spectrometer (for ^{1}H and ^{13}C, respectively). Chemical shifts were calibrated to the residual proton and carbon resonances of the solvent; DMSO-d6 (δH = 2.54, δC = 39.5), CDCl3 (δH = 7.26, δC = 77.16). Chemical shifts (δ) are given in ppm and coupling constants (J) in Hz. GC-MS analyses were performed in a GC Agilent 6890 (Agilent Technologies, Santa Clara, CA, USA), which was fitted with a mass detector Agilent Network 5973, using a 30 m capillary column, i.d. of 0.25 mm and film thickness 0.25 μm. GC conditions were: injection split 1:10, injector temperature 250 ℃, detector temperature 280 ℃. Gas carrier: helium (1.2 mL/min). Temperature program: from 50 ℃ (5min) to 100 ℃ (1min) at 10 ℃/min, to 230 ℃ (1min) at 20 ℃/min, to 300 ℃ (5 min) at 20 ℃/min. The cations were determined with a Perkin Elmer Optima 7000 (Perkin Elmer, Waltham, MA, USA) inductively coupled plasma-optical emission spectrometer (ICP-OES). rGO synthesis was carried out in a professional MW reactor (Monowave 400/200, Anton Paar GmbH, Graz, AT) using reaction vial G10. Thermogravimetric analyses were performed using a thermogravimetric analyzer TGA 4000 (Perkin Elmer) at 10 ℃ min^{-1} operating under argon (80 ml min-1) with alumina crucibles containing 6-8 mg of rGO derivatives. Samples were previously overnight stove dried at 80 ℃, then the samples were heated up to 800 ℃ (starting temperature: 50 ℃; temperature increase rate: 10 ℃/min; argon flow: 80 ml/min). Total mass loss was attributed to functional groups which were covalently attached to the sidewalls. The number of functional groups was calculated considering a fixed thermogram temperature. Functionalization amounts were expressed in mmol of adducts per 100 mg of rGO or NDs. rGO or NDs carbon atoms were excluded in the calculation of the molecular weight of cycloaddition adducts. Centrifuge Microfuge 18 (Beckmann Coulter) and Centrikon T-42K (Kontron Instruments). UV absorption measurements were performed on a UV-Vis dual-beam spectrophotometer (Agilent Technologies Cary 60, G6860AA) equipped with a 1 cm path length quartz cuvette. Raman measurements were assessed with a conventional micro-spectrometer (Horiba Jobin Yvon HR800), with optical excitation given by a continuous 532 nm laser focused with a 100× air objective or a Renishaw Raman spectrometer (blue laser at 442 nm).

8.2.2. Experimental procedures

General procedure for the synthesis of Fmoc protected amino aldehydes
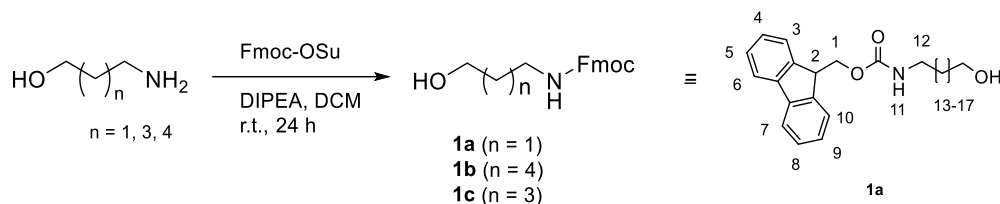
Scheme 35. Synthesis of Fmoc-aldehydes **1a-c.**

General procedure for the FMOC protection of amino alcohol to products (1a-1c)

Amino alcohol (6 mmol) was dissolved in 25 mL of CH_2Cl_2 and 9-fluoromethyl succinimidyl carbonate (2 g, 5.9 mmol) and DIPEA (2.1 ml, 12 mmol) were added. After being stirred at room temperature for 24 h, the mixture was diluted with acidulated water (25 mL) and extracted with CH_2Cl_2. The organic layer was washed with water and Brine, dried over Na_2SO_4 and concentrated under vacuum to provide white solids 1a-1c in 84%, 91%,74% yield respectively.

(9H-fluoren-9-yl)methyl(3-hydroxypropyl)carbamate (**1a**)[495] White solid (1.5 g, 84% yield). R_f 0.51 (CH_2Cl_2/CH_3OH 9:1).

^{1}H NMR (300 MHz, $CDCl_3$) δ 7.79-7-77 (d, J = 7.5 Hz, 2H, *H-6, H-7*), 7.62-7.59 (d, J = 7.2 Hz, 2H, *H-3, H-10*), 7.44-7.42 (t, J = 7.2 Hz, 2H, *H-5, H-8*), 7.33-7.31 (t, J = 7.9 Hz, 2H, *H-4, H-9*), 5.08-4.88 (brs, 1H, *H-11*), 4.47-4.45 (d, J = 6.8 Hz, 2H, *H-1*), 4.26-4.20 (t, J= 6.8Hz, 1H, *H-2*), 3.68-3.64 (t, J = 5.7 Hz, 2H, *H-14*), 3.36 (m, 2H, *H-12*), 1.65 (m, overlayed, water 2H, *H-13*) ppm.

^{13}C NMR (75 MHz, $CDCl_3$) δ 157.8, 144.28, 141.75, 128.11, 127.47, 125.39, 120.40, 67.08, 59.88, 47.70, 38.02, 32.97 ppm.

ESI-MS[+]: m/z calc for $C_{18}H_{19}NO_3$ 298.14; [M+H][+] found 298.59; [M+Na][+] found 320.64.

(9H-fluoren-9-yl)methyl(6-hydroxyhexyl)carbamate (**1b**)[496] White solid (1.85 g, 91% yield). R_f 0.54 (CH_2Cl_2/CH_3OH 9:1).

^{1}H NMR (600 MHz, $CDCl_3$): δ 7.77 (d, *J* = 7.8 Hz, 2H, *H-6, H-7*), 7.60 (d, *J* = 7.8 Hz, 2H, *H-3, H-10*), 7.40 (t, *J* = 7.2 Hz, 2H, *H-5, H-8*), 7.31 (t, *J* = 7.2 Hz, 2H, *H-4, H-9*), 4.76 (s, 1H, *H-11*), 4.41 (d, *J* = 7.2 Hz, 2H, *H-1*), 4.21 (t, *J* = 7.2 Hz, 1H, *H-2*), 3.64 (t, *J* = 6.6 Hz, 2H, *H-17*), 3.19 (m, 2H, *H-12*), 1.59-1.51 (m, 4H, *H-13, H-16*), 1.41-1.33 (m, 4H, *H-14, H-15*) ppm.

^{13}C NMR (151 MHz, $CDCl_3$): δ 144.32, 141.38, 127.80, 127.13, 125.16, 120.07, 66.63, 62.88, 47.47, 41.04, 32.70, 30.10, 26.51, 25.39 ppm.

ESI-MS$^+$: m/z calc for $C_{21}H_{25}NO_3$ 339.18; [M+H]$^+$ 340.19, found 340.15; [M+Na]$^+$ 362.17, found 362.17.

(9H-fluoren-9-yl)methyl(5-hydroxypentyl) carbamate (**1c**)[497] Yellow solid (1.78 g, 74% yield). R_f 0.57 (CH$_2$Cl$_2$/ CH$_3$OH: 9:1).

^{1}H NMR (300 MHz, CDCl$_3$) δ 7.79-7.77 (d, J = 7.4 Hz, 2H, *H-6, H-7*), 7.59 (d, J = 7.4 Hz, 2H, *H-3, H-10*), 7.42 (t, J = 7.0 Hz, 2H, *H-5, H-8*), 7.32-7.30 (t, J = 7.0 Hz, 2H, *H-4, H-9*), 4.8 (brs, 1H, *H-11*), 4.43-4.41 (d, J = 6.6 Hz, 2H, *H-1*), 4.25-4.21 (t, J = 6.6. 1H, *H-2*), 3.69-3.64 (t, J = 6.4 Hz, 2H, *H-16*), 3.22 (m, 2H, *H-12*), 1.55-1.41 (m, 6H, *H-13, H-14, H-15*) ppm.

^{13}C NMR (75 MHz, CDCl$_3$) δ 155.63, 142.97, 140.29, 126.66, 126.02, 124.00, 118.96, 65.50, 61.43, 46.26, 39.90, 31.15, 28.68, 21.88 ppm.

ESI-MS$^+$: m/z calc for $C_{20}H_{23}NO_3$ 325.17; [M+H]$^+$ found 326.63; [M+Na]$^+$ found 348.54.

General procedure for the oxidation of N-Fmoc ammino alcohols to N-Fmoc ammino aldehydes (2a), (2b) and to product (3)
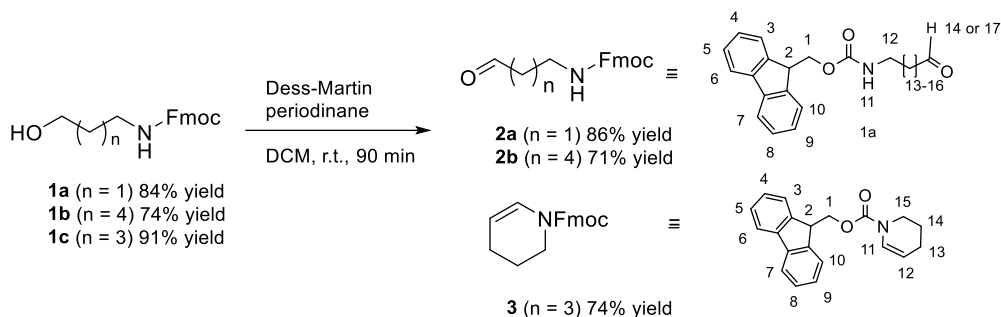
Scheme 36. Synthesis of products 2a, 2b and 3.

N-Fmoc ammino alcohol **1a-1c** (1.68 mmol) were dissolved in 5 mL of CH$_2$Cl$_2$ and Dess-Martin periodinane (785 mg, 1.85 mmol) was added. After being stirred r.t. for 90 min, under nitrogen, the mixture was diluted with NaHCO$_3$ saturated solution (20 mL) and extracted with CH$_2$Cl$_2$. The organic layer was washed with water and brine, dried over Na$_2$SO$_4$ and concentrated under vacuum. The crude product was purified over silica (PE/EtOAc 5:5)

(9H-fluoren-9-yl)methyl(3-oxopropyl)carbamate (**2a**)[498] Yellow solid (476 mg, 86% yield). R_f 0.74 (PE/EtOAc 5:5).

^{1}H NMR (300 MHz, CDCl$_3$) δ 9.80 (s, 1H, *H-14*), 7.79-7.76 (d, *J* = 7.5 Hz, 2H, *H-6, H-7*), 7.58 (d, *J* = 7.4 Hz, 2H, *H-3, H-10*), 7.42 (q, *J* = 7.5 Hz, 2H, *H-5, H-8*), 7.33-7.28 (q, *J* = 7.4 Hz, 2H, *H-4, H-9*), 5.30 (brs, 1H, *H-11*), 4.42-4.40 (d, *J* = 6.8 Hz, 2H, *H-1*), 4.21 (m, 1H, *H-2*), 3.50-3.49 (q, *J* = 11.4, 5.6 Hz, 2H, *H-13*), 2.75-2.71 (m, 2H, *H-12*) ppm.

^{13}C NMR (75 MHz, CDCl$_3$) δ 201.75, 156.80, 144.28, 141.73, 128.12, 127.46, 125.44, 120.40, 67.09, 47.64, 44.42, 34.87 ppm.

ESI-MS$^+$: m/z calc for C$_{18}$H$_{17}$NO$_3$ 295.33; [M+H]$^+$ found 296.

(9H-fluoren-9-yl)methyl (5-oxohexyl)carbamate **(2b)** White solid (367 mg, 71% yield). R$_f$ 0.84 (PE/EtOAc 5:5).

^{1}H NMR (600 MHz, CDCl$_3$): δ 9.77 (s, 1H, *H-17*), 7.77 (d, *J* = 7.8 Hz, 2H, *H-6, H-7*), 7.60 (d, *J* = 7.8 Hz, 2H, *H-3, H-10*), 7.40 (t, *J* = 7.2 Hz, 2H, *H-5, H-8*), 7.32 (t, *J* = 7.2 Hz, 2H, *H-4, H-9*), 4.79 (s, 1H, *H-11*), 4.41 (d, *J* = 7.2 Hz, 2H, *H-1*), 4.21 (t, *J* = 7.2 Hz, 1H, *H-2*), 3.21 (m, 2H, *H-12*), 1.66 (t, *J* = 7.2 Hz, 2H, *H-16*), 1.53 (m, 2H, *H-13*), 1.36 (m, 2H, *H-15*), 1.26 (m, 2H, *H-14*) ppm.

^{13}C NMR (150 MHz, CDCl$_3$): δ 202.81, 156.76, 144.29, 141.66, 128.00, 127.36, 125.36, 120.31, 66.83, 47.62, 44.07, 41.09, 30.11, 26.54, 21.95

ESI-MS$^+$: m/z calc for C$_{21}$H$_{23}$NO$_3$ 337.41; [M+H]$^+$ found 338.1; [M+Na]$^+$ found 360.18; [M+K]$^+$ found 376.16.

(9H-fluoren-9-yl)methyl 3,4-dihydroxypiyridine-1(2H)carboxylate (**3**) Yellow-white solid (1.78 g, 74% yield). R$_f$ 0.79 (PE/EtOAc 8:2).

^{1}H NMR (300 MHz, CDCl$_3$) δ 7.81-7.79 (d, J = 7.6 Hz, 2H, *H-6, H-7*), 7.63-7.61 (d, J = 7.4 Hz, 2H, *H-3, H-10*), 7.46-7.44 (q, J = 7.0 Hz, 2H, *H-5, H-8*), 7.35 (q, 2H, *H-4, H-9*), 6.93-6.84 (dd, J = 18.4, 8.2 Hz, 1H, *H-11*), 4.99-4.96 (m, 1H, *H-12*), 4.45 (d, J = 13.8, 8.9 Hz, 2H, *H-1*), 4.30 (t, J = 15.2, 8.2 Hz, 1H, *H-2*), 3.67 (m, J = 11.4, 7.6 Hz, 2H, *H-15*), 2.10 (t, 2H, *H-13*), 1.89 (m, J = 17.0, 11.4 Hz, 2H, *H-14*) ppm.

^{13}C NMR (75 MHz, CDCl$_3$) δ 138.09, 135.75, 123.35, 122.75, 120.91, 120.53, 116.29, 104.27, 68.60, 49.70, 45.33, 26.37, 26.25 ppm.

ESI-MS$^+$: m/z calc for C$_{20}$H$_{19}$NO$_2$ 305.37; [M+H]$^+$ found 306.36; [M+Na]$^+$ found 328.53.

Synthesis of Fmoc-chloroxime (5)

150

Scheme 37. Synthesis of aliphatic Fmoc-chloroxime **4**.
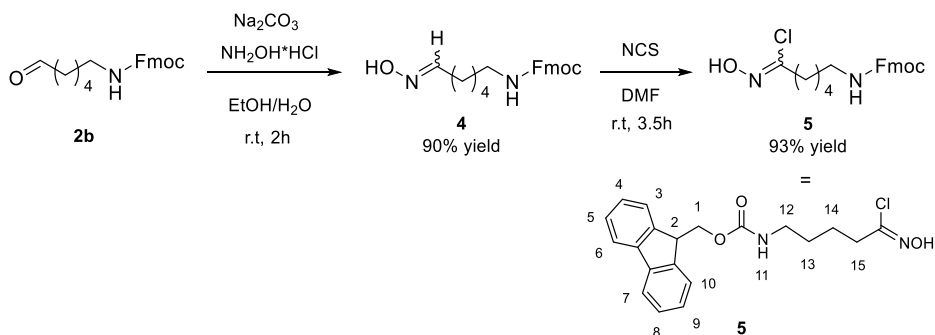
Synthesis of Fmoc protected oxime (4)

To a stirred solution of aldehyde 5 (500 mg, 1.48 mmol) in EtOH (3.5 mL) was added hydroxylamine hydrochloride (113 mg, 1.63 mmol) previously solubilized in H_2O (0.62 mL). A solution of Na_2CO_3 (86.4 mg, 0.815 mmol) in H_2O (0.48 mL) was added dropwise. After being stirred at r.t. for 2 h, EtOH was dried and the mixture was extracted with DCM. The organic layer was washed with water, dried over Na_2SO_4 and concentrated under vacuum.

(9H-fluoren-9-yl)methyl(6-(hydroxyimino)hexyl)carbamate (**4**) White solid (469 mg, yield 90%). R_f 0.74 (PE/EtOAc 5:5). R_f 0.74 (PE/EtOAc 5:5).

^{1}H NMR (600 MHz, CDCl$_3$) δ 7.77 (d, J = 7.8 Hz, 2H, *H-6, H-7*), 7.60 (d, J = 7.8 Hz, 2H, *H-3, H-10*), 7.40 (t, J = 7.2 Hz, 2H, *H-5, H-8*), 7.31 (t, J = 7.2 Hz, 2H, *H-4, H-9*), 6.71 (s, 1H, *H-17*), 4.40 (d, J = 7.2 Hz, 2H, *H-1*), 4.21 (t, J = 7.2 Hz, 1H, *H-2*), 3.19 (m, 2H, *H-12*), 1.52 (m, 2H, *H-16*), 1.39-1.35 (m, 4H, *H-13, H-15*), 1.25 (m, 2H, *H-14*) ppm.

^{13}C NMR (600 MHz, CDCl$_3$) δ 157.16, 152.44, 144.13, 141.40, 127.84, 127.16, 125.15, 120.05, 66.56, 47.39, 41.12, 29.78, 29.24, 26.14, 24.92 ppm

ESI-MS[+]: m/z calc for $C_{21}H_{24}N_2O_3$ 352.43; [M+H]$^+$ found 353.26; [M+Na]$^+$ found 375.15.

Synthesis of Fmoc protected alkyl chloroxime (5)[499]

To a stirred solution of **5** (500 mg, 1.42 mmol) in DMF (1.6 mL) was added N-chlorosuccinimmide (227 mg, 1.7 mmol). After being stirred at r.t. for 3 h 30 min, H_2O and diethyl ether were added. The organic layer was washed with water and saturated NaCl solution, dried over Na_2SO_4 and concentrated under vacuum to give **8**.

(9H-fluoren-9-yl)methyl (6-chloro-6-(hydroxyimino)hexyl)carbamate (**5**) Yellow oil (511 mg, 93% yield).

^{1}H NMR (600 MHz, CDCl$_3$) δ 7.74 (d, *J* = 7.8 Hz, 2H, *H-6,H-7*), 7.57 (d, *J* = 7.8 Hz, 2H, *H-3, H-10*), 7.37 (t, *J* = 7.2 Hz, 2H, *H-5, H-8*), 7.28 (t, *J* = 7.2 Hz, 2H, *H-4, H-9*), 4.99 (s, 1H, *H-1*), 4.36 (d, *J* = 7.2 Hz, 2H, *H-11*), 4.18 (t, *J* = 7.2 Hz, 1H, *H-2*), 3.16 (m, 2H, *H-12*), 2.47 (t, *J* = 7.2 Hz, 2H, *H-16*), 1.64 (m, 2H, *H-13, H15*), 1.50 (m, 2H, *H-14*), 1.33 (m, 2H, *H-10*) ppm.

^{13}C NMR (600 MHz, CDCl$_3$) δ 147.10, 144.10, 141.45, 127.75, 127.05, 125.02, 120.05, 66.57, 47.24, 29.71, 29.59, 18.16 ppm.

Synthesis of Fmoc-protected p-amino benzaldehyde (9)
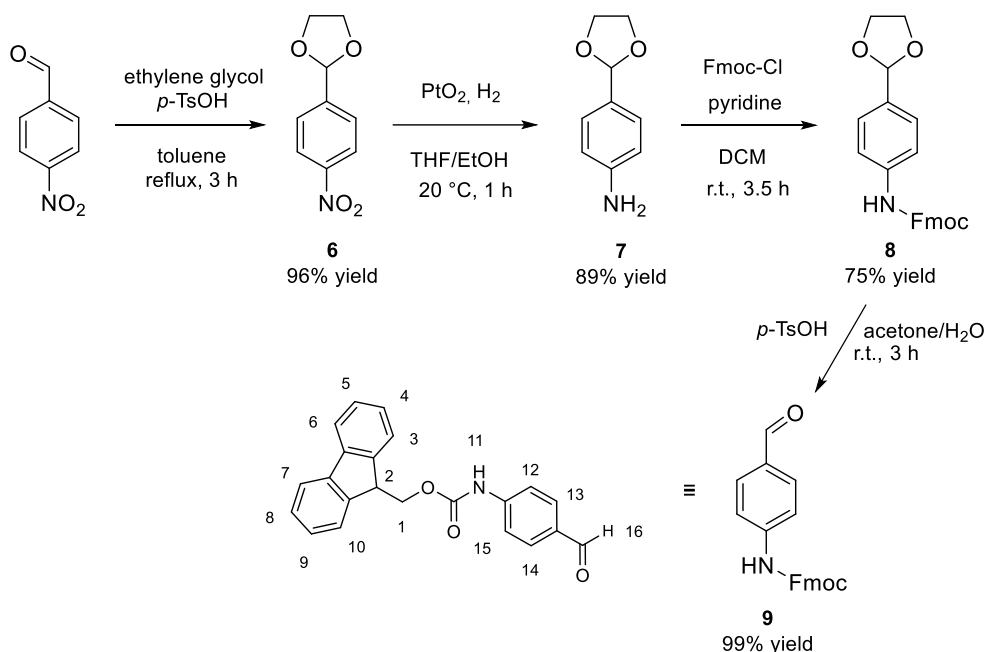
Scheme 38. Synthesis of Fmoc-protected p-amino benzaldehyde **9**.

Protection of p-nitro benzaldehyde to product (6)[500]

4-Nitrobenzaldehyde (15 g, 99.2 mmol) and p-toluenesulfonic acid monohydrate (377.6 mg, 1.98 mmol) were dissolved in toluene (180 mL). Ethylene glycol (12.43 mL, 222 mmol) was added, and the solution was refluxed for 3 h with a Dean-Stark trap, to remove the water. After that, the solution was allowed to cool, and 240 mL of EtOAc were added. The organic layer was washed with saturated NaHCO$_3$ solution (2 x 120 mL) and then washed with saturated NaCl solution (120 mL). The organic layer was dried with Na$_2$SO$_4$ and the solvent was removed under reduced pressure to give the desired protected aldehyde **6**.

2-(4-nitrophenyl)-1,3-dioxolane (**6**) Light yellow powder (18.62 g, 96% yield).

^{1}H NMR (300 MHz, CDCl$_3$): δ 8.26-8.23 (d, J = 8.5Hz, 2H, *H-1, H-4*), 7.67-7.64 (d, J= 8.5 Hz, 2H, *H-2, H-3*), 5.90 (s, 1H, *H-5*), 4.13-4.07 (m, 4H, *H-6, H-7*) ppm.

^{13}C NMR (75 MHz, CDCl$_3$) δ 148.80, 145.35, 127.84, 124.00, 102.65, 65.90 ppm. (See Fig S28)

ESI-MS$^+$: *m/z* calcd for C$_9$H$_9$NO$_4$ 195.05, [M+H]$^+$ found 195.99; [M+Na]$^+$ found 217.97; [M+K]$^+$ 235.98.

Reduction of nitrobenzene derivative to obtain product (7)[501]

Compound **6** (1 g) was dissolved in a mixture of EtOH:THF anhydrous 1: 1 (11 mL). PtO_2 (20 mg) was added. After being stirred at r.t. for 5 h with 4 bar of H_2 pressure, the reaction mixture was filtered through celite, washed with anhydrous EtOH, dried with Na_2SO_4 and the solvent was removed under reduced pressure to give the desired product **7**

4-(1,3-dioxolan-2-yl)aniline (**7**) Light yellow oil (735.2 mg, 89% yield).

^{1}H NMR (600 MHz, CDCl$_3$): δ 7.25 (d, *J* = 8.3 Hz, 2H, *H-1, H-4*), 6.66 (d, *J* = 8.5 Hz, 2H, *H-2, H-3*), 5.69 (s, 1H, *H-5*), 4.13 – 4.09 (m, 2H, *H-6*), 4.00 – 3.97 (m, 2H, *H-7*), 3.77 – 3.65 (brs, 2H) ppm.

^{13}C NMR (151 MHz, CDCl$_3$): δ 147.48, 127.89, 127.65, 114.83, 104.15, 65.26 ppm.

MALDI-TOF: *m/z* calcd for $C_9H_{11}NO_2$ 165.08, found 165.

Fmoc protection of aniline (7) to obtain product (8)

To a stirred solution of compound **7** (729 mg, 4.42 mmol) and dry pyridine (0.427 mL, 5.3 mmol) in dry DCM (1.5 mL), at 0 °C was added a Fmoc-Cl solution (1.26 g, 4.86 mmol) in dry DCM (2.5 mL). After being stirred at r.t. for 3 h 30 min, the solution was extracted with DCM and a saturated solution of NH_4Cl, dried with Na_2SO_4 and the crude product was purified on silica column chromatography (hexane, EtOAc). Product **11** was recovered.

(9H-fluoren-9-yl)methyl(4-(1,3-dioxolan-2-yl)phenyl)carbamate (**8**) White powder (1.2 g, 75% yield). The product, after purification shows 10% deprotected benzaldehyde derivative

^{1}H NMR (600 MHz, CDCl$_3$): δ 7.78 (d, *J* = 7.4 Hz, 2H, *H-6, H-7*), 7.62 (d, *J* = 7.1 Hz, 2H, *H-3, H-10*), 7.42 (dd, *J* = 14.6, 7.2 Hz, 6H, *H-5, H-8, H-12, H-13, H-14, H-15*), 7.34 (q, *J* = 6.9 Hz, 2H, *H-4, H-9*), 6.71 (s, 1H, *H-11*), 5.76 (s, 1H, *H16*), 4.55 (d, *J* = 6.4 Hz, 2H, *H-1*), 4.28 (t, *J* = 6.5 Hz, 1H, *H-2*), 4.12 (t, *J* = 6.9 Hz, 2H, *H-17*), 4.02 (t, *J* = 6.9 Hz, 2H, *H-18*) ppm.

^{13}C NMR (151 MHz, CDCl$_3$) δ 191.26, 144.02, 141.70, 131.60, 128.20, 127.74, 127.50, 125.20, 120.43, 103.78, 65.60, 47.43 ppm.

ESI-MS$^+$: m/z calcd for $C_{24}H_{21}NO_4$, 387,43; [M+H]$^+$ found 388.22.

Deprotection of acetal 8 to obtain benzaldehyde (9)

Compound **8** (500 mg, 1.30 mmol) and p-toluenesulfonic acid monohydrate (98.2 mg, 0.516 mmol) were dissolved in acetone (40 mL) and H_2O was added (2 mL). After being stirred at r.t.

for 3 h, EtOAc was added and the solution was extracted, dried with Na_2SO_4 and the solvent was removed under reduced pressure to give product **12**.

(9H-fluoren-9-yl)methyl(4-formylphenyl)carbamate (**9**) Light yellow powder (445 mg, 99% yield).

^{1}H NMR (600 MHz, CDCl$_3$): δ 9.90 (s, 1H, *H-16*), 7.82 (d, *J* = 8.5 Hz, 2H, *H-13, H-14*), 7.79 (d, *J* = 7.6 Hz, 2H, *H-6, H-7*), 7.61 (dd, *J* = 7.5, 2H, *H-3, H-10*), 7.53 (d, 2H, *H-12, H-15*), 7.42 (dd, *J* = 10.8, 2H, *H-5, H-8*), 7.33 (td, *J* = 7.5, 2H, *H-4, H-9*), 7.03 (s, 1H, *H-11*), 4.60 (d, *J* = 6.3 Hz, 2H, *H-1*), 4.28 (t, *J* = 6.4 Hz, 1H, *H-2*) ppm.

^{13}C NMR (151 MHz, CDCl$_3$) δ 191.32, 153.15, 143.79, 143.74, 141.72, 132.05, 131.61, 128.24, 127.52, 125.14, 120.46, 118.40, 67.47, 47.32 ppm.

ESI-MS[+]: m/z calcd for $C_{22}H_{17}NO_3$, 343.38; found 344.05 [M+H][+].

Synthesis of Fmoc-protected p-amino benzene chloroxime
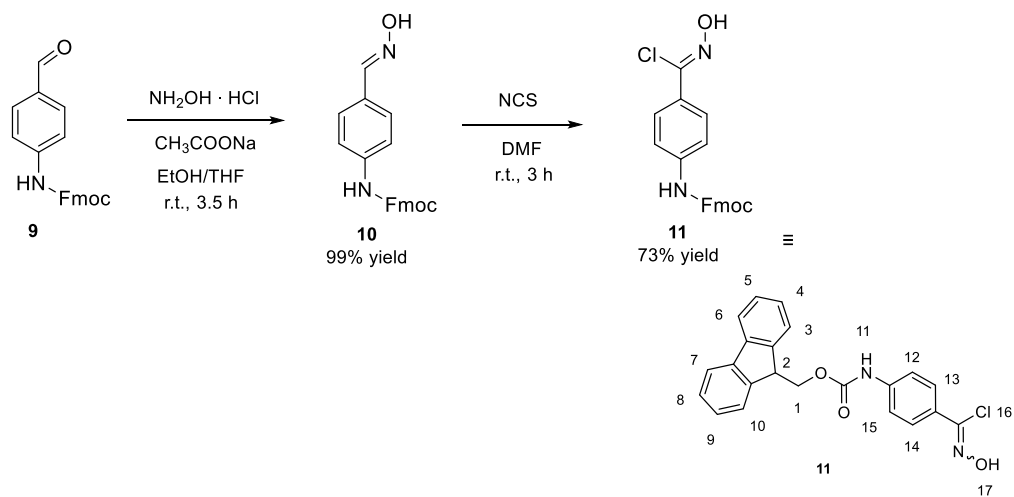
Scheme 39. Synthesis of chloroxyme derivative (11).

Compound **9** (100 mg, 0.291 mmol) was dissolved in a dry mixture of EtOH:THF 3:1 (9 mL) and hydroxylamine hydrochloride (202 mg, 2.91 mmol) and anhydrous sodium acetate (716 mg, 8.73 mmol) were added. After being stirred at r.t. for 3 h 30 min, the reaction mixture was extracted with EtOAc, dried with Na_2SO_4 and the solvent was removed under reduced pressure to give product **10**.

(9H-fluoren-9-yl)methyl (4-((hydroxyimino)methyl)phenyl)carbamate (**10**) Light yellow powder (103 mg, 99% yield).

^{1}H NMR (600 MHz, DMSO-d$_6$): δ 11.01 (s, 1H, *H-16*), 9.83 (s, 1H, *H-17*), 8.00 (d, 2H, *H-13, H-14*), 7.87 (d, *J* = 7.5 Hz, 2H, *H-6, H-7*), 7.71 (d, *J* = 7.4 Hz, 2H, *H-3, H-10*), 7.44 (d, 2H, *H-12, H-15*), 7.39 (t, *J* = 7.4 Hz, 2H, *H-5, H-8*), 7.31 (td, *J* = 7.4, 2H, *H-4, H-9*), 4.46 (d, *J* = 5.0 Hz, 2H, *H-1*), 4.28 (t, *J* = 6.5 Hz, 1H *H-2*) ppm.

^{13}C NMR (151 MHz, DMSO-d$_6$): δ 182.30, 153.84, 148.19, 144.27, 141.34, 128.24, 127.66, 125.64, 120.73, 118.71, 66.21, 47.11 ppm.

ESI-MS$^+$: m/z calcd for $C_{22}H_{18}N_2O_3$, 358.39; calc for [M+Na]$^+$ 381,38 found 381,27.

Synthesis of Chloroxime (11)

To a stirred solution of **10** (100 mg, 0.279 mmol) in DMF (2.5 mL) was added N-chlorosuccinimmide (44.7 mg, 0.335 mmol). After being stirred at r.t. for 3 h, H$_2$O and diethyl ether were added. The organic layer was washed with water and saturated NaCl solution, dried over Na$_2$SO$_4$ and concentrated under vacuum to give **11** that was reacted without further purification

(9H-fluoren-9-yl)methyl (4-(chloro(hydroxyimino)methyl)phenyl)carbamate) (**11**) Yellow oil (80 mg, 73% yield).

Synthesis of hydroxylamine precursors (13) and (15)

Synthesis of aromatic hydroxylamine (13)
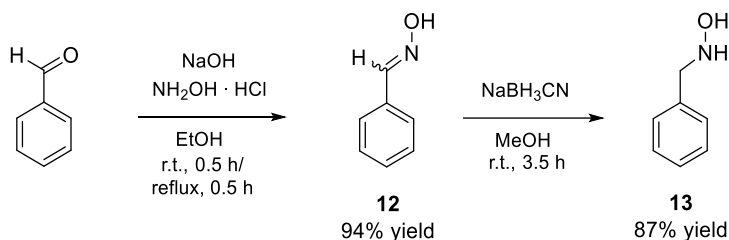
Scheme 40. Synthesis of N-benzylhydroxylamine.

Synthesis of benzaldehyde oxime (12)[501]

To a solution of benzaldehyde (500 mg, 4.71 mmol) and hydroxylamine hydrochloride (1.09 g, 15.7 mmol) in EtOH (15.7 mL), NaOH (1.69 g, 42.4 mmol) was added powdered in small portions. The mixture was stirred at r.t. for 30 min and then refluxed for another 30 min. The reaction mixture was then cooled to r.t., poured into a mixture of concentrated HCl (1.88 mL) and water (7.23 mL), carefully concentrated to one third of the original volume and finally extracted with CH$_2$Cl$_2$. The organic layer was washed with brine, dried with Na$_2$SO$_4$ and concentrated under vacuum. Benzaldehyde oxime **12** was obtained.

Benzaldehyde oxime (12) Colorless oil (535 mg, 94% yield).

^{1}H NMR (600 MHz, CDCl[3]): δ 8.16 (s, 1H, *H-6*), 7.58 (m, 2H, *H-3, H-4*), 7.40-7.39 (m, 3H, *H-1, H-2, H-5*) ppm.

^{13}C NMR (600 MHz, CDCl[3]) δ 150.52, 132.05, 130.22, 128.94, 127.15 ppm.(.

ESI-MS$^+$: m/z calc for C[7]H[7]NO 121.14; found 121.87.

Synthesis of N-benzylhydroxylamine (13)

To a solution of benzaldehyde oxime **12** (204 mg, 1.68 mmol) in MeOH (2.5 mL), NaBH[3]CN (211.6 mg, 3.37 mmol) and a trace of methyl orange were added. At 0 °C, 12 N HCl was added dropwise until the color remained pink. The reaction mixture was allowed to stir at r.t. for 3.5 h. The reaction mixture was concentrated under vacuum and 6 N NaOH was added until pH~10. The product was extracted with CH[2]Cl[2], washed with water and saturated NaCl solution, dried over Na[2]SO[4] and concentrated under vacuum to give the *N*-benzyl-hydroxylamine **17.**

N-benzylhydroxylamine (13) White solid (180 mg, 87% yield).

^{1}H NMR (600 MHz, CDCl[3]): δ 7.36-7.33 (m, 5H, *H-1, H-2, H-3, H-4, H-5*), 5.92 (s, 1H, *H-7*), 4.02 (s, 2H, *H-6*) ppm.

^{13}C NMR (600 MHz, CDCl[3]) δ 135.77, 129.42, 128.78, 128.15, 57.86 ppm.

ESI-MS$^+$: m/z calc for C[7]H[9]NO 123.14; [M+H]$^+$ found 123.90.

Synthesis of aliphatic hydroxylamine (15)
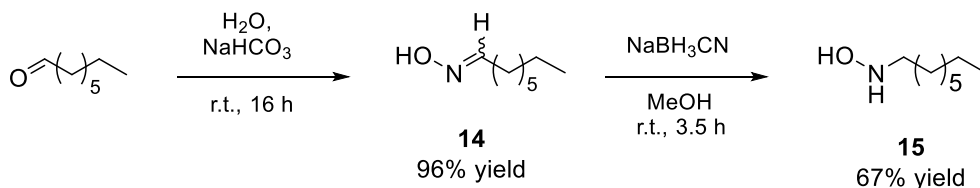
Scheme 41. Synthesis of *N*-octylhydroxylamine **15.**

Synthesis of octanal oxime (14)

A solution of octanal (1.30 g, 9.44 mmol) in 15 mL of ethanol is added to a solution of hydroxylamine hydrochloride (720 mg, 10.4 mmol) in 3.8 mL of water, then 3.2 mL of an aqueous solution of sodium carbonate (548 mg, 5.19 mmol) are added dropwise. The mixture was stirred at r.t. overnight. The reaction mixture was then concentrated under vacuum and washed three times with dichloromethane. The organic layer was washed with brine, dried with Na[2]SO[4] and concentrated under vacuum. Octanal oxime **14** was obtained.

Octanal oxime (14) Colorless oil (1.30 g, 96% yield).

^{1}H NMR (600 MHz, CDCl$_3$): δ 7.42/6.73 (s, 1H, *H-8*), 2.38/2.19 (m, 2H, *H-7*), 1.48 (m, 2H, *H-6*), 1.32-1.26 (m, 8H, *H-5, H-4, H-3, H-2*), 0.87 (t, J = 6.6 Hz, 3H, *H-1*) ppm.

^{13}C NMR (600 MHz, CDCl$_3$) δ 153.14/152.56, 31.81, 29.60, 29.03, 26.68, 26.16, 22.74, 14.27 ppm.

ESI-MS$^+$: m/z calc for C$_8$H$_{17}$NO 143.23; [M+H]$^+$ found 144.10.

Synthesis of N-octylhydroxylamine (15)

To a solution of octanal oxime **14** (240 mg, 1.40 mmol) in MeOH (6.5 mL), NaBH$_3$CN (105 mg, 1.81 mmol) and a trace of methyl orange were added. At 0 °C, 12 N HCl was added dropwise until the color remained pink. The reaction mixture was allowed to stir at r.t. for 3.5 h. The reaction mixture was concentrated under vacuum and 6 N NaOH was added until pH~10. The product was extracted with CH$_2$Cl$_2$, washed with water and saturated NaCl solution, dried over Na$_2$SO$_4$ and concentrated under vacuum to give the *N*-octyl-hydroxylamine **15**.

N-octylhydroxylamine (15) White solid (136 mg, 67% yield).

^{1}H NMR (600 MHz, CDCl3): δ 5.08 (s, 1H, *H-9*), 2.93 (t, J = 7.2 Hz, 2H, *H-8*), 1.53 (m, 2H, *H-7*), 1.31-1.25 (m, 10H, *H-6, H-5, H-4, H-3, H-2*), 0.87 (t, J = 6.6 Hz, 3H, *H-1*) ppm.

^{13}C NMR (600 MHz, CDCl$_3$) δ 53.95, 31.95, 29.63, 29.33, 27.26, 26.98, 22.79, 14.22 ppm.

ESI-MS$^+$: m/z calc for C$_8$H$_{19}$NO 145.23; [M+H]$^+$ found 146.17.

Synthesis of Fmoc protected nitrone derivatives (16-19)
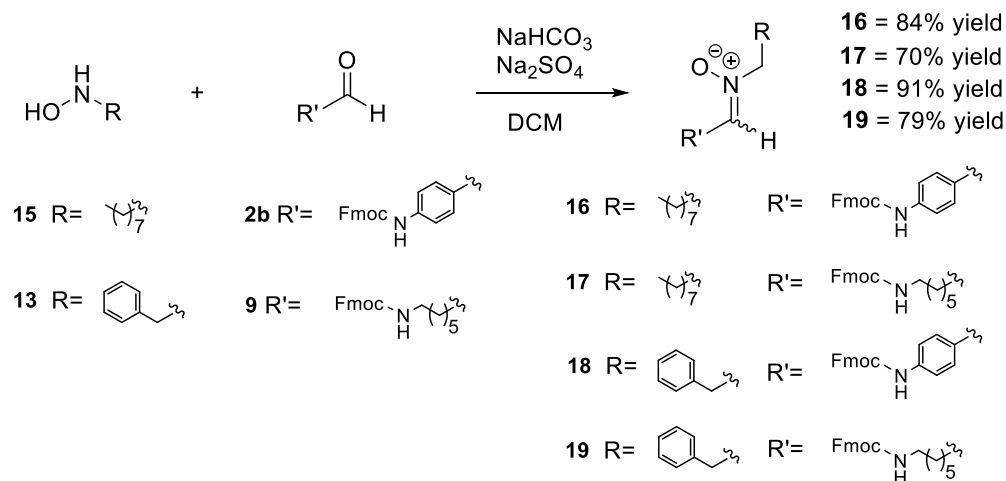
Scheme 42. General synthesis of nitrones.

157

General procedure for nitrones synthesis

Hydroxylamine derivative (0.35 mmol), aldehyde (0.35 mmol), Na_2SO_4 (50 mg, 0.35 mmol) and a trace of $NaHCO_3$ in DCM (4 mL) were stirred at 0 °C, under nitrogen atmosphere, overnight. The mixture was filtered and the filtrate was removed under reduced pressure to give desired products **16-19**.

N-(4-((((9H-fluoren-9-yl)methoxy)carbonyl)amino)benzylidene)octan-1-amine oxide (**16**) Pale yellow oil (137 mg, 84% yield).

^{1}H NMR (600 MHz, $CDCl_3$): δ 8.21-7.83 (s, 1H, *H-16*), 7.78 (d, J = 7.2 Hz, 2H, *H-6, H-7*), 7.61 (d, J = 7.2 Hz, 2H, *H-3, H-10*), 7.54 (m, 2H, *H-13, H-14*), 7.46 (d, J = 8.4 Hz, 2H, *H-12, H-15*), 7.42 (m, 2H, *H-5, H-8*), 7.33 (m, 2H, *H-4, H-9*), 4.57 (d, J= 7.2 Hz, 2H, *H-1*), 4.28 (t, J = 7.2 Hz, 1H, *H-2*), 3.92 (t, J = 6.6 Hz, 2H, *H-17*), 1.99 (m, 2H, *H-18*), 1.38-1.25 (m, 10H, *H-19, H-20, H-21, H-22, H-23*), 0.87 (m, 3H, *H-24*) ppm.

^{13}C NMR (600 MHz, $CDCl_3$) δ 190.85, 143.67, 143.36, 141.57, 131.78, 131.57, 130.08, 127.95, 127.31, 124.96, 120.22, 66.99, 52.20, 47.15, 31.81, 29.33, 27.95, 27.26, 26.66, 22.68, 14.24 ppm.

ESI-MS[+]: m/z calc for $C_{30}H_{34}N_2O_3$ 470.60; [M+H][+] found 471.33; [M+Na][+] found 493.35.

N-(4-((((9H-fluoren-9-yl)methoxy)carbonyl)amino)benzylidene)octan-1-amine oxide (**17**) Pale yellow oil (114 mg, 70% yield).

^{1}H NMR (600 MHz, $CDCl_3$): 7.76 (d, *J* = 7.6 Hz, 2H, *H-6, H-7*), 7.58 (d, *J* = 7.5 Hz, 2H, *H-3, H-10*), 7.38 (t, *J* = 7.5 Hz, 2H, *H-5, H-8*), 7.31 (t, *J* = 8.0 Hz, 2H *H-4, H-9*), 6,67 (m, 1H, H-11), 4.38 (d, J= 7.2 Hz, 2H, *H-1*), 4.20 (t, J = 7.2 Hz, 1H, *H-2*), 3.92 (t, J = 6.6 Hz, 2H, *H-18*), 3.17 (d, *J* = 6.5 Hz, 2H, *H-16*), 2.49 (d, *J* = 6.6 Hz, 2H, *H-12*), 1.84 (m, 2H, *H-19*), 1.62 – 1.4 (m, 14H, *H-13, H-14, H-15, H20-H24*), 0.87 (m, 3H, *H-25*) ppm.

^{13}C NMR (600 MHz, $CDCl_3$) δ 156.58, 144.08, 141,39, 127,81, 127.11, 125.03, 120.05, 66.58, 65.52, 53.48, 47.38, 43.81, 40.83, 31.82, 29.15, 27.53, 26.53, 25,30, 22,68, 14.15 ppm

ESI-MS[+]: m/z calc for $C_{29}H_{40}N_2O_3$ 464,30; [M+H][+] found 465,4; [M+Na][+] found 487.43.

N,N-(4-((((9H-fluoren-9-yl)methoxy)carbonyl)amino)benzylidene)-1-phenylmethanamine oxide **(18)** colourless oil (140 mg, 91% yield).

^{1}H NMR (600 MHz, $CDCl_3$): δ 8.16 (t, 1H, *H-16*), 7.79 (d, J = 7.2 Hz, 2H, *H-6, H-7*), 7.61 (d, J = 7.2 Hz, 2H, *H-3, H-10*), 7.53 (m, 2H, *H-13, H-14*), 7.47 (d, J = 8.4 Hz, 2H, *H-12, H-15*), 7.41 (m, 6H, *H-5, H-8, H-18, H-19, H-21, H-22*), 7.38 (m, 1H, *H-20*), 7.32 (m, 2H, *H-4, H-9*), 5.07 (s, 2H, *H-17*), 4.58 (d, J= 7.2 Hz, 2H, *H-1*), 4.27 (t, J = 7.2 Hz, 1H, *H-2*) ppm.

^{13}C NMR (600 MHz, $CDCl_3$) δ 191.53, 158.59, 143.72, 143.54, 141.06, 131.42, 129.55, 129.32, 129.21, 128.05, 127.34, 125.31, 125.25, 125.02, 124.98, 120.26, 67.33, 53.22, 47.22 ppm.

ESI-MS[+]: m/z calc for $C_{29}H_{24}N_2O_3$ 448.51; [M+H][+] found 449.31; [M+Na][+] found 471.33.

N-(6-((((9H-fluoren-9-yl)methoxy)carbonyl)amino)hexylidene)-1-phenylmethanamine oxide (**19**) a pale yellow oil (122 mg, 79% yield).

^{1}H NMR (600 MHz, CDCl$_3$): δ 7.76 (t, *J* = 7.6 Hz, 2H, *H-6, H-7*), 7.59 (d, *J* = 7.5 Hz, 2H, *H-3, H-10*), 7.39 (d, *J* = 7.6 Hz, 7H, *H-5, H-8, H-19, H-20, H-21, H-22, H-23*), 7.31 (t, *J* = 8.0 Hz, 2H *H-4, H-9*), 6.63 (t, *J* = 5.8 Hz, 1H, *H-17*), 4.87 (s, 2H, *H-18*), 4.40 (d, *J* = 6.9 Hz, 2H, *H-1*), 4.21 (t, *J* = 6.8 Hz, 1H, *H-2*), 3.17 (d, *J* = 6.5 Hz, 2H, *H-16*), 2.49 (d, *J* = 6.6 Hz, 2H, *H-12*), 1.60 – 1.28 (m, 6H, *H-13, H-14, H-15*).

^{13}C NMR (151 MHz, CDCl$_3$): δ 156.80, 144.33, 141.64, 133.18, 129.67, 129.30, 128.00, 127.36, 125.38, 120.31, 69.55, 66.80, 47.62, 44.07, 41.06, 29.76, 26.75, 25.47.

ESI-MS[+]: m/z calc for $C_{28}H_{30}N_2O_3$ 442.56; [M+H][+] found 443.14.

Procedure for rGO and Nanodiamonds functionalization

Synthesis of GO

GO was prepared by a modified Hummers method[502]: graphite powder (0.5 g) was added to a cold (0 °C) solution of concentrated H_2SO_4 containing 0.25 g of NaNO$_3$. KMnO$_4$ (1.5 g) was gradually added, while stirring and keeping the reaction temperature below 20 °C. The mixture was stirred at 35 °C for 30 min. Then, distilled water (25 mL) was added and the temperature was kept at 98 °C for 45 min. Finally, 70 mL of distilled water were added, followed by 2 mL of 30% H_2O_2. The mixture was filtered and washed three times with water and 10% HCl. At the end, it was dried in the oven at 80 °C for 12 h.

Synthesis of rGO[503, 504] under conventional heating

GO was dispersed in water (1 mg/mL). The dispersion was sonicated in an ultrasound bath until no particles are visible. A brown/yellow solution was formed. Hydrazine monohydrate was subsequently added to the suspension (32.1 mmol for 100 mg of GO), and the mixture was stirred at 100 °C for 24 h, yielding a black precipitation of rGO powder. After cooling at room temperature, the mixture was filtered, washed with water and dried in the oven at 80 °C for 12 h.

Synthesis of rGO under MW irradiation

GO was dispersed in water (1 mg/mL). The dispersion was sonicated in an ultrasound bath until no particles are visible. A brown/yellow solution was formed. Hydrazine monohydrate was subsequently added to the suspension (32.1 mmol for 100 mg of GO), and the mixture was irradiated in a MW reactor at 120 °C for 10 min, yielding a black precipitation of rGO powder.

After cooling at room temperature, the mixture was filtered, washed with water and dried in the oven at 80 °C for 12 h.

General procedure for rGO and NDs functionalization with azomethine ylides (rGO/NDs-AMY-Ala-n1, rGO/NDs-AMY-Ala-n4, rGO-AMY-Ser-n1, rGO-AMY-Ser-n4)

In a typical experiment, 15 mg of rGO or NDs were suspended in DFM (4 mL) with 0.48 mmol of the corresponding aldehyde **2a** (141 mg) or **2b** (162 mg), and alanine (50,73 mg, 0,57 mmol) or serine (60 mg, 0.57 mmol) in a MW glass tube. The tube was closed and the mixture was irradiated for 2 h at 130 °C. The dispersion was filtered and washed with water, methanol and DCM and dried overnight in an oven (80 °C). The products were further characterized by TGA, Raman, FT-IR or DRIFT.

The MW irradiation was applied at fixed temperature. Anton Paar Monowave 300 and CEM Discover SP was used. 2 min were required to reach the reaction temperature (130 °C) using the program: "heat as quickly as possible" (Maximum power 400 W). When performing the reaction at fixed temperature, the program "hold" was selected in order to main the temperature constant (130 °C) during the reaction. In this mode, the MW-reactor automatically adjusts the power to reach the indicated temperature. Reaction time: 2 h.

General procedure for rGO and NDs functionalization with nitrile oxides (rGO/NDs-NO-1-2)

15 mg of rGO or NDs were suspended in dioxane (2 mL) with $KHCO_3$ (12.5 mg, 0.125 mmol). A solution of chloro oxime **5** or **11** (0.125 mmol) in dioxane (2 mL) was added dropwise. After being stirred at 30 °C for 2 h, the collected solid was washed several times with H_2O and dioxane and dried overnight in an oven (80 °C), affording functionalized **rGO/NDs-NO-1-2**.

General procedure for rGO and NDs functionalization with nitrones 16-19 (rGO/NDs-Nitrone-16-19)

15 mg of rGO or NDs were suspended in toluene (2 mL) and nitrone **16-19** (0.125 mmol) was added. The reaction mixture was heated up at 100 °C for 12 h. After that, the reaction was allowed to cool down at room temperature, the solid was collected by filtration and washed several times with $CHCl_3$, dried overnight in an oven (80 °C), affording functionalized **rGO/NDs-Nitrone-16-19.**

UV analysis

The indirect UV determination of functionalized rGO and NDs was measured after Fmoc deprotection of a weighted amount of derivatized rGO or NDs. 3-5 mg of samples were suspended in 5 mL of piperidine solution (20% in DMF) and stirred at r.t. for 30 min. 5 mL of MeOH were added and the solution was filtered through syringe filters. The solution was diluted 1:1 with MeOH. The absorbance at 301 nm was measured on a spectrophotometer Cary 60 UV-Vis (Agilent), using quartz cells. The results are shown in the main text and are consistent with the TGA ones.

8.3. Study of heterogeneous catalyst design and applications for metathesis reactions

8.3.1. General working conditions

All the reagents were purchased by Sigma Aldrich and used without further purification. rGO synthesis and derivatization were carried out in a professional MW reactor (Monowave 400/200, Anton Paar GmbH, Graz, AT) using reaction vial G10. Thermogravimetric analyses were performed using a thermogravimetric analyzer TGA 4000 (Perkin Elmer) at 10 °C min^{-1} operating under argon (80 mL min-1) with alumina crucibles containing 6-8 mg of rGO derivatives. Samples were previously overnight stove dried at 80 °C, then the samples were heated up to 800 °C (starting temperature: 50 °C; temperature increase rate: 10 °C/min; argon flow: 80mL/min). Total mass loss was attributed to functional groups which were covalently attached to the sidewalls. The number of functional groups was calculated considering a fixed thermogram temperature. Functionalization amounts were expressed in mmol of adducts per 100 mg of rGO. rGO carbon atoms were excluded in the calculation of the molecular weight of cycloaddition adducts.

8.3.2. Experimental procedures

Synthesis of GO

GO was prepared by a modified Hummers method[502]: graphite powder (0.5 g) was added to a cold (0°C) solution of concentrated H_2SO_4 containing 0.25 g of $NaNO_3$. $KMnO_4$ (1.5 g) was gradually added, while stirring and keeping the reaction temperature below 20°C. The mixture was stirred at 35°C for 30 min. Then, distilled water (25 mL) was added and the temperature was kept at 98°C for 45 min. Finally, 70 mL of distilled water were added, followed by 2 mL of 30% H_2O_2. The mixture was filtered and washed three times with water and 10% HCl. At the end, it was dried in the oven at 80°C for 12 h.

Synthesis of rGO under MW irradiation

GO was dispersed in water (1 mg/mL). The dispersion was sonicated in an ultrasound bath until no particles are visible. A brown/yellow solution was formed. Hydrazine monohydrate was subsequently added to the suspension (32.1 mmol for 100 mg of GO), and the mixture was irradiated in a MW reactor at 120°C for 10 min, yielding a black precipitation of rGO powder. After cooling at room temperature, the mixture was filtered, washed with water and dried in the oven at 80°C for 12 h.

Procedure for rGO functionalization to obtain rGO-Glutamic

Paraformaldehyde (PFA, 0.333 mmol, 1 equiv), glutamic acid (1.2 equiv) and rGO (20 mg) were mixed in 3 mL of anhydrous DMF. The dispersion was irradiated in a MW reactor at 130℃ for 2 h. After cooling at room temperature, the dispersion was filtered and washed with water, methanol and DCM and dried overnight in an oven (80 ℃).

Procedure for rGO functionalization to obtain rGO-Aspartic

Paraformaldehyde (PFA, 0.333 mmol, 1 equiv), aspartic acid (1.2 equiv) and rGO (20 mg) were mixed in 3 mL of anhydrous DMF. The dispersion was irradiated in a MW reactor at 130℃ for 2 h. After cooling at room temperature, the dispersion was filtered and washed with water, methanol and DCM and dried overnight in an oven (80 ℃).

Procedure for rGO functionalization to obtain rGO-Lys

Paraformaldehyde (PFA, 0.333 mmol, 1 equiv), lysine (1.2 equiv) and rGO (20 mg) were mixed in 3 mL of anhydrous DMF. The dispersion was irradiated in a MW reactor at 130℃ for 2 h. After cooling at room temperature, the dispersion was filtered and washed with water, methanol and DCM and dried overnight in an oven (80 ℃).

Procedure for rGO-Lys modification to obtain rGO-Succinic, rGO-Citric, rGO-Phthalic

rGO-Lys (15 mg) was suspended in 0,900 mL of anhydrous DMF. Citric anhydride (16 mg), succinic anhydride (34 mg) or phthalic anhydride (24 mg) and pyridine (0.013 mL) were added and the mixture was stirred at 40 ℃ for 24 h. The dispersion was filtered and washed with water, methanol and DCM and dried overnight in an oven (80 ℃).

8.4. Improving the electrocatalytic performance of sustainable Co/carbon materials for the oxygen evolution reaction by ultrasound and microwave assisted synthesis

8.4.1. General working conditions

All the reagents employed in the synthesis and in the reactions were of analytical grade purity and were used without any further purification. They were purchased from Sigma-Aldrich Inc. (St. Louis, MO, USA). Green Malaysian tea was bought from a local market in Turin (Italy). Pinecones were collected from "Parco Valentino" nearby the University of Turin (Italy). US bath irradiation at was performed in a ultrasound bath supplied by Weber ULTRASONICS GMBH. When reactions were carried out in a combined system MW/US the device has been designed in our laboratory by inserting a sonic horn made of pirex inside a RotoShynth (Milestone) microwave chamber. Ethos microwave (Milestones Srl, Bergamo, Italy) equipped with an infrared sensor combined with an *in situ* temperature sensor was used. Thermogravimetric analyses (TGA) were carried out with a Mettler Toledo TGA/SDTA 851 analyser operating with alumina crucibles. The samples were heated from 25 °C up to 900 °C at 5 °C min^{-1} in a nitrogen atmosphere (50 mL min^{-1}). Prior to analysis, the materials were conditioned at 25 °C under a nitrogen flux (50 mL min^{-1}) for 20 min. XRD patterns were recorded using a Bruker D8 DISCOVER A25 diffractometer (PanAnalytic/Philips, Lelyweg, Almelo, Netherlands) using CuKa (λ = 1.5418 A) radiation. Wide angle scanning patterns ° were collected over a 2q range from 10° to 80° with a step size of 0.018° and a counting time of 5" per step. Inductively coupled plasma mass spectrometry (ICP-MS) analysis was carried out at the Research Support Service (SCAI) by digesting the samples in a solution HNO$_3$: HCl = 3 : 1. SEM images were recorded in a JEOL JSM-6300 scanning microscope (JEOL Ltd., Peabody, MA, USA) equipped with an Energy-dispersive X-ray spectrometer (SEM-EDX) at 15 kV at the Research Support Service Centre (SCAI) of the University of Cordoba. Transmission electron microscopy (TEM) images were obtained using a JEOL JEM 1400 TEM microscope (JEOL Ltd., Peabody, MA, USA), operating at an accelerating voltage of 80 kV at the Research Support Service Centre (SCAI) of the University of Cordoba. The specific surface area (SSA), and micro- and mesopore volume were calculated by gas-volumetric analysis measuring N$_2$ adsorption–desorption isotherms at the liquid nitrogen temperature using an ASAP 2020 physisorption analyser (Micromeritics). The SSA was calculated by the Langmuir method. The mesopore volume was determined by means of the Barrett–Joyner–Halenda (BJH) method, on the adsorption branch of nitrogen isotherms. The micropore volume was calculated by the t-plot method. Before the measurements, the samples were outgassed at 100 °C overnight. ICP-MS analysis was performed after microwave-assisted acidic digestion of the samples and using a Perkin Elmer NexionX Spectrometer to measure the total amount of cobalt (%wt) contained. XPS studies were performed on a Physical Electronics spectrometer (PHI Versa Probe II Scanning XPS Microprobe) with monochromatic X-ray Al Ka radiation (100 mm, 100 W, 20 kV, 1486.6 eV) and

a dual-beam charge neutralizer. The spectrometer was calibrated with Au $4f_{7/2}$, Ag $3d_{5/2}$ and Cu $2p_{3/2}$ photoelectron lines at 84.0, 368.2 and 932.7 eV, respectively. The Au $4f_{7/2}$ line was recorded with 0.73 eV FWHM at a binding energy (BE) of 84.0 eV, under a constant pass energy mode at 23.5 eV condition. XPS spectra were analyzed using PHI SmartSoft software and processed using the MultiPak 9.3 package. The binding energy values were referenced to the adventitious C 1s signal at 284.8 eV. The recorded spectra were fitted using Gauss–Lorentz curves. The atomic concentration percentages of the constituent elements of the surfaces were determined considering the corresponding area sensitivity factor for the different measured spectral regions.

8.4.2. Experimental procedures

Preparation of cobalt/pinecone catalyst

Prior to the utilization, pinecones were washed in an US bath for 30′ with a 1:1:1 mixture of water, acetone and acetonitrile, and sequentially dried in a 100 °C oven, in order to remove resins and organic traces. Washed pinecones were carbonized at 600 °C (30 min at 1500 W) in an Ethos microwave equipped with an infrared sensor combined with an *in situ* temperature sensor. Where necessary, before carbonization, pinecones were smashed together with urea using a blender (in order to obtain 10% (wt) of nitrogen in the final product). Sequentially, the carbonaceous materials were activated through KOH impregnation: carbon material was washed with an aqueous solution of KOH (KOH:carbon = 2:1) in an US bath, and directly filtered, avoiding the evaporation of water. The derived activated pinecone carbon was filtered, washed several times with distilled water in an US bath and carbonized at 900 °C (30 min at 1500 W) in an Ethos microwave.

Adsorption of Co on pinecone carbon

A metal/ carbon mixture was prepared by mixing 300 mg of pinecone carbon (or commercially available activated carbon), 3 mL of ethanol solution and 81 mmol of $Co(OAc)_2$ (43 mg). The mixture was stirred for 24 h at room temperature.

Preparation of polyphenol solution

6 g of green Malaysian tea were mixed with 150 mL of ethanol and sequentially irradiated with combined MW-US at 50 °C for 15 min (100 W MW + 40 W US).

Preparation of cobalt N-doped carbon materials

9 mL of polyphenol solution (or ethanol, for samples not containing polyphenols) were added to the mixture of metal/carbon. The resulting solution was heated at 45 °C for 1 h in an oil bath

or in a MW-oven or in a US bath or in a combined MW-US apparatus. The resulting powders were filtered, washed several times with ethanol and dried at 80 °C for 24 h prior to determine the final weight.

Preparation of the electrocatalyst materials

Each sample was firstly dispersed (5 mg mL^{-1}, 15 min in an US bath) in a mixture made of 15 mL 30% vol isopropanol in water and 5 mL of a Naflon 117 solution (~5%). 2D working electrodes were prepared by drop-casting the different solutions over glassy carbon (GC) discs of 5 mm diameters (Pine Instruments Company, Grove City, USA). Before each usage, the GC electrodes were washed and cleaned. Specifically, the discs were firstly sonicated for 15 min in pure isopropanol in order to remove any residual Naflon. Sequentially, the electrodes were polished using two distinct alumina (Al$_2$O$_3$) powders with different particle sizes (0.2 and 0.05 mm), which were previously mixed with water on the polishing pad, making a paste. After polishing, the electrodes were sonicated again at least three times (15′ each one) in ultrapure water. Finally, the discs were electrochemically cleaned by performing 100 cyclic voltammetric (CV) scans in an aqueous electrolyte composed of nitrogen-saturated 0.5 M H$_2$SO$_4$ plus 0.5 M NaCl, at a scan rate of 50 mV s^{-1}. RuO$_2$ NPs were used as a reference electrocatalyst material and were synthesized according to the precipitation method reported in the literature.[505]

Electrochemical measurements

Linear-sweep voltammetric (LSV) measurements were con-ducted using a three-electrode electrochemical cell connected to a potentiostat/galvanostat tool (AUTOLAB PGSTAT30). Ag/AgCl and Pt foil were used as reference and counter electrodes. The experiments were performed in an alkaline aqueous solution of KOH 0.5 M. Electrochemical measurements were performed operating in the potential range 0.00–0.90 V vs. Ag/AgCl, using a scan rate of 2 mV s^{-1} and a rotation rate of 1600 rpm. Current densities were obtained considering the geometric surface area, whilst all potentials were referenced to the RHE according to the Nernst equation. The number of active sites was determined according to the work by Stevens et al. More in detail, a sequence of cyclic voltammetry (CVs) measurements were performed in a narrow potential window of -0.717 V to -0.817 V vs. RHE (i.e. where no faradaic reactions occurred) at different scan rates (12–48 mV s^{-1} at an interval of 4 mV s^{-1}). Sequentially, the slope of the lines of the scan rate vs. Janodic - Jcathodic graph (at -0.767 V vs. RHE) was used to determine the number of active sites as well as the electrochemical surface area.

8.5.   Multifunctional amino-citrate-β-CD coated iron oxide nanoparticles: an efficient nanosystem for Magnetic Resonance Imaging (MRI)

8.5.1. General working conditions

All commercially available reagents and solvents were purchased from Sigma-Aldrich (Milan, Italy) and used without further purification. β-CD was provided by Wacker Chemie (München, Germany). US irradiation at 20.2 kHz was performed with a titanium immersion horn made by Danacamerini s.a.s. (Italy). When reactions were carried out in a combined system MW/US the device has been designed in our laboratory by inserting a sonic horn made of pirex inside a RotoShynth (Milestone) microwave chamber. Thermogravimetric analyses were performed using a thermogravimetric analyzer TGA 4000 (PerkinElmer) at 10 °C min^{-1} operating with alumina crucibles that contained 10−20 mg of sample. The analyses were performed under an argon atmosphere at a starting temperature of 50 °C and an end temperature of 800 °C. Total mass loss was attributed to the functional groups that were covalently attached to the sidewalls. UV−vis absorption spectra were measured on a dual-beam spectrophotometer (Agilent Technologies Cary 60, G6860AA) equipped with a 1 cm path length quartz cuvette. FT-IR analyses were recorder on Shimadzu FT-IR 8001 spectrophotometer. MCT detector was used with a resolution of 4 cm^{-2} and 32 scans. NMR spectra were performed on Bruker Advance (600 MHz and 75 or 125 MHz for ^{1}H and ^{13}C respectively). Chemical shifts were calibrated to the residual proton and carbon resonances of the solvent: DMSO-d6 (δH = 2.54, δC = 39.5), D$_2$O (δH = 4.79), acetone (δH = 2.09, δC = 205.87). Chemical shifts (δ) are given in ppm and coupling constants (J) in Hz. Hydrodynamic particle diameter, polidispersity index (PDI), zeta potential and electrical stability of the colloidal iron oxide suspensions were measured by Dynamic Light Scattering (DLS) (Malvern Instrument, Zetasizer nanoseries). To this purpose the suspensions were diluted 1:10 in bidistilled water. Measurements were performed in triplicate. MNPs size and morphology were analysed by transmission electron microscopy (TEM JEOL JEM-3010, 300 kV, 0.17 nm of resolution, with Gatan camera US1000 CCD and OXFORD detector. INCA softwer was used).

The 1/T$_1$ nuclear magnetic relaxation dispersion profiles (NMRD) of all the preparations were measured over a continuum of magnetic field strength from 0.00024 to 0.5 T (corresponding to 0.01–20 MHz proton Larmor frequency), on the fast field cycling (Stelar Spinmaster FFC 2000 relaxometer) equipped with a resistive low inductance air cored solenoid, made in silver and used in Fast Field Cycling NMR relaxometers The relaxometer operates under complete computer control with an absolute uncertainty in the 1/T$_1$ values of ±1%. The observation field was set at 16 MHz. T$_1$ was determined by the saturation recovery method. 16 values of delay between pulses have been used. The number of averaged experiments was 2. Water proton T$_1$ measurements at fixed frequency were carried out on a Stelar Spin Master Spectrometer [Stelar S.n.c., Mede (PV), Italy] operating in the range from 20 to 80 MHz, by means of the

inversion recovery method (16 delays values, two averages). Water proton T_1 and T_2, and respective R_1 and R_2, at 21.5 MHz were recovered using Spin Master 21.5 MHz, Stelar PC-NMR. Analysis were carried out at 25 °C.

To check the stability of the prepared suspensions both in bidistilled water and in physiological media, longitudinal relaxivity measurements (21.5 MHz, 25°C) was carried out at different time points for seven days. The preparations were diluted 1:1 in bidistilled water, 1:1 in human serum (Seronorm TM) or 1:1 in HEPES/NaCl buffer (300 mOsm, pH 7.3) added with 2.4 mM human serum albumin (final concentration 1.2 mM). For relaxometric measurements resulting samples (80 µL total volume) were transferred in sealed NMR tubes and kept at 37°C into a Thermomixer (EchoTherm™ SC20 Orbital Mixing Chilling/Heating Dry Bath, Torrey Pines Scientific) under gentle vortexing (level 2) from day 0 to day 7. Before each measurement samples were kept 5 min at room temperature to reach 25°C.

J774A.1 cells (from American Type Culture Collection, ATCC,) were used for *in vitro* cell viability studies in presence of MNPs@CA-β-CD and MNPs@CA-Citramide. Cells were cultured at 37°C and 5% CO_2 with Dulbecco's Modified Eagle Medium (DMEM) supplemented with 1% pen/strep, 10% foetal bovine serum (FBS) and 4 mM L-glutamine. When cells reached confluence, they were detached by scraping, counted and seeded into 96 well plates at a density of 10×10^3 cells/cm^2. 24 h later synthesized MNPs diluted at different concentrations (0.2, 0.5, 2, 5, 10 20 µg/mL, 100 µL total volume) in complete culture medium were added into each well and incubation was carried out for 1, 4 and 24 h. Cells incubated with complete medium were used as control. Then the MNPs were removed, cells were extensively washed, MTT (methyl thiazolyl tetrazolium) was added in each well and incubated for 4 h (37°C, 5% CO_2). Then, MTT solution was removed, 150 µl of DMSO were added to each well and the well plates were gently shaken for 15 min at room temperature. At the end, the absorbance was measured using iMark^{TM} Microplate Absorbance Reader (λ range =400 - 750 nm) and the percentage cell viability was calculated as follows:

$$\% \, Cell \, Viability = \frac{Abs \, Sample \, x}{Abs \, Control \, Sample} \, x \, 100$$

Where *Abs Sample x* is the absorbance of each incubated sample, while *Abs Control Sample* is the absorbance of non incubated cells. Each measurement was performend in triplicate.

8.5.2. Experimental procedures

Synthesis of bare MNPs via coprecipitation method

Conventional technique

$FeCl_3 \cdot 6 H_2O$ (8.64 mmol, 2.34 g) and $FeCl_2 \cdot 4 H_2O$ (4.32 mmol) were dissolved in 40 mL of deionized water. The solution was degassed with nitrogen and heated up to 80 °C for 1 h, followed by the addition of 5 mL of 30% ammonia aqua. The heating was continued for 30 min. The mixture was cooled at room temperature and the magnetic nanoparticles were collected by an external magnet, rinsed with deionized water and dried under vacuum.

MW-US irradiation

$FeCl_3 \cdot 6 H_2O$ (8.64 mmol, 2.34 g) and $FeCl_2 \cdot 4 H_2O$ (4.32 mmol) were dissolved in 40 mL of deionized water. The solution was degassed with nitrogen and irradiated by combined MW and US irradiation at 80 °C for 30 min (ultrasound power: 40 W, microwave power :70 W). 5 mL of 30% ammonia aqua where added. The suspension was further irradiated at 80 °C for 15 min. The mixture was cooled at room temperature and the magnetic nanoparticles were collected by an external magnet, rinsed with deionized water and dried under vacuum.

Synthesis of MNPs@CMDx via chemical assembly

Conventional technique

CMDx (0.1 g) was dissolved in 20 mL of water. Bare MNPs (0.1 g) were added. The suspension was stirred for 1 h at 80 °C. After cooling at room temperature, MNPs were collected using an external magnet, rinsed with water and dried under vacuum.

US irradiation

CMDx (0.1 g) was dissolved in 20 mL of water. Bare MNPs (0.1 g) were added. The suspension was irradiated by US irradiation for 1 h at 65 °C. After cooling at room temperature, MNPs were collected using an external magnet, rinsed with water and dried under vacuum.

Synthesis of MNPs@CA via chemical assembly

Conventional technique

Bare MNPs (1 g) were dispersed in 20 mL of a citric acid solution (2.4 M). The suspension was stirred for 1 h at 80 °C. After cooling at room temperature, MNPs were collected using an external magnet, rinsed with ethanol and dried under vacuum.

US irradiation

Bare MNPs (1 g) were dispersed in 20 mL of a citric acid solution (2.4 M). The suspension was irradiated by US irradiation for 1 h at 65 °C. After cooling at room temperature, MNPs were collected using an external magnet, rinsed with ethanol and dried under vacuum.

Synthesis of MNPs@StA

Conventional technique

$FeCl_3 \cdot 6 H_2O$ (0.31 mmol, 83 mg), $FeCl_2 \cdot 4 H_2O$ (0.15 mmol) and stearic acid (0.15 mmol) were added in 20 mL of deionized water. 0.30 mL of 30% ammonia aqua was added dropwise. The solution was stirred at room temperature for 24 h. The magnetic NPs were collected by an external magnet, rinsed with deionized water and dried under vacuum.

US irradiation

$FeCl_3 \cdot 6 H_2O$ (0.31 mmol, 83 mg), $FeCl_2 \cdot 4 H_2O$ (0.15 mmol) and stearic acid (0.15 mmol) were added in 20 mL of deionized water. The mixture was irradiated by US irradiation and 0.30 mL of 30% ammonia aqua was added dropwise. The solution was irradiated at 65 °C for 30 min. The suspension was cooled at room temperature and the magnetic NPs were collected by an external magnet, rinsed with deionized water and dried under vacuum.

Synthesis of MNPs@CMDx via ligand exchange

MNPs@StA (25 mg) were finely dispersed in 15 mL of toluene. Carboxymethyl dextran (25 mg) was dissolved in 30 mL of basic deionized water (0.50 mL of KOH 1 N). The solutions were combined, and the mixture was refluxed 24 h. The organic layer was removed, MNPs were collected from the aqueous phase by an external magnet, rinsed with deionized water and acetone and dried under vacuum.

Synthesis of MNPs@CA via ligand exchange

MNPs@StA (25 mg) were finely dispersed in 15 mL of toluene. Citric acid (25 mg) was dissolved in 30 mL of basic deionized water (0.50 mL of KOH 1 N). The solutions were combined, and the mixture was refluxed 24 h. The organic layer was removed, MNPs were collected from the aqueous phase by an external magnet, rinsed with deionized water and acetone and dried under vacuum.

Synthesis of MNPs@CA-β-CD via ligand exchange

MNPs@StA (25 mg) were finely dispersed in 50 mL of petroleum ether. Citric acid (25 mg) and β-CD (50 mg) were dissolved in 50 mL of deionized water. The solutions were combined, and the mixture was vigorously stirred at room temperature 24 h. The organic layer was removed, MNPs were collected from the aqueous phase by an external magnet, rinsed with deionized water and acetone and dried under vacuum.

Synthesis of MNPs@CA-Citramide via ligand exchange

MNPs@StA (25 mg) were finely dispersed in 50 mL of petroleum ether. Citric acid (25 mg) and β-CD citrate (citramide) (61 mg) were dissolved in 50 mL of deionized water. The solutions were combined, and the mixture was vigorously stirred at room temperature 24 h. The organic layer was removed, MNPs were collected from the aqueous phase by an external magnet, rinsed with deionized water and acetone and dried under vacuum.

Synthesis of citric acid anhydride

Citric acid (2.61 mmol, 0.50 mg) was added to a mixture of glacial acetic acid (0.232 mL) and acetic anhydride (0.486 mL). The solution was stirred at 38 °C for 24 h and finally dried under vacuum to obtain the product. White powder (MW: 174.11 g/mol. 0.354 g. 78% yield). (iPrOH/H_2O/EtOAc/NH_4OH 5:3:1:1).

^{1}H NMR (600 MHz, Acetone) δ 3.45 (d, 1H, H-a), 3.19 (d, 1H, H-c), 3.14 (d, 1H, H-d), 3.06 (d, 1H, H-b) ppm (five terms citric acid anhydride). δ 3.34 (d, 1H, H-e), 3.24 (d, 1H, H-f) ppm (six terms citric acid anhydride). δ 3.51 (d, 1H, H-g), 3.41 (d, 1H, H-i), 2.12 (s, 3H, H-j) ppm (six terms acetylated citric acid anhydride).

Synthesis of 6^I-O-p-Toluenesulfonyl-β-CD

βCD (2.80 mmol, 3.17 g) was dissolved in 90 mL of deionized water. The solution was heated up to 55 °C, 1-(p-toluenesulfonyl)imidazole (1.12 mmol) was added and the solution was stirred at room temperature for 2 h. A water solution of NaOH (1.66 g in 6.60 mL) was added dropwise and a precipitate was formed. The suspension was filtered and the filtered was further stirred

for 30 min. NH$_4$Cl (3.97 g) was added and a precipitated was obtained. It was recovered by filtration under vacuum, washed with acetone and dried. White powder (MW: 1289.17 g/mol. 0.830 g. 23% yield). Rf 0.44 (iPrOH/H$_2$O/EtOAc/NH$_4$OH 5:1:3:1).

^{1}H NMR (600 MHz, DMSO-d6): δ 7.71 (d, J = 8.3 Hz, 2H), 7.39 (d, J = 8.2 Hz, 2H), 5.72 (dt, J = 24.0, 14H), 4.79 (d, J = 7.5 Hz, 5H), 4.73 (d, J = 3.2 Hz, 2H), 4.51 − 4.39 (m, 5H), 4.37 − 4.25 (m, 1H), 3.69 − 3.38 (m, 28H), 2.39 (s, 3H).

Synthesis of 6^I-diethylentriamine-6^I-monodeoxy-βCD

6^I-O-p-Toluenesulfonyl-β-CD (0.31 mmol, 0.40 mg) was added to 0.80 mL of diethylentriamine. After complete solubilization the mixture was stirred at 100 °C for 7 h. The product was precipitated by adding 2-propanol. The precipitated was filtered under vacuum, washed several times with 2-propanol and dried. White powder (MW: 1220.14 g/mol. 0.366 g. 96% yield). (iPrOH/H$_2$O/EtOAc/NH$_4$OH 5:3:1:1).

^{1}H NMR (600 MHz, D$_2$O): δ 4.91 (s, 7H, H-1), 3.84 − 3.65 (m, 27H, 7×H-3, 7×H-5, 12×H-6, 1×H-4), 3.51 − 3.39 (m, 13H, 7×H-2, 6×H-4), 3.03 (d, J = 6.1 Hz, 1H, H-4), 2.96-2.92 (m, 1H, H-6a), 2.72 (t, J = 6.4 Hz, 4H, 2×H-1', 2×H-2'), 2.61 (dd, J = 16.4 Hz, 5H, 2×H-3', 2×H-4', 1×H-6b,) ppm.

Synthesis of β-CD citrate (citramide)

Citric acid anhydride (71 mg) was dissolved in 6 mL of dry dimethylformamide (DMF). 100 mg of 6^I-diethylentriamine-6^I-monodeoxy-βCD and 1 mL of pyridine were added and the solution was heated up at 40 °C for 24 h. The product was precipitated by adding acetone. The precipitated was filtered under vacuum, washed several times with acetone and dried. White powder (MW: 1394.26 g/mol. 0.082 g. 71% yield). (H$_2$O/1,4-dioxane/NH$_4$OH 1:1:0.1).

ESI-MS$^+$: m/z calc for C$_{52}$H$_{87}$N$_3$O$_{40}$ 1394.26; [M+H]$^+$ found 1395.25.

Synthesis of carboxymethyl dextran

Dextran (6000 g/mol, 0.50 g, 3.09 mmol) were dissolved in 10.62 mL of tert-butanol. Subsequently, 1.8 mL of sodium hydroxide at concentrations of 3.8 M were added dropwise to the dextran solution. Then, the solution was stirred at room temperature for 1 h. Monobromoacetic acid (7.71 mmol) was added. The reaction mixture was stirred at 60 °C for 90 min. Afterward the mixture was cooled to room temperature and then neutralized with glacial acetic acid. Finally, the product was precipitated and washed twice with methanol, filtered under vacuum and dried. This process was repeated three times. After the carboxymethylation reaction, the modified dextrans are in the form of a carboxylate sodium salt (–CH$_2$COONa). An acid wash was used to obtain the free acid form (–CH$_2$COOH). For this, 1 g of CMDx was

washed 10 min with 14 mL of a solution of methanol and chloridric acid 37 %v/v (20:1). The acid liquor was removed by vacuum filtration and the solid product was subsequently washed several times with ethanol to remove all traces of the acid reagent and dried under vacuum. Afterward, the amount of carboxylic (–COOH) groups per CMDx chain were determined by acidimetric titration. For the acidimetric titration, a solution at 1% w/v of CMDx in a mixture of distilled water/acetone (1:1) was prepared. NaOH 0.012 N was added dropwise and then the solution was titrated with hydrochloric acid 0.012 N, using phenolphthalein as indicator. From the titration data, the equivalents of –COOH groups per gram of CMDx were calculated and 30% of degree of substitution was obtained. White powder (MW: 179.84 g/mol, 75% yield).

FT-IR νmax (KBr, cm^{-1}): 3318, 2938, 1737, 1635, 1384, 1231, 1157, 1020, 917.

Sorption experiments

Phenolphthalein – A buffer solution was prepared from 13.2 g of Na_2CO_3 and 2.1 g of $NaHCO_3$ dissolved in 250 mL of ultrapure water (pH 10.5). Php powder was dissolved in ethanol to obtain a 5 mM Php stock solution, and β-CD powder was dissolved in ultrapure water to obtain a 0.88 mM β-CD stock solution. The Php stock solution was diluted in the buffer solution (pH 10.5) to achieve a constant Php concentration of 0.008 mM and was mixed with the β-CD stock solution to achieve β-CD concentrations of 0, 7.9, 9.6, 11.3, 13, 14.7, 16.4, and 18.1 mmol L^{-1}. The absorbance of the CD calibration solutions was measured at a wavelength of 553 nm at room temperature. The MNPs samples (5 mg) were dispersed in a Php solution in buffer (0.008 mM, 5 mL). The mixture was stirred for 15 min in an US bath and the MNPs were collected magnetically. UV absorbance was recorded at 553 nm.

Adamantane amine – A solution of adamantane amine dissolved in methanol (2 mL) (1, 2, 4, 8, 10 mg/mL) and MNPs (2 mg) were added to a test tube and stirred for 2 h in an US batch. After the elimination of the solid *via* magnetic attraction, the solution was analyzed by GC-FID. Concentration was determined using a calibration curve, and the adsorption capacity was calculated.

Relaxometric analysis

The proton longitudinal relaxation rate (R_1) and the proton transverse relaxation rate (R_2) were calculated from the relaxation time T_1 and T_2, respectively:

$$R_i = \frac{1}{T_i} = [s^{-1}]$$

where i = 1 or 2.

The relaxivity was calculated:

$$r_{ip} = \frac{R_i - 0.38}{[Fe^{3+}]} = mM^{-1} s^{-1}$$

where i = 1 or 2, and 0.38 is the water contribution.

The iron concentration (Fe^{3+}) was determined *via* relaxometric measurements: a suspension of coated MNPs was diluted with HNO_3 (1 : 10 v/v) and the mixture was allowed to stay at 120 °C for 12 h, in order to oxidize all the metallic ions to Fe^{3+}. Finally, the proton longitudinal relaxation rate (R_1) was measured and the amount of Fe^{3+} was calculated as follows:

$$R_{1obs} = [Fe^{3+}] \cdot r_{1p} + R_{1dia}$$

where, at 21.5 MHz and at 298 K, $R_{1dia} = 0.481$ e $r_{1p} = 18.47 \; s^{-1} mM^{-1}$, thus:

$$[Fe^{3+}] = \frac{R_{1obs} - 0.481}{18.47} = mM$$

The efficiency of the contrast was calculated as follows:

$$\frac{r_2}{r_1}$$

8.6. Continuous flow chemistry for the synthesis of drugs

8.6.1. General working conditions

Reagents used in the following experimental procedures were purchased from Sigma Aldrich or Merck and were used without further purification. Reactions were monitored with thin-layer chromatography on aluminium-backed Merck silica gel 60 F_{254} plates or pre-coated TLC sheets ALUGRAM Xtra SIL G/UV. Synthesised compounds were visualised on TLC under UV light (254 nm). Purification of compounds was carried out with column chromatography on Merck silica gel 60 (particle size 0.063-0.2 mm) using appropriate combinations of solvent mixtures. Analytical techniques were used to fully characterize isolated compounds. Nuclear Magnetic Resonance spectra were recorded using a 300 MHz Varian VNMRS (75 MHz for ^{13}C), a 400 MHz Varian Unity Inova (100 MHz for ^{13}C) or a Bruker Avance-400 (400 MHz) spectrometers. Chemical shifts (δ) are reported in ppm and *J*-values are given in Hz. Chemical shifts were recorded relative to a reference compound – residual $CDCl_3$ or d_6-DMSO. All NMR spectra were obtained at 25 °C. Infrared spectra were recorded from 4000 to 500 cm^{-1} using a Bruker spectrometer, and peaks (umax) are reported in wavenumbers (cm^{-1}). High-performance liquid chromatography (HPLC) data was obtained using Agilent 1100 with a UV detector. HPLC analysis was performed on ACE Generix 5 C18(2) column (150 mm × 4.6 mm i.d) at ambient temperature using an isocratic system. The mobile phase consisted of 35% water and 65% MeCN or 35% H_2O and 65% MeOH or 100% MeCN, depending on the analyzed molecules. A Bruker Alpha FT-IR spectrophotometer was used to acquire FT-IR spectra, through OPUS 7.5 Software. The sample injection volume was 1 μL, eluted at a flow rate of 1 mL/min, and detected at 254 nm. A pump system Chemyx Inc. Fusion 101 was used to perform continuous flow processes and reagents were purged onto Trajan Supelco SGE Syringes, 10 mL, Luer Loch. A flow reactor system LTF – Mr-Lab-Ms 115 x 60 x 6.4 mm coupled with a LTF – Mr-Lab-V 115 x 60 x 6.4 mm was used. All units were connected using PTFE tubing (0.2 mm internal diameter). A Zaiput back pressure regulator was used.

Set-up for the packed bed reactor unit

The experimental setup consisted of a syringe pump (Chemyx Inc. Fusion 101), a packed bed reactor (PBR) ((Omnifit EZ column 6.6 mm/100 mm) and an oil bath. All units were connected using PTFE tubing (0.2 mm internal diameter). The PBR was heated by immersing the reactor inside the oil bath.

The bed volume was calculated as follow: once the packed bed reactor was filled with the catalyst, the internal volume was determined by weighing the freshly PBR (Mass 1) and then pumping a solvent through the reactor to fill the void with it. The packed bed reactor was then weighed again (Mass 2). The reactor volume was determined by Rv = (Mass 2 – Mass 1)/ solvent density.

175

$$R_v = \frac{Mass_2 - Mass_1}{Solvent\ density}$$

8.6.2. Experimental procedures

General procedure for the synthesis of 6-aminouracil camptothecin analogue

Synthesis of 6-aminouracil camptothecin analogue (7) via conventional heating and O₂ atmosphere

4-Nitrobenzaldehyde (0.4 mmol, 60 mg), 6-aminouracile (0.4 mmol, 51 mg) and 1,3-indanedione (0.4 mmol, 58 mg) are suspended in DMF (0.8 mL, 0.5 M). Acetic acid (0.8 mmol, 0.046 mL) and acetic anhydride (0.8 mmol, 0.076 mL) are added. The reaction mixture is heated for 4 h at 160 °C under O_2 atmosphere and then allowed to cool to room temperature. Water is added (4.90 mL) and the formed precipitate is isolated by filtration, washed with ethanol and diethyl ether and dried under vacuum overnight.

Orange powder (154 mg, 99% yield). R_f 0.65 (DCM/MeOH, 9:1).

Synthesis of 6-aminouracil camptothecin analogue (7) via conventional heating and CuCl₂ oxidation

4-Nitrobenzaldehyde (0.4 mmol, 60 mg), 6-aminouracile (0.4 mmol, 51 mg) and 1,3-indanedione (0.4 mmol, 58 mg) are suspended in DMF (0.8 mL, 0.5 M). Acetic acid (0.8 mmol, 0.046 mL), acetic anhydride (0.8 mmol, 0.076 mL) and $CuCl_2$ (0.04 mmol, 5.4 mg) are added. The reaction mixture is heated for 4 h at 160 °C and then allowed to cool to room temperature. Water is added (4.90 mL) and the formed precipitate is isolated by filtration, washed with ethanol and diethyl ether and dried under vacuum overnight.

Orange powder (146 mg, 94% yield). R_f 0.65 (DCM/MeOH, 9:1).

Synthesis of 6-aminouracil camptothecin analogue (7) via MW heating and CuCl₂ oxidation

4-Nitrobenzaldehyde (0.4 mmol, 60 mg), 6-aminouracile (0.4 mmol, 51 mg) and 1,3-indanedione (0.4 mmol, 58 mg) are suspended in DMF (0.8 mL, 0.5 M). Acetic acid (0.8 mmol, 0.046 mL), acetic anhydride (0.8 mmol, 0.076 mL) and $CuCl_2$ (0.04 mmol, 5.4 mg) are added. The reaction mixture is heated for 1 h at 160 °C under MW irradiation and then allowed to cool to room temperature. Water is added (4.90 mL) and the formed precipitate is isolated by filtration, washed with ethanol and diethyl ether and dried under vacuum overnight.

Orange powder (98 mg, 93% yield). R_f 0.65 (DCM/MeOH, 9:1).

Synthesis of 6-aminouracil camptothecin analogue (6) and (7) via flow chemistry

A solution of 4-Nitrobenzaldehyde (5 mmol) in DMSO (10 mL) premixed with an acid catalyst (10 mmol) and a solution of 1,3-indanedione (5 mmol) and 6-aminouracile (5 mmol) in DMSO (10 mL) are pumped using two separate full 10 mL glass syringes into a 0.2 mL glass mixer, followed by a 1.7 mL glass reactor, held at 160 °C for 45 min residence time to afford intermediate (**6**). Subsequently, chloranil (10 mmol) in DMSO (8 mL) was pumped using a full 10 mL glass syringe into a 0.2 mL glass reactor, at 160 °C for 5 seconds residence time, to give product (**7**). Water is added to the collected reaction mixture and the formed precipitate is filtered off, washed with water and dried under vacuum.

Product (**6**): orange powder (63% yield – measured by HPLC, MeOH : H_2O / 65 : 35, isocratic, 8 min).

^{1}H NMR (400 MHz, DMSO-d_6) δ 11.01 (s, 1H), 10.49 (s, 2H), 8.15 (d, J = 8.7 Hz, 2H), 7.60 (d, J = 8.7 Hz, 2H), 7.55 – 7.48 (m, 2H), 7.42 (td, J = 7.0, 1H), 7.33 (d, J = 7.1 Hz, 1H), 4.88 (s, 1H).

^{13}C NMR (151 MHz, DMSO-d_6) δ 190.93, 163.78, 154.45, 153.13, 153.13, 146.19, 145.58, 136.46, 131.23, 130.38, 129.92, 128.21, 122.35, 119.33, 108.47, 107.06, 104.68, 90.49.

Product (**7**): orange/brown powder (99% yield).

^{1}H NMR (300 MHz, DMSO-d_6) δ 12.33 (s, 1H), 11.41 (s, 1H), 8.26 (d, J = 8.8 Hz, 2H), 7.83 (d, J = 7.4 Hz, 1H), 7.76 (t, J = 7.9 Hz, 1H), 7.66 – 7.54 (m, 4H).

^{13}C NMR (151 MHz, DMSO-d_6) δ 188.64, 168.81, 161.75, 157.93, 150.32, 149.24, 147.55, 142.71, 140.71, 136.43, 136.15, 133.63, 129.70, 122.87, 122.21, 120.84, 107.06.

General procedure for the synthesis of Praziquantel

Synthesis of N-Phenylethylformamide

2-Phenylethylamine (0.4 mmol, 51 µL) is added to formamide (2 mL). The reaction mixture is stirred and heated up to 120 °C. After 15 h the reaction is cooled down to room temperature, extracted with ethyl acetate and water. Sequentially, the organic layer is washed with a saturated ammonium chloride solution, then with a saturated sodium chloride solution, dried over sodium sulphate and finally dried under reduced pressure. The isolated product is stored at -4 °C.

Yellow oil (51.6 mg, 86% yield). R_f 0.71 (DCM/MeOH, 9:1).

^{1}H NMR (300 MHz, CDCl$_3$) δ 8.09 (s, 1H), 7.31 (dd, J = 8.0 Hz, 2H), 7.26 – 7.16 (m, 3H), 5.84 (s, 1H), 3.55 (dd, J = 13.1 Hz, 2H), 2.83 (t, J = 7.0 Hz, 2H).

^{13}C NMR (75 MHz, CDCl$_3$) δ 161.57, 136.66, 128.80, 128.68, 127.27, 39.63, 34.47.

Synthesis of N-phenylethylisocyanide (11)

To a solution of N-phenylethylformamide (3.35 mmol, 500 mg) in CH$_2$Cl$_2$ (1.67 mL), Et$_3$N (16.7 mmol) and POCl$_3$ (3.35 mmol, 514 mg) are added keeping the solution at 0 °C. The reaction mixture is stirred at 0 °C for 10 min. After that, the reaction mixture is directly poured onto a column loaded with silica in diethylether, that is used as mobile phase. The desired isocyanide is obtained.

Yellow oil (374 mg, 83% yield). R$_f$ 0.71 (DCM).

^{1}H NMR (300 MHz, CDCl$_3$) δ 7.38 – 7.28 (m, 3H), 7.25 – 7.21 (m, 2H), 3.64 – 3.58 (m, 2H), 3.04 – 2.95 (m, 2H).

^{13}C NMR (75 MHz, CDCl$_3$) δ 156.49, 136.66, 128.80, 128.68, 127.27, 42.90, 35.69.

Synthesis of N-(2,2-dimethoxyethyl)-N-(2-oxo-2-(2-phenethylamino)-ethyl)cyclohexane carboxamide (Ugi reaction) (12) under conventional heating

To a solution of formaldehyde (37% in MeOH, 1 mmol), cyclohexancarboxylic acid (1 mmol, 128 mg) and amino acetaldehyde dimethylacetal (1 mmol, 106 mg) in MeOH/CH$_3$CN (1:1, 2 mL), isocyanide (1 mmol, 132 mg) is added dropwise at 0 °C. The resulting solution is stirred at 80 °C for 1 h. The reaction mixture is extracted with diethyl ether and water, dried over anhydrous sodium sulphate and finally the solvent is removed under reduced pressure.

Yellow oil (250 mg, 66% yield). R$_f$ 0.34 (Hexane/EtOAC, 1:2).

Synthesis of N-(2,2-dimethoxyethyl)-N-(2-oxo-2-(2-phenethylamino)-ethyl)cyclohexane carboxamide (Ugi reaction) (12) under MW irradiation

To a solution of formaldehyde (37% in MeOH, 1 mmol), cyclohexancarboxylic acid (1 mmol, 128 mg) and amino acetaldehyde dimethylacetal (1 mmol, 106 mg) in MeOH/CH$_3$CN (1:1, 2 mL), isocyanide (1 mmol, 132 mg) is added dropwise at 0 °C. The resulting solution is heated up to at 80 °C under MW irradiation and stirred for 15 min. The reaction mixture is extracted with diethyl ether and water, dried over anhydrous sodium sulphate and finally the solvent is removed under reduced pressure.

Yellow oil (198 mg, 53% yield). R$_f$ 0.34 (Hexane/EtOAC, 1:2).

Synthesis of N-(2,2-dimethoxyethyl)-N-(2-oxo-2-(2-phenethylamino)-ethyl)cyclohexane carboxamide (Ugi reaction) (12) via continuous flow chemistry

Isocyanide (10 mmol, 1.32 g) and amino acetaldehyde dimethylacetal (1o mmol, 1.06 g) are premixed in MeOH/CH₃CN (1:1, 10 mL, 1 M) and poured onto a 10 mL glass syringe. Formaldehyde (37% in MeOH, 10 mmol) and cyclohexancarboxylic acid (10 mmol, 1.28 g) are premixed in MeOH/CH₃CN (1:1, 10 mL, 1 M) and poured onto a 10 mL glass syringe. The solutions are pumped into a 0.2 mL glass mixer, followed by a 1.7 mL glass reactor, held at 100 °C for 15 min residence time to afford intermediate (13) (flow rate 0.0633 mL/min).

Yellow oil (291 mg, 78% yield). R_f 0.34 (Hexane/EtOAC, 1:2). HPCL conditions: H_2O : CH_3CN / 35 : 65, isocratic, 9 min.

¹H NMR (400 MHz, CDCl₃) δ 7.33 – 7.26 (m, 2H), 7.24 – 7.13 (m, 3H), 7.00 (t, J = 5.2 Hz, 1H), 6.49 (t, J = 5.1 Hz, 1H), 4.57 (t, J = 5.1 Hz, 1H), 4.39 (t, J = 5.2 Hz, 1H), 3.98 (d, J = 7.2 Hz, 2H), 3.55 (dd, J = 13.1 Hz, 1H), 3.48 (dd, J = 13.0 Hz, 1H), 3.41 (t, J = 5.7 Hz, 2H), 3.37 (s, 3H), 3.33 (s, 3H), 2.84 – 2.75 (m, 2H), 2.57 (t, J = 11.6 Hz, 1H), 2.25 (dd, J = 23.9, 11.4 Hz, 1H), 1.80 – 1.69 (m, 2H), 1.62 (dd, J = 19.1, 10.0 Hz, 2H), 1.50 – 1.37 (m, 2H), 1.33 – 1.16 (m, 4H).

¹³C NMR (101 MHz, CDCl₃) δ 177.85, 169.55, 128.85 – 128.40, 126.51, 103.44, 102.66, 55.45, 55.05, 54.05, 52.13, 51.49, 50.32, 41.04, 40.55, 40.26, 35.56, 29.30, 25.60.

Synthesis of 2-(cyclohexanecarbonyl)-2,3,6,7,11b-hexahydro-pyrazino[2,1-a]isoquinolin-4-one (Praziquantel) (Pictet–Spengler reaction) (13) under conventional heating

N-(2,2-Dimethoxyethyl)-N-(2-oxo-2-(2-phenethylamino)ethyl)cyclohexanecarboxamide (12) (0.266 mmol, 100 mg) is added portionwise to methanesulfonic acid (5.31 mmol, 510 mg) at 0 °C. After heating up to 70 °C for 6 h, the reaction mixture is poured into an ice/water mixture and adjusted to pH 8 with an aqueous solution of NaOH (20%). The solution is extracted with diethyl ether, the organic layer is dried over anhydrous sodium sulphate and concentrated under reduced pressure.

Yellow oil (55 mg, 66% yield). R_f 0.62 (Hexane/EtOAC, 1:2).

Synthesis of 2-(cyclohexanecarbonyl)-2,3,6,7,11b-hexahydro-pyrazino[2,1-a]isoquinolin-4-one (Praziquantel) (Pictet–Spengler reaction) (13) via continuous flow chemistry

A solution of N-(2,2-Dimethoxyethyl)-N-(2-oxo-2-(2-phenethylamino)ethyl)cyclohexane carboxamide (12) in MeOH/CH₃CN (1:1, 0.5 M) is poured onto a 10 mL glass syringe and pumped into a 0.2 mL glass mixer, followed by a 1.7 mL glass reactor, contemporary at a

solution of MsOH (1 equiv, MeOH/CH$_3$CN (1:1, 1 M)), held at 100 °C for 30 min residence time to afford intermediate (**13**).

Yellow oil (73 mg, 88% yield). R$_f$ 0.62 (Hexane/EtOAC, 1:2). HPCL conditions: H$_2$O : CH$_3$CN / 35 : 65, isocratic, 9 min.

^{1}H NMR (400 MHz, CDCl$_3$) δ 7.27 − 7.13 (m, 4H), 5.14 (d, J = 10.5 Hz, 1H), 4.79 (d, J = 10.9 Hz, 2H), 4.46 (d, J = 17.7 Hz, 1H), 4.07 (d, J = 17.4 Hz, 1H), 2.95 − 2.73 (m, 4H), 2.49 − 2.40 (m, 1H), 1.87 − 1.67 (m, 5H), 1.59 − 1.47 (m, 2H), 1.26 (d, J = 10.2 Hz, 3H).

^{13}C NMR (101 MHz, CDCl$_3$) δ 174.68, 164.33, 134.60, 132.58, 129.28, 127.32, 126.85, 125.11, 54.97, 48.84, 45.09, 40.23, 39.13, 29.42, 28.55, 28.08, 25.62.

General procedure for the synthesis of 4-[4-(4-Methoxyphenyl)piperazin-1-yl]-aniline

Synthesis of copper nanoparticles

A Copper (II) sulfate solution (1.5 mL of a 0.01 M solution in water/glycerol 5:1) was stirred and was followed dropwise by addition of 2 M NaOH aqueous solution to adjust the solution pH up to 11. After stirring for 10 min, 0.5 M NaBH$_4$ in water (0.092 mL) was added into the flask, keeping the solution in an US bath. Firstly, the deep blue solution gradually became colourless, and then it turned burgundy, which shows the formation of copper colloid. The copper nanoparticles were filtered on a Büchner funnel with a sintered glass disc using water and methanol to wash the catalyst.

Synthesis of supported copper nanoparticles

A Copper (II) sulfate solution (1.5 mL of a 0.01 M solution in water/glycerol 5:1) was stirred and was followed dropwise by addition of 2 M NaOH aqueous solution to adjust the solution pH up to 11. After stirring for 10 min, celite powder (50 mg) is added, followed by the addition of 0.5 M NaBH$_4$ in water (0.092 mL), keeping the solution in an US bath. After the addition of NaBH$_4$, the supported copper nanoparticles were filtered on a Büchner funnel with a sintered glass disc using water and methanol to wash the catalyst.

Synthesis of Bis-(2-chloroethyl)-amine hydrochloride (15)

Diethanolamine (4.7 mmol, 500 mg) is dissolved in CHCl$_3$ (2 mL). A second mixed solution is prepared by mixing SOCl$_2$ (10.9 mmol, 1.30 g) in CHCl$_3$ (1.5 mL). The first mixed solution is dropped to the second mixed solution while stirring at 0 °C. Thereafter, the resulting mixture is stirred for 5 h at 50 °C. After the reaction a white precipitate is formed, 500 μL of CH$_3$OH are

added to the reaction mixture and after being cooled at room temperature, the solvents are removed under reduced pressure to obtain a white powder.

White powder (819 mg, 97% yield).

^{1}H NMR (400 MHz, DMSO-d$_6$) δ 9.72 (s, 1H), 3.93 (t, J = 6.4 Hz, 4H), 3.33 (t, J = 6.4 Hz, 4H).

^{13}C NMR (101 MHz, DMSO-d$_6$) δ 48.35

Synthesis of 1-(4-methoxyphenyl)piperazine (16)

To a stirred mixture of bis-(2-chloroethyl)-amine hydrochloride (4.2 mmol, 750 mg) and nBuOH (3.25 mL) is added slowly a solution of 4-methoxyaniline (3.8 mmol, 470 mg) in nBuOH (0.5 mL). The resulting reaction mixture is heated up at reflux conditions for 24 h. The hot mixture is filtered and the precipitate is washed with cold nBuOH and dried under vacuum.

White powder (67% yield). R$_f$ 0.73 (DCM/MeOH, 8:2).

^{1}H NMR (300 MHz, DMSO-d$_6$) δ 6.89 (dd, J = 26.7 Hz, 4H), 3.69 (s, 3H), 3.36 (brs, 1H), 3.20 (d, J = 4.6 Hz, 8H).

^{13}C NMR (75 MHz, DMSO-d$_6$) δ 154.08, 144.79, 118.56, 114.82, 55.66, 47.28, 43.20.

Synthesis of 1-(4-Methoxyphenyl)-4-(4-nitrophenyl)piperazine (17)

1-(4-methoxyphenyl)piperazine (0.78 mmol, 150 mg) is dissolved in DMSO (1.5 mL), K$_2$CO$_3$ (0.82 mmol, 113 mg) and 1-chloro-4-nitrobenzene (0.75 mmol, 118 mg) are added. The reaction mixture is stirred at 160 °C for 15 h. The reaction is allowed to cool down at room temperature, the generated solid precipitate is filtered, washed with ethanol and dried under vacuum.

Yellow powder (230 mg, 98% yield). R$_f$ 0.52 (PE/EtOAc, 5:5).

^{1}H NMR (400 MHz, CDCl$_3$) δ 8.15 (d, J = 9.4 Hz, 2H), 6.95 (d, J = 9.2 Hz, 2H), 6.88 (d, J = 7.8 Hz, 4H), 3.78 (s, 3H), 3.61 – 3.55 (m, 4H), 3.26 – 3.19 (m, 4H).

^{13}C NMR (101 MHz, CDCl$_3$) δ 154.77, 154.41, 145.06, 138.65, 125.95, 118.70, 114.57, 112.82, 55.56, 50.52, 47.27.

Synthesis of 4-[4-(4-Methoxyphenyl)piperazin-1-yl]-aniline (18) under conventional heating and Pd/C as catalyst

To a solution of 1-(4-Methoxyphenyl)-4-(4-nitrophenyl)piperazine (0.319 mmol, 100 mg) in EtOH or DMF (12 mL, 0.025 M), hydrazine monohydrate (3.19 mmol, 160 mg) and Pd/C (5% loaded, 0.0319 mmol, 68 mg) are added. The reaction mixture is stirred and heated at reflux conditions for 15 h. Then, the catalyst is filtered off and the solution is extracted with water and

ethyl acetate. The organic layer is dried over sodium sulphate and finally dried under reduced pressure.

Yellow powder (81 mg, 89% yield). R_f 0.16 (PE/EtOAc, 5:5).

Synthesis of 4-[4-(4-Methoxyphenyl)piperazin-1-yl]-aniline (18) under conventional heating and Cu(0) NPs as catalyst (0.08 M)

Cu(0) NPs (10 mol%, 2 mg) are finely dispersed in glycerol (4 mL) by US irradiation. KOH (0.638 mmol, 36 mg) and 1-(4-Methoxyphenyl)-4-(4-nitrophenyl)piperazine (0.319 mmol, 100 mg) are added. The resulting reaction mixture is heated up to 130 °C and stirred for 5 h. The reaction is allowed to cool down at room temperature, the Cu(0) NPs are filtered off and the solution is extracted with water and ethyl acetate. The organic layer is dried over sodium sulphate and finally dried under reduced pressure.

Yellow powder (48 mg, 53% yield). R_f 0.16 (PE/EtOAc, 5:5).

Synthesis of 4-[4-(4-Methoxyphenyl)piperazin-1-yl]-aniline (18) under conventional heating and supported Cu(0) NPs as catalyst (0.08 M)

Celite supported Cu(0) NPs (5% loaded, 10 mol%, 40 mg) are finely dispersed in glycerol (4 mL) by US irradiation. KOH (0.638 mmol, 36 mg) and 1-(4-Methoxyphenyl)-4-(4-nitrophenyl)piperazine (0.319 mmol, 100 mg) are added. The resulting reaction mixture is heated up to 130 °C and stirred for 8 h. The reaction is allowed to cool down at room temperature, the supported Cu(0) NPs are filtered off and the solution is extracted with water and ethyl acetate. The organic layer is dried over sodium sulphate and finally dried under reduced pressure.

Yellow powder (56 mg, 62% yield). R_f 0.16 (PE/EtOAc, 5:5).

Synthesis of 4-[4-(4-Methoxyphenyl)piperazin-1-yl]-aniline (18) via continuous flow chemistry and supported Cu(0) NPs as catalyst (0.005 M)

1-(4-Methoxyphenyl)-4-(4-nitrophenyl)piperazine (0.5 mmol, 160 mg) and KOH (1 mmol, 56 mg) in ethylene glycol (100 mL, 0.005 M) are passed through celite supported Cu(0) NPs (5% loaded) packed into a bed reactor and kept at 130 °C, residence time 3.42 min. The collected solution is extracted with water and ethyl acetate. The organic layer is dried over sodium sulphate and finally dried under reduced pressure.

Brown powder (87% conversion, measured by HPLC (HPLC conditions: CH_3CN 100%, isocratic, 5 min). R_f 0.16 (PE/EtOAc, 5:5).

^{1}H NMR (300 MHz, CDCl$_3$) δ 6.98 (d, J = 9.0 Hz, 4H), 6.89 (d, J = 6.9 Hz, 6H), 6.70 (d, J = 8.6 Hz, 3H), 3.80 (s, 5H), 3.23 (d, J = 2.4 Hz, 16H).

^{13}C NMR (101 MHz, CDCl$_3$) δ 153.92, 145.69, 144.44, 140.31, 118.79, 118.38, 116.20, 114.45, 55.56, 51.23, 50.98.

Synthesis of 4-[4-(4-Methoxyphenyl)piperazin-1-yl]-aniline (18) via continuous flow chemistry and Pd/C as catalyst (0.025 M)

1-(4-Methoxyphenyl)-4-(4-nitrophenyl)piperazine (0.25 mmol, 78 mg) and hydrazine monohydrate (2.5 mmol, 125 mg) in DMF (10 mL, 0.025 M) are passed through Pd/C (5% loaded) packed into a bed reactor and kept at 100 °C, residence time 2.16 min. The collected solution is extracted with water and ethyl acetate. The organic layer is dried over sodium sulphate and finally dried under reduced pressure.

Brown powder (79% yield). R$_f$ 0.16 (PE/EtOAc, 5:5).

Appendix

9.1.   Sonochemically-promoted preparation of β-cyclodextrin-silica hybrid systems for efficient copper catalysis

6I-O-p-Toluenesulfonyl-β-CD
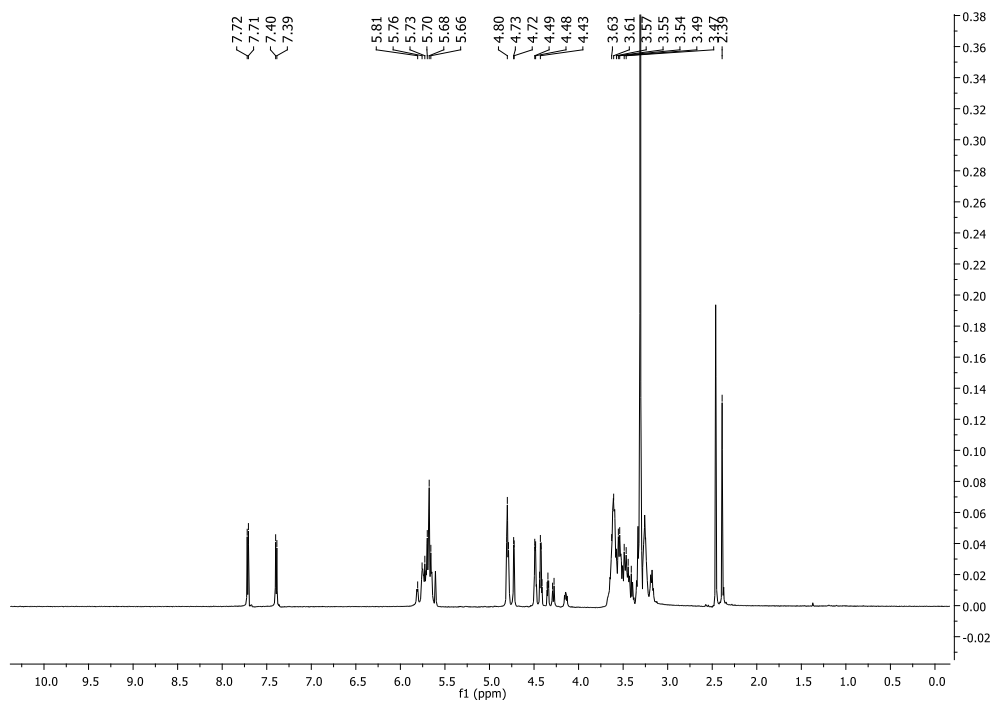
Figure 66. ¹H NMR of 6ᴵ-O-p-Toluenesulfonyl-β-CD.

1,5-bis(1-benzyl-1H-1,2,3-triazol-4-yl)pentane
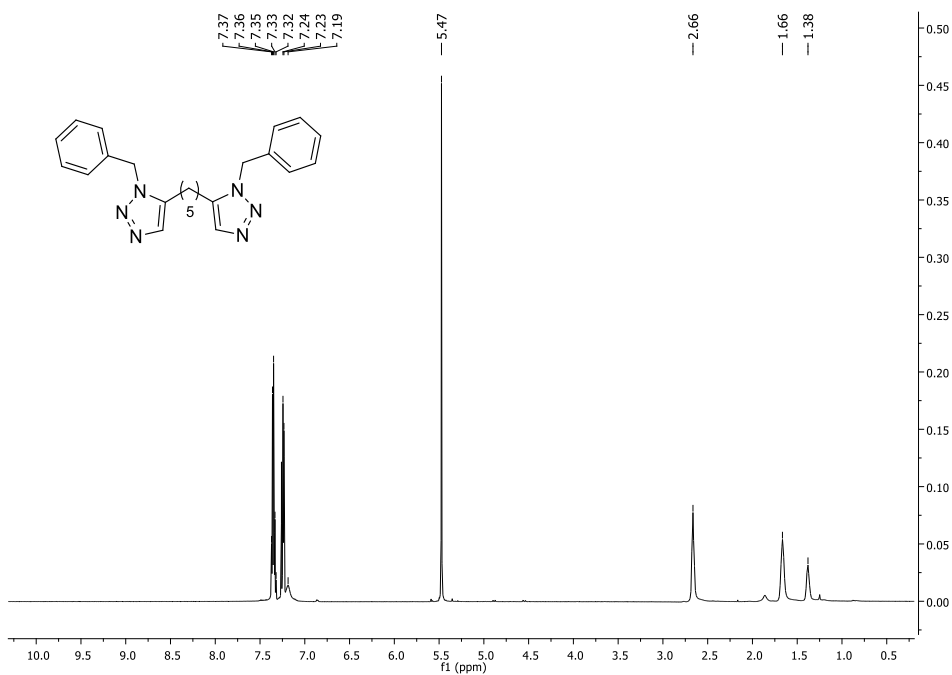
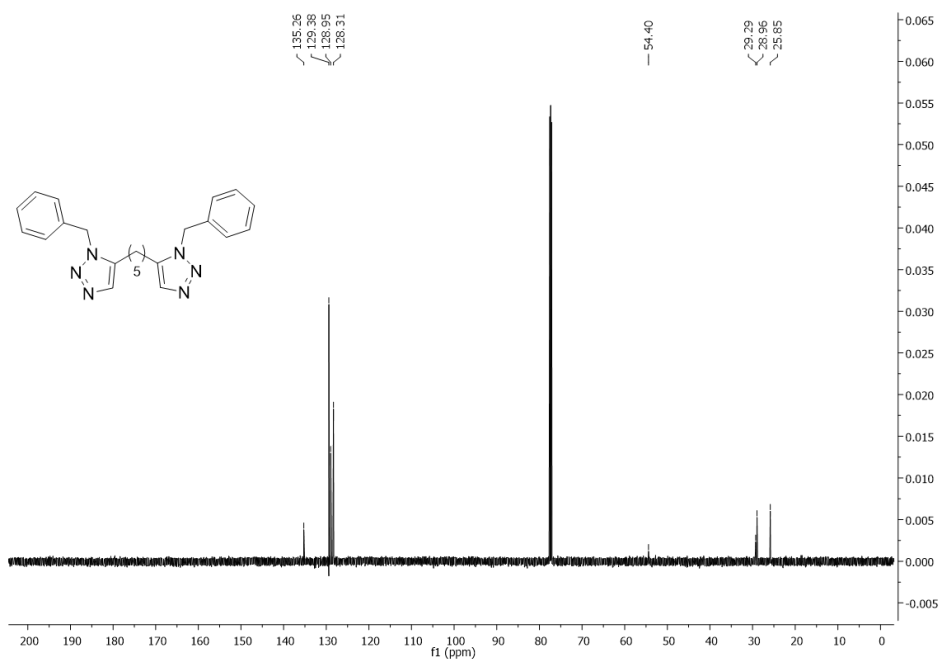**Figure 67.** ^{1}H NMR of 1,5-bis(1-benzyl-1H-1,2,3-triazol-4-yl)pentane.

Figure 68. ^{13}C NMR of 1,5-bis(1-benzyl-1H-1,2,3-triazol-4-yl)pentane.
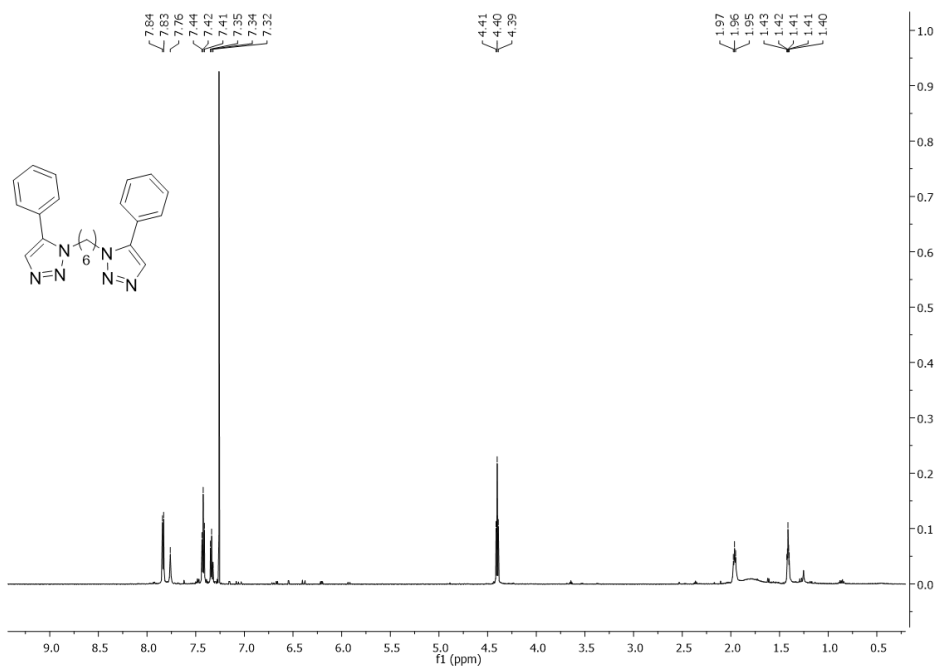
185

1,6-bis(5-phenyl-1H-1,2,3-triazol-1-yl)hexane

Figure 69. ^{1}H NMR of 1,6-bis(5-phenyl-1H-1,2,3-triazol-1-yl)hexane.
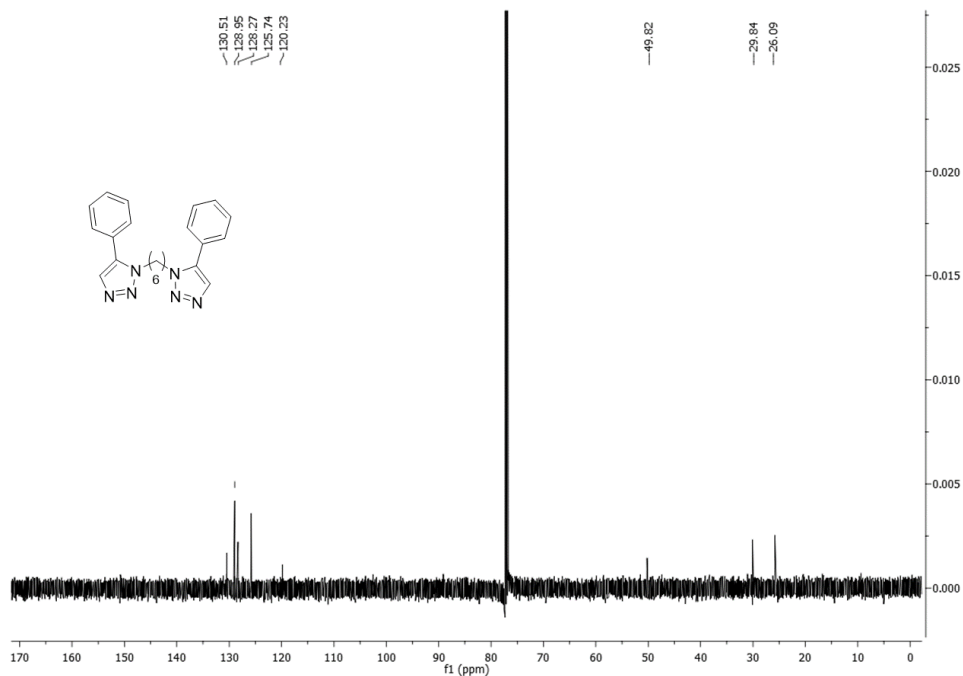
Figure 70. ^{13}C NMR of 1,6-bis(5-phenyl-1H-1,2,3-triazol-1-yl)hexane.
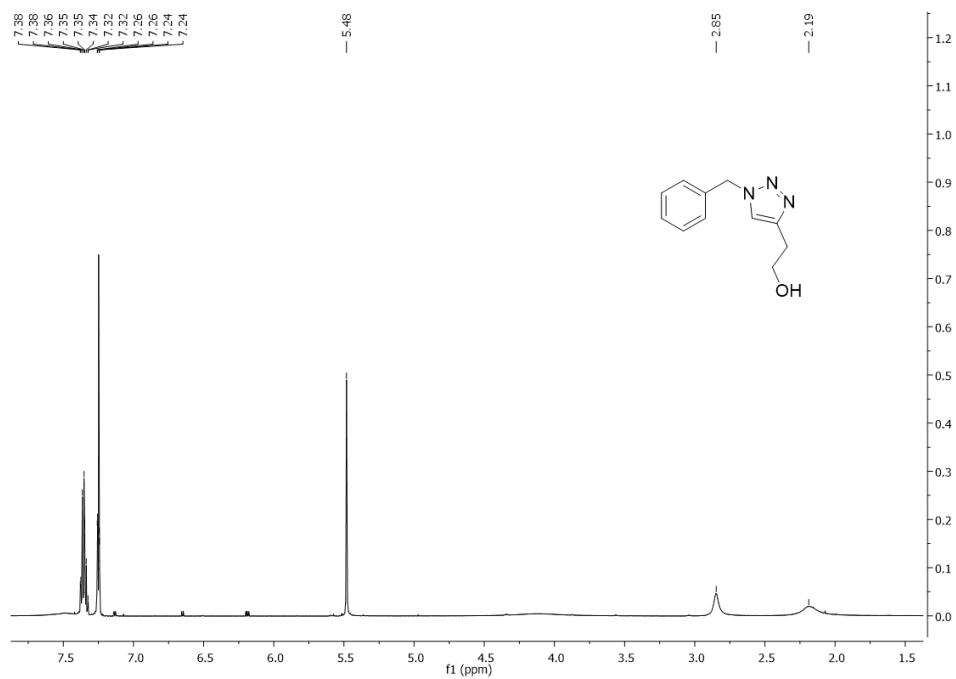
2-(1-benzyl-1H-1,2,3-triazol-4-yl)ethan-1-ol

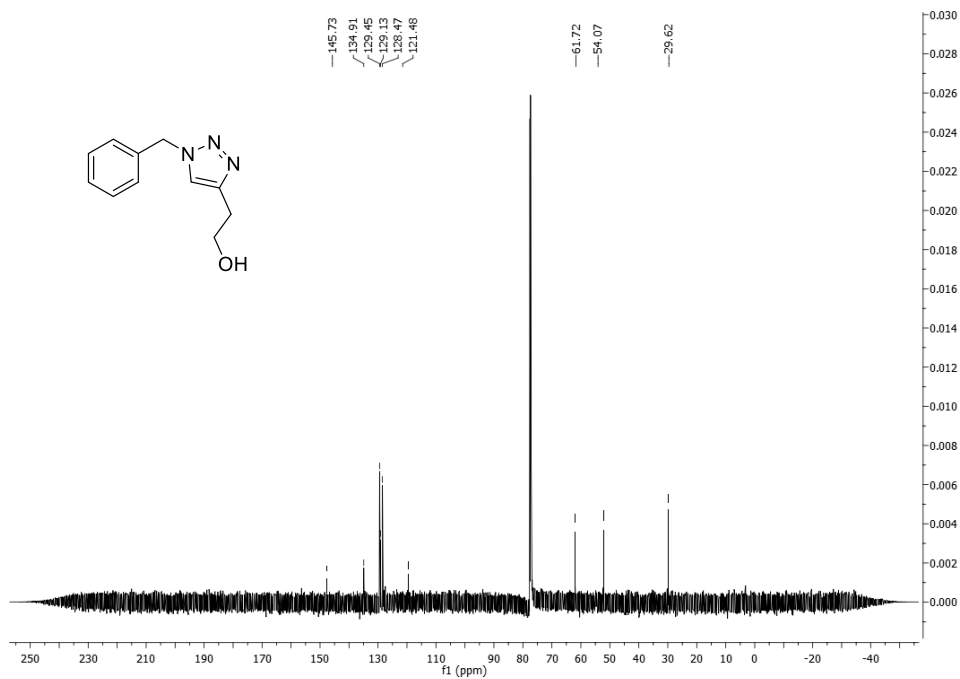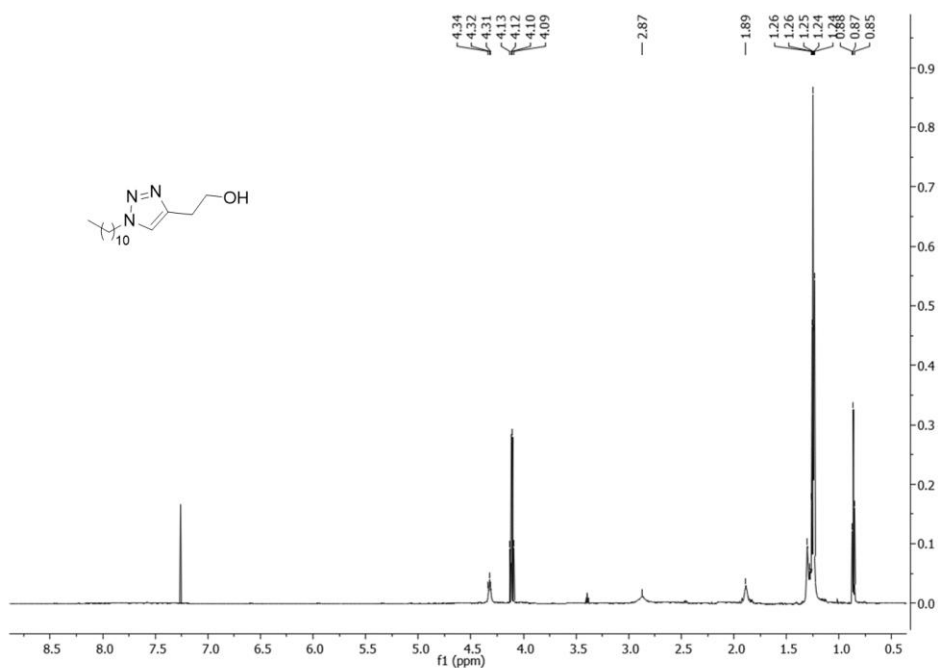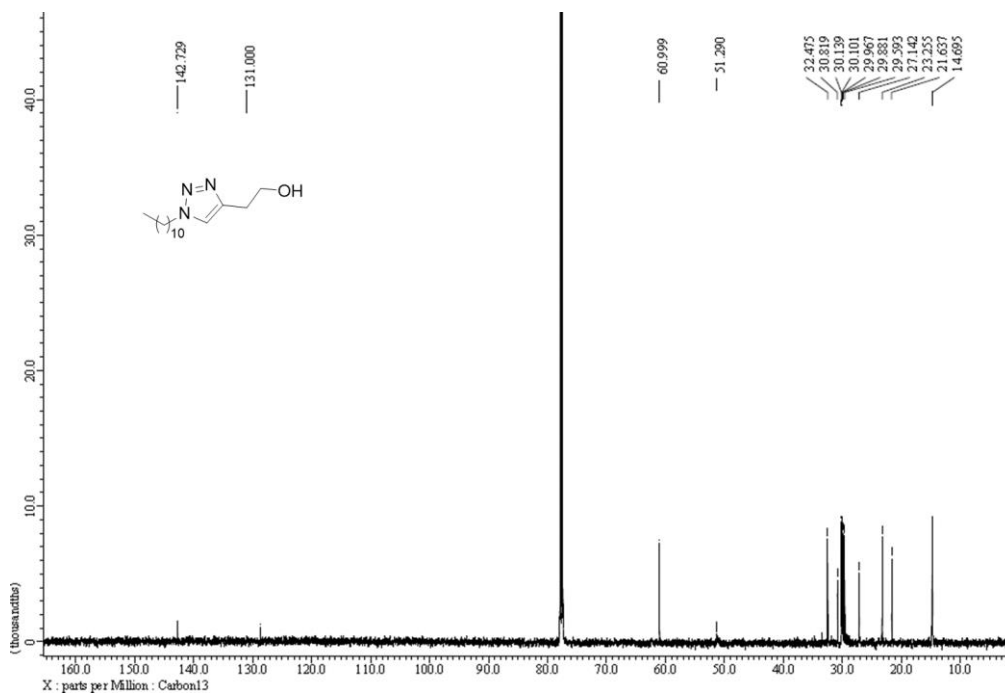**Figure 71.** ^{1}H NMR of 2-(1-benzyl-1H-1,2,3-triazol-4-yl)ethan-1-ol.

Figure 72. ^{13}C NMR of 2-(1-benzyl-1H-1,2,3-triazol-4-yl)ethan-1-ol.

2-(1-undecyl-1H-1,2,3-triazol-4-yl)ethan-1-ol

Figure 73. ^{1}H NMR of 2-(1-undecyl-1H-1,2,3-triazol-4-yl)ethan-1-ol.

Figure 74. ^{13}C NMR of 2-(1-undecyl-1H-1,2,3-triazol-4-yl)ethan-1-ol.
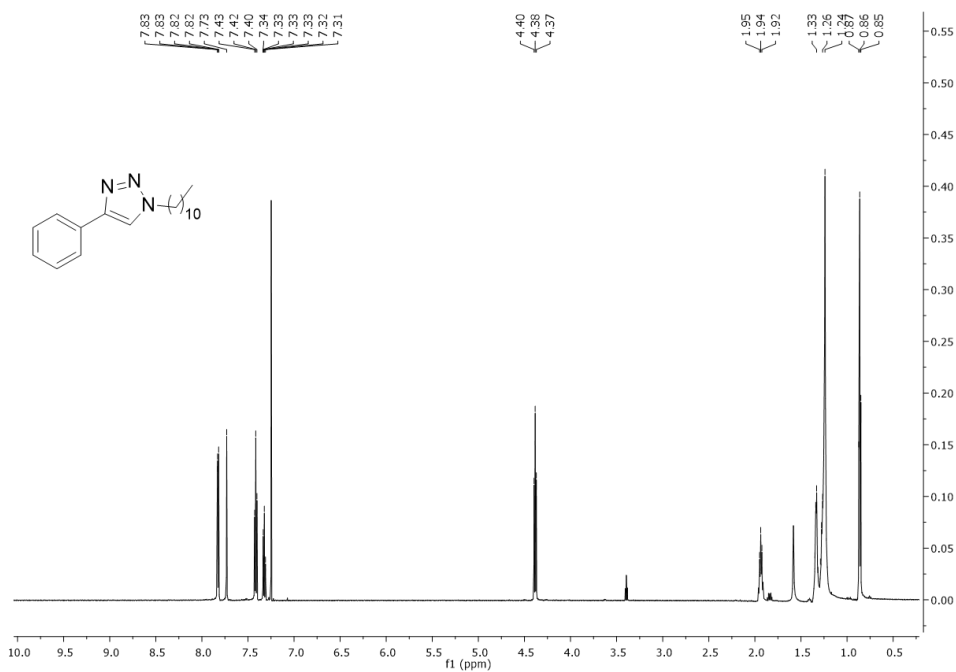
4-phenyl-1-undecyl-1H-1,2,3-triazole

Figure 75. ^{1}H NMR of 4-phenyl-1-undecyl-1H-1,2,3-triazole.
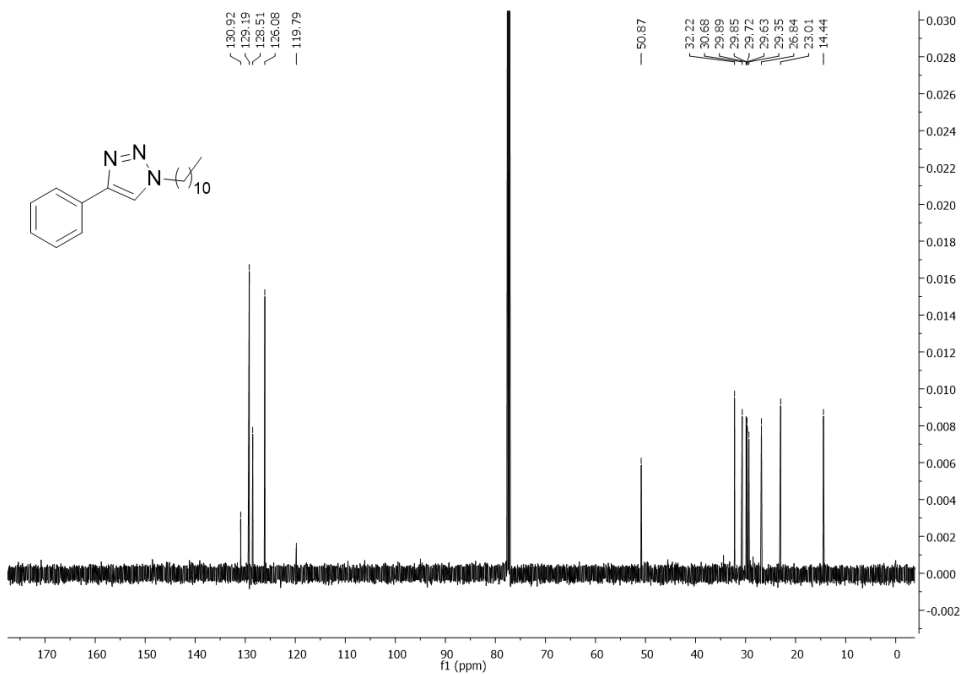

Figure 76. ^{13}C NMR of 4-phenyl-1-undecyl-1H-1,2,3-triazole.

9.2. Surface modification of carbon-based nanomaterials: a study to obtain high degree of functionalization with different dipols

Structural characterization of functionalized rGO and NDs
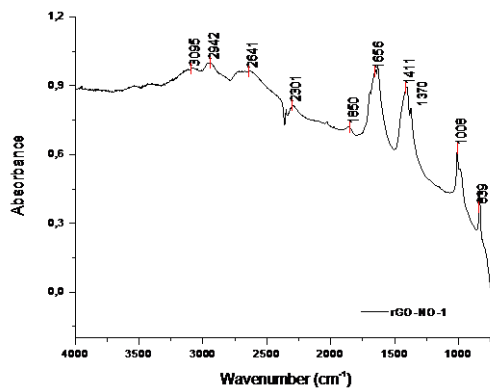

Figure 77. FT-IR spectrum of rGO-NO-1.

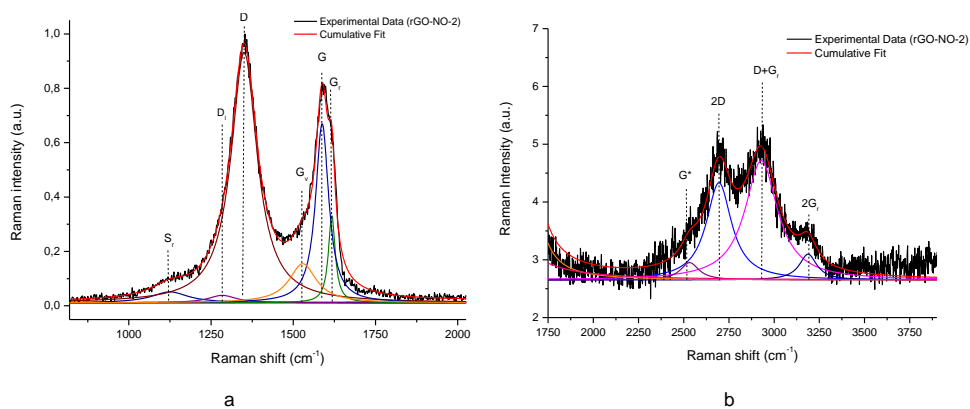a   b

Figure 78. Deconvoluted Raman spectrum of rGO-NO-2.
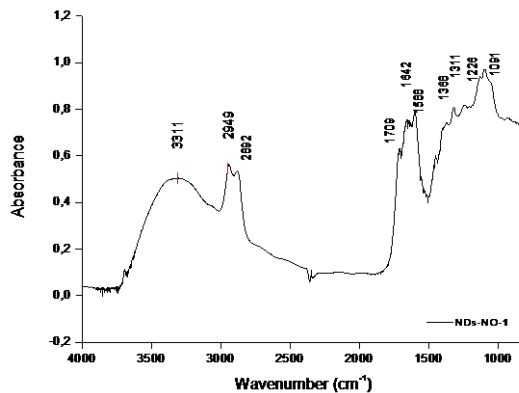

Figure 79. DRIFT spectrum of NDs-NO-1.
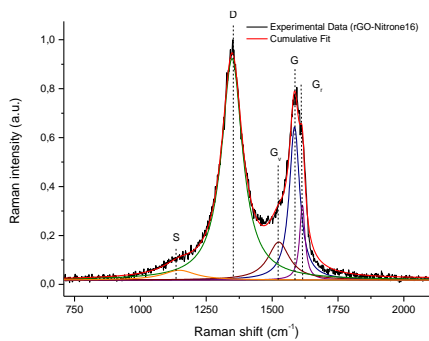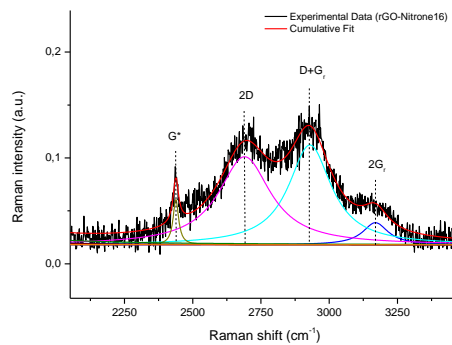
Figure 80. Deconvoluted Raman spectrum of rGO-Nitrone16.
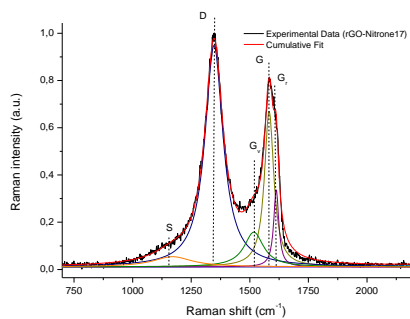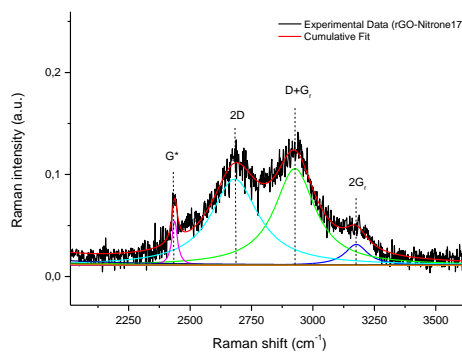
Figure 81. Deconvoluted Raman spectrum of rGO-Nitrone17.
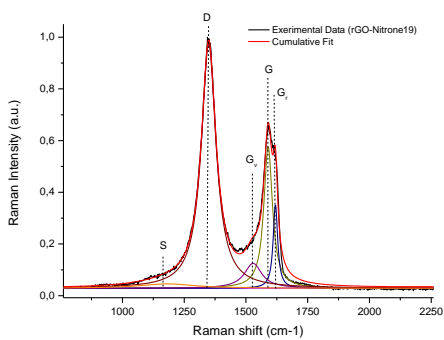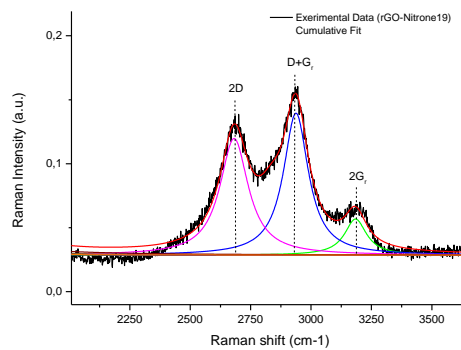
Figure 82. Deconvoluted Raman spectrum of rGO-Nitrone19.

NMR characterization

(9H-fluoren-9-yl)methyl(3-hydroxypropyl)carbamate
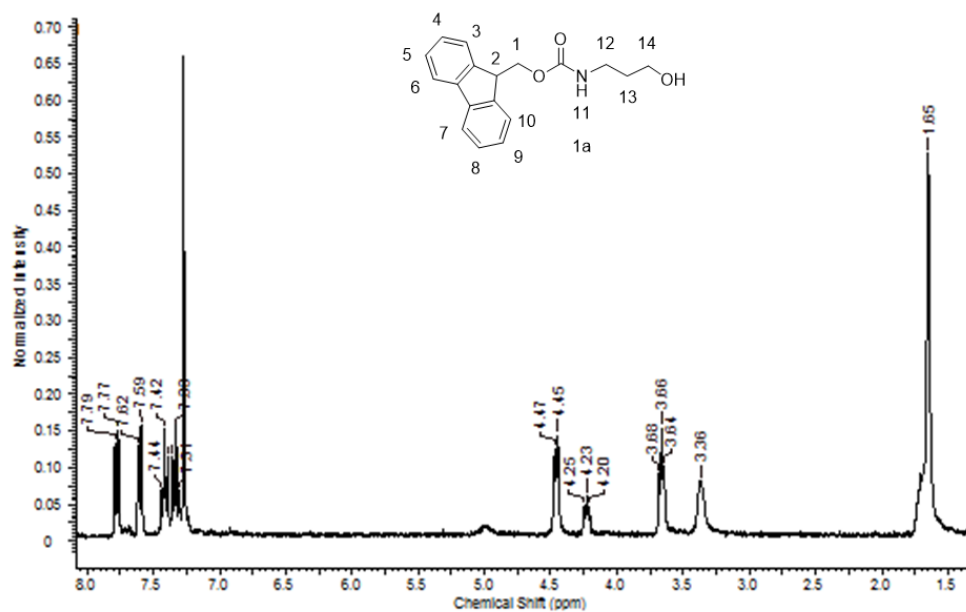
Figure 83. ^{1}H NMR of **1a.**
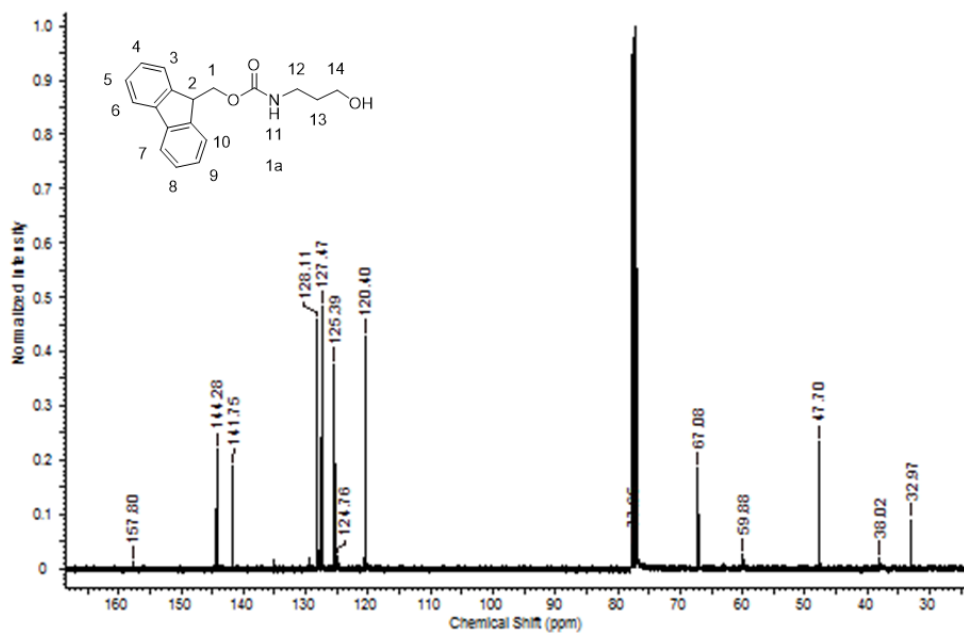
Figure 84. ^{13}C NMR of **1a.**

Figure 85. ESI-MS of **1a.**
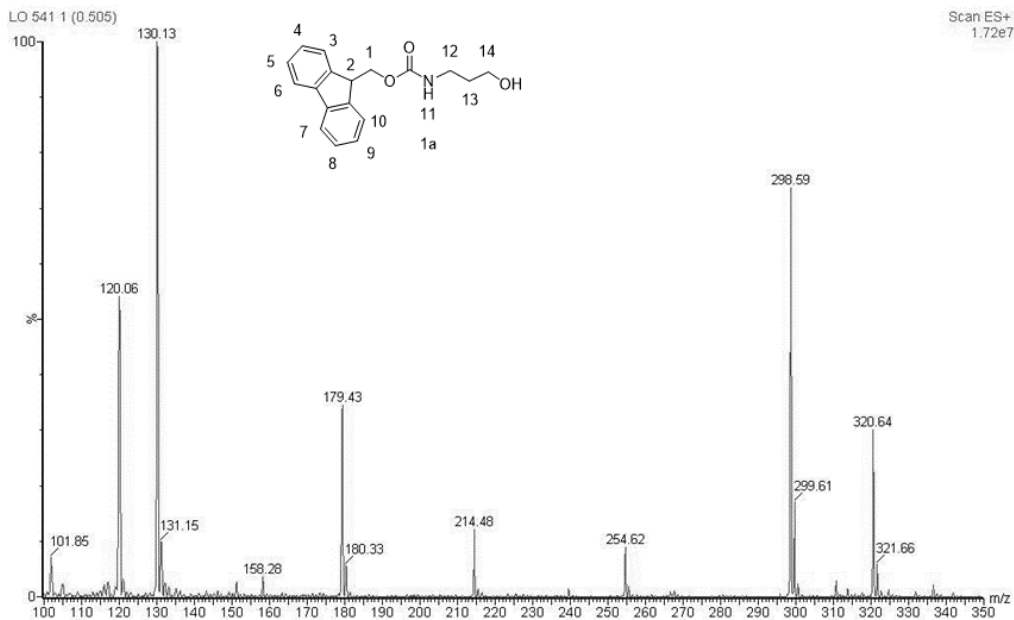
(9H-fluoren-9-yl)methyl(6-hydroxyhexyl)carbamate

Figure 86. ¹H NMR of **1b.**
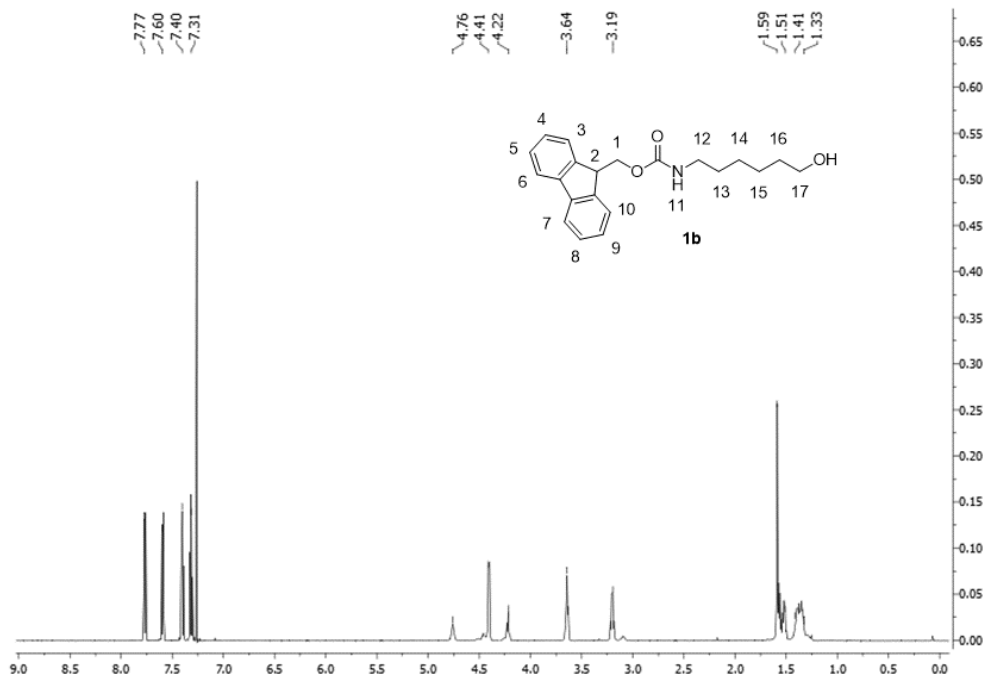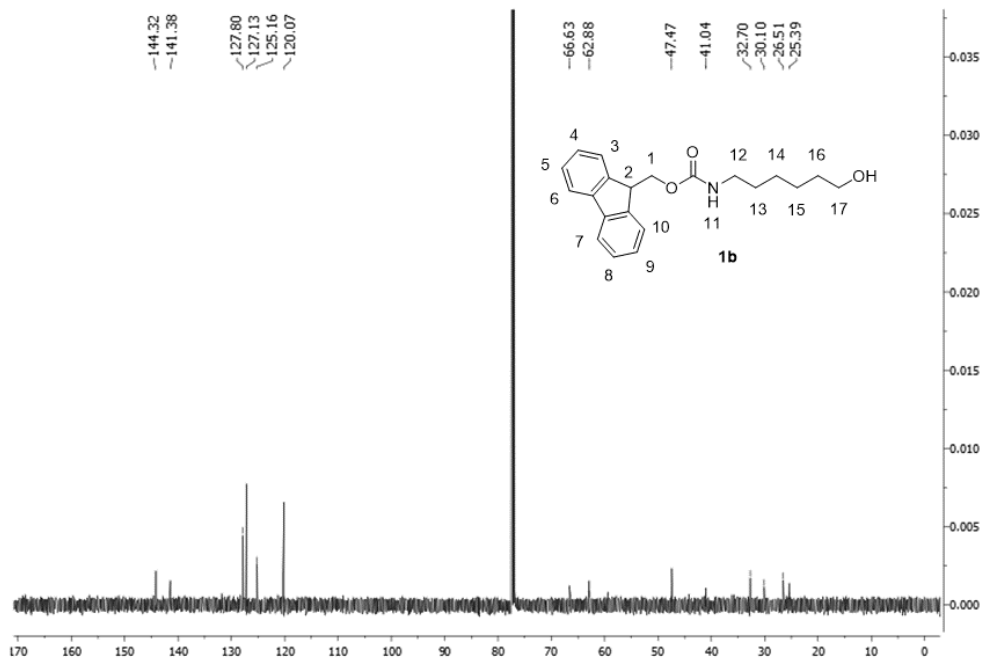
Figure 87. ^{13}C NMR of **1b.**
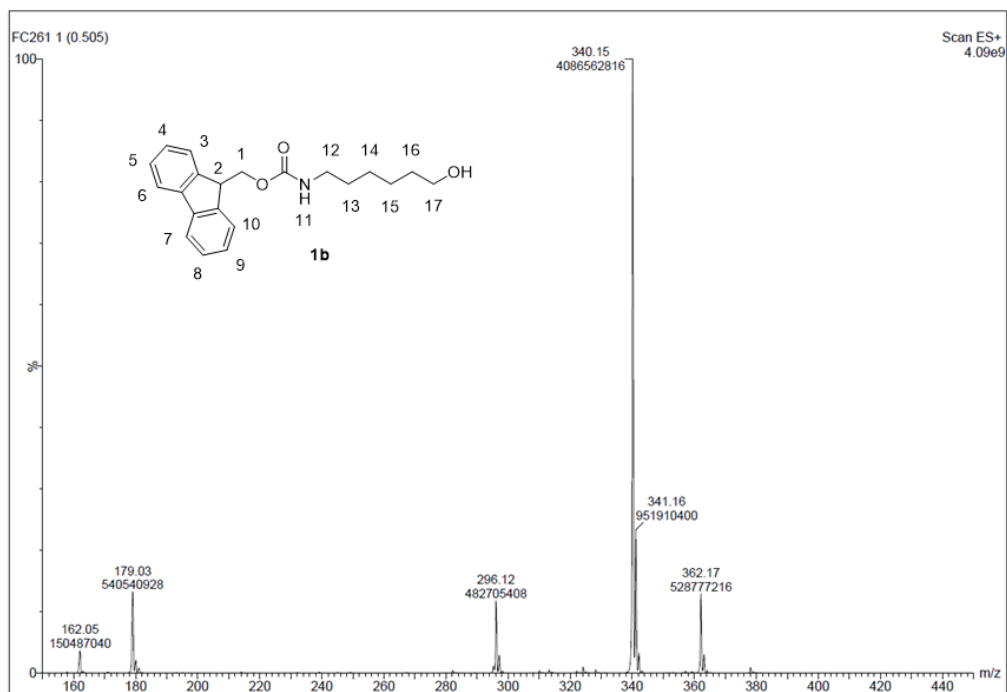
Figure 88. ESI-MS of **1b.**

(9H-fluoren-9-yl)methyl(5-hydroxypentyl) carbamate
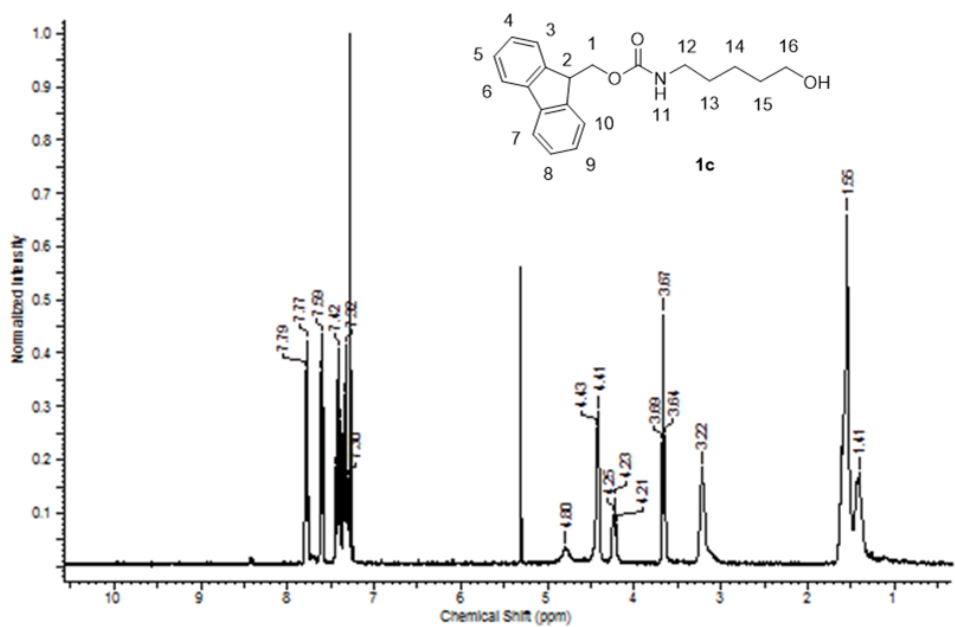
Figure 89. ^{1}H NMR of **1c.**
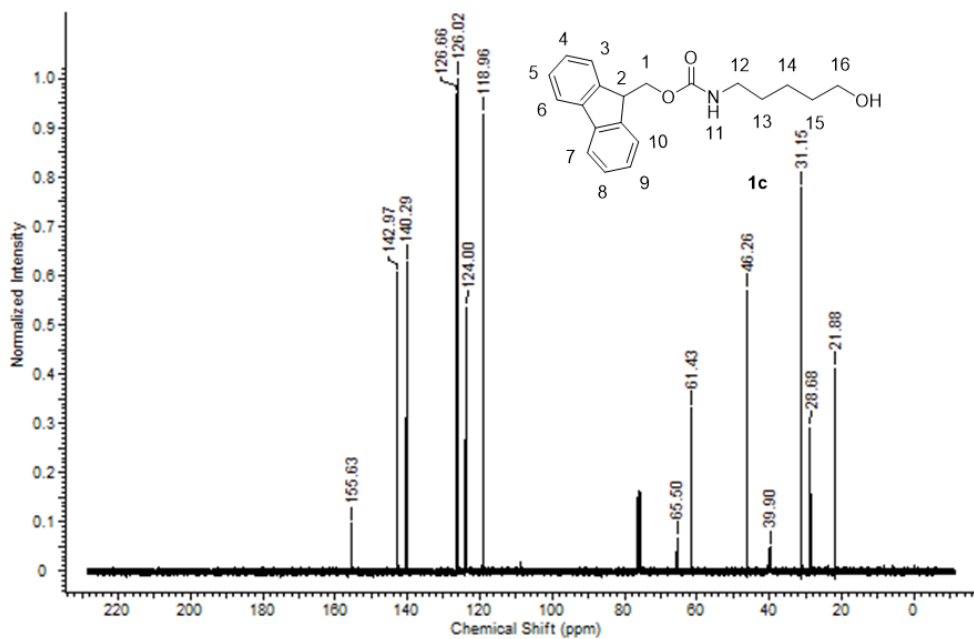
Figure 90. ^{13}C NMR of **1c.**
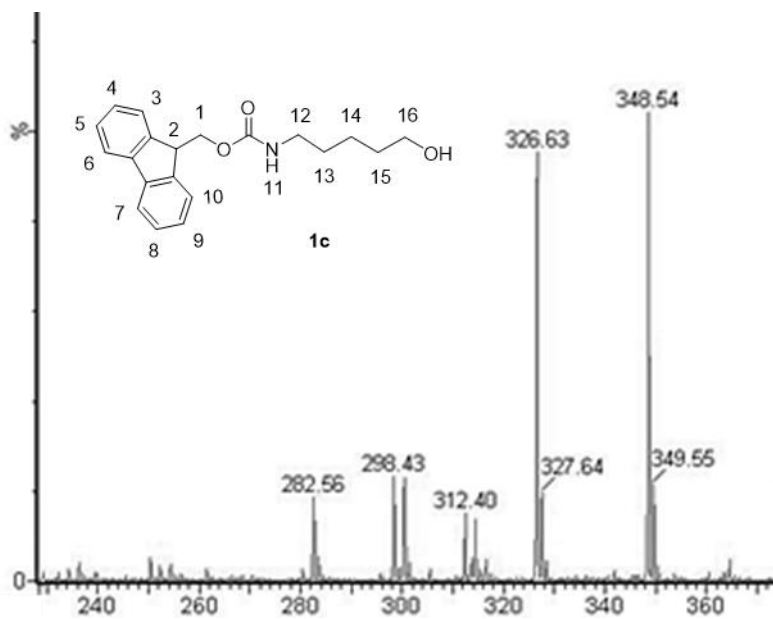
Figure 91. ESI-MS of **1c.**

(9H-fluoren-9-yl)methyl(3-oxopropyl)carbamate
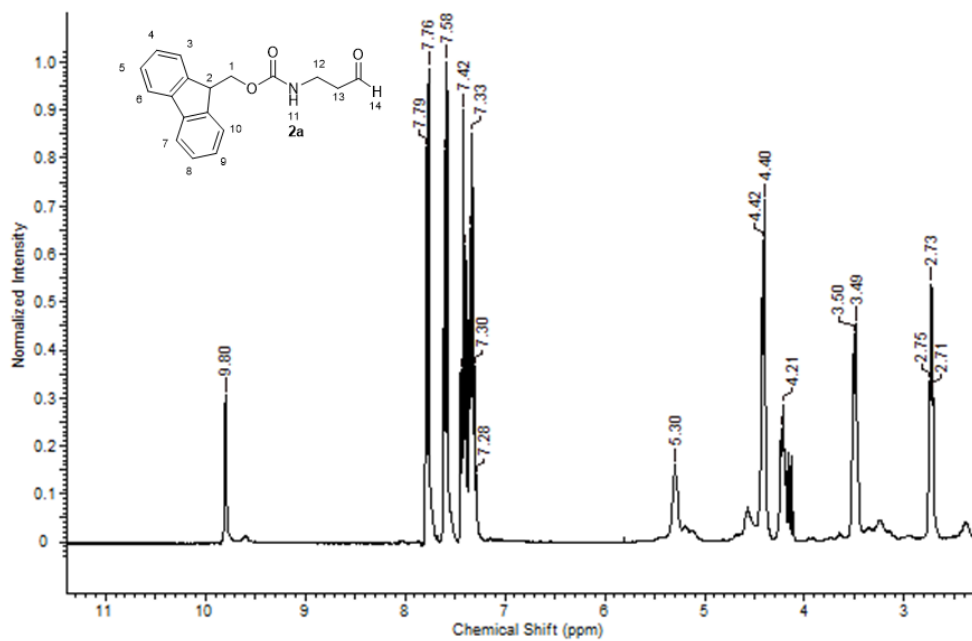
Figure 92. ^{1}H NMR of **2a.**

Figure 93. ^{13}C NMR of **2a.**

SPEC: lo542ai   23-JUL-99   Elapse: 00:01:01.7   46
Samp: 23/07/2014   Start : 15:00:41   72
Comm: id ci iBu 5500 mtorr (295)
Mode: CI +QlMS LMR UP LR
Oper: d. l.   Client: Giancarlo Cravotto   Inlet : DIP
Base: 296.2   Inten : 3334296   Masses: 230 > 350
Norm: 296.2   RIC   : 5026770   #peaks: 104
Peak: 1000.00   mmu
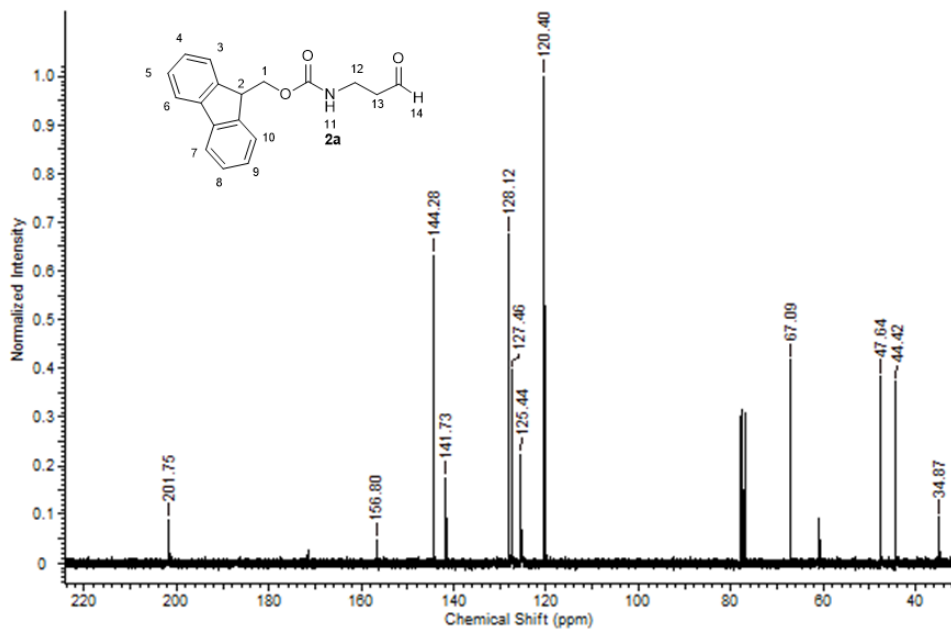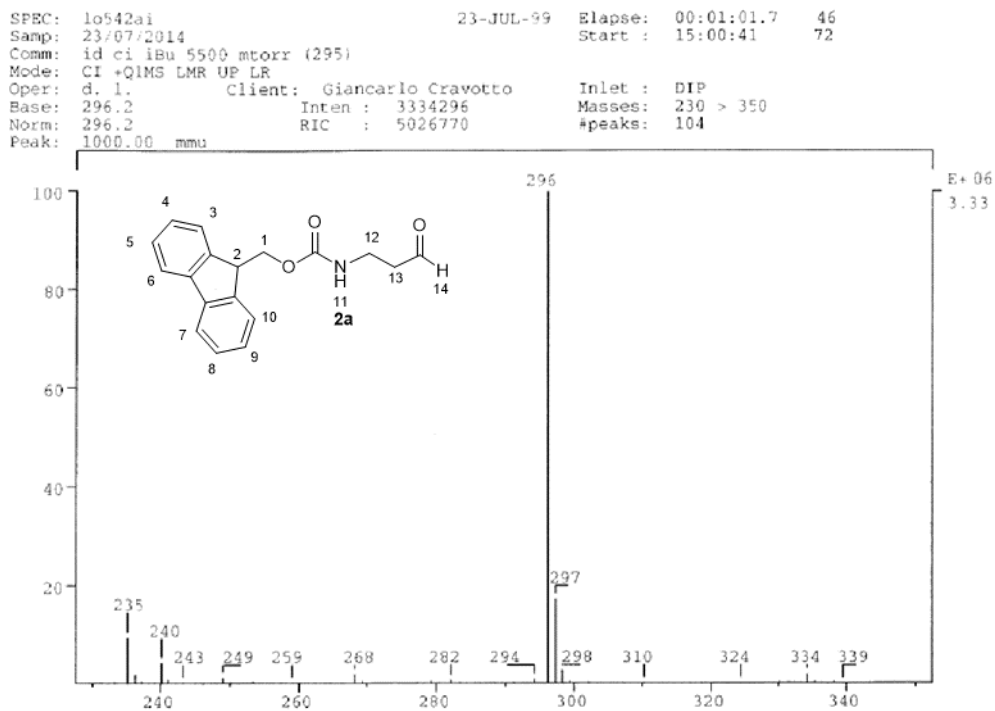
Figure 94. CI-MS spectrum of **2a.**

(9H-fluoren-9-yl)methyl (5-oxohexyl)carbamate (5)
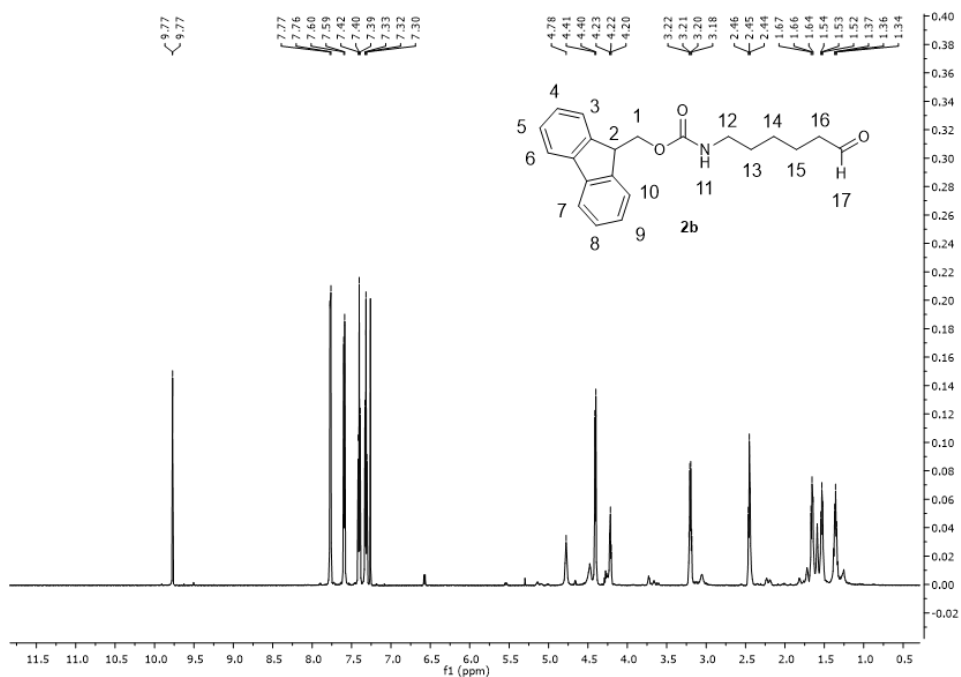
Figure 95. ^{1}H NMR of **2b.**
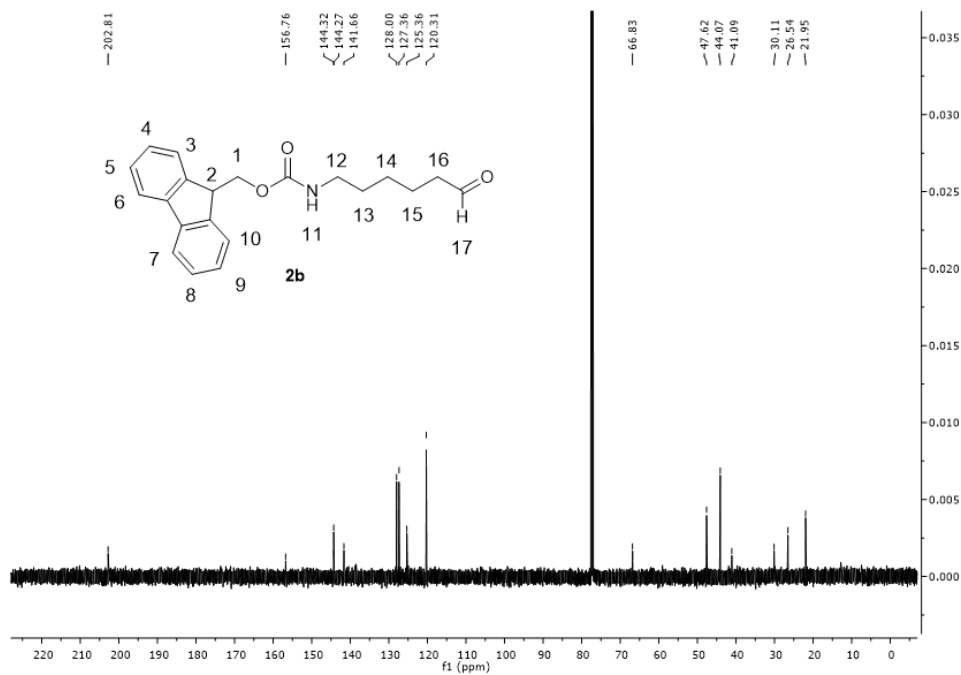
Figure 96. ^{13}C NMR of **2b.**
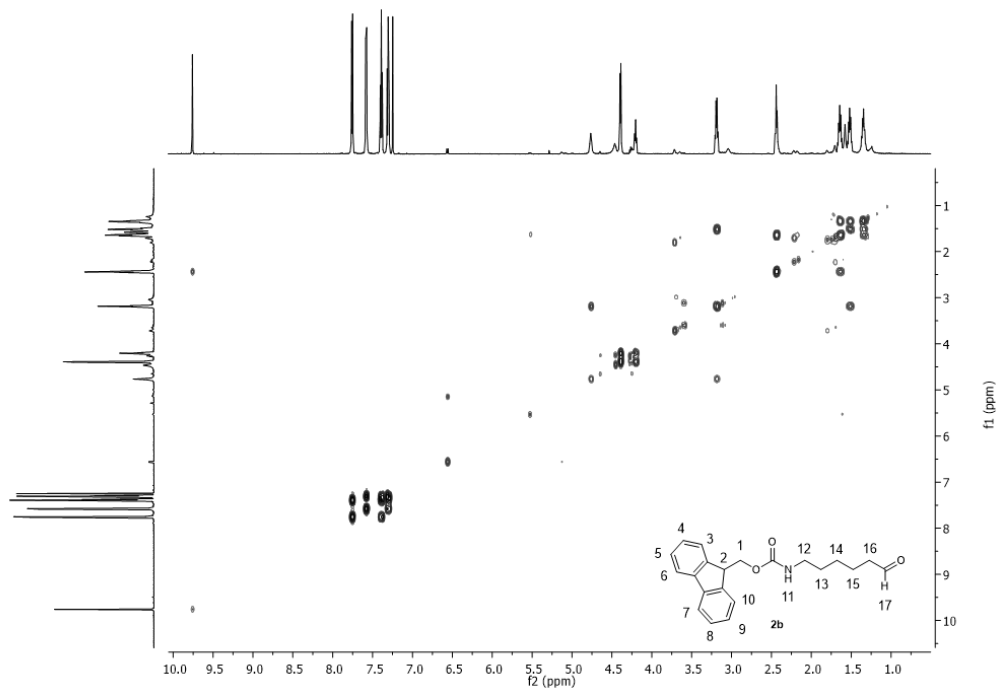
Figure 97. COSY NMR of **2b.**

9
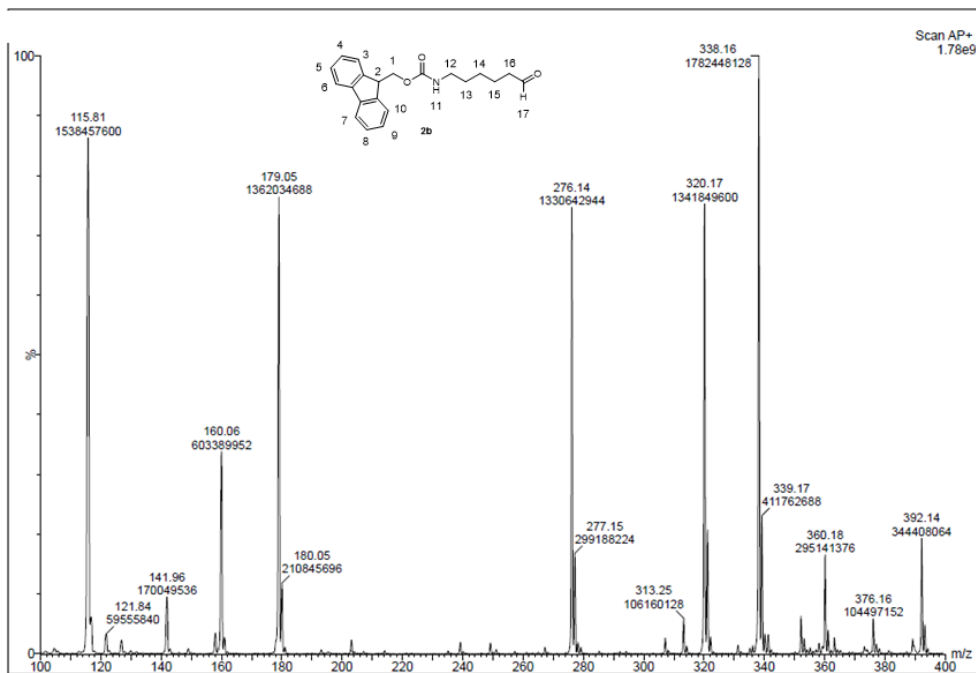
Figure 98. ESI-MS of **2b.**

(9H-fluoren-9-yl)methyl 3,4-dihydroxypiyridine-1(2H)carboxylate

Figure 99. ^{1}H NMR of **3.**

Figure 100. ^{13}C NMR of **3**.
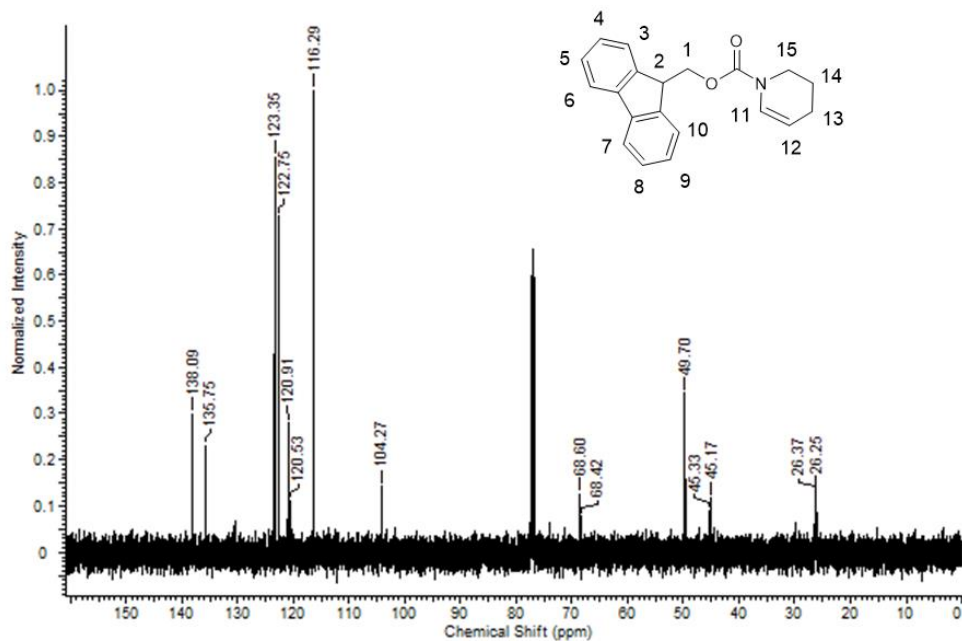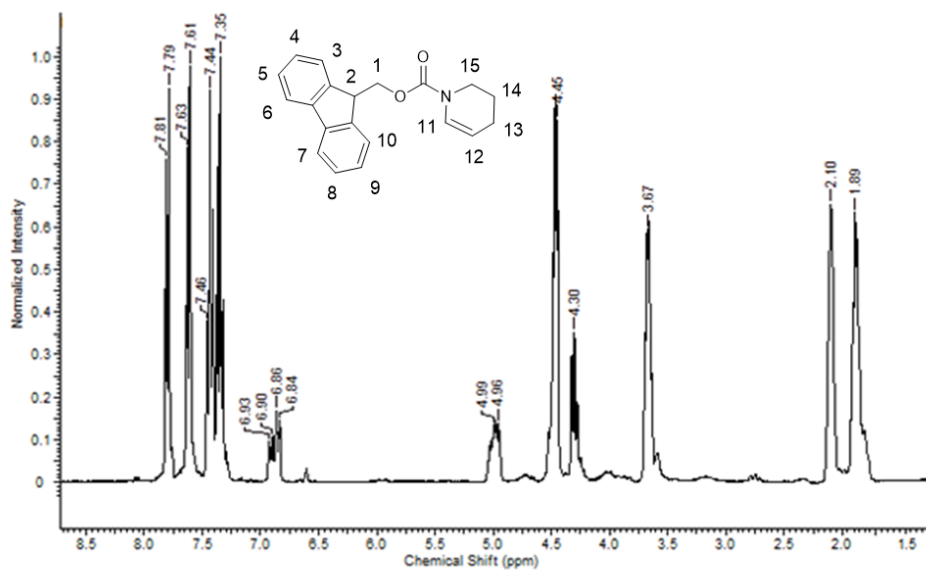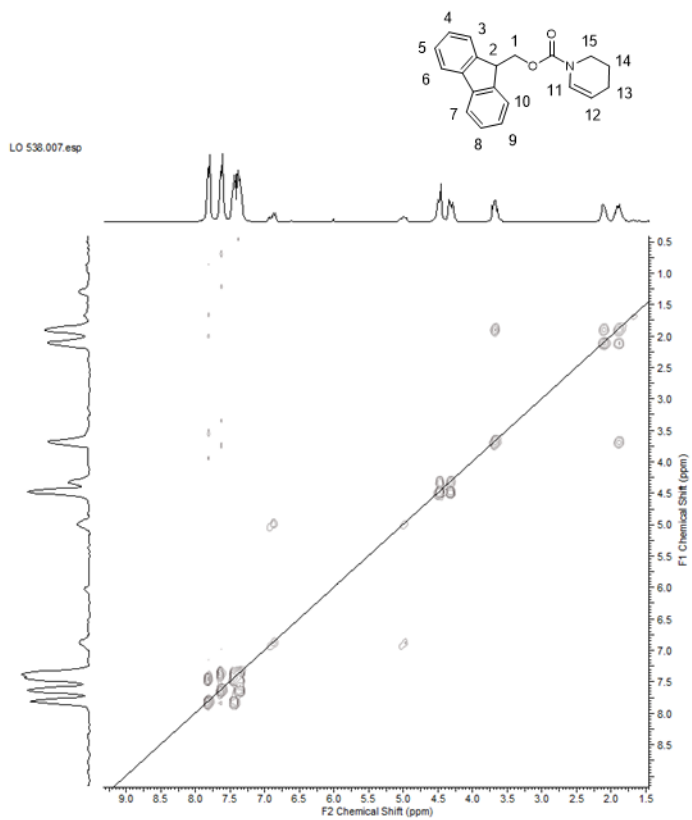
Figure 101. COSY NMR of **3**.
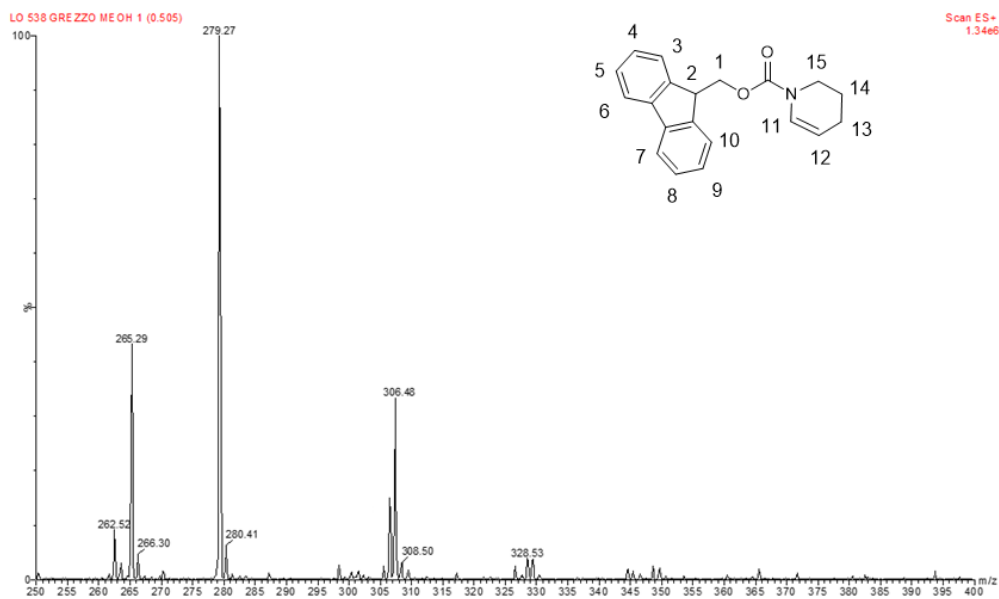
Figure 102. ESI-MS of **3**.

(9H-fluoren-9-yl)methyl(6-(hydroxyimino)hexyl)carbamate
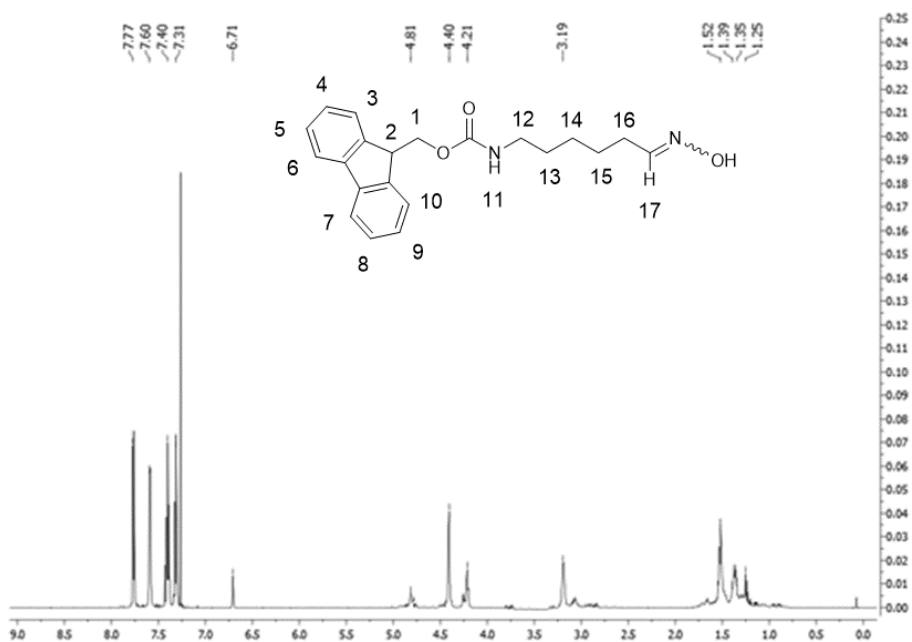
Figure 103. ^{1}H NMR of **4.**
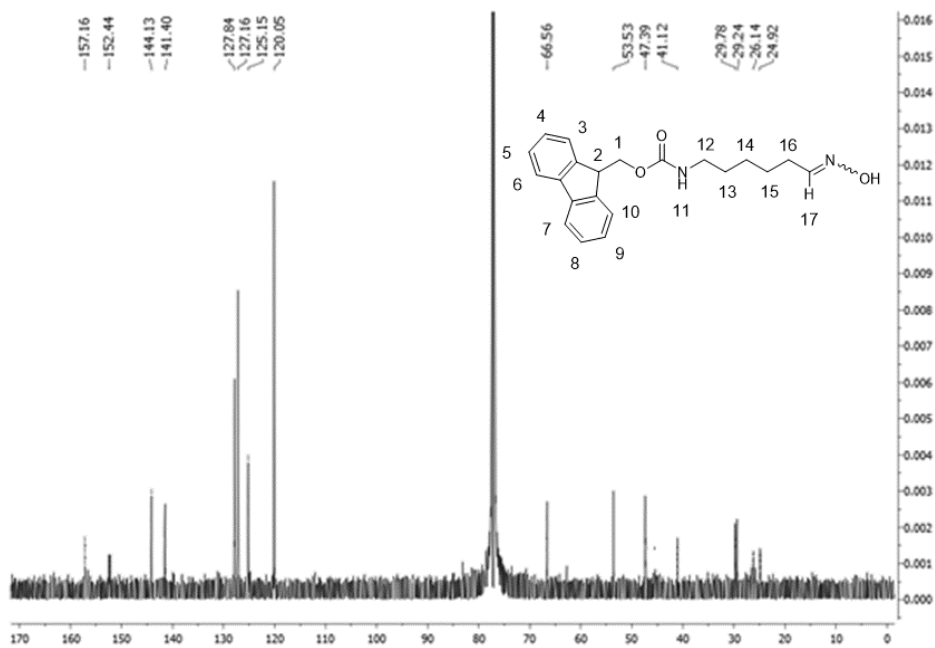
Figure 104. ^{13}C NMR of **4.**
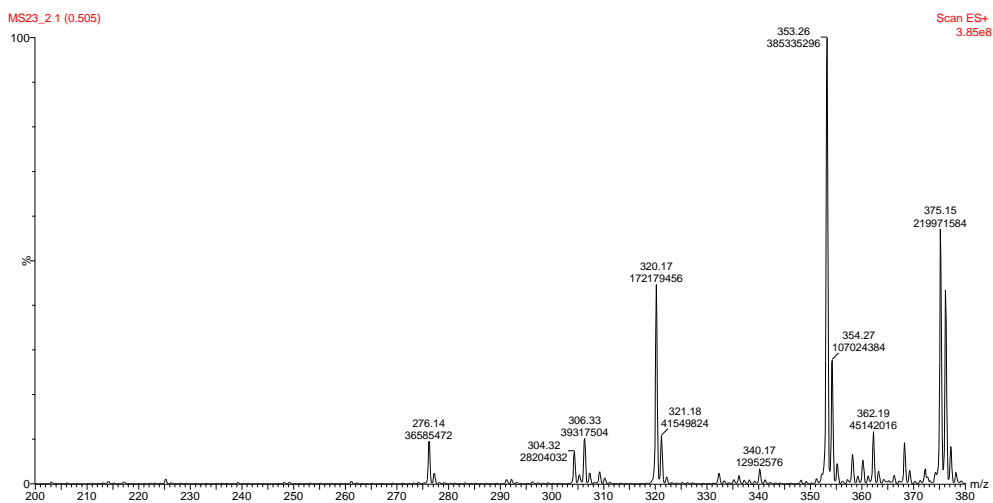
Figure 105. ESI-MS of **4**.

(9H-fluoren-9-yl)methyl (6-chloro-6-(hydroxyimino)hexyl)carbamate
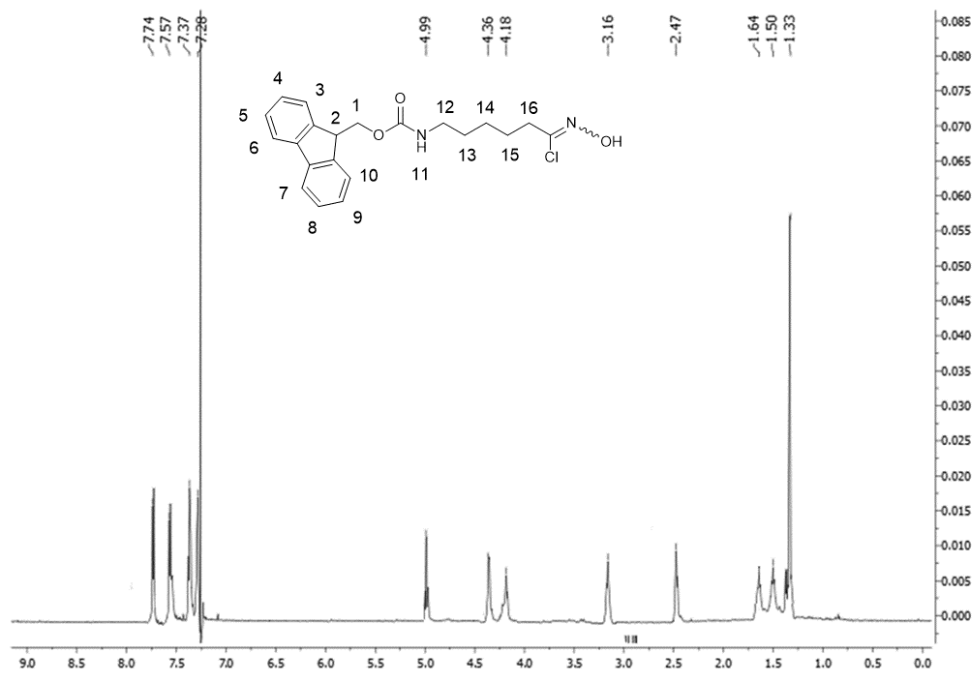
Figure 106. ^{1}H NMR of **5.**
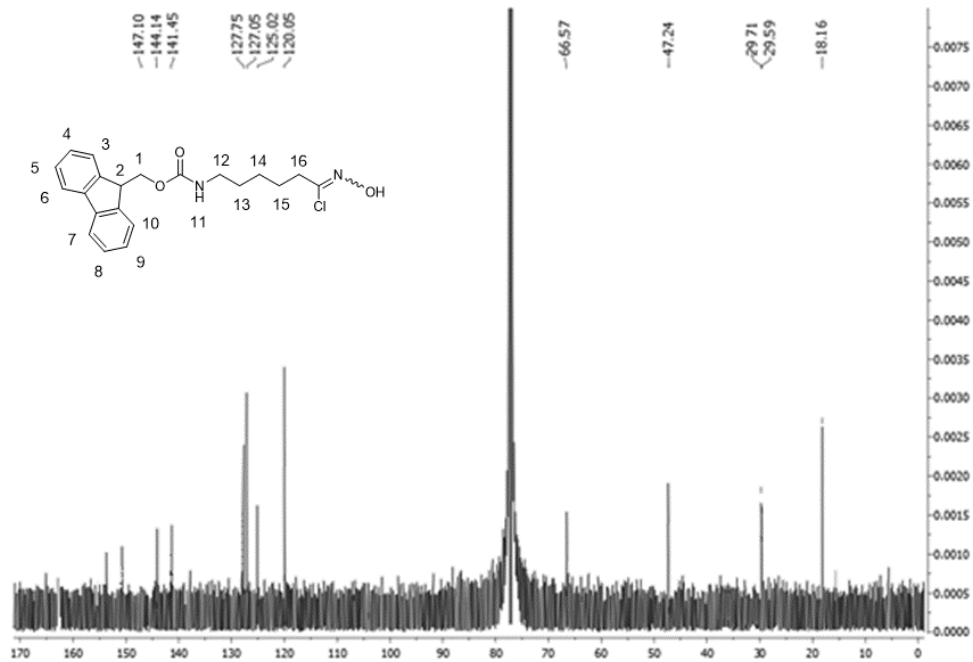
Figure 107. ^{13}C NMR of **5.**
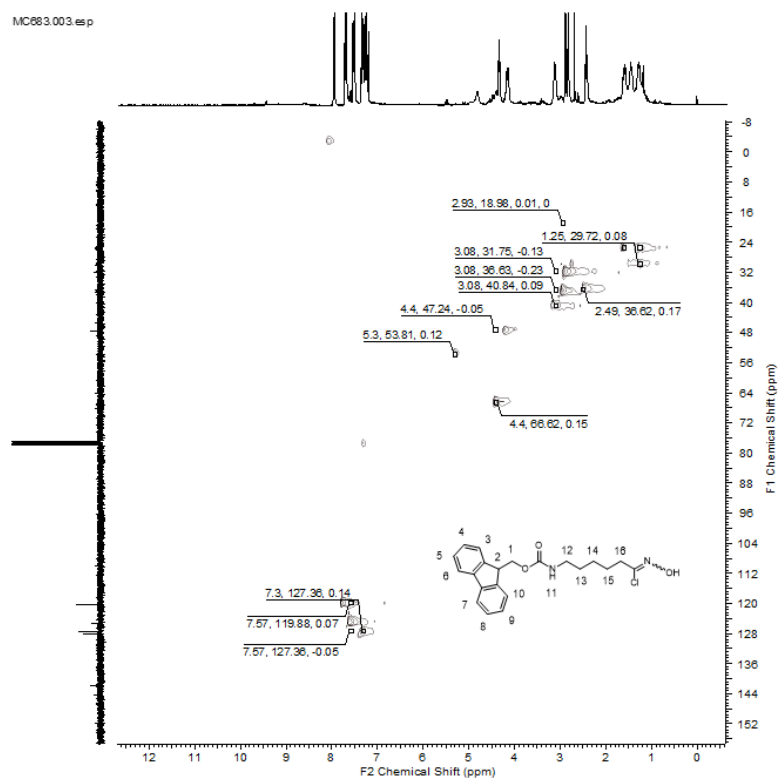
Figure 108. HMQC (^{1}H, ^{13}C) NMR of **5.**

2-(4-nitrophenyl)-1,3-dioxolane
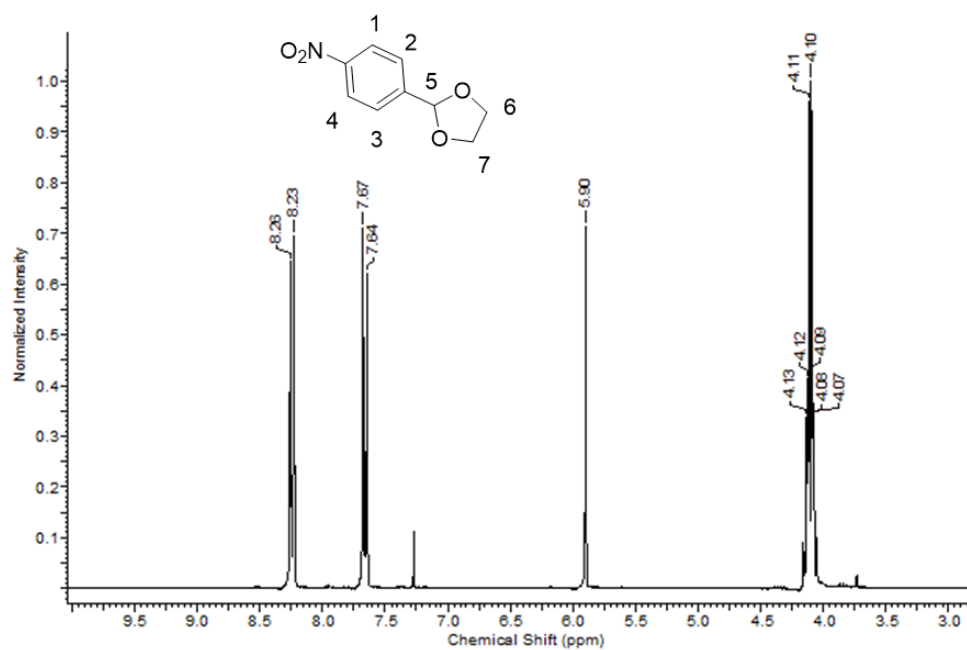
Figure 109. ^{1}H NMR of **6.**
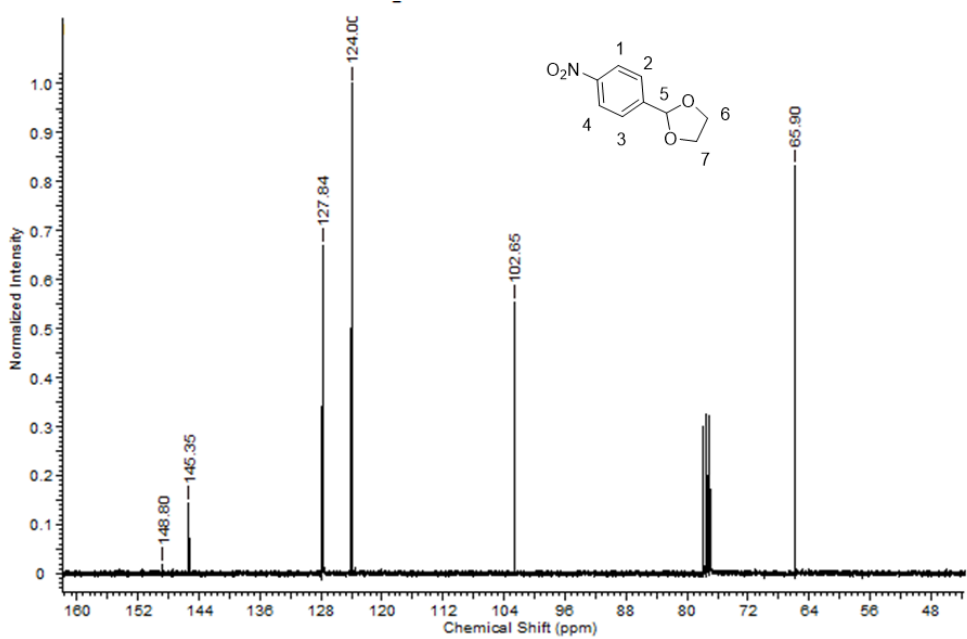
Figure 110. ^{13}C NMR of **6.**

Figure 111. ESI-MS of **6**.
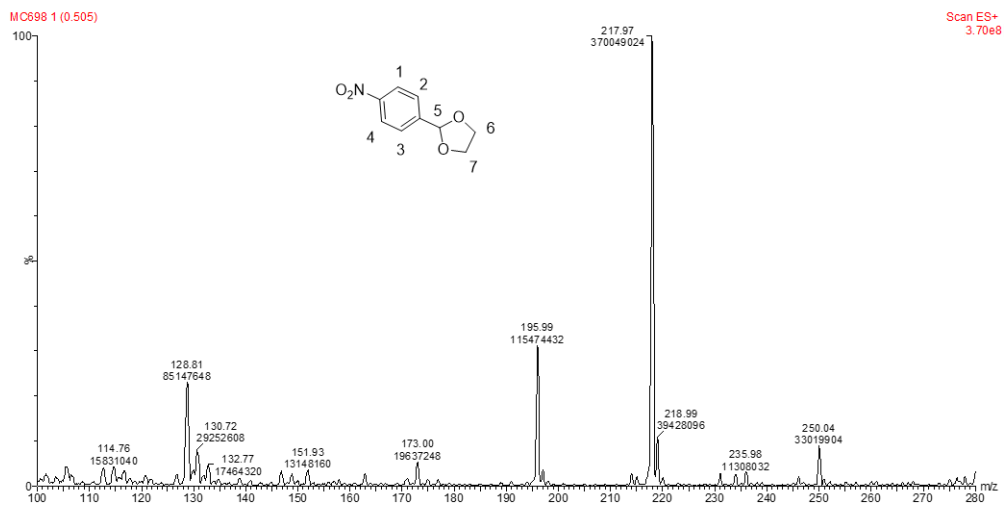
4-(1,3-dioxolan-2-yl)aniline

Figure 112. ^{1}H NMR of **7.**
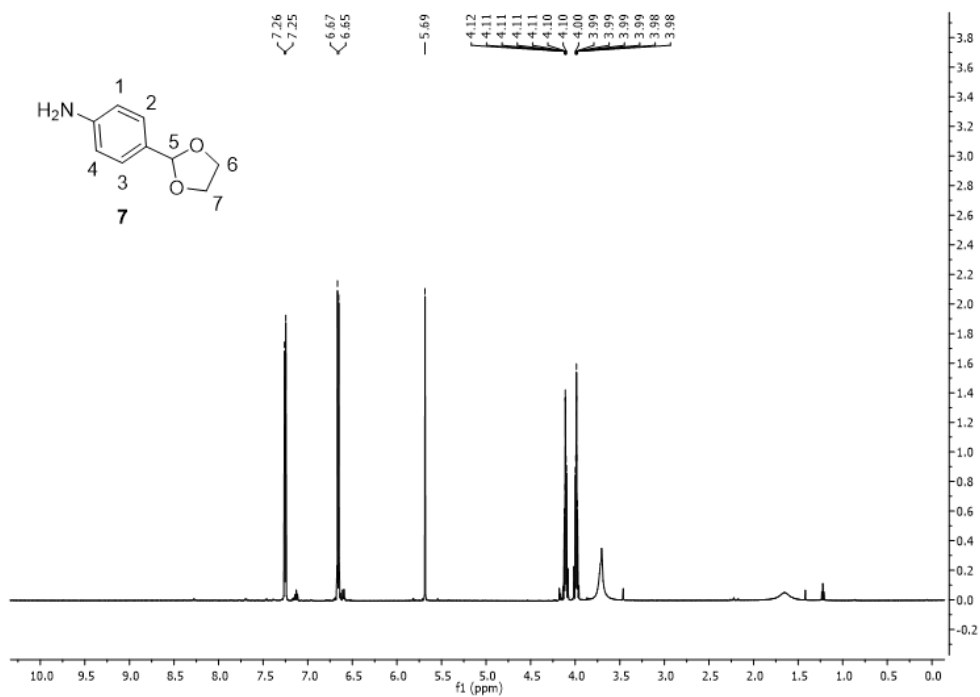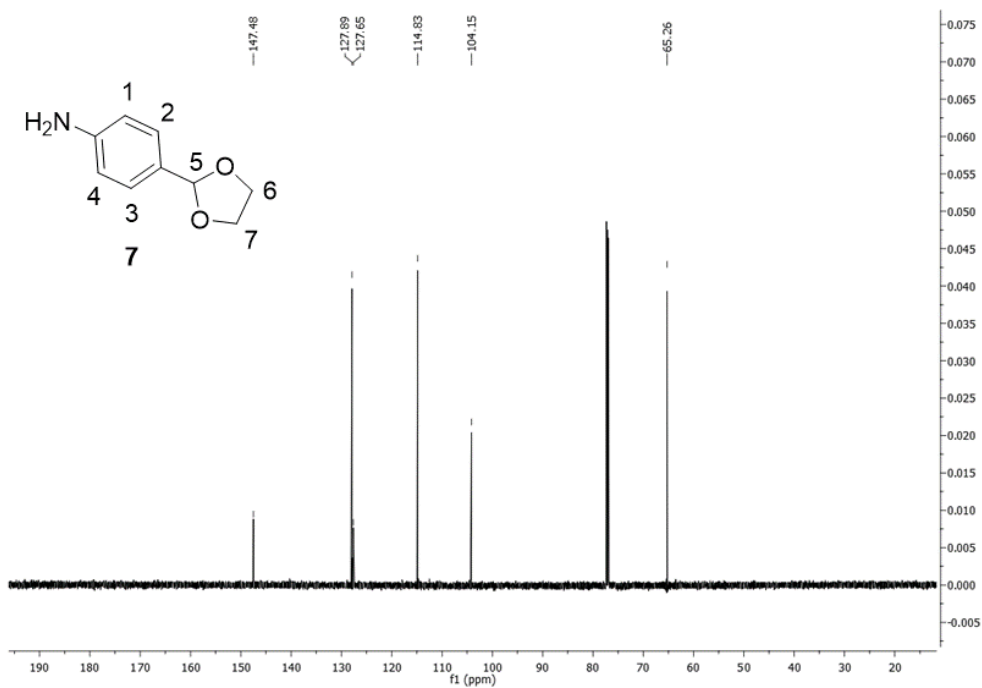
Figure 113. ^{13}C NMR of **7.**
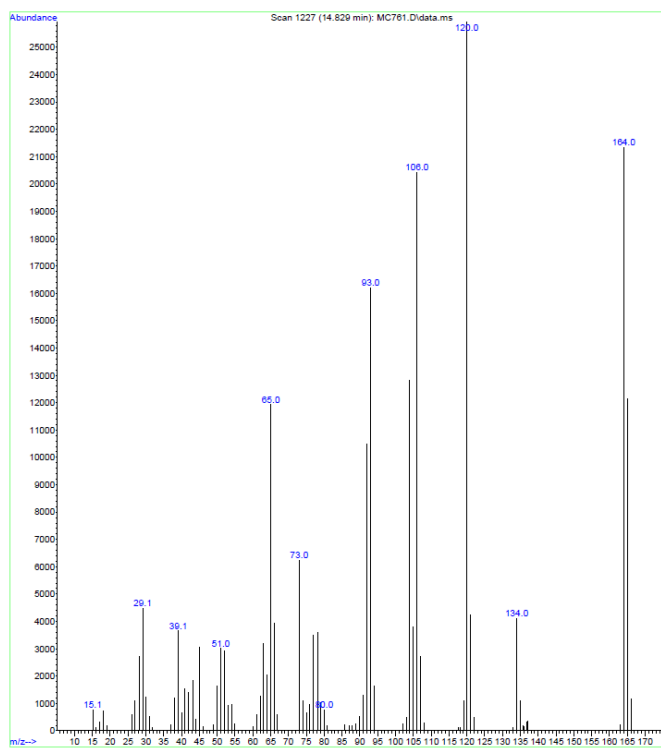
Figure 114. EI-MS of **7.**

207

(9H-fluoren-9-yl)methyl(4-(1,3-dioxolan-2-yl)phenyl)carbamate
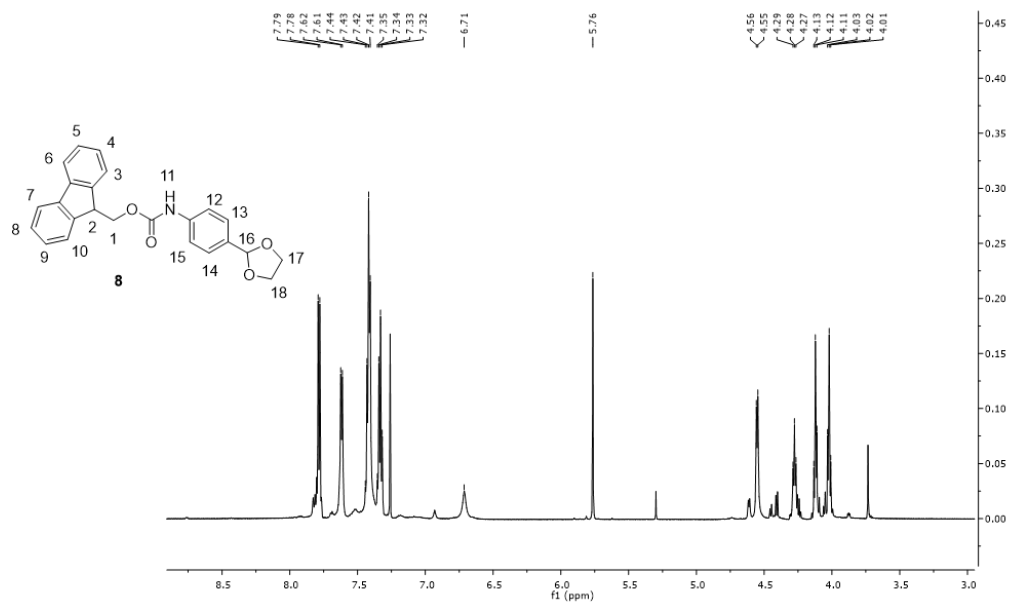
Figure 115. ^{1}H NMR of **8.**
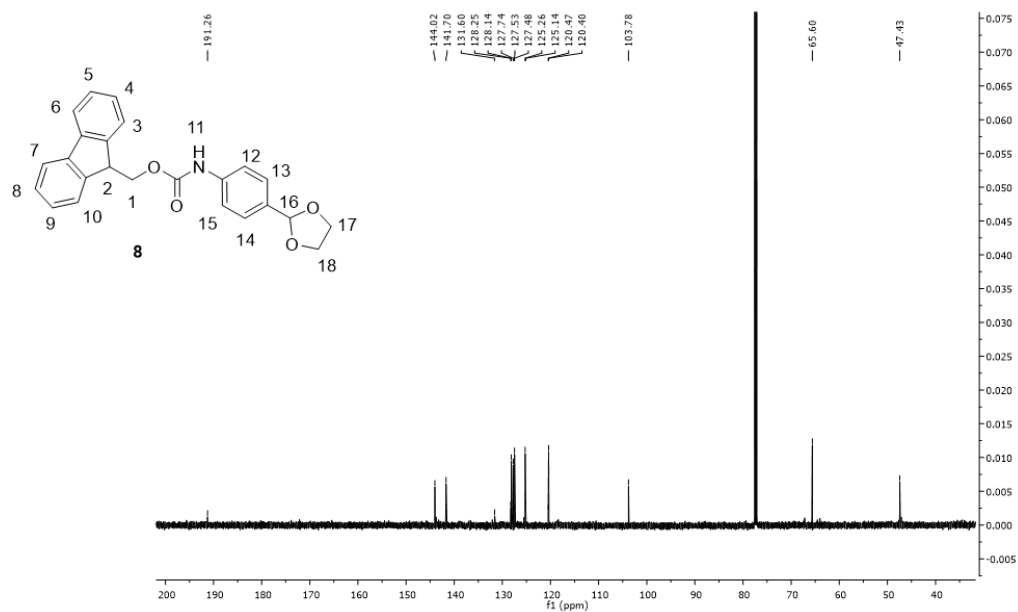
Figure 116. ^{13}C NMR of **8.**

208
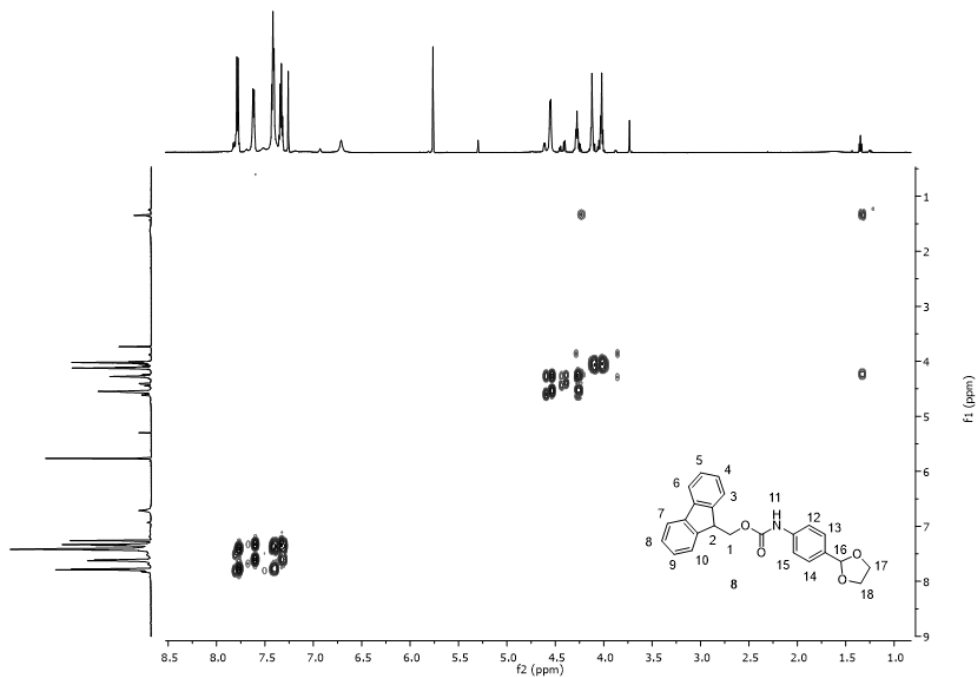
Figure 117. COSY NMR of **8.**
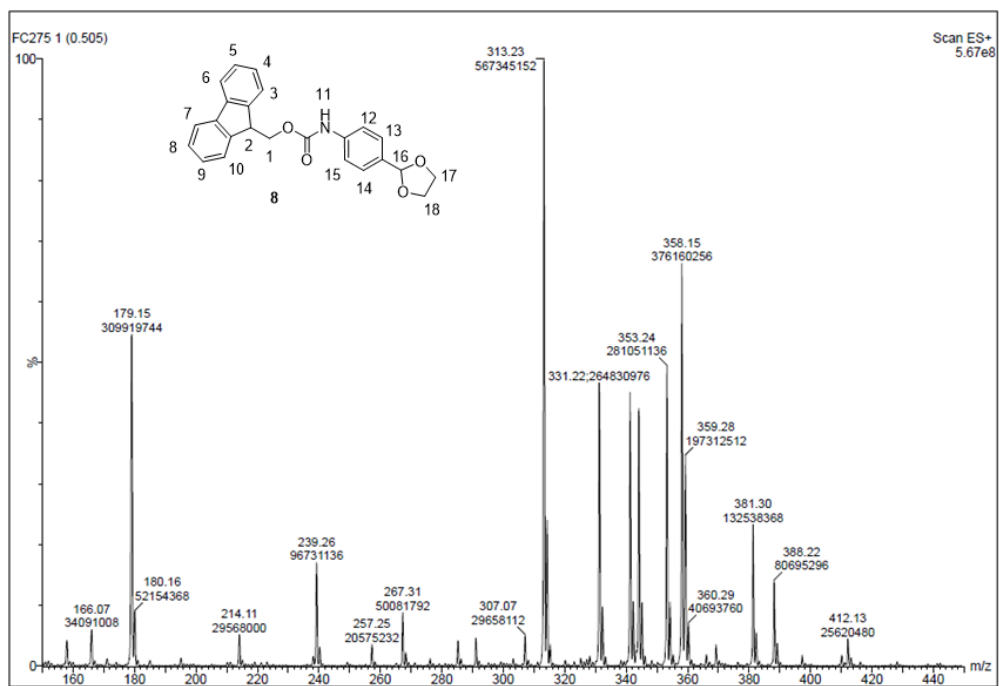
Figure 118. ESI-MS of **8.**

(9H-fluoren-9-yl)methyl(4-formylphenyl)carbamate
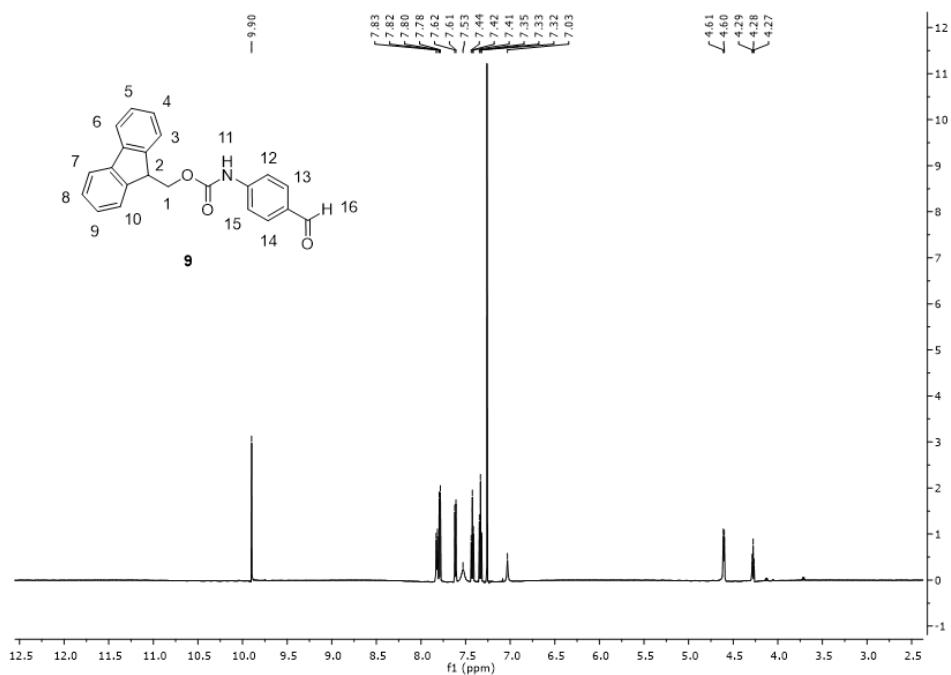
Figure 119. ^{1}H NMR of **9.**
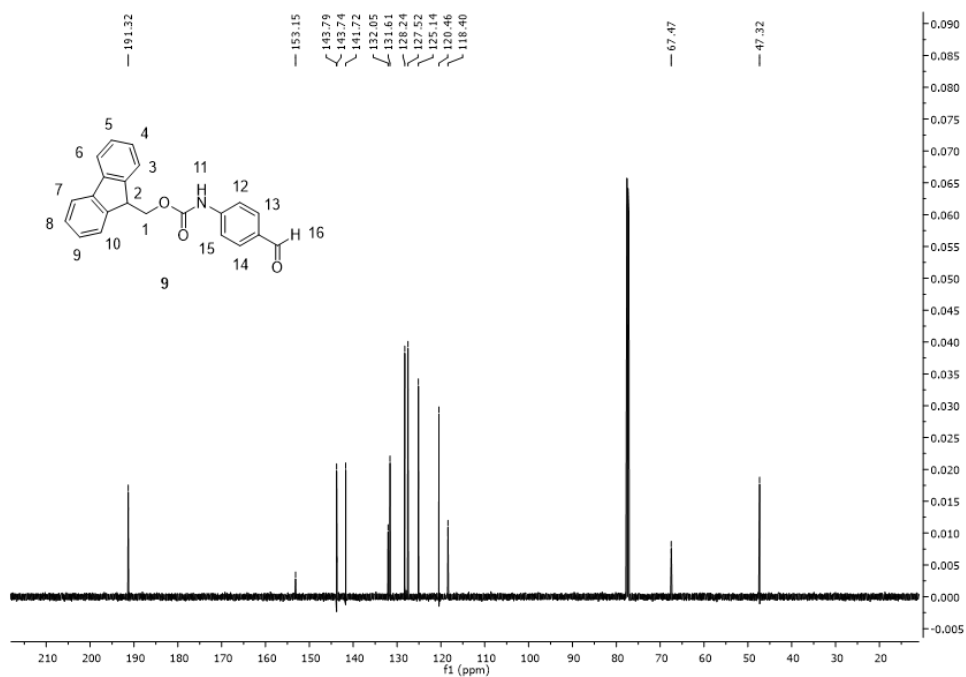
Figure 120. ^{13}C NMR of **9.**
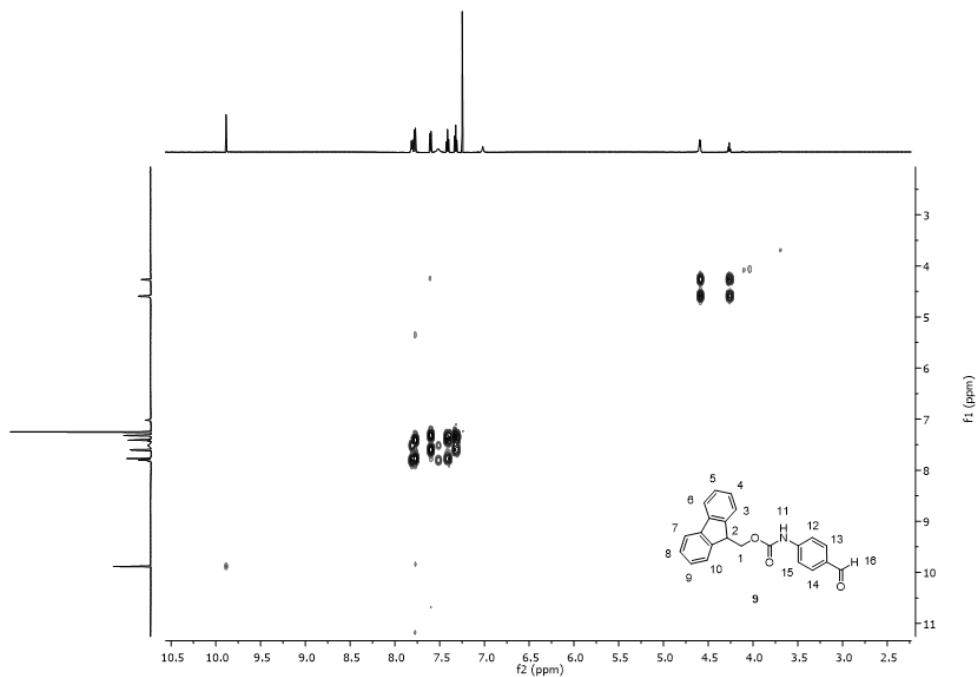
Figure 121. COSY NMR of **9.**
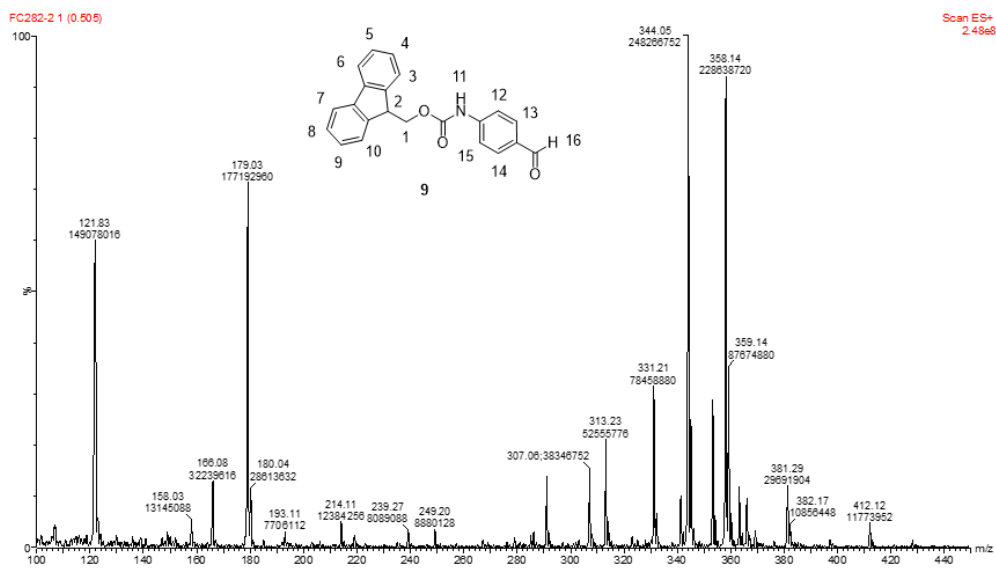
Figure 122. ESI-MS of **9**.

(9H-fluoren-9-yl)methyl (4-((hydroxyimino)methyl)phenyl)carbamate
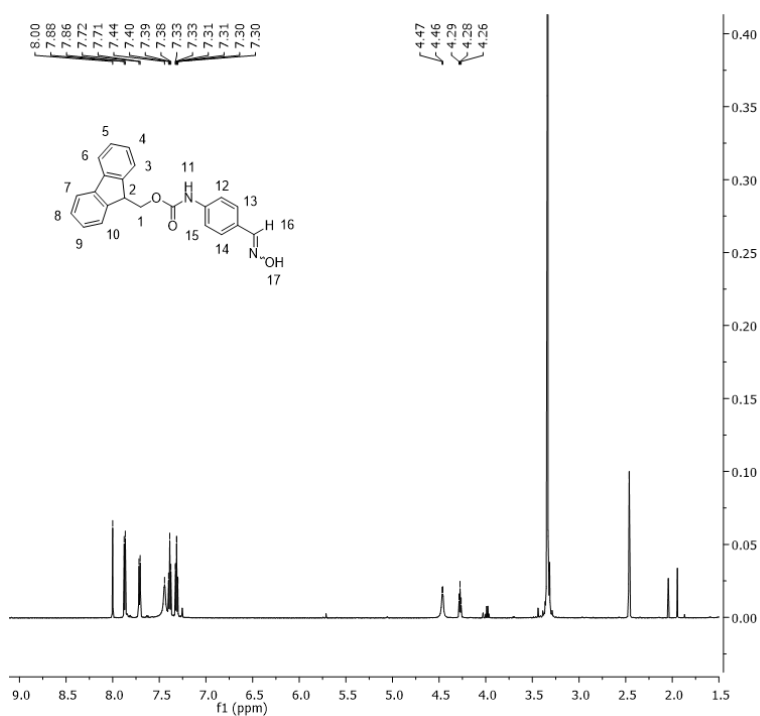
Figure 123. ^{1}H NMR of **10.**
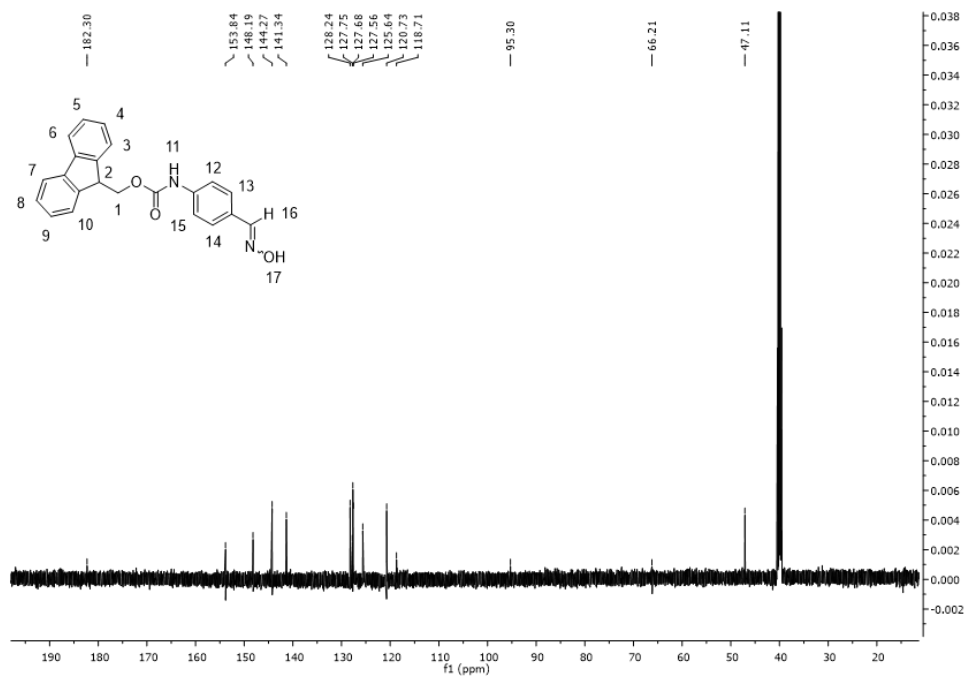
Figure 124. ^{13}C NMR of **10.**
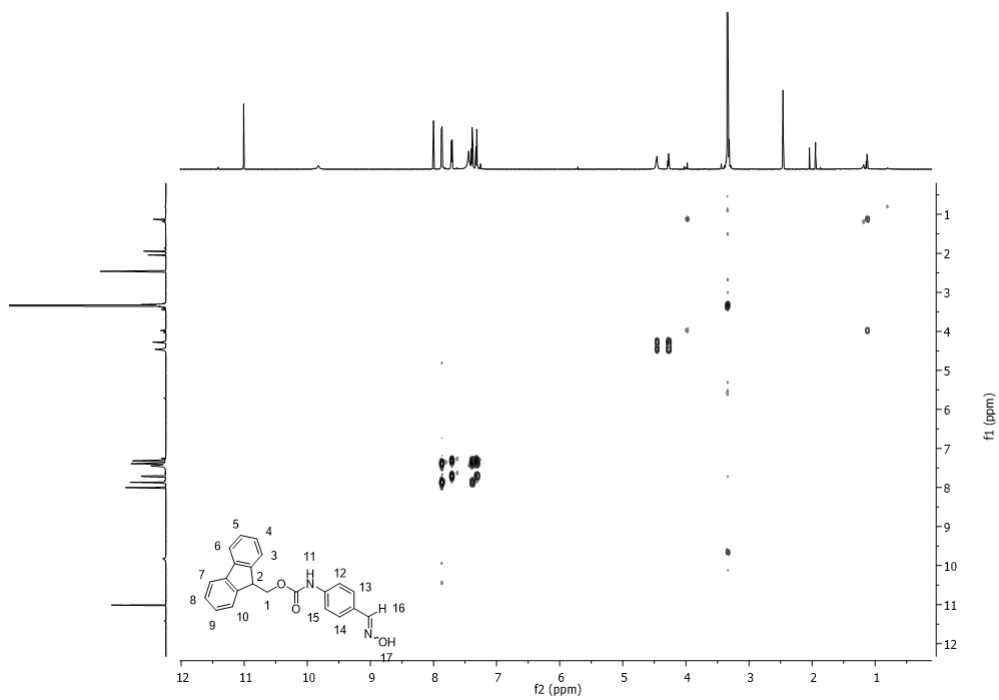
Figure 125. COSY NMR of **10.**
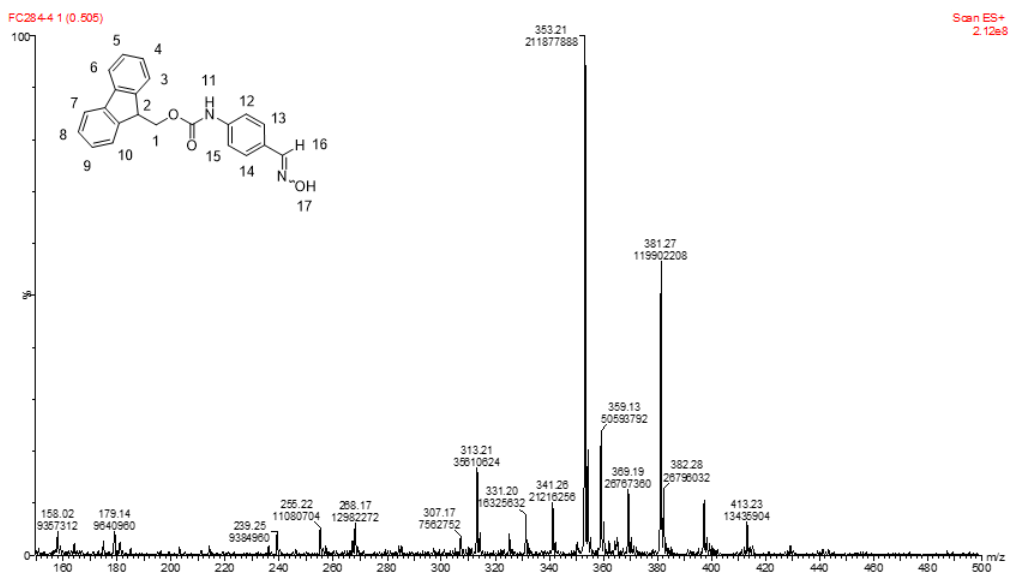
Figure 126. ESI-MS of **10**.

Benzaldehyde oxime

Figure 127. ^{1}H NMR of **12.**

Figure 128. ^{13}C NMR of **12.**
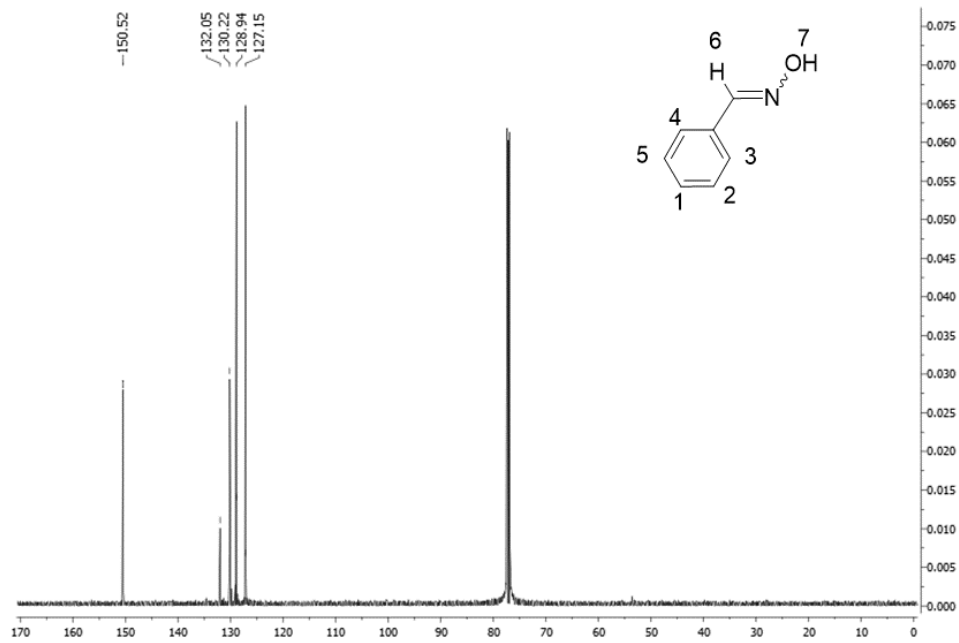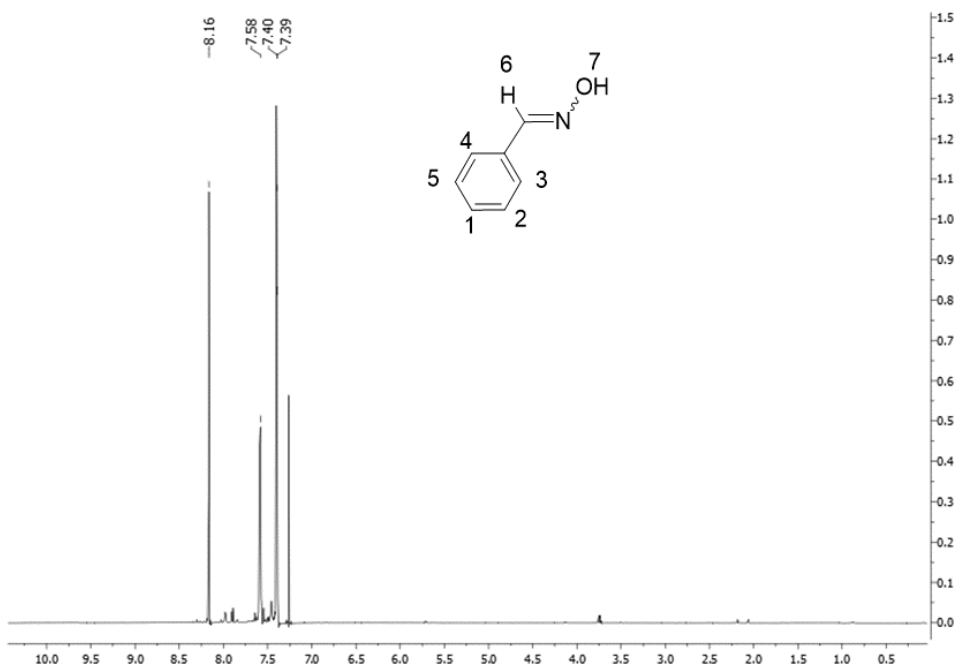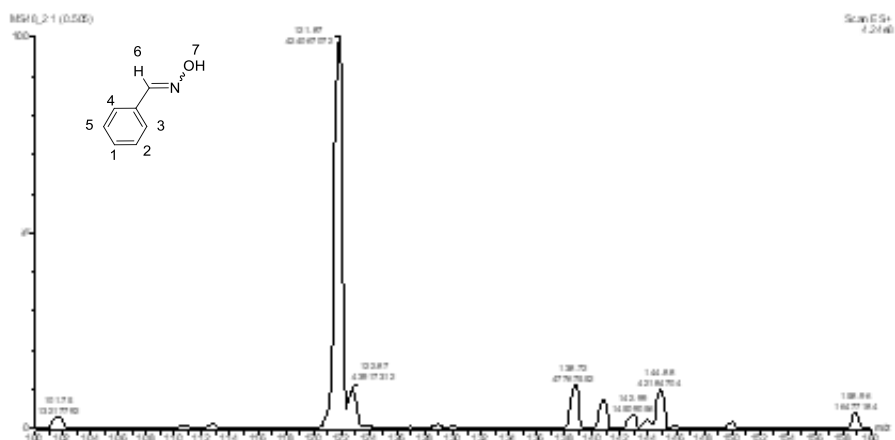
Figure 129. ESI-MS of **12.**

N-benzylhydroxylamine
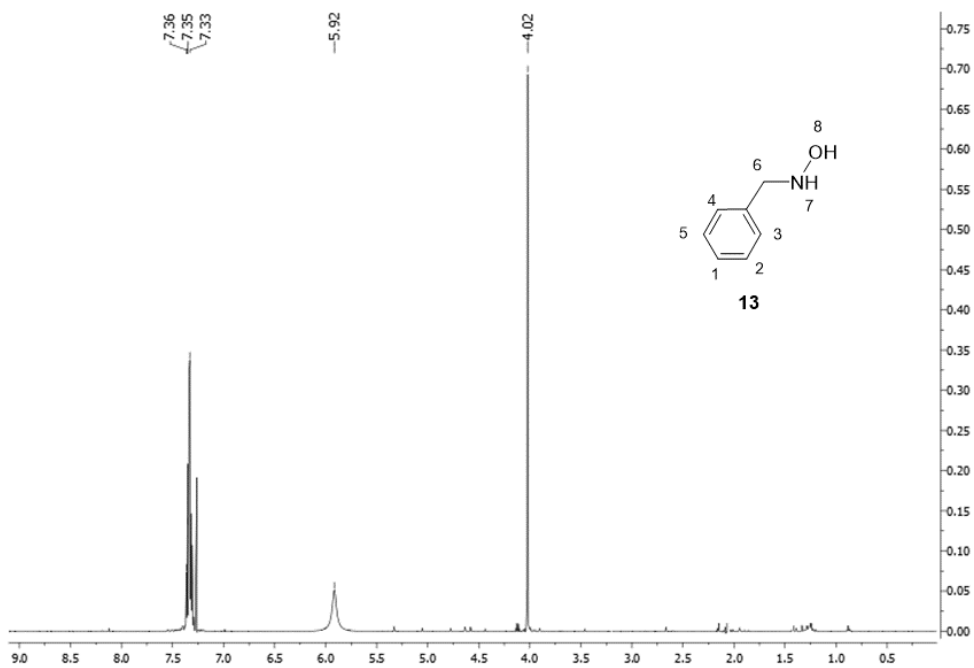
Figure 130. ¹H NMR of **13.**
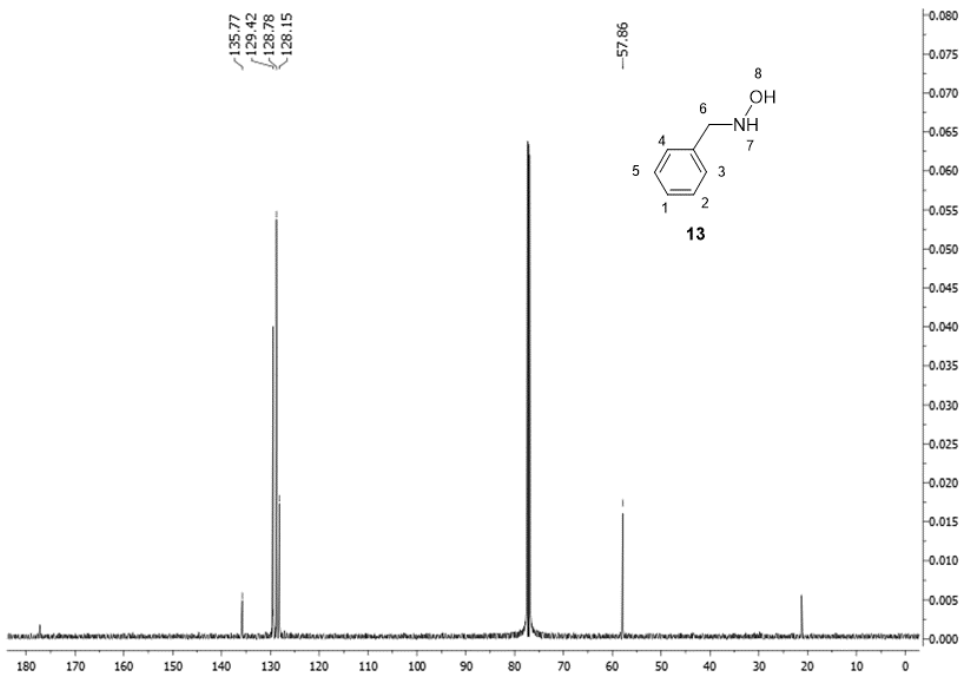
Figure 131. ^{13}C NMR of **13.**
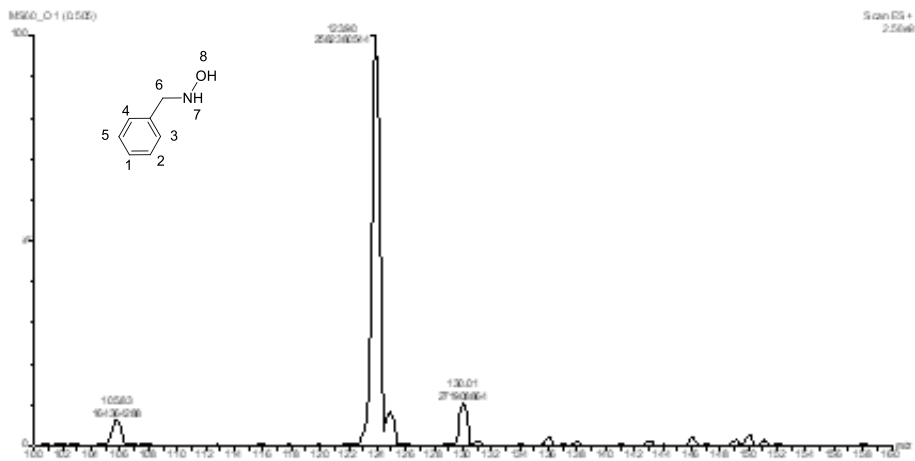
Figure 132. ESI-MS of **13.**

Octanal oxime
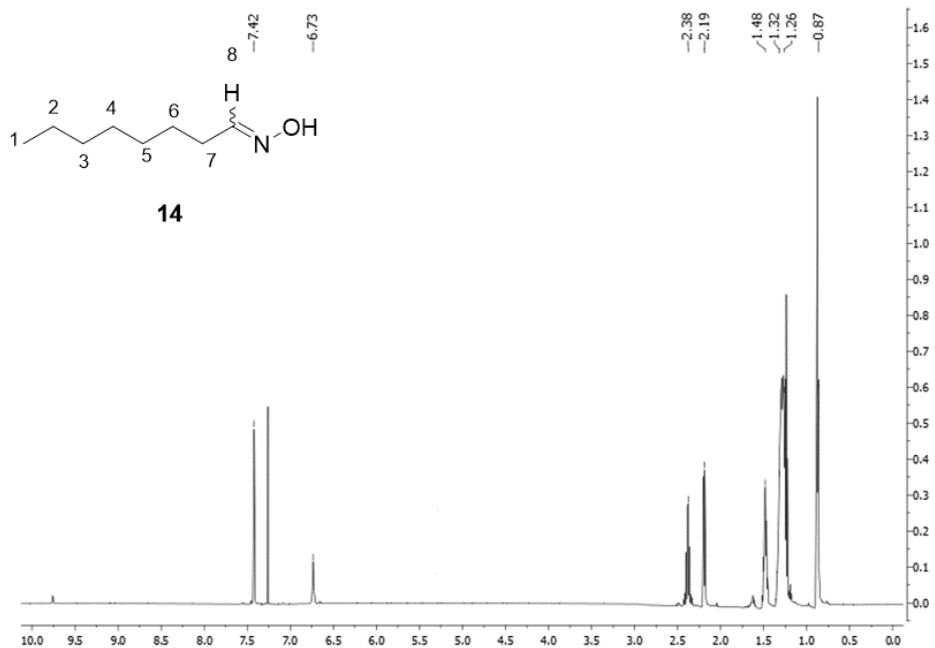
Figure 133. ^{1}H NMR of **14.**
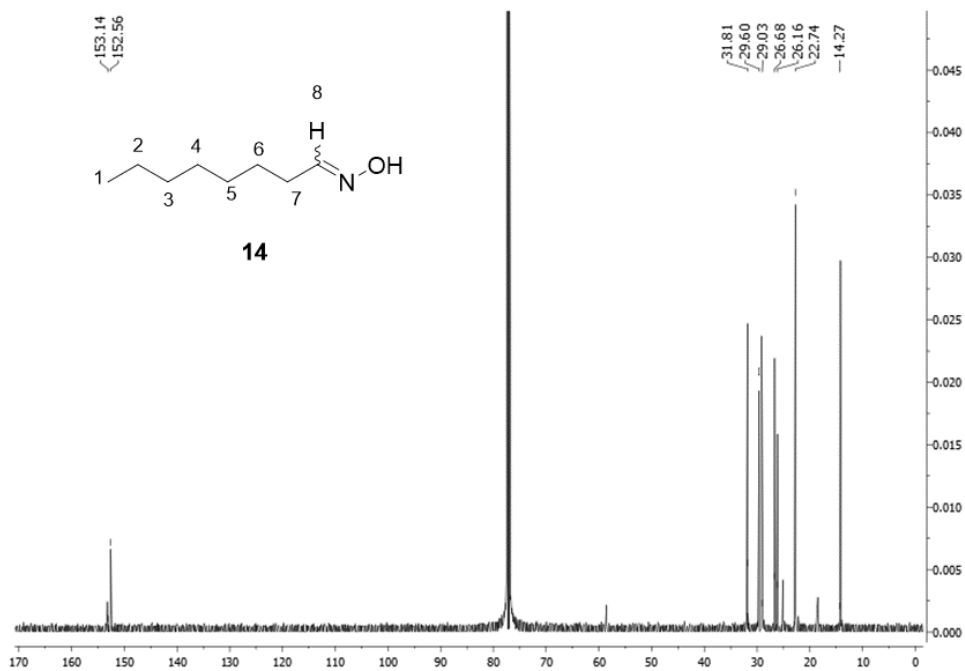
Figure 134. ^{13}C NMR of **14.**

217
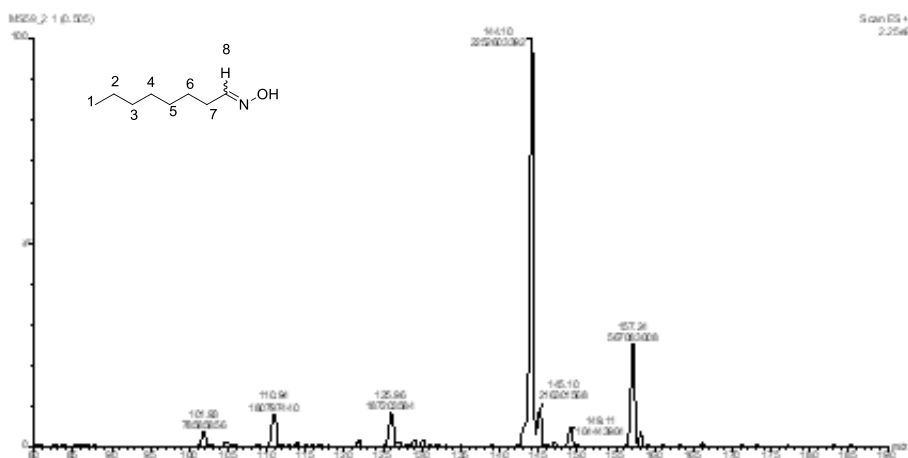
Figure 135. ESI-MS of **14.**

N-octylhydroxylamine
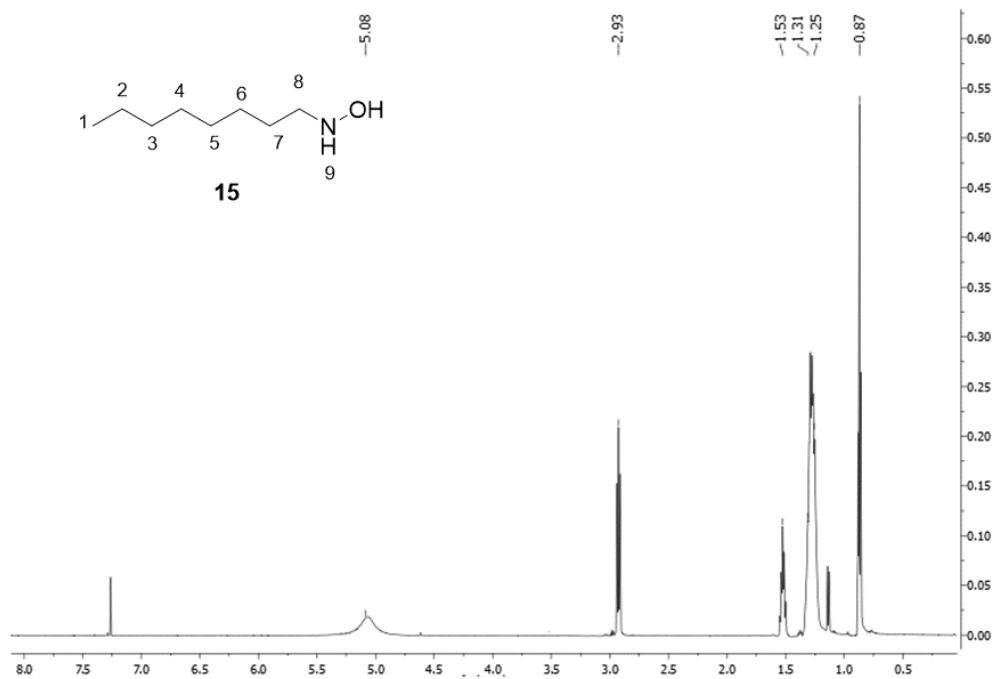
Figure 136. ¹H NMR of **15.**
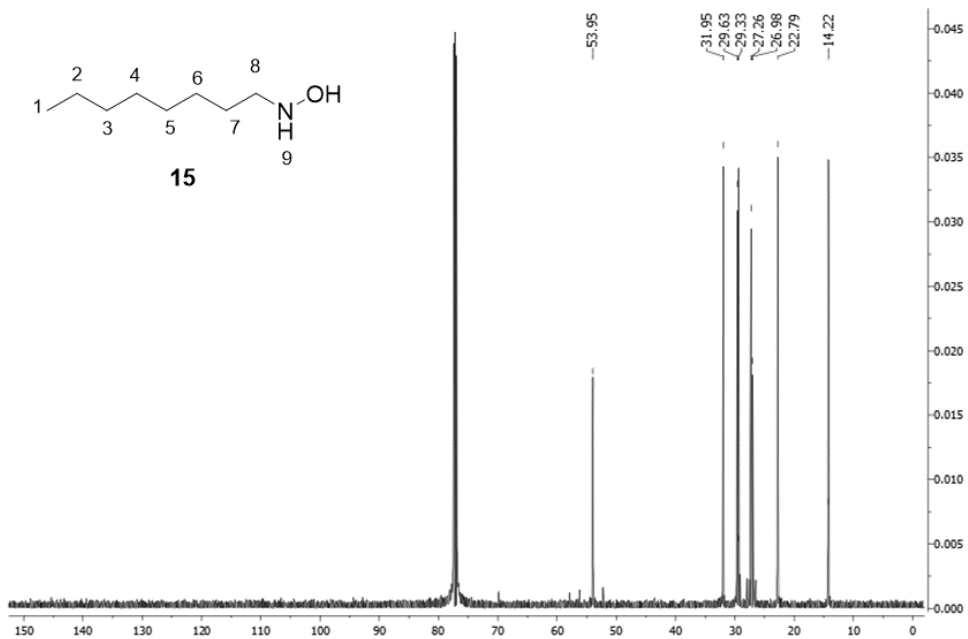
Figure 137. ^{13}C NMR of **15.**
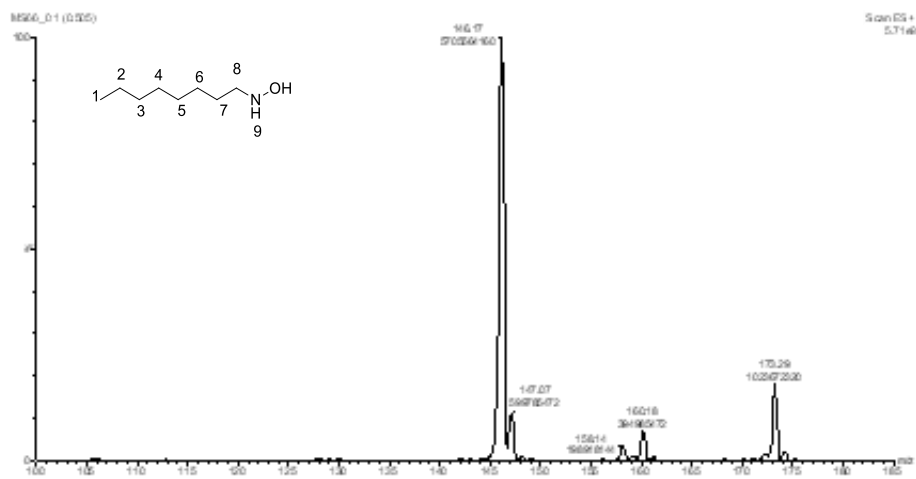
Figure 138. ESI-MS of **15.**

219

N-(4-((((9H-fluoren-9-yl)methoxy)carbonyl)amino)benzylidene)octan-1-amine oxide
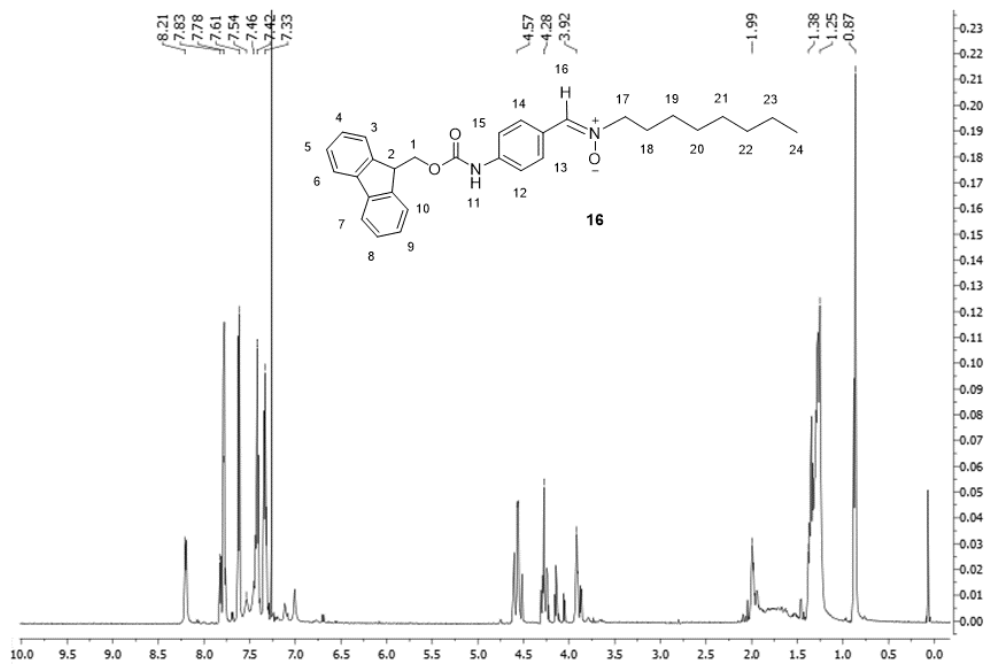
Figure 139. ^{1}H NMR of **16**.
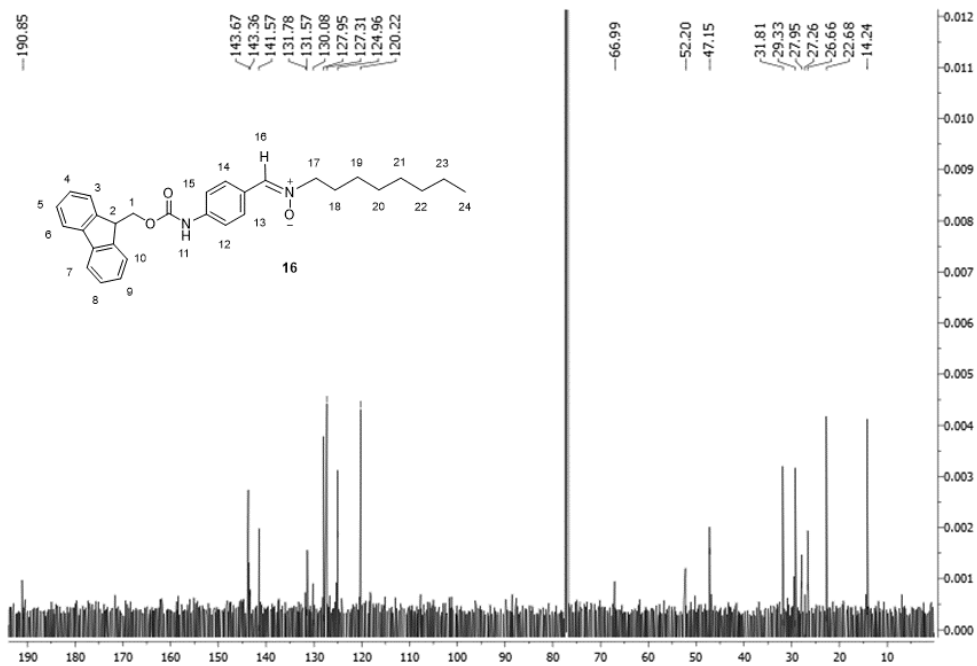
Figure 140. ^{13}C NMR of **16**.

Figure 141. ESI-MS of **16.**

N-(4-((((9H-fluoren-9-yl)methoxy)carbonyl)amino)benzylidene)octan-1-amine oxide
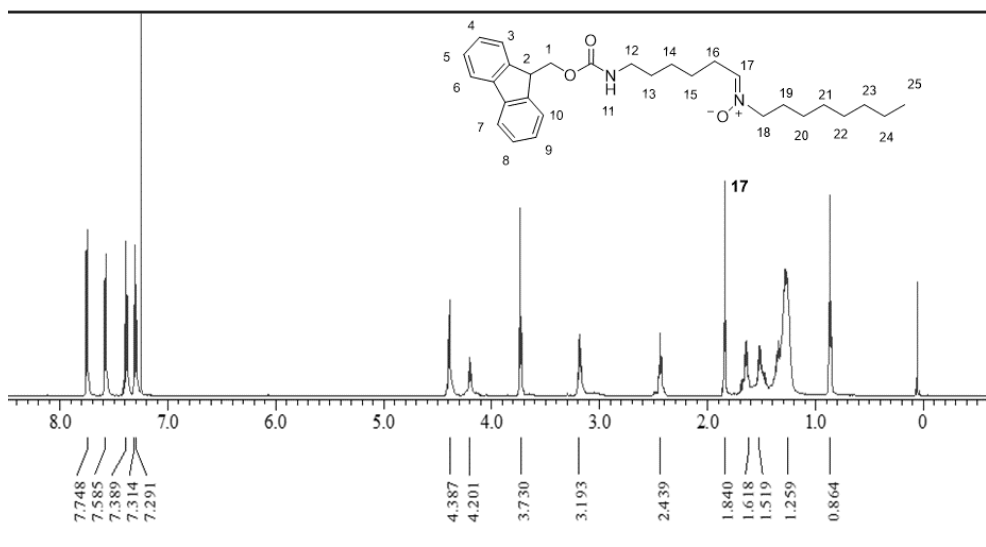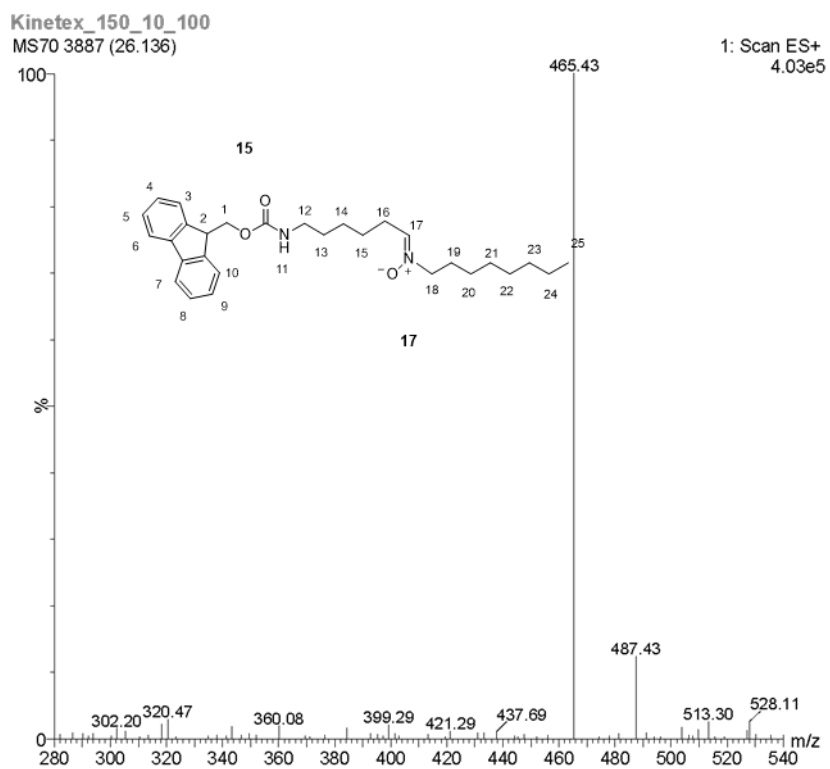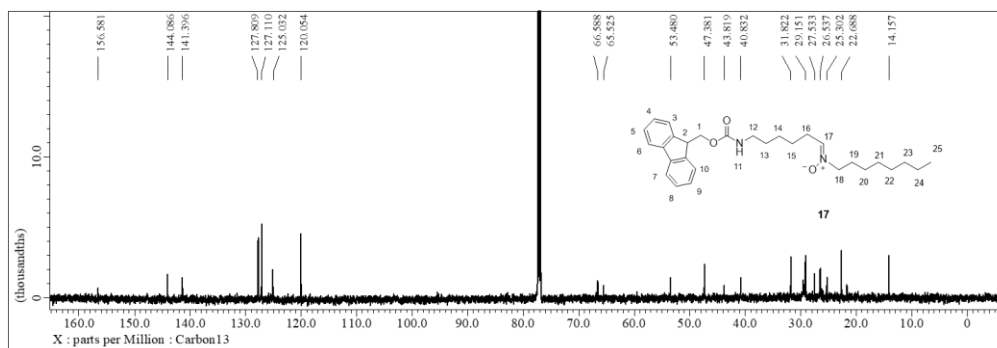
Figure 142. ^{1}H NMR of **17.**

Figure 143. ^{13}C NMR of **17.**

Figure 144. ESI-MS of **17.**

N,N-(4-((((9H-fluoren-9-yl)methoxy)carbonyl)amino)benzylidene)-1-phenylmethanamine oxide
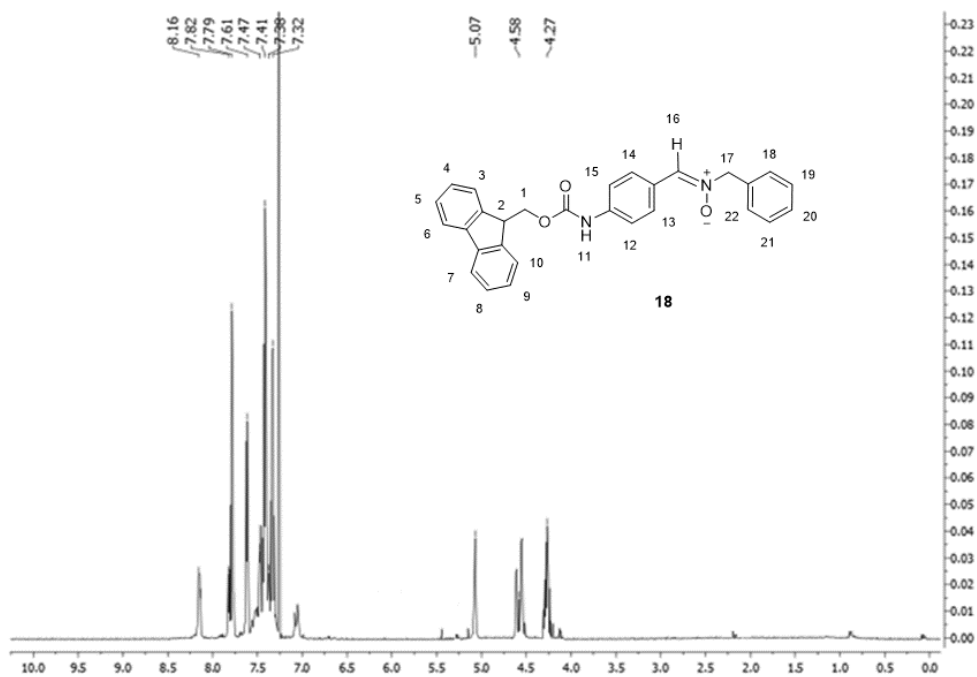
Figure 145. ^{1}H NMR of **18.**
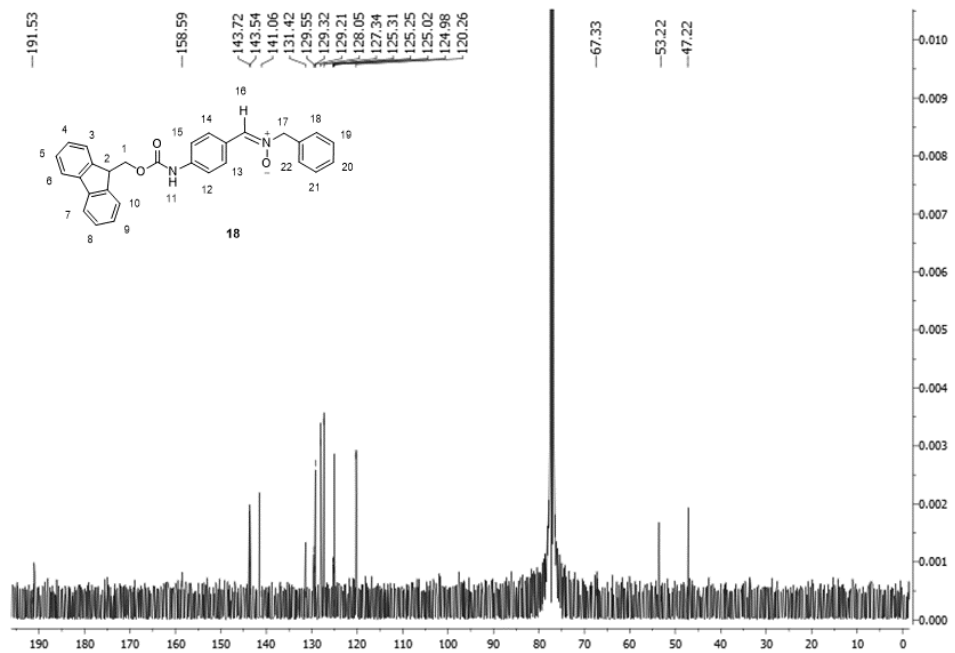
Figure 146. ^{13}C NMR of **18.**
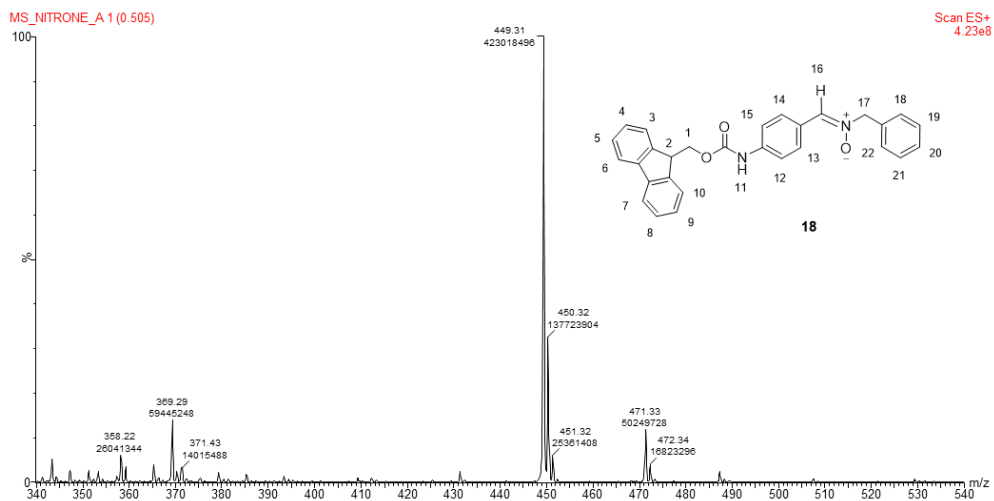
Figure 147. ESI-MS of **18.**

N-(6-((((9H-fluoren-9-yl)methoxy)carbonyl)amino)hexylidene)-1-phenylmethanamine oxide

Figure 148. ¹H NMR of **19.**
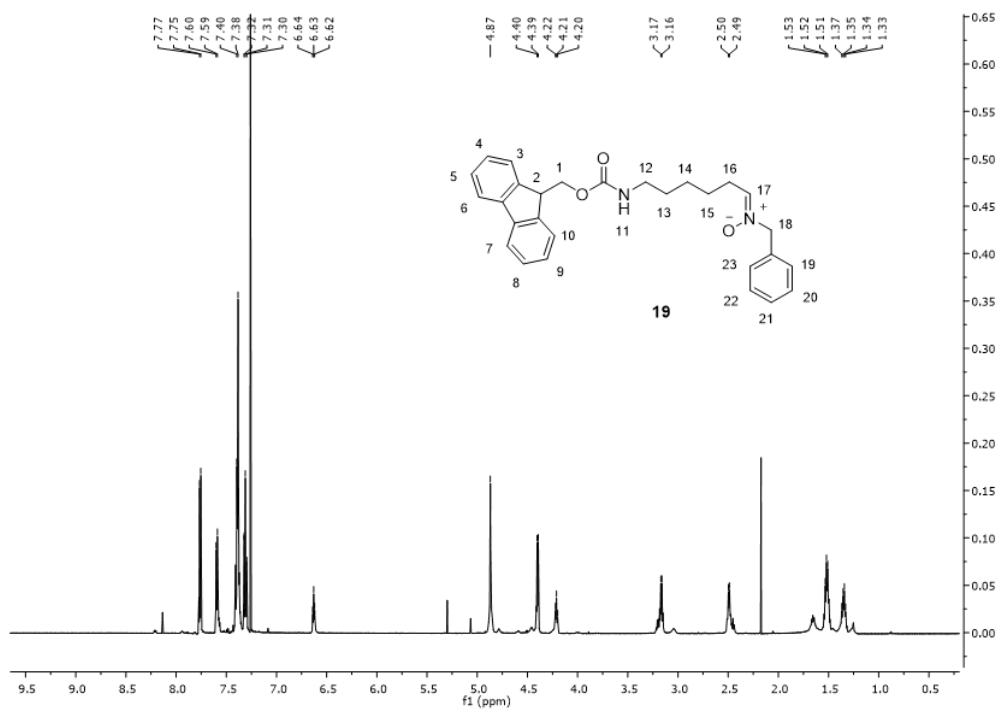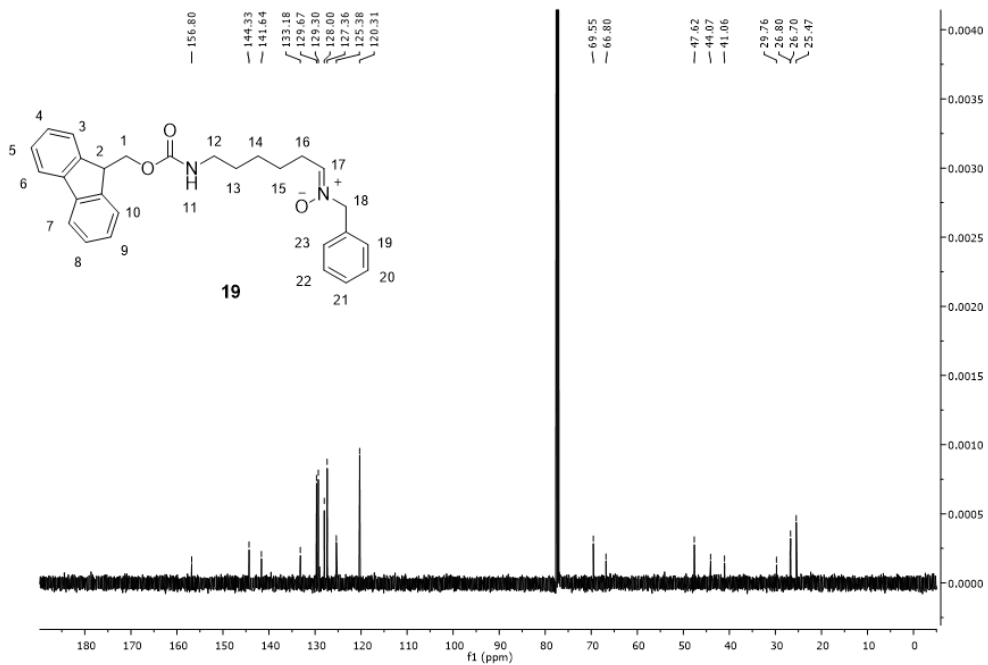
Figure 149. ^{13}C NMR of **19.**
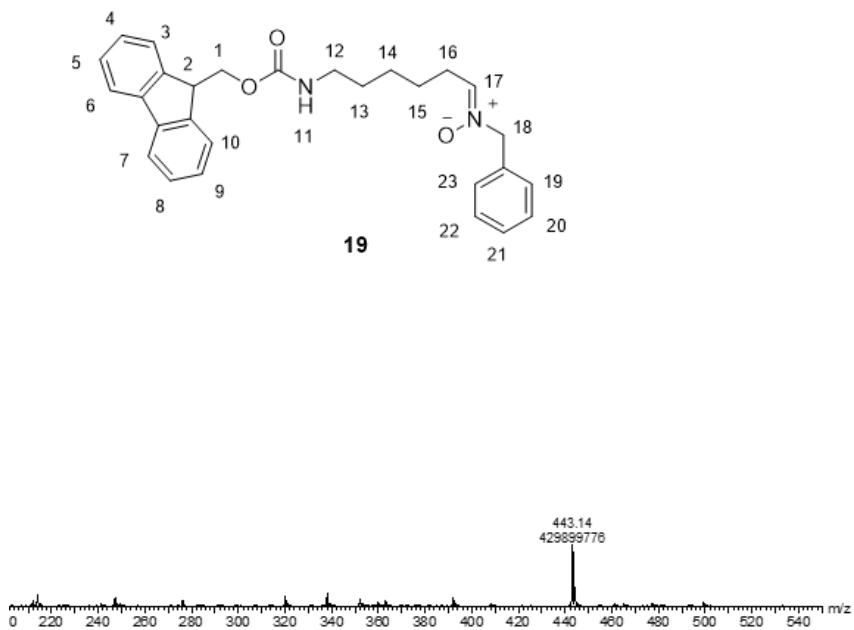
Figure 150. ESI-MS of **19.**

225

9.3. Improving the electrocatalytic performance of sustainable Co/carbon materials for the oxygen evolution reaction by ultrasound and microwave assisted synthesis

Co-Polyphenol materials characterization
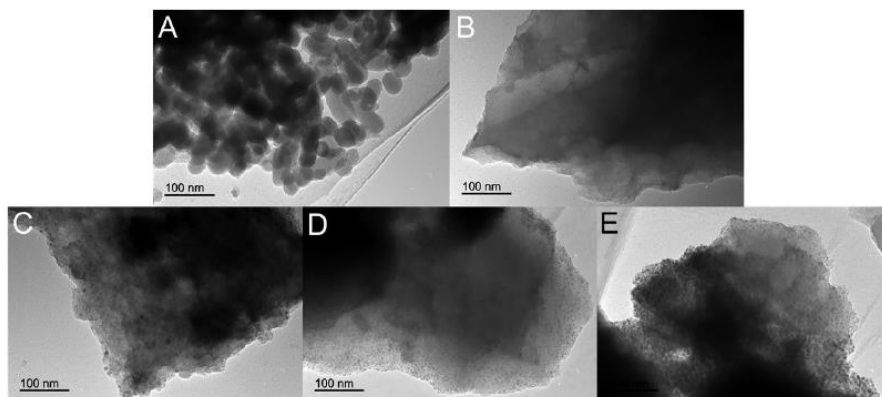
Figure 151. Representative TEM images of Co/CC (A), N-PC (B), Co/N-PC-pp-M (C), Co/N-PC-pp-U (D) and Co/N-PC-pp-MU€ samples.
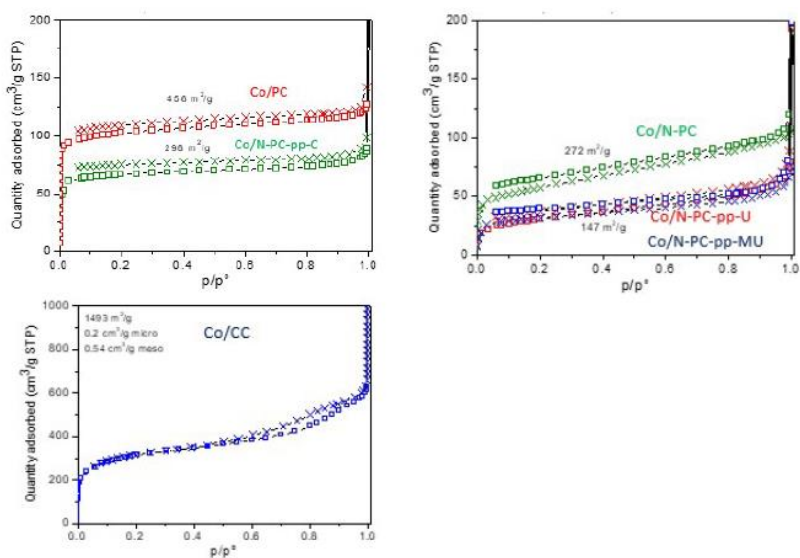
Figure 152. N$_2$ adsorption-desorption isotherms of the Co/ PC, Co/N-PC, Co/N-PC-pp-C, Co/N-PC-pp-M, Co/N-PC-pp-U and Co/N-PC-pp-MU.
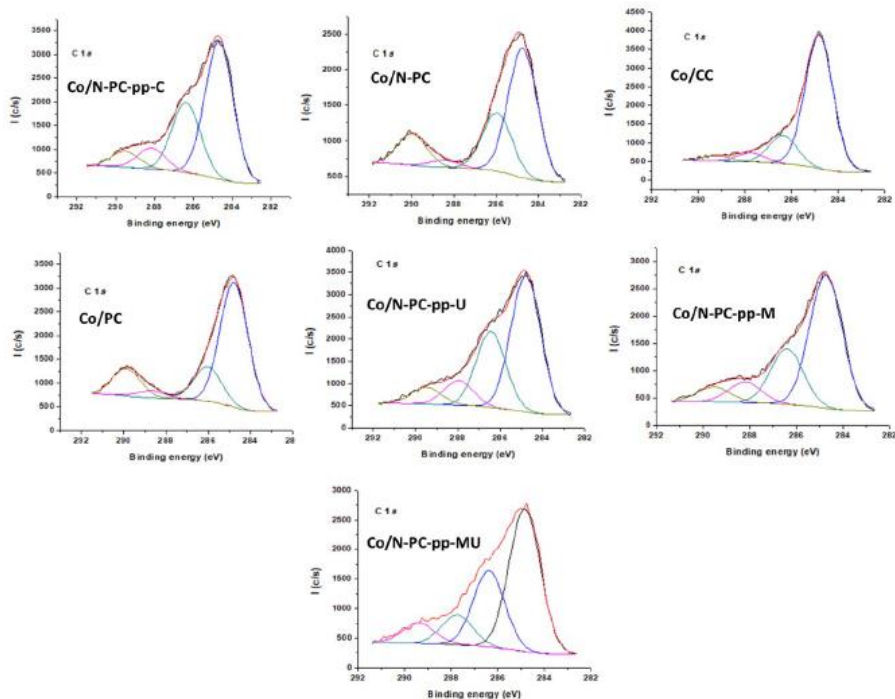
Figure 153. HR-XPS C 1s core level spectra for Co/CC, Co/PC, Co/N-PC and Co/N-PC-pp-C, Co/N-PC-pp-U, Co/N-PC-pp-M and Co/N-PC-pp-MU samples.
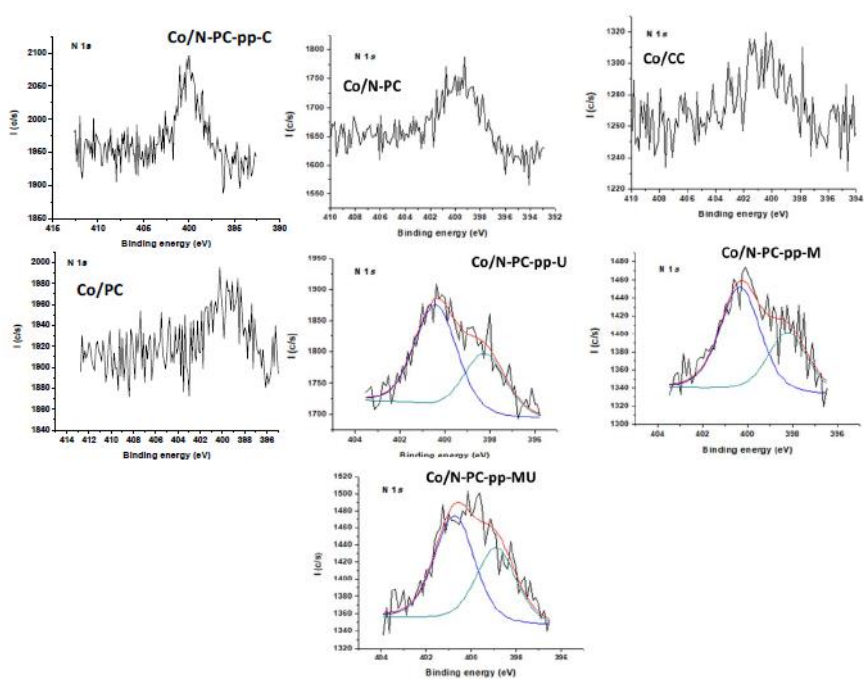
Figure 154. HR-XPS N 1s core level spectra for Co/CC, Co/PC, Co/N-PC and Co/N-PC-pp-C, Co/N-PC-pp-U, Co/N-PC-pp-M and Co/N-PC-pp-MU samples.
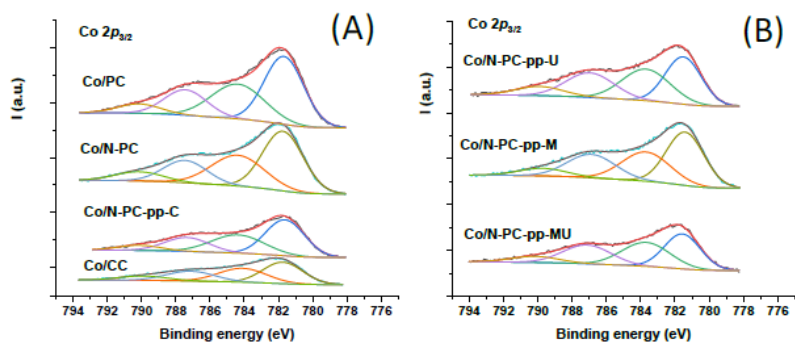
Figure 155. Deconvoluted XPS spectra of the Co 2p3/2 region for the different samples.
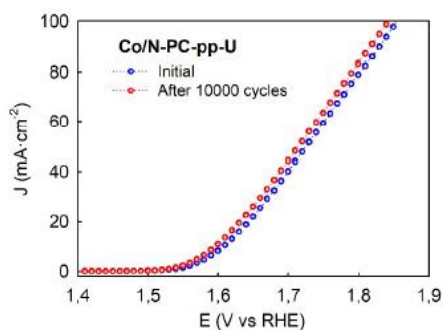
Figure 156. LSV curves of Co/N-PC-pp-U sample before and after performing 10000 cycles of cyclic voltammetry at the same OER conditions.

Table 28. Co 2p3/2 spectral fitting parameters and (Co 2p3/2-Co 2p1/2) (in eV).

Sample	Peak 1	Peak 2	Peak 3	Peak 4	Δ (Co 2p$_{3/2}$-Co 2p$_{1/2}$)
Co/CC	781.8 (39%)	784.1 (30%)	787.1 (21%)	789.9 (10%)	-
Co/PC	781.7 (44%)	784.4 (31%)	787.4 (18%)	790.1 (7%)	16.0
Co/N-PC	781.8 (44%)	784.4 (30%)	787.5 (18%)	790.1 (8%)	16.1
Co/N-PC-pp-C	781.6 (44%)	784.4 (30%)	787.4 (19%)	790.0 (7%)	16.1
Co/N-PC-pp-M	781.4 (41%)	783.7 (29%)	786.9 (23%)	789.7 (7%)	16.0
Co/N-PC-pp-U	781.5 (35%)	783.7 (31%)	787.0 (24%)	789.9 (10%)	16.1
Co/N-PC-pp-MU	781.6 (35%)	783.7 (32%)	787.1 (25%)	790.2 (8%)	16.3

Table 29. Comparison of the OER electrocatalytic parameters of the Co/N-PC with the state-of-the-art Co-based carbon catalysts.

Sample	Peak 1	Peak 2	Peak 3	Peak 4	Δ (Co $2p_{3/2}$–Co $2p_{1/2}$)
Co/CC	781.8 (39%)	784.1 (30%)	787.1 (21%)	789.9 (10%)	-
Co/PC	781.7 (44%)	784.4 (31%)	787.4 (18%)	790.1 (7%)	16.0
Co/N-PC	781.8 (44%)	784.4 (30%)	787.5 (18%)	790.1 (8%)	16.1
Co/N-PC-pp-C	781.6 (44%)	784.4 (30%)	787.4 (19%)	790.0 (7%)	16.1
Co/N-PC-pp-M	781.4 (41%)	783.7 (29%)	786.9 (23%)	789.7 (7%)	16.0
Co/N-PC-pp-U	781.5 (35%)	783.7 (31%)	787.0 (24%)	789.9 (10%)	16.1
Co/N-PC-pp-MU	781.6 (35%)	783.7 (32%)	787.1 (25%)	790.2 (8%)	16.3

Table 30. OER electrocatalytic parameters obtained for Co/N-PC-pp-M at different temperatures.

Co/N-PC-pp-M				
Working temperature (°C)	Onset potential (V)	Overpotential (mV) at 10 mA·cm^{-2}	Maximum current density (mA·cm^{-2})	Tafel slope (mV·dec^{-1})
r.t.	1.57	526	27.1	78
60	1.55	440	70.0	74
80	1.52	380	106.1	69

Table 31. OER electrocatalytic parameters obtained for Co/N-PC-pp-U at different temperatures.

Co/N-PC-pp-U				
Working temperature (°C)	Onset potential (V)	Overpotential (mV) at 10 mA·cm^{-2}	Maximum current density (mA·cm^{-2})	Tafel slope (mV·dec^{-1})
r.t.	1.56	497	32.0	94
60	1.54	428	76.6	61
80	1.51	365	126.2	58

9.4. Multifunctional amino-citrate-β-CD coated iron oxide nanoparticles: an efficient nanosystem for Magnetic Resonance Imaging (MRI)
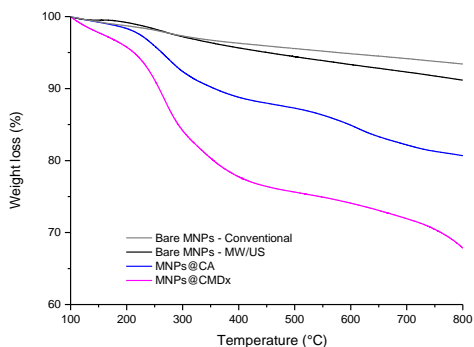
Figure 157. TGA profiles of bare MNPs obtained by co-precipitation method *via* conventional and MW/US heating and coated MNPs prepared *via* physical assembly.

Sorption experiments

Phenolphthalein

Equation	y = a + b*x	
Adj. R-Square	0,99942	
		Value
Abs	*Intercept*	0,40196
Abs	*Slope*	-7,56542
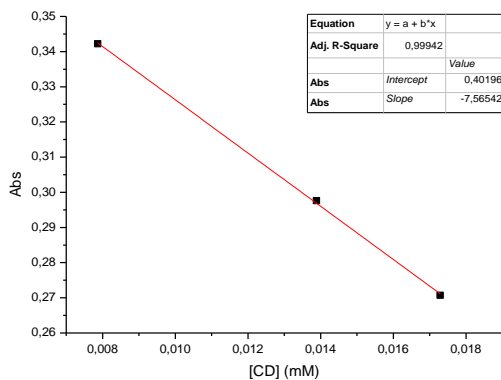
Figure 158. Calibration curve of Php-CD inclusion complex at 553 nm wavelength.

Adamantane amine

Equation	y = a + b*x	
Adj. R-Squa	0,99191	
		Value
Area	Intercept	10
Area	Slope	1079,428
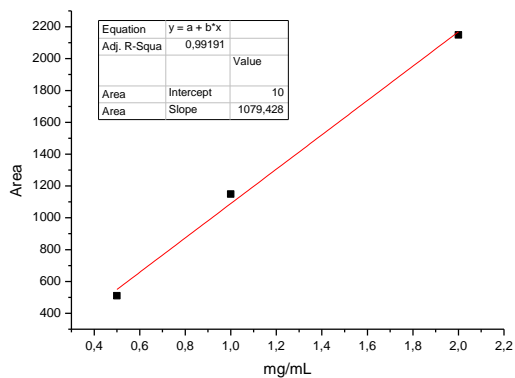
Figure 159. Calibration curve of adamantane amine measured using GC-FID.

Stability assays

Water stability

Serum stability

Albumin stability
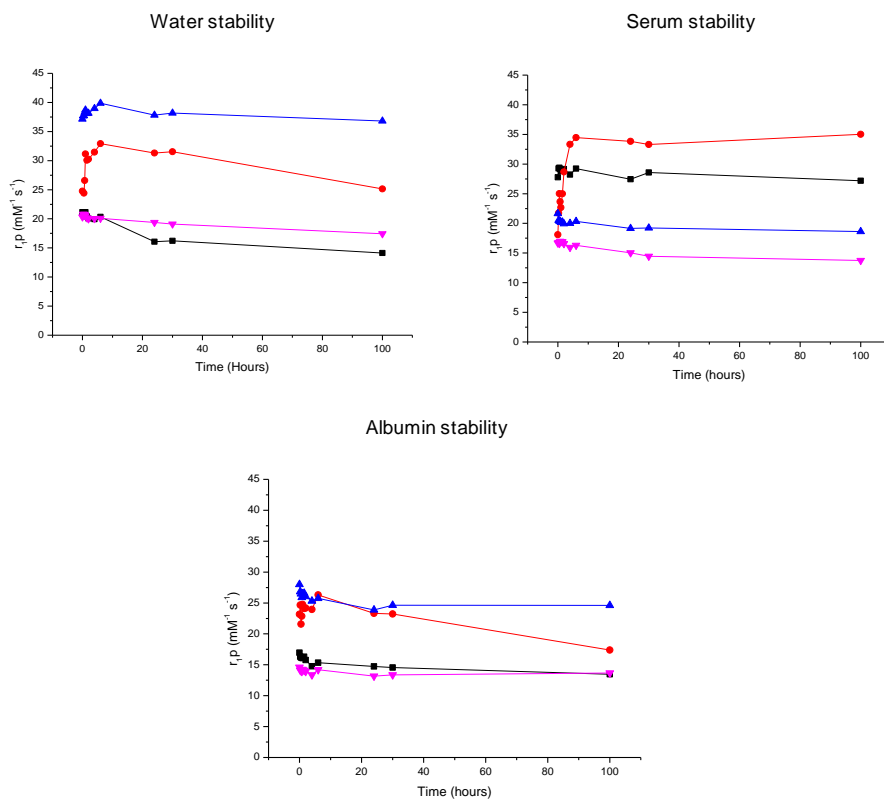
Figure 160. Graphic representation of r_1p (mM^{-1} s^{-1}) stability in function of time (h) of MNPs@CA (black line), MNPs@CMDx (pink line), MNPs@CA-Citramide (red line), MNPs@CA-β-CD (blue line).

R₂/R₁ ratio
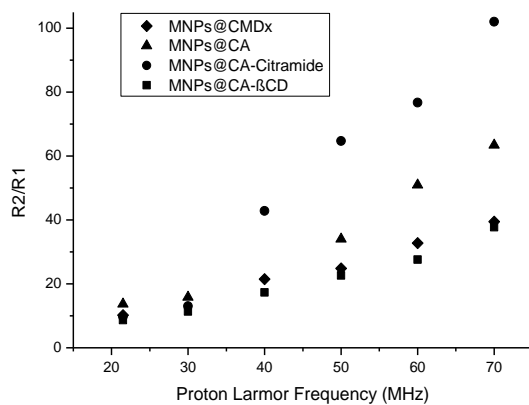
Figure 161. R$_2$/R$_1$ ratio of MNPs@CMDx, MNPs@CA, MNPs@CA-β-CD and MNPs@CA-Citramide.

MRI
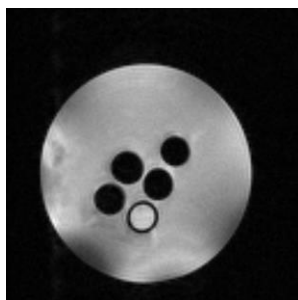
Figure 162. Magnetic resonance imaging of MNPs@CMDx, MNPs@CA, MNPs@CA-β-CD and MNPs@CA-Citramide.

TEM analysis

Bare MNPs-Conventional technique
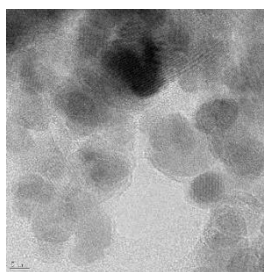
Bare MNPs-MW/US technique

MNPs@CMDx – ligand exchange   MNPs@CA – ligand exchange   MNPs@β-CD-CA – ligand exchange
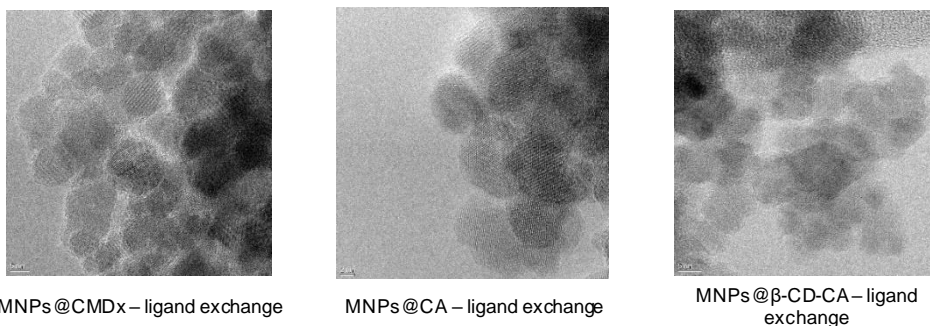
Figure 163. TEM images of bare MNPs, prepared through co-precipitation method (conventional heating and MW/US combined irradiation), MNPs@CMDx, MNPs@CA, MNPs@β-CD-CA prepared following ligand exchange technique.

Structural characterization

Citric acid anhydride
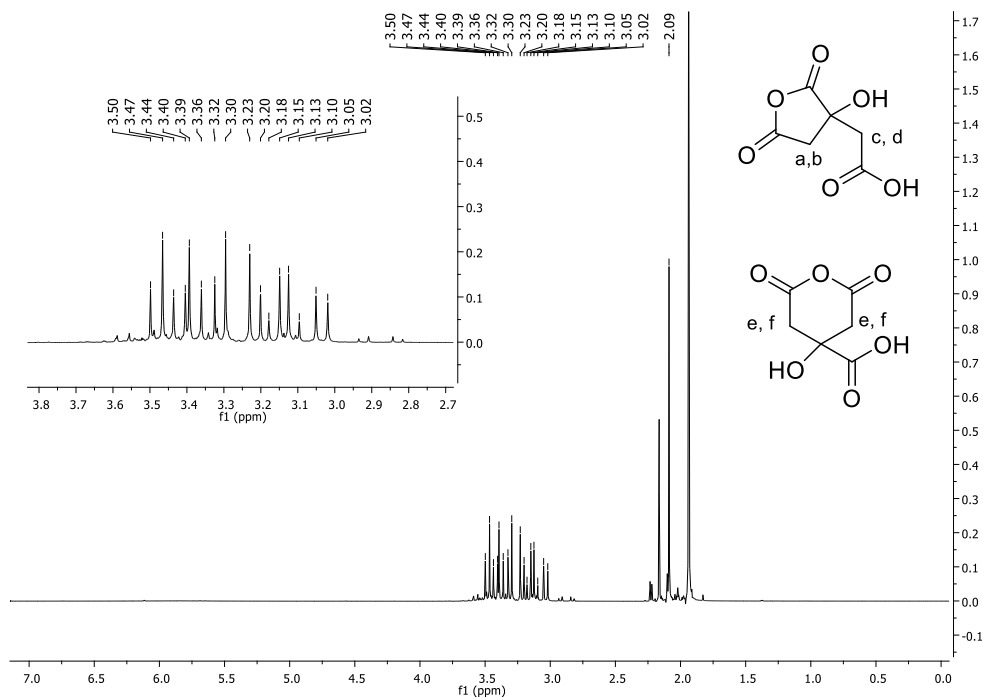
Figure 164. ^{1}H NMR of citric acid anhydride.
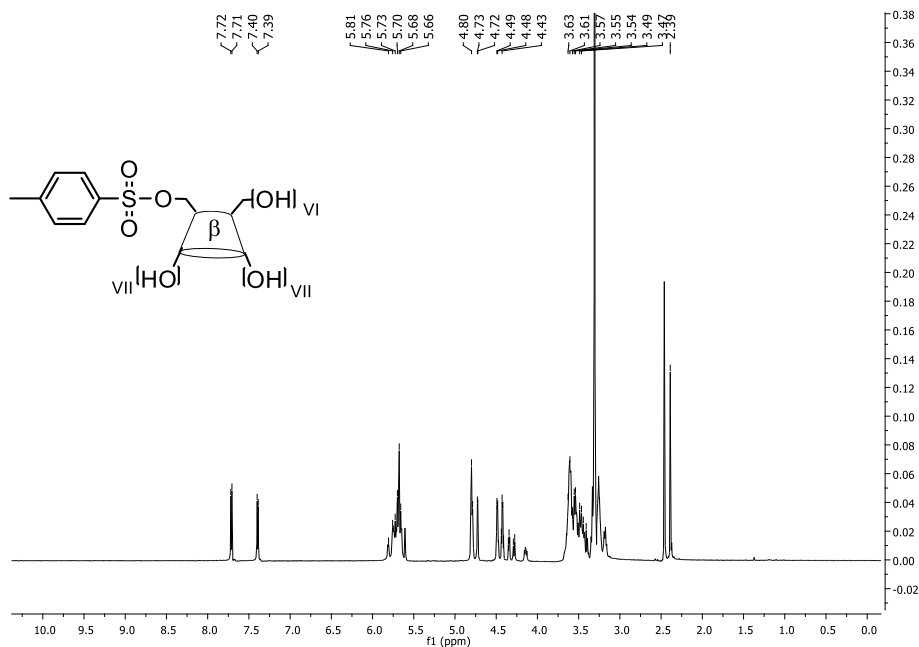
233

6^I-O-p-Toluenesulfonyl-β-CD

6ᴵ-O-p-Toluenesulfonyl-β-CD

Figure 165. ^{1}H NMR of 6I-O-p-Toluenesulfonyl-β-CD.

of 6ᴵ-diethylentriamine-6ᴵ-monodeoxy-βCD

of 6ᴵ-diethylentriamine-6ᴵ-monodeoxy-βCD
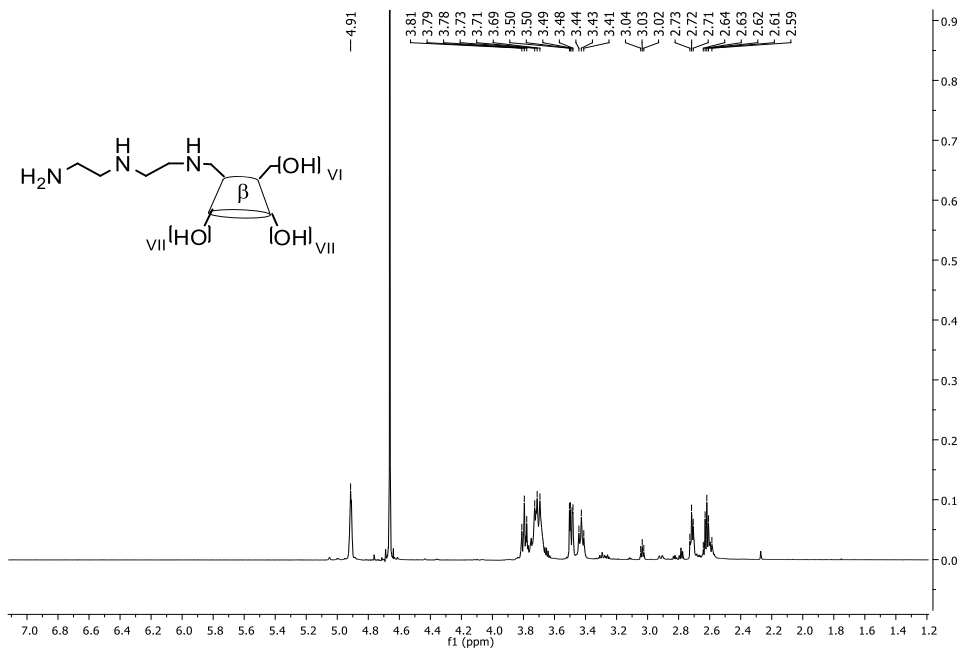
Figure 166. ^{1}H NMR of 6^I-diethylentriamine-6^I-monodeoxy-βCD.
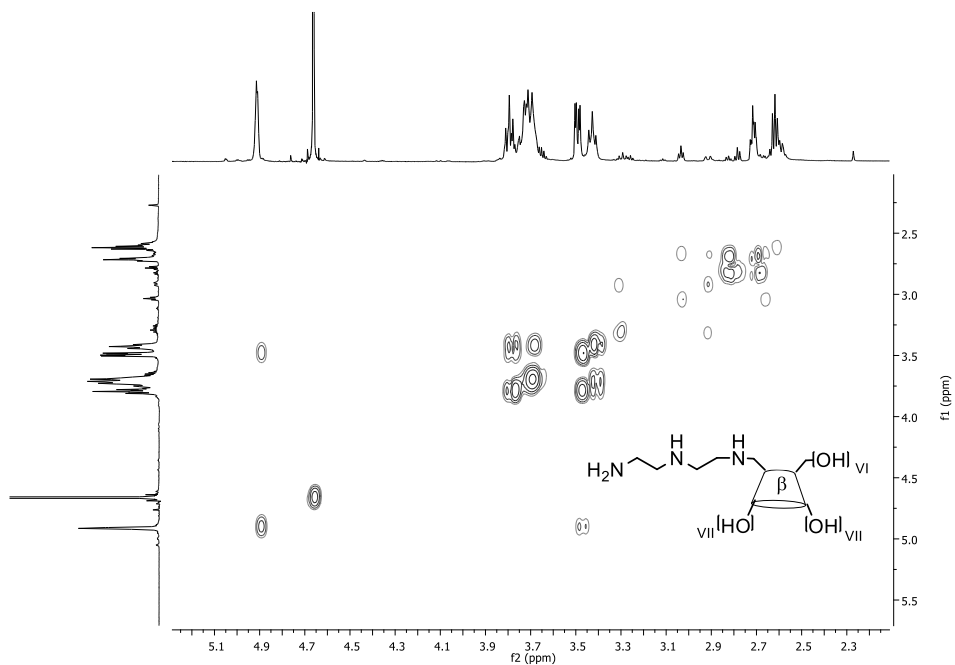
Figure 167. COSY NMR of 6^I-diethylentriamine-6^I-monodeoxy-βCD.

*β*CD citrate (citramide)
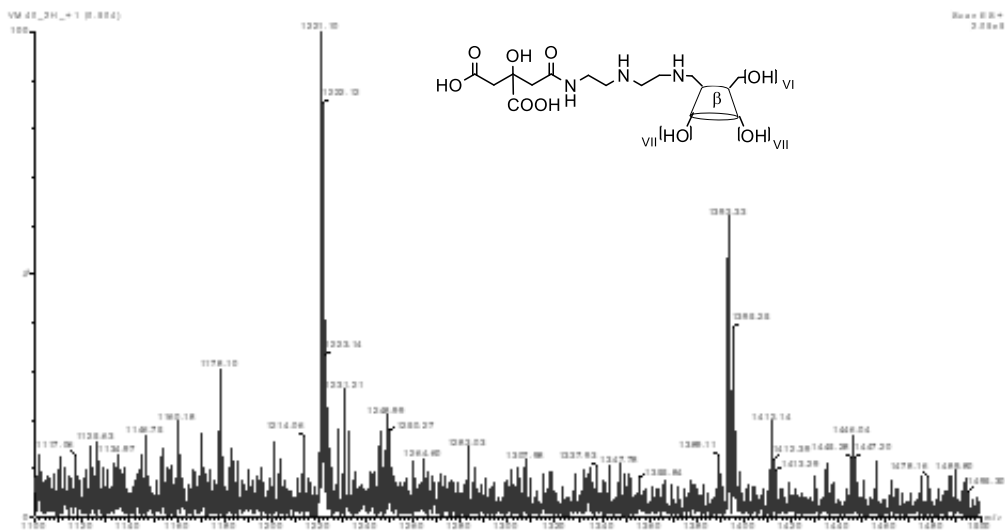
Figure 168. ESI-MS$^+$ of amino citrate-βCD (citramide).

Carboxymethyl dextran
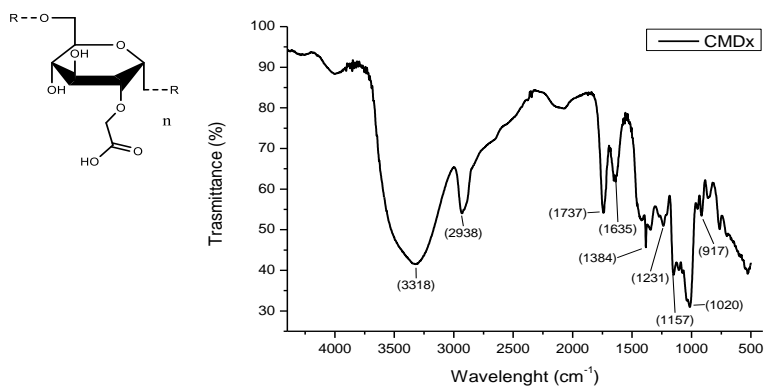
Figure 169. FT-IR of carboxymethyl dextran.

9.5.   Flow chemistry for the synthesis of drugs

NMR characterization

Camptothecin analogue
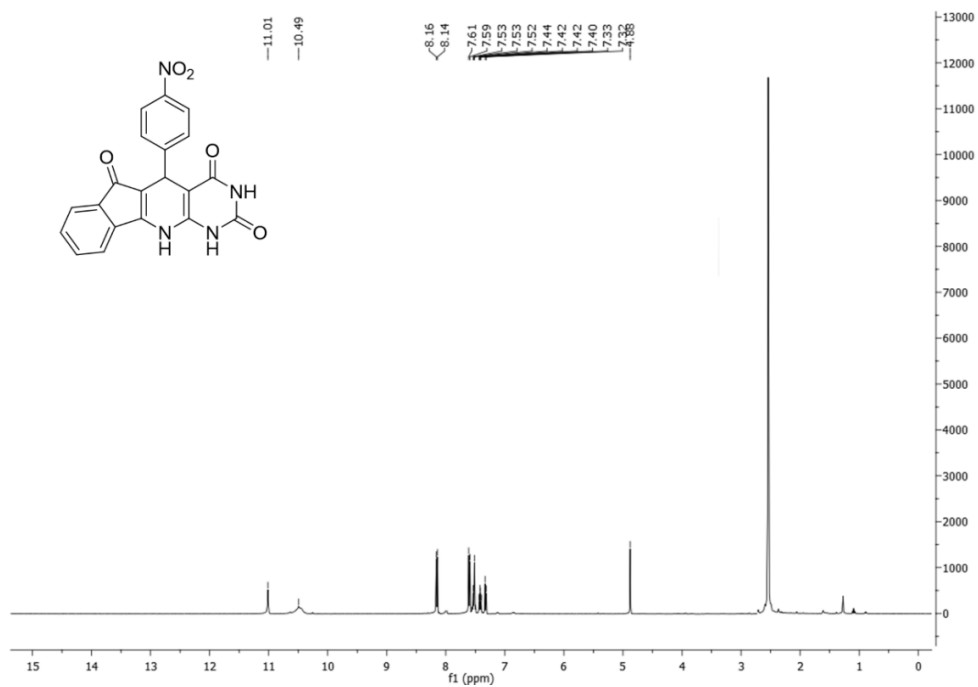
Figure 170. ^{1}H NMR of 6-aminouracil camptothecin analogue (**6**).
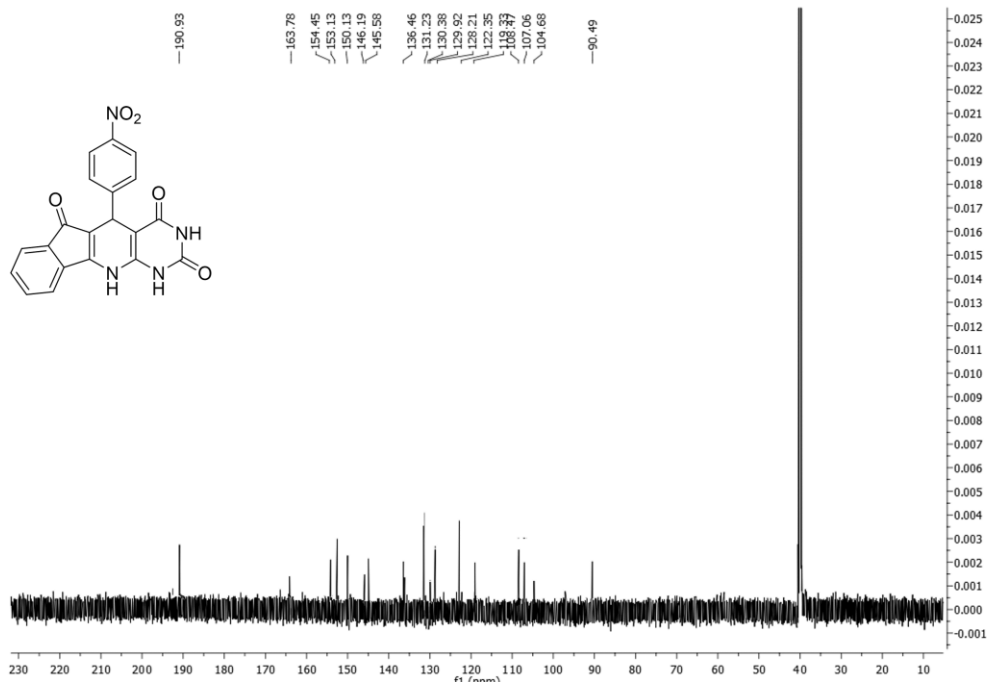
Figure 171. ^{13}C NMR of 6-aminouracil camptothecin analogue (**6**).
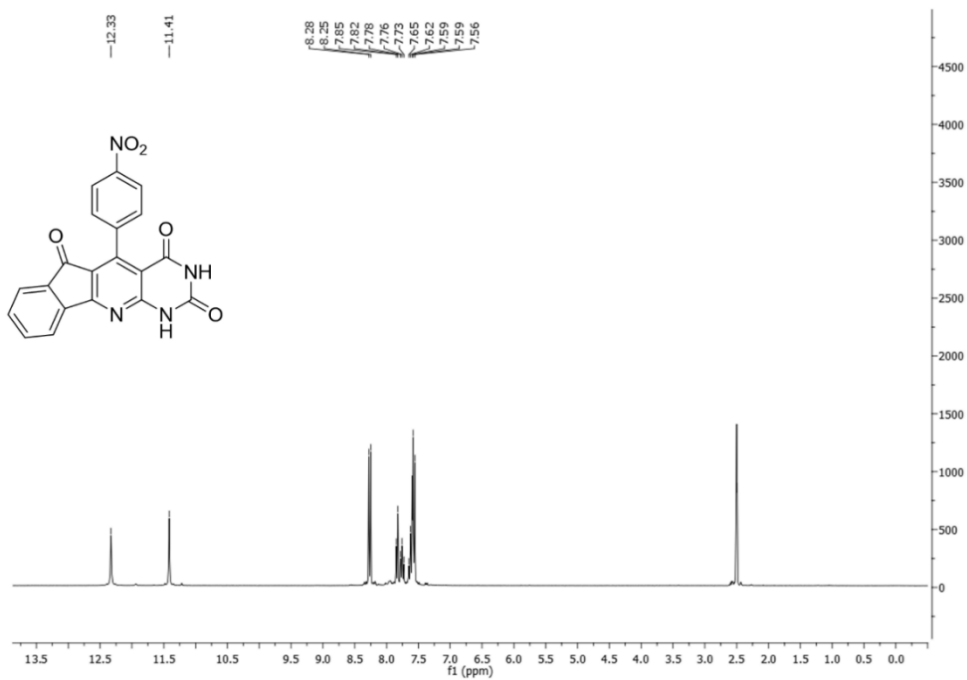
Figure 172. ^{1}H NMR of 6-aminouracil camptothecin analogue (**7**).

238
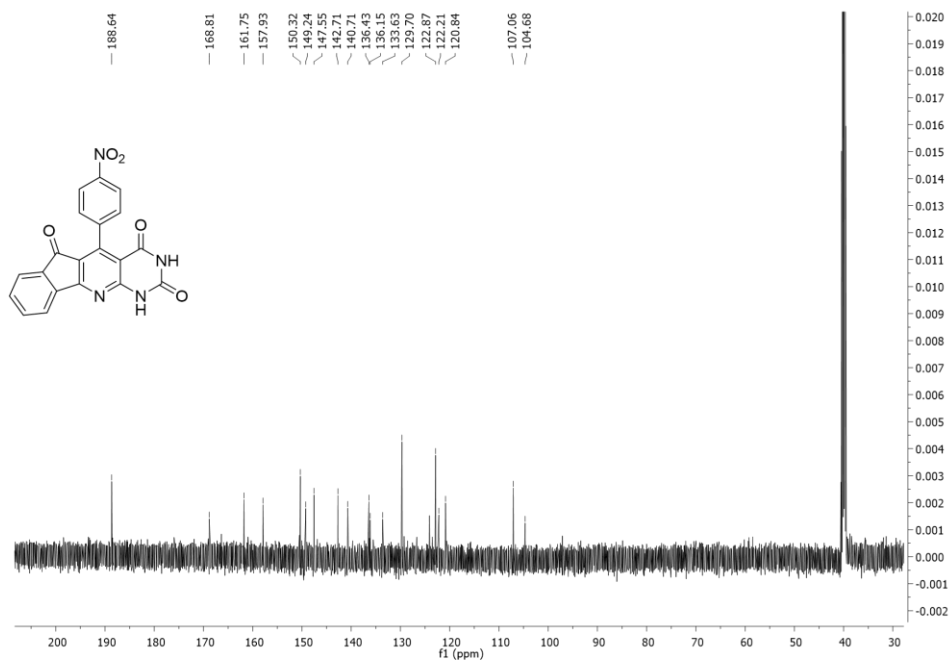
Figure 173. ^{13}C NMR of 6-aminouracil camptothecin analogue (**7**).

N-Phenylethylformamide
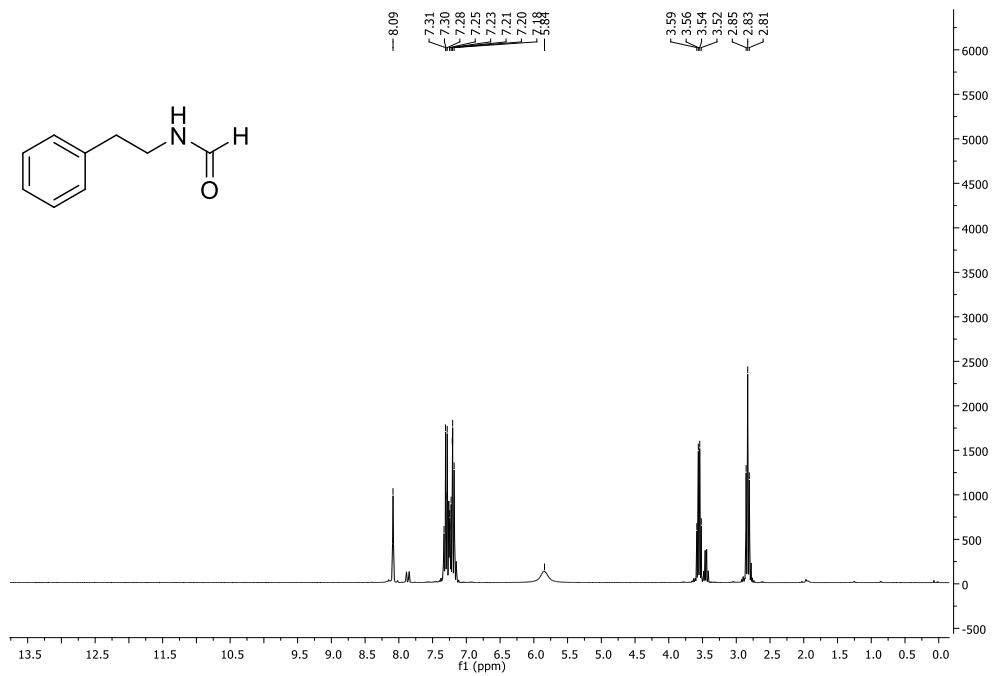
Figure 174. ^{1}H NMR of N-Phenylethylformamide.
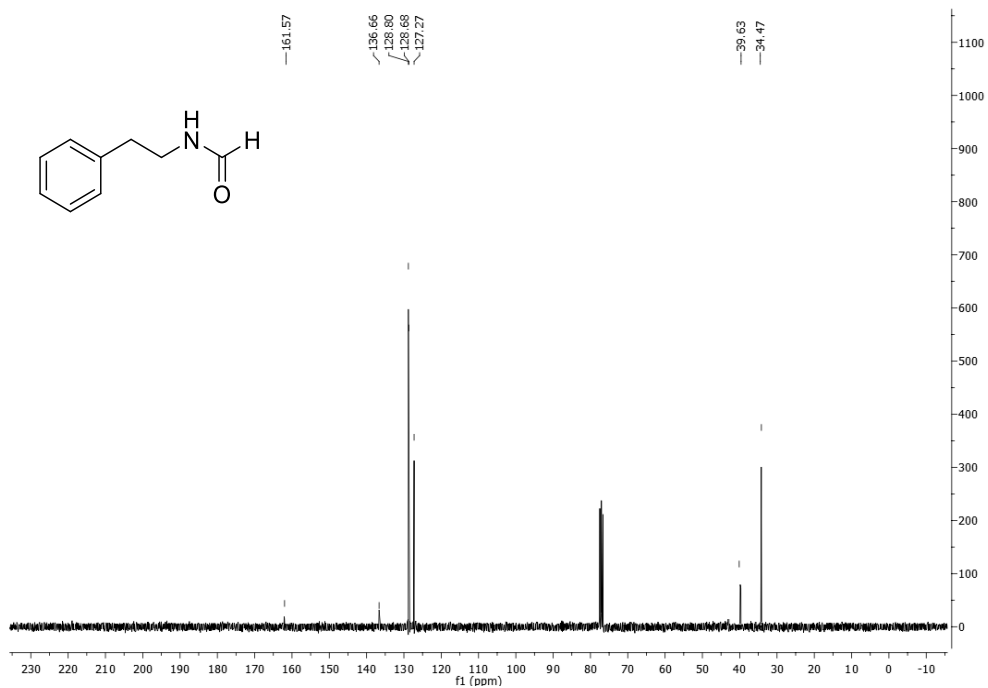
Figure 175. ^{13}C NMR of N-Phenylethylformamide.

N-phenylethylisocyanide
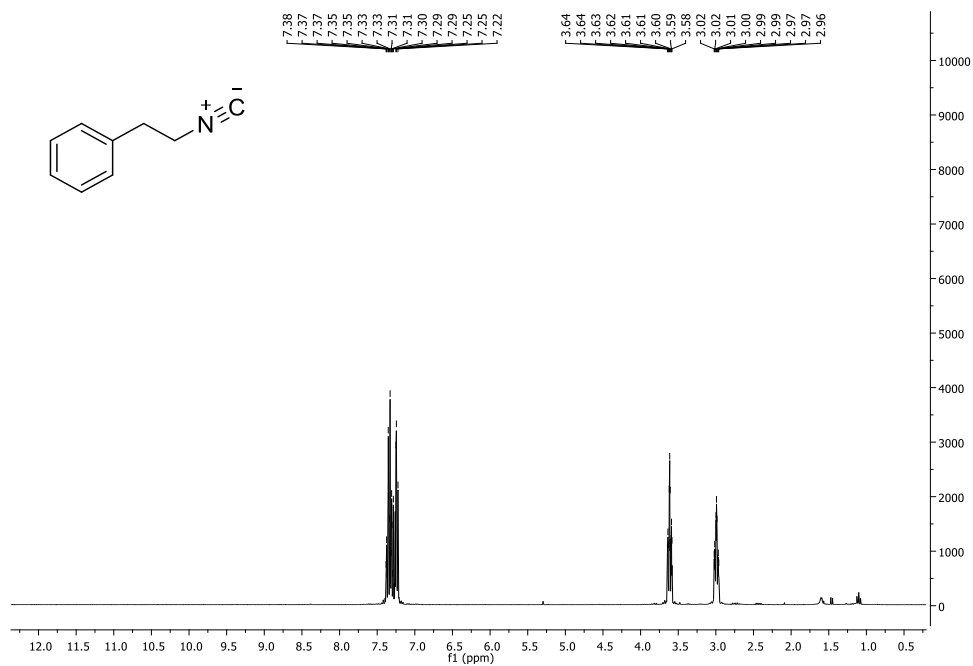
Figure 176. ^{1}H NMR of N-phenylethylisocyanide (**11**).
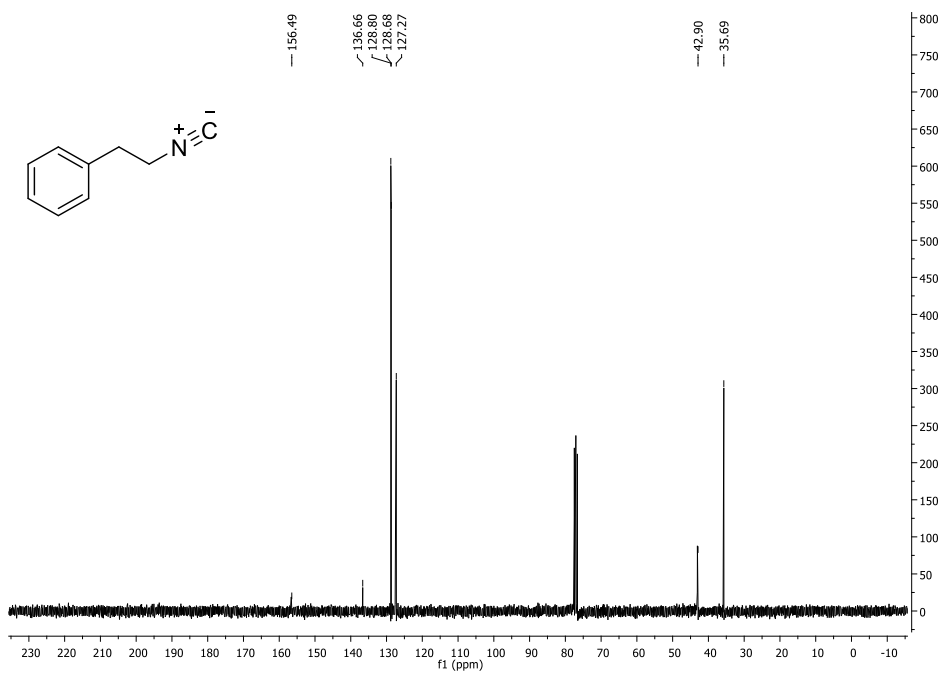
Figure 177. ^{13}C NMR of N-phenylethylisocyanide (**11**).

N-(2,2-dimethoxyethyl)-N-(2-oxo-2-(2-phenethylamino)-ethyl)cyclohexane carboxamide
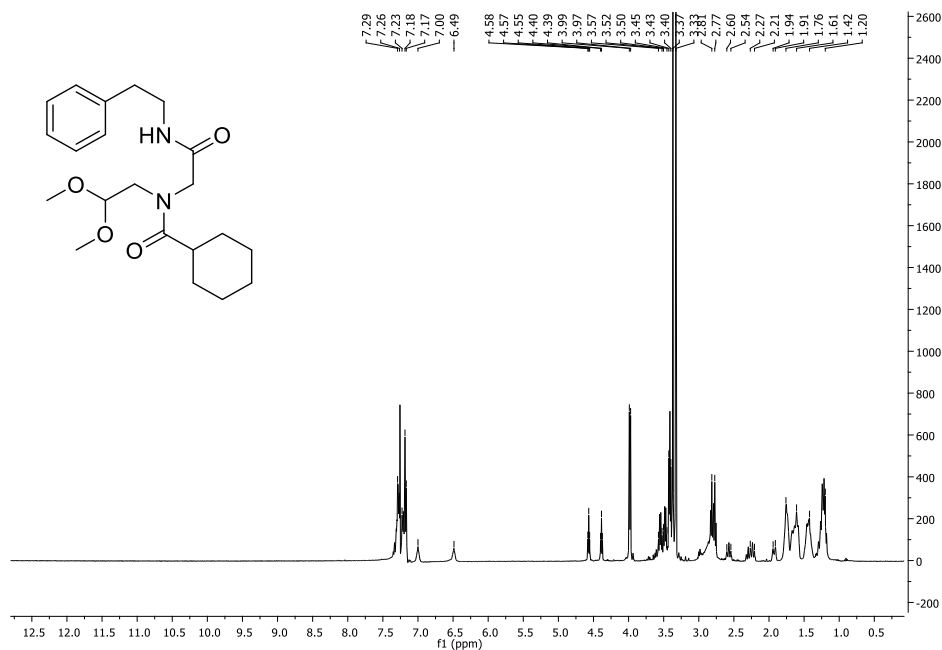
Figure 178. ^{1}H NMR of N-(2,2-dimethoxyethyl)-N-(2-oxo-2-(2-phenethylamino)-ethyl)cyclohexane carboxamide (Ugi reaction) (**12**).
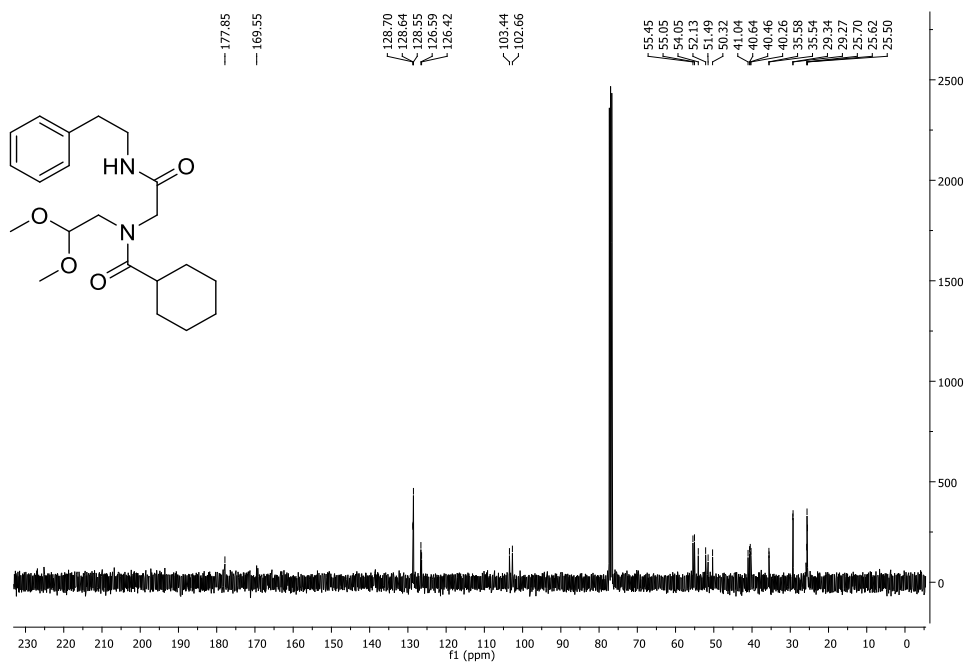
Figure 179. ^{13}C NMR of N-(2,2-dimethoxyethyl)-N-(2-oxo-2-(2-phenethylamino)-ethyl)cyclohexane carboxamide (Ugi reaction) (**12**).

2-(cyclohexanecarbonyl)-2,3,6,7,11b-hexahydro-pyrazino[2,1-a]isoquinolin-4-one (Praziquantel)
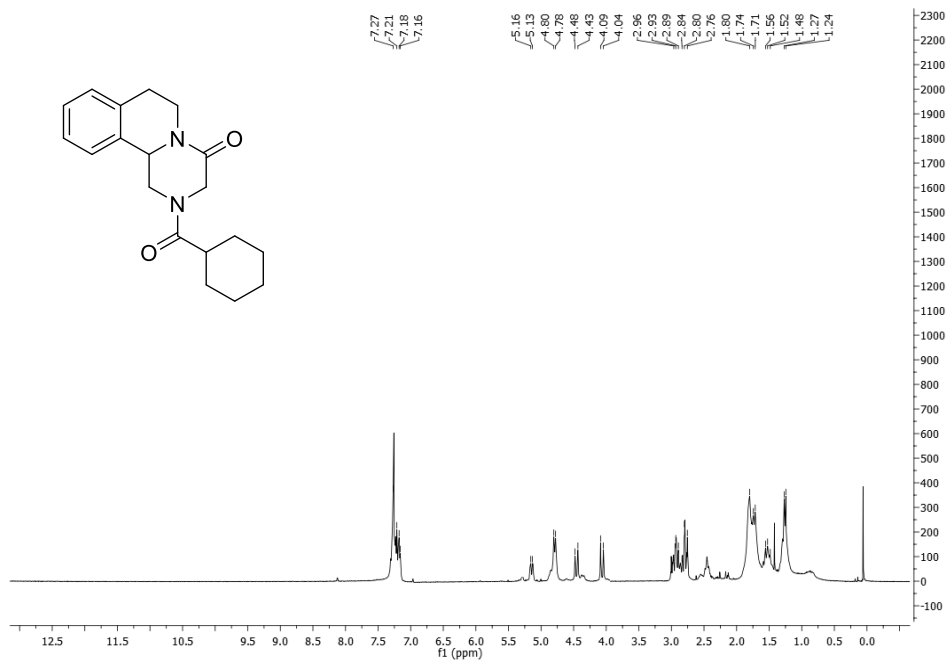
Figure 180. ^{1}H NMR of 2-(cyclohexanecarbonyl)-2,3,6,7,11b-hexahydro-pyrazino[2,1-a]isoquinolin-4-one (Praziquantel) (Pictet−Spengler reaction) (13).
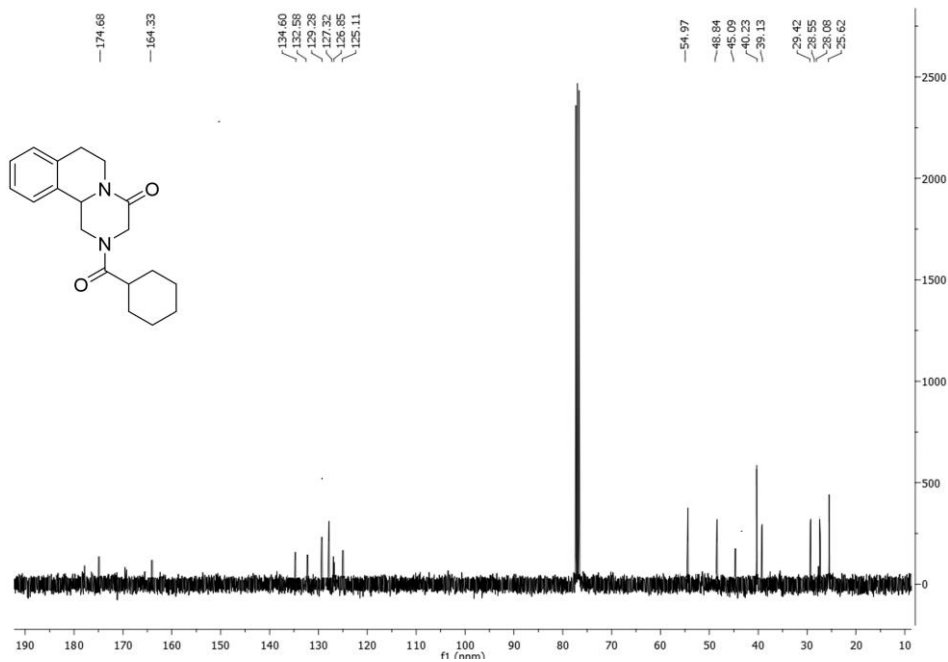
Figure 181. ^{13}C NMR of 2-(cyclohexanecarbonyl)-2,3,6,7,11b-hexahydro-pyrazino[2,1-a]isoquinolin-4-one (Praziquantel) (Pictet−Spengler reaction) (**13**).

243

Bis-(2-chloroethyl)-amine hydrochloride
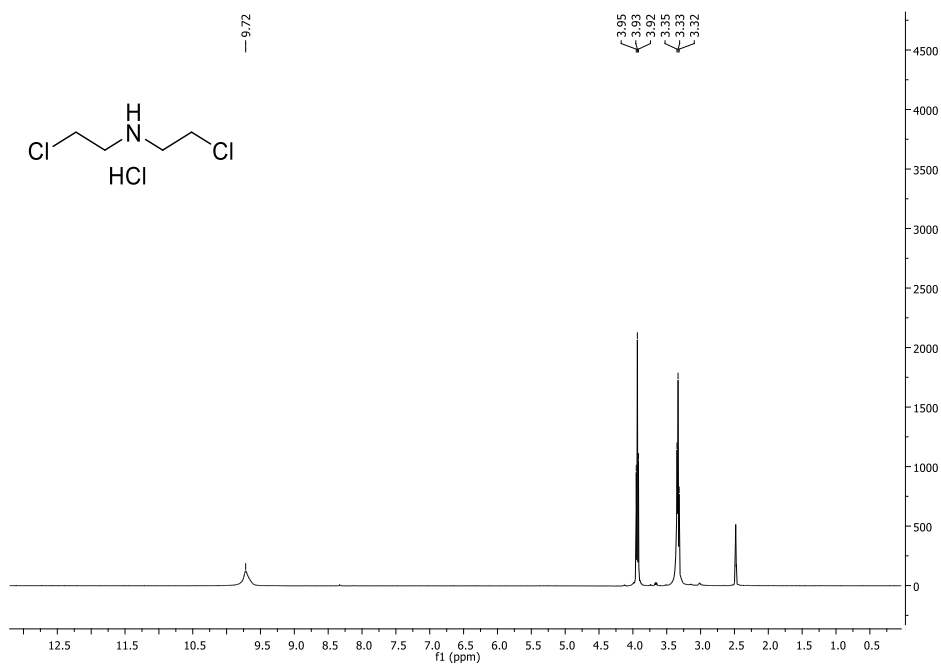
Figure 182. ^{1}H NMR of Bis-(2-chloroethyl)-amine hydrochloride (**15**).
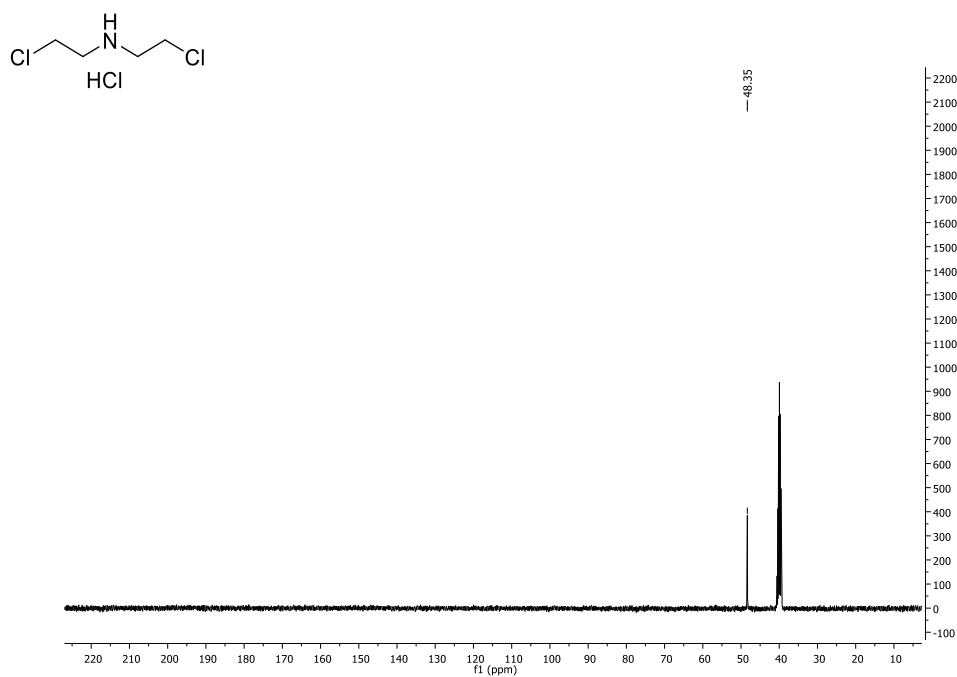
Figure 183. ^{13}C NMR of Bis-(2-chloroethyl)-amine hydrochloride (**15**).

1-(4-methoxyphenyl)piperazine
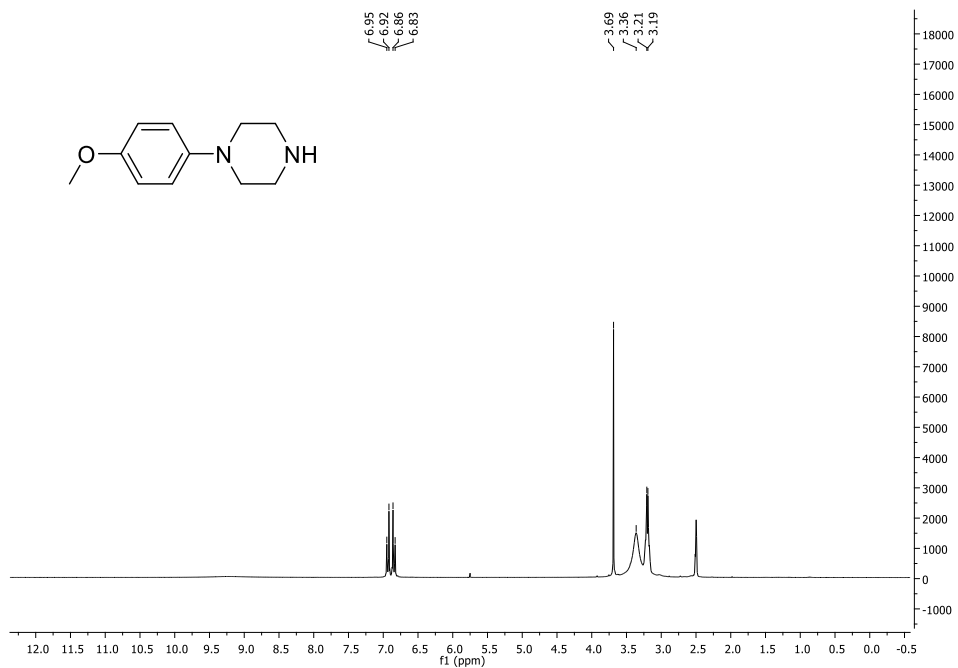
Figure 184. ^{1}H NMR of 1-(4-methoxyphenyl)piperazine (**16**).
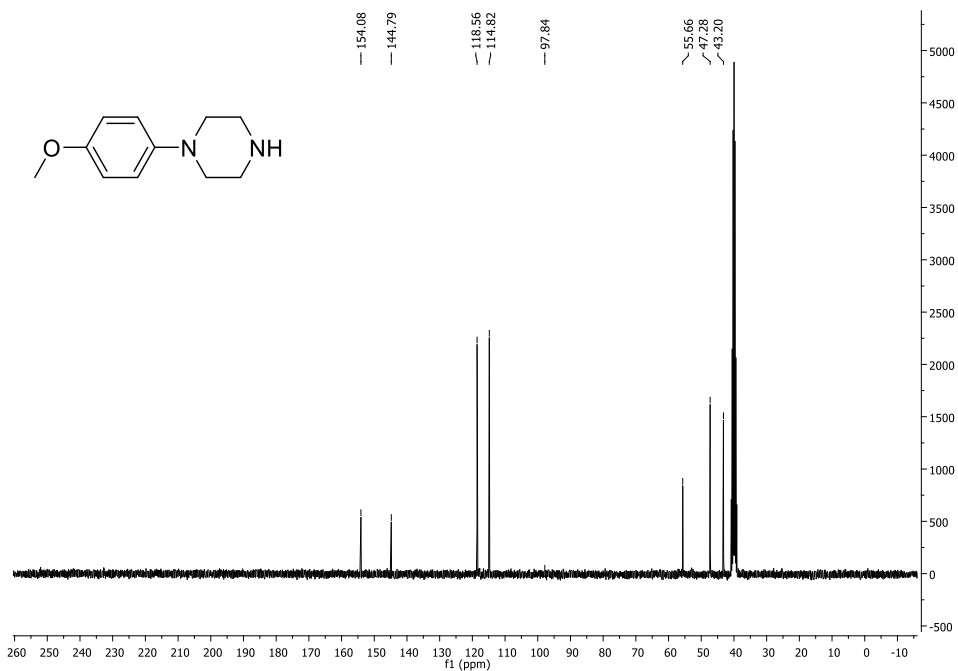
Figure 185. ^{13}C NMR of 1-(4-methoxyphenyl)piperazine (**16**).

1-(4-Methoxyphenyl)-4-(4-nitrophenyl)piperazine
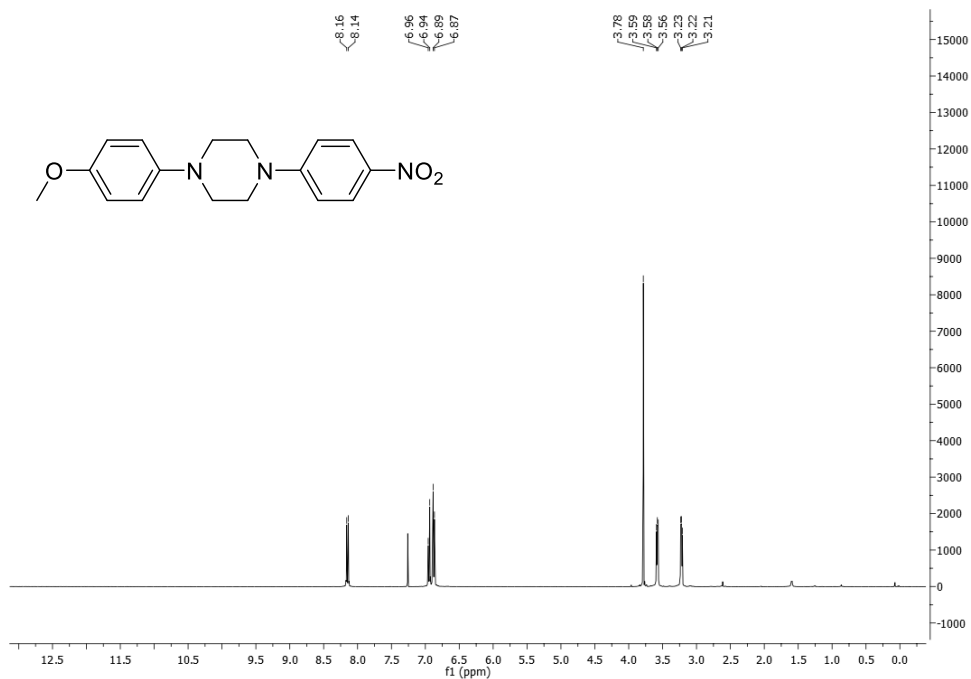
Figure 186. ^{1}H NMR of 1-(4-Methoxyphenyl)-4-(4-nitrophenyl)piperazine (**17**).
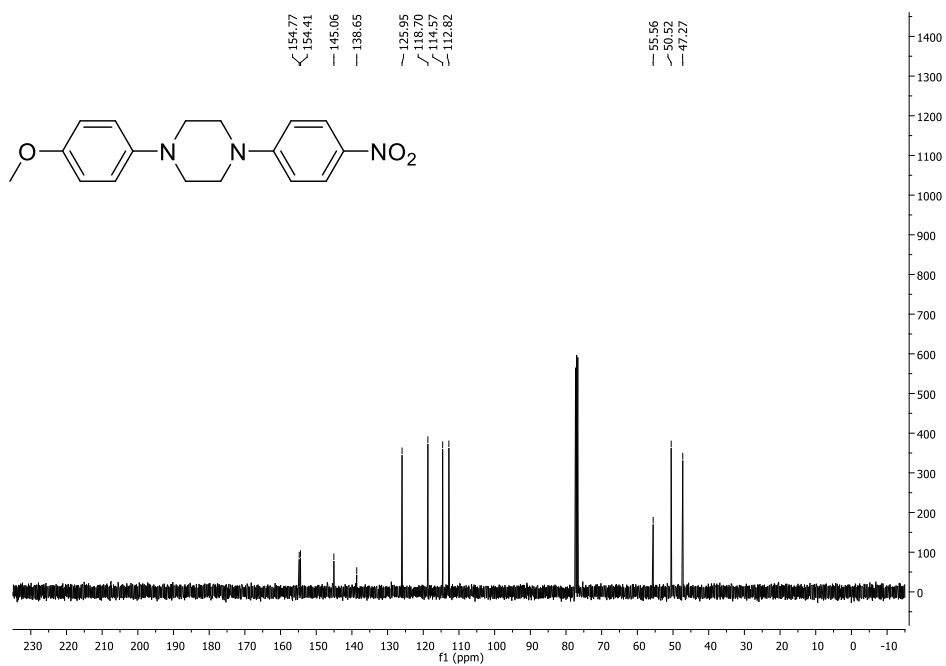
Figure 187. ^{13}C NMR of 1-(4-Methoxyphenyl)-4-(4-nitrophenyl)piperazine (**17**).

4-(4-(4-Methoxyphenyl)piperazin-1-yl)-aniline
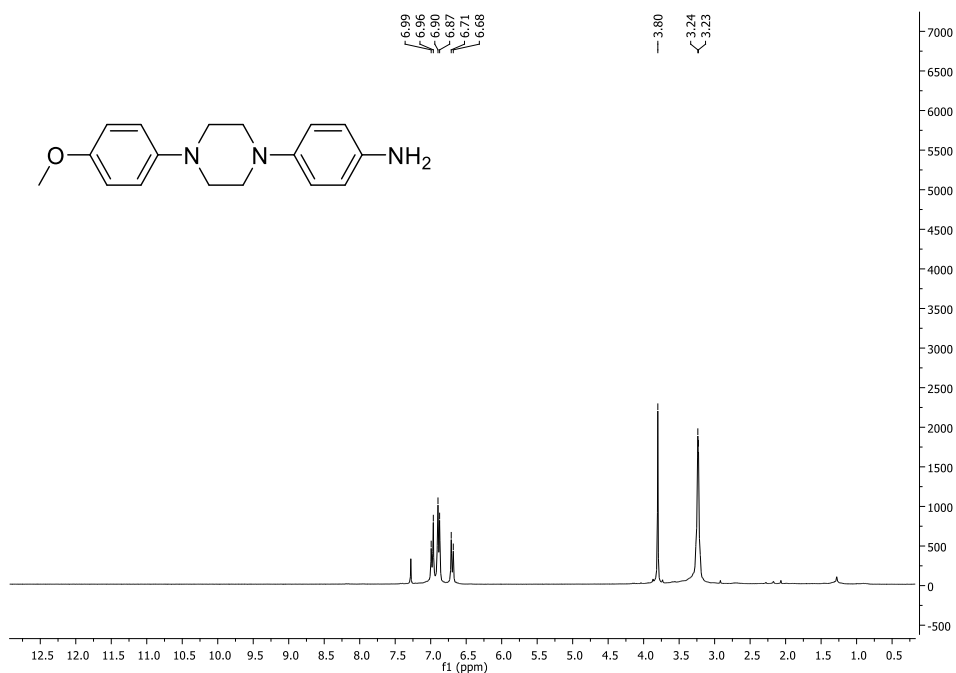
Figure 188. ^{1}H NMR of 4-[4-(4-Methoxyphenyl)piperazin-1-yl]-aniline (**18**).
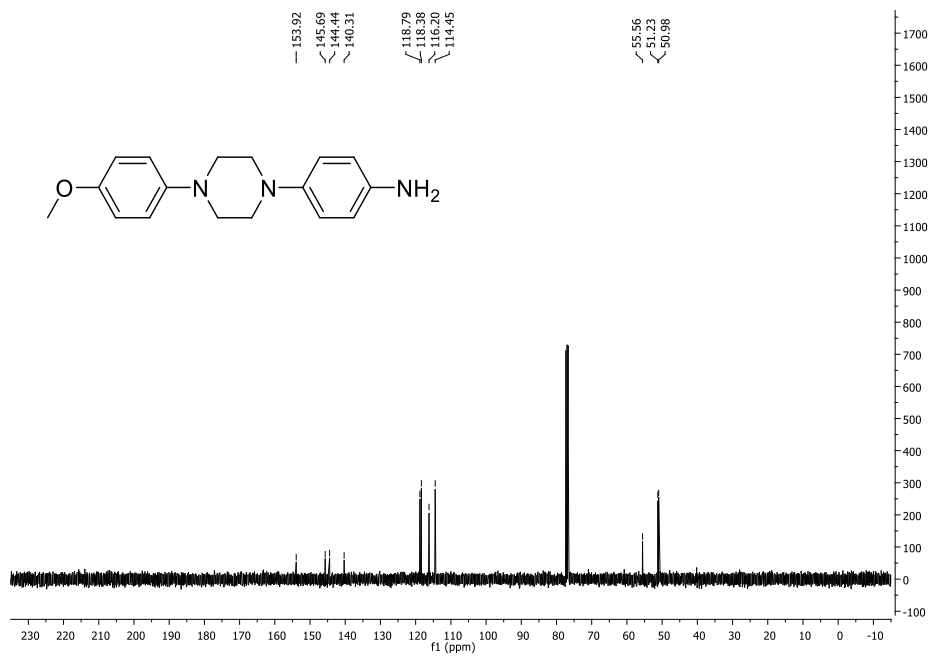
Figure 189. ^{13}C NMR of 4-[4-(4-Methoxyphenyl)piperazin-1-yl]-aniline (**18**).

Final remarks

The present work was focused on the development of new eco-friendly chemical procedures for the preparation and application of heterogeneous catalysts, aiming at saving energy and increasing process efficiency, following the Green Chemistry's principles. In particular the attention was focused on: 1) the comparison of classic methods with non-conventional energy sources and techniques, 2) the development of mild, simple and inexpensive heterogeneous catalytic systems, and 3) application of such catalysts for sustainable synthetic processes.

In this contest, the use of the so-called enabling technologies, such as MW, US and flow chemistry, generated high-energy microenvironments that were exploited in different fields: from the preparation of solid supports, material functionalization and metal immobilization, to the synthesis of fine chemicals and active pharmaceutical intermediates.

Effective preparation and specific derivatization have been performed on silica, carbon-based materials and iron oxide nanoparticles. Different functionalization strategies were specifically chosen on the basis of the selected material and specific organic portions were added to study their influence on support stabilization and/or metal complexation.

More specifically, Cu(II) supported on polyamino and β-CD derivatized silica materials were prepared by a condensation reaction between the silanol group of the silica surface and alkoxysilane derivatives. The interposition of an organic flexible polyamino spacer was proven to influence the catalytic activity of these systems.

Secondly, mild and efficient synthetic protocols based on 1,3-DCA were studied and exploited for the derivatization of graphitic layers (rGO and NDs). A new accurate and non-destructive quantification method, based on the Fmoc deprotection, was validated. The selective derivatization of these systems could offer the opportunity to prepare specific supporting materials for metal immobilization.

Then, a sustainable procedure for the preparation of Co(II) supported and stabilized on carbon-based nanoparticles was investigated. Carbon derived from pinecones was used as support for the immobilization and stabilization of cobalt nanocluster, ensured by the presence of polyphenols. This system could be classified as as an "excellent" electrocatalyst for the OER.

Finally, negatively charged hydrophilic β-CDs grafted IONPs were prepared to study the combination of citric acid and amino citrate modified β-CDs into their adsorption capacity, stability, cytotoxicity and relaxometric properties.

The efficacy of MW, US or combined MW/US systems in the preparation of the above-mentioned well-defined solid materials was deeply demonstrated, supported by the comparison with conventional technologies. Moreover, the catalytic efficiency of prepared catalysts was tested under non-conventional energy sources. They offered more energy efficiency in

promoting catalytic organic reactions than classical synthetic methods, because of their excellent heat and mass transfer, resulting in promising technologies, also exploitable in industrial processes.

Finally, flow chemistry was exploited as innovative reaction set-up for continuous realization of green production processes of pharmaceuticals. The possibility to improve reaction parameters, enhance safety, reduce reaction time and preserve yields was tested on the synthesis of 6-aminouracil Camptothecin analogue, Praziquantel and Itraconazole. Good conversion and isolated yields of the products were obtained, suggesting an innovative, green and cost-effective methodology for the application of flow chemistry for the synthesis of APIs.

Based on these good results and on the versatility of such systems, usable for instance in the field of regenerative medicine, where graphene scaffold could have an impact on stem cell differentiation, or in drug carrier applications, using derivatized NDs or magnetic IONPs, that can also be driven to a specific area thanks to an external magnet, or, simply as catalytic systems, thanks to the availability, environmental acceptability, corrosion resistance, and unique surface properties of selected supporting systems, I hope this work will be a starting point for other investigations and applications.

Acknowledgments

Ai miei amici, ai miei colleghi, a tutte le persone che ho incrociato durante il mio cammino in questi tre, bellissimi, anni. Grazie.

Infine, a te Pietro, che sei entrato nella mia via durante questo percorso, va il pensiero più dolce. Hai reso frizzante ogni momento di questo tempo, che è diventato il nostro tempo. Un enorme grazie va a te, alla meravigliosa persona che sei. All'amore, alle attenzioni, ai consigli e al supporto. Il grazie più grande è rivolto alla tua spensieratezza, alla calma, alla serenità, alla libertà, all'energia che mi trasmetti ogni giorno. È con te che voglio concludere questa tesi e sapere che saremo accolti semplicemente da un altro, meraviglioso, splendido inizio.

Bibliography

1.   Anastas, P. T.; Warner, J. C., *Green Chemistry: Theory and Practice*. Oxford University Press: New York, 1998.
2.   Anastas, P. T.; Zimmerman, J. B., Peer Reviewed: Design Through the 12 Principles of Green Engineering. *Environmental Science & Technology* **2003,** *37* (5), 94A-101A.
3.   Tang, S. L. Y.; Smith, R. L.; Poliakoff, M., Principles of green chemistry: PRODUCTIVELY. *Green Chemistry* **2005,** *7* (11).
4.   Tang, S. Y.; Bourne, R. A.; Smith, R. L.; Poliakoff, M., The 24 Principles of Green Engineering and Green Chemistry: "IMPROVEMENTS PRODUCTIVELY". *Green Chemistry* **2008,** *10* (3).
5.   Anastas, P.; Eghbali, N., Green chemistry: principles and practice. *Chemical Society Reviews* **2010,** *39* (1), 301-12.
6.   Anastas Paul T., B. L. B., Kirchhoff Mary M., Williamson Tracy C., The role of catalysis in the design, development, and implementation of green chemistry. *Catalysis Today* **2000,** *55*, 11-22.
7.   Copéret, C., Design and understanding of heterogeneous alkene metathesis catalysts. *Dalton Transactions* **2007,** (47), 5498-5504.
8.   Balcar, H.; Cejka, J., Mesoporous Molecular Sieves Based Catalysts for Olefin Metathesis and Metathesis Polymerization. In *Green Metathesis Chemistry: Great Challenges in Synthesis, Catalysis and Nanotechnology*, Dragutan, V.; Demoncean, A.; Dragutan, I.; Finkelshtein, E. S., Eds. 2010; pp 101-114.
9.   Buchmeiser, M. R., Polymer-Supported Well-Defined Metathesis Catalysts. *Chemical Reviews* **2009,** *109* (2), 303-321.
10.   Ma, Z.; Zaera, F., Heterogeneous Catalysis by Metals. *Encyclopedia of Inorganic and Bioinorganic Chemistry* **2014,** 1-16.
11.   Sanchez, C.; Soler-Illia, G.; Ribot, F.; Lalot, T.; Mayer, C. R.; Cabuil, V., Designed hybrid organic-inorganic nanocomposites from functional nanobuilding blocks. *Chemistry of Materials* **2001,** *13* (10), 3061-3083.
12.   Gomez-Romero, P., Hybrid organic-inorganic materials - In search of synergic activity. *Adv. Mater.* **2001,** *13* (3), 163-174.
13.   Corma, A.; Diaz, U.; Garcia, T.; Sastre, G.; Velty, A., Multifunctional Hybrid Organic-Inorganic Catalytic Materials with a Hierarchical System of Well-Defined Micro- and Mesopores. *Journal of the American Chemical Society* **2010,** *132* (42), 15011-15021.
14.   Karimi, B.; Zamani, A.; Clark, J. H., A Bipyridyl Palladium Complex Covalently Anchored onto Silica as an Effective and Recoverable Interphase Catalyst for the Aerobic Oxidation of Alcohols. *Organometallics* **2005,** *24* (19), 4695-4698.
15.   Guo, H.; Gong, C.; Zeng, X.; Xu, H.; Zeng, Q.; Zhang, J.; Zhong, Z.; Xie, J., Isopolymolybdate-based inorganic–organic hybrid compounds constructed by multidentate N-donor ligands: syntheses, structures and properties. *Dalton Transactions* **2019,** *48* (17), 5541-5550.
16.   Goni, M. A.; Rosenberg, E.; Meregude, S.; Abbott, G., A methods study of immobilization of PONOP pincer transition metal complexes on silica polyamine composites (SPC). *Journal of Organometallic Chemistry* **2016,** *807*, 1-10.
17.   Dolbecq, A.; Dumas, E.; Mayer, C. R.; Mialane, P., Hybrid Organic−Inorganic Polyoxometalate Compounds: From Structural Diversity to Applications. *Chemical Reviews* **2010,** *110* (10), 6009-6048.
18.   Mir, S. H.; Nagahara, L. A.; Thundat, T.; Mokarian-Tabari, P.; Furukawa, H.; Khosla, A., Review-Organic-Inorganic Hybrid Functional Materials: An Integrated Platform for Applied Technologies. *Journal of the Electrochemical Society* **2018,** *165* (8), B3137-B3156.
19.   Lei, B.; Li, B.; Zhang, H.; Zhang, L.; Li, W., Synthesis, Characterization, and Oxygen Sensing Properties of Functionalized Mesoporous SBA-15 and MCM-41 with a Covalently Linked Ruthenium(II) Complex. *The Journal of Physical Chemistry C* **2007,** *111* (30), 11291-11301.
20.   Sanchez, C.; Julian, B.; Belleville, P.; Popall, M., Applications of hybrid organic-inorganic nanocomposites. *Journal of Materials Chemistry* **2005,** *15* (35-36), 3559-3592.
21.   Benzaqui, M.; Semino, R.; Carn, F.; Tavares, S. R.; Menguy, N.; Giménez-Marqués, M.; Bellido, E.; Horcajada, P.; Berthelot, T.; Kuzminova, A. I.; Dmitrenko, M. E.; Penkova, A. V.; Roizard, D.; Serre, C.; Maurin, G.; Steunou, N., Covalent and Selective Grafting of Polyethylene Glycol Brushes at the Surface of ZIF-8 for the Processing of Membranes for Pervaporation. *ACS Sustainable Chemistry & Engineering* **2019,** *7* (7), 6629-6639.
22.   Georgakilas, V.; Otyepka, M.; Bourlinos, A. B.; Chandra, V.; Kim, N.; Kemp, K. C.; Hobza, P.; Zboril, R.; Kim, K. S., Functionalization of Graphene: Covalent and Non-Covalent Approaches, Derivatives and Applications. *Chemical Reviews* **2012,** *112* (11), 6156-6214.
23.   Ziarani, G. M.; Lashgari, N.; Badiei, A., Sulfonic acid-functionalized mesoporous silica (SBA-Pr-SO3H) as solid acid catalyst in organic reactions. *Journal of Molecular Catalysis a-Chemical* **2015,** *397*, 166-191.
24.   Ziarani, G. M.; Badiei, A.; Mousavi, S.; Lashgari, N.; Shahbazi, A., Application of Amino-Functionalized SBA-15 Type Mesoporous Silica in One-Pot Synthesis of Spirooxindoles. *Chinese Journal of Catalysis* **2012,** *33* (11), 1832-1839.

25. Bhanja, P.; Modak, A.; Chatterjee, S.; Bhaumik, A., Bifunctionalized Mesoporous SBA-15: A New Heterogeneous Catalyst for the Facile Synthesis of 5-Hydroxymethylfurfural. *Acs Sustainable Chemistry & Engineering* **2017,** *5* (3), 2763-2773.

26. Bied, C.; Gauthier, D.; Moreau, J. J. E.; Man, M. W. C., Preparation and characterization of new templated hybrid materials containing a chiral diamine ligand. *Journal of Sol-Gel Science and Technology* **2001,** *20* (3), 313-320.

27. Du, J. Z.; Chen, Y. M., Organic-inorganic hybrid nanoparticles with a complex hollow structure. *Angewandte Chemie-International Edition* **2004,** *43* (38), 5084-5087.

28. Allain, C.; Favette, S.; Chamoreau, L. M.; Vaissermann, J.; Ruhlmann, L.; Hasenknopf, B., Hybrid organic-inorganic porphyrin-polyoxometalate complexes. *European Journal of Inorganic Chemistry* **2008,** (22), 3433-3441.

29. Zhang, J.; Jiang, P. P.; Shen, Y. R.; Zhang, W. J.; Bian, G., Covalent anchoring of Mo(VI) Schiff base complex into SBA-15 as a novel heterogeneous catalyst for enhanced alkene epoxidation. *Journal of Porous Materials* **2016,** *23* (2), 431-440.

30. Zare, M.; Moradi-Shoeili, Z.; Ashouri, F.; Bagherzadeh, M., Heterogeneous SBA-15-supported Oxoperoxomolybdenum(VI) complex for enhanced olefin epoxidation. *Catalysis Communications* **2017,** *88*, 9-12.

31. Bhar, S.; Ananthakrishnan, R., Ru(II)-Metal complex immobilized mesoporous SBA-15 hybrid for visible light induced photooxidation of chlorophenolic compounds in aqueous medium. *Photochemical & Photobiological Sciences* **2017,** *16* (8), 1290-1300.

32. Férey, G.; Latroche, M.; Serre, C.; Millange, F.; Loiseau, T.; Percheron-Guégan, A., Hydrogen adsorption in the nanoporous metal-benzenedicarboxylate M(OH)(O2C–C6H4–CO2) (M = Al3+, Cr3+), MIL-53. *Chemical Communications* **2003,** (24), 2976-2977.

33. Boury, B.; Corriu, R. J. P., Auto-organisation of hybrid organic–inorganic materials prepared by sol–gel chemistry. *Chemical Communications* **2002,** (8), 795-802.

34. Corriu, R. J. P.; Mehdi, A.; Reyé, C.; Thieuleux, C., Control of coordination chemistry in both the framework and the pore channels of mesoporous hybrid materials. *New Journal of Chemistry* **2003,** *27* (6), 905-908.

35. Merle, N.; Mazoyer, E.; Szeto, K. C.; Rouge, P.; de Mallmann, A.; Berrier, E.; Delevoye, L.; Gauvin, R. M.; Nicholas, C. P.; Basset, J.-M.; Taoufik, M., Synthesis of an oxo trialkyl tungsten fluoride complex and its dual reactivity with silica dehydroxylated at high temperature. *Journal of Organometallic Chemistry* **2018,** *869*, 11-17.

36. Kallmeier, F.; Irrgang, T.; Dietel, T.; Kempe, R., Highly Active and Selective Manganese C=O Bond Hydrogenation Catalysts: The Importance of the Multidentate Ligand, the Ancillary Ligands, and the Oxidation State. *Angewandte Chemie International Edition* **2016,** *55* (39), 11806-11809.

37. Ortuño, M. A.; López, N., Reaction mechanisms at the homogeneous–heterogeneous frontier: insights from first-principles studies on ligand-decorated metal nanoparticles. *Catalysis Science & Technology* **2019,** *9* (19), 5173-5185.

38. Marshall, S. T.; O'Brien, M.; Oetter, B.; Corpuz, A.; Richards, R. M.; Schwartz, D. K.; Medlin, J. W., Controlled selectivity for palladium catalysts using self-assembled monolayers. *Nature Materials* **2010,** *9* (10), 853-858.

39. Albani, D.; Li, Q.; Vilé, G.; Mitchell, S.; Almora-Barrios, N.; Witte, P. T.; López, N.; Pérez-Ramírez, J., Interfacial acidity in ligand-modified ruthenium nanoparticles boosts the hydrogenation of levulinic acid to gamma-valerolactone. *Green Chemistry* **2017,** *19* (10), 2361-2370.

40. Wang, A. L.; Xu, H.; Feng, J. X.; Ding, L. X.; Tong, Y. X.; Li, G. R., Design of Pd/PANI/Pd sandwich-structured nanotube array catalysts with special shape effects and synergistic effects for ethanol electrooxidation. *Journal of the American Chemical Society* **2013,** *135* (29), 10703-10709.

41. Berben, L. A.; de Bruin, B.; Heyduk, A. F., Non-innocent ligands. *Chemical Communications* **2015,** *51* (9), 1553-1554.

42. Luca, O. R.; Crabtree, R. H., Redox-active ligands in catalysis. *Chemical Society Reviews* **2013,** *42* (4), 1440-1459.

43. Praneeth, V. K.; Ringenberg, M. R.; Ward, T. R., Redox-active ligands in catalysis. *Angewante Chemie International Edition* **2012,** *51* (41), 10228-10234.

44. Copéret, C.; Basset, J. M., Strategies to Immobilize Well-Defined Olefin Metathesis Catalysts: Supported Homogeneous Catalysisvs. Surface Organometallic Chemistry. *Advanced Synthesis & Catalysis* **2007,** *349* (1-2), 78-92.

45. Ding, K.; Gulec, A.; Johnson, A. M.; Drake, T. L.; Wu, W.; Lin, Y.; Weitz, E.; Marks, L. D.; Stair, P. C., Highly Efficient Activation, Regeneration, and Active Site Identification of Oxide-Based Olefin Metathesis Catalysts. *ACS Catalysis* **2016,** *6* (9), 5740-5746.

46. Dewaele, A.; Verpoort, F.; Sels, B., Opportunities of Immobilized Homogeneous Metathesis Complexes as Prominent Heterogeneous Catalysts. *ChemCatChem* **2016,** *8* (19), 3010-3030.

47. Balcar, H.; Čejka, J., Mesoporous molecular sieves as advanced supports for olefin metathesis catalysts. *Coordination Chemistry Reviews* **2013,** *257* (21-22), 3107-3124.

48. Conley, M. P.; Copéret, C.; Thieuleux, C., Mesostructured Hybrid Organic–Silica Materials: Ideal Supports for Well-Defined Heterogeneous Organometallic Catalysts. *ACS Catalysis* **2014,** *4* (5), 1458-1469.

49.   Copéret, C., Molecular design of heterogeneous catalysts: the case of olefin metathesis. *New Journal of Chemistry* **2004,** *28* (1), 1-10.

50.   Bing, W.; Wei, M., Recent advances for solid basic catalysts: Structure design and catalytic performance. *Journal of Solid State Chemistry* **2019,** *269*, 184-194.

51.   Takaya, J., Catalysis using transition metal complexes featuring main group metal and metalloid compounds as supporting ligands. *Chemical Science* **2021,** *12* (6), 1964-1981.

52.   Elsby, M. R.; Baker, R. T., Strategies and mechanisms of metal–ligand cooperativity in first-row transition metal complex catalysts. *Chemical Society Reviews* **2020,** *49* (24), 8933-8987.

53.   Henrici-Olivé, G.; Olivé, S., Influence of Ligands on the Activity and Specificity of Soluble Transition Metal Catalysts. *Angewandte Chemie International Edition* **1971,** *10* (2), 105-115.

54.   Diesendruck, C. E.; Tzur, E.; Ben-Asuly, A.; Goldberg, I.; Straub, B. F.; Lemcoff, N. G., Predicting the Cis−Trans Dichloro Configuration of Group 15−16 Chelated Ruthenium Olefin Metathesis Complexes: A DFT and Experimental Study. *Inorganic Chemistry* **2009,** *48* (22), 10819-10825.

55.   Pump, E.; Leitgeb, A.; Kozłowska, A.; Torvisco, A.; Falivene, L.; Cavallo, L.; Grela, K.; Slugovc, C., Variation of the Sterical Properties of the N-Heterocyclic Carbene Coligand in Thermally Triggerable Ruthenium-Based Olefin Metathesis Precatalysts/Initiators. *Organometallics* **2015,** *34* (22), 5383-5392.

56.   Ivry, E.; Nechmad, N. B.; Baranov, M.; Goldberg, I.; Lemcoff, N. G., Influence of Anionic Ligand Exchange in Latent Sulfur-Chelated Ruthenium Precatalysts. *Inorganic Chemistry* **2018,** *57* (24), 15592-15599.

57.   Eivgi, O.; Phatake, R. S.; Nechmad, N. B.; Lemcoff, N. G., Light-Activated Olefin Metathesis: Catalyst Development, Synthesis, and Applications. *Accounts of Chemical Research* **2020,** *53* (10), 2456-2471.

58.   Rozenberg, I.; Eivgi, O.; Frenklah, A.; Butilkov, D.; Kozuch, S.; Goldberg, I.; Lemcoff, N. G., Synthesis and Catalytic Properties of Sulfur-Chelated Ruthenium Benzylidenes Bearing a Cyclic (Alkyl)(amino)carbene Ligand. *ACS Catalysis* **2018,** *8* (9), 8182-8191.

59.   Ben-Asuly, A.; Tzur, E.; Diesendruck, C. E.; Sigalov, M.; Goldberg, I.; Lemcoff, N. G., A Thermally Switchable Latent Ruthenium Olefin Metathesis Catalyst. *Organometallics* **2008,** *27* (5), 811-813.

60.   Thieuleux, C., Heterogeneous well-defined catalysts for metathesis of inert and not so inert bonds. *Journal of Molecular Catalysis A: Chemical* **2004,** *213* (1), 47-57.

61.   Coperet, C.; Chabanas, M.; Saint-Arroman, R. P.; Basset, J.-M., Homogeneous and heterogeneous catalysis: bridging the gap through surface organometallic chemistry. *Angewante Chemie, International Edition* **2003,** *42* (2), 156-181.

62.   Qureshi, Z. S.; Hamieh, A.; Barman, S.; Maity, N.; Samantaray, M. K.; Ould-Chikh, S.; Abou-hamad, E.; Falivene, L.; D'Elia, V.; Rothenberger, A.; Llorens, I.; Hazemann, J.-L.; Basset, J.-M., SOMC-Designed Silica Supported Tungsten Oxo Imidazolin-2-iminato Methyl Precatalyst for Olefin Metathesis Reactions. *Inorganic Chemistry* **2017,** *56* (2), 861-871.

63.   Corma, A.; García, H.; Llabrés i Xamena, F. X., Engineering Metal Organic Frameworks for Heterogeneous Catalysis. *Chemical Reviews* **2010,** *110* (8), 4606-4655.

64.   O'Neill, B. J.; Jackson, D. H. K.; Lee, J.; Canlas, C.; Stair, P. C.; Marshall, C. L.; Elam, J. W.; Kuech, T. F.; Dumesic, J. A.; Huber, G. W., Catalyst Design with Atomic Layer Deposition. *ACS Catalysis* **2015,** *5* (3), 1804-1825.

65.   Liu, M.; Zhao, Z.; Duan, X.; Huang, Y., Nanoscale Structure Design for High-Performance Pt-Based ORR Catalysts. *Advanced Materials* **2019,** *31* (6), 18022-18034.

66.   Jeevanandam, J.; Barhoum, A.; Chan, Y. S.; Dufresne, A.; Danquah, M. K., Review on nanoparticles and nanostructured materials: history, sources, toxicity and regulations. *Beilstein Journal of Nanotechnologies* **2018,** *9*, 1050-1074.

67.   Niu, Z.; Li, Y., Removal and Utilization of Capping Agents in Nanocatalysis. *Chemistry of Materials* **2014,** *26* (1), 72-83.

68.   El Badawy, A. M.; Luxton, T. P.; Silva, R. G.; Scheckel, K. G.; Suidan, M. T.; Tolaymat, T. M., Impact of Environmental Conditions (pH, Ionic Strength, and Electrolyte Type) on the Surface Charge and Aggregation of Silver Nanoparticles Suspensions. *Environmental Science & Technology* **2010,** *44* (4), 1260-1266.

69.   Varma, R. S., Greener approach to nanomaterials and their sustainable applications. *Current Opinion in Chemical Engineering* **2012,** *1* (2), 123-128.

70.   Tang, S. C. N.; Lo, I. M. C., Magnetic nanoparticles: Essential factors for sustainable environmental applications. *Water Research* **2013,** *47* (8), 2613-2632.

71.   Pârvulescu, V. I.; Hardacre, C., Catalysis in Ionic Liquids. *Chemical Reviews* **2007,** *107* (6), 2615-2665.

72.   Varma, R. S., Greener approach to nanomaterials and their sustainable applications. *Curr. Opin. Chem. Eng.* **2012,** *1* (2), 123-128.

73.   Polshettiwar, V.; Varma, R. S., Green chemistry by nano-catalysis. *Green Chemistry* **2010,** *12* (5), 743-754.

74.   Yang, F.; Deng, D.; Pan, X.; Fu, Q.; Bao, X., Understanding nano effects in catalysis. *National Science Review* **2015,** *2* (2), 183-201.

75.   Astruc, D.; Lu, F.; Aranzaes, J. R., Nanoparticles as Recyclable Catalysts: The Frontier between Homogeneous and Heterogeneous Catalysis. *Angewandte Chemie International Edition* **2005,** *44* (48), 7852-7872.

76.   Santosh Bahadur Singh, P. K. T., Catalysis: A Brief Review on Nano-Catalyst. *Journal of Energy and Chemical Engineering* **2014,** *2* (3), 106-115.

77.   Yang, X.-F.; Wang, A.; Qiao, B.; Li, J.; Liu, J.; Zhang, T., Single-Atom Catalysts: A New Frontier in Heterogeneous Catalysis. *Accounts of Chemical Research* **2013,** *46* (8), 1740-1748.

78.   Liu, L.; Corma, A., Metal Catalysts for Heterogeneous Catalysis: From Single Atoms to Nanoclusters and Nanoparticles. *Chemical Reviews* **2018,** *118* (10), 4981-5079.

79.   Santosh Bahadur Singh, P. K. T., Catalysis: A Brief Review on Nano-Catalyst. *Journal of Energy and Chemical Engineering* **2014,** *2*, 106-115.

80.   Gedye, R.; Smith, F.; Westaway, K.; Ali, H.; Baldisera, L.; Laberge, L.; Rousell, J., The use of microwave ovens for rapid organic synthesis. *Tetrahedron Letters* **1986,** *27* (3), 279-282.

81.   Mandal, A. K.; Sen, R., An overview on microwave processing of material: A special emphasis on glass melting. *Materials and Manufacturing Processes* **2016,** *32* (1), 1-20.

82.   Pelle Lidstrom, J. T., Bernard Wathey, Jacob Westman, Microwave assisted organic synthesis. *Tetrahedron* **2001,** *57*, 9225-9283.

83.   Kappe, C. O.; Dallinger, D., The impact of microwave synthesis on drug discovery. *Nature Reviews Drug Discovery* **2006,** *5* (1), 51-63.

84.   Horikoshi, S.; Serpone, N., Role of microwaves in heterogeneous catalytic systems. *Catalysis Science & Technology* **2014,** *4* (5), 1197-1210.

85.   Zhu, Y. J.; Chen, F., Microwave-assisted preparation of inorganic nanostructures in liquid phase. *Chemical Reviews* **2014,** *114* (12), 6462-6555.

86.   https://cem.com/it/microwave-chemistry/solvent-choice. (accessed 23/02/2022).

87.   Gawande, M. B.; Shelke, S. N.; Zboril, R.; Varma, R. S., Microwave-assisted chemistry: synthetic applications for rapid assembly of nanomaterials and organics. *Accounts of Chemical Research* **2014,** *47* (4), 1338-1348.

88.   Kuznetsov, D. V.; Raev, V. A.; Kuranov, G. L.; Arapov, O. V.; Kostikov, R. R., Microwave Activation in Organic Synthesis. *Russian Journal of Organic Chemistry* **2005,** *41* (12), 1719-1749.

89.   Zhu, Y. J.; Chen, F., Microwave-assisted preparation of inorganic nanostructures in liquid phase. *Chem Rev* **2014,** *114* (12), 6462-555.

90.   Ahmed, F.; Li, J.; Zhu, J.; Zhao, J., Biosynthesis of Controllable Size and Shape Gold Nanoparticles by Black Seed (Nigella Sativa) Extract. *Journal of nanoscience and nanotechnology* **2012,** *12*, 2337-2345.

91.   Rutkowska, M.; Namieśnik, J.; Konieczka, P., Chapter 10 - Ultrasound-Assisted Extraction. In *The Application of Green Solvents in Separation Processes*, Pena-Pereira, F.; Tobiszewski, M., Eds. Elsevier: 2017; pp 301-324.

92.   Lupacchini, M.; Mascitti, A.; Giachi, G.; Tonucci, L.; d'Alessandro, N.; Martinez, J.; Colacino, E., Sonochemistry in non-conventional, green solvents or solvent-free reactions. *Tetrahedron* **2017,** *73* (6), 609-653.

93.   Ammar, H. B.; Chtourou, M.; Frikha, M. H.; Trabelsi, M., Green condensation reaction of aromatic aldehydes with active methylene compounds catalyzed by anion-exchange resin under ultrasound irradiation. *Ultrasonics Sonochemistry* **2015,** *22*, 559-564.

94.   Vivekanand, P. A.; Wang, M.-L., Sonocatalyzed synthesis of 2-phenylvaleronitrile under controlled reaction conditions – A kinetic study. *Ultrasonics Sonochemistry* **2011,** *18* (5), 1241-1248.

95.   Sancheti, S. V.; Gogate, P. R., A review of engineering aspects of intensification of chemical synthesis using ultrasound. *Ultrasonics Sonochemistry* **2017,** *36*, 527-543.

96.   Saurabh, P.; Balbir, K.; Anupama, P.; Harish, K., Applications of Ultrasound in Organic Synthesis - A Green Approach. *Current Organic Chemistry* **2013,** *17* (16), 1790-1828.

97.   Cravotto, G.; Cintas, P., Power ultrasound in organic synthesis: moving cavitational chemistry from academia to innovative and large-scale applications. *Chemical Society Reviews* **2006,** *35* (2), 180-196.

98.   Wu, Z.; Borretto, E.; Medlock, J.; Bonrath, W.; Cravotto, G., Effects of Ultrasound and Microwaves on Selective Reduction: Catalyst Preparation and Reactions. *ChemCatChem* **2014,** *6* (10), 2762-2783.

99.   Luche, J.-L., Effect of ultrasound on heterogeneous systems. *Ultrasonics Sonochemistry* **1994,** *1* (2), S111-S118.

100.   Cintas, P.; Palmisano, G.; Cravotto, G., Power ultrasound in metal-assisted synthesis: From classical Barbier-like reactions to click chemistry. *Ultrasonics Sonochemistry* **2011,** *18* (4), 836-841.

101.   Cintas, P.; Tagliapietra, S.; Caporaso, M.; Tabasso, S.; Cravotto, G., Enabling technologies built on a sonochemical platform: Challenges and opportunities. *Ultrasonics Sonochemistry* **2015,** *25*, 8-16.

102.   Rup, S.; Sindt, M.; Oget, N., Catalytic oxidative cleavage of olefins by RuO4 organic solvent-free under ultrasonic irradiation. *Tetrahedron Letters* **2010,** *51* (23), 3123-3126.

103.   Varma, R. S., "Greener" chemical syntheses using mechanochemical mixing or microwave and ultrasound irradiation. *Green Chemistry Letters and Reviews* **2007,** *1* (1), 37-45.

104.   Martina, K.; Cravotto, G.; Varma, R. S., Impact of Microwaves on Organic Synthesis and Strategies toward Flow Processes and Scaling Up. *The Journal of Organic Chemistry* **2021,** *86* (20), 13857-13872.

105.   Straathof, N. J. W.; Tegelbeckers, B. J. P.; Hessel, V.; Wang, X.; Noel, T., A mild and fast photocatalytic trifluoromethylation of thiols in batch and continuous-flow. *Chemical Science journal* **2014,** *5* (12), 4768-4773.

106.   Wang, J.; Guo, Z.; Zhao, J.; Yang, Q.; Dai, Y.; Yang, Y.; Wang, C., Preparation of silica as catalyst supports with controlled surface property using continuous flow reactor. *Applied Catalysis A: General* **2019,** *585*, 117-212.

107.   Akwi, F. M.; Watts, P., Continuous flow chemistry: where are we now? Recent applications, challenges and limitations. *Chemical Communications* **2018,** *54* (99), 13894-13928.

108.   Sagandira, C. R.; Moyo, M.; Watts, P., Continuous flow synthesis of pharmaceuticals in Africa. *ARKIVOC (Gainesville, FL, U. S.)* **2020,** (3), 24-39.

109.   Jensen, K. F., Flow chemistry—Microreaction technology comes of age. *AIChE Journal* **2017,** *63* (3), 858-869.

110.   Koenig, S. G.; Sneddon, H. F., Recent advances in flow chemistry in the pharmaceutical industry. *Green Chemistry* **2017,** *19* (6), 1418-1419.

111.   Tsubogo, T.; Oyamada, H.; Kobayashi, S., Multistep continuous-flow synthesis of (R)- and (S)-rolipram using heterogeneous catalysts. *Nature* **2015,** *520*, 329-332.

112.   Wang, Y.; Wang, X.; Antonietti, M., Polymeric Graphitic Carbon Nitride as a Heterogeneous Organocatalyst: From Photochemistry to Multipurpose Catalysis to Sustainable Chemistry. *Angewandte Chemie International Edition* **2012,** *51* (1), 68-89.

113.   Porta, R.; Benaglia, M.; Puglisi, A., Flow Chemistry: Recent Developments in the Synthesis of Pharmaceutical Products. *Organic Process Research & Development* **2016,** *20* (1), 2-25.

114.   Gutmann, B.; Cantillo, D.; Kappe, C. O., Continuous-Flow Technology-A Tool for the Safe Manufacturing of Active Pharmaceutical Ingredients. *Angewante Chemie International Edition* **2015,** *54* (23), 6688-6728.

115.   Heo, J. H.; Im, S. H.; Noh, J. H.; Mandal, T. N.; Lim, C. S.; Chang, J. A.; Lee, Y. H.; Kim, H. J.; Sarkar, A.; Nazeeruddin, M. K.; Gratzel, M.; Seok, S. I., Efficient inorganic-organic hybrid heterojunction solar cells containing perovskite compound and polymeric hole conductors. *Nature Photonics* **2013,** *7* (6), 487-492.

116.   Parola, S.; Julian-Lopez, B.; Carlos, L. D.; Sanchez, C., Optical Properties of Hybrid Organic-Inorganic Materials and their Applications. *Advanced Functional Materials* **2016,** *26* (36), 6506-6544.

117.   Taleghani, S.; Mirzaei, M.; Eshtiagh-Hosseini, H.; Frontera, A., Tuning the topology of hybrid inorganic-organic materials based on the study of flexible ligands and negative charge of polyoxometalates: A crystal engineering perspective. *Coordination Chemistry Reviews* **2016,** *309*, 84-106.

118.   Cui, J. D.; Jia, S. R., Organic-inorganic hybrid nanoflowers: A novel host platform for immobilizing biomolecules. *Coordination Chemistry Reviews* **2017,** *352*, 249-263.

119.   Rostamnia, S.; Doustkhah, E., Nanoporous silica-supported organocatalyst: a heterogeneous and green hybrid catalyst for organic transformations. *RSC Advances* **2014,** *4* (54), 28238-28248.

120.   Férey, G., Hybrid porous solids: past, present, future. *Chemical Society Reviews* **2008,** *37* (1), 191-214.

121.   Wen, J.; Wilkes, G. L., Organic/Inorganic Hybrid Network Materials by the Sol−Gel Approach. *Chemistry of Materials* **1996,** *8* (8), 1667-1681.

122.   Salvo, A. M. P.; Giacalone, F.; Gruttadauria, M., Advances in Organic and Organic-Inorganic Hybrid Polymeric Supports for Catalytic Applications. *Molecules* **2016,** *21* (10), 1288.

123.   Lashgari, N.; Badiei, A.; Mohammadi Ziarani, G., Modification of mesoporous silica SBA-15 with different organic molecules to gain chemical sensors: a review. *Nanochemistry Research* **2016,** *1* (1), 127-141.

124.   Singh, S.; Kumar, R.; Setiabudi, H. D.; Nanda, S.; Vo, D.-V. N., Advanced synthesis strategies of mesoporous SBA-15 supported catalysts for catalytic reforming applications: A state-of-the-art review. *Applied Catalysis A: General* **2018,** *559*, 57-74.

125.   Ndolomingo, M. J.; Meijboom, R., Noble and Base-Metal Nanoparticles Supported on Mesoporous Metal Oxides: Efficient Catalysts for the Selective Hydrogenation of Levulinic Acid to γ-Valerolactone. *Catalysis Letters* **2019**.

126.   Chen, D.; Zhang, P.; Fang, Q.; Wan, S.; Li, H.; Yang, S.; Huang, C.; Dai, S., Coordination-supported organic polymers: mesoporous inorganic–organic materials with preferred stability. *Inorganic Chemistry Frontiers* **2018,** *5* (8), 2018-2022.

127.   Azeez, A.; Polio, L.; Hanson, J. E.; Gorun, S. M., Photoreactive Superhydrophobic Organic–Inorganic Hybrid Materials Composed of Poly(vinylidene fluoride) and Titanium Dioxide-Supported Perfluorinated Phthalocyanines. *ACS Applied Polymer Materials* **2019,** *1* (6), 1514-1523.

128.   Fedorov, P. P.; Luginina, A. A.; Kuznetsov, S. V.; Voronov, V. V.; Lyapin, A. A.; Ryabochkina, P. A.; Chernov, M. V.; Mayakova, M. N.; Pominova, D. V.; Uvarov, O. V.; Baranchikov, A. E.; Ivanov, V. K.; Pynenkov, A. A.; Nishchev, K. N., Preparation and properties of methylcellulose/nanocellulose/CaF2:Ho polymer-inorganic composite films for two-micron radiation visualizers. *Journal of Fluorine Chemistry* **2017,** *202*, 9-18.

129. Ahadi, N.; Bodaghifard, M. A.; Mobinikhaledi, A., Cu (II)-β-cyclodextrin complex stabilized on magnetic nanoparticles: A retrievable hybrid promoter for green synthesis of spiropyrans. *Applied Organometallic Chemistry* **2019,** *33* (2), e4738.

130. Fallahi, M.; Ahmadi, E.; Mohamadnia, Z., Effect of inorganic oxide supports on the activity of chromium-based catalysts in ethylene trimerization. *Applied Organometallic Chemistry* **2019,** *0* (0), e4975.

131. Li, W.; Zhang, Y.; Li, Q.; Zhang, G., Metal−organic framework composite membranes: Synthesis and separation applications. *Chemical Engineering Science* **2015,** *135*, 232-257.

132. Yin, P. T.; Shah, S.; Chhowalla, M.; Lee, K.-B., Design, Synthesis, and Characterization of Graphene–Nanoparticle Hybrid Materials for Bioapplications. *Chemical Reviews* **2015,** *115* (7), 2483-2531.

133. Zhang, N.; Liu, X.; Huang, Y.; Wang, M.; Li, S.; Zong, M.; Liu, P., Novel nanocomposites of cobalt ferrite covalently-grafted on graphene by amide bond as superior electromagnetic wave absorber. *Journal of Colloid and Interface Science* **2019,** *540*, 218-227.

134. Shinde, P. S.; Suryawanshi, P. S.; Patil, K. K.; Belekar, V. M.; Sankpal, S. A.; Delekar, S. D.; Jadhav, S. A., A Brief Overview of Recent Progress in Porous Silica as Catalyst Supports. *Journal of Composites Science* **2021,** *5* (3).

135. Musso, F.; Ugliengo, P.; Sodupe, M., Do H-Bond Features of Silica Surfaces Affect the H2O and NH3 Adsorption? Insights from Periodic B3LYP Calculations. *The Journal of Physical Chemistry A* **2011,** *115* (41), 11221-11228.

136. Zhuravlev, L. T., The surface chemistry of amorphous silica. Zhuravlev model. *Physicochemical and Engineering Aspects* **2000,** *173*, 1-38.

137. Pal, N.; Bhaumik, A., Mesoporous materials: versatile supports in heterogeneous catalysis for liquid phase catalytic transformations. *RSC Advances* **2015,** *5* (31), 24363-24391.

138. Wang, J.; Guo, Z.; Zhao, J.; Yang, Q.; Dai, Y.; Yang, Y.; Wang, C., Preparation of silica as catalyst supports with controlled surface property using continuous flow reactor. *Applied Catalysis A: General* **2019,** *585*.

139. Reck, B. K.; Graedel, T. E., Challenges in Metal Recycling. *Science* **2012,** *337* (6095), 690.

140. Song, B. Q.; Wang, X. L.; Sun, C. Y.; Zhang, Y. T.; Wu, X. S.; Yang, L.; Shao, K. Z.; Zhao, L.; Su, Z. M., An organic-inorganic hybrid photocatalyst based on sandwich-type tetra-Co-substituted phosphotungstates with high visible light photocatalytic activity. *Dalton Transactions* **2015,** *44* (31), 13818-13822.

141. Wei, X. L.; Lu, X. H.; Ma, X. T.; Peng, C.; Jiang, H. Z.; Zhou, D.; Xia, Q. H., Synthesis and catalytic activity of organic-inorganic hybrid catalysts coordinated with cobalt(II) ions for aerobic epoxidation of styrene. *Catalysis Communications* **2015,** *61*, 48-52.

142. Barbe, J. M.; Canard, G.; Brandes, S.; Guilard, R., Organic-inorganic hybrid sol-gel materials incorporating functionalized cobalt(III) corroles for the selective detection of CO. *Angewandte Chemie-International Edition* **2005,** *44* (20), 3103-3106.

143. Al-Rehili, S.; Fhayli, K.; Hammami, M. A.; Moosa, B.; Patil, S.; Zhang, D. L.; Alharbi, O.; Hedhili, M. N.; Mohwald, H.; Khashab, N. M., Anisotropic Self-Assembly of Organic-Inorganic Hybrid Microtoroids. *Journal of the American Chemical Society* **2017,** *139* (30), 10232-10238.

144. Parmeggiani, C.; Cardona, F., Transition metal based catalysts in the aerobic oxidation of alcohols. *Green Chemistry* **2012,** *14* (3), 547-564.

145. Hojoh, K.; Ohmiya, H.; Sawamura, M., Synthesis of alpha-Quaternary Formimides and Aldehydes through Umpolung Asymmetric Copper Catalysis with Isocyanides. *Journal of the American Chemical Society* **2017,** *139* (6), 2184-2187.

146. Zhang, K.; Lu, L. Q.; Yao, S.; Chen, J. R.; Shi, D. Q.; Xiao, W. J., Enantioconvergent Copper Catalysis: In Situ Generation of the Chiral Phosphorus Ylide and Its Wittig Reactions. *Journal of the American Chemical Society* **2017,** *139* (36), 12847-12854.

147. Hickman, A. J.; Sanford, M. S., High-valent organometallic copper and palladium in catalysis. *Nature* **2012,** *484* (7393), 177-185.

148. Chen, Z. F.; Meyer, T. J., Copper(II) Catalysis of Water Oxidation. *Angewandte Chemie-International Edition* **2013,** *52* (2), 700-703.

149. Wang, D. H.; Zhu, N.; Chen, P. H.; Lin, Z. Y.; Liu, G. S., Enantioselective Decarboxylative Cyanation Employing Cooperative Photoredox Catalysis and Copper Catalysis. *Journal of the American Chemical Society* **2017,** *139* (44), 15632-15635.

150. Saunthwal, R. K.; Patel, M.; Kumar, S.; Verma, A. K., Cu(II)-catalyzed tandem synthesis of 2-imino 1,3 benzothiazines from 2-aminoaryl acrylates via thioamidation and concomitant chemoselective thia-Michael addition. *Tetrahedron Letters* **2015,** *56* (5), 677-681.

151. Zhang, G. F.; Han, X. W.; Luan, Y. X.; Wang, Y.; Wen, X.; Xu, L.; Ding, C. R.; Gao, J. R., Copper-catalyzed aerobic alcohol oxidation under air in neat water by using a water-soluble ligand. *Rsc Advances* **2013,** *3* (42), 19255-19258.

152. Maity, R.; Naskar, S.; Das, I., Copper(II)-Catalyzed Reactions of alpha-Keto Thioesters with Azides via C-C and C-S Bond Cleavages: Synthesis of N-Acylureas and Amides. *Journal of Organic Chemistry* **2018,** *83* (4), 2114-2124.

153. Jiang, N.; Ragauskas, A. J., Cu(II)-catalyzed selective aerobic oxidation of alcohols under mild conditions. *Journal of Organic Chemistry* **2006,** *71* (18), 7087-7090.

154.   Kitanosono, T.;   Xu, P. Y.; Kobayashi, S., Heterogeneous versus Homogeneous Copper(II) Catalysis in Enantioselective Conjugate-Addition Reactions of Boron in Water. *Chemistry-an Asian Journal* **2014,** *9* (1), 179-188.

155.   Fedorov, A.;   Liu, H. J.; Lo, H. K.; Coperet, C., Silica-Supported Cu Nanoparticle Catalysts for Alkyne Semihydrogenation: Effect of Ligands on Rates and Selectivity. *Journal of the American Chemical Society* **2016,** *138* (50), 16502-16507.

156.   Meng, X.; Zhang, J. Q.; Chen, B. H.; Jing, Z. Q.; Zhao, P. Q., Copper supported on H+ -modified manganese oxide octahedral molecular sieves (Cu/H-OMS-2) as a heterogeneous biomimetic catalyst for the synthesis of imidazo 1,2-a -N-heterocycles. *Catalysis Science & Technology* **2016,** *6* (3), 890-896.

157.   Zou, Y. D.; Wang, X. X.; Ai, Y. J.; Liu, Y. H.; Ji, Y. F.; Wang, H. Q.; Hayat, T.; Alsaedi, A.; Hu, W. P.; Wang, X. K., beta-Cyclodextrin modified graphitic carbon nitride for the removal of pollutants from aqueous solution: experimental and theoretical calculation study. *Journal of Materials Chemistry A* **2016,** *4* (37), 14170-14179.

158.   Kaboudin, B.; Abedi, Y.; Yokomatsu, T., Cu-II-beta-Cyclodextrin Complex as a Nanocatalyst for the Homo- and Cross-Coupling of Arylboronic Acids under Ligand- and Base-Free Conditions in Air: Chemoselective Cross-Coupling of Arylboronic Acids in Water. *European Journal of Organic Chemistry* **2011,** (33), 6656-6662.

159.   Kaboudin, B.; Abedi, Y.; Yokomatsu, T., One-pot synthesis of 1,2,3-triazoles from boronic acids in water using Cu(II)-beta-cyclodextrin complex as a nanocatalyst. *Organic & Biomolecular Chemistry* **2012,** *10* (23), 4543-4548.

160.   Gupta, D.; Mishra, A.; Kundu, S., Cu (II)-beta-CD as Water-Loving Catalyst for One-Pot Synthesis of Triazoles and Biofuels Intermediate at Room Temperature without Any Other Additive. *Chemistryselect* **2017,** *2* (10), 2997-3008.

161.   Skorjanc, T.; Benyettou, F.; Olsen, J. C.; Trabolsi, A., Design of Organic Macrocycle-Modified Iron Oxide Nanoparticles for Drug Delivery. *Chemistry* **2017,** *23* (35), 8333-8347.

162.   Han, B.-H.; Antonietti, M., One-step synthesis of copper nanoparticles containing mesoporous silica by nanocasting of binuclear copper(ii) complexes with cyclodextrins. *Journal of Materials Chemistry* **2003,** *13* (7), 1793-1796.

163.   Bahadorikhalili, S.; Ma'mani, L.; Mahdavi, H.; Shafiee, A., Copper supported β-cyclodextrin functionalized PEGylated mesoporous silica nanoparticle -graphene oxide hybrid: An efficient and recyclable nano-catalyst for straightforward synthesis of 2-arylbenzimidazoles and 1,2,3-triazoles. *Microporous and Mesoporous Materials* **2018,** *262*, 207-216.

164.   Ye, R.-P.; Lin, L.; Liu, C.-Q.; Chen, C.-C.; Yao, Y.-G., One-Pot Synthesis of Cyclodextrin-Doped Cu-SiO2 Catalysts for Efficient Hydrogenation of Dimethyl Oxalate to Ethylene Glycol. *ChemCatChem* **2017,** *9* (24), 4587-4597.

165.   Fedorova, A. A.; Morozov, I. V.; Kotovshchikov, Y. N.; Romanovsky, B. V.; Sirotin, S. V.; Knyazeva, E. E.; Lermontov, A. S.; Shaporev, A. S., Preparation and characterization of copper- and iron-containing mesoporous silica using β-cyclodextrin as a structure-directing agent. *Mendeleev Communications* **2011,** *21* (3), 171-172.

166.   Han, B.-H.; Polarz, S.; Antonietti, M., Cyclodextrin-based Porous Silica Materials as in Situ Chemical "Nanoreactors" for the Preparation of Variable Metal−Silica Hybrids. *Chemistry of Materials* **2001,** *13* (11), 3915-3919.

167.   Khalafi-Nezhad, A.; Panahi, F., Size-Controlled Synthesis of Palladium Nanoparticles on a Silica–Cyclodextrin Substrate: A Novel Palladium Catalyst System for the Heck Reaction in Water. *ACS Sustainable Chemistry & Engineering* **2014,** *2* (5), 1177-1186.

168.   Martina, K.; Baricco, F.; Caporaso, M.; Berlier, G.; Cravotto, G., Cyclodextrin -Grafted Silica-Supported Pd Nanoparticles: An Efficient and Versatile Catalyst for Ligand-Free C−C Coupling and Hydrogenation. *ChemCatChem* **2016,** *8* (6), 1176-1184.

169.   Jayaprabha, K. N.; Joy, P. A., Citrate modified β-cyclodextrin functionalized magnetite nanoparticles: A biocompatible platform for hydrophobic drug delivery. *RSC Advances* **2015,** *5* (28), 22117-22125.

170.   Bagabas, A. A.; Frasconi, M.; Iehl, J.; Hauser, B.; Farha, O. K.; Hupp, J. T.; Hartlieb, K. J.; Botros, Y. Y.; Stoddart, J. F., γ-Cyclodextrin Cuprate Sandwich-Type Complexes. *Inorganic Chemistry* **2013,** *52* (6), 2854-2861.

171.   Shin, J.-A.; Lim, Y.-G.; Lee, K.-H., Copper-Catalyzed Azide–Alkyne Cycloaddition Reaction in Water Using Cyclodextrin as a Phase Transfer Catalyst. *The Journal of Organic Chemistry* **2012,** *77* (8), 4117-4122.

172.   Kaboudin, B.; Abedi, Y.; Yokomatsu, T., CuII−β-Cyclodextrin Complex as a Nanocatalyst for the Homo- and Cross-Coupling of Arylboronic Acids under Ligand- and Base-Free Conditions in Air: Chemoselective Cross-Coupling of Arylboronic Acids in Water. *European Journal of Organic Chemistry* **2011,** *2011* (33), 6656-6662.

173.   Sadeghzadeh, S. M.; Zhiani, R.; Moradi, M., KCC-1 Supported Cu(II)-β-Cyclodextrin Complex as a Reusable Catalyst for the Synthesis of 3-Aryl-2-oxazolidinones from Carbon Dioxide, Epoxide, Anilines. *ChemistrySelect* **2018,** *3* (12), 3516-3522.

174.   Gupta, D.; Mishra, A.; Kundu, S., Cu (II)-β-CD as Water-Loving Catalyst for One-Pot Synthesis of Triazoles and Biofuels Intermediate at Room Temperature without Any Other Additive. *ChemistrySelect* **2017,** *2* (10), 2997-3008.

175.   Martina, K.; Calsolaro, F.; Zuliani, A.; Berlier, G.; Chavez-Rivas, F.; Moran, M. J.; Luque, R.; Cravotto, G., Sonochemically-Promoted Preparation of Silica-Anchored Cyclodextrin Derivatives for Efficient Copper Catalysis. *Molecules* **2019,** *24* (13).

176.   Ye, R. P.; Lin, L.; Liu, C. Q.; Chen, C. C.; Yao, Y. G., One-Pot Synthesis of Cyclodextrin-Doped Cu-SiO2 Catalysts for Efficient Hydrogenation of Dimethyl Oxalate to Ethylene Glycol. *Chemcatchem* **2017,** *9* (24), 4587-4597.

177.   Duan, Z. B.; Ding, X. C.; Wang, Y.; Zhu, L.J.; Xia, D. H., A New Strategy for Fuel Desulfurization by Molecular Inclusion with Copper(II)-beta-cyclodextrin@SiO2@Fe3O4 for Removing Thiophenic Sulfides. *Energy & Fuels* **2018,** *32* (11), 11421-11431.

178.   Khalafi-Nezhad, A.; Panahi, F., Immobilized palladium nanoparticles on a silica-starch substrate (PNP-SSS): as an efficient heterogeneous catalyst for Heck and copper-free Sonogashira reactions in water. *Green Chemistry* **2011,** *13* (9), 2408-2415.

179.   Mohanazadeh, F.; Amini, H., Silica chloride mediated alkylation of electron-rich aromatics by benzyl or tert-butyl chloride. *Bulletin of the Korean Chemical Society* **2010,** *31* (10), 3038-3040.

180.   Martina, K.; Baricco, F.; Berlier, G.; Caporaso, M.; Cravotto, G., Efficient Green Protocols for Preparation of Highly Functionalized β-Cyclodextrin-Grafted Silica. *ACS Sustainable Chemistry & Engineering* **2014,** *2* (11), 2595-2603.

181.   Bagabas, A. A.; Frasconi, M.; Iehl, J.; Hauser, B.; Farha, O. K.; Hupp, J. T.; Hartlieb, K. J.; Botros, Y. Y.; Stoddart, J. F., γ-Cyclodextrin Cuprate Sandwich-Type Complexes. *Inorg. Chem.* **2013,** *52* (6), 2854-2861.

182.   Matsui, Y.; Kurita, T.; Yagi, M.; Okayama, T.; Mochida, K.; Date, Y., The Formation and Structure of Copper(II) Complexes with Cyclodextrins in an Alkaline Solution. *Bulletin of the Chemical Society of Japan* **1975,** *48* (7), 2187-2191.

183.   Liu, J.; He, P.; Wang, L.; Liu, H.; Cao, Y.; Li, H., An efficient and stable Cu/SiO2 catalyst for the syntheses of ethylene glycol and methanol via chemoselective hydrogenation of ethylene carbonate. *Chinese Journal of Catalysis* **2018,** *39* (8), 1283-1293.

184.   Musso, G. E.; Bottinelli, E.; Celi, L.; Magnacca, G.; Berlier, G., Influence of surface functionalization on the hydrophilic character of mesoporous silica nanoparticles. *Physical Chemistry Chemical Physics* **2015,** *17* (21), 13882-13894.

185.   Zhu, M.; Lerum, M. Z.; Chen, W., How To Prepare Reproducible, Homogeneous, and Hydrolytically Stable Aminosilane-Derived Layers on Silica. *Langmuir* **2012,** *28* (1), 416-423.

186.   Negri, C.; Signorile, M.; Porcaro, N. G.; Borfecchia, E.; Berlier, G.; Janssens, T. V. W.; Bordiga, S., Dynamic CuII/CuI speciation in Cu-CHA catalysts by in situ Diffuse Reflectance UV–vis-NIR spectroscopy. *Applied Catalysis A: General* **2019,** *578*, 1-9.

187.   Velasco, M. I.; Krapacher, C. R.; de Rossi, R. H.; Rossi, L. I., Structure characterization of the non-crystalline complexes of copper salts with native cyclodextrins. *Dalton Transactions* **2016,** *45* (26), 10696-10707.

188.   Velasco, M. I.; Krapacher, C. R.; de Rossi, R. H.; Rossi, L. I., Structure characterization of the non-crystalline complexes of copper salts with native cyclodextrins. *Dalton Trans* **2016,** *45* (26), 10696-707.

189.   Negri, C.; Signorile, M.; Porcaro, N. G.; Borfecchia, E.; Berlier, G.; Janssens, T. V. W.; Bordiga, S., Dynamic Cu-II/Cu-I speciation in Cu-CHA catalysts by in situ Diffuse Reflectance UV-vis-NIR spectroscopy. *Applied Catalysis A-General* **2019,** *578*, 1-9.

190.   Kaboudin, B.; Abedi, Y.; Yokomatsu, T., One-pot synthesis of 1,2,3-triazoles from boronic acids in water using Cu(II)-β-cyclodextrin complex as a nanocatalyst. *Organic & Biomolecular Chemistry* **2012,** *10* (23), 4543-8.

191.   Bordiga, S.; Groppo, E.; Agostini, G.; van Bokhoven, J. A.; Lamberti, C., Reactivity of Surface Species in Heterogeneous Catalysts Probed by In Situ X-ray Absorption Techniques. *Chemical Reviews* **2013,** *113* (3), 1736-1850.

192.   Solomon, E. I.; Heppner, D. E.; Johnston, E. M.; Ginsbach, J. W.; Cirera, J.; Qayyum, M.; Kieber-Emmons, M. T.; Kjaergaard, C. H.; Hadt, R. G.; Tian, L., Copper Active Sites in Biology. *Chemical Reviews* **2014,** *114* (7), 3659-3853.

193.   Negri, C.; Borfecchia, E.; Cutini, M.; Lomachenko, K. A.; Janssens, T. V. W.; Berlier, G.; Bordiga, S., Evidence of Mixed-Ligand Complexes in Cu-CHA by Reaction of Cu Nitrates with NO/NH3 at Low Temperature. *Chemcatchem* **2019,** *11* (16), 3828-3838.

194.   Borfecchia, E.; Beato, P.; Svelle, S.; Olsbye, U.; Lamberti, C.; Bordiga, S., Cu-CHA - a model system for applied selective redox catalysis. *Chemical Society Reviews* **2018,** *47* (22), 8097-8133.

195.   W, J., The Elements, Their Origin, Abundance and Distribution: P.A. Cox: Oxford University Press, 1989, pp.207, price £25 (hardback): £9.95 (paperback). ISBN 0-19-855275-0. *Journal of Molecular Structure* **1990,** *240*, 339.

196.   Mauter, M. S.; Elimelech, M., Environmental Applications of Carbon-Based Nanomaterials. *Environmental Science & Technology* **2008,** *42* (16), 5843-5859.

197.	Hu, C.; Qu, J.; Xiao, Y.; Zhao, S.; Chen, H.; Dai, L., Carbon Nanomaterials for Energy and Biorelated Catalysis: Recent Advances and Looking Forward. *ACS Central Science* **2019**.

198.	Kroto, H. W.; Heath, J. R.; O'Brien, S. C.; Curl, R. F.; Smalley, R. E., C60: Buckminsterfullerene. *Nature* **1985,** *318* (6042), 162-163.

199.	Heimann, R. B.; Evsvukov, S. E.; Koga, Y., Carbon allotropes: a suggested classification scheme based on valence orbital hybridization. *Carbon* **1997,** *35* (10), 1654-1658.

200.	Castro Neto, A. H.; Guinea, F.; Peres, N. M. R.; Novoselov, K. S.; Geim, A. K., The electronic properties of graphene. *Reviews of Modern Physics* **2009,** *81* (1), 109-162.

201.	Rao, C. N.; Sood, A. K.; Subrahmanyam, K. S.; Govindaraj, A., Graphene: the new two-dimensional nanomaterial. *Angewante Chemie International Edition* **2009,** *48* (42), 7752-77.

202.	Geim, A. K. N., K. S. , The rise of graphene. *Nature Materials* **2007,** *6*, 183-191.

203.	Katsnelson, M. I., Graphene: carbon in two dimensions. *Materials Today* **2007,** *10* (1-2), 20-27.

204.	Wu, Y.; Zhu, J.; Huang, L., A review of three-dimensional graphene-based materials: Synthesis and applications to energy conversion/storage and environment. *Carbon* **2019,** *143*, 610-640.

205.	Kumar, A.; Sharma, K.; Dixit, A. R., A review of the mechanical and thermal properties of graphene and its hybrid polymer nanocomposites for structural applications. *Journal of Materials Science* **2019,** *54* (8), 5992-6026.

206.	Wang, Y.; Yang, P.; Zheng, L.; Shi, X.; Zheng, H., Carbon nanomaterials with sp or/and sp hybridization in energy conversion and storage applications: A review. *Energy Storage Materials* **2020,** *26*, 349-370.

207.	Harris, P. J. F., Engineering carbon materials with electricity. *Carbon* **2017,** *122*, 504-513.

208.	Araujo, P. T.; Terrones, M. S.; Dresselhaus, M. S., Defects and impurities in graphene-like materials. *Materials Today* **2012,** *15* (3), 98-109.

209.	W. Tian; W. Li; W. Yu; Liu, X., A Review on Lattice Defects in Graphene: Types, Generation, Effects and Regulation. *Micromachines* **2017,** *8* (5).

210.	Liu, L.; Qing, M.; Wang, Y.; Chen, S., Defects in Graphene: Generation, Healing, and Their Effects on the Properties of Graphene: A Review. *Journal of Materials Science & Technology* **2015,** *31* (6), 599-606.

211.	Rao, C. N.; Sood, A. K.; Subrahmanyam, K. S.; Govindaraj, A., Graphene: the new two-dimensional nanomaterial. *Angew Chem Int Ed Engl* **2009,** *48* (42), 7752-77.

212.	Oliveira, A. E. F.; Braga, G. B.; Tarley, C. R. T.; Pereira, A. C., Thermally reduced graphene oxide: synthesis, studies and characterization. *Journal of Materials Science* **2018,** *53* (17), 12005-12015.

213.	Sundaram, R. S., 3 - Chemically derived graphene. In *Graphene*, Skákalová, V.; Kaiser, A. B., Eds. Woodhead Publishing: 2014; pp 50-80.

214.	Pendolino, F.; Armata, N., Synthesis, Characterization and Models of Graphene Oxide. In *Graphene Oxide in Environmental Remediation Process*, 2017; pp 5-21.

215.	Arthi G, P. B.; Bd, L., A Simple Approach to Stepwise Synthesis of Graphene Oxide Nanomaterial. *Journal of Nanomedicine & Nanotechnology* **2015,** *06* (01).

216.	Gao, X.; Jang, J.; Nagase, S., Hydrazine and Thermal Reduction of Graphene Oxide: Reaction Mechanisms, Product Structures, and Reaction Design. *The Journal of Physical Chemistry C* **2009,** *114* (2), 832-842.

217.	Georgakilas, V.; Otyepka, M.; Bourlinos, A. B.; Chandra, V.; Kim, N.; Kemp, K. C.; Hobza, P.; Zboril, R.; Kim, K. S., Functionalization of graphene: covalent and non-covalent approaches, derivatives and applications. *Chem Rev* **2012,** *112* (11), 6156-214.

218.	Bo, Z.; Shuai, X.; Mao, S.; Yang, H.; Qian, J.; Chen, J.; Yan, J.; Cen, K., Green preparation of reduced graphene oxide for sensing and energy storage applications. *Scientific Reports* **2014,** *4*, 4684.

219.	Tang, Q.; Zhou, Z.; Chen, Z., Graphene-related nanomaterials: tuning properties by functionalization. *Nanoscale* **2013,** *5* (11), 4541-83.

220.	Yan, M., Pristine graphene: functionalization, fabrication, and nanocomposite materials. *Journal of Physics: Conference Series* **2018**.

221.	Kuila, T.; Bose, S.; Mishra, A. K.; Khanra, P.; Kim, N. H.; Lee, J. H., Chemical functionalization of graphene and its applications. *Progress in Materials Science* **2012,** *57* (7), 1061-1105.

222.	Kasprzak, A.; Zuchowska, A.; Poplawska, M., Functionalization of graphene: does the organic chemistry matter? *Beilstein J Org Chem* **2018,** *14*, 2018-2026.

223.	Chua, C. K.; Pumera, M., Covalent chemistry on graphene. *Chemical Society Reviews* **2013,** *42* (8), 3222-33.

224.	Niu, X. H.; Yang, X.; Mo, Z. L.; Guo, R. B.; Liu, N. J.; Zhao, P.; Liu, Z. Y., Perylene-functionalized graphene sheets modified with beta-cyclodextrin for the voltammetric discrimination of phenylalanine enantiomers. *Bioelectrochemistry* **2019,** *129*, 189-198.

225.	Leung, F. C. M.; Yam, V. W. W., Covalent and Non-covalent Conjugation of Few-Layered Graphene Oxide and Ruthenium(II) Complex Hybrids and Their Energy Transfer Modulation via Enzymatic Hydrolysis. *Acs Applied Materials & Interfaces* **2018,** *10* (18), 15582-15590.

226.	Bonaccorso, F.; Colombo, L.; Yu, G.; Stoller, M.; Tozzini, V.; Ferrari, A. C.; Ruoff, R. S.; Pellegrini, V., 2D materials. Graphene, related two-dimensional crystals, and hybrid systems for energy conversion and storage. *Science* **2015,** *347* (6217), 1246501.

227. Huang, X.; Yin, Z.; Wu, S.; Qi, X.; He, Q.; Zhang, Q.; Yan, Q.; Boey, F.; Zhang, H., Graphene-based materials: synthesis, characterization, properties, and applications. *Small* **2011,** *7* (14), 1876-902.

228. Geim, A. K. N., K. S. , The rise of graphene. *Nat. Mater.* **2007,** *6*, 183-191.

229. Kongkanand, A.; Martínez Domínguez, R.; Kamat, P. V., Single Wall Carbon Nanotube Scaffolds for Photoelectrochemical Solar Cells. Capture and Transport of Photogenerated Electrons. *Nano Letters* **2007,** *7* (3), 676-680.

230. Novoselov, K. S.; Fal'ko, V. I.; Colombo, L.; Gellert, P. R.; Schwab, M. G.; Kim, K., A roadmap for graphene. *Nature* **2012,** *490* (7419), 192-200.

231. Kulakova, I. I., Surface chemistry of nanodiamonds. *Physical Solid State* **2004,** *46* (4), 636-643.

232. Reina, G.; Zhao, L.; Bianco, A.; Komatsu, N., Chemical Functionalization of Nanodiamonds: Opportunities and Challenges Ahead. *Angewandte Chemie International Edition* **2019,** *58* (50), 17918-17929.

233. Desai, C.; Mitra, S., Microwave induced carboxylation of nanodiamonds. *Diamond and Related Materials* **2013,** *34*, 65-69.

234. Stehlik, S.; Glatzel, T.; Pichot, V.; Pawlak, R.; Meyer, E.; Spitzer, D.; Rezek, B., Water interaction with hydrogenated and oxidized detonation nanodiamonds — Microscopic and spectroscopic analyses. *Diamond and Related Materials* **2016,** *63*, 97-102.

235. Desai, C.; Chen, K.; Mitra, S., Aggregation behavior of nanodiamonds and their functionalized analogs in an aqueous environment. *Environmental Science: Processes & Impacts* **2014,** *16* (3), 518-523.

236. Xiong, L.; Yu, M.; Liu, J.; Li, S.; Xue, B., Preparation and evaluation of the microwave absorption properties of template-free graphene foam-supported Ni nanoparticles. *RSC Advances* **2017,** *7* (24), 14733-14741.

237. Yan, K.; Yin, F.; Pang, C.; Zuo, X.; Zhang, Q.; Shen, L.; Fan, R.; Bao, N., Broadband microwave absorber constructed by reduced graphene oxide/La0.7Sr0.3MnO3 composites. *RSC Advances* **2019,** *9* (71), 41817-41823.

238. Chen, C.-Y.; Pu, N.-W.; Liu, Y.-M.; Huang, S.-Y.; Wu, C.-H.; Ger, M.-D.; Gong, Y.-J.; Chou, Y.-C., Remarkable microwave absorption performance of graphene at a very low loading ratio. *Composites Part B: Engineering* **2017,** *114*, 395-403.

239. Meng, F.; Wang, H.; Huang, F.; Guo, Y.; Wang, Z.; Hui, D.; Zhou, Z., Graphene-based microwave absorbing composites: A review and prospective. *Composites Part B: Engineering* **2018,** *137*, 260-277.

240. Tian, W.; Li, W.; Yu, W.; Liu, X., A Review on Lattice Defects in Graphene: Types, Generation, Effects and Regulation. *Micromachines* **2017,** *8* (5).

241. Quintana, M.; Vazquez, E.; Prato, M., Organic Functionalization of Graphene in Dispersions. *Accounts of Chemical Research* **2013,** *46* (1), 138-148.

242. Cunha, E.; Ren, H.; Lin, F.; Kinloch, I. A.; Sun, Q.; Fan, Z.; Young, R. J., The chemical functionalization of graphene nanoplatelets through solvent-free reaction. *RSC Advances* **2018,** *8* (58), 33564-33573.

243. Georgakilas, V.; Bourlinos, A. B.; Ntararas, E.; Ibraliu, A.; Gournis, D.; Dimos, K.; Kouloumpis, A.; Zboril, R., Graphene nanobuds: Synthesis and selective organic derivatisation. *Carbon* **2016,** *110*, 51-55.

244. Neri, G.; Scala, A.; Fazio, E.; Mineo, P. G.; Rescifina, A.; Piperno, A.; Grassi, G., Repurposing of oxazolone chemistry: gaining access to functionalized graphene nanosheets in a top-down approach from graphite. *Chemical Science* **2015,** *6* (12), 6961-6970.

245. Suggs, K.; Reuven, D.; Wang, X.-Q., Electronic Properties of Cycloaddition-Functionalized Graphene. *The Journal of Physical Chemistry C* **2011,** *115*.

246. Yang, T.; Zhao, X.; Nagase, S., 1,3-Dipolar cycloadditions of Stone–Wales defective single-walled carbon nanotubes: A theoretical study. *Journal of Computational Chemistry* **2013,** *34* (26), 2223-2232.

247. Lu, X.; Tian, F.; Xu, X.; Wang, N.; Zhang, Q., A Theoretical Exploration of the 1,3-Dipolar Cycloadditions onto the Sidewalls of (n,n) Armchair Single-Wall Carbon Nanotubes. *Journal of the American Chemical Society* **2003,** *125* (34), 10459-10464.

248. Cao, Y.; Houk, K. N., Computational assessment of 1,3-dipolar cycloadditions to graphene. *Journal of Materials Chemistry* **2011,** *21* (5), 1503-1508.

249. Tagmatarchis, N.; Prato, M., Functionalization of carbon nanotubes via 1,3-dipolar cycloadditions. *Journal of Materials Chemistry* **2004,** *14* (4), 437-439.

250. Quintana, M.; Spyrou, K.; Grzelczak, M.; Browne, W. R.; Rudolf, P.; Prato, M., Functionalization of Graphene via 1,3-Dipolar Cycloaddition. *ACS Nano* **2010,** *4* (6), 3527-3533.

251. Zhao, S.; Wang, H.; Xin, L.; Cui, J.; Yan, Y., A Versatile Platform of 2-(3,4-Dihydroxyphenyl) Pyrrolidine Grafted Graphene for Preparation of Various Graphene-derived Materials. *Chemistry – An Asian Journal* **2015,** *10* (5), 1177-1183.

252. Kasprzak, A.; Nowicka, A. M.; Sek, J. P.; Fronczak, M.; Bystrzejewski, M.; Koszytkowska-Stawinska, M.; Poplawska, M., Addition of azomethine ylides to carbon-encapsulated iron nanoparticles. *Dalton Transactions* **2018,** *47* (1), 30-34.

253. Popławska, M.; Żukowska, G. Z.; Cudziło, S.; Bystrzejewski, M., Chemical functionalization of carbon-encapsulated magnetic nanoparticles by 1,3-dipolar cycloaddition of nitrile oxide. *Carbon* **2010,** *48* (4), 1318-1320.

254. Meier, M. S.; Poplawska, M., The addition of nitrile oxides to C60. *Tetrahedron* **1996,** *52* (14), 5043-5052.

255. Herman, A. P.; Boncel, S., Nitrile N-oxides in programmable one-pot functionalization of multi-wall carbon nanotubes via 1,3-dipolar cycloaddition. *RSC Advances* **2016,** *6* (68), 64129-64132.

256. Alvaro, M.; Atienzar, P.; de la Cruz, P.; Delgado, J. L.; Troiani, V.; Garcia, H.; Langa, F.; Palkar, A.; Echegoyen, L., Synthesis, Photochemistry, and Electrochemistry of Single-Wall Carbon Nanotubes with Pendent Pyridyl Groups and of Their Metal Complexes with Zinc Porphyrin. Comparison with Pyridyl-Bearing Fullerenes. *Journal of the American Chemical Society* **2006,** *128* (20), 6626-6635.

257. Ghini, G.; Luconi, L.; Rossin, A.; Bianchini, C.; Giambastiani, G.; Cicchi, S.; Lascialfari, L.; Brandi, A.; Giannasi, A., Can nitrones functionalize carbon nanotubes? *Chemical Communications* **2010,** *46* (2), 252-254.

258. Giofrè, S. V.; Tiecco, M.; Celesti, C.; Patanè, S.; Triolo, C.; Gulino, A.; Spitaleri, L.; Scalese, S.; Scuderi, M.; Iannazzo, D., Eco-Friendly 1,3-Dipolar Cycloaddition Reactions on Graphene Quantum Dots in Natural Deep Eutectic Solvent. *Nanomaterials (Basel)* **2020,** *10* (12), 2549.

259. Tagliapietra, S.; Cravotto, G.; Gaudino, E. C.; Visentin, S.; Mussi, V., Functionalization of Single-Walled Carbon Nanotubes through 1,3-Cyclo-addition of Carbonyl Ylides under Microwave Irradiation. *Synletters* **2012,** *23* (10), 1459-1462.

260. Monajati, M.; Borandeh, S.; Hesami, A.; Mansouri, D.; Tamaddon, A. M., Immobilization of -asparaginase on aspartic acid functionalized graphene oxide nanosheet: Enzyme kinetics and stability studies. *Chemical Engineering Journal* **2018,** *354*, 1153-1163.

261. Marcano, D. C.; Kosynkin, D. V.; Berlin, J. M.; Sinitskii, A.; Sun, Z.; Slesarev, A.; Alemany, L. B.; Lu, W.; Tour, J. M., Improved Synthesis of Graphene Oxide. *ACS Nano* **2010,** *4* (8), 4806-4814.

262. Calcio Gaudino, E.; Tagliapietra, S.; Martina, K.; Barge, A.; Lolli, M.; Terreno, E.; Lembo, D.; Cravotto, G., A novel SWCNT platform bearing DOTA and β-cyclodextrin units. "One shot" multidecoration under microwave irradiation. *Organic & Biomolecular Chemistry* **2014,** *12* (26), 4708-4715.

263. Bhaskar, R.; Joshi, H.; Sharma, A. K.; Singh, A. K., Reusable Catalyst for Transfer Hydrogenation of Aldehydes and Ketones Designed by Anchoring Palladium as Nanoparticles on Graphene Oxide Functionalized with Selenated Amine. *ACS Appl Mater Interfaces* **2017,** *9* (3), 2223-2231.

264. Zhang, Q.; Li, Q.-L.; Xiang, S.; Wang, Y.; Wang, C.; Jiang, W.; Zhou, H.; Yang, Y.-W.; Tang, J., Covalent modification of graphene oxide with polynorbornene by surface-initiated ring-opening metathesis polymerization. *Polymer* **2014,** *55* (23), 6044-6050.

265. Eissler, S.; Kley, M.; Bächle, D.; Loidl, G.; Meier, T.; Samson, D., Substitution determination of Fmoc-substituted resins at different wavelengths. *Journal of Peptide Science* **2017,** *23* (10), 757-762.

266. Sheppeck, J. E.; Kar, H.; Hong, H., A convenient and scaleable procedure for removing the Fmoc group in solution. *Tetrahedron Letters* **2000,** *41* (28), 5329-5333.

267. Yu, C.; Hu, L., A facile synthesis of cyclic enecarbamates using Dess–Martin periodinane. *Tetrahedron Letters* **2001,** *42* (31), 5167-5170.

268. Rebelo, S. L. H.; Guedes, A.; Szefczyk, M. E.; Pereira, A. M.; Araújo, J. P.; Freire, C., Progress in the Raman spectra analysis of covalently functionalized multiwalled carbon nanotubes: unraveling disorder in graphitic materials. *Physical Chemistry Chemical Physics* **2016,** *18* (18), 12784-12796.

269. Luo, S.-X. L.; Liu, R. Y.; Lee, S.; Swager, T. M., Electrocatalytic Isoxazoline–Nanocarbon Metal Complexes. *Journal of the American Chemical Society* **2021,** *143* (27), 10441-10453.

270. Bogdanov, D.; Bogdanov, A.; Plotnikov, V.; Makarov, S.; Yelisseyev, A.; Chepurov, A., Core growth of detonation nanodiamonds under high-pressure annealing. *RSC Advances* **2021,** *11* (21), 12961-12970.

271. Aleksenskii, A., Technology of Preparation of Detonation Nanodiamond. 2014; pp 37-72.

272. Ducrozet, F.; Girard, H. A.; Leroy, J.; Larquet, E.; Florea, I.; Brun, E.; Sicard-Roselli, C.; Arnault, J. C., New Insights into the Reactivity of Detonation Nanodiamonds during the First Stages of Graphitization. *Nanomaterials (Basel)* **2021,** *11* (10).

273. Safaei-Ghomi, J.; Masoomi, R., An efficient comparison of methods involving conventional, grinding and ultrasound conditions for the synthesis of fulleroisoxazolines. *Ultrasonics Sonochemistry* **2015,** *23*, 212-218.

274. López-Díaz, D.; López Holgado, M.; García-Fierro, J. L.; Velázquez, M. M., Evolution of the Raman Spectrum with the Chemical Composition of Graphene Oxide. *The Journal of Physical Chemistry C* **2017,** *121* (37), 20489-20497.

275. Merino, P.; Tejero, T.; Delso, I.; Matute, R., New mechanistic interpretations for nitrone reactivity. *Organic & Biomolecular Chemistry* **2017,** *15* (16), 3364-3375.

276. Ess, D. H.; Houk, K. N., Distortion/Interaction Energy Control of 1,3-Dipolar Cycloaddition Reactivity. *Journal of the American Chemical Society* **2007,** *129* (35), 10646-10647.

277. Rios-Gutierrez, M.; Perez, P.; Domingo, L. R., A bonding evolution theory study of the mechanism of [3+2] cycloaddition reactions of nitrones with electron-deficient ethylenes. *RSC Advances* **2015,** *5* (72), 58464-58477.

278. Hamer, J.; Macaluso, A., Nitrones. *Chemical Reviews* **1964,** *64* (4), 473-495.

279.	Domingo, L. R., Molecular Electron Density Theory: A Modern View of Reactivity in Organic Chemistry. *Molecules* **2016,** *21* (10), 1319.

280.	Domingo, L. R.; Ríos-Gutiérrez, M.; Pérez, P., How does the global electron density transfer diminish activation energies in polar cycloaddition reactions? A Molecular Electron Density Theory study. *Tetrahedron* **2017,** *73* (13), 1718-1724.

281.	Domingo, L. R., A new C–C bond formation model based on the quantum chemical topology of electron density. *RSC Advances* **2014,** *4* (61), 32415-32428.

282.	Domingo, L. R.; Sáez, J. A., Understanding the mechanism of polar Diels–Alder reactions. *Organic & Biomolecular Chemistry* **2009,** *7* (17), 3576-3583.

283.	Murahashi, S.-I.; Imada, Y., Synthesis and Transformations of Nitrones for Organic Synthesis. *Chemical Reviews* **2019,** *119* (7), 4684-4716.

284.	Hoveyda, A. H.; Malcolmson, S. J.; Meek, S. J.; Zhugralin, A. R., Catalytic Enantioselective Olefin Metathesis in Natural Product Synthesis. Chiral Metal-Based Complexes that Deliver High Enantioselectivity and More. *Angewandte Chemie International Edition* **2010,** *49* (1), 34-44.

285.	Dong, Y.; Matson, J. B.; Edgar, K. J., Olefin Cross-Metathesis in Polymer and Polysaccharide Chemistry: A Review. *Biomacromolecules* **2017,** *18* (6), 1661-1676.

286.	Deraedt, C.; d'Halluin, M.; Astruc, D., Metathesis Reactions: Recent Trends and Challenges. *European Journal of Inorganic Chemistry* **2013**, n/a-n/a.

287.	Grubbs, R. H.; Chang, S., Recent advances in olefin metathesis and its application in organic synthesis. *Tetrahedron* **1998,** *54* (18), 4413-4450.

288.	Vidal, V.; Theolier, A.; Thivolle-Cazat, J.; Basset, J.-M., Metathesis of alkanes catalyzed by silica-supported transition metal hydrides. *Science (Washington, D. C.)* **1997,** *276* (5309), 99-102.

289.	Schrock, R. R.; Hoveyda, A. H., Molybdenum and Tungsten Imido Alkylidene Complexes as Efficient Olefin-Metathesis Catalysts. *Angewandte Chemie International Edition* **2003,** *42* (38), 4592-4633.

290.	Astruc, D., The metathesis reactions: from a historical perspective to recent developments. *New Journal of Chemistry* **2005,** *29* (1), 42-56.

291.	Ibrahim, M. A.; Akhtar, M. N.; Čejka, J.; Montanari, E.; Balcar, H.; Kubů, M.; Al-Khattaf, S. S., Metathesis of 2-pentene over Mo and W supported mesoporous molecular sieves MCM-41 and SBA-15. *Journal of Industrial and Engineering Chemistry* **2017,** *53*, 119-126.

292.	Wang, C.; Jiang, F.; Zuo, G.; Liu, B.; Li, H.; Liu, X., Remarkably enhanced performance of the metathesis reaction of ethylene and 1-butene to propene using one-step prepared W-MCM-41 catalysts. *RSC Advances* **2019,** *9* (69), 40618-40627.

293.	Howell, J. G.; Li, Y.-P.; Bell, A. T., Propene Metathesis over Supported Tungsten Oxide Catalysts: A Study of Active Site Formation. *ACS Catalysis* **2016,** *6* (11), 7728-7738.

294.	Wu, J.-F.; Ramanathan, A.; Snavely, W. K.; Zhu, H.; Rokicki, A.; Subramaniam, B., Enhanced metathesis of ethylene and 2-butene on tungsten incorporated ordered mesoporous silicates. *Applied Catalysis A: General* **2016,** *528*, 142-149.

295.	Larabi, C.; Merle, N.; Le Quéméner, F.; Rouge, P.; Berrier, E.; Gauvin, R. M.; Le Roux, E.; de Mallmann, A.; Szeto, K. C.; Taoufik, M., New synthetic approach towards well-defined silica supported tungsten bis-oxo, active catalysts for olefin metathesis. *Catalysis Communications* **2018,** *108*, 51-54.

296.	Mougel, V.; Chan, K.-W.; Siddiqi, G.; Kawakita, K.; Nagae, H.; Tsurugi, H.; Mashima, K.; Safonova, O.; Copéret, C., Low Temperature Activation of Supported Metathesis Catalysts by Organosilicon Reducing Agents. *ACS Central Science* **2016,** *2* (8), 569-576.

297.	Gayapan, K.; Sripinun, S.; Panpranot, J.; Praserthdam, P.; Assabumrungrat, S., Effect of pretreatment atmosphere of WOx/SiO2 catalysts on metathesis of ethylene and 2-butene to propylene. *RSC Advances* **2018,** *8* (21), 11693-11704.

298.	Lwin, S.; Wachs, I. E., Catalyst Activation and Kinetics for Propylene Metathesis by Supported WOx/SiO2 Catalysts. *ACS Catalysis* **2017,** *7* (1), 573-580.

299.	Liu, N.; Ding, S.; Cui, Y.; Xue, N.; Peng, L.; Guo, X.; Ding, W., Optimizing activity of tungsten oxides for 1-butene metathesis by depositing silica on γ-alumina support. *Chemical Engineering Research and Design* **2013,** *91* (3), 573-580.

300.	Tao, K.; Ma, Q.; Tsubaki, N.; Zhou, S.; Han, L., Molybdenum containing cage like mesoporous KIT-5 for enhanced catalytic conversion of 1-butene and ethylene to propene. *Journal of Molecular Catalysis A: Chemical* **2016,** *416*, 39-46.

301.	Sripinun, S.; Gayapan, K.; Tolek, W.; Suriye, K.; Praserthdam, P.; Assabumrungrat, S., Catalyst pellet design of WO3/Si-Al and hydrotalcite binder for propylene self-metathesis. *Catalysis Today* **2020**.

302.	Grekov, D.; Bouhoute, Y.; Szeto, K. C.; Merle, N.; De Mallmann, A.; Lefebvre, F.; Lucas, C.; Del Rosal, I.; Maron, L.; Gauvin, R. M.; Delevoye, L.; Taoufik, M., Silica-Supported Tungsten Neosilyl Oxo Precatalysts: Impact of the Podality on Activity and Stability in Olefin Metathesis. *Organometallics* **2016,** *35* (13), 2188-2196.

303.	Rouge, P.; Szeto, K. C.; Bouhoute, Y.; Merle, N.; De Mallmann, A.; Delevoye, L.; Gauvin, R. M.; Taoufik, M., Ethenolysis of Renewable Methyl Oleate Catalyzed by Readily Accessible Supported Group VI Oxo Catalysts. *Organometallics* **2020,** *39* (7), 1105-1111.

304.	Merle, N.; Le Quéméner, F.; Bouhoute, Y.; Szeto, K. C.; De Mallmann, A.; Barman, S.; Samantaray, M. K.; Delevoye, L.; Gauvin, R. M.; Taoufik, M.; Basset, J.-M., Well-Defined Molybdenum

Oxo Alkyl Complex Supported on Silica by Surface Organometallic Chemistry: A Highly Active Olefin Metathesis Precatalyst. *Journal of the American Chemical Society* **2017**, *139* (6), 2144-2147.

305. Bouhoute, Y.; Del Rosal, I.; Szeto, K. C.; Merle, N.; Grekov, D.; De Mallmann, A.; Le Roux, E.; Delevoye, L.; Gauvin, R. M.; Maron, L.; Taoufik, M., Modification of silica-supported tungsten neosilyl oxo precatalysts: impact of substituted phenol on activity and stability in olefin metathesis. *Catalysis Science & Technology* **2016**, *6* (24), 8532-8539.

306. Pucino, M.; Inoue, M.; Gordon, C. P.; Schowner, R.; Stoehr, L.; Sen, S.; Hegedues, C.; Robe, E.; Toth, F.; Buchmeiser, M. R.; Coperet, C., Promoting Terminal Olefin Metathesis with a Supported Cationic Molybdenum Imido Alkylidene N-Heterocyclic Carbene Catalyst. *Angewante Chemie International Edition* **2018**, *57* (44), 14566-14569.

307. Unnu, V. S.; Cetinkaya, S., Synthesis and Catalytic Activity of PolyHIPE-Supported NHC-Bearing Ruthenium Initiator for ROMP. *Catalysis Letters* **2018**, *148* (8), 2432-2445.

308. Choluj, A.; Nogas, W.; Patrzalek, M.; Krzesinski, P.; Chmielewski, M. J.; Kajetanowicz, A.; Grela, K., Preparation of ruthenium olefin metathesis catalysts immobilized on MOF, SBA-15, and 13X for probing heterogeneous boomerang effect. *Catalysts* **2020,** *10* (4), 438.

309. Kaczanowska, K.; Chwalba, M.; Pastva, J.; Kubu, M.; Ruszczynska, A.; Bulska, E.; Balcar, H.; Skowerski, K., Carboxyl Graphene as a Superior Support for Bulky Ruthenium-Based Olefin Metathesis Catalyst. *Organometallics* **2018**, *37* (12), 1837-1844.

310. Xia, L.; Peng, T.; Wang, G.; Wen, X.; Zhang, S.; Wang, L., Grubbs Catalysts Immobilized on Merrifield Resin for Metathesis of Leaf Alcohols by using a Convenient Recycling Approach. *ChemistryOpen* **2019**, *8* (1), 45-48.

311. Renom-Carrasco, M.; Mania, P.; Sayah, R.; Veyre, L.; Occhipinti, G.; Gajan, D.; Lesage, A.; Jensen, V. R.; Thieuleux, C., Supported Ru olefin metathesis catalysts via a thiolate tether. *Dalton Transactions* **2019,** *48* (9), 2886-2890.

312. Ehrhorn, H.; Tamm, M., Well-Defined Alkyne Metathesis Catalysts: Developments and Recent Applications. *Chemistry – A European Journal* **2019**, *25* (13), 3190-3208.

313. Merle, N.; Taoufik, M.; Nayer, M.; Baudouin, A.; Le Roux, E.; Gauvin, R. M.; Lefebvre, F.; Thivolle-Cazat, J.; Basset, J.-M., Development of a well-defined silica-supported tungstenocarbyne complex as efficient heterogeneous catalyst for alkyne metathesis. *Journal of Organometallic Chemistry* **2008**, *693* (10), 1733-1737.

314. Merle, N.; Taoufik, M.; Nayer, M.; Baudouin, A.; Le Roux, E.; Gauvin, R. M.; Lefebvre, F.; Thivolle-Cazat, J.; Basset, J.-M., Development of a well-defined silica-supported tungstenocarbyne complex as efficient heterogeneous catalyst for alkyne metathesis. *J. Organomet. Chem.* **2008**, *693* (10), 1733-1737.

315. Estes, D. P.; Gordon, C. P.; Fedorov, A.; Liao, W.-C.; Ehrhorn, H.; Bittner, C.; Zier, M. L.; Bockfeld, D.; Chan, K. W.; Eisenstein, O.; Raynaud, C.; Tamm, M.; Coperet, C., Molecular and Silica-Supported Molybdenum Alkyne Metathesis Catalysts: Influence of Electronics and Dynamics on Activity Revealed by Kinetics, Solid-State NMR, and Chemical Shift Analysis. *Journal of the American Chemical Society* **2017**, *139* (48), 17597-17607.

316. Weissman, H.; Plunkett, K. N.; Moore, J. S., A highly active, heterogeneous catalyst for alkyne metathesis. *Angewante Chemie International Edition* **2006,** *45* (4), 585-588.

317. Cho, H. M.; Weissman, H.; Moore, J. S., Synthetic Applications with Use of a Silica-Supported Alkyne Metathesis Catalyst. *The Journal of Organic Chemistry* **2008**, *73* (11), 4256-4258.

318. Riache, N.; Dery, A.; Callens, E.; Poater, A.; Samantaray, M.; Dey, R.; Hong, J.; Li, K.; Cavallo, L.; Basset, J.-M., Silica-Supported Tungsten Carbynes (≡SiO)xW(≡CH)(Me)y (x = 1, y = 2; x = 2, y = 1): New Efficient Catalysts for Alkyne Cyclotrimerization. *Organometallics* **2015,** *34* (4), 690-695.

319. Coutelier, O.; Nowogrocki, G.; Paul, J.-F.; Mortreux, A., Selective terminal alkyne metathesis: synthesis and use of a unique triple bonded dinuclear tungsten alkoxy complex containing a hemilabile ligand. *Advanced Synthesis & Catalysis* **2007,** *349* (14+15), 2259-2263.

320. Bendjeriou-Sedjerari, A.; Sofack-Kreutzer, J.; Minenkov, Y.; Abou-Hamad, E.; Hamzaoui, B.; Werghi, B.; Anjum, D. H.; Cavallo, L.; Huang, K. W.; Basset, J. M., Tungsten(VI) Carbyne/Bis(carbene) Tautomerization Enabled by N-Donor SBA15 Surface Ligands: A Solid-State NMR and DFT Study. *Angew Chem Int Ed Engl* **2016,** *55* (37), 11162-6.

321. Maity, N.; Barman, S.; Callens, E.; Samantaray, M. K.; Abou-Hamad, E.; Minenkov, Y.; D'Elia, V.; Hoffman, A. S.; Widdifield, C. M.; Cavallo, L.; Gates, B. C.; Basset, J.-M., Controlling the hydrogenolysis of silica-supported tungsten pentamethyl leads to a class of highly electron deficient partially alkylated metal hydrides. *Chemical Science* **2016,** *7* (2), 1558-1568.

322. Mazar, M. N.; Al-Hashimi, S.; Bhan, A.; Cococcioni, M., Alkane Metathesis by Tantalum Metal Hydride on Ferrierite: A Computational Study. *The Journal of Physical Chemistry C* **2011,** *115* (20), 10087-10096.

323. Huang, J.; Wang, D.; Yue, Z.; Li, X.; Chu, D.; Yang, P., Ruthenium Dye N749 Covalently Functionalized Reduced Graphene Oxide: A Novel Photocatalyst for Visible Light H2 Evolution. *The Journal of Physical Chemistry C* **2015,** *119* (50), 27892-27899.

324. Vinoth, R.; Babu, S. G.; Bharti, V.; Gupta, V.; Navaneethan, M.; Bhat, S. V.; Muthamizhchelvan, C.; Ramamurthy, P. C.; Sharma, C.; Aswal, D. K.; Hayakawa, Y.; Neppolian, B.,

Ruthenium based metallopolymer grafted reduced graphene oxide as a new hybrid solar light harvester in polymer solar cells. *Scientific Reports* **2017,** *7* (1), 43133.

325.   Xiao, B.; Wang, X.; Huang, H.; Zhu, M.; Yang, P.; Wang, Y.; Du, Y., Improved Superiority by Covalently Binding Dye to Graphene for Hydrogen Evolution from Water under Visible-Light Irradiation. *The Journal of Physical Chemistry C* **2013,** *117* (41), 21303-21311.

326.   Ventura-Espinosa, D.; Vicent, C.; Baya, M.; Mata, J. A., Ruthenium molecular complexes immobilized on graphene as active catalysts for the synthesis of carboxylic acids from alcohol dehydrogenation. *Catalysis Science & Technology* **2016,** *6* (22), 8024-8035.

327.   Cannon, J. S.; Zou, L.; Liu, P.; Lan, Y.; O'Leary, D. J.; Houk, K. N.; Grubbs, R. H., Carboxylate-assisted C(sp(3))-H activation in olefin metathesis-relevant ruthenium complexes. *Journal of the American Chemical Society* **2014,** *136* (18), 6733-43.

328.   Gawin, R.; Grela, K., Synthesis of Stable Ruthenium Olefin Metathesis Catalysts with Mixed Anionic Ligands. *European Journal of Inorganic Chemistry* **2012,** *2012* (9), 1477-1484.

329.   Şen, B.; Lolak, N.; Paralı, Ö.; Koca, M.; Şavk, A.; Akocak, S.; Şen, F., Bimetallic PdRu/graphene oxide based Catalysts for one-pot three-component synthesis of 2-amino-4H-chromene derivatives. *Nano-Structures & Nano-Objects* **2017,** *12*, 33-40.

330.   Guadagno, L.; Mariconda, A.; Agovino, A.; Raimondo, M.; Longo, P., Protection of graphene supported ROMP catalyst through polymeric globular shell in self-healing materials. *Composites Part B: Engineering* **2017,** *116*, 352-360.

331.   Ge, H.; Zou, W., Preparation and characterization of L-glutamic acid-functionalized graphene oxide for adsorption of Pb(II). *Journal of Dispersion Science and Technology* **2016,** *38* (2), 241-247.

332.   Wang, D.; Huang, J.; Li, K.; Zhang, C.; Du, Y.; Yang, P., A robust and efficient visible light driven photocatalyst for hydrogen evolution based on ruthenium dye N3 covalently immobilized on reduced graphene oxide. *RSC Advances* **2016,** *6* (41), 34699-34707.

333.   Ge, L.; Wang, Y.; Yang, H.; Yang, P.; Cheng, X.; Yan, M.; Yu, J., A photoelectrochemical biosensor using ruthenium complex-reduced graphene oxide hybrid as the photocurrent signal reporter assembled on rhombic TiO2 nanocrystals driven by visible light. *Analytica Chimica Acta* **2014,** *828*, 27-33.

334.   Renom-Carrasco, M.; Mania, P.; Sayah, R.; Veyre, L.; Occhipinti, G.; Gajan, D.; Lesage, A.; Jensen, V. R.; Thieuleux, C., Supported Ru olefin metathesis catalysts via a thiolate tether. *Dalton Trans.* **2019,** *48* (9), 2886-2890.

335.   Segalovich-Gerendash, G.; Rozenberg, I.; Alassad, N.; Nechmad, N. B.; Goldberg, I.; Kozuch, S.; Lemcoff, N. G., Imposing Latency in Ruthenium Sulfoxide-Chelated Benzylidenes: Expanding Opportunities for Thermal and Photoactivation in Olefin Metathesis. *ACS Catalysis* **2020,** *10* (8), 4827-4834.

336.   Mol, J. C., Industrial applications of olefin metathesis. *Journal of Molecular Catalysis A: Chemical* **2004,** *213* (1), 39-45.

337.   Hafner, A.; van der Schaaf, P. A.; Mühlebach, A.; Paul, B.; Schaedeli, U.; Karlen, T.; Ludi, A., Thermal- and photoinduced ring-opening metathesis polymerization (ROMP)/(PROMP): an efficient tool in polymer chemistry. *Progress in Organic Coatings* **1997,** *32* (1), 89-96.

338.   Choinopoulos, I., Grubbs' and Schrock's Catalysts, Ring Opening Metathesis Polymerization and Molecular Brushes—Synthesis, Characterization, Properties and Applications. *Polymers* **2019,** *11* (2).

339.   Brik, A., Metathesis in Peptides and Peptidomimetics. *Advanced Synthesis & Catalysis* **2008,** *350* (11-12), 1661-1675.

340.   Lin, Y. A.; Chalker, J. M.; Davis, B. G., Olefin Metathesis for Site-Selective Protein Modification. *ChemBioChem* **2009,** *10* (6), 959-969.

341.   Kaur, N., Ruthenium catalysis in six-membered O-heterocycles synthesis. *Synthetic Communications* **2018,** *48* (13), 1551-1587.

342.   Morzycki, J. W., Application of olefin metathesis in the synthesis of steroids. *Steroids* **2011,** *76* (10), 949-966.

343.   Gaich, T.; Mulzer, J., Recent applications of olefin ring-closing metathesis (RCM) in the synthesis of biologically important alkaloids, terpenoids, polyketides and other secondary metabolites. *Current topics in medicinal chemistry* **2005,** *5* (15), 1473-94.

344.   Jehrod, B. B.; Stephen, F. M., Ring-Closing Metathesis as a Construct for the Synthesis of Polycyclic Alkaloids. *Current Organic Chemistry* **2005,** *9* (15), 1535-1549.

345.   Koffi Senam, E.; Alice, N.; Nelly Tshibalonza, N.; Albert, D.; Lionel, D.; Ileana, D.; Valerian, D., Microwave-assisted Olefin Metathesis as Pivotal Step in the Synthesis of Bioactive Compounds. *Current Medicinal Chemistry* **2017,** *24* (41), 4538-4578.

346.   Pierre, V. d. W.; Jacques, E., The Application of Olefin Metathesis to the Synthesis of Biologically Active Macrocyclic Agents. *Current topics in medicinal chemistry* **2005,** *5* (15), 1495-1519.

347.   dos Santos, E. N.; Granato, A. V.; Santos, A. G., Metal-catalysed Metathesis Reactions for Greener Synthon/Drug Synthesis. In *Sustainable Synthesis of Pharmaceuticals: Using Transition Metal Complexes as Catalysts*, The Royal Society of Chemistry: 2018; pp 230-252.

348.   Jana, A.; Zieliński, G. K.; Czarnocka-Śniadała, S.; Grudzień, K.; Podwysocka, D.; Szulc, M.; Kajetanowicz, A.; Grela, K., Synthesis of Substituted β-Functionalised Styrenes by Microwave-Assisted Olefin Cross-Metathesis and Scalable Synthesis of Apremilast. *ChemCatChem* **2019,** *11* (23), 5808-5813.

349. Mori, M., Recent Progress on Enyne Metathesis: Its Application to Syntheses of Natural Products and Related Compounds. *Materials* **2010,** *3* (3).

350. Cao, R.; Lee, J.-S.; Liu, M.; Cho, J., Recent Progress in Non-Precious Catalysts for Metal-Air Batteries. *Advanced Energy Materials* **2012,** *2* (7), 816-829.

351. To, J. W. F.; Ng, J. W. D.; Siahrostami, S.; Koh, A. L.; Lee, Y.; Chen, Z.; Fong, K. D.; Chen, S.; He, J.; Bae, W.-G.; Wilcox, J.; Jeong, H. Y.; Kim, K.; Studt, F.; Nørskov, J. K.; Jaramillo, T. F.; Bao, Z., High-performance oxygen reduction and evolution carbon catalysis: From mechanistic studies to device integration. *Nano Research* **2017,** *10* (4), 1163-1177.

352. Li, Y.; Lu, Y.; Zhao, C.; Hu, Y.-S.; Titirici, M.-M.; Li, H.; Huang, X.; Chen, L., Recent advances of electrode materials for low-cost sodium-ion batteries towards practical application for grid energy storage. *Energy Storage Materials* **2017,** *7*, 130-151.

353. Albertus, P.; Babinec, S.; Litzelman, S.; Newman, A., Status and challenges in enabling the lithium metal electrode for high-energy and low-cost rechargeable batteries. *Nature Energy* **2018,** *3* (1), 16-21.

354. Cova, C. M.; Zuliani, A.; Puente Santiago, A. R.; Caballero, A.; Muñoz-Batista, M. J.; Luque, R., Microwave-assisted preparation of Ag/Ag2S carbon hybrid structures from pig bristles as efficient HER catalysts. *Journal of Materials Chemistry A* **2018,** *6* (43), 21516-21523.

355. Hui, L.; Xue, Y.; Yu, H.; Liu, Y.; Fang, Y.; Xing, C.; Huang, B.; Li, Y., Highly Efficient and Selective Generation of Ammonia and Hydrogen on a Graphdiyne-Based Catalyst. *Journal American Chemical Society* **2019,** *141* (27), 10677-10683.

356. Khan Shahed, U. M.; Al-Shahry, M.; Ingler William, B., Efficient Photochemical Water Splitting by a Chemically Modified n-TiO2. *Science* **2002,** *297* (5590), 2243-2245.

357. Kudo, A.; Miseki, Y., Heterogeneous photocatalyst materials for water splitting. *Chemical Society Reviews* **2009,** *38* (1), 253-278.

358. Xu, H.; Ci, S.; Ding, Y.; Wang, G.; Wen, Z., Recent advances in precious metal-free bifunctional catalysts for electrochemical conversion systems. *Journal of Materials Chemistry A* **2019,** *7* (14), 8006-8029.

359. Suen, N.-T.; Hung, S.-F.; Quan, Q.; Zhang, N.; Xu, Y.-J.; Chen, H. M., Electrocatalysis for the oxygen evolution reaction: recent development and future perspectives. *Chemical Society Reviews* **2017,** *46* (2), 337-365.

360. Reier, T.; Oezaslan, M.; Strasser, P., Electrocatalytic Oxygen Evolution Reaction (OER) on Ru, Ir, and Pt Catalysts: A Comparative Study of Nanoparticles and Bulk Materials. *ACS Catalysis* **2012,** *2* (8), 1765-1772.

361. Zou, X.; Zhang, Y., Noble metal-free hydrogen evolution catalysts for water splitting. *Chemical Society Reviews* **2015,** *44* (15), 5148-5180.

362. Wang, J.; Cui, W.; Liu, Q.; Xing, Z.; Asiri, A. M.; Sun, X., Recent Progress in Cobalt-Based Heterogeneous Catalysts for Electrochemical Water Splitting. *Advanced Materials* **2016,** *28* (2), 215-230.

363. Deng, D.; Novoselov, K. S.; Fu, Q.; Zheng, N.; Tian, Z.; Bao, X., Catalysis with two-dimensional materials and their heterostructures. *Nature Nanotechnology* **2016,** *11* (3), 218-230.

364. Wu, X.; Li, S.; Wang, B.; Liu, J.; Yu, M., From biomass chitin to mesoporous nanosheets assembled loofa sponge-like N-doped carbon/g-C3N4 3D network architectures as ultralow-cost bifunctional oxygen catalysts. *Microporous and Mesoporous Materials* **2017,** *240*, 216-226.

365. Wang, G.; Deng, Y.; Yu, J.; Zheng, L.; Du, L.; Song, H.; Liao, S., From Chlorella to Nestlike Framework Constructed with Doped Carbon Nanotubes: A Biomass-Derived, High-Performance, Bifunctional Oxygen Reduction/Evolution Catalyst. *ACS Applied Materials & Interfaces* **2017,** *9* (37), 32168-32178.

366. Sathiskumar, C.; Ramakrishnan, S.; Vinothkannan, M.; Rhan Kim, A.; Karthikeyan, S.; Yoo, D. J., Nitrogen-Doped Porous Carbon Derived from Biomass Used as Trifunctional Electrocatalyst toward Oxygen Reduction, Oxygen Evolution and Hydrogen Evolution Reactions. *Nanomaterials* **2020,** *10* (1).

367. Banza Lubaba Nkulu, C.; Casas, L.; Haufroid, V.; De Putter, T.; Saenen, N. D.; Kayembe-Kitenge, T.; Musa Obadia, P.; Kyanika Wa Mukoma, D.; Lunda Ilunga, J. M.; Nawrot, T. S.; Luboya Numbi, O.; Smolders, E.; Nemery, B., Sustainability of artisanal mining of cobalt in DR Congo. *Nature Sustainability* **2018,** *1* (9), 495-504.

368. Skrabalak, S. E., Ultrasound-assisted synthesis of carbon materials. *Physical Chemistry Chemical Physics* **2009,** *11* (25), 4930-4942.

369. Schwenke, A. M.; Hoeppener, S.; Schubert, U. S., Synthesis and Modification of Carbon Nanomaterials utilizing Microwave Heating. *Adv Mater* **2015,** *27* (28), 4113-41.

370. Hülsey, M. J.; Lim, C. W.; Yan, N., Promoting heterogeneous catalysis beyond catalyst design. *Chemical Science journal* **2020,** *11* (6), 1456-1468.

371. Menéndez, J. A.; Arenillas, A.; Fidalgo, B.; Fernández, Y.; Zubizarreta, L.; Calvo, E. G.; Bermúdez, J. M., Microwave heating processes involving carbon materials. *Fuel Processing Technology* **2010,** *91* (1), 1-8.

372. Zuliani, A.; Balu, A. M.; Luque, R., Efficient and Environmentally Friendly Microwave-Assisted Synthesis of Catalytically Active Magnetic Metallic Ni Nanoparticles. *ACS Sustainable Chemistry & Engineering* **2017,** *5* (12), 11584-11587.

373.   Martina, K.; Calsolaro, F.; Zuliani, A.; Berlier, G.; Chávez-Rivas, F.; Moran, M. J.; Luque, R.; Cravotto, G., Sonochemically-Promoted Preparation of Silica-Anchored Cyclodextrin Derivatives for Efficient Copper Catalysis. *Molecules* **2019,** *24* (13).

374.   Aijaz, A.; Masa, J.; Rösler, C.; Xia, W.; Weide, P.; Botz, A. J.; Fischer, R. A.; Schuhmann, W.; Muhler, M., Co@Co3O4 Encapsulated in Carbon Nanotube-Grafted Nitrogen-Doped Carbon Polyhedra as an Advanced Bifunctional Oxygen Electrode. *Angewante Chemie International Edition Engl* **2016,** *55* (12), 4087-91.

375.   Zhao, J.; Quan, X.; Chen, S.; Liu, Y.; Yu, H., Cobalt Nanoparticles Encapsulated in Porous Carbons Derived from Core-Shell ZIF67@ZIF8 as Efficient Electrocatalysts for Oxygen Evolution Reaction. *ACS Appl Mater Interfaces* **2017,** *9* (34), 28685-28694.

376.   Kumar, A.; Gupta, V.; Gaikwad, K. K., Microfibrillated cellulose from pine cone: extraction, properties, and characterization. *Biomass Conversion and Biorefinery* **2021.**

377.   Argun, M. E.; Dursun, S.; Karatas, M.; Gürü, M., Activation of pine cone using Fenton oxidation for Cd(II) and Pb(II) removal. *Bioresource Technology* **2008,** *99* (18), 8691-8698.

378.   Değirmen, G.; Kılıç, M.; Çepelioğullar, Ö.; Pütün, A. E., Removal of copper(II) and cadmium(II) ions from aqueous solutions by biosorption onto pine cone. *Water Science and Technology* **2012,** *66* (3), 564-572.

379.   Wurster, B.; Grumelli, D.; Hötger, D.; Gutzler, R.; Kern, K., Driving the Oxygen Evolution Reaction by Nonlinear Cooperativity in Bimetallic Coordination Catalysts. *Journal American Chemical Society* **2016,** *138* (11), 3623-6.

380.   Shi, H.-T.; Li, X.-X.; Wu, F.-H.; Yu, W.-B., Electrocatalytic oxygen evolution with a cobalt complex. *Dalton Transactions* **2017,** *46* (46), 16321-16326.

381.   Tahir, M.; Pan, L.; Idrees, F.; Zhang, X.; Wang, L.; Zou, J.-J.; Wang, Z. L., Electrocatalytic oxygen evolution reaction for energy conversion and storage: A comprehensive review. *Nano Energy* **2017,** *37*, 136-157.

382.   Igalavithana, A. D.; Lee, S.-E.; Lee, Y. H.; Tsang, D. C. W.; Rinklebe, J.; Kwon, E. E.; Ok, Y. S., Heavy metal immobilization and microbial community abundance by vegetable waste and pine cone biochar of agricultural soils. *Chemosphere* **2017,** *174*, 593-603.

383.   Lin, Z.; Waller, G.; Liu, Y.; Liu, M.; Wong, C.-P., Facile Synthesis of Nitrogen-Doped Graphene via Pyrolysis of Graphene Oxide and Urea, and its Electrocatalytic Activity toward the Oxygen-Reduction Reaction. *Advanced Energy Materials* **2012,** *2* (7), 884-888.

384.   Antonetti, E.; Iaquaniello, G.; Salladini, A.; Spadaccini, L.; Perathoner, S.; Centi, G., Waste-to-Chemicals for a Circular Economy: The Case of Urea Production (Waste-to-Urea). *ChemSusChem* **2017,** *10* (5), 912-920.

385.   Huang, C.; Li, Y.; Wang, N.; Xue, Y.; Zuo, Z.; Liu, H.; Li, Y., Progress in Research into 2D Graphdiyne-Based Materials. *Chemical Reviews* **2018,** *118* (16), 7744-7803.

386.   Li, L.; Song, L.; Guo, H.; Xia, W.; Jiang, C.; Gao, B.; Wu, C.; Wang, T.; He, J., N-Doped porous carbon nanosheets decorated with graphitized carbon layer encapsulated Co9S8 nanoparticles: an efficient bifunctional electrocatalyst for the OER and ORR. *Nanoscale* **2019,** *11* (3), 901-909.

387.   Sun, M.; Liu, H.; Qu, J.; Li, J., Earth-Rich Transition Metal Phosphide for Energy Conversion and Storage. *Advanced Energy Materials* **2016,** *6* (13), 1600087.

388.   Saif, M. J.; Zia, K. M.; Fazal ur, R.; Usman, M.; Hussain, A. I.; Chatha, S. A., Removal of Heavy Metals by Adsorption onto Activated Carbon Derived from Pine Cones of Pinus roxburgh ii. *Water Environment Research* **2015,** *87* (4), 291-7.

389.   Wang, J.; Kaskel, S., KOH activation of carbon-based materials for energy storage. *Journal of Materials Chemistry* **2012,** *22* (45), 23710-23725.

390.   McDonald, M.; Mila, I.; Scalbert, A., Precipitation of Metal Ions by Plant Polyphenols: Optimal Conditions and Origin of Precipitation. *Journal of Agricultural and Food Chemistry* **1996,** *44*.

391.   Renjith, A.; Lakshminarayanan, V., Single-Step Electrochemical Synthesis of Cobalt Nanoclusters Embedded on Dense Graphite Sheets for Electrocatalysis of the Oxygen Evolution Reaction. *ACS Applied Nano Materials* **2020,** *3* (3), 2705-2712.

392.   Yu, H.; Shang, L.; Bian, T.; Shi, R.; Waterhouse, G. I.; Zhao, Y.; Zhou, C.; Wu, L. Z.; Tung, C. H.; Zhang, T., Nitrogen-Doped Porous Carbon Nanosheets Templated from g-C3 N4 as Metal-Free Electrocatalysts for Efficient Oxygen Reduction Reaction. *Advanced Materials* **2016,** *28* (25), 5080-6.

393.   Travlou, N. A.; Giannakoudakis, D. A.; Algarra, M.; Labella, A. M.; Rodríguez-Castellón, E.; Bandosz, T. J., S- and N-doped carbon quantum dots: Surface chemistry dependent antibacterial activity. *Carbon* **2018,** *135*, 104-111.

394.   Huang, Z.-F.; Song, J.; Du, Y.; Xi, S.; Dou, S.; Nsanzimana, J. M. V.; Wang, C.; Xu, Z. J.; Wang, X., Chemical and structural origin of lattice oxygen oxidation in Co–Zn oxyhydroxide oxygen evolution electrocatalysts. *Nature Energy* **2019,** *4* (4), 329-338.

395.   Sayed, D. M.; El-Nagar, G. A.; Sayed, S. Y.; El-Anadouli, B. E.; El-Deab, M. S., Activation/deactivation behavior of nano-NiOx based anodes towards the OER: Influence of temperature. *Electrochimica Acta* **2018,** *276*, 176-183.

396.   Nurlaela, E.; Shinagawa, T.; Qureshi, M.; Dhawale, D. S.; Takanabe, K., Temperature Dependence of Electrocatalytic and Photocatalytic Oxygen Evolution Reaction Rates Using NiFe Oxide. *ACS Catalysis* **2016,** *6* (3), 1713-1722.

397. Wu, W.; Jiang, C. Z.; Roy, V. A. L., Designed synthesis and surface engineering strategies of magnetic iron oxide nanoparticles for biomedical applications. *Nanoscale* **2016,** *8* (47), 19421-19474.

398. Vangijzegem, T.; Stanicki, D.; Laurent, S., Magnetic iron oxide nanoparticles for drug delivery: applications and characteristics. *Expert Opinion on Drug Delivery* **2019,** *16* (1), 69-78.

399. Xu, Q.; Zhang, T.; Wang, Q.; Jiang, X.; Li, A.; Li, Y.; Huang, T.; Li, F.; Hu, Y.; Ling, D.; Gao, J., Uniformly sized iron oxide nanoparticles for efficient gene delivery to mesenchymal stem cells. *International Journal of Pharmaceutics* **2018,** *552*, 443-452.

400. Sun, C.; Lee, J. S. H.; Zhang, M., Magnetic nanoparticles in MR imaging and drug delivery. *Advanced Drug Delivery Reviews* **2008,** *60* (11), 1252-1265.

401. Ruggiero, M. R.; Crich, S. G.; Sieni, E.; Sgarbossa, P.; Forzan, M.; Cavallari, E.; Stefania, R.; Dughiero, F.; Aime, S., Magnetic hyperthermia efficiency and 1H-NMR relaxation properties of iron oxide/paclitaxel-loaded PLGA nanoparticles. *Nanotechnology* **2016,** *27* (28), 1-27.

402. Shubayev, V. I.; Pisanic, T. R.; Jin, S., Magnetic nanoparticles for theragnostics. *Advanced Drug Delivery Reviews* **2009,** *61* (6), 467-477.

403. Gupta, A. K.; Gupta, M., Synthesis and surface engineering of iron oxide nanoparticles for biomedical applications. *Biomaterials* **2005,** *26* (18), 3995-4021.

404. Nisticò, R.; Cesano, F.; Garello, F., Magnetic Materials and Systems : Domain Structure Visualization and Other Characterization Techniques for the Application in the Materials Science and Biomedicine. *Inorganics* **2020,** *8*, 6-6.

405. Tomoiaga, A. M.; Vasile, A.; Alexandroaei, M.; Sandu, I., Ultrasound-assisted rapid growth of water compatible magnetite nanoparticles. *Journal of Optoelectronics and Advanced Materials* **2014,** *16* (1-2), 221-226.

406. Laurent, S.; Forge, D.; Port, M.; Roch, A.; Robic, C.; Vander Elst, L.; Muller, R. N., Magnetic iron oxide nanoparticles: Synthesis, stabilization, vectorization, physicochemical characterizations, and biological applications (Chemical Reviews (2008) 108 (2064)). *Chemical Reviews* **2010,** *110* (4), 2574-2574.

407. Xu, C.; Sun, S., New forms of superparamagnetic nanoparticles for biomedical applications. *Advanced Drug Delivery Reviews* **2013,** *65* (5), 732-743.

408. Wu, W.; Wu, Z.; Yu, T.; Jiang, C.; Kim, W.-S., Recent progress on magnetic iron oxide nanoparticles: synthesis, surface functional strategies and biomedical applications. *Science and Technology of Advanced Materials* **2015,** *16* (2), 023501.

409. Shaterabadi, Z.; Nabiyouni, G.; Soleymani, M., High impact of in situ dextran coating on biocompatibility, stability and magnetic properties of iron oxide nanoparticles. *Materials Science and Engineering C* **2017,** *75*, 947-956.

410. Mirabello, G.; Lenders, J. J. M.; Sommerdijk, N. A. J. M., Bioinspired synthesis of magnetite nanoparticles. *Chemical Society Reviews* **2016,** *45*, 5085-5106.

411. Wang, Y.; Nkurikiyimfura, I.; Pan, Z., Sonochemical Synthesis of Magnetic Nanoparticles. *Chemical Engineering Communications* **2015,** *202* (5), 616-621.

412. Boustani, K.; Shokri, A.; Shayesteh, S. F.; Jafari, A., Ultrasound-Assisted Synthesis and Tuning the Magnetic and Structural Features of Superparamagnetic Fe3O4 Nanoparticles by Using Ethylenediamine as a Precipitating Agent. *Journal of Superconductivity and Novel Magnetism* **2020**.

413. Poddar, M. K.; Arjmand, M.; Sundararaj, U.; Moholkar, V. S., Ultrasound-assisted synthesis and characterization of magnetite nanoparticles and poly(methyl methacrylate)/magnetite nanocomposites. *Ultrasonics Sonochemistry* **2018,** *43* (December 2017), 38-51.

414. Aliramaji, S.; Zamanian, A.; Sohrabijam, Z., Characterization and Synthesis of Magnetite Nanoparticles by Innovative Sonochemical Method. *Procedia Materials Science* **2015,** *11*, 265-269.

415. Wang, N.; Zhu, L.; Wang, D.; Wang, M.; Lin, Z.; Tang, H., Sono-assisted preparation of highly-efficient peroxidase-like Fe3O4 magnetic nanoparticles for catalytic removal of organic pollutants with H2O2. *Ultrasonics Sonochemistry* **2010,** *17* (3), 526-533.

416. Wang, S.; Li, E.; Li, Y.; Li, J.; Du, Z.; Cheng, F., Enhanced Removal of Dissolved Humic Acid from Water Using Eco-Friendly Phenylalanine-Modified-Chitosan Fe3O4 Magnetic Nanoparticles. *ChemistrySelect* **2020,** *5* (14), 4285-4291.

417. Chen, S.; Xie, F., Selective adsorption of Copper (II) ions in mixed solution by Fe3O4-MnO2-EDTA magnetic nanoparticles. *Applied Surface Science* **2020,** *507*, 145090.

418. Shen, Y. F.; Tang, J.; Nie, Z. H.; Wang, Y. D.; Ren, Y.; Zuo, L., Preparation and application of magnetic Fe3O4 nanoparticles for wastewater purification. *Separation and Purification Technology* **2009,** *68*, 312-319.

419. Yong-mei, H.; Man, C.; Zhong-bo, H., Effective removal of Cu (II) ions from aqueous solution by amino-functionalized magnetic nanoparticles. *Journal of Hazardous Materials* **2010,** *184* (1-3), 392-399.

420. Skorjanc, T.; Benyettou, F.; Olsen, J.-c.; Trabolsi, A., Design of Organic Macrocycle-Modified Iron Oxide Nanoparticles for Drug Delivery. *Chemistry - A European Journal* **2017,** 8333-8347.

421. Hayashi, K.; Ono, K.; Suzuki, H.; Sawada, M.; Moriya, M., High-Frequency, Magnetic-Field-Responsive Drug Release from Magnetic Nanoparticle / Organic Hybrid Based on Hyperthermic Effect. *ACS applied materials and interfaces* **2010,** *2* (7), 1903-1911.

422.   Shahverdi, N.; Heydarinasab, A.; Panahi, A.; Moniri, E., Synthesis and Evaluation of Enalapril-Loaded PVA / PMC Modified Magnetic Nanoparticles as a Novel Efficient Nano-Carrier. *ChemistrySelect* **2019**, 5246-5250.

423.   Wang, L.; Li, L.-l.; Fan, Y.-s.; Wang, H., Host – Guest Supramolecular Nanosystems for Cancer Diagnostics and Therapeutics. *Advanced Materials* **2013**, 3888-3898.

424.   Skorjanc, T.; Benyettou, F.; Olsen, J.-c.; Trabolsi, A., Design of Organic Macrocycle-Modified Iron Oxide Nanoparticles for Drug Delivery. **2017**, 8333-8347.

425.   Sun, X.; Dong, B.; Xu, H.; Xu, S.; Zhang, X.; Lin, Y.; Xu, L.; Bai, X.; Zhang, S.; Song, H., Amphiphilic Silane Modified Multifunctional Nanoparticles for Magnetically Targeted Photodynamic Therapy. *ACS Applied Materials & Interfaces* **2017,** *9* (13), 11451-11460.

426.   Sattarzadeh, E.; Amini, M. M.; Kakaei, S.; Khanchi, A., 68Ga-radiolabeled magnetic nanoparticles for PET–MRI imaging. *Journal of Radioanalytical and Nuclear Chemistry* **2018,** *317* (3), 1333-1339.

427.   Yamaura, M.; Camilo, R. L.; Sampaio, L. C.; Macêdo, M. A.; Nakamura, M.; Toma, H. E., Preparation and characterization of (3-aminopropyl)triethoxysilane-coated magnetite nanoparticles. *Journal of Magnetism and Magnetic Materials* **2004,** *279* (2), 210-217.

428.   Liu, Y.; Li, Y.; Li, X.-M.; He, T., Kinetics of (3-Aminopropyl)triethoxylsilane (APTES) Silanization of Superparamagnetic Iron Oxide Nanoparticles. *Langmuir* **2013,** *29* (49), 15275-15282.

429.   Wang, X.-Y.; Mertz, D.; Blanco-Andujar, C.; Bora, A.; Ménard, M.; Meyer, F.; Giraudeau, C.; Bégin-Colin, S., Optimizing the silanization of thermally-decomposed iron oxide nanoparticles for efficient aqueous phase transfer and MRI applications. *RSC Advances* **2016,** *6* (96), 93784-93793.

430.   Wan, X.; Song, Y.; Song, N.; Li, J.; Yang, L.; Li, Y.; Tan, H., The preliminary study of immune superparamagnetic iron oxide nanoparticles for the detection of lung cancer in magnetic resonance imaging. *Carbohydrate Research* **2016,** *419*, 33-40.

431.   Grootendorst, D. J.; Jose, J.; Fratila, R. M.; Visscher, M.; Velders, A. H.; Ten Haken, B.; Van Leeuwen, T. G.; Steenbergen, W.; Manohar, S.; Ruers, T. J., Evaluation of superparamagnetic iron oxide nanoparticles (Endorem®) as a photoacoustic contrast agent for intra-operative nodal staging. *Contrast Media Mol Imaging* **2013,** *8* (1), 83-91.

432.   Pinkernelle, J.; Teichgraeber, U.; Neumann, F.; Lehmkuhl, L.; Ricke, J.; Scholz, R.; Jordan, A.; Bruhn, H., Imaging of single human carcinoma cells in vitro using a clinical whole-body magnetic resonances scanner at 3.0 T. *Magnetic Resonance in Medicine* **2005,** *53* (5), 1187-1192.

433.   Lunov, O.; Syrovets, T.; Büchele, B.; Jiang, X.; Röcker, C.; Tron, K.; Nienhaus, G. U.; Walther, P.; Mailänder, V.; Landfester, K.; Simmet, T., The effect of carboxydextran-coated superparamagnetic iron oxide nanoparticles on c-Jun N-terminal kinase-mediated apoptosis in human macrophages. *Biomaterials* **2010,** *31* (19), 5063-5071.

434.   Reimer, P.; Balzer, T., Ferucarbotran (Resovist): a new clinically approved RES-specific contrast agent for contrast-enhanced MRI of the liver: properties, clinical development, and applications. *European Radiology* **2003,** *13* (6), 1266-1276.

435.   Sharma, A.; Cornejo, C.; Mihalic, J.; Geyh, A.; Bordelon, D. E.; Korangath, P.; Westphal, F.; Gruettner, C.; Ivkov, R., Physical characterization and in vivo organ distribution of coated iron oxide nanoparticles. *Scientific Reports* **2018,** *8* (1), 4916.

436.   Mandawala, C.; Chebbi, I.; Durand-Dubief, M.; Le Fèvre, R.; Hamdous, Y.; Guyot, F.; Alphandéry, E., Biocompatible and stable magnetosome minerals coated with poly-l-lysine, citric acid, oleic acid, and carboxy-methyl-dextran for application in the magnetic hyperthermia treatment of tumors. *Journal of Materials Chemistry B* **2017,** *5* (36), 7644-7660.

437.   Schweiger, C.; Hartmann, R.; Zhang, F.; Parak, W. J.; Kissel, T. H.; Rivera-Gil, P., Quantification of the internalization patterns of superparamagnetic iron oxide nanoparticles with opposite charge. *Journal of Nanobiotechnology* **2012,** *10* (1), 1-1.

438.   Feng, Q.; Liu, Y.; Huang, J.; Chen, K.; Huang, J.; Xiao, K., Uptake, distribution, clearance, and toxicity of iron oxide nanoparticles with different sizes and coatings. *Scientific Reports* **2018,** *8* (1), 1-13.

439.   Monteiro, A. P. F.; Caminhas, L. D.; Ardisson, J. D.; Paniago, R.; Cortés, M. E.; Sinisterra, R. D., Magnetic nanoparticles coated with cyclodextrins and citrate for irinotecan delivery. *Carbohydrate Polymers* **2017,** *163*, 1-9.

440.   Press, D., Nanoparticles in magnetic resonance imaging : from simple to dual contrast agents. *International Journal of Nanomedicine* **2015**, 1727-1741.

441.   Joos, A.; Löwa, N.; Wiekhorst, F.; Gleich, B.; Haase, A., Size-dependent MR relaxivities of magnetic nanoparticles. *Journal of Magnetism and Magnetic Materials* **2017,** *427* (June 2016), 122-126.

442.   Terreno, E.; Castelli, D. D.; Viale, A.; Aime, S., Challenges for Molecular Magnetic Resonance Imaging. *Chemical Reviews* **2010,** (Ii), 3019-3042.

443.   Kim, B. H.; Lee, N.; Kim, H.; An, K.; Park, Y. I.; Choi, Y.; Shin, K.; Lee, Y.; Kwon, S. G.; Na, H. B.; Park, J.-g.; Ahn, T.-y.; Kim, Y.-w.; Moon, W. K.; Choi, S. H.; Hyeon, T., Large-Scale Synthesis of Uniform and Extremely Small-Sized Iron Oxide Nanoparticles for High-Resolution T 1 Magnetic Resonance Imaging Contrast Agents. *Journal of the American Chemical Society* **2011**, 12624-12631.

444.   Laconte, L. E. W.; Nitin, N.; Zurkiya, O.; Caruntu, D.; Connor, C. J. O.; Hu, X., Coating Thickness of Magnetic Iron Oxide Nanoparticles Affects R 2 Relaxivity. *Journal of Magnetic Resonance Imaging* **2007,** *1641*, 1634-1641.

445.   Cheraghipour, E.; Javadpour, S.; Mehdizadeh, A. R., Citrate capped superparamagnetic iron oxide nanoparticles used for hyperthermia therapy. *Journal of Biomedical Science and Engineering* **2012,** *Vol.05No.12,* 5.

446.   Arefi, M.; Kazemi Miraki, M.; Mostafalu, R.; Satari, M.; Heydari, A., Citric acid stabilized on the surface of magnetic nanoparticles as an efficient and recyclable catalyst for transamidation of carboxamides, phthalimide, urea and thiourea with amines under neat conditions. *Journal of the Iranian Chemical Society* **2019,** *16* (2), 393-400.

447.   Sahoo, Y.; Goodarzi, A.; Swihart, M. T.; Ohulchanskyy, T. Y.; Kaur, N.; Furlani, E. P.; Prasad, P. N., Aqueous Ferrofluid of Magnetite Nanoparticles: Fluorescence Labeling and Magnetophoretic Control. *The Journal of Physical Chemistry B* **2005,** *109* (9), 3879-3885.

448.   Can, H. K.; Kavlak, S.; ParviziKhosroshahi, S.; Güner, A., Preparation, characterization and dynamical mechanical properties of dextran-coated iron oxide nanoparticles (DIONPs). *Artificial Cells, Nanomedicine and Biotechnology* **2018,** *46* (2), 421-431.

449.   Li, Y. S.; Church, J. S.; Woodhead, A. L.; Moussa, F., Preparation and characterization of silica coated iron oxide magnetic nano-particles. *Spectrochimica Acta - Part A: Molecular and Biomolecular Spectroscopy* **2010,** *76* (5), 484-489.

450.   Liu, G.; Hong, R. Y.; Guo, L.; Li, Y. G.; Li, H. Z., Preparation, characterization and MRI application of carboxymethyl dextran coated magnetic nanoparticles. *Applied Surface Science* **2011,** *257* (15), 6711-6717.

451.   Ghosh, S.; Badruddoza, A. Z. M.; Uddin, M. S.; Hidajat, K., Adsorption of chiral aromatic amino acids onto carboxymethyl-β-cyclodextrin bonded Fe3O4/SiO2 core-shell nanoparticles. *Journal of Colloid and Interface Science* **2011,** *354* (2), 483-492.

452.   Răcuciu, M.; Creangă, D. E.; Airinei, A., Citric-acid-coated magnetite nanoparticles for biological applications. *European Physical Journal E* **2006,** *21* (2), 117-121.

453.   Martina, K.; Baricco, F.; Berlier, G.; Caporaso, M.; Cravotto, G., Efficient Green Protocols for Preparation of Highly Functionalized β-Cyclodextrin-Grafted Silica. *ACS Sustainable Chemistry and Engineering* **2014,** *2,* 2595-2603.

454.   Zhang, Y.; Zhang, L.; Song, X.; Gu, X.; Sun, H.; Fu, C.; Meng, F., Synthesis of Superparamagnetic Iron Oxide Nanoparticles Modified with MPEG-PEI via Photochemistry as New MRI Contrast Agent. *Journal of Nanomaterials* **2015,** *2015,* 1-6.

455.   Sharifi Dehsari, H.; Ksenofontov, V.; Möller, A.; Jakob, G.; Asadi, K., Determining Magnetite/Maghemite Composition and Core–Shell Nanostructure from Magnetization Curve for Iron Oxide Nanoparticles. *The Journal of Physical Chemistry C* **2018,** *122* (49), 28292-28301.

456.   Bordonali, L.; Kalaivani, T.; Sabareesh, K. P. V.; Innocenti, C.; Fantechi, E.; Sangregorio, C.; Casula, M. F.; Lartigue, L.; Larionova, J.; Guari, Y.; Corti, M.; Arosio, P.; Lascialfari, A., NMR-D study of the local spin dynamics and magnetic anisotropy in different nearly monodispersed ferrite nanoparticles. *Journal of Physics Condensed Matter* **2013,** *25* (6).

457.   Roch, A.; Muller, R. N.; Gillis, P., Theory of proton relaxation induced by superparamagnetic particles. *Journal of Chemical Physics* **1999,** *110* (11), 5403-5411.

458.   Caspani, S. M., R.; Araújo, J.P.; Sousa, C.T., Magnetic Nanomaterials as Contrast Agents for MRI. *Materials* **2020,** *13,* 2586.

459.   Svenskaya, Y.; Garello, F.; Lengert, E.; Kozlova, A.; Verkhovskii, R.; Bitonto, V.; Ruggiero, M. R.; German, S.; Gorin, D.; Terreno, E., Biodegradable polyelectrolyte/magnetite capsules for MR imaging and magnetic targeting of tumors. *Nanotheranostics* **2021,** *5* (3), 362-377.

460.   Wegner, J.; Ceylan, S.; Kirschning, A., Flow Chemistry – A Key Enabling Technology for (Multistep) Organic Synthesis. *Advanced Synthesis & Catalysis* **2012,** *354* (1), 17-57.

461.   Kirschning, A.; Altwicker, C.; Drager, G.; Harders, J.; Hoffmann, N.; Hoffmann, U.; Schonfeld, H.; Solodenko, W.; Kunz, U., PASSflow syntheses using functionalized monolithic polymer/glass composites in flow-through microreactors. *Angewante Chemie International Edition* **2001,** *40* (21), 3995-3998.

462.   Ruijter, E.; Orru, R. V., Multicomponent reactions - opportunities for the pharmaceutical industry. *Drug Discovery Today Technologies* **2013,** *10* (1), e15-20.

463.   Kalinski, C.; Lemoine, H.; Schmidt, J.; Burdack, C.; Kolb, J.; Umkehrer, M.; Ross, G., Multicomponent reactions as a powerful tool for generic drug synthesis. *Synthesis* **2008,** (24), 4007-4011.

464.   Bossert, F.; Meyer, H.; Wehinger, E., 4-Aryldihydropyridine, a new class of highly active calcium antagonists. *Angewante Chemie* **1981,** *93* (9), 755-63.

465.   Rossen, K.; Pye, P. J.; DiMichele, L. M.; Volante, R. P.; Reider, P. J., An efficient asymmetric hydrogenation approach to the synthesis of the Crixivan piperazine intermediate. *Tetrahedron Letters* **1998,** *39* (38), 6823-6826.

466.   Carofiglio, T.; Cozzi, P. G.; Floriani, C.; Chiesi-Villa, A.; Rizzoli, C., Nonorganometallic pathway of the Passerini reaction assisted by titanium tetrachloride. *Organometallics* **1993,** *12* (7), 2726-36.

467.   Doemling, A.; Khoury, K., Praziquantel and Schistosomiasis. *ChemMedChem* **2010,** *5* (9), 1420-1434.

468.   Mohammad Hakimi Roknabadi, M. H. M., Razieh Mohebat, Efficient synthesis of a novel series of indeno-fused pyrido[2,3-d]pyrimidines using a deep eutectic solvent system comprised of choline chloride/urea. *Journal of chemical research* **2017,** *41,* 430-433.

469.   Jairo Quiroga, D. C., Braulio Insuasty, Rodrigo Abonía, Regioselective Three-component Synthesis of Novel Indeno[1,2-b]-pyrazolo[4,3-e]pyridines-Fused Derivatives of 4-Azafluorenone Alkaloid. *Heterocyclic chemistry* **2008,** *45*, 155.

470.   Manpadi, M.; Uglinskii, P. Y.; Rastogi, S. K.; Cotter, K. M.; Wong, Y. S.; Anderson, L. A.; Ortega, A. J.; Van Slambrouck, S.; Steelant, W. F.; Rogelj, S.; Tongwa, P.; Antipin, M. Y.; Magedov, I. V.; Kornienko, A., Three-component synthesis and anticancer evaluation of polycyclic indenopyridines lead to the discovery of a novel indenoheterocycle with potent apoptosis inducing properties. *Organic & Biomolecular Chemistry* **2007,** *5* (23), 3865-72.

471.   Mabasa, T. F.; Mabasa, J.; Simelane, M.; Vatsha, B.; Makhubela, B. C. E.; Kinfe, H. H., Acetic Anhydride–Acetic Acid as a New Dehydrating Agent of Aldoximes for the Preparation of Nitriles: Preparation of 2-Cyanoglycals. *Synlett* **2020,** *31* (10), 991-996.

472.   Barge, M.; Salunkhe, R., Aqueous extract of Balanites roxburghii fruit: a green dispersant for C– C bond formation. *RSC Advances* **2014,** *4* (59), 31177-31183.

473.   Cui, X.; Lin, J.-J.; Wang, S.; Li, J.-P.; Xia, X.-S.; Huang, C., Electronic effect control of regioselectivity in the Michael-Addition inspired cascade reaction of 1,3-dimethyl-6-amino-uracil and 2-hydroxychalcones. *Tetrahedron Letters* **2022,** *89*, 153603.

474.   Shim, J. L.; Niess, R.; Broom, A. D., Acylation of some 6-aminouracil derivatives. *The Journal of Organic Chemistry* **1972,** *37* (4), 578-581.

475.   Bernier, J. L.; Henichart, J. P.; Warin, V.; Trentesaux, C.; Jardillier, J. C., 5-Cinnamoyl-6-aminouracil derivatives as novel anticancer agents. Synthesis, biological evaluation, and structure-activity relationships. *Journal of Medicinal Chemistry* **1985,** *28* (4), 497-502.

476.   Boess, E.; Van Hoof, M.; Birdsall, S. L.; Klussmann, M., Investigating the Oxidation Step in the CuCl2-Catalyzed Aerobic Oxidative Coupling Reaction of N-Aryl Tetrahydroisoquinolines. *The Journal of Organic Chemistry* **2020,** *85* (4), 1972-1980.

477.   Qadir, S.; Khan, K. Z.; Jan, A., Reaction of Dimethyl Sulfoxide-Acetic Anhydride with 4-Hydroxy-coumarin and Its Derivatives Under Microwave Conditions. *Asian Journal of Chemistry* **2013,** *25* (6), 3019-3022.

478.   Yang, Q.; Sheng, M.; Li, X.; Tucker, C.; Vásquez Céspedes, S.; Webb, N. J.; Whiteker, G. T.; Yu, J., Potential Explosion Hazards Associated with the Autocatalytic Thermal Decomposition of Dimethyl Sulfoxide and Its Mixtures. *Organic Process Research & Development* **2020,** *24* (6), 916-939.

479.   Domling, A.; Khoury, K., Praziquantel and schistosomiasis. *ChemMedChem* **2010,** *5* (9), 1420-34.

480.   Jia, M.; Zhang, H.; Lin, Y.; Chen, D.; Chen, Y.; Xia, Y., Consecutive Lossen rearrangement/transamidation reaction of hydroxamic acids under catalyst- and additive-free conditions. *Organic & Biomolecular Chemistry* **2018,** *16* (19), 3615-3624.

481.   Patil, P.; Ahmadian-Moghaddam, M.; Dömling, A., Isocyanide 2.0. *Green Chemistry* **2020,** *22* (20), 6902-6911.

482.   Cao, H.; Liu, H.; Domling, A., Efficient multicomponent reaction synthesis of the schistosomiasis drug praziquantel. *Chemistry* **2010,** *16* (41), 12296-8.

483.   Yin, H.; Xu, Y.; Qian, X., Novel antitumor agent family of 1H-benzo[c,d]indol-2-one with flexible basic side chains: synthesis and biological evaluation. *Bioorganic & Medicinal Chemistry* **2007,** *15* (3), 1356-62.

484.   Zhou, B.; Ji, M.; Cai, J., Design, synthesis and biological evaluation of bitopic arylpiperazine-hexahydro-pyrazinoquinolines as preferential dopamine D3 receptor ligands. *Bioorganic Chemistry* **2018,** *77*, 125-135.

485.   Jun O. Liu, C. R. C., Jing Xu, Jun Lu, Shridhar Bhat Chirally pure isomers of Itraconazole and inhibitors of Lanosterol 14A-demethylase for use as angiogenesis inhibitors. 2011.

486.   Moran, M. J.; Martina, K.; Baricco, F.; Tagliapietra, S.; Manzoli, M.; Cravotto, G., Tuneable Copper Catalysed Transfer Hydrogenation of Nitrobenzenes to Aniline or Azo Derivatives. *Advanced Synthesis & Catalysis* **2020,** *362* (13), 2689-2700.

487.   Moran, M. J.; Martina, K.; Stefanidis, G. D.; Jordens, J.; Gerven, T. V.; Goovaerts, V.; Manzoli, M.; Groffils, C.; Cravotto, G., Glycerol: An Optimal Hydrogen Source for Microwave-Promoted Cu-Catalyzed Transfer Hydrogenation of Nitrobenzene to Aniline. *Frontiers in Chemistry* **2020,** *8*, 34.

488.   Pace, J. R.; DeBerardinis, A. M.; Sail, V.; Tacheva-Grigorova, S. K.; Chan, K. A.; Tran, R.; Raccuia, D. S.; Wechsler-Reya, R. J.; Hadden, M. K., Repurposing the Clinically Efficacious Antifungal Agent Itraconazole as an Anticancer Chemotherapeutic. *Journal of Medicinal Chemistry* **2016,** *59* (8), 3635-49.

489.   Kumari, S.; Mishra, C. B.; Tiwari, M., Design, synthesis and pharmacological evaluation of N-[4-(4-(alkyl/aryl/heteroaryl)-piperazin-1-yl)-phenyl]-carbamic acid ethyl ester derivatives as novel anticonvulsant agents. *Bioorganic & Medicinal Chemistry Letters* **2015,** *25* (5), 1092-9.

490.   Trotta, F.; Martina, K.; Robaldo, B.; Barge, A.; Cravotto, G., Recent advances in the synthesis of cyclodextrin derivatives under microwaves and power ultrasound. *Journal of Inclusion Phenomena and Macrocyclic Chemistry* **2007,** *57* (1-4), 3-7.

491.   Dent, A. J.; Cibin, G.; Ramos, S.; Smith, A. D.; Scott, S. M.; Varandas, L.; Pearson, M. R.; Krumpa, N. A.; Jones, C. P.; Robbins, P. E., B18: A core XAS spectroscopy beamline for Diamond. In *14th*

International Conference on X-Ray Absorption Fine Structure, DiCicco, A.; Filipponi, A., Eds. 2009; Vol. 190.

492.   Ravel, B.; Newville, M., Athena, artemis, hephaestus: data analysis for X-ray absorption spectroscopy using IFEFFIT. *Journal of Synchrotron Radiation* **2005,** *12*, 537-541.

493.   Khalafi-Nezhad, A.; Panahi, F., Immobilized palladium nanoparticles on a silica-starch substrate (PNP-SSS): as an efficient heterogeneous catalyst for Heck and copper-free Sonogashira reactions in water. *Green Chem.* **2011,** *13* (9), 2408-2415.

494.   Trotta, F.; Martina, K.; Robaldo, B.; Barge, A.; Cravotto, G., Recent advances in the synthesis of cyclodextrin derivatives under microwaves and power ultrasound. *Journal of Inclusion Phenomena and Macrocyclic Chemistry* **2007,** *57* (1), 3-7.

495.   Gening, M. L.; Tsvetkov, Y. E.; Pier, G. B.; Nifantiev, N. E., The study of the reaction of terminated oligomerization in the synthesis of oligo-(β1-6)-glucosamines. *Russian Journal of Bioorganic Chemistry* **2006,** *32* (4), 389-399.

496.   Nakamura, J.; Yamashiro, H.; Hayashi, S.; Yamamoto, M.; Miura, K.; Xu, S.; Doi, T.; Maki, H.; Yoshida, O.; Arimoto, H., Elucidation of the Active Conformation of Vancomycin Dimers with Antibacterial Activity against Vancomycin-Resistant Bacteria. *Chemistry – A European Journal* **2012,** *18* (40), 12681-12689.

497.   Park, H.; Kwon, Y.; Shin, J. E.; Kim, W.-J.; Hwang, S.; Lee, S.; Kim, S., Orthoester in Cyclodehydration of Carbamate-Protected Amino Alcohols under Acidic Conditions. *Synthesis* **2017,** *49* (12), 2761-2767.

498.   Ghosh, A. K.; Rodriguez, S., An enantioselective synthesis of the C3–C21 segment of the macrolide immunosuppressive agent FR252921. *Tetrahedron Letters* **2016,** *57* (26), 2884-2887.

499.   Liu, K.-C.; Shelton, B. R.; Howe, R. K., A particularly convenient preparation of benzohydroximinoyl chlorides (nitrile oxide precursors). *The Journal of Organic Chemistry* **1980,** *45* (19), 3916-3918.

500.   Queiroz Jr, L. H. K.; Giraudeau, P.; dos Santos, F. A. B.; de Oliveira, K. T.; Ferreira, A. G., Real-time mechanistic monitoring of an acetal hydrolysis using ultrafast 2D NMR. *Magnetic Resonance in Chemistry* **2012,** *50* (7), 496-501.

501.   Walton, R.; Lahti, P. M., An Efficient, Simple Synthesis of 4-Azidobenzaldehyde. *Synthetic Communications* **1998,** *28* (6), 1087-1092.

502.   Monajati, M.; Borandeh, S.; Hesami, A.; Mansouri, D.; Tamaddon, A. M., Immobilization of l-asparaginase on aspartic acid functionalized graphene oxide nanosheet: Enzyme kinetics and stability studies. *Chemical Engineering Journal* **2018,** *354*, 1153-1163.

503.   Stankovich, S.; Dikin, D. A.; Piner, R. D.; Kohlhaas, K. A.; Kleinhammes, A.; Jia, Y.; Wu, Y.; Nguyen, S. T.; Ruoff, R. S., Synthesis of graphene-based nanosheets via chemical reduction of exfoliated graphite oxide. *Carbon* **2007,** *45* (7), 1558-1565.

504.   Park, S.; An, J.; Potts, J. R.; Velamakanni, A.; Murali, S.; Ruoff, R. S., Hydrazine-reduction of graphite- and graphene oxide. *Carbon* **2011,** *49* (9), 3019-3023.

505.   Tsele, T. P.; Adekunle, A. S.; Fayemi, O. E.; Ebenso, E. E., Electrochemical detection of Epinephrine using Polyaniline nanocomposite films doped with TiO2 and RuO2 Nanoparticles on Multi-walled Carbon Nanotube. *Electrochimica Acta* **2017,** *243*, 331-348.